Vol. 10 No. 2
October 2026

ISSN 2579-5821
e-ISSN 2579-5546

S2 sinta
Science and Technology Index

Jurnal Geocelebes

Published by:
Geophysics Department
Hasanuddin University
Makassar, Indonesia

JURNAL GEOCELEBES
Geophysics Department | Faculty of Mathematics and Natural Sciences | Hasanuddin University

Volume 10 Number 2, October 2026

P-ISSN: 2579-5821
E-ISSN: 2579-5546

Published by:
Geophysics Department, Math and Natural Science Faculty
Hasanuddin University

JURNAL GEOCELEBES

Volume 10 Number 1, October 2026

ISSN: 2579 – 5821 (Print)
ISSN: 2579 – 5546 (Online)
URL address: http://journal.unhas.ac.id/index.php/geocelebes

Diterbitkan berkala dua kali setahun oleh/ **Published periodically two times annually by**
Dept. Geofisika Universitas Hasanuddin/ **Geophysics Dept., Hasanuddin University**

Dewan Redaksi/ Editor Board

Editor Kepala (Chief Editor) : Muh. Altin Massinai / Universitas Hasanuddin

Redaksi yang bertugas pada Volume 10/ The editorial team assigned to Volume 10

Dewan Editor / Editorial Board:

- Muhammad Altin Massinai / Geophysics Department, Hasanuddin University, Indonesia.
- Javid Hussain / Institute of Rock and Soil Mechanics, Wuhan, Hubei, China.
- Saaduddin / Geophysics Department, Hasanuddin University, Indonesia – School of Earth and Environment, University of Leeds, UK.
- Bilal Wadood / Department of Geology, University of Swabi, Pakistan
- Ayusari Wahyuni / Physics Dept. Alauddin State Islamic University, Makassar, Indonesia – National Taipei University of Technology, Civil Engineering, Taipei, Taiwan.
- Muhammad Fawzy Ismullah M. / Geophysics Department, Hasanuddin University, Indonesia.
- Sakka / Geophysics Department, Hasanuddin University, Makassar, Indonesia.

Mitra Bestari/ Reviewer

- Mostafa Mohamed Sayed / Department of Geology, Faculty of Earth Sciences, Geography and Astronomy, University of Vienna, 1090 Vienna, Austria; Department of Palaeontology, Faculty of Earth Sciences, Geography and Astronomy, University of Vienna, 1090 Vienna, Austria; Geology Department, Faculty of Science, Beni-Suef University, Beni-Suef 62511, Egypt.
- Arifin / Department of Geography, University College London, UK
- Yohannes Yihdego / Adjunct Research Fellow, Department of Environment and Genetics, School of Agriculture, Biomedicine and Environment, La Trobe University, Australia
- Mohamad Ramdhan / Pusat Riset Kebencanaan Geologi, Badan Riset dan Inovasi Nasional (BRIN), Indonesia.
- Masoud Sharifi-Yazdi / Department of Geology, University of Vienna, Vienna, Austria.
- Alexandr Yablokov / Trofimuk Institute of Petroleum Geology and Geophysics, Siberian Branch, Russian Academy of Sciences, Novosibirsk, Russia; Novosibirsk State University, Novosibirsk, Russia; Schmidt Institute of Physics of the Earth, Russian Academy of Sciences, Moscow, Russia
- Nurul Ashikin Mabahwi / School of Housing, Building and Planning, Universiti Sains Malaysia, Malaysia
- Nanang Sugianto / Geophysics Department, Faculty of Mathematics and Natural Science, Universitas Bengkulu, Indonesia.
- Annisa Aulia Lukman / Departemen Oseanografi, Fakultas Perikanan dan Ilmu Kelautan, Universitas Diponegoro, Indonesia.

- Purwaditya Nugraha/ Program Studi Teknik Geofisika, Jurusan Teknologi Produksi dan Industri, Institut Teknologi Sumatera, Indonesia.
- Syamsul Bahri Agus / Department of Marine Science and Technology, Faculty of Fisheries and Marine Science, IPB University, Indonesia.
- Andika / Geophysics Department, Hasanuddin University, Indonesia.
- Erlangga Ibrahim Fattah / Program Studi Teknik Geofisika, Jurusan Teknologi Produksi dan Industri, Institut Teknologi Sumatera, Indonesia.
- Jamaluddin / Departemen Teknik Geologi, STT-Migas Balikpapan, Indonesia.
- Muhammad Ulin Nuha / Institut Teknologi Sumatera, Lampung, Indonesia.
- Siti Umiyatun Choiriah / Department of Geological Engineering, Universitas Pembangunan Nasional "Veteran" Yogyakarta, Indonesia
- Hita Pandita / Department of Geology, Institut Teknologi Nasional Yogyakarta, Indonesia
- Meutia Farida / Department of Geological Engineering, Hasanuddin University, Indonesia
- Arin Wildani / Universitas Islam Madura, Indonesia.
- Rohima Wahyu Ningrum / Program Studi Pendidikan Fisika, Universitas Khairun, Ternate, Indonesia
- Wien Lestari / Departemen Teknik Geofisika; Fakultas Teknik Sipil, Perencanaan, dan Kebumian; Institut Teknologi Sepuluh Nopember, Surabaya, IndonesiaSadewa Purba Sejati / Program Studi Geografi, Fakultas Sains dan Teknologi, Universitas AMIKOM Yogyakarta, Indonesia.
- Amir Yarkhasy Yuliardi / Program Studi Ilmu Kelautan, Fakultas Perikanan dan Ilmu Kelautan, Universitas Jenderal Soedirman, Indonesia.
- Wildan Tri Koesmawardani / Teknik Geologi Universitas Trisakti, Indonesia.
- Wahidah / Geofisika, Universitas Mulawarman, Indonesia
- Nabila Afifah Azuga / Jurusan Ilmu Kelautan, Fakultas Perikanan dan Kelautan, Universitas Riau, Indonesia.
- Masita Dwi Mandini Manessa / Department of Geography, Faculty of Mathematics and Natural Sciences, Universitas Indonesia, Indonesia.
- Muhammad Taufiq Rafie / Geophysics Department, Hasanuddin University, Indonesia.
- Muhammad Dikman Maheng / Jurusan Teknik Lingkungan, Universitas Muhammadiyah Kendari, Indonesia.
- Andi Ihwan / Jurusan Fisika FMIPA, Universitas Tanjungpura, Indonesia.
- Agus Setyawan / Departemen Fisika, Universitas Diponegoro, Semarang, Indonesia
- Gatot Yuliyanto / Departemen Fisika, Universitas Diponegoro, Semarang, Indonesia.
- Andri Kurniawan / Teknik Geofisika, Universitas Lampung, Indonesia.
- Dian Kusumawati / Postdoctoral Research Fellow, Research Center for Geological Disaster, Indonesian National Research, and Innovation Agency (BRIN), Indonesia
- Muhammad Abdus Salam Jawwad / Department of Environmental Engineering, Faculty of Engineering, University of Pembangunan Nasional Veteran Jawa Timur, Indonesia
- Yudha Gusti Wibowo / Department of Mining Engineering, Faculty of Technology Industry, Institut Teknologi Sumatera, Lampung, 35365, Indonesia
- Ajimas Pascaning Setiahadiwibowo / Teknik Geofisika UPN Veteran Yogyakarta, Indonesia.
- Rifa Salma Salsabila / Teknik Geofisika, Universitas Syiah Kuala, Indonesia
- Aswar Syafnur / Departemen Geofisika, Universitas Hasanuddin, Makassar, Indonesia.
- Hidayat / Pusat Riset Limnologi dan Sumber Daya Air, Organisasi Riset Kebumian dan Maritim, BRIN, Indonesia.
- Ashari Wicaksono / Ilmu Kelautan Universitas Trunojoyo Madura, Indonesia
- Ridwan Rahmanto / Teknik Geologi, Universitas Pertamina, Indonesia
- Riza Adriat / Jurusan Fisika Fakultas MIPA Universitas Tanjungpura, Indonesia.
- Arif Wijaya / Teknik Pertambangan, Universitas Muhammadiyah Mataram, NTB, Indonesia

- Nurul Dzakiya / Institut Sains dan Teknologi AKPRIND Yogyakarta, Indonesia; National Taipei University of Technology, Taipei city, Taiwan
- Mashuri / Teknik Sipil, Institut Teknologi Sumatera, Indonesia.
- Afrinia Lisditya Permatasari / Program Studi Geografi, Fakultas Sains dan Teknologi, Universitas AMIKOM Yogyakarta, Indonesia.
- Muhammad Hakiem Sedo Putra / Program Studi Rekayasa Tata Kelola Air Terpadu, Institut Teknologi Sumatera, Indonesia

Sekretariat/ Secretariat:
Departemen Geofisika, FMIPA Universitas Hasanuddin
Gedung MIPA, Kampus Unhas Tamalanrea - Jalan Perintis Kemerdekaan, Makassar, Sulawesi Selatan, 90245.
E-mail: geocelebes@sci.unhas.ac.id

Jurnal Geocelebes is a scientific journal published by the Department of Geophysics, Hasanuddin University. This journal is intended as a means of scientific publication in the field of geophysics ranging from theoretical topics to geophysical applications in various fields topics. The articles are original research results, reviews of recent advances in a particular topic, case studies of geophysical applications or reviews of software related to geophysics. Papers should be sent to the editorial website in softcopy using the template provided. Each accepted paper will be reviewed for eligibility through a rigorous reviewing process by the Editorial Board.

Contents

JURNAL GEOCELEBES

Volume 10, Number 1, April 2026

ISSN: 2579 – 5821 (Print)
ISSN: 2579 – 5546 (Online)

URL: http://journal.unhas.ac.id/index.php/geocelebes

Cover ---------- i
Editorial boards ---------- iii
Contents ---------- vi
Preface ---------- ix

Distribution of Vs30 by Microzonation Using Microtremor Method in the Expansion Area of Pondok Kelapa Sub-district, Central Bengkulu, Bengkulu ---------- 133
Olga Triutami, Refrizon, M. Farid, Andre Rahmat Al Ansory

Receiver-Fault Variability and Depth-Dependent Coulomb Stress Changes in the 2019 Mw 7.2 Halmahera Earthquake Sequence --------- 145
Rizki Wulandari, Cahli Suhendi, Yudha Styawan

Metal Corrosion Indicators for Sulfur Exposure Assessment in Urban and Volcanic Areas of East Java ---------- 160
Yuansyah Dhaniar Ramadhan, Muhammad Tegar Rahmawan, Ayunita Haq, Nayla Rohmatul Maulidiyah, Daryll Alfaraby Noorlaksono, Arie Realita, Madlazim, Muhammad Nurul Fahmi, Adedio Daniel Situmeang, Zunan Faruq Ardiansyah

Integration of Ground Penetrating Radar (GPR) and Well Logging Data for Mapping Coal Seams in Pit "NS", South Palembang Sub-Basin ---------- 177
Neta Gresiana Santi Siregar, Andri Yadi Paembonan, Putu Pradnya Andika, Muhammad Alamshah

Aquifer Characterization through Vertical Electrical Sounding (VES), Well Logging, Petrographic Analysis, and Pumping Tests in the Monitoring Well Area, Lampung ---------- 192
Cherly Rizka Susanti, Astrik Yati, Rizka

GIS-Based Flood Susceptibility Mapping Using Weighted Overlay Method in Barabai Sub-District, South Kalimantan, Indonesia ---------- 217
Sandri Erfani, Nailatussa'adah, Rosna Amaliaatul Ma'rifah, M. Rayya Andisa Putra, Eka Andika, Andri Kurniawan

Spatial Model of Forest Cover Change using Moisture Index in Kolaka Regency ---------- 241
Septianto Aldiansyah, Amniar Ati, Fitriyani Saudi

Calcareous Nannofossils from Bojongsana River, Purbalingga Regency: Implication for Identifying the Age of Tapak Formation ---- 258
Akmaluddin, Efrilia Mahdilah Nurhidayah

Tidal Wave Transformation in the Mahakam Delta: Integrating Observations and Machine Learning ---------- 269
Muhammad Riza, Nanda Khoirunisa, Zetsaona Sihotang, Idris Mandang

Analysis Distribution and Deformation Changes of Mount Dukono in 2024 using the SBAS – InSAR Method ---------- 287
Nova Triyani Siagian, Erlangga Ibrahim Fattah

Physically Consistent Peak Ground Acceleration Prediction in Bali Using Ensemble Machine Learning ---------- 306
Rayhan Irfan Hielmy, Muzli

Characteristics of Land-Sea Breeze Circulations along the West Coast of West Sumatra Using Observations and WRF-ARW Simulations ---------- 322
Reinal Taruna Wahyu Halawa, Latifah Nurul Qomariyatuzzamzami, Yosafat Donni Haryanto, Avrionesti

Multi-Attribute Analysis and Probabilistic Neural Network (PNN) Method for Predicting Carbonate Volume and Water Saturation in Biogenic Gas Reservoir: A Case Study of the Nias Basin, North Sumatra ---------- 343
Chikita Mery Yuliani, Renita Dwi Vadila, Mokhammad Puput Erlangga, Harnanti Yogaputri Hutami, Egie Wijaksono

Multi-Sensor Remote Sensing and GIS for Potential CO_2 Leakage Mapping in Gundih CCUS Field ---------- 359
Tirta Khayru Putra, Ridwan Rahmanto, Syahrbanu

ENSO and IOD Teleconnection with Sumbawa Rainfall: Seasonal Predictability Beyond Monthly Lag Structure ---------- 371
Romi Aprianto, Akbar Tawaqqal, Syaharuddin

Estimation of Meteorological Drought in West Kalimantan Using the Random Forest Model ---------- 397
Nurputri, Muhammad Ishak Jumarang, Andi Ihwan

Intraseasonal Ocean Surface Variability Response to the Madden-Julian Oscillation: A Comparative Study of the Malacca Strait and the Indian Ocean ---------- 413
Nabila Afifah Azuga, Ahmad Dhuha Habibullah, Bintal Amin, Rianti Putri, Mubarak, Ilham Ilahi, Rifardi

Comparison of Window Scan and Digital Outcrop Model Approaches for Fracture Characterisation Along the Lampung–Panjang Fault Zone ---------- 432
Rezki Naufan Hendrawan, David Kurniawan, Muhammad Eval Juni Wijaya, Luhut Pardamean Siringoringo

Projected Changes in Rainy Season Onset, Retreat, and Duration over the Brantas Watershed Using Downscaled CMIP6 Climate Models ---------- 443
Gilang Aulia Herlambang, Lalu Muhamad Jaelani

Preface

Jurnal Geocelebes managed by the Department of Geophysics, Faculty of Mathematics and Natural Sciences, Hasanuddin University Makassar has entered its tenth year. The Editorial Board expresses gratitude to God Almighty for this achievement and expresses gratitude for the commitment of the Editorial Board, in carrying out this mandate. In particular, the Editorial Board expresses its gratitude and highest appreciation to all authors who have submitted their scientific works and to the Reviewers who have been willing to take the time to provide constructive suggestions and corrections to each article in each issue of the Jurnal Geocelebes.

In the edition of Volume 10 Number 2 October 2026 there are nineteen articles. The articles published generally discuss the implementation of the role of geosciences, especially geophysics in natural resource exploration and other fields that are in accordance with the focus and scope of the field published by the Jurnal Geocelebes. The language used in this volume is English, which shows that Jurnal Geocelebes deserves to be an international journal in the future. With deep gratitude, we announce that based on the assessment conducted by Arjuna DIKTI, Jurnal Geocelebes has successfully obtained SINTA 2 accreditation rating based on the Keputusan Direktur Jenderal Riset dan Pengembangan Kementerian Pendidikan Tinggi, Sains dan Teknologi number 295/C/C3/KPT/2026 dated 2 January 2026. The official accreditation certificate can be downloaded on main page of Jurnal Geocelebes website. Jurnal Geocelebes welcomes participation from academics, researchers, industry practitioners, students, and others in the field of geosciences in both theoretical and application perspectives, which of course will go through a series of processes which are submitting, reviewing, editing, and publishing.

The Editorial Board of Jurnal Geocelebes is open to suggestions and constructive criticism for future improvements. All suggestions and criticisms can be sent via email geocelebes@sci.unhas.ac.id

Makassar, October 2026

The Editorial Board of Jurnal Geocelebes

ISSN: 2579 - 5821 (Print)
ISSN: 2579 - 5546 (Online)
URL address: http://journal.unhas.ac.id/index.php/geocelebes
DOI: 10.70561/geocelebes.v10i2.34686

Jurnal Geocelebes Vol. 10 No. 2, October 2026, 133 – 144

Distribution of Vs30 in Pondok Kelapa Sub-District, Central Bengkulu, Bengkulu Based on Microtremor Data

Olga Triutami[1], Refrizon[2]*, M. Farid[3]*, Andre Rahmat Al Ansory[3]

[1]Geophysics Study Program, University of Bengkulu, Jl. WR Supratman, Bengkulu, 38371, Indonesia.
[2]Centre for Disaster Mitigation Studies, University of Bengkulu, Jl. WR Supratman, Bengkulu, 38371, Indonesia.
[3]Mitigation and Exploration Laboratory, Floor 2, Integrated Laboratory, University of Bengkulu, Jl. WR Supratman, Bengkulu, 38371, Indonesia.

*Corresponding author. Email: refrizon@unib.ac.id, mfarid@unib.ac.id

Manuscript received: 30 April 2024; Received in revised form: 22 July 2024; Accepted: 14 August 2024

Abstract

Pondok Kelapa is among the sub-districts in Central Bengkulu Regency adjacent to major Sumatran faults, which are the Manna Fault and the Musi Fault, making it vulnerable to earthquakes. Therefore, regional planning and infrastructure development are needed to reduce the impact of earthquakes. This study aims to look at the state of the subsurface layers, the seismic vulnerability index, and the distribution of the average shear wave velocity value at a depth of 30 m (Vs30) and see the soil site class based on the Vs30 value. Field data acquisition used the HVSR methodology, while data analysis used microtremor data. Microtremor data was processed employing Geopsy software to gain H/V curves, which were then inversed using H/Inv software. The results are presented as shear wave velocity value distribution maps. The results showed the A0 (amplification factor value) ranged from 0.73 – 7.41, the dominant frequency (f_0) between 0.74 – 16.84 Hz, and the seismic susceptibility index value (Kg) ranged from 0.11 – 37.12 with the highest seismic susceptibility index value located in the East area of the research location. At the same time, the Vs30 value of the HVSR curve inversion results obtained ranged from 157 – 516 m/s. Site Class in the study area has SC, SD, and SE types, which are dominated by the SD type site class.

Keywords: Bengkulu; HVSR inversion; microtremor; Pondok Kelapa; Vs30.

Citation: Triutami, O., Refrizon, R., Farid, M., & Al Ansory, A. R. (2026). Distribution of Vs30 in Pondok Kelapa Sub-District, Central Bengkulu, Bengkulu Based on Microtremor Data. *Jurnal Geocelebes*, 10(2): 133–144, doi: 10.70561/geocelebes.v10i2.34686

Introduction

Pondok Kelapa is a sub-district in Central Bengkulu Regency, Bengkulu Province, with rock formations in alluvium and lake deposits (Gafoer et al., 1992). Rock formations with the lowest seismic wave velocity and bulk density values due to a lack of rock compactness are those that may make more vulnerable to earthquake disasters (Hadi et al., 2021).

Bengkulu Central is located near the Manna Fault and the Musi Fault on the Great Sumatra Fault. The city is also located on the outskirts of Sumatra Island, with direct access to the Indian Ocean (Natawidjaja, 2018; Al Ansory et al., 2023). The impact of one of the active segments on the Sumatra Fault, especially the Musi segment along the Bukit Barisan, makes Central Bengkulu highly vulnerable to earthquake disasters that trigger building collapses (Hamzah et al., 2020). Infrastructure development should be adapted to local geological conditions to reduce the risk of earthquake casualties and building damage (Nakamura et al., 2000).

© 2026 Dept. of Geophysics Hasanuddin University

One of the first stages of earthquake mitigation efforts to estimate the seismic hazard that could arise is local area micro zonation, which assesses the regional seismic risk. One of the factors used when creating microzoning maps is assessing the potential earthquake hazard (Bignardi et al., 2016). Analysis of ground shaking strength generated from bedrock shaking and amplification of ground motion variables are part of determining the possible earthquake hazard. The estimated value of the ground motion amplification potential involves the identification of local site characteristics, utilizing the average shear wave velocity value as low as 30 m s to classify local sites (Thamarux et al., 2019; Ghanbari et al., 2018).

The average shear wave velocity at a depth of thirty meters (Vs30) and the investigation of the impact of local soil properties on earthquake shaking are crucial components of ground motion prediction (Sunardi et al., 2018). Shows site characteristics, such as soil classification and site amplification, which are essential for building codes and seismic design using borehole geophysical methods (Kim & Hong, 2022). However, these methods are costly and time-consuming. Therefore, microtremor observation using the horizontal-to-vertical spectrum (HVSR) method can present the local dynamic characteristics without drilling (Nakamura, 1989).

Research that distributes Vs30 has been conducted by Mase et al. (2021). It is using microtremor data and inversion techniques to obtain secondary wave velocity (Vs) values. According to the study results, following the guidelines set by the NEHRP (National Earthquake Hazard Reduction Program) standard, the city of Bengkulu is conquered by site classes SC (Hard, Very Hard, Compacted Soil and Soft Rock) and SD (Medium Soil). Nabhan et al. (2023) used HVSR inversion on the alternative Central Bengkulu – Kepahiang road to determine soil type as a preventive measure for earthquake hazards, showing that the Vs30 value was generally high. Vs30 values remain in the SC to SB (Rock) site classes. Furthermore, Farid et al. (2024) employed the HVSR method to investigate the rate of shoreline change resulting from coastal abrasion in Central Bengkulu Regency. The study generated Vs30 values within the SC site class heading, ranging from 227 – 1235 m/s.

However, the Vs30 value generated in the previous study cannot describe the overall subsurface layer conditions in the Central Bengkulu area, especially the Pondok Kelapa sub-district, because the research station points are less spread in the research area. As a result, the author intends to examine the subsurface layers to determine the soil site class based on the Vs30, the distribution of the layers' shear wave velocity values, and the seismic vulnerability index.

This research is expected to be helpful for the advancement of science related to Vs30. Furthermore, Central Bengkulu Regency's regional development can be built upon the spatial distribution of Vs30, particularly in the Pondok Kelapa Sub-district area, where earthquake risk reduction is imperative due to its designation as a regional development area. This may also be taken into account while designing infrastructure that is earthquake-resistant in the beginning.

Pondok Kelapa sub-district is in Central Bengkulu Regency, Bengkulu Province, Indonesia. Based on the geological map (Gafoer et al., 1992), the research point is located in a geological area consisting of various rock formations, depending on the location and geological conditions Figure 1. The geological map shows the area's different rock formations and geological structures, such as the Alluvium formation (Qa) consisting of medium–sized sedimentary rocks, such as pebbles, gravel, sand, silt, mud, and clay. Alluvium

© 2026 Dept. of Geophysics Hasanuddin University

Terraces (Qat2) consist of large sedimentary rocks, such as sand, silt, clay, and gravel. Bintunan (Qtb) consists of fine-sized sedimentary rocks such as conglomerate, tuffaceous claystone, and reef limestone. Swamp Deposits (Qs) consist of large sedimentary stones such as mud, silt, sand, clay, and plant remains. Qa, Qtb, Qs, and Qat rock formations have different hardness levels, which affect their ability to resist earthquake-induced ground movement. Rock formations with lower hardness levels, such as Qa and Qtb, are more susceptible to ground movement, while rock formations with higher hardness levels, such as Qs and Qat, are more resistant to ground movement (Sugianto et al., 2017).

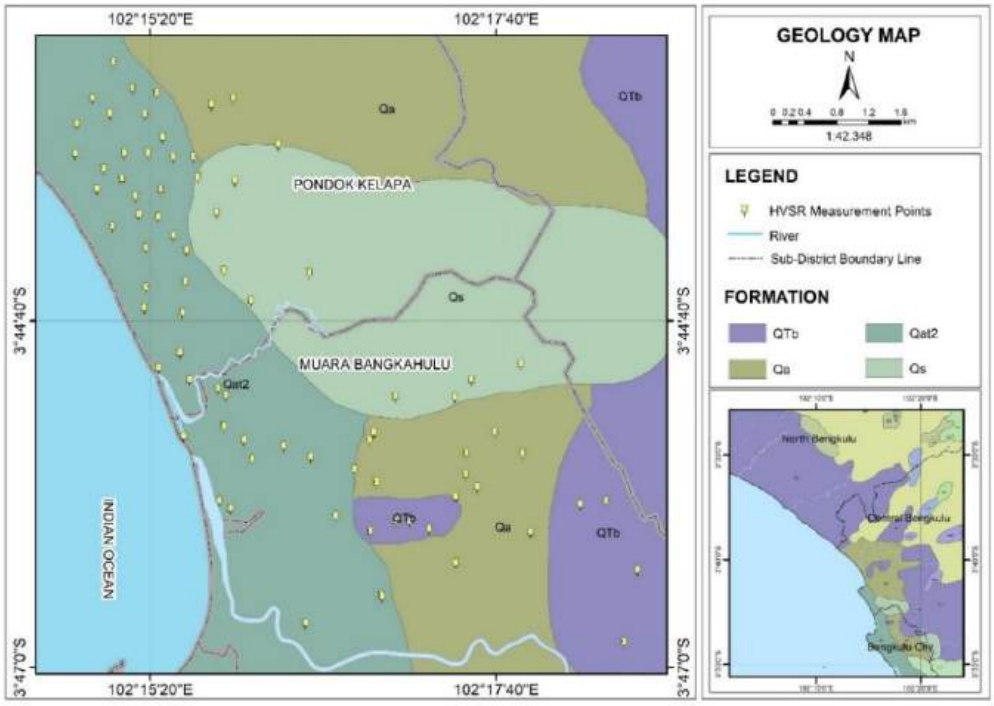


Figure 1. Geological of study area and HVSR measurement point.

Materials and Methods

This research took 78 location points with the microtremor method to estimate the seismic susceptibility value and determine the subsurface layer based on the Vs. Value and the dispersal of Vs30 values in the Bengkulu City expansion area in Pondok Kelapa District, Central Bengkulu. The locations spread towards Muara Bangkahulu Sub-district, Bengkulu City. The recording duration is 960 seconds at each location, while the interval between measurement stations is 200 – 400 m apart. The equipment used is a Portable Short Period Seismometer Gemini 2 Sn-1405 model, laptop, GPS, geological compass, camera, and software such as Geopsy, HV-Inv Beta, and ArcGIS. Figure 2 reveals a distribution map of the measurement points.

Geopsy software processes the microtremor data recording findings obtained directly from the field (Wathelet et al., 2020). by inputting the signal. Then, the windowing process is carried out to separate microtremor data and transient data. The microtremor data that has been separated is then carried out in the calculation stage of the ratio between the three components (Vertical, North-South, and East-West) to produce the HVSR spectrum (SESAME, 2004). The peak of the HVSR spectrum is based on SESAME criteria (Kang, 2024) to acquire the prevailing f_0 (frequency value) and the A_0 (amplification factor value) and then obtain the H/V curve (Handayani et al., 2021). They are shown in Figure 3.

© 2026 Dept. of Geophysics Hasanuddin University

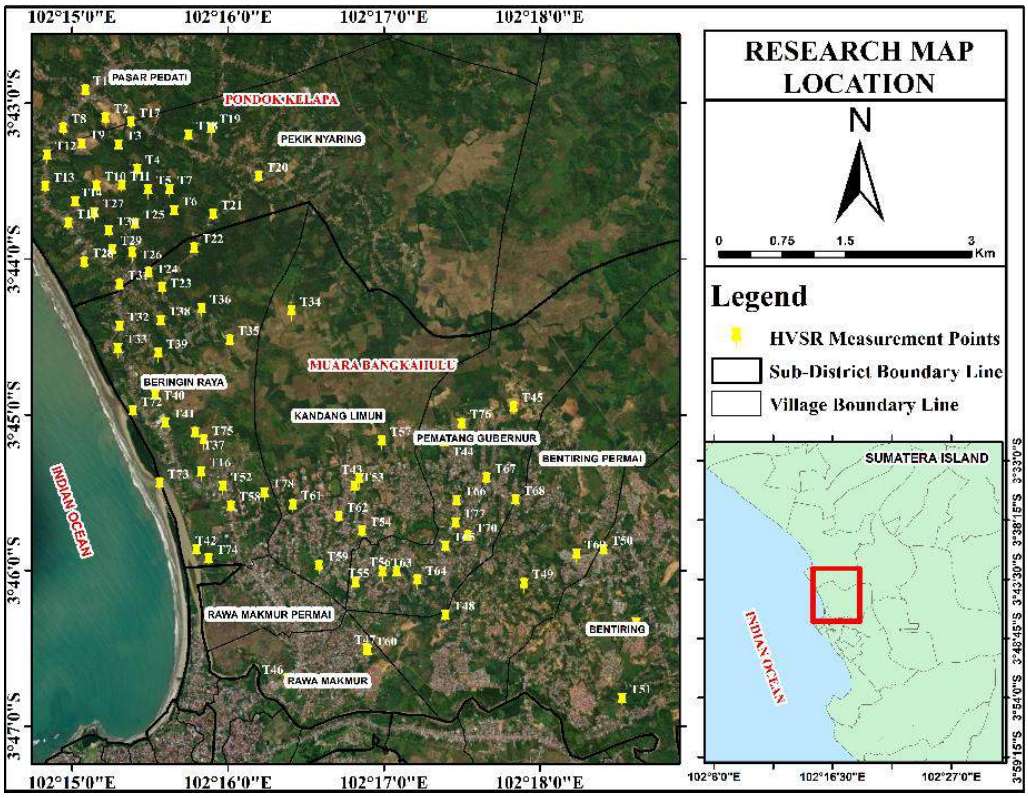


Figure 2. Research location map.

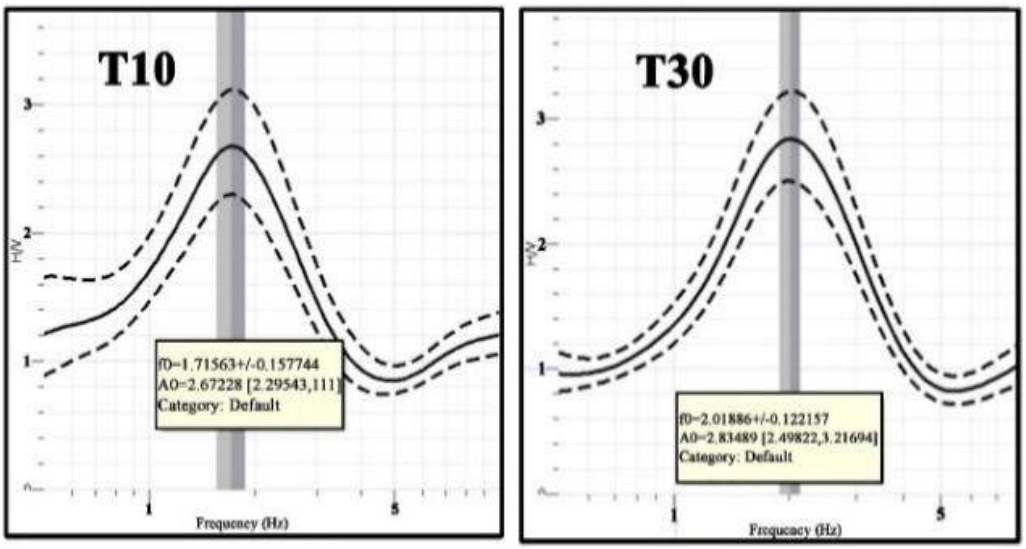


Figure 3. HVSR curve at points T10 and T30.

The seismic susceptibility index (Kg) can be deliberate by considering the central frequency and amplification factor as the determining variables (Yutaka, 1997):

$$Kg = \frac{(A_0)^2}{f_0} \qquad (1)$$

where A_0 dan f_0 representing the amplification factor and dominant frequency, respectively. The Kg estimates areas susceptible to cracking and the potential level of soil deformation due to earthquakes (Nakamura, 1989). Soils with soft sedimentary rock lithologies typically have low Kg values, which suggests that the region is prone to earthquakes. In contrast, areas with high Kg values are usually found in soils composed of solid and stable rock, indicating that the area experiences only minor shaking when an earthquake occurs (Tanjung et al., 2021).

© 2026 Dept. of Geophysics Hasanuddin University

The HVSR inversion procedure minimizes the detached job, which is the difference between the intentional and experimental HVSR, to calculate the shear wave velocity value (Syamsuddin et al., 2022). Shear wave profiles can be employed to describe the geotechnical conditions of soil layers with the HV-Inv Beta software (García-Jerez et al., 2016). HVSR curve inversion using the Forward Modelling (FWD) principle. The subsurface layer is assumed to be a homogenous layer comprising two layered viscoelastic layers. The properties of the layer are density (Rho), thickness (H), associated attenuation factors (Qp, Qs), and compressive and shear wave velocity (Vp, Vs) (Wijayanto et al., 2022).

The Vs, which describes the shear features of the soil structure, is one of the essential metrics that illustrates the dynamics of soil properties (Tawakal et al., 2020). Vs30 is the average shear wave speed at a depth of 30 meters to see the impact of the local site, especially the sediment layer above the bedrock.

Based on the National Standardization Agency rules, the value of Vs30 is estimated using the equation (BSN, 2019):

$$Vs30 = \frac{30}{\sum_{i=1}^{n} \frac{di}{Vs_i}} \quad (2)$$

where d_i is the layer thickness at 0 to 30 m depth, The quantity of layers up to a depth of 30 meters (n) determines the speed of the shear waves (Vs). Table 1 reveals the cataloging of soil site classes established on SNI 1726:2019 (BSN, 2019).

Table 1. Classification of site based on Vs30 data.

Class Site	Vs30 (m/s)
SA (Hard Rocks)	> 1500
SB (Medium Rocks)	750 – 1500
SC (Hard, Very Hard, Compacted Soil and Soft Rock)	350 – 750
SD (Medium Soil)	175 – 350
SE (Soft Soil)	< 175

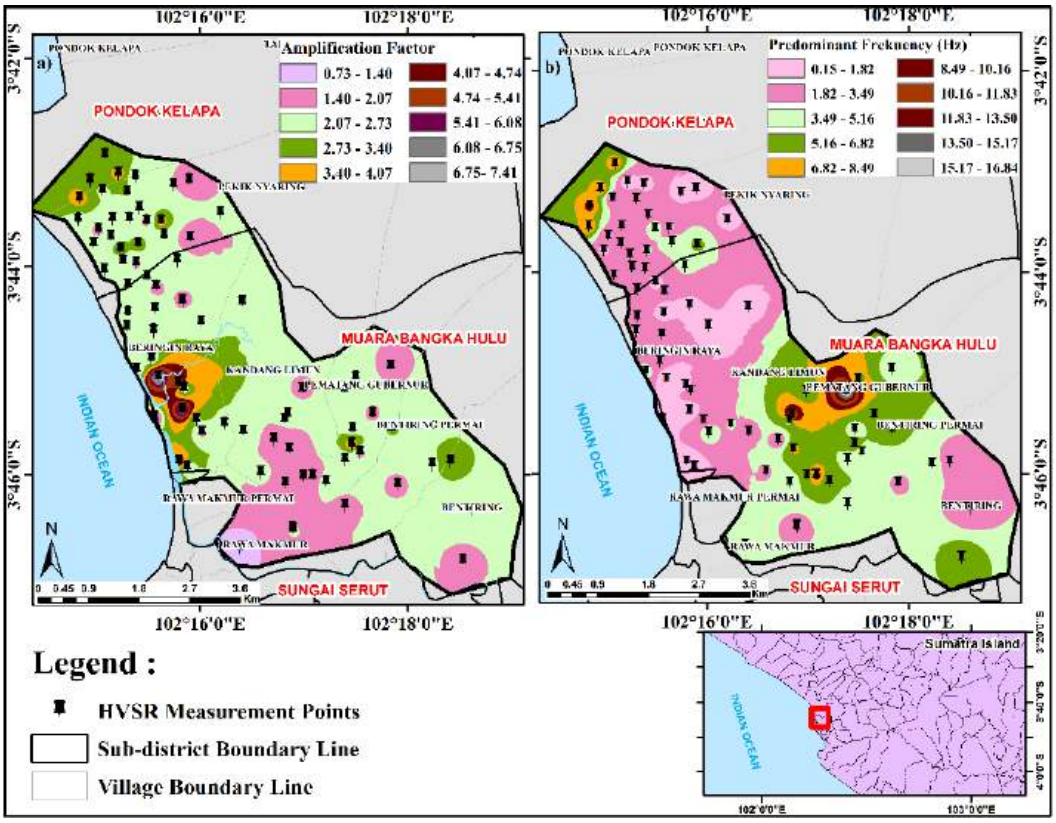


Figure 4. Scatter map of (a) Amplification Factor (b) Dominant Frequency.

© 2026 Dept. of Geophysics Hasanuddin University

Results and Discussion

Based on the field research, the resulting amplification factor values range between 0.73 and 7.41, indicating that most of the amplification factor distribution is low. Amplification values with a low classification of < 3 Are almost spread throughout the research site, marked by geological formations Qa (Alluvium), Qs (Swamp Deposits), and QTb (Bintunan), where the characteristics of these formations are relatively soft sedimentary rocks, meaning that the earthquake shaking felt on the ground is relatively more minor than the original shaking in the earth. The amplification value with a medium to high classification of $3 < A < 7$ is shown in some areas of the Qat (Alluvium Terraces) geological formation, which is characterized by relatively large and more complex sedimentary rocks, meaning that the earthquake shaking felt at ground level is greater than the original shaking in the earth (Figure 4a) and the dominant frequency value is between 0.74 to 16.84 Hz. Based on the classification of the dominant frequency according to Kanai (Ridwan et al., 2021).

In this study, the soil classification by Kanai (Table 2) includes Type I, II, III, and IV soils. Type I and II, with a frequency of < 2.5 Hz, are in the eastern direction, composed of alluvial rocks formed from delta sedimentation, top, soil, and mud exceeding 30 meters. Type III, with a frequency of 2.5 – 4 Hz, is in the west and consists of alluvial rocks > 5 m thick, comprised of alluvial loam, sandy gravel, and sandy hard clay. Type IV type I, a frequency of 67 -20 Hz, is composed of tertiary rocks consisting of Hard sandy and gravel, and Type II, a frequency of 10 – 20 Hz, thickness of 5 m, sandy–gravelly, sandy–hard, clayey, and alluvial rocks located in the Pematang Gubernur and Pasar Pedati areas seen in (Figure 4b).

Table 2. Kanai's classification of soil based on dominant frequency values (Al Ansory et al., 2023).

Classification of Soils		Dominant Frequency (Hz)	Kanai Classification	Descriptions
Type	Class			
IV	I	6.67 – 20	Tertiary or older rocks. Consists of Hard rock, gravel, sandy, etc.	The thickness of the surface sediments is very thin, dominated by hard rocks.
III	II	4 – 10	Alluvial rocks, with a thickness of 5m. consist of sandy, loam, gravel, sandy hard clay, etc.	Its surface sediment thickness falls into the medium category of 5 – 10 m.
II	III	2.5 – 4	Alluvial rocks, > 5m thick, consisting of sandy-gravel, sandy hard clay, loam, etc.	The thickness of the surface sediments is in the thick category, about 10 – 30 m.
I	IV	< 2.5	Alluvial rocks, which are formed from sedimentation of delta, top soil, mud, etc. With a depth of ≥ 30 m.	The sediment surface is very thick.

Seismic Vulnerability Index

Based on the formulas and calculations carried out, Seismic vulnerability index values are strongly influenced by maximum amplitude and natural frequency. The seismic vulnerability index will be more significant for larger amplitude and lower natural frequency values. Conversely, lower amplitude values and higher natural frequency values lead to lower seismic risk index values. The soil structure stability in an area is lower when the seismic vulnerability index is elevated, so the possibility of building damage will increase during an earthquake shock (Maimun et al., 2020).

Based on the data taken at 78 measurement points, the seismic susceptibility index

© 2026 Dept. of Geophysics Hasanuddin University

value in the research area ranges from 0.11 – 37.12 as shown in Figure 5. According to Satria et al. (2020) vulnerability index values are divided into three zones in the study area: the low zone with a Kg value < 3, the medium zone with a Kg value of 3 – 6, and the high zone with a Kg value > 6. The low zone indicates a zone that is safe from land surface movement. The zone is distributed in most of the study area, including Pekik Nyaring, Kandang Limun, Pematang Gubernur, Bentiring Permai, Bentiring, Rawa Makmur Permai, and Rawa Makmur villages. The medium zone indicates a safe zone with relatively small levels of land surface movement. The zone is in a tiny portion of the southern Pasar Pedati area, the northern Beringin Raya area, and the northern Pekik Nyaring area. In line with moderately high amplification factors, the high zone is concentrated in the southern part of Beringin Raya village, a coastal area.

Soils characterized by soft sedimentary rock lithologies typically exhibit low Kg values, such as the condition of the study area, which has Alluvium, Alluvium Terraces, Bintunan, and Swamp deposit formations. This indicates that the area is susceptible to vibration. On the other hand, soils with strong and stable constituent rocks tend to have high Kg values, indicating that the region experiences only small shocks during vibration.

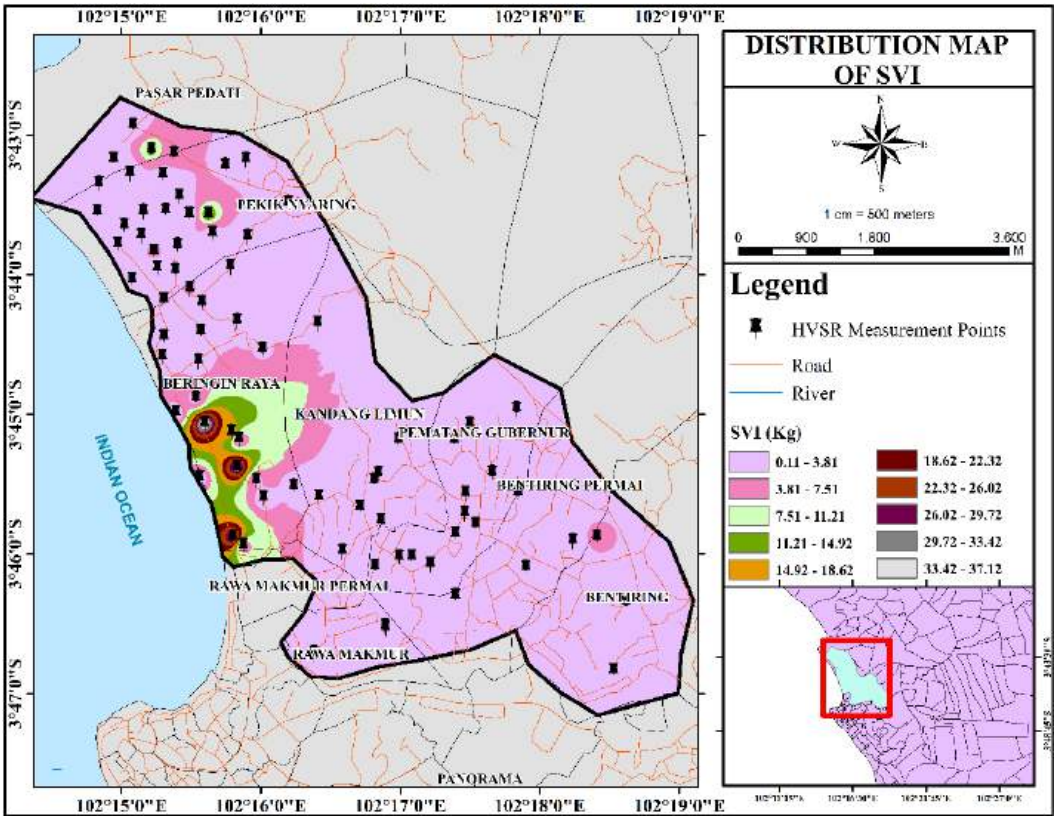


Figure 5. Distribution map of seismic vulnerability index at the research site.

Vs30

Figure 6 shows a spread of Vs30 values, falling between 157 m/s to 516 m/s. Based on the study area's Vs30 readings, most areas are dominated by the SD rock type category triggered in Table 1. Specifically, medium soils have Vs. Values range from 175 to less than 350 m/s; medium soils have a clay texture and minerals that are easy to detach, lift, move, or are prone to land movement. Vs. Values between 350 m/s to 516 m/s are the SC rock type category with hard, thorny soil, compacted soil, and soft rock, which is in Kelurahan Kandang

© 2026 Dept. of Geophysics Hasanuddin University

Limun, Pematang Gubernur, and East Rawamakmur. A tiny portion is included in the SE category that exhibits a range of Vs. Values below 175 m/s, which is soft soil located in a part of Pasar Pedati village, marked with light green. In areas with soft and medium soil types, seismic waves that propagate will propagate slowly to the ground and buildings above them after being reflected by the medium (Edison et al., 2022).

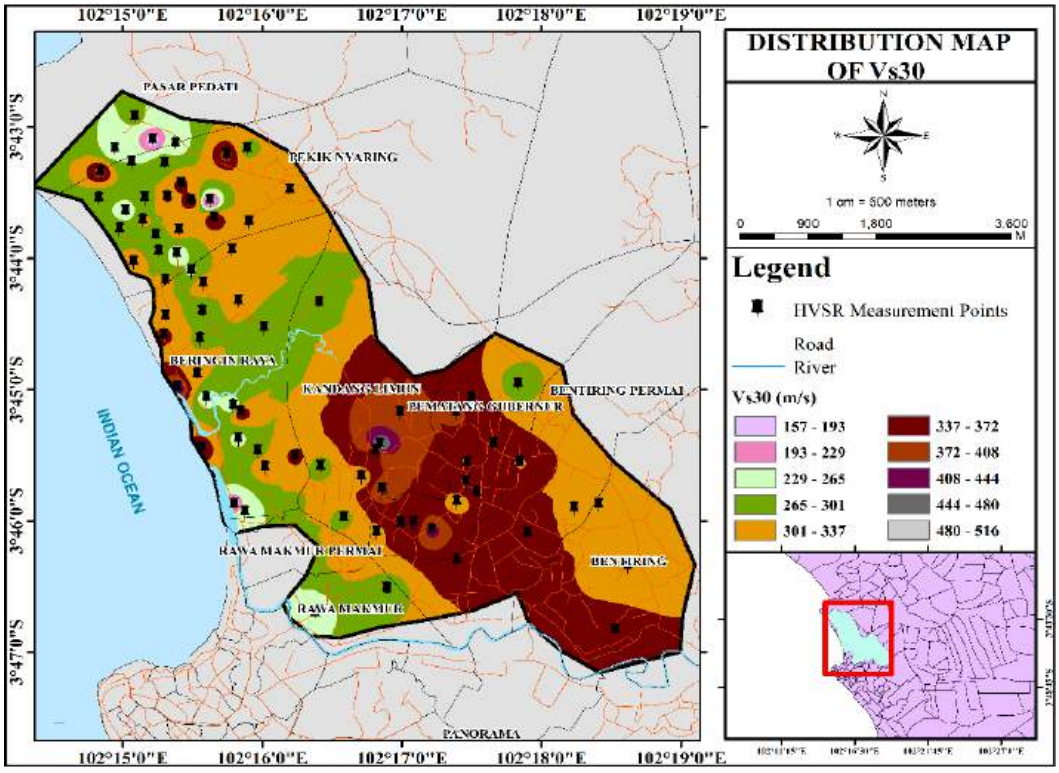


Figure 6. Map of the distribution of Vs30 values at the study site.

A study that employed the same idea was carried out by Nabhan et al. (2023). In the Central Bengkulu-Kepahiang Road section region, the results in the site class SC to SB have a Vs30 value in the 511 – 1422 m/s range. This area tends to have a high value because it is in the andesite-basalt volcanic rock formation, Bal formation, seat formation, and Hulusimpang formation. Furthermore, research in the same area has been conducted by Farid et al. (2024) using the HVSR method and obtaining Vs30 values ranging from 227 – 1235 m/s, which are included in the SC classification (Very Solid Soil and Rigid Soil). This research was only conducted in part of the coastal area and covered only some regions in the sub-district of Pondok Kelapa, Central Bengkulu.

Figure 7 is a 3D profile of the shear wave velocity (Vs) distribution in the northern part of the research region shows Vs values falling between 171 – 593 m/s, with a purple to red gradation. At a depth of 0 – 10 m, the purple to dark blue degradation shows the Vs value is getting more significant with a shear wave velocity of 171 – 276 m/s, which spreads to the north and west. Soil layers with values of 276 – 382 m/s with green color degradation spread to the south and west at 11 – 20m depth. Soil layers with high Vs. Values of 382 – 593 m/s with yellow to red color degradation at a 21 – 30 m/s complexity. Based on the criteria for classifying soil types in Table 1, the Pondok Kelapa area is dominated by type SC, type SD, and a small portion of type SE, which is composed of material types dominated by soft mud, dry sand, and clay. This area has a low Vs value

© 2026 Dept. of Geophysics Hasanuddin University

because it is in an alluvial rock formation composed of gravel, sand, silt, mud, and clay.

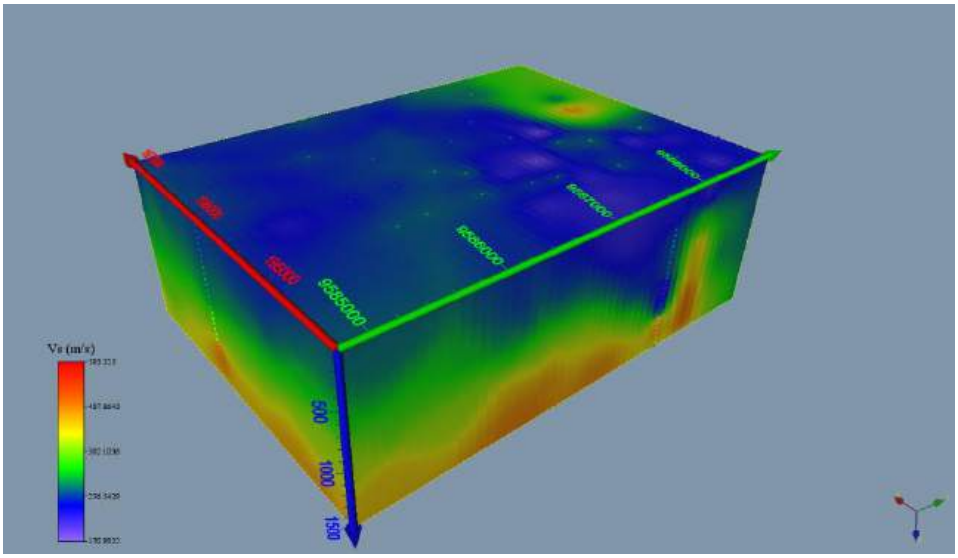


Figure 7. 3D layer profile Vs Pondok Kelapa sub-district.

Based on research findings, the level of risk due to earthquakes in the Pondok Kelapa area and its surroundings is relatively high. This can be used as a reference for building construction. The shaking caused by an earthquake tends to be larger in soft rock than in hard or solid rock. If the shaking gets bigger, potential earthquake damage will be higher. Therefore, it is better to construct buildings in relatively safe areas and make them earthquake-resistant to avoid severe damage.

When viewed from the Vs30 distribution map in Figure 6 areas that are safe for high-rise buildings are areas that have relatively high Vs values with brown to dark brown colour degradation, which are in the North and East Muara Bangka Hulu sub-districts. For areas that have soft soil conditions, the construction of the building must be stronger than the soil conditions that are denser or harder.

Conclusion

Based on research findings, the distribution of A_0 values ranges from 0.73 – 7.41, where the Eastern area has a high amplification factor value compared to other places, and the f_0 between 0.74 – 16.84 Hz with the highest value in the Western area, and Kg ranged start 0.11 – 37.12, with the highest values in the study site's eastern region. While the Vs30 value obtained ranges from 157 – 516 m/s, indicating that the Pondok Kelapa and Rawa Makmur sub-districts have Site Class SC, SD, and SE, which are dominated by the SD type site class, this illustrates that the area has a significant vulnerability to earthquake hazards so that it requires earthquake-resistant buildings to build buildings.

Acknowledgements

We want to thank the Geophysical Laboratory of FMIPA Bengkulu University for the facilities and equipment provided to support this research, as well as thanks to friends who have helped the process of making this article better.

Author Contribution

The main author in this article is Olga Triutami, who has overall duties starting from the initial idea, data collection, data processing, analysis and manuscript writing until completion. However, the author

© 2026 Dept. of Geophysics Hasanuddin University

collaborated with the Bengkulu University Geophysics research team, which are Andre Rahmat, Refrizon and M. Farid.

Conflict of Interest

The author declare that the data published in the manuscript has no conflict of interest to any parties.

References

Al Ansory, A. R., Raihana, H., Farid, M., & Hadi, A. I. (2023). Investigation of Sediment Layer Thickness Estimation at Bengkulu University Hospital Based on A0, f0, and T0 Values. *Jurnal Geocelebes*, 8(1), 1–10. https://doi.org/10.20956/geocelebes.v8i1.28144

Bignardi, S., Mantovani, A., & Abu Zeid, N. (2016). OpenHVSR: Imaging the subsurface 2D/3D elastic properties through multiple HVSR modeling and inversion. *Computers and Geosciences*, 93, 103–113. https://doi.org/10.1016/j.cageo.2016.05.009

BSN. (2019). SNI 1726:2019 Tata Cara Perencanaan Ketahanan Gempa untuk Struktur Bangunan Gedung dan Nongedung *Badan Standar Nasional Indonesia*.

Edison, R., Prakowo, W. A., & Rohadi, S. (2022). Pemetaan Vs30 Dengan Menggunakan Korelasi Zhao Di Pesisir Cilacap. *Jurnal Geosaintek*, 8(1), 181–190. https://doi.org/10.12962/j25023659.v8i1.12601

Farid, M., Hadi, A. I., Refrizon., Suhartoyo, H., Litman., Fadli, D. I., & Putriani, E. (2024). The Combination of Hvsr and Masw Methods with Landsat 8 Imagery to Assess the Changing Shoreline along the Coastal Area of Central Bengkulu. *Trends in Sciences*, 21(5), 1–11. https://doi.org/10.48048/tis.2024.7544

Gafoer, S., Amin, T. C., & Pardede, R. (1992). *Peta Geologi Lembar Bengkulu, Sumatera*. Pusat Survei Geologi. https://geologi.esdm.go.id/geomap/pages/preview/peta-geologi-lembar-bengkulu-sumatera

García-Jerez, A., Piña-Flores, J., Sánchez-Sesma, F. J., Luzón, F., & Perton, M. (2016). A computer code for forward calculation and inversion of the H/V spectral ratio under the diffuse field assumption. *Computers and Geosciences*, 97, 67–78. https://doi.org/10.1016/j.cageo.2016.06.016

Ghanbari, A., Daghigh, Y., & Hassanvand, F. (2018). Risks of Solely Relying on VS30 in Ground Motion Response Studies. *Civil Engineering Journal*, 4(12), 2937–2945. https://doi.org/10.28991/cej-03091210

Hadi, A. I., Refrizon, R., Halauddin, H., Lidiawati, L., & Edo, P. (2021). Interpretasi Tingkat Kekerasan Batuan Bawah Permukaan di Daerah Rawan Gempa Bumi Kota Bengkulu. *Indonesian Journal of Applied Physics*, 11(1), 11–24. https://doi.org/10.13057/ijap.v11i1.46525

Hamzah, A., Amri, M. R., Rozita, E., & Yunus, R. (2020). Penilaian Bangunan Sederhanadi Kawasan Rawan Gempabumi (Studi Kasus di Kota Bengkulu dan Kabupaten Bengkulu Tengah). *Jurnal Dialog Penanggulangan Bencana*, 11(1), 13–21. https://jdpb.bnpb.go.id/index.php/jurnal/article/view/155

Handayani, I. P., La Hamimu., Manan, A., & Puspitafuri, C. (2021). Analisis Spektrum HVSR Untuk Pendugaan Potensi Kerusakan Akibat Gempabumi di Daratan Pesisir Kecamatan Wangi-Wangi Selatan Kabupaten Wakatobi. *Jurnal Rekayasa Geofisika Indonesia*, 3(03),

© 2026 Dept. of Geophysics Hasanuddin University

123–130. https://ojs.uho.ac.id/index.php/jrgi/article/view/23051/14555

Kang, S. Y. (2024). Mapping Bedrock Topography and Detecting Blind Faults using the Fundamental Resonance of Microtremor: a case study of the Pohang Basin, southeastern Korea. *Geophysical Journal International*, 238(2), 806–819. https://doi.org/10.1093/gji/ggae194

Kim, B., & Hong, T.-K. (2022). A National V_{S30} Model for South Korea to Combine Nationwide Dense Borehole Measurements With Ambient Seismic Noise Analysis. *Earth and Space Science*, 9(1), e2021EA002066. https://doi.org/10.1029/2021EA002066

Maimun, A, K., Silvia, U. N., Julia, V., & Ariyanto, P. (2020). Analisis Indeks Kerentanan Seismik, Periode Dominan, Dan Faktor Amplifikasi Menggunakan Metode HVSR di Stage Of Tangerang. *Jurnal Meteorologi Klimatologi Dan Geofisika*, 7(2), 24–30. https://jurnal.stmkg.ac.id/index.php/jmkg/article/view/194

Mase, L. Z., Sugianto, N., & Refrizon. (2021). Seismic hazard microzonation of Bengkulu City, Indonesia. *Geoenvironmental Disasters*, 8(5), 1–17. https://doi.org/10.1186/s40677-021-00178-y

Nabhan, M. A., Hadi, A. I., Fadli, D. I., Harlianto, B., Refrizon., & Ramdani, R. (2023). Distribusi Vs30 Secara Mikrozonasi Berdasarkan Data Inversi Seismik Pasif di Sepanjang Jalan Provinsi Alternatif Kabupaten Bengkulu Tengah-Kepahiang. *Jurnal Ilmiah Geomatika*, 25(2), 67–76. https://www.big.go.id/uploads/content/produk/Geomatika/Vol29.2/1.1206.pdf

Nakamura, Y. (1989). AMethod for dynamic characteristics estimation of subsurface using microtremor on the ground surface. *Railway Technical Research Institute*, 30(1), 25–33. https://www.sdr.co.jp/papers/hv_1989.pdf

Nakamura, Y., Sato, T., & Nishinaga, M. (2000). Local Site Effect of Kobe Based on Microtremor. *Proceedings of the Sixth International Conference on Seismic Zonation (6ISCZ) EERI, November 12-15, 2000/ Palm Springs. California*.

Natawidjaja, D. H. (2018). Updating active fault maps and sliprates along the Sumatran Fault Zone, Indonesia. *IOP Conference Series: Earth and Environmental Science*, 118(1), 012001. https://doi.org/10.1088/1755-1315/118/1/012001

Ridwan, M., Yatini, Y., & Pramono, S. (2021). Mapping of Potential Damages Area in Lombok Island Base on Microtremor Data. *Jurnal Pendidikan Fisika Indonesia*, 17(1), 49–59. https://doi.org/10.15294/jpfi.v17i1.27028

Satria, A., Resta, I. L., & MZ, N. (2020). Analisis Ketebalan Lapisan Sedimen dan Indeks Kerentanan Sismik Kota Jambi Bagian Timur. *Jurnal Geofisika Eksplorasi*, 6(1), 18–30. https://doi.org/10.23960/jge.v6i1.58

SESAME. (2004). *Guidelines for the Implementation of the H / V Spectral Ratio Technique on Ambient Vibrations*. *December*, 1–69.

Sugianto, N., Farid, M., & Suhendra, S. (2017). Kondisi Geologi Lokal Kota Bengkulu Berdasarkan Ground Shear Strain (GSS). *Spektra: Jurnal Fisika Dan Aplikasinya*, 2(1), 29–36. https://doi.org/10.21009/spektra.021.05

Sunardi, B., Naimah, S., Haryoko, U., Rohadi, S., Sulatri., & Rasmid. (2018). Vs30 Mapping and Soil Classification in The Southern Part of Kulon Progo Using Rayleigh Wave Ellipticity Inversion. *JGISE: Journal of Geospatial Information Science and*

© 2026 Dept. of Geophysics Hasanuddin University

Engineering, 1(2), 58–64. https://doi.org/10.22146/jgise.39780

Syamsuddin, E., Aswad, S., Assegaf, M. A. H., Rasimeng, S., Sakka, S., Syamsuddin, S., Nasri, M., & Syihab, M. F. (2022). Seismic Site Classification Using the Multichannel Analysis of Surface Waves Method. *Positron*, 12(2), 149–155. https://doi.org/10.26418/positron.v12i2.53869

Tanjung, N. A. F., Permatasari, I., & Yuniarto, A. H. P. (2021). Mapping of weathered layer thickness and Seismic Vulnerability in Tegal using HVSR method. *Journal of Physics: Conference Series*, 1951(1), 012053. https://doi.org/10.1088/1742-6596/1951/1/012053

Tawakal, M. I., Haris, A., & Martha, A. A. (2020). Estimating shear wave velocity (Vs30) of East Java, Indonesia, using ambient noise inversion of horizontal to vertical spectral ratio (HVSR). *IOP Conference Series: Earth and Environmental Science*, 538(1), 012012. https://doi.org/10.1088/1755-1315/538/1/012012

Thamarux, P., Matsuoka, M., Poovarodom, N., & Iwahashi, J. (2019). VS30 seismic microzoning based on a geomorphology map: Experimental case study of Chiang mai, Chiang rai, and Lamphun, Thailand. *ISPRS International Journal of Geo-Information*, 8(7), 309. https://doi.org/10.3390/ijgi8070309

Wathelet, M., Chatelain, J.-L., Cornou, C., Di Giulio, G., Guillier, B., Ohrnberger, M., & Savvaidis, A. (2020). Geopsy: A user-friendly open-source tool set for ambient vibration processing. *Seismological Research Letters*, 91(3), 1878–1889. https://doi.org/10.1785/0220190360

Wijayanto., Mardiatno, D., Daryono., Nehren, U., Marfai, M. A., & Pramono, S. (2022). Spatial Distribution of Vs30 Based on Masw and Microtremor Inversion in Gunungkidul, Yogyakarta, Indonesia. *International Journal of GEOMATE*, 22(94), 29–38. https://doi.org/10.21660/2022.94.2463

Yutaka, N. (1997). Seismic Vulnerability Indices for Ground and Structures using Microtremor. *World Congress on Railway Research*, Florence, Nov. 1997.

© 2026 Dept. of Geophysics Hasanuddin University

ISSN: 2579-5821 (Print)
ISSN: 2579-5546 (Online)
URL address: http://journal.unhas.ac.id/index.php/geocelebes
DOI: 10.70561/geocelebes.v10i2.47046

Jurnal Geocelebes Vol. 10 No. 2, October 2026, 145 – 159

Receiver-Fault Variability and Depth-Dependent Coulomb Stress Changes in the 2019 Mw 7.2 Halmahera Earthquake Sequence

Rizki Wulandari[1,2], Cahli Suhendi[1,3]*, Yudha Styawan[1,2]

[1]Geophysical Engineering, Faculty of Industrial Technology, Institut Teknologi Sumatera, 35365, Indonesia
[2]Center of Earthquake and Tsunami Disaster Mitigation, Institut Teknologi Sumatera, 35365, Indonesia
[3] Earth Science and Engineering Program, Physical Science and Engineering Division, King Abdullah Univerity of Science and Technology, 23955-6900, Kingdom of Saudi Arabia

*Corresponding author. Email: cahli.suhendi@tg.itera.ac.id

Manuscript received: 8 September 2025; Received in revised form: 25 April 2026; Accepted: 21 May 2026

Abstract

This study investigates the relationship between fault geometry, Coulomb stress transfer, and aftershock distribution in the Halmahera region after the 2019 Mw 7.2 Halmahera Earthquake. Analysis of focal mechanism solutions reveals two distinct clusters: Cluster 1 is located southwest of the mainshock around Bacan Island and is dominated by normal faulting that suggests local extension, whereas Cluster 2 trends southeast of the mainshock along southern Halmahera and exhibits a mix of strike-slip and normal. Coulomb stress modeling shows that when only the maximum ΔCFS across the depth column is considered, aftershocks appear to occur within positive stress-change zones (ΔCFS ≥ ~0.1 bar). Evaluation at the actual hypocentral depths reveals that many aftershocks are concentrated within zones of apparent stress-reduction at shallow levels (0–10 km). This observation may be due to mismatches in receiver-fault geometry, spatial heterogeneity in the background stress/strength field, or processes that are not captured by static ΔCFS. By applying a fault-variability approach, we demonstrate that small variations in receiver-fault orientation can substantially alter ΔCFS outcomes and better reproduce the observed aftershock distribution. These results underscore the importance of receiver-fault geometry and segmentation specific to the Halmahera region in interpreting stress transfer.

Keywords: Extensional area; Receiver fault variability; Seismic triggering; Stress shadow; Strike-slip kinematics.

Citation: Wulandari, R., Suhendi, C., & Styawan, Y. (2026). Receiver-Fault Variability and Depth-Dependent Coulomb Stress Changes in the 2019 Mw 7.2 Halmahera Earthquake Sequence. *Jurnal Geocelebes*, 10(2): 145–159, doi: 10.70561/geocelebes.v10i2.47046

Introduction

The Mw 7.2 earthquake that struck south of Halmahera Island, Indonesia, on 14 July 2019 at 09:10:51 UTC (16:10:51 local time, WIB) was one of the most significant seismic events in the North Maluku region (Figure 1 – 2). The seismicity of southern Halmahera is regionally controlled by segments of the nearby fault systems, including the Sorong fault and Sula fault, which extend westward from Papua (Figure 3). Recent high-resolution multibeam bathymetry mapping has defined the detailed strands of the Sorong Fault Zone, including the Molucca-Sorong and Salawati-Obi segments that trend through the region near Bacan and Halmahera (Watkinson and Hall, 2017). Furthermore, prevailing stress conditions indicate that the northwestern part of Halmahera exhibits significant stress accumulation due to continuous subduction processes, signaling a high potential for large-magnitude earthquakes in this complex tectonic setting (Wajedy et al., 2026). The regional structural context is illustrated in Figure 4b. According to the United States Geological Survey (USGS), the finite-fault solution for this earthquake indicates a left-lateral strike-slip mechanism with a steep fault geometry (strike = 124°, dip = 79°) and

© 2026 Dept. of Geophysics Hasanuddin University

complex rupture characteristics (USGS, 2019). These finite-fault parameters form the structural basis for Coulomb stress change calculations in this study. Tsunami and teleseismic inversion modeling of the 2019 event further suggests that the region is prone to high dip-angle splay faulting, emphasizing its extreme structural complexity (Heidarzadeh et al., 2021).

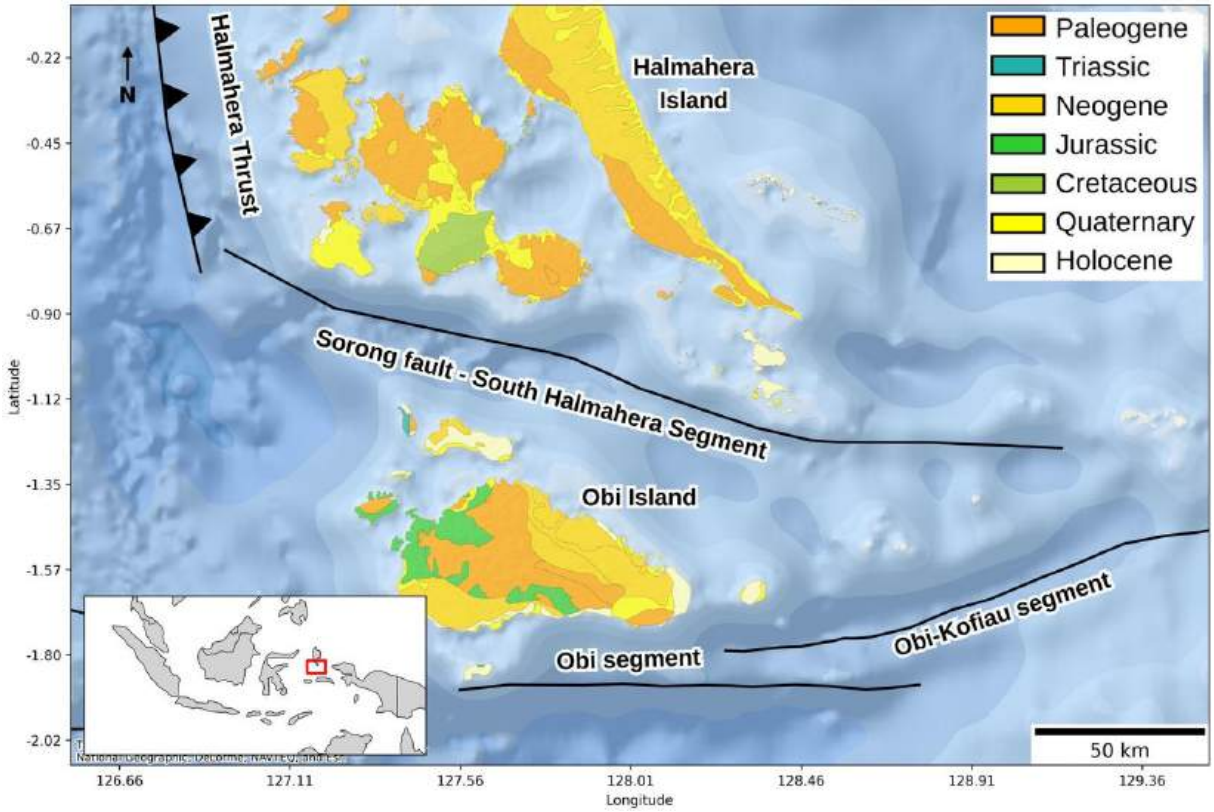


Figure 1. Regional geological map of the Halmahera–Obi area showing the distribution of lithological units by age (Triassic to Holocene) and major tectonic structures, including the Sorong Fault (South Halmahera segment), Obi segment, and Obi–Kofiau segment. The Halmahera Thrust is also identified in the northwestern part of the map. This figure highlights the complex tectonic setting of the region, which plays a significant role in its geological evolution and seismic hazard potential. The inset indicates the location of the study area within Indonesia.

Coulomb stress change analysis has long been used to evaluate static stress transfer between fault segments, which may promote aftershocks or trigger subsequent earthquakes in nearby regions. The core hypothesis posits that a positive value of Coulomb failure stress (ΔCFS) indicates that the earthquake-induced stress changes push the receiver fault closer to rupture (Liu et al., 2023), a mechanism frequently linked to the domino-style triggering of large events on neighboring segments (Altunel et al., 2024). In the Indonesian archipelago, studies have shown that zones of increased Coulomb stress often correlate with aftershock distributions and triggered events, such as those observed following the 2018 Palu earthquake, the 2006 Yogyakarta earthquake, the Pasaman earthquake 2022, and volcanic-seismic interactions in Halmahera (Supendi et al., 2020; Ramdhan et al., 2025; Wulandari et al., 2023; Sinaga et al., 2021). For example, analysis of the 2023 Türkiye earthquake doublet demonstrated that over 81% of aftershocks occurred in regions of increased Coulomb stress (Dai et al., 2024). However, this correlation is not always consistent: aftershocks have also been observed in areas of low or even negative stress change (Hardebeck & Harris, 2022), which is commonly attributed to

© 2026 Dept. of Geophysics Hasanuddin University

heterogeneity in the background stress field or variations in fault orientation. High-resolution remote sensing studies of recent megathrust and crustal events, such as the optical satellite mapping of co-seismic surface ruptures in the 2023 Türkiye earthquakes by Provost et al. (2024), empirically confirm that actual fault zones exhibit massive geometric complexity, sub-parallel splays, and variable rupture widths that static models often oversimplify. In the complex submarine terrain of the Molucca Sea and Halmahera, such geometric heterogeneity is highly likely yet inherently obscured, providing a plausible mechanism for why uniform stress models fail to capture localized triggering

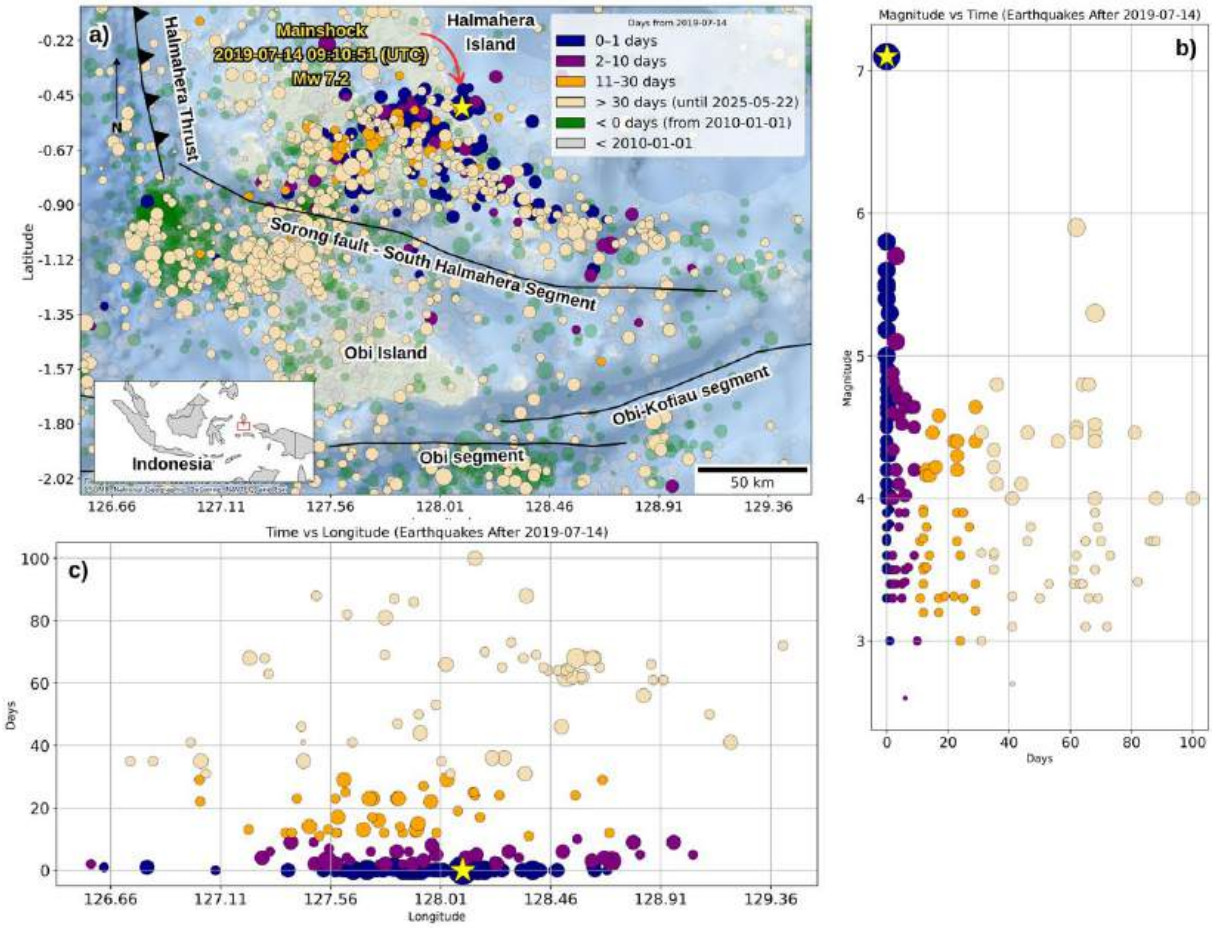


Figure 2. (a) Seismicity in the southern Halmahera region and surrounding areas from the ISC catalog (April 22, 1925 – May 22, 2025). The mainshock location (yellow star) is based on the NEIC preliminary solution, also adopted as the reference for the USGS Finite Fault Solution. (b) Magnitude distribution of aftershocks as a function of time within 100 days. (c) Longitude distribution of aftershocks as a function of time within 100 days.

Despite the importance of the 2019 Halmahera earthquake, no comprehensive study has been conducted to investigate the stress transferred from the earthquake event and its correlation with aftershock distribution in this region. In the context of active Indonesian faults, similar anomalies have been recorded; for instance, post-seismic analysis of the 2016 Mw 6.5 Pidie Jaya earthquake revealed that while stress increases triggered subsequent events on previously unmapped sinistral faults, numerous aftershocks still occurred within theoretical stress shadow areas (Muzli et al., 2018; Kusumawati et al., 2019). Preliminary seismicity analyses suggest that aftershocks cluster in the north of the South Halmahera segment, part of the Sorong Fault system, and do not extend linearly to the NNW but rather propagate to

© 2026 Dept. of Geophysics Hasanuddin University

the SSW. This pattern may indicate a complex tectonic setting in the region, including the possible involvement of secondary fault structures (Figure 1). Although similar Coulomb stress transfer approaches have been extensively applied in other tectonically active regions (e.g., Siwi et al., 2020; Souisa & Sapulete, 2021; Liu et al., 2023; Dai et al., 2024), no comprehensive analysis has yet addressed the Halmahera region, where detailed assessment of fault interactions and depth-dependent stress changes remains lacking. These observations highlight the need to investigate the spatial relationship between Coulomb stress changes and aftershock occurrence in this tectonically complex region.

This study addresses this gap by utilizing the USGS finite fault model (Figure 4c), to calculate Coulomb stress changes at several key depths using the formulation of Reasenberg & Simpson (1992). By integrating these calculations with aftershock data, the study aims to quantify stress transfer patterns and evaluate their correlation with the aftershock distribution and nearby fault segments. The overarching goal is to provide new insights into fault interactions and aftershock triggering mechanisms associated with the 2019 Mw 7.2 Halmahera earthquake, thereby contributing to a broader understanding of seismic hazard in the North Maluku region.

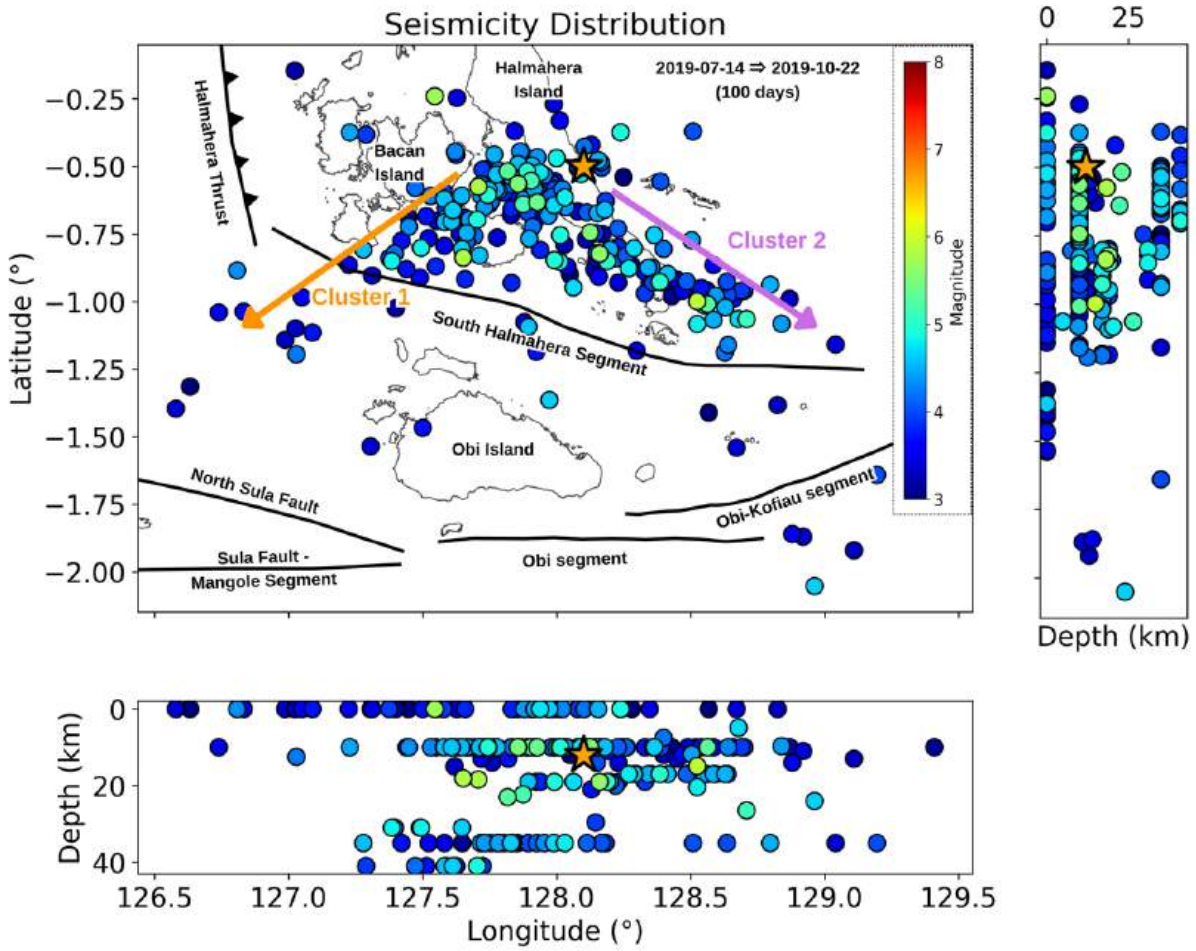


Figure 3. Spatial and depth distribution of seismicity between July 4, 2019 and October 22, 2019 (100 days). The aftershocks extend in two directions, toward the southwest (Cluster 1) and southeast (Cluster 2) from the mainshock.

© 2026 Dept. of Geophysics Hasanuddin University

Materials and Methods

The seismicity data used in this study were obtained from the International Seismological Centre (ISC) catalog (International Seismological Centre, 2026; Storchak et al., 2020), covering the period from 22 April 1925 to 22 May 2025 (Figure 2). For the purpose of Coulomb stress change and aftershock analyses, the dataset was restricted to a 100-day time window following the mainshock, spanning from 4 July 2019 to 22 October 2019 (Figure 3). During this period, seismicity rates were high within the first 10 days after the mainshock, characterized by rapid magnitude releases, and events with magnitudes up to 6 suprisingly occured after 60 days. This restriction allows for a focused examination of aftershock activity that is most likely influenced by the static stress perturbations of the mainshock. To decipher the kinematics and orientation of the fault planes driving the Halmahera sequence, complementary focal mechanism data were systematically compiled from the focal mechanism catalog managed by the International Seismological Centre (International Seismological Centre, 2026; Lentas et al., 2019) up to the year 2024 (Figure 4a,b). This repository aggregates diverse moment tensor inversion solutions, including datasets from the Global Centroid Moment Tensor (GCMT) project, providing the high-fidelity structural parameters necessary to construct the ternary diagram analysis.

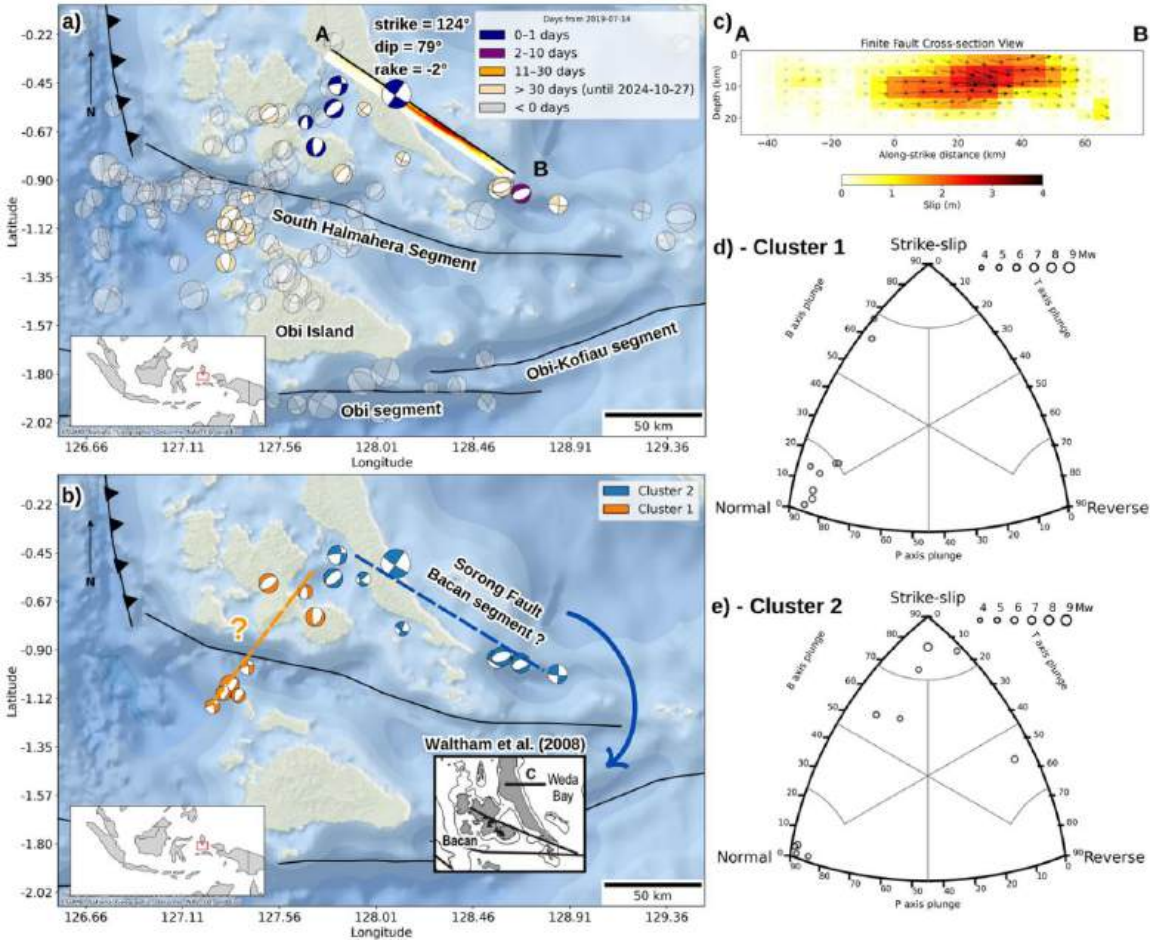


Figure 4. (a) Focal mechanism distribution from available ISC solutions. (b) Focal mechanisms within 100 days of the mainshock, showing two trends, one of which (southeastward) may correspond to the Bacan segment. (c) Slip distribution and orientation from the USGS Finite Fault Solution, with fault location indicated in panel (a) (USGS, 2019). (d–e) Ternary diagrams of focal mechanism types for Cluster 1 and Cluster 2 obtained using FMC (Álvarez-Gómez, 2019), with cluster locations shown in panel (b). Cluster 1 is dominated by normal faulting, whereas Cluster 2 comprises strike-slip and normal faulting events.

© 2026 Dept. of Geophysics Hasanuddin University

For Coulomb stress change calculations, we adopted the finite-fault solution provided by the USGS (2019), which specifies a left-lateral strike-slip mechanism with strike 124°, dip 79°, and rake –2° (Figure 4a,c). These parameters served as the source input for stress transfer modeling in this study.

Information on active fault segments was derived from the 2017 Indonesian Earthquake Source and Hazard Map compiled by Pusat Studi Gempa Nasional (PuSGeN, 2017) (Figure 2). The South Halmahera segment is the closest fault to the mainshock, followed sequentially by the Obi, Obi–Kofiau, North Kofiau, Sagewin, and Dampier segments, all of which are part of the broader Sorong Fault System that dominates the tectonic framework of the region. In addition, the North Sula and Mangole segments, which belong to the Sula Fault, are also present in the surrounding area, underscoring the structural complexity of this tectonic setting.

To begin with, seismic event data were restricted to the maximum depth of 50 km to ensure the analysis focused on shallow crustal earthquakes. The ISC catalog provides multiple magnitude types for each event; therefore, a magnitude priority scheme was applied, giving preference to Mw, followed by Ms, Ml, and Mb, respectively. This hierarchy was determined based on the reliability of the magnitude type (e.g., degree of saturation). In terms of availability, the majority of magnitudes were reported as MLv, Ms, Mb, Ml, and Mw. The primary contributors were DJA for MLv, IDC for Mb and Ml, and GCMT for Mw, with additional data provided by NEIC, EIDC, and others. To ensure consistency, all magnitudes were converted to Mw using the equations from PuSGeN (2017) shows on Table 1. In these equations, Ml/ Mlv was treated as directly equivalent to Mw, as the empirical analysis in the PuSGeN study showed that both magnitude scales exhibit a near-linear relationship with $R^2 = 0.85$. Nevertheless, this assumption may introduce regional uncertainties and could be refined in future studies through updated magnitude calibration analyses specific in the research location. After processing, a total of 3,261 earthquake events were retained.

Table 1. Equations of magnitude type conversion used in this study (PuSGeN, 2017).

Magnitude type	Valid Range	Conversion equation to Mw
mB	mB ≤ 8.2	Mw = 1.0107 × mB + 0.0801
MS	MS ≤ 6.1	Mw = 0.6016 × MS + 2.476
MS	MS ≥ 6.2	Mw = 0.9239 × MS + 0.5671
MLv	All values	Mw = MLv (assumed equivalent)
ML	All values	Mw = ML (assumed equivalent)

Focal mechanism data were primarily obtained from the Global CMT (GCMT) solutions as distributed through the ISC database (Ekström et al., 2012). When GCMT solutions were unavailable, alternative sources were considered. For the mainshock, we adopted the mechanism provided in the USGS finite-fault model, which is based on the NEIC solution (USGS, 2019), to ensure consistency between the mainshock source parameters and the stress modeling framework. The aftershock sequence within 100 days following the mainshock was analyzed to determine the dominant faulting style. This analysis was conducted using the ternary diagram approach of Álvarez-Gómez (2019), which classifies earthquake focal mechanisms into relative proportions of strike-slip, normal, and reverse faulting. Based on this approach, the events were grouped into two main clusters, corresponding to the Bacan segment and a second area hypothesized to represent an unrecognized fault structure (Figure 4).

© 2026 Dept. of Geophysics Hasanuddin University

The static Coulomb stress change was calculated using the finite-fault model published by the USGS. The computation was performed within the spatial bounds of longitude 125.0931°–131.0931° and latitude −3.529°–2.471°, with a grid spacing of 6.67 km. Elastic parameters included a Poisson's ratio of 0.25, Young's modulus of 8×10^5 bar (≈ 80 GPa), and a friction coefficient of 0.4. These values are widely adopted in Coulomb stress modeling as representative of average crustal conditions: a Poisson's ratio of ~0.25 reflects typical elastic behavior of crystalline and consolidated sedimentary rocks (Gercek, 2007), a Young's modulus of ~80 GPa corresponds to the upper–mid crustal lithologies (Durkin et al., 2019), and a friction coefficient of ~0.4 falls within the broader range of μ = 0.25–0.80 reported for natural fault zones, reflecting the strength heterogeneity observed in fault rocks (Smith & Faulkner, 2010). Together, these parameters provide a simplified yet realistic approximation for evaluating static stress transfer in the study area. The finite-fault model corresponds to a seismic moment of 6.5×10^{26} dyne·cm, equivalent to a moment magnitude (Mw) of 7.14. The receiver fault geometry was initially defined to be the same as that of the mainshock, consistent with the finite-fault solution reported by the USGS (2019). This assumption was adopted because detailed geological or focal mechanism constraints for individual aftershocks are not available for the study area. While this simplification provides a first-order approximation of the regional stress transfer pattern, it may not fully capture local variations in fault orientation or segmentation. These limitations are further addressed by applying a fault-variability approach in the subsequent analysis. Stress changes were evaluated over a depth range of 0–30 km at 2 km intervals, and the maximum Coulomb stress value was extracted for each grid point. We employed Coulomb 3.4 software, an updated version of 3.3 (Toda et al., 2011) to calculate Coulomb stress change. The Coulomb failure stress change is calculated using the following equation (Toda et al., 2011):

$$\Delta CFS = \Delta\tau + \mu'\Delta\sigma_n \quad (1)$$

Where:
$\Delta\tau$ = shear stress change on the receiver fault in the slip direction,
$\Delta\sigma_n$ = normal stress change (positive for unclamping),
μ' = effective friction coefficient.

In addition, Coulomb stress changes were evaluated on nearby fault segments by discretizing each segment into smaller receiver elements (hereafter referred to as subfaults). In contemporary finite-fault modeling, the term subfault refers to a discretized fault patch with its own slip amplitude, used to reconstruct complex rupture distributions within active fault systems (Supendi et al., 2023). In this study, however, the term is used more generally to describe the subdivision of larger receiver-fault segments into smaller geometric elements in order to resolve spatial variations in stress changes along the fault. Each subfault was assigned a geometry consistent with left-lateral strike-slip motion, represented by a dip of 90° and rake of 0°. This uniform assumption provides a simplified reference for evaluating regional stress transfer, although local variations in dip and rake may exist and could influence detailed stress patterns. Such variability is beyond the scope of this study but may be explored in future work. As in the main calculation, depths were evaluated from 0–30 km at 2 km intervals, and the maximum ΔCFS value was assigned to each subfault.

Focal mechanism data of aftershocks were used to compute Coulomb stress changes by incorporating the strike, dip, rake, and focal depth of each event. Because it is generally uncertain which nodal plane represents the true fault plane, both nodal planes were evaluated. For classification,

© 2026 Dept. of Geophysics Hasanuddin University

the plane with the smaller strike value was assigned as nodal plane 1, while the other was treated as nodal plane 2.

For aftershocks lacking focal mechanism solutions, a fault-variability approach was employed. In this method, each earthquake was assigned 1,500 random fault geometries, generated with a standard deviation of 30° around the mainshock orientation (Sharma et al., 2020). For each event, the geometry with Coulomb stress change ≥ 0.1 bar was selected as the preferred solution; if no such geometry existed, the configuration with the highest Coulomb stress was chosen instead. The resulting solutions were divided into two clusters and analyzed using ternary diagrams. To further visualize faulting patterns, composite focal mechanism plots (beachballs) were generated for each cluster, highlighting the dominant strike orientations of the aftershock population.

Results and Discussion

Figure 3 and 4b illustrates the contrasting aftershocks and their focal mechanism patterns observed in the two main clusters. Cluster 2, which is interpreted as the Bacan segment and is likely associated with a splay fault system, is dominated by strike-slip and normal mechanisms (Figure 4e). In contrast, Cluster 1, which may represent a newly developed and previously unidentified structure, exhibits dominantly normal faulting (Figure 4d). The occurrence of normal faulting suggests that this area is undergoing extensional deformation, possibly driven by opposing strike-slip faults at its boundaries. This tectonic environment is consistent with the complex zones of distributed crustal deformation and the reactivation of unidentified secondary fault systems documented in northern Sumatra (Muzli et al., 2018). Nonetheless, further investigation is required to validate this interpretation.

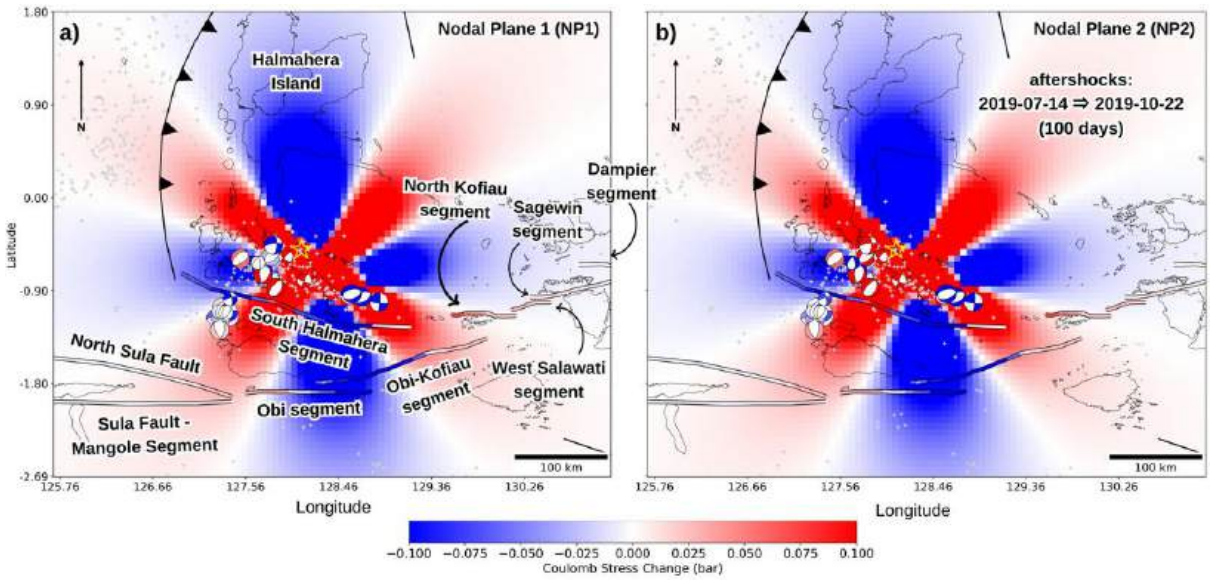


Figure 5. Spatial distribution of maximum Coulomb stress change (0–30 km depth, 2 km intervals) for receiver faults with the same geometry as the source fault. Coulomb stress changes are shown for focal mechanisms in Figure 4b, comparing (a) Nodal Plane 1 and (b) Nodal Plane 2. Nodal Plane 1 exhibits a smaller strike angle than Nodal Plane 2. Grey dots represent aftershock locations (Figure 3). Fault segments also show stress change values consistent with their geometry (strike from subfault orientation, dip = 90°, rake = 0°).

According to Wu et al. (2017), a Coulomb stress change of approximately 0.1 bar can be sufficient to trigger aftershocks. As shown in Figure 5a-b, regions with positive Coulomb stress change generally coincide with the aftershock distribution. However,

© 2026 Dept. of Geophysics Hasanuddin University

many of the surrounding faults are associated with negative Coulomb stress changes. These negative changes were consistent with the depth-variant stress change on the faults (0-30 km) (Figure 6a-d). These include the nearby South Halmahera segment, most of the Obi segment, and the Obi–Kofiau segment. Although slight stress increases are observed along parts of the North Kofiau segment, the western Obi segment, and the central portion of the South Halmahera segment, these faults did not host significant aftershock activity (Figure 3). Depth variations further confirm this pattern, as demonstrated in Figure 6a-d, reinforcing the idea that the mainshock did not substantially trigger the adjacent fault systems.

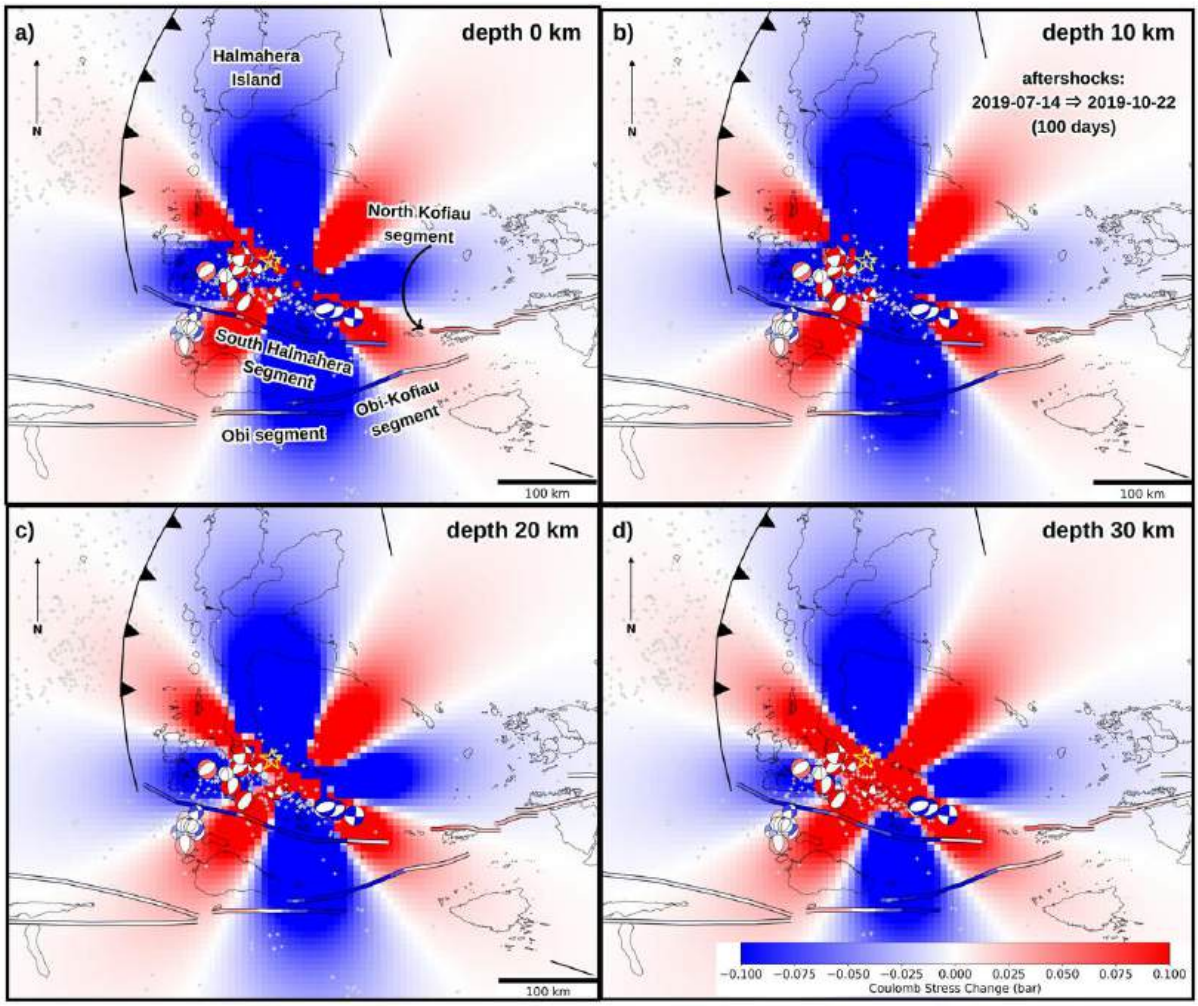


Figure 6. Spatial distribution of Coulomb stress change at depths of (a) 0 km, (b) 10 km, (c) 20 km, and (d) 30 km. Similar stress based on depths are observed in the fault segment closest to the mainshock. The nodal planes shown are selected based on the larger Coulomb stress change value.

The focal mechanisms of aftershocks shown in Figure 5 also reveal intriguing behavior. In the southeastern part of the study area, three aftershocks consistently situated at stress decreases, in contrast with the northwestern and southwestern regions where the distribution of focal mechanisms varies with nodal plane geometry but is predominantly associated with positive stress changes. This contrast may be linked to differences in local stress orientation and fault plane compatibility with the imposed stress field, suggesting a spatially heterogeneous stress transfer process. The spatially heterogeneous stress transfer documented here aligns with observations

© 2026 Dept. of Geophysics Hasanuddin University

from the contemporaneous 2019 Ambon sequence, where stress redistribution effectively promoted seismicity on specific fault strands with varying source mechanisms (Rohadi et al., 2021). This complexity is consistent with high-resolution satellite observations of recent major strike-slip events, which demonstrate that rupture zones are not simple linear traces but often consist of multiple sub-parallel strands and diffuse deformation regions. Such physical heterogeneity likely drives the localized variations in stress orientation observed in the Halmahera sequence.

Table 2. Comparison of Coulomb stress change results using identical fault parameters and the fault variability approach in the aftershocks (14/7/2019 – 22/10/2019).

Metric	Same Fault Parameters (N)	Same Fault Parameters (%)	Fault Variability Approach (N)	Fault Variability Approach (%)
Positive Coulomb events	56	23.43	232	97.07
Negative Coulomb events	183	76.57	7	2.93
Total events	239	100.00	239	100.00
Events with Mw ≥ 5.0	17	7.11	17	7.11
Positive Coulomb events with Mw ≥ 5.0	3	17.65	17	100.00
Negative Coulomb events with Mw ≥ 5.0	14	82.35	0	0.00

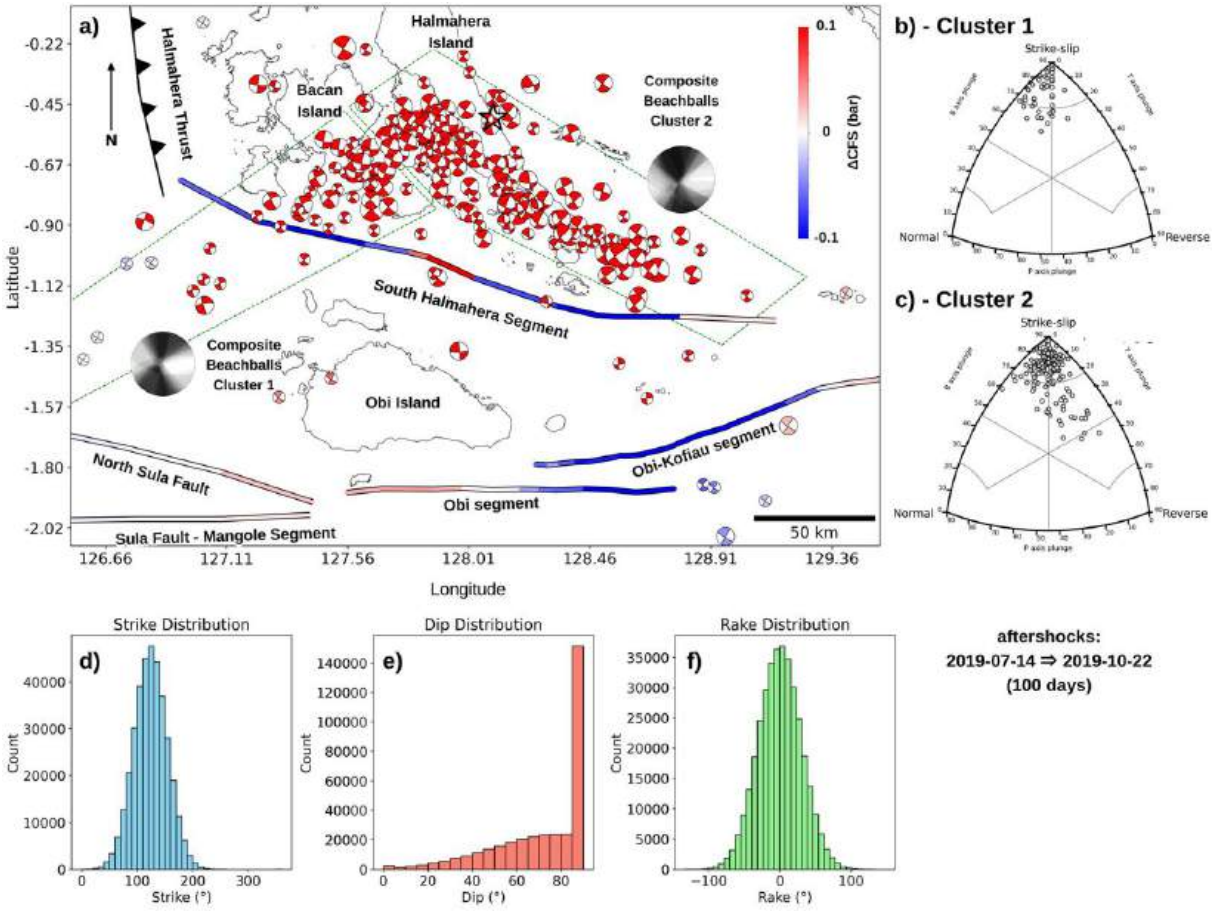


Figure 7. Coulomb stress change distribution for aftershocks using the Fault Variability approach with a normal distribution and 30° standard deviation of the mainshock geometry. (a) Aftershock fault geometries selected based on proximity to the mainshock geometry and showing positive stress changes ≥ 0.1 bar, or alternatively the geometry with the maximum stress change. (b–c) Ternary diagrams of focal mechanism distributions for Cluster 1 and Cluster 2 dominated by strike-slip faulting. Each cluster has a composite of the beachballs in panel (a). (d–f) Strike, dip, and rake distributions for 1500 random geometries of each aftershock, giving a total of 1500 multiplied by the number of aftershocks (within 100 days of the mainshock).

© 2026 Dept. of Geophysics Hasanuddin University

The apparent correlation between aftershock occurrence and regions of increased stress in Figure 5 requires further examination when depth distribution is taken into account. As illustrated in Figure 6, the depth range of 0–10 km is characterized by a reduction in Coulomb stress, yet most aftershocks occurred within this shallow interval (Figure 3). This observation raises the question of whether the aftershock zone corresponds to a shadow stress region. A definitive conclusion cannot be made, since the dominant fault orientations are not well constrained. It indicates further study that focus on the characterization of the complex tectonic in this region is important. The presence of numerous aftershocks in the shallow interval (0–10 km), despite a modeled reduction in Coulomb stress, may be explained by the findings of Provost et al. (2024), who documented that real-world fault zones exhibit an average width of 1 km with a standard deviation of up to 2.5 km. This suggests that localized zone widening or the existence of secondary splays at shallow depths, which are often oversimplified in uniform planar models, could shift these events into positive stress-change environments.

However, one way to address this limitation, we applied a fault variability approach that incorporates uncertainty by assuming aftershocks occur in areas of potential positive stress change shown in Table 2. The results, presented in Figure 7, demonstrate that even minor variations in fault orientation can shift the stress outcome from negative to positive. This is clearly depicted in the ternary diagram, where strike-slip mechanisms dominate, and the composite beachball solutions suggest fault geometries broadly consistent with that of the mainshock. These findings underscore the importance of incorporating receiver fault geometry in Coulomb stress analyses to avoid misinterpretations that place aftershocks in apparent stress shadow regions. Nonetheless, this approach also has limitations, particularly in cases where independent evidence for shadow stress effects may exist.

Conclusion

The results of this study highlight the complex interaction between fault geometry, stress transfer, and aftershock distribution in the investigated region. The different focal mechanisms observed in the two clusters suggest the coexistence of strike-slip and normal faulting processes, might indicate local extensional regimes possibly driven by surrounding strike-slip faulting activities.

Coulomb stress analysis further reveals that aftershock occurrence is not always consistent with maximum positive stress changes. This emphasizes the limitations of assuming a uniform receiver fault geometry. By applying the fault variability approach, we demonstrate that the proportion of aftershocks falling within positive stress zones ($\Delta CFS \geq 0.1$ bar) increased significantly from 23.43% to 97.07%. These findings underscore the importance of considering geometric uncertainty to avoid misleading interpretations, such as placing aftershocks in apparent stress shadow regions.

However, this study has limitations, as it primarily investigates static stress changes. We do not account for dynamic stress triggering or postseismic effects, which may also influence aftershock distribution. Despite these limitations, our results provide vital insights for improving seismic hazard assessments in Halmahera. Understanding these localized stress interactions is essential for better predicting future fault ruptures and mitigating earthquake risks in North Maluku.

Acknowledgements

© 2026 Dept. of Geophysics Hasanuddin University

The authors would like to thank the editor and reviewers of *Jurnal Geocelebes* for their valuable comments and constructive suggestions that greatly improved this manuscript.

Author Contribution

Rizki Wulandari conducted the data processing, analysis, and manuscript drafting; Cahli Suhendi supervised the research design, provided critical revisions, and coordinated the submission process; while Yudha Styawan contributed to the interpretation of results and refinement of the discussion.

Conflict of Interest

The authors declare that there is no conflict of interest regarding the publication of this manuscript.

References

Altunel, E., Kozacı, Ö., Yıldırım, C., Sbeinati, R. M., & Meghraoui, M. (2024). Potential domino effect of the 2023 Kahramanmaraş earthquake on the centuries-long seismic quiescence of the Dead Sea fault: Inferences from the North Anatolian fault. *Scientific Reports*, 14(1), 15440. https://doi.org/10.1038/s41598-024-65906-4

Álvarez-Gómez, J. A. (2019). FMC—Earthquake focal mechanisms data management, cluster and classification. *SoftwareX*, 9, 299–307. https://doi.org/10.1016/j.softx.2019.03.008

Dai, X., Liu, X., Liu, R., Song, M., Zhu, G., Chang, X., & Guo, J. (2024). Coseismic Slip Distribution and Coulomb Stress Change of the 2023 MW 7.8 Pazarcik and MW 7.5 Elbistan Earthquakes in Turkey. *Remote Sensing*, 16(2), 240. https://doi.org/10.3390/rs16020240

Durkin, W., Kachuck, S., & Pritchard, M. (2019). The Importance of the Inelastic and Elastic Structures of the Crust in Constraining Glacial Density, Mass Change, and Isostatic Adjustment From Geodetic Observations in Southeast Alaska. *Journal of Geophysical Research: Solid Earth*, 124(1), 1106–1119. https://doi.org/10.1029/2018JB016399

Ekström, G., Nettles, M., & Dziewoński, A. M. (2012). The global CMT project 2004–2010: Centroid-moment tensors for 13,017 earthquakes. *Physics of the Earth and Planetary Interiors,* 200–201, 1–9. https://doi.org/10.1016/j.pepi.2012.04.002

Gercek, H. (2007). Poisson's ratio values for rocks. *International Journal of Rock Mechanics and Mining Sciences*, 44(1), 1–13. https://doi.org/10.1016/j.ijrmms.2006.04.011

Hardebeck, J. L., & Harris, R. A. (2022). Earthquakes in the shadows: Why aftershocks occur at surprising locations. *The Seismic Record*, 2(3), 207–216. https://doi.org/10.1785/0320220023

Heidarzadeh, M., Ishibe, T., Harada, T., Natawidjaja, D. H., Pranantyo, I. R., & Widyantoro, B. T. (2021). High potential for splay faulting in the Molucca Sea, Indonesia: November 2019 Mw 7.2 earthquake and tsunami. *Geophysical Research Letters*, 48(10), e2020GL083989. https://doi.org/10.1029/2020GL083989

International Seismological Centre. (2026). *On-line Bulletin*. https://doi.org/10.31905/D808B830

Kusumawati, D., Sahara, D. P., Nugraha, A. D., & Puspito, N. T. (2019). Sensitivity of static Coulomb stress change in relation to source fault geometry and regional stress magnitude: case study of the 2016 Pidie Jaya, Aceh earthquake (Mw =

© 2026 Dept. of Geophysics Hasanuddin University

6.5), Indonesia. *Journal of Seismology*, 23, 1391–1403. https://doi.org/10.1007/s10950-019-09878-3

Lentas, K., Di Giacomo, D., Harris, J., & Storchak, D. A. (2019). The ISC Bulletin as a comprehensive source of earthquake source mechanisms. *Earth System Science Data*, 11, 565–578, https://doi.org/10.5194/essd-11-565-2019

Liu, C., Lay, T., Wang, R., Taymaz, T., Xie, Z., Xiong, X., Irmak, T. S., Kahraman, M., & Erman, C. (2023). Complex multi-fault rupture and triggering during the 2023 earthquake doublet in southeastern Türkiye. *Nature Communications*, 14(1), 5564. https://doi.org/10.1038/s41467-023-41404-5

Muzli, M., Umar, M., Nugraha, A. D., Bradley, K. E., Widiyantoro, S., Erbas, K., Jousset, P., Rohadi, S., Nurdin, I., & Wei, S. (2018). The 2016 Mw 6.5 Pidie Jaya, Aceh, North Sumatra, Earthquake: Reactivation of an unidentified sinistral fault in a region of distributed deformation. *Seismological Research Letters*, 89(5), 1761-1772. https://doi.org/10.1785/0220180068

Provost, F., Karabacak, V., Malet, J.-P., Van der Woerd, J., Meghraoui, M., Masson, F., Ferry, M., Michéa, D., & Pointal, E. (2024). High-resolution co-seismic fault offsets of the 2023 Türkiye earthquake ruptures using satellite imagery. *Scientific Reports*, 14(1), 6834. https://doi.org/10.1038/s41598-024-55009-5

Pusat Studi Gempa Nasional (PuSGeN). (2017). *Peta Sumber dan Bahaya Gempa Indonesia Tahun 2017.* Bandung: Pusat Penelitian dan Pengembangan Perumahan dan Permukiman, Kementerian Pekerjaan Umum dan Perumahan Rakyat.

Ramdhan, M., Palgunadi, K. H., Mukti, M. M., Librian, V., Daniarsyad, G., Muttaqy, F., Hidayat, E., Syuhada, S., Hanif, M., Mursitantyo, A., Lühr, B.-G., Nugraha, A. D., Widiyantoro, S., Setyonegoro, W., & Febriani, F. (2025). Aftershock sequence of the Yogyakarta earthquake 2006 (Mw ~ 6.4), Indonesia, based on analysis of hypocenter relocation, static, and dynamic stress. *Natural Hazards*, 121, 16559–16579. https://doi.org/10.1007/s11069-025-07440-8

Reasenberg, P. A., & Simpson, R. W. (1992). Response of regional seismicity to the static stress change produced by the Loma Prieta earthquake. *Science*, 255(5052), 1687-1690. https://doi.org/10.1126/science.255.5052.1687

Rohadi, S., Perdana, Y. H., Herayndoko, N., Sunardi, B., Prakoso, T. A., Suliyanti, S., Sunardi, S., Florida, N., Edison, R., & Karnawati, D. (2021). The M 6.5 Ambon earthquake 26 September 2019: the source mechanism and the aftershock sequence characteristics. *IOP Conference Series: Earth and Environmental Science*, 873(1), 012013. https://doi.org/10.1088/1755-1315/873/1/012013

Sharma, S., Hainzl, S., Zöeller, G., & Holschneider, M. (2020). Is coulomb stress the best choice for aftershock forecasting? *Journal of Geophysical Research: Solid Earth*, 125(9), e2020JB019553. https://doi.org/10.1029/2020JB019553

Sinaga, G. H. D., Zarlis, M., Sitepu, M., Prasetyo, R. A., & Simanullang, A. (2021). Coulomb stress analysis of West Halmahera earthquake Mw=7.2 to Mount Soputan and Gamalama volcanic activities. *IOP Conference Series: Earth and Environmental Science*, 56(1), 012005. https://doi.org/10.1088/1755-1315/56/1/012005

© 2026 Dept. of Geophysics Hasanuddin University

Siwi, P. W., Sriyanto, S. P. D., Rondonuwu, A. T., & Silangen, P. M. (2020). Perubahan Coulomb Stress Akibat Gempa Bumi Laut Maluku 7 Januari 2019. *Jurnal Geosaintek*, 6(3), 137–142. https://doi.org/10.12962/j25023659.v6i3.7030

Smith, S. A. F., & Faulkner, D. R. (2010). Laboratory measurements of the frictional properties of the Zuccale low-angle normal fault, Elba Island, Italy. *Journal of Geophysical Research: Solid Earth*, 115(B2), 2008JB006274. https://doi.org/10.1029/2008JB006274

Souisa, M., & Sapulete, S. M. (2021). Analysis of the Impact of Coulomb Stress Changes of Tehoru Earthquake, Central Maluku Regency, Maluku Province. *Jurnal Penelitian Pendidikan IPA*, 7(4), 593–600. https://doi.org/10.29303/jppipa.v7i4.975

Storchak, D. A., Harris, J., Brown, L., Lieser, K., Shumba, B., & Di Giacomo, D. (2020). Rebuild of the Bulletin of the International Seismological Centre (ISC)—part 2: 1980–2010. *Geoscience Letters*, 7(1), 18. https://doi.org/10.1186/s40562-020-00164-6

Supendi, P., Nugraha, A. D., Widiyantoro, S., Pesicek, J. D., Thurber, C. H., Abdullah, C. I., Daryono, D., Shiddiqi, H. A., & Rosalia, S. (2020). Relocated aftershocks and background seismicity in eastern Indonesia shed light on the 2018 Lombok and Palu earthquake sequences. *Geophysical Journal International*, 221(3), 1845-1855. https://doi.org/10.1093/gji/ggaa118

Supendi, P., Rawlinson, N., Prayitno, B. S., Sianipar, D., Simanjuntak, A., Widiyantoro, S., Palgunadi, K. H., Kurniawan, A., Ash Shiddiqi, H., Nugraha, A. D., Sahara, D. P., Daryono, D., Triyono, R., Adi, S. P., Karnawati, D., Daniarsyad, G., Ahadi, S., Fatchurohman, I., Anugrah, S. D., Heryandoko, N., & Sudrajat, A. (2023). A previously unidentified fault revealed by the February 25, 2022 (Mw 6.1) Pasaman earthquake, West Sumatra, Indonesia. *Physics of the Earth and Planetary Interiors*, 334, 106973. https://doi.org/10.1016/j.pepi.2022.106973

Toda, S., Stein, R. S., Sevilgen, V., & Lin, J. (2011). *Coulomb 3.3 Graphic-rich deformation and stress-change software for earthquake, tectonic, and volcano research and teaching-user guide* (2011–1060). U.S. Geological Survey. https://doi.org/10.3133/ofr20111060

USGS**.** (2019). *Finite fault model for the M 7.2 earthquake 155 km SSE of Sofifi, Indonesia (2019-07-14 09:10:51 UTC)*. U.S. Geological Survey. https://earthquake.usgs.gov/earthquakes/eventpage/us70004jyv/finite-fault

Wajedy, M. F., Saaduddin, S., Massinai, M. A., Fahruddin, F., & Thariq, A. (2026). Seismic hazard and tectonic stress in Halmahera, Indonesia based on b-value and apparent stress analyses. *Physics of the Earth and Planetary Interiors*, 372, 107512. https://doi.org/10.1016/j.pepi.2026.107512

Watkinson, I. M., & Hall, R. (2017). Fault systems of the eastern Indonesian triple junction: evaluation of Quaternary activity and implications for seismic hazards. *Geological Society, London, Special Publications*, 441(1), 71–120. https://doi.org/10.1144/SP441.8

Wu, J., Cai, Y., Li, W., & Feng, Q. (2017). Strong Aftershock Study Based on Coulomb Stress Triggering—A Case Study on the 2016 Ecuador Mw 7.8 Earthquake. *Applied Sciences*, 7(1), 88. https://doi.org/10.3390/app7010088

Wulandari, R., Chan, C.-H., & Wibowo, A.

© 2026 Dept. of Geophysics Hasanuddin University

(2023). The 2022 Mw6.2 Pasaman, Indonesia, earthquake sequence and its implication of seismic hazard in central-west Sumatra. *Geoscience Letters*, 10(1), 25. https://doi.org/10.1186/s40562-023-00279-6

© 2026 Dept. of Geophysics Hasanuddin University

ISSN: 2579-5821 (Print)
ISSN: 2579-5546 (Online)
URL address: http://journal.unhas.ac.id/index.php/geocelebes
DOI: 10.70561/geocelebes.v10i2.49863

Jurnal Geocelebes Vol. 10 No. 2, October 2026, 160 – 176

Metal Corrosion Indicators for Sulfur Exposure Assessment in Urban and Volcanic Areas of East Java

Yuansyah Dhaniar Ramadhan[1], Muhammad Tegar Rahmawan[1], Ayunita Haq[1], Nayla Rohmatul Maulidiyah[2], Daryll Alfaraby Noorlaksono[3], Arie Realita[1]*, Madlazim[1], Muhammad Nurul Fahmi[1], Adedio Daniel Situmeang[1], Zunan Faruq Ardiansyah[4]

[1]Department of Physics, Universitas Negeri Surabaya, Surabaya, 60231, Indonesia.
[2]Department of Chemistry, Universitas Negeri Surabaya, Surabaya, 60231, Indonesia.
[3]Department of Biology, Universitas Negeri Surabaya, Surabaya, 60231, Indonesia.
[4]Department of Geography, Universitas Negeri Malang, Malang, 65145, Indonesia.

*Corresponding author. Email: arierealita@unesa.ac.id

Manuscript received: 8 February 2026; Received in revised form: 28 May 2026; Accepted: 1 June 2026

Abstract

This study investigates the relationship between sulfur content in commercial fuels and metal corrosion behavior as an environmental indicator of sulfur exposure in urban and volcanic areas of East Java. The research aims to evaluate corrosion characteristics of iron materials immersed in various commercial fuels and to examine their potential relevance to regional sulfur-related atmospheric conditions. Corrosion experiments were conducted using iron spheres immersed for 21 days in several fuel types, including diesel, gasoline, Pertamax, Pertalite, and Pertasol variants. Sulfur characterization was performed using an Oil Sulfur Analyzer based on X-ray Fluorescence (XRF) principles, while corrosion rates were determined using the weight-loss method. The results indicate that fuels with higher sulfur content generally produced higher corrosion rates. Diesel fuel exhibited the highest corrosion rate (1.0300 mpy), while low-sulfur fuels such as Pertamax showed significantly lower corrosion behavior (0.4120 mpy). Spatial interpretation of sulfur-related environmental conditions in East Java suggests contrasting characteristics between urban regions dominated by anthropogenic fuel combustion and volcanic areas influenced by natural sulfur degassing. Estimated sulfur dioxide emissions and their associated radiative forcing values demonstrate that sulfur-rich fuels potentially contribute to greater atmospheric sulfur loading and sulfate aerosol formation. Overall, the findings suggest that metal corrosion indicators have potential applicability as supporting proxies for sulfur-related environmental assessment.

Keywords: Environmental assessment; Fuel sulfur; Metal corrosion indicators; Sulfur dioxide; Urban and volcanic environments.

Citation: Ramadhan, Y. D., Rahmawan, M. T., Haq, A., Maulidiyah, N. R., Noorlaksono, D. A., Realita, A., Madlazim, M., Fahmi, M. N., Situmeang, A. D., & Ardiansyah, Z. F. (2026). Metal Corrosion Indicators for Sulfur Exposure Assessment in Urban and Volcanic Areas of East Java. *Jurnal Geocelebes*, 10(2): 160–176, doi: 10.70561/geocelebes.v10i2.49863

Introduction

Sulfur dioxide (SO_2) is one of the major atmospheric pollutants generated from anthropogenic and geogenic activities and plays an important role in atmospheric chemistry, aerosol formation, environmental degradation, and climate-related processes (IPCC, 2021; Bond et al., 2013). Anthropogenic SO_2 emissions are primarily produced by fossil fuel combustion, industrial operations, and transportation sectors, whereas geogenic sulfur emissions mainly originate from volcanic degassing processes (Carn et al., 2017). Geological and geotechnical characteristics also influence environmental instability processes because weathering and erosion mechanisms may accelerate material

© 2026 Dept. of Geophysics Hasanuddin University

degradation and increase susceptibility to environmental disturbances under reactive surface conditions (Firoozi et al., 2024). In rapidly urbanizing tropical regions characterized by active volcanic systems, sulfur-related environmental dynamics become increasingly complex because urban-industrial emissions coexist with natural volcanic sulfur sources (Henley & Fischer, 2021). Sulfur dioxide oxidation processes in the atmosphere contribute to sulfate aerosol formation and atmospheric acidity under humid environmental conditions (Burns et al., 2016).

East Java represents one of the most environmentally dynamic regions in Indonesia because it combines densely populated urban-industrial corridors with active volcanic systems within the same regional environment (Ibrahim et. al., 2025). Urban areas such as Surabaya, Sidoarjo, and Gresik are characterized by intensive transportation activity, industrial fuel consumption, and increasing population density, all of which contribute to anthropogenic sulfur emissions (Crippa et al., 2020; World Bank, 2023). At the same time, southern and eastern parts of East Java are strongly influenced by active volcanic systems associated with the Sunda volcanic arc, including Mount Semeru, Bromo, Ijen, and the Lamongan volcanic field (Ibrahim et al., 2025). These volcanic systems are characterized by continuous volcanic activity, degassing processes, and sulfur-bearing gas emissions that contribute significantly to regional sulfur loading and atmospheric environmental dynamics in East Java (Carn et al., 2017; Moktikanana et al., 2024). The coexistence of anthropogenic sulfur emissions from urban-industrial activities and geogenic sulfur emissions from volcanic systems creates a mixed sulfur environment that potentially influences regional atmospheric conditions and environmental quality (Moktikanana et al., 2024).

Recent studies have widely investigated sulfur emissions, sulfate aerosol formation, atmospheric pollution, and urban environmental degradation (IPCC, 2021). Other studies have demonstrated that sulfur-containing compounds accelerate electrochemical degradation processes on metallic materials by destabilizing protective oxide layers and enhancing acidic oxidation mechanisms (Gao et al., 2022). Sulfur-bearing fuels may therefore create more aggressive corrosive environments and increase sulfur-related environmental exposure. In addition, atmospheric oxidation of sulfur dioxide contributes to sulfate aerosol formation, which influences atmospheric radiation scattering and environmental conditions (Kusumaningtyas et al., 2022).

Although sulfur emissions, corrosion mechanisms, and atmospheric sulfur dynamics have been studied separately, integrated studies combining fuel sulfur characterization, laboratory corrosion indicators, and sulfur related spatial environmental interpretation remain limited, particularly in tropical urban volcanic systems such as East Java (Granados-Bolaños et al., 2021). Previous studies have mainly focused on atmospheric monitoring, industrial emissions, volcanic degassing, or material corrosion independently, while comparative environmental interpretation integrating anthropogenic and geogenic sulfur systems has received less attention (Wang et al., 2024).

Metal corrosion behavior has potential applicability as a supporting physicochemical proxy for evaluating sulfur-related environmental characteristics because sulfur compounds intensify electrochemical oxidation processes on iron surfaces (Gao et al., 2022). Consequently, understanding the relationship between sulfur content, corrosion behavior, and sulfur-related environmental patterns is important for evaluating sulfur-related

© 2026 Dept. of Geophysics Hasanuddin University

environmental conditions in mixed urban–volcanic regions.

This study aims to evaluate the corrosion characteristics of iron materials exposed to different commercial fuels, analyze the relationship between fuel sulfur content and corrosion behavior, and examine sulfur-related environmental characteristics in urban and volcanic regions of East Java. Corrosion experiments were conducted using iron sphere immersion methods combined with sulfur characterization using an Oil Sulfur Analyzer based on X-ray Fluorescence (XRF) principles. The findings are expected to provide additional insights into the environmental implications of sulfur-containing fuels and the potential use of metal corrosion indicators as supporting proxies for sulfur-related environmental assessment.

Materials and Methods

Study Area

This study was conducted in urban and volcanic regions of East Java, Indonesia, representing environmental systems influenced by both anthropogenic and geogenic sulfur sources. Urban areas include Surabaya, Sidoarjo, Gresik, and Mojokerto, which are characterized by high population density, industrial activities, transportation intensity, and commercial fuel consumption. Volcanic regions include Malang Regency, Batu City, Pasuruan, and surrounding areas influenced by volcanic systems such as Mount Semeru, Bromo–Tengger, and Arjuno–Welirang. These volcanic systems continuously release sulfur-bearing gases through degassing processes and therefore contribute to regional atmospheric sulfur loading (Carn et al., 2017).

The selection of East Java was based on its environmental complexity, where urban-industrial emissions coexist with active volcanic sulfur emissions. This environmental setting provides an appropriate regional framework for evaluating sulfur-related environmental characteristics from an environmental geophysics' perspective (IPCC, 2021).

Fuel Sample Preparation

Seven commercial fuel samples were analyzed in this study, consisting of diesel fuel, gasoline, Pertamax, Pertalite, and Pertasol variants (CA, CB, and CC). All fuel samples were obtained from commercial distributors in East Java and stored in sealed laboratory containers to minimize contamination and evaporation prior to analysis.

Each fuel sample was prepared under identical laboratory conditions to ensure consistency during corrosion testing and sulfur characterization. Fuel samples were maintained at room temperature during the experimental period following laboratory fuel handling recommendations described in fuel chemistry studies (Gao et al., 2022).

Corrosion Rate Measurement

Corrosion experiments were conducted using spherical iron specimens with a diameter of 6.35 mm. Each iron sphere was immersed separately in individual fuel samples for 21 days under sealed conditions at room temperature to minimize external environmental influences such as humidity fluctuations and airborne contamination. Sulfur-bearing environments may accelerate oxidation behavior and metallic degradation processes under reactive conditions (Han et al., 2019).

Daily visual observations were performed to identify changes in surface appearance, oxidation intensity, and deposit formation. After the immersion period, the iron specimens were removed, cleaned using distilled water and ethanol, dried under controlled laboratory conditions, and weighed using a digital analytical balance. Corrosion processes on metallic materials are strongly influenced by acidic sulfur-

© 2026 Dept. of Geophysics Hasanuddin University

bearing environments that accelerate electrochemical oxidation reactions.

The corrosion rate was determined using the weight-loss method based on ASTM G31 standard principles for laboratory immersion corrosion testing. The corrosion rate equation is expressed as (ASTM G31-21, 2021):

$$\text{CR}\ (Corrosion\ Rate) = \frac{K\,.W}{\rho\,.\,A\,.t} \qquad (1)$$

where:

CR : corrosion rate (mm.year^{-1})
K : conversion constant (8.76×10^4 for mm.year^{-1} when W is expressed in grams)
W : mass loss of the metal due to corrosion (g)
ρ : metal density (g.cm^{-3})
A : exposed surface area of the metal (cm^2)
t : exposure time (h)

The corrosion rate values were used as physicochemical indicators representing the relative influence of sulfur-containing fuel environments on metallic degradation processes (Gao et al., 2022; ASTM G31-21, 2021).

Sulfur Characterization using Oil Sulfur Analyzer

Sulfur characterization of fuel samples was conducted using an Oil Sulfur Analyzer based on X-ray fluorescence (XRF) spectroscopy principles. This method enables qualitative to semi-quantitative identification of sulfur concentrations within liquid hydrocarbon matrices.

The XRF method operates through excitation of sulfur atoms by primary X-rays, producing secondary characteristic fluorescence emissions whose intensities are proportional to sulfur concentration (Skoog et al., 2017). The obtained sulfur concentration values were used to compare sulfur characteristics among different fuel types and to support interpretation of corrosion behavior.

The sulfur measurements in this study were intended for comparative environmental assessment rather than absolute atmospheric sulfur quantification.

Sulfur Emission Estimation

Potential sulfur dioxide (SO_2) emissions were estimated theoretically based on sulfur concentrations measured in fuel samples. The estimation assumes complete oxidation of sulfur during combustion processes according to stoichiometric sulfur oxidation principles described in atmospheric chemistry studies. The SO_2 emission estimation is expressed as (Seinfeld & Pandis, 2016):

$$SO_2 Emissions = Sulfur\ Content\ x\ 2\,.10^{-3} \qquad (2)$$

The total mass of sulfur dioxide emitted (M_{SO2}) was subsequently estimated by multiplying the calculated SO_2 emission value by the volume of the fuel sample used in the experiment. This simplified sulfur emission estimation approach follows sulfur mass balance concepts commonly applied in atmospheric environmental assessments, expressed as (IPCC, 2021):

$$Total\ emissions\ of\ SO_2(MSO_2) = SO_2 Emissions\ x\ sample\ volume = \cdots . g \qquad (3)$$

The estimated sulfur dioxide emissions were then converted into simplified sulfur-related radiative forcing indicators using sulfur aerosol forcing coefficients adapted from atmospheric aerosol forcing studies. The simplified radiative forcing relationship is expressed as (Haywood & Boucher, 2021):

$$RF = \frac{M_{SO_2}}{1\ x\ 10^9\ g}\ x\ (-0{,}3) W/m^2 \qquad (4)$$

where:

M_{SO2} : mass of SO_2 released (grams)
–0.3W/m^2 : approximate global mean negative radiative forcing coefficient associated with anthropogenic sulfate aerosols derived from SO_2

© 2026 Dept. of Geophysics Hasanuddin University

emissions (IPCC, 2021)

The negative radiative forcing coefficient reflects the cooling effect produced by sulfate aerosols formed through atmospheric oxidation of sulfur dioxide, which increases shortwave radiation scattering in the atmosphere (Seinfeld & Pandis, 2016). The resulting values therefore represent simplified relative sulfur-related atmospheric indicators rather than direct atmospheric SO_2 measurements or comprehensive climate-scale radiative transfer calculations (Loveridge et al., 2025).

This estimation approach was adapted from simplified sulfur emission relationships commonly used in atmospheric environmental assessments and aerosol forcing interpretation studies (IPCC, 2021).

Spatial Environmental Interpretation

Spatial interpretation of sulfur-related environmental conditions was conducted using regional sulfur distribution maps, population density information, and volcanic distribution data in East Java.

The sulfur distribution maps were interpreted as supporting environmental datasets to qualitatively compare sulfur characteristics between urban-industrial regions and volcanic regions. Population density data used in this study were obtained from the Ministry of Home Affairs of the Republic of Indonesia to support urban spatial interpretation and regional demographic analysis (Ministry of Home Affairs of the Republic of Indonesia, 2022). Volcanic distribution data were interpreted based on regional geological and volcanic frameworks of Java Island (van Bemmelen, 1949).

The spatial interpretation in this study was performed qualitatively and semi-quantitatively to distinguish anthropogenic sulfur signatures in urban regions from geogenic sulfur influences in volcanic regions. This approach emphasizes comparative environmental interpretation based on sulfur-related spatial patterns rather than applying complex atmospheric dispersion simulations, which generally require detailed meteorological parameters, advection–diffusion modeling, and computational atmospheric transport analysis (Leelőssy et al., 2018; Erfani & Mitchell, 2026). Therefore, the spatial assessment presented in this study was intended to support environmental characterization of sulfur-related conditions in East Java rather than conduct comprehensive atmospheric dispersion modeling (Granados-Bolaños et al., 2021).

Results and Discussion

At a regional scale, population density dynamics play a crucial role in shaping the interaction between anthropogenic activities, energy consumption, and atmospheric geophysical processes. Uneven population growth intensifies the demand for transportation, industrial operations, and commercial fuel usage, particularly in densely populated areas, thereby increasing the potential release of sulfur dioxide (SO_2) into the atmosphere. From a geophysical environmental perspective, population distribution functions as an important indicator of anthropogenic pressure on atmospheric composition, as high-density regions generally correspond to elevated emission intensities and altered atmospheric chemical processes. Consequently, population density mapping provides a critical demographic framework for interpreting SO_2 spatial distribution and proxies for assessing regional sulfur dynamics in East Java (Gao et al., 2022).

Based on the 2022 population density distribution map of Java Island shown in Figure 1, population concentration forms a continuous west–east urban corridor extending from the Jakarta metropolitan region in West Java to Surabaya and its surrounding industrial belt in East Java.

© 2026 Dept. of Geophysics Hasanuddin University

The highest density clusters are visible in the Jakarta–Bekasi–Karawang area, Bandung Basin, Semarang, and the Surabaya – Gresik – Sidoarjo corridor, reflecting strong metropolitan expansion, industrial agglomeration, and transportation network intensity. Recent demographic and urban assessments indicate that rapid urban concentration in Southeast Asia, including Indonesia, significantly increases energy demand and fossil fuel consumption, thereby intensifying anthropogenic air pollutant emissions (United Nations, 2022; World Bank, 2023). The strong coupling between urban density and emission intensity has also been emphasized in recent emission inventory studies showing that densely populated megacities contribute disproportionately to regional sulfur dioxide (SO_2) loading (Crippa et al., 2020).

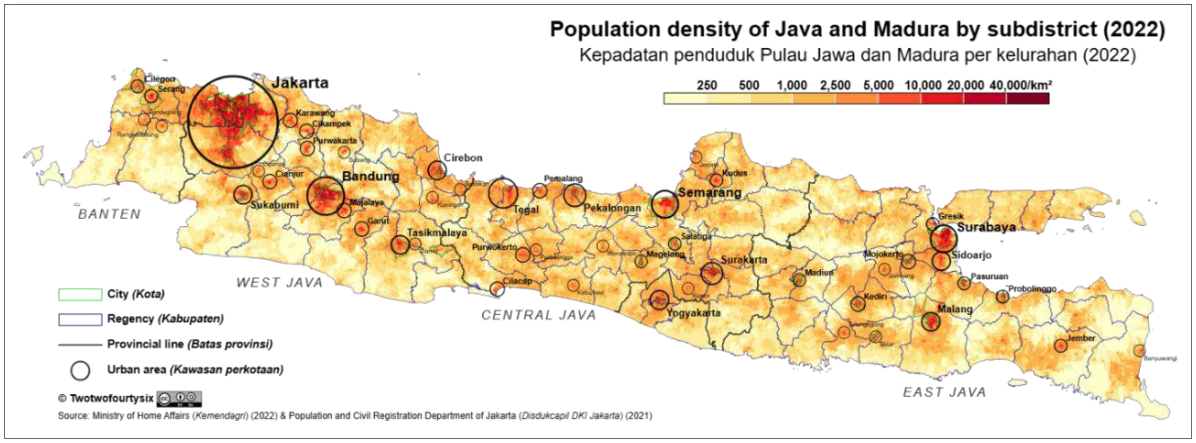


Figure 1. Distribution of population density in Java Island 2022 (Ministry of Home Affairs of the Republic of Indonesia, 2022).

In East Java specifically, the Surabaya metropolitan region exhibits high-density clustering consistent with industrial and port-centered development, which is closely linked to transportation-related fuel combustion. Contemporary air quality evaluations in Indonesian urban regions confirm that transportation and industrial fuel use remain dominant contributors to SO_2 variability in major cities (World Health Organization, 2021). In contrast, areas such as Malang and Pasuruan display moderate to high population densities but are situated along active volcanic corridors associated with Mount Semeru, Bromo, and Arjuno–Welirang. In these regions, atmospheric sulfur dynamics are influenced not only by anthropogenic combustion but also by persistent volcanic degassing, which has been identified as a major natural contributor to regional SO_2 emissions in Indonesia (Bani et al., 2022).

The coexistence of dense urban populations and active volcanic systems therefore creates a dual-source sulfur environment in East Java (Figure 2). Recent atmospheric chemistry assessments emphasize that interactions between anthropogenic emissions and natural volcanic inputs can amplify localized sulfate aerosol formation and alter regional radiative balance (IPCC, 2021). Consequently, the 2022 population density pattern across Java Island provides an essential demographic framework for interpreting spatial SO_2 variability, particularly when distinguishing purely urban emission signatures from mixed urban–volcanic atmospheric systems.

The distribution of volcanoes in East Java and Central Java Provinces follows a well-defined east–west alignment that corresponds to the active Sunda volcanic arc formed by the subduction of the Indo-Australian Plate beneath the Eurasian Plate (Wandono et al., 2025). This tectonic setting results in a high concentration of Quaternary volcanoes extending from Central Java (e.g., Merapi–Merbabu

© 2026 Dept. of Geophysics Hasanuddin University

volcanic complex) through East Java, including major volcanic systems such as Semeru, Bromo–Tengger, Kelud, Ijen, and Raung. These volcanoes are predominantly located along structural zones such as the Kendeng Zone and the Southern Mountains, where magmatic ascent is facilitated by crustal weaknesses (Berghuis et al., 2022). The spatial clustering of active and potentially active volcanoes in these regions makes them significant natural sources of sulfur dioxide (SO_2), continuously contributing to the regional atmospheric sulfur background through volcanic degassing. This geological configuration provides a critical geophysical context for interpreting sulfur anomalies observed in East Java, as illustrated by the elevated SO_2 concentrations mapped in the volcanic sector shown in Figure 3, where the correspondence between volcanic locations and high sulfur intensity highlights the strong influence of geogenic emissions on atmospheric sulfur distribution (Blessing et al., 2025).

The sulfur distribution patterns illustrated in Figure 3 reveal a clear spatial differentiation between urban areas and regions influenced by volcanic activity in East Java, which is closely related to variations in emission sources and fuel characteristics. As shown in Figure 1, urban centers such as Surabaya and Sidoarjo are characterized by relatively low SO_2 column densities, indicated by cooler color gradients. This pattern suggests that sulfur accumulation in these areas remains comparatively controlled despite high levels of industrial and transportation activity, reflecting the influence of low-sulfur fuel standards and improved combustion efficiency in urban environments (Anastasopolos et al., 2023).

A more detailed spatial representation in Figure 3 highlights localized increases in sulfur concentrations within several suburban and peri-urban industrial zones, indicating mixed contributions from local anthropogenic emissions and regional atmospheric transport. In contrast, the southern and highland regions associated with volcanic systems particularly around Malang, Malang City, and Batu City consistently exhibit elevated sulfur levels. The dominance of warmer color tones in these areas signifies substantial sulfur loading driven primarily by continuous volcanic degassing processes, which contribute significantly to the regional atmospheric sulfur background.

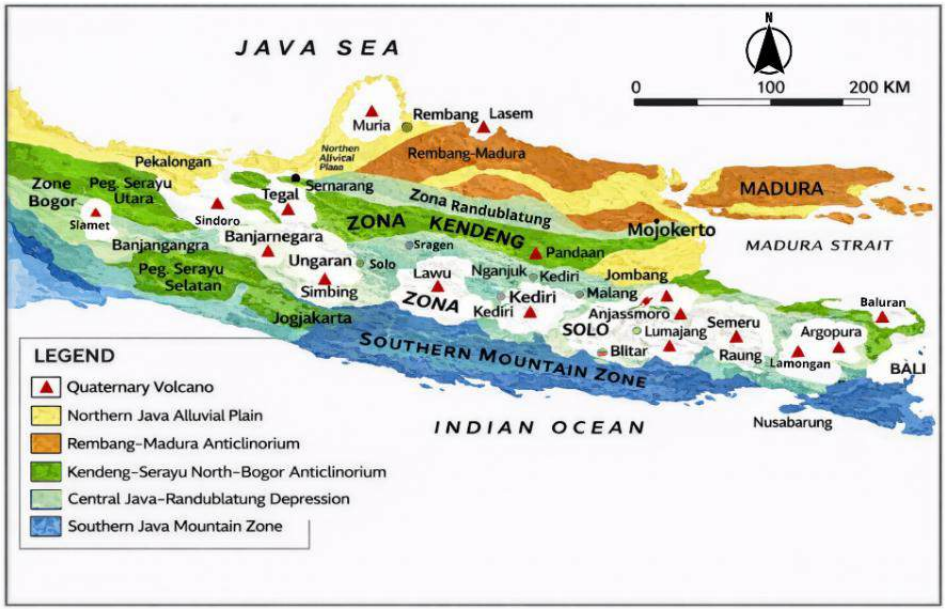


Figure 2. Distribution of Volcanoes in East Java and Central Java Provinces (modified from van Bemmelen, 1949).

© 2026 Dept. of Geophysics Hasanuddin University

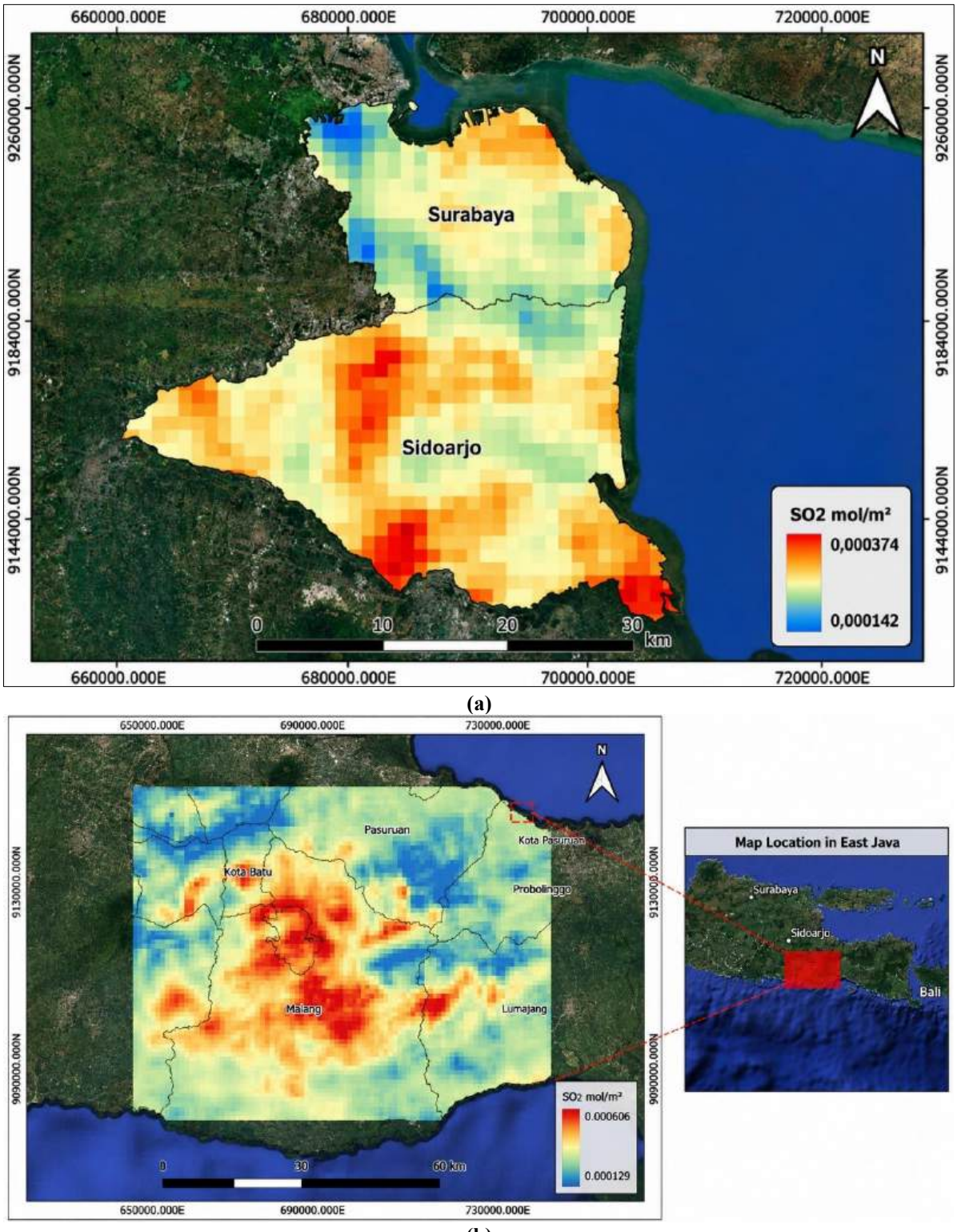


Figure 3. Sulfur Dioxide (SO_2) distribution map (a) Urban areas (b) Volcanic areas of East Java.

The experimental data presented in Table 1 and Figure 4 reveal distinct variations in corrosion rates among the tested fuel types, underscoring their differing impacts on iron degradation and their relevance as supporting indicators of sulfur-related environmental exposure. The measured corrosion rates (CR) range from 0.4120 to 1.0300 mpy, with diesel fuel exhibiting the highest value (1.0300 mpy), followed by Pertasol CC (0.8930 mpy) and Pertasol CA and CB (0.8240 mpy). Figure 4 clearly

© 2026 Dept. of Geophysics Hasanuddin University

illustrates this trend, showing a progressive increase in corrosion intensity from low-sulfur fuels toward sulfur-rich fuels. The graphical distribution highlights diesel fuel as the dominant corrosive medium, while Pertamax exhibits the lowest corrosion behavior among all tested samples. These differences reflect variations in sulfur concentration among commercial fuels and support the interpretation that corrosion behavior may provide physicochemical information regarding sulfur-related environmental conditions (Cao et al, 2023).

Table 1. Corrosion rate values for each fuel sample.

Type of Material	Diameter (cm)	Areas (cm^2)	T (Hour) (21 Days)	Initial Mass (gr)	Final Mass (gr)	Δm (gr)	Cr (mpy)
Pertasol CA	0.635	1.266	504	1.0311	1.0299	0.0012	0.8240
Pertasol CB	0.635	1.266	504	1.0311	1.0305	0.0012	0.8240
Pertasol CC	0.635	1.266	504	1.0311	1.0298	0.0013	0.8930
Diesel	0.635	1.266	504	1.0311	1.0301	0.0015	1.0300
Gasoline	0.635	1.266	504	1.0311	1.0210	0.0010	0.6870
Pertamax	0.635	1.266	504	1.0311	1.0305	0.0006	0.4120
Pertalite	0.635	1.266	504	1.0311	1.0301	0.0010	0.6870

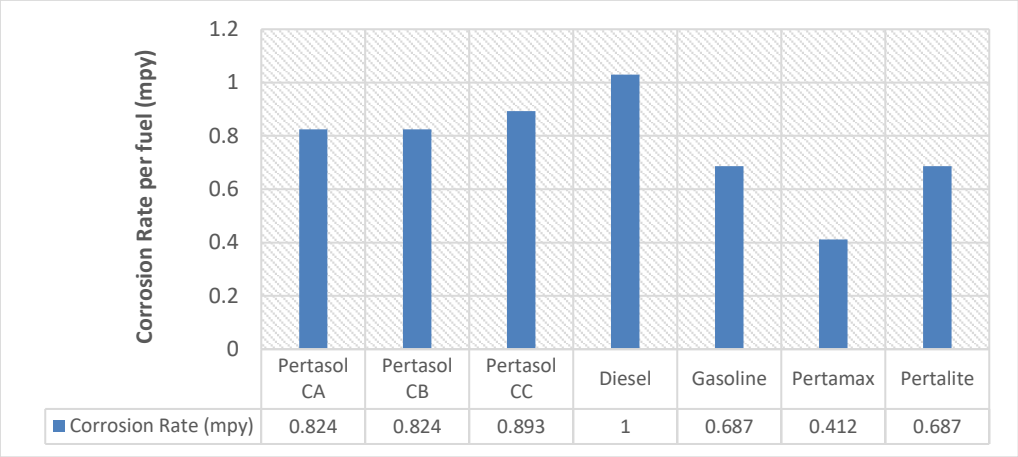


Figure 4. Graph of corrosion rate per fuel (mpy).

Diesel fuel demonstrates the most pronounced corrosive effect, consistent with its highest mass loss (Δm = 0.0015 g), indicating a more aggressive sulfur-bearing chemical environment (Nguyen & Vu, 2019). The sharp increase in corrosion rate observed in Figure 4 for diesel fuel suggests stronger electrochemical degradation processes compared to gasoline-based fuels. This behavior is associated with elevated sulfur fractions that may undergo oxidation to form sulfur dioxide (SO_2) and sulfur-derived acidic compounds under oxidizing and humid conditions, thereby accelerating electrochemical reactions at the metal surface (Schmitz & Linderholm, 2018). Sulfate ions may enhance electrochemical activity by increasing ionic conductivity and accelerating interfacial charge transfer kinetics on metallic surfaces under reactive conditions (Reddy et al., 2025). These electrochemical processes intensify metallic degradation behavior and indicate a potential relationship between sulfur-containing fuels, corrosion mechanisms, and sulfur-related environmental loading.

Similarly, Pertasol CA, CB, and CC exhibit intermediate to high corrosion rates (0.8240–0.8930 mpy), consistent with their relatively higher sulfur characteristics compared to gasoline-based fuels. Figure 4 demonstrates that the Pertasol fuels form a clustered corrosion pattern below diesel but substantially above Pertamax and gasoline

© 2026 Dept. of Geophysics Hasanuddin University

fuels, indicating moderate-to-high corrosive characteristics. Although Pertasol CA and CB present identical mass losses (Δm = 0.0012 g), the slightly greater mass reduction in Pertasol CC (Δm = 0.0013 g) produces a measurable increase in corrosion rate, emphasizing the sensitivity of metallic corrosion processes to subtle sulfur–metal chemical interactions. This trend is consistent with corrosion studies showing that sulfur-containing environments accelerate oxidation kinetics and electrochemical degradation processes on iron surfaces (Gao et al., 2022).

In contrast, low-sulfur fuels such as Pertamax and Pertalite display substantially lower corrosion rates, 0.4120 mpy and 0.6870 mpy respectively, accompanied by minimal mass loss (Δm = 0.0006–0.0010 g). Figure 4 further emphasizes the distinct reduction in corrosion intensity for Pertamax, which appears significantly lower than all other fuel samples. These findings indicate relatively improved chemical stability toward metallic materials and correspond to stricter sulfur regulation standards applied to modern fuel products. Low-sulfur fuels such as Pertamax and Pertalite exhibited lower corrosion rates, indicating improved chemical stability toward metallic materials and reduced sulfur-related degradation potential (Gao et al., 2022). Previous studies have demonstrated that sulfur-containing compounds promote anodic dissolution and destabilize protective oxide films on iron surfaces (Ottosson et al., 2018). Sulfur-derived ionic species may enhance electrochemical reaction kinetics by increasing interfacial charge transfer activity and ionic conductivity at the metal–fuel interface under reactive conditions (Reddy et al., 2025). Prolonged exposure to sulfur-bearing fuels may therefore intensify localized metallic degradation processes, including pitting corrosion and micro-galvanic interactions on iron surfaces.

The corrosion characteristics identified experimentally in Table 1 and visualized comparatively in Figure 4 can be qualitatively associated with the sulfur-related spatial patterns shown in Figure 3. Urban-industrial regions such as Surabaya and Sidoarjo display moderate sulfur-related anomalies associated with transportation activity, industrial combustion, and intensive commercial fuel utilization. In contrast, volcanic regions surrounding Malang, Pasuruan, and the Bromo–Semeru volcanic corridor exhibit relatively stronger sulfur-related spatial anomalies, which are interpreted as environmental indications of additional geogenic sulfur influence from volcanic degassing systems (Bani et al., 2022).

From an environmental geophysics' perspective, the coexistence of anthropogenic sulfur emissions from fuel combustion and natural volcanic sulfur emissions creates spatially variable sulfur exposure conditions across East Java. The laboratory corrosion results therefore provide supporting physicochemical evidence that fuels characterized by higher sulfur content possess greater potential to contribute to sulfur-related environmental loading under both urban and volcanic atmospheric systems (Cao et al., 2023). Figure 4 particularly supports this interpretation by demonstrating a consistent relationship between fuel type and corrosion intensity, where sulfur-rich fuels systematically produce greater metallic degradation compared to low-sulfur fuels.

However, it is important to emphasize that the corrosion experiment conducted in this study represents a laboratory-scale physicochemical assessment and does not directly measure atmospheric SO_2 concentration or atmospheric sulfur dispersion. Consequently, the sulfur-related spatial interpretation presented in Figure 3 should be regarded as supporting environmental context rather than direct validation of corrosion measurements.

© 2026 Dept. of Geophysics Hasanuddin University

The simplified sulfur-related atmospheric indicators calculated in this study show a consistent dependence on sulfur concentration, indicating that fuels with higher sulfur content possess greater potential to contribute to sulfur-related atmospheric loading through sulfate aerosol formation. Diesel fuel (950 ppm sulfur) produced the highest estimated sulfur dioxide emission potential (0.0009500 mol/m²) and the largest relative sulfur-related atmospheric indicator (-5.7×10^{-10} W/m²), whereas low-sulfur fuels such as Pertamax (18.6 ppm) generated substantially lower estimated sulfur emissions (0.0000186 mol/m²) and weaker atmospheric indicator values (-1.1×10^{-11} W/m²), as presented in Table 2.

Table 2. Radiative forcing value of each fuel sample (W/m²)

Material Type	Sulfur Content (ppm)	Emissions SO_2 (mol/m²)	Total SO_2 Emissions(mol/m²)	Radiative Forcing (W/m²)
Pertasol CA	182.2	0.3644	0.0001822	-1.093×10^{-10}
Pertasol CB	259.9	0.5198	0.0002599	-1.559×10^{-10}
Pertasol CC	306.3	0.6126	0.0003063	-1.837×10^{-10}
Diesel	950.0	1.9000	0.0009500	-5.700×10^{-10}
Gasoline	176.6	0.3532	0.0001766	-1.059×10^{-10}
Pertamax	18.6	0.0372	0.0000186	-1.116×10^{-11}
Pertalite	56.6	0.1132	0.0000566	-3.396×10^{-11}

This trend is consistent with atmospheric chemistry principles indicating that sulfur dioxide may undergo oxidation processes to form sulfate aerosols, which can increase shortwave radiation scattering and contribute to atmospheric cooling effects (Seinfeld & Pandis, 2016). At the global scale, sulfate aerosol forcing associated with anthropogenic sulfur emissions has been estimated to produce net negative radiative forcing on the order of −0.3 W/m² (IPCC, 2021), demonstrating that sulfur-derived aerosols influence atmospheric radiative balance.

However, the forcing-related values calculated in this study should not be interpreted as direct atmospheric radiative forcing measurements or comprehensive climate-scale forcing simulations. Atmospheric dispersion and radiative processes generally require complex advection–diffusion modeling, meteorological parameter integration, and large-scale atmospheric transport analysis to produce quantitative predictions (Alrammah et al., 2022; Leelőssy et al., 2018). Therefore, the obtained values in this study represent simplified relative environmental indicators derived from theoretical sulfur emission estimations based on fuel sulfur content and are intended only for comparative interpretation among fuel types rather than quantitative climate prediction (Darwish et al., 2025).

From a regional environmental perspective, fuels characterized by lower sulfur concentrations demonstrate relatively smaller sulfur-related atmospheric influence compared to sulfur-rich fuels (Dudziak et al., 2023). Reduced sulfur content may decrease sulfur dioxide emission potential and limit sulfate aerosol formation, thereby minimizing possible atmospheric and material degradation impacts under sulfur-related environmental exposure conditions (Liu et al., 2025).

When compared with the sulfur-related spatial patterns presented in Figure 3, the relative atmospheric indicator results demonstrate qualitative consistency with observed sulfur anomaly distributions in East Java. The volcanic sector shown in Figure 3(b) exhibits relatively stronger sulfur-related anomalies, particularly within the Malang–Pasuruan and Bromo–Semeru volcanic corridor, which is spatially associated with active volcanic sulfur degassing systems (Carn et al., 2017; Ibrahim et al., 2025). These volcanic

© 2026 Dept. of Geophysics Hasanuddin University

emissions contribute natural geogenic sulfur input capable of increasing regional sulfur background conditions independently of anthropogenic fuel combustion.

In contrast, the urban-industrial sector shown in Figure 3(a) demonstrates relatively moderate and spatially fragmented sulfur-related patterns across Surabaya and Sidoarjo. These spatial sulfur characteristics are interpreted as being associated with anthropogenic emission intensity driven by transportation density, industrial activities, and fuel consumption patterns in urban environments. Similar spatiotemporal emission studies have shown that urban atmospheric pollutant distributions are strongly influenced by human activities, industrial development, traffic density, and emission variability across metropolitan regions (Lou et al., 2025).

The comparison between urban and volcanic regions therefore illustrates a dual-source sulfur system in East Java, where anthropogenic fuel combustion and volcanic degassing jointly contribute to regional sulfur-related environmental characteristics. Sulfur-rich fuels potentially increase localized sulfur-related atmospheric influence, while volcanic systems contribute persistent natural sulfur background conditions that may enhance sulfate aerosol formation processes (Nwankwo & David, 2025).

From an environmental geophysics' perspective, the integration of corrosion behavior, sulfur characterization, simplified atmospheric indicators, and sulfur-related spatial interpretation provides a comparative framework for understanding sulfur-related environmental dynamics in East Java (Granados-Bolaños et al., 2021; Li et al., 2024). Nevertheless, it should be emphasized that the relationship established in this study is qualitative to semi-quantitative and does not represent direct atmospheric sulfur dispersion modeling or comprehensive radiative transfer simulation. Consequently, the interpretation presented here should be regarded as a supporting environmental assessment approach rather than a direct climate-scale atmospheric evaluation (Nisticò et al., 2025).

Conclusion

This study demonstrates that sulfur content in commercial fuels influences metallic corrosion behavior and contributes to sulfur-related environmental characteristics in East Java. Experimental results show that fuels with higher sulfur concentrations generally produced greater corrosion rates, with diesel fuel exhibiting the highest corrosion intensity (CR = 1.0300 mpy), while low-sulfur fuels such as Pertamax and Pertalite displayed substantially lower corrosion behavior. These findings support the interpretation that sulfur-bearing compounds contribute to electrochemical degradation processes on iron surfaces under sulfur-containing fuel environments.

The integration of sulfur characterization, corrosion measurements, simplified sulfur-related atmospheric indicators, and spatial environmental interpretation suggests that East Java represents a mixed sulfur system influenced by both anthropogenic fuel combustion and geogenic volcanic emissions (Ibrahim et al., 2025). Urban-industrial regions such as Surabaya and Sidoarjo are primarily associated with transportation and industrial sulfur emissions, whereas volcanic regions surrounding Malang and Pasuruan demonstrate additional sulfur influence related to volcanic degassing activity. The qualitative consistency between laboratory corrosion behavior and sulfur-related spatial patterns indicates that corrosion indicators may have potential applicability as supporting physicochemical proxies for comparative sulfur-related environmental assessment (Gao et al., 2022). In addition,

© 2026 Dept. of Geophysics Hasanuddin University

fuels characterized by lower sulfur concentrations demonstrated relatively smaller sulfur-related atmospheric implications, suggesting the importance of fuel sulfur reduction for minimizing environmental and material degradation effects. Nevertheless, this study represents a qualitative to semi-quantitative environmental assessment approach and does not constitute direct atmospheric sulfur dispersion modeling or comprehensive radiative transfer analysis (Haywood & Boucher, 2021). Future studies integrating direct atmospheric SO_2 observations, satellite-based monitoring, and atmospheric transport modeling are recommended to improve understanding of sulfur-related environmental dynamics in mixed urban–volcanic systems.

Acknowledgements

The authors would like to express their sincere gratitude to the lecturers of Physics Departmen, laboratory assistants, and technical staff of the Oil and Gas Laboratory (Laboratorium Migas) Cepu for their valuable support in fuel characterization, laboratory measurements, and data acquisition that significantly contributed to this research. The authors also gratefully acknowledge all supporting institutions, colleagues, and field assistants whose guidance, technical assistance, and encouragement contributed to the successful completion of this study. Special appreciation is extended to the reviewers and editors for their constructive comments, valuable suggestions, and insightful feedback, which significantly improved the scientific quality and clarity of this manuscript.

Author Contribution

Yuansyah Dhaniar Ramadhan: Conceptualization, Methodology, Investigation, Formal analysis, Data curation, Writing original draft. Muhammad Tegar Rahmawan: Investigation, Data curation, Validation. Ayunita Haq: Methodology, Investigation, Formal analysis. Nayla Rohmatul Maulidiyah: Investigation, Data curation. Daryll Alfaraby Noorlaksono: Software, Data curation, Visualization. Arie Realita: Conceptualization, Supervision, Writing, Review & Editing, Project administration. Madlazim: Methodology, Formal analysis, Writing, Review & Editing, Supervision. Muhammad Nurul Fahmi: Conceptualization methodology, Supervision. Adedio Daniel Situmeang: Spatial analysis, Sulfur distribution map interpretation, Visualization. Zunan Faruq Ardiansyah: Mapping visualization, Spatial imaging assistance, GIS support. All authors have read and approved the final version of the manuscript and agree to be accountable for the content of the work.

Conflict of Interest

The authors declare no conflict of interest

References

Alrammah, I., Saeed, I. M. M., Mhareb, M. H. A., & Alotiby, M. (2022). Atmospheric dispersion modeling and radiological environmental impact assessment for normal operation of a proposed pressurized water reactor in the eastern coast of Saudi Arabia. *Progress in Nuclear Energy*, 145, 104121. https://doi.org/10.1016/j.pnucene.2022.104121

Anastasopolos, A. T., Hopke, P. K., Sofowote, U. M., Mooibroek, D., Zhang, J. J. Y., Rouleau, M., Peng, H., & Sundar, N. (2023). Evaluating the effectiveness of low-sulphur marine fuel regulations at improving urban ambient PM2.5 air quality: Source apportionment of PM2.5 at Canadian Atlantic and Pacific coast cities with implementation of the North American Emissions Control Area. *Science of The Total Environment*, 904, 166965. https://doi.org/10.1016/j.scitotenv.20

© 2026 Dept. of Geophysics Hasanuddin University

23.166965

ASTM International. (2021). *ASTM G31-21: Standard Guide for Laboratory Immersion Corrosion Testing of Metals*. ASTM International. https://doi.org/10.1520/G0031-21

Bani, P., Oppenheimer, C., Tsanev, V., Scaillet. B., Primulayana, S., Saiing, U. B., Alfianti, H., & Marlia, M. (2022). Modest volcanic SO_2 emissions from the Indonesian archipelago. *Nature Communications*, 13, 3366. https://doi.org/10.1038/s41467-022-31043-7

Berghuis, H. W. K., van Kolfschoten, T., Adhityatama, S., Troelstra, S. R., Noerwidi, S., Suriyanto, R. A., Wibowo, U. P., Pop, E., Kurniawan, I., Hilgen, S. L., Veldkamp, A., & Joordens, J. C. A. (2022). The eastern Kendeng Hills (Java, Indonesia) and the hominin-bearing beds of Mojokerto, a re-interpretation. *Quaternary Science Reviews*, 294, 107716. https://doi.org/10.1016/j.quascirev.2022.107692

Blessing, M., Lerouge, C., Gal, F., Lahfid, A., Fléhoc, C., & Kloppmann, W. (2025). Geogenic greenhouse gas emissions and shale weathering: lessons learned from an alpine "eternal flame". *Science of The Total Environment*, 987, 179799. https://doi.org/10.1016/j.scitotenv.2025.179799

Burns, D. A., Aherne, J., Gay, D. A., & Lehmann, C. M. B. (2016). Acid rain and its environmental effects: Recent scientific advances. *Atmospheric Environment*, 146, 1–4. https://doi.org/10.1016/j.atmosenv.2016.10.019

Cao, X., Nan, F., Zhang, J., Chen, L., Gao, H., & He, W. (2023). Effect of sulfuric residual acid on the physicochemical properties, thermal behavior, and decomposition kinetics of nitrocellulose. *Thermochimica Acta*, 729, 179605. https://doi.org/10.1016/j.tca.2023.179605

Carn, S. A., Fioletov, V. E., McLinden, C. A., Li, C., & Krotkov, N. A. (2017). A decade of global volcanic SO_2 emissions measured from space. *Scientific Reports*, 7, 44095. https://doi.org/10.1038/srep44095

Crippa, M., Solazzo, E., Huang, G., Guizzardi, D., Koffi, E., Muntean, M., Schieberle, C., Friedrich, R., & Janssens-Maenhout, G. (2020). High-resolution temporal profiles in the Emissions Database for Global Atmospheric Research. *Scientific Data*, 7, 121. https://doi.org/10.1038/s41597-020-0462-2

Darwish, H., AlHmoud, I. W., Turlapaty, A. C., & Gokaraju, B. (2025). Predicting the future climate: Integrating renewable energy and machine learning to address temperature and GHG emissions. *Energy Reports*, 14, 2399–2419. https://doi.org/10.1016/j.egyr.2025.09.004

Dudziak, T., Rząd, E., Morgiel, J., Kirchner, A., Polczyk, T., Moskal, G., Klöden, B., Weißgärber, T., Toboła, D., & Wójcicki, M. (2023). Influence of a rich sulphur atmosphere on the phase development and kinetic behaviour of differentially processed RNT650 γ-TiAl alloys. *Journal of Materials Research and Technology*, 23, 1753–1760. https://doi.org/10.1016/j.jmrt.2023.01.120

Erfani, E., & Mitchell, D. L. (2026). Constraining a Radiative Transfer Model with Satellite Retrievals: Contrasts between cirrus formed via homogeneous and heterogeneous freezing and their implications for cirrus cloud thinning. *Atmospheric Chemistry and Physics*, 26(1), 523-546. https://doi.org/10.5194/acp-26-523-2026

© 2026 Dept. of Geophysics Hasanuddin University

Firoozi, A. A., & Firoozi, A. A. (2024). Water erosion processes: Mechanisms, impact, and management strategies. *Results in Engineering*, 24, 103237. https://doi.org/10.1016/j.rineng.2024.103237

Gao, J., Jia, S., Xu, Q., Wu, S., & Sui, H. (2022). Spontaneous combustion mechanism and influencing factors of sulfur corrosion products in petroleum refining equipment. *American Journal of Applied and Industrial Chemistry*, 6(2), 29–37. https://www.sciencepublishinggroup.com/article/10.11648/j.ajaic.20220602.12

Granados-Bolaños, S., Quesada-Román, A., & Alvarado, G. E. (2021). Low-cost UAV applications in dynamic tropical volcanic landforms. *Journal of Volcanology and Geothermal Research*, 410, 107143. https://doi.org/10.1016/j.jvolgeores.2020.107143

Han, X., Wang, Y., Peng, S., & Zhang, H. (2019). Oxidation behavior of FeCrAl-coated Zry-4 under high-temperature steam environment. *Corrosion Science*, 149, 45–53. https://doi.org/10.1016/j.corsci.2019.01.004

Haywood, J., & Boucher, O. (2000). Estimates of the direct and indirect radiative forcing due to tropospheric aerosols: A review. *Reviews of Geophysics*, 38(4), 513–543. https://doi.org/10.1029/1999RG000078

Henley, R. W., & Fischer, T. P. (2021). Sulfur sequestration and redox equilibria in volcanic gases. *Journal of Volcanology and Geothermal Research*, 414, 107181. https://doi.org/10.1016/j.jvolgeores.2021.107181

Ibrahim, K., Bijaksana, S., Abdurrachman, M., Sahara, D. P., Suryanata, P. B., Zulaikah, S., Wirawan, R., Harlianti, U., Widagdo, T. A. M., Fajar, S. J., Noya, Y., & Suandayani, N. K. T. (2025). Contrasting magmatic structures and tectonic controls from integrated gravity and magnetic data in the Bromo–Tengger–Semeru complex and the Lamongan Volcanic Field, East Java, Indonesia. *Journal of Volcanology and Geothermal Research*, 468, 108455. https://doi.org/10.1016/j.jvolgeores.2025.108455

IPCC. (2021). *Climate Change 2021: The Physical Science Basis*. Cambridge University Press. https://doi.org/10.1017/9781009157896

Kusumaningtyas, S. D. A., Tonokura, K., Aldrian, E., Giles, D. M., Holben, B. N., Gunawan, D., Lestari, P., & Iriana, W. (2022). Aerosols optical and radiative properties in Indonesia based on AERONET version 3. *Atmospheric Environment*, 282, 119174. https://doi.org/10.1016/j.atmosenv.2022.119174

Leelőssy, Á., Lagzi, I., Kovács, A., & Mészáros, R. (2018). A review of numerical models to predict the atmospheric dispersion of radionuclides. *Journal of Environmental Radioactivity*, 182, 20–33. https://doi.org/10.1016/j.jenvrad.2017.11.009

Li, X., Jia, J., Liu, C., Xu, Q., & Fan, X. (2024). Characterization of corrosion products formed on Q235 carbon steel and T2 copper in the Antarctic atmosphere. *Journal of Materials Research and Technology*, 29, 364–375. https://doi.org/10.1016/j.jmrt.2024.01.063

Liu, Z., Dai, Z., Song, X., Yang, L., Yu, F., & Chen, S. (2025) Swelling and chemical degradation of sulfur-bearing fillers in high-speed railway subgrade: Effect of pH on ion release and material deterioration. *Transportation Geotechnics*, 51,

© 2026 Dept. of Geophysics Hasanuddin University

101546. https://doi.org/10.1016/j.trgeo.2025.101546

Lou, Y., Chen, Y., Chen, X., & Li, R. (2025). Spatiotemporal estimates of anthropogenic NOx emissions across China during 2015–2022 using a deep learning model. *Journal of Hazardous Materials*, 487, 137308. https://doi.org/10.1016/j.jhazmat.2025.137308.

Loveridge, J. R., Fu, D., & Di Girolamo, L. (2025). Validating machine learning retrievals of the cloud-top droplet effective radius over oceans that account for 3D radiative transfer effects. *Journal of Geophysical Research: Atmospheres*, 130(23), e2025JD044317. https://doi.org/10.1029/2025JD044317

Ministry of Home Affairs & Population and Civil Registration Department of Jakarta (2022). *Population density map of Java and Madura by subdistrict (kelurahan) (2022)*.

Moktikanana, M. L. A., Ohba, T., Harijoko, A., Wibowo, H. E., Gurusinga, M. A., & Cahyani, S. M. (2024). Geology, chronology, and temporal evolution of basaltic to dacitic magma system in Raung volcano, East Java, Indonesia. *Journal of Volcanology and Geothermal Research*, 452, 108126. https://doi.org/10.1016/j.jvolgeores.2024.108126

Nguyen, X. P., & Vu, H. N. (2019). Corrosion of the metal parts of diesel engines in biodiesel-based fuels. *International Journal of Renewable Energy Development*, 8(2), 119-132. https://doi.org/10.14710/ijred.8.2.119-132

Nisticò, F., Messina, G., Quercioli, C., Errico, S., Fanti, E., Frilli, E., Postiglione, M., De Luca, A., D'Urso, A., & Nante, N. (2025). Can "fine scale" data on air pollution be an evaluation tool for public health professionals? *Atmospheric Pollution Research*, 16(6), 102487. https://doi.org/10.1016/j.apr.2025.102487

Nwankwo, N. E., & David, J. C. (2025). A review of sulfur-containing compounds of natural origin with insights into their pharmacological and toxicological impacts. *Discover Chemistry*, 2, 207. https://doi.org/10.1007/s44371-025-00286-w

Ottosson, M., Boman, M., Berastegui, P., Andersson, Y., Hahlin, M., Korvela, M., & Berger, R. (2018). Response to the comments by P. Szakálos, T. Åkermark and C. Leygraf on the paper "Copper in ultrapure water, a scientific issue under debate". *Corrosion Science*, 142, 308–311. https://doi.org/10.1016/j.corsci.2018.02.003

Reddy, I. N., Veerla, S. C., Bhargav, A., Dhanasekar, M., Shim, J., & Bai, C. (2025). Investigating the impact of sulfate (SO_4^{2-}) and hydroxide (OH^-) ions on photocurrent density and reaction kinetics in $WO_3/FeWO_4$ pyramid structures under illumination for electrochemical applications. *Journal of Alloys and Compounds*, 1032, 181203. https://doi.org/10.1016/j.jallcom.2025.181203.

Schmitz, M., & Linderholm, C. (2018). Chemical looping combustion of biomass in 10- and 100-kW pilots – Analysis of conversion and lifetime using a sintered manganese ore. *Fuel*, 231, 73–84. https://doi.org/10.1016/j.fuel.2018.05.071

Seinfeld, J. H., & Pandis, S. N. (2016). *Atmospheric Chemistry and Physics: From Air Pollution to Climate Change* (3rd ed.). Wiley. https://www.wiley.com/en-gb/Atmospheric+Chemistry+and+Physics%3A+From+Air+Pollution+to+Climate+Change%2C+3rd+Edition-p-9781118947401

© 2026 Dept. of Geophysics Hasanuddin University

Skoog, D. A., Holler, F. J., & Crouch, S. R. (2017). *Principles of Instrumental Analysis* (6th ed.). Cengage Learning.

United Nations. (2022). *World Urbanization Prospects: The 2022 Revision*. Department of Economic and Social Affairs, Population Division. United Nations, New York.

van Bemmelen, R. W. (1949). *The Geology of Indonesia*. Government Printing Office.

Wandono, W., Ramdhan, M., Aulia, A. N., Pangestu, A. B., Hidayat, E., Syuhada, S., Widiyantoro, S., Rawlinson, N., Anggono, T., Pranata, B., Mukti, M. M., & Maulana, M. P. (2025). Seismic velocity structure beneath the western Java region, Indonesia, from local earthquake tomography. *Journal of Volcanology and Geothermal Research*, 468, 108472. https://doi.org/10.1016/j.jvolgeores.2025.108472

Wang, C., Luo, A., Qu, S., Liang, X., Xiao, B., Mu, W., Wang, Y., & Yu, R. (2024). Anthropogenic processes drive spatiotemporal variability of sulfate in groundwater from a multi-aquifer system: Dilution caused by mine drainage. *Journal of Contaminant Hydrology*, 264, 104358. https://doi.org/10.1016/j.jconhyd.2024.104358

World Bank. (2023). *Indonesia Economic Prospects: Urbanization and Infrastructure Development*. World Bank.

World Health Organization. (2021). *WHO Global Air Quality Guidelines*. World Health Organization, Geneva.

© 2026 Dept. of Geophysics Hasanuddin University

ISSN: 2579-5821 (Print)
ISSN: 2579-5546 (Online)
URL address: http://journal.unhas.ac.id/index.php/geocelebes
DOI: 10.70561/geocelebes.v10i2.50664

Jurnal Geocelebes Vol. 10 No. 2, October 2026, 177 – 191

Integration of Ground Penetrating Radar (GPR) and Well Logging Data for Mapping Coal Seams in Pit "NS", South Palembang Sub-Basin

Neta Gresiana Santi Siregar[1]*, Andri Yadi Paembonan[1], Putu Pradnya Andika[1], M. Alamshah[2]

[1]Geophysical Engineering Study Program , Faculty of Industrial Technology, Sumatera Institute of Technology, Lampung 35365, Indonesia
[2]PT. Bukit Asam Tbk., Jl. Parigi No. 1, Tanjung Enim, Muara Enim, South Selatan 31716, Indonesia

*Corresponding author. Email: netasiregar13@gmail.com

Manuscript received: 17 April 2026; Received in revised form: 5 June 2026; Accepted: 12 June 2026

Abstract

Coal seam continuity is an important aspect in coal exploration and mine planning, particularly in the Muara Enim Formation, South Sumatra Basin, which is one of Indonesia's major coal-bearing formations. This study aims to identify and evaluate the lateral and vertical continuity of coal seams in Pit "NS", South Palembang Sub-Basin, by integrating Ground-Penetrating Radar (GPR), drill, and outcrop data. GPR data were acquired along four survey lines with lengths of 418 m, 611 m, 158 m, and 517 m using a 25 MHz antenna. The data were processed through static correction, dewow filtering, gain application, bandpass filtering, background removal, running-average filtering, and depth conversion using an electromagnetic-wave velocity of 0.14 m/ns. The processed radargrams show strong, continuous, high-amplitude reflectors interpreted as coal seams, supported by drill and outcrop observations. The interpreted coal seams occur at depths of approximately 5–42 m, with thicknesses ranging from 8 to 12 m, varying across the survey lines. The integration of GPR with geological control data improves the reliability of coal seam interpretation and demonstrates that GPR is effective for evaluating shallow coal seam continuity in the study area.

Keywords: Coal; Drilling Data; Ground Penetrating Radar (GPR); Outcrop.

Citation: Siregar, N. G. S., Paembonan, A. Y., Andika, P. P., & Alamshah, M. (2026). Integration of Ground Penetrating Radar (GPR) Method and Drill Data to Map Coal Seams in Pit "NS" South Palembang Sub-Basin. *Jurnal Geocelebes*, 10(2): 177–191, doi: 10.70561/geocelebes.v10i2.50664

Introduction

Coal constitutes one of Indonesia's strategic energy resources and remains an important commodity supporting domestic energy supply and industrial development. The South Sumatra Basin is recognized as one of Indonesia's major coal-producing regions, with the Muara Enim Formation hosting extensive, economically significant coal deposits (ESDM, 2023). Accurate delineation of coal seam geometry, thickness, and continuity is fundamental for resource estimation, mine planning, and operational decision-making. Although drilling and well logging provide reliable information regarding lithological characteristics and coal seam occurrence, these methods are inherently limited to discrete observation points and often fail to adequately characterize lateral seam continuity between boreholes (Ramadhana et al., 2022).

Ground Penetrating Radar (GPR) has been widely applied as a near-surface geophysical technique for subsurface imaging due to its ability to detect electromagnetic property contrasts between geological materials. In coal-bearing environments, differences in dielectric permittivity between coal and surrounding

© 2026 Dept. of Geophysics Hasanuddin University

lithologies generate distinctive reflection responses that can be utilized to delineate seam boundaries and geometry. Previous studies have demonstrated GPR's capability to identify coal seam distribution, estimate seam thickness, and map shallow subsurface structures with high spatial resolution (Ibrahim et al., 2018; Wahidah & Basid, 2018).

Despite the proven effectiveness of GPR for coal exploration, most studies have focused primarily on interpreting radargram reflection patterns without comprehensive integration with geological control data. Consequently, uncertainties may arise in distinguishing coal-related reflectors from other subsurface features and in evaluating seam continuity beyond localized observations. Furthermore, studies integrating GPR interpretation with borehole logs and outcrop observations within the coal-bearing sequences of the Muara Enim Formation remain relatively limited. The integration of these datasets has the potential to improve the reliability of interpretation by combining continuous geophysical imaging with direct geological evidence.

Accordingly, this study employs an integrated approach involving GPR data, borehole logs, and outcrop observations to evaluate the depth, thickness, geometry, and lateral continuity of coal seams in Pit "NS" in the South Palembang Sub-basin. By combining geophysical and geological information, this approach is expected to enhance the accuracy of coal seam delineation and provide a more representative characterization of coal distribution both vertically and laterally. The results are anticipated to contribute to resource evaluation, exploration activities, and mine planning within the Muara Enim Formation.

Material and Methods

Geological Setting

The study area is stratigraphically located within the Muara Enim Formation, which represents the principal coal-bearing formation in the South Sumatra Basin (Figure 1). The formation is generally composed of interbedded coal seams, claystone, mudstone, siltstone, sandstone, and locally limestone deposits, reflecting deposition in fluvial, delta plain, and shallow marginal marine environments (Nasution & Nalendra, 2017; Ramadhana et al., 2022).

To support coal seam identification, this study employed GPR, a near-surface geophysical method that utilizes electromagnetic waves to detect contrasts in subsurface electromagnetic properties. The method provides high-resolution information on subsurface conditions both laterally and vertically. Previous studies have demonstrated that GPR is effective for identifying coal seam geometry, boundaries, and continuity by analyzing electromagnetic wave reflection responses and correlating them with borehole data (Ibrahim et al., 2018).

The application of GPR in coal-bearing environments is particularly effective because coal generally exhibits different electromagnetic properties from the surrounding lithologies, resulting in distinct reflection responses on radargrams. These contrasts enable the delineation of coal seam boundaries and continuity with relatively high spatial resolution. Therefore, the interpretation of GPR data in this study was based on the analysis of electromagnetic wave propagation, attenuation, reflection characteristics, and depth conversion principles, which are described in the following section.

Ground Penetrating Radar (GPR)

Ground Penetrating Radar (GPR) is an active geophysical method that uses high-frequency electromagnetic waves, generally ranging from 10 MHz to 2 GHz, to image subsurface conditions (Čeru et al.,

© 2026 Dept. of Geophysics Hasanuddin University

2018). Ground Penetrating Radar has become one of the most widely applied near-surface geophysical methods because of its high resolution, rapid acquisition, and ability to characterize subsurface materials based on electromagnetic property contrasts (Rangole et al., 2024; Syam et al., 2019). In this study, a 25 MHz antenna was used because lower frequencies provide deeper penetration, allowing the method to reach depths of up to approximately 40 meters under suitable subsurface conditions. In GPR, there are various measurement configurations, one of which is the Continuous Reflecting Profiling (CRP) used in this study. This method operates by moving the GPR device along a predetermined path, maintaining a constant distance between transmitter and receiver (Figure 2). When waves propagate, they are distorted by variations in the material's electromagnetic properties such as conductivity, permeability, and dielectric permittivity. The dielectric constant of the medium in GPR greatly affects the speed, attenuation, reflection, refraction, and transmission of electromagnetic waves (Feng, 2023).

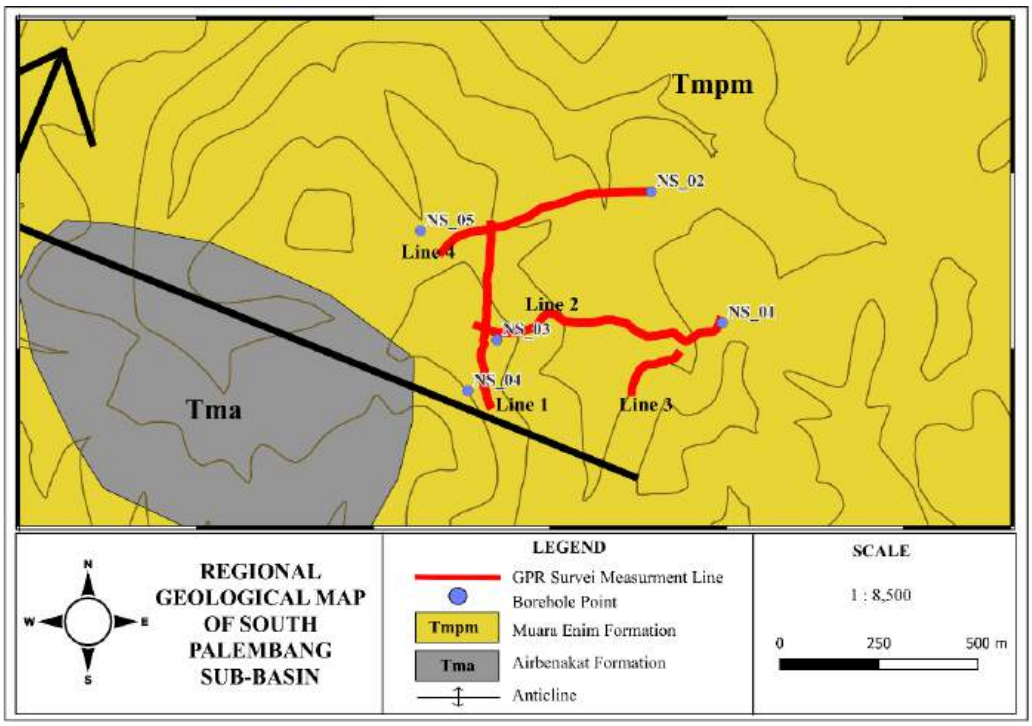


Figure 1. Regional geological map of South Sumatra showing the location of the 'NS' Field (Gafoer et al., 1986).

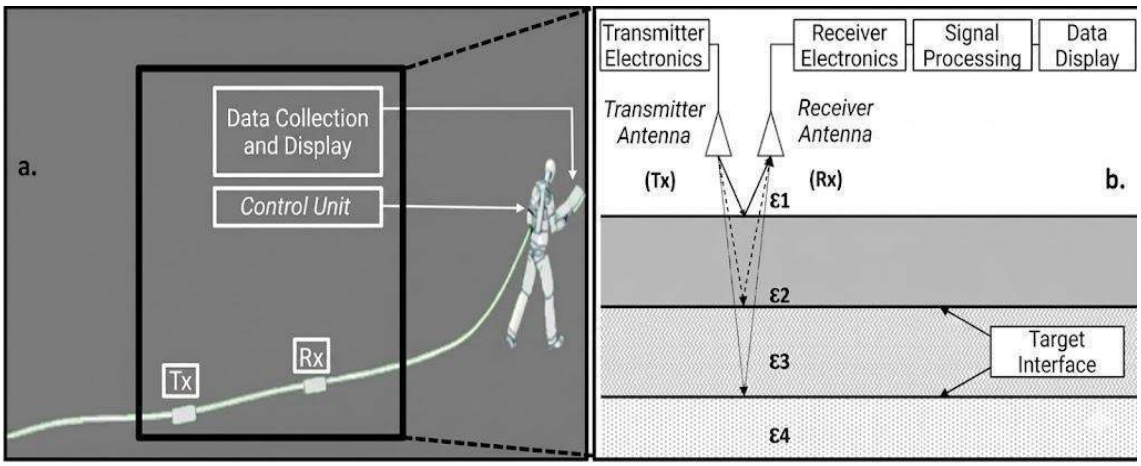


Figure 2. (a) Ground Penetrating Radar (GPR) data acquisition process in the field; (b) Schematic of the working principle of GPR based on the emission and reflection of electromagnetic waves (Daniels, 2004).

© 2026 Dept. of Geophysics Hasanuddin University

Electromagnetic waves used in Ground Penetrating Radar (GPR) are described by Maxwell's equations, which relate an electric field to a magnetic field. In the GPR method, the electromagnetic waves emitted propagate through the soil and reflect when they cross the boundary between layers with different electromagnetic properties. The difference in permittivity between the coal layer and the surrounding rocks produces a strong reflection on the radargram (Hamdaoui et al., 2020). Therefore, the interpretation of GPR data is based on analyzing reflection patterns to identify the presence and continuity of the coal seam. The conductivity of a material or rock can vary with time, temperature, pressure, and other environmental factors. In contrast to permittivity and electrical conductivity, permeability usually does not depend on the strength of the electric field but is more influenced by the magnetic field. The electromagnetic properties of a material are related to its composition and moisture content, which is the main controller of the propagation velocity and attenuation of electromagnetic waves in the material (Gao et al., 2021).

In the propagation of electromagnetic waves, especially when passing through different mediums, the amplitude of the signal will be attenuated due to energy loss as expressed in Equation (1). This occurs as a result of the reflection and transmission events that occur when radar waves pass through the boundary plane between mediums.

$$\alpha \approx \frac{\sigma}{2}\sqrt{\frac{\mu}{\varepsilon}};\ \sigma < \omega\varepsilon \qquad (1)$$

where (σ) is the electrical conductivity, (μ) is the magnetic permeability, (α) is the dielectric permittivity, and (ω) is the angular frequency (Daniels, 2004).

The penetration capability of electromagnetic waves is commonly represented by skin depth (δ) using Equation (2) defined as the depth at which the signal amplitude decreases to 1/e (37%) of its original value. Skin depth can be estimated using (Daniels, 2004):

$$\delta \approx 0{,}0053\frac{\sqrt{\varepsilon_r}}{\sigma};\sigma < \omega\varepsilon \qquad (2)$$

When GPR waves arrive at the interface of two layers with different dielectric properties, some of the energy is reflected to the surface. Propagation velocity and amplitude of the electromagnetic wave signal reflected in the survey GPR are strongly influenced by the relative dielectric constant contrast between adjacent rock layers (Putro et al., 2019). The reflection coefficient between two subsurface layers is calculated using Equation (3). The value of this reflection coefficient depends on the difference in the relative dielectric constant (ε) between the first layer (ε_1) and the second layer (ε_2). The magnitude of the reflection coefficient can be calculated using the following equation:

$$R = \frac{\sqrt{\varepsilon_2} - \sqrt{\varepsilon_1}}{\sqrt{\varepsilon_2} + \sqrt{\varepsilon_1}} \qquad (3)$$

The reflected signals recorded by the GPR system are initially represented in two-way travel time and must be converted into depth using an appropriate electromagnetic wave velocity model. The accuracy of depth estimation is strongly influenced by the selected propagation velocity (Ghazali et al., 2019). To obtain the actual depth of subsurface reflectors, the travel time must be converted into depth was performed using Equation (4). The depth conversion is expressed as:

$$z = \frac{v\,.\,t}{2} \qquad (4)$$

where (z) is the reflector depth (m), (v) is the electromagnetic wave velocity in the medium (m/ns), and (t) is the two-way travel time (ns). The division by two accounts for the travel path from the transmitting antenna to the reflector and back to the receiving antenna (Daniels, 2004). In this study, an average velocity of

© 2026 Dept. of Geophysics Hasanuddin University

0.14 m/ns was used based on the dielectric characteristics of coal and the surrounding lithologies.

Data and Processing Steps

This study was conducted in the operational area of PT "X", located within the South Palembang Sub-basin of the South Sumatra Basin. Stratigraphically, the study area belongs to the Muara Enim Formation, a Late Miocene–Pliocene coal-bearing unit that constitutes the principal coal-producing formation in the South Sumatra Basin. The formation is generally composed of interbedded claystone, siltstone, sandstone, carbonaceous mudstone, and coal seams deposited in fluvial to deltaic environments (Nasution & Nalendra, 2017). Locally, the main coal seam identified in the study area is Seam C (Petai Seam), with a thickness of 7.2 to 11.4 m and thin carbonaceous clay intercalations. The coal seam generally occurs at shallow to intermediate depths, while interpreted reflector depths from GPR data range from approximately 5 to 42 m, depending on topographic conditions and survey line orientation.

A total of 4 GPR survey lines were analyzed: Line 1 (418 m), Line 2 (611 m), Line 3 (158 m), and Line 4 (517 m). Data acquisition was performed using a 25 MHz Rough Terrain Antenna (RTA), selected for deeper penetration suitable for imaging coal seams to depths of approximately 40 m. Survey lines were determined based on borehole locations, interpreted seam continuity, and field accessibility conditions.

The penetration depth and resolution of GPR data are strongly influenced by antenna frequency. Lower-frequency antennas generally provide greater penetration depth but lower vertical resolution, whereas higher-frequency antennas provide higher vertical resolution but shallower penetration depth (Indelicato, 2017; Lombardi et al., 2022). Figure 3 describes the depth of penetration of GPR signals in various mediums.

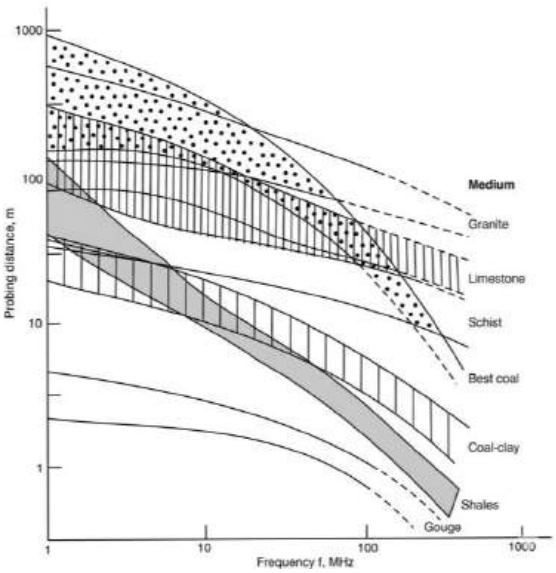


Figure 3. The depth of penetration of the GPR signal in the medium (Reynolds, 1997).

The use of 25 MHz antennas allows deeper penetration, but at the cost of lower vertical resolution. This causes the ability to distinguish thin layers to be limited, especially in layers with small thicknesses that have a reflection response like the surrounding lithology (Lai et al., 2018).

Meanwhile, the supporting data used are elevation data, aerial photos, outcrops, log borings, local geological maps, and local stratigraphic columns in the research area. The results of the GPR measurement will yield the resolution of the raw data, which will then be processed further to minimize the influence of any direct waves or tool-related errors during measurements in the research field.

Recent developments in GPR processing have shown that advanced signal enhancement techniques can significantly improve the reliability of reflector identification and interpretation (Afrasiabi et al., 2025). To obtain a reliable radargram for interpretation, the raw GPR data were processed using several sequential processing steps. The workflow employed in this study is presented in Figure 4.

© 2026 Dept. of Geophysics Hasanuddin University

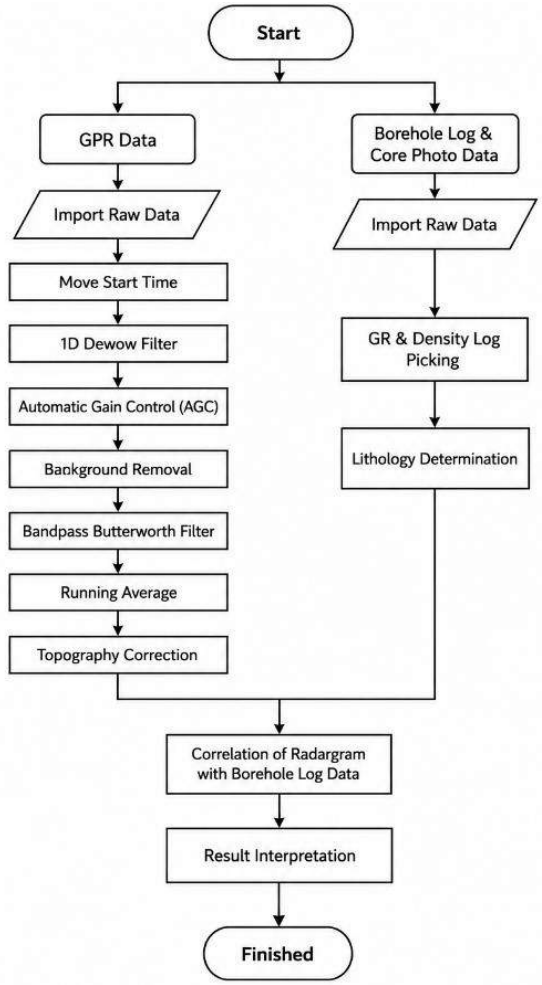


Figure 4. Workflow of integrated GPR and borehole log interpretation for coal seam analysis.

The processing workflow consisted of static correction, dewow filtering, Automatic Gain Control (AGC), bandpass filtering, background removal, running-average smoothing, and topographic correction. These procedures were applied to improve radargram quality and facilitate a more reliable interpretation of subsurface conditions. Overall, this processing stage aims to improve the quality of the data radargram so that the interpretation of subsurface conditions can be carried out more accurately (Afrasiabi et al., 2025; Rumansah et al., 2025; Zadhoush & Giannopoulos, 2021).

The GPR method for coal seam estimation applications is based on measuring electromagnetic wave reflection, which is directly proportional to the difference in dielectric permittivity (r) of the underlying medium. Electromagnetic waves are reflected when they encounter boundaries between materials with contrasting electromagnetic properties, allowing subsurface objects and lithological contacts to be identified from radargram reflections (Sugiarto et al., 2018). Depth conversion was performed using an average electromagnetic wave velocity of 0.14 m/ns based on the dielectric characteristics of coal and the surrounding lithologies. The value of 0.14 m/ns was selected based on previous Ground Penetrating Radar (GPR) investigations conducted in the same coal mining area of Tanjung Enim by Ibrahim et al. (2007). The study demonstrated that an electromagnetic wave velocity of 0.14 m/ns provided a representative approximation for coal-bearing formations and associated lithologies in the area. The following are the characteristic values for the Earth's material (Table 1).

Table 1. Characteristic values of dielectric constants (*K*) and velocity (v) for earth materials (Daniels, 2004).

Material	*K*	v (m/ns)
Air	1	0.3
Clay (wet)	8 – 15	0.086 – 0.11
Clay (dry)	3	0.173
Sandstone (wet)	6	0.112
Coal	4 – 5	0.134 – 0.15

Table 1 presents the dielectric permittivity and electromagnetic wave velocities of common subsurface materials used as references for GPR interpretation. Differences in the electromagnetic properties of coal and its surrounding lithologies generate reflection contrasts that can be identified on radargrams. Based on these characteristics, coal seams are generally interpreted as continuous, high-amplitude reflectors resulting from dielectric contrasts at lithological boundaries (Daniels, 2004).

To improve interpretation reliability and reduce ambiguity in reflector identification, GPR data were validated against borehole logs. Borehole logs provide direct

© 2026 Dept. of Geophysics Hasanuddin University

information on lithological variations and the occurrence of coal seams in the subsurface. In addition, well-log responses can be used to support lithological discrimination and depositional environment interpretation in coal-bearing formations (Setiawan et al., 2025). In this study, Borehole log interpretation was carried out using WellCAD software. Gamma-ray and density logs were analyzed to identify lithological boundaries and coal-bearing intervals by characterizing variations in radioactivity and bulk density. Gamma-ray logs are commonly used to distinguish clay-rich formations from cleaner lithologies, whereas density logs provide information on bulk density variations across different rock types. Coal intervals are typically characterized by low gamma-ray and density responses compared with surrounding sedimentary rocks, making them distinguishable from claystone and sandstone units (Setiahadiwibowo, 2017). In contrast, claystone generally exhibits high gamma ray values and higher density responses, while sandstone is characterized by relatively lower gamma ray values and moderate to high density responses. These characteristic log responses were used as reference markers for coal seam identification prior to correlation with GPR radargrams.

The integration of GPR, borehole logs, and outcrop observations enabled the validation of interpreted reflectors and provided a more reliable assessment of coal seam geometry, thickness, and lateral continuity throughout the study area.

The lithological characteristics summarized in Table 2 were subsequently used to correlate borehole log responses with GPR reflection patterns and outcrop observations.

Table 2. Rock log characteristics (Adrian & Mulyatno, 2020).

Material	Log characteristics	
	Gamma ray	Density
Sandstone	Slightly Low	Moderate
Coal	Low	Low
Clay	Moderate	Moderate

Results and Discussions

Well logging data are interpreted to identify the lithology and characteristics of the subsurface layer based on the rock's physical responses to specific parameters, such as gamma-ray values and density (Sujiman & Ramadhani, 2023). Based on gamma-ray log interpretation, coal seams are characterized by relatively low gamma-ray values, indicating a lower concentration of naturally radioactive materials compared to clay-rich lithologies. In addition, density logs show lower density values for coal than for the surrounding claystone and sandstone units, enabling clear seam identification (Farahdila & Setiawan, 2023).

The interpretation of borehole logs at NS-01 and NS-03 was conducted using gamma ray and density log responses to identify lithological boundaries and coal seam intervals. The interpreted lithological sequence and coal seam distribution for both boreholes are presented in Figure 5.

© 2026 Dept. of Geophysics Hasanuddin University

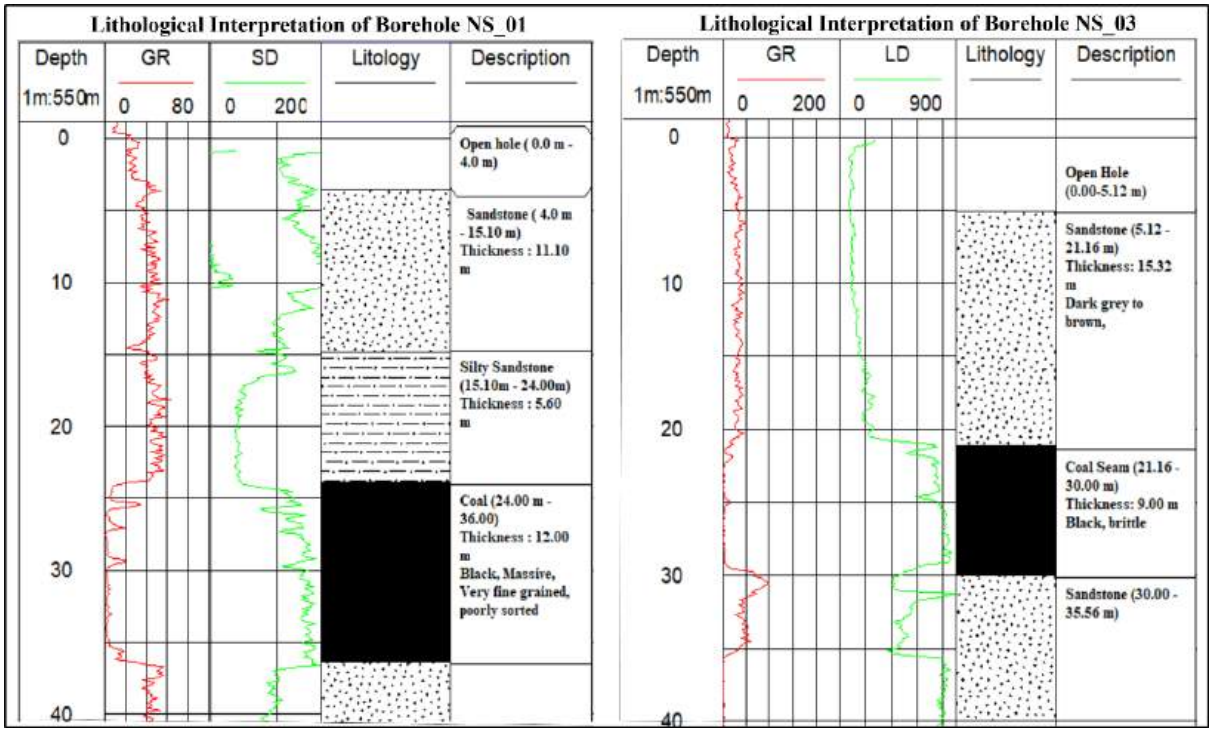


Figure 5. Lithological interpretation of boreholes NS-01 and NS-03 derived from gamma ray and density logs, indicating the depth and thickness of the interpreted coal seams.

The borehole log interpretation successfully identified coal seam intervals based on characteristic low gamma-ray and low-density responses. Coal seams and surrounding lithologies identified in the borehole logs were verified through visual examination of the corresponding core photographs. The validation process involved correlating the interpreted GPR reflectors with the depth and thickness of coal seams observed in the borehole records and confirmed by core documentation. These data provide reliable information regarding coal seam depth, thickness, and lithological variations at each borehole location. However, borehole logs capture vertical conditions at discrete points and cannot fully capture the lateral continuity of the coal seam between boreholes. Therefore, GPR data were integrated to extend the interpretation laterally and evaluate coal seam geometry and continuity throughout the study area. The processed GPR radargrams provide two-dimensional images of subsurface reflection patterns, with the vertical axis representing two-way travel time and depth, and the horizontal axis representing survey distance along each profile. Coal seams are interpreted as continuous high-amplitude reflectors resulting from contrasts in electromagnetic properties between coal and the surrounding lithologies. Similar interpretation approaches based on reflector continuity and amplitude contrast have been successfully applied in previous GPR studies (Jannah et al., 2024). Variations in reflector continuity, depth, and geometry observed along the survey lines are influenced by topographic conditions, survey-line orientation relative to seam strike, and local geological factors such as erosion and structural deformation. The interpretation results for each survey line are presented in the following sections.

Line 1 is oriented south–north and located in the western part of the study area, with a survey length of 418 m running subparallel to the coal seam strike (Figure 6). Three high-amplitude reflector zones were identified at depths of approximately 21–30 m and interpreted as Seam C based on reflector continuity, amplitude characteristics, and correlation with borehole NS_03 and outcrop data. The

© 2026 Dept. of Geophysics Hasanuddin University

seam has an estimated thickness of approximately 9 m.

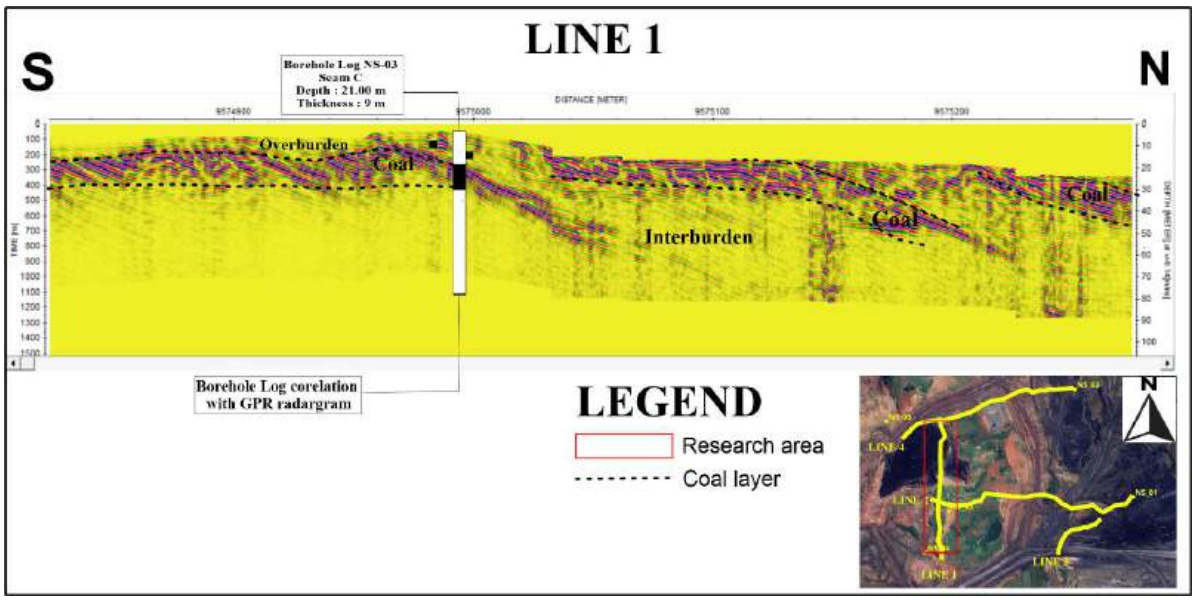


Figure 6. Interpretation of the GPR radargram of Line 1 showing strong amplitude reflectors interpreted as coal seams at depths of 21–30 m.

The strong, continuous reflections are attributed to the significant dielectric contrast between coal and the surrounding claystone and mudstone units, which serve as overburden and interburden. Coal exhibits lower dielectric permittivity and conductivity, producing a more distinct reflection response than the adjacent lithologies. Correlation with borehole data shows a depth difference of only 1–2 m, indicating good agreement between GPR interpretation and subsurface geological conditions. Reflector continuity decreases in the central part of the profile, while strong reflections persist in the southern and northern sections. This pattern is interpreted as the result of local erosion and topographic variation near the outcrop zone, suggesting that the seam was originally continuous but has been partially modified by post-depositional processes.

Line 2 is oriented west–east with a survey length of 611 m and exhibits a laterally continuous high-amplitude reflector zone at depths of approximately 24–36 m (Figure 7). Based on reflector continuity, amplitude characteristics, and correlation with borehole data NS_01 this reflector is interpreted as Seam C with an estimated thickness of 11–12 m. The strong reflection response is attributed to the significant dielectric contrast between coal and the surrounding claystone and mudstone units, allowing the coal seam to be clearly distinguished from the overburden and interburden lithologies.

The interpreted seam exhibits better lateral continuity than that observed along Line 1, suggesting relatively stable depositional conditions and limited erosional influence. Similar high-amplitude and continuous reflector patterns associated with coal seams have been reported in previous GPR studies (Ibrahim et al., 2018). The reflection response becomes weaker toward the eastern part of the profile, which is interpreted as the effect of increasing topographic elevation and mining excavation activities in the mine front area. These conditions cause the coal seam to occur at greater relative depths and locally affect reflector continuity on the radargram.

© 2026 Dept. of Geophysics Hasanuddin University

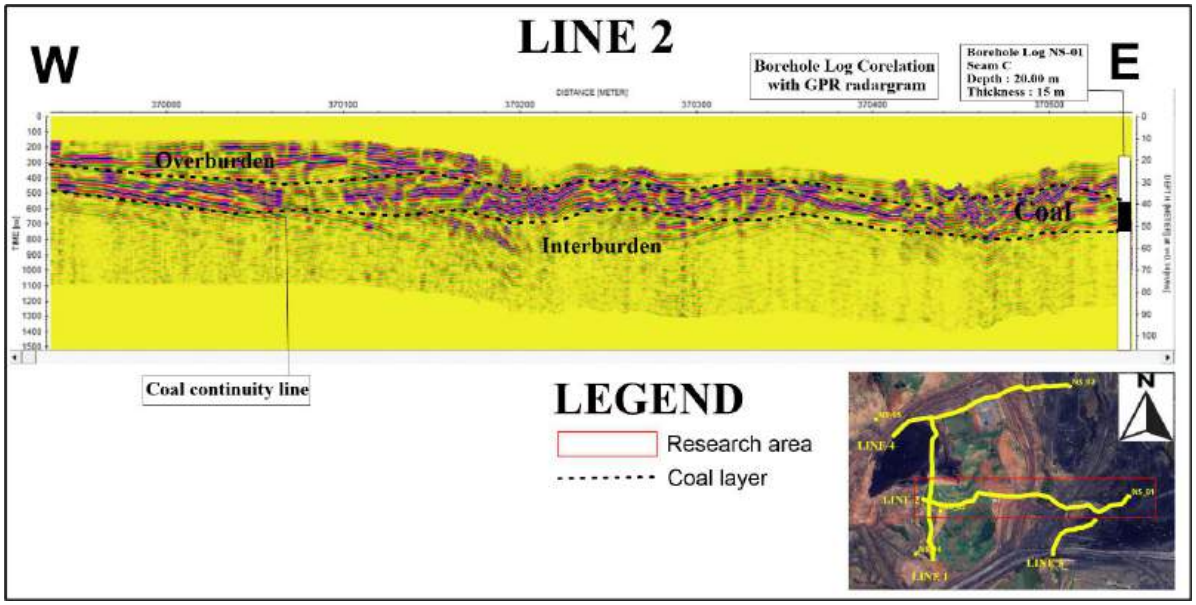


Figure 7. Interpretation of the GPR radargram of Line 2 showing a relatively continuous high-amplitude reflector interpreted as a coal seam at depths of 24–36 m with an estimated thickness of 11–12 m.

Line 3 has a survey length of 158 m and identified two potential coal zones at depths of approximately 5–13 m, characterized by medium- to high-amplitude reflectors (Figure 8). These reflections are interpreted as coal-bearing intervals due to their relatively strong amplitudes compared to the surrounding overburden and interburden lithologies. One reflector zone is supported by field observations and is therefore interpreted with higher confidence, whereas the second zone remains tentative because of its limited lateral continuity. Compared to Lines 1 and 2, reflector continuity along Line 3 is relatively poor. This is primarily attributed to changes in survey orientation, which shifts from south–north to southwest–northeast along the profile. Such variations reduce the consistency of reflector imaging and complicate seam correlation along the survey line. Consequently, although potential coal-bearing zones can be identified, Line 3 is considered less representative for evaluating coal seam geometry and continuity.

Line 4 has a total length of 517 m and is oriented approximately west–east, intersecting the coal seam strike direction. Field measurements indicate a strike of 350° and a dip of 8°, suggesting that the coal seam trends nearly north–south and dips gently (Table 3). Because the survey line is oriented nearly perpendicular to the strike direction, the radargram provides a representative cross-sectional view of the coal seam geometry and depth variation along the profile.

Table 3. Strike and Dip measurements along GPR survey Line 4.

Strike (°)	Dip (°)
350	8

Two coal zones characterized by strong and continuous reflection contrasts were identified in the western and eastern sections of the radargram (Figure 9). Correlation with borehole data shows that the interpreted reflector depths differ by less than 1 m from the drilled coal seam intervals, indicating good agreement between GPR interpretation and subsurface lithology. The interpreted coal seam thickness ranges from approximately 10 to 11 m and is further supported by outcrop observations that confirm the upper and lower boundaries of Seam C.

© 2026 Dept. of Geophysics Hasanuddin University

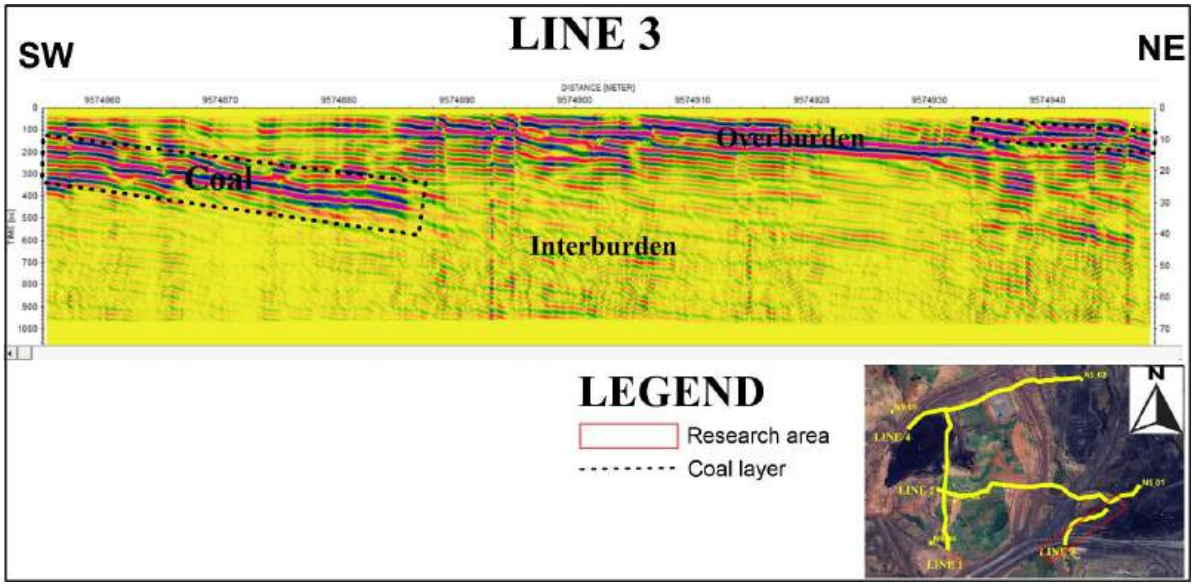


Figure 8. Interpretation of the GPR radargram of Line 3 two coal zones characterized by medium to high amplitude reflectors at depths of approximately 5–13 m.

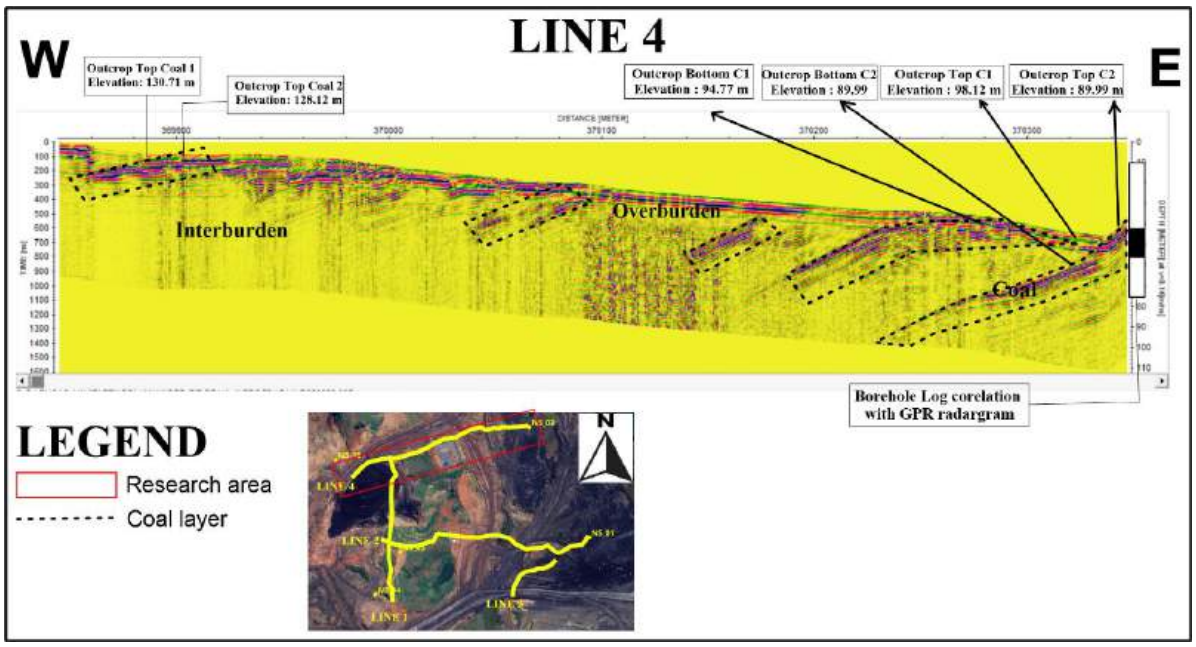


Figure 9. Interpretation of the GPR radargram of Line 4 showing strong amplitude reflectors interpreted as coal seams with an estimated thickness of 10–11 m.

The measured dip angle of 8° indicates that the coal seam is relatively gently inclined, which is consistent with the generally continuous reflector geometry observed along the profile. However, the absence of a strong reflector in the central portion of the radargram suggests an interruption in seam continuity. This discontinuity is interpreted as associated with topographic erosion rather than significant structural deformation, as the low dip value indicates only a minor bedding inclination. The decreasing topography along the survey line likely contributed to erosion of the coal seam in the central section, leading to the apparent separation of the western and eastern coal zones.

Overall, the interpretation of the four GPR survey lines indicates that Seam C is present throughout the study area with varying depths and lateral continuity (Table 4). The interpreted coal seam occurs at depths of approximately 5–42 m and has a

© 2026 Dept. of Geophysics Hasanuddin University

thickness of about 8–12 m. Comparison with borehole log data shows good agreement in both seam depth and thickness, confirming the reliability of the interpreted reflectors. Variations in reflector continuity observed along several survey lines are interpreted to be influenced by local topographic conditions and erosional processes. These results demonstrate that integrating GPR and borehole data provides a representative characterization of coal seam geometry and continuity within the study area.

Table 4. Interpretation of Coal Layer Geometry.

Survey Line	Direction	Line Distance (m)	Coal Seam Interpreted from GPR		Coal Seam Interpreted from Log	
			Depth (m)	Thickness (m)	Depth (m)	Thickness (m)
1	N – S	418	21 – 30	9 – 10	21.16 – 30	9
2	W – E	611	24 – 36	11 – 12	24 – 36	12
3	SW – NE	158	5 – 13	8 – 10	–	–
4	W – E	517	31 – 42	10 – 11	31.22 – 42.88	11.66

Conclusion

This study demonstrates that Ground Penetrating Radar (GPR) successfully identified and delineated Seam C within the Muara Enim Formation by detecting continuous high-amplitude reflectors generated by contrasts in electromagnetic properties between coal and surrounding lithologies. The interpreted coal seam was identified at depths of 5–42 m, with an estimated thickness of 8–12 m, indicating that GPR can image the geometry and continuity of near-surface coal seams.

The interpreted reflector depths show very good agreement with borehole logs, cores, and outcrop data, with depth discrepancies generally less than 1 m. This result indicates a high level of correlation between GPR interpretation and geological observations, confirming the reliability of the interpreted coal seam boundaries and reducing uncertainty in subsurface characterization.

Unlike previous studies that primarily focused on coal seam detection based on radargram responses, this study emphasizes evaluating coal seam continuity through the integration of GPR, gamma-ray, and density logs, core data, and outcrop observations. The integrated interpretation not only confirms the presence of coal but also provides a more representative characterization of seam geometry, lateral continuity, and distribution patterns.

Acknowledgements

The authors would like to thank PT Bukit Asam (Persero) Tbk and the Exploration Work Unit for the opportunity, support, and permission to publish this research, which was conducted as part of a final-year project internship.

The authors also gratefully acknowledge the Geophysical Engineering Study Program at Sumatera Institute of Technology for its academic guidance, valuable discussions, and continuous support throughout the research process. The faculty members' constructive insights and encouragement have greatly contributed to the development and completion of this work.

Author Contribution

Neta Gresiana Santi Siregar was responsible for studying conceptualization, the research, data processing and analysis, and writing the manuscript, and Andri Yadi Paembonan supervised the research, provided critical guidance throughout the research process, and contributed to the interpretation of the results. Putu Pradnya Andika provided expertise in data analysis, contributed to

© 2026 Dept. of Geophysics Hasanuddin University

data interpretation, and provided valuable insights during manuscript preparation. M. Alamshah provided the data and served as field supervisor during the data acquisition process. All authors contributed to the writing and revision of the manuscript.

Conflict of Interest

The authors declare that they have no conflicts of interest relevant to the content of this publication.

References

Adrian, D., & Mulyatno, B. S. (2020). Identifikasi dan Estimasi Sumber Daya Batubara Menggunakan Metode Poligon Berdasarkan Intepretasi Data Logging pada Lapangan ”Ada”, Sumatera Selatan. *Jurnal Geofisika Eksplorasi*, 4(1), 73–87. https://doi.org/10.23960/jge.v4i1.8

Afrasiabi, A. F., Faramarzi, A., Chapman, D., & Keshavarzi, A. (2025). Optimising Ground Penetrating Radar data interpretation: A hybrid approach with AI-assisted Kalman Filter and Wavelet Transform for detecting and locating buried utilities. *Journal of Applied Geophysics*, 232, 363–370. https://doi.org/10.1016/j.jappgeo.2024.105567

Čeru, T., Dolenec, M., & Gosar, A. (2018). Application of Ground Penetrating Radar Supported by Mineralogical-Geochemical Methods for Mapping Unroofed Cave Sediments. *Remote Sensing*, 10(4), 639. https://doi.org/10.3390/rs10040639

Daniels, D. J. (2004). *Ground Penetrating Radar (2nd ed.)*. London: The Institution of Engineering and Technology. https://doi.org/10.1049/PBRA015E

ESDM. (2023). *Handbook of energy and economic statistics of Indonesia 2023*. https://www.esdm.go.id/assets/media/content/content-handbook-of-energy-and-economic-statistics-of-indonesia-2023.pdf

Farahdila, S., & Setiawan, B. (2023). Pemodelan Sebaran Ketebalan Batubara dan Sumberdata Batubara pada Tambang SBJ di PT. Bukit Asam Tanjung Enim, Sumatera Selatan. *Jurnal Penelitian Sains*, 25(3), 233–241. https://doi.org/10.56064/jps.v25i3.866

Feng, D., Liu, Y., Zhang, B., & Wang, X. (2023). Special Issue on Ground Penetrating Radar: Theory, Methods, and Application. *Applied Sciences*, 13(17), 9847. https://doi.org/10.3390/app13179847

Gafoer, S., Cobrie, T., & Purnomo, J. (1986). *Peta Geologi Lembar Lahat, Sumatra Selatan*, *Skala 1:250.000*. Pusat Survei Geologi. https://geologi.esdm.go.id/geomap//pages/preview/peta-geologi-lembar-lahat-sumatera-selatan

Gao, L., Dachena, C., Wu, K., Fedeli, A., Pastorino, M., Randazzo, A., Wu, X., & Lambot, S. (2021). Full-Wave Modeling and Inversion of UWB Radar Data for Wave Propagation in Cylindrical Objects. *Remote Sensing*, 13(12), 2370. https://doi.org/10.3390/rs13122370

Ghazali, R., Rasam, A. R. A., Razali, M. H., Razali, R., & Latif, Z. A. (2019). Estimation of different subsurface materials depth using Ground Penetrating Radar. *International Journal of Advanced Trends in Computer Science and Engineering*, 8(1.3), 363–370. https://doi.org/10.30534/ijatcse/2019/6581.32019

Hamdaoui, M., Faize, A., Rochdi, M., & Alsharahi, G. (2020). Effect of electromagnetic parameters of the medium on the GPR data. *International Journal of Emerging Trends in Engineering Research*, 8(5), 1749–1755.

© 2026 Dept. of Geophysics Hasanuddin University

https://doi.org/10.30534/ijeter/2020/42852020

Ibrahim, E., Basri, H., & Alam, I. S. (2007). Penggunaan Metode GPR dan Geolistrik Pada Eksplorasi Batubara. *Prosiding Seminar Nasional XIII - FTI-ITS*, 436-1–436-8. https://repository.unsri.ac.id/9496/1/Penggunaan_Metode_GPR_dan_Geolistrik_Pada_Eksplorasi_Batubara_SNTI_XIII_ITS_2007.pdf

Ibrahim, E., Maulana, Y., & Hendrajaya, L. (2018). New method of Ground Penetrating Radar for delineation and mapping of shallow coal seam. *International Conference on Natural Resources and Sustainable Development*, 107–111. https://doi.org/10.5220/0009898400002480

Indelicato, A. (2017). The Impact of Frequency in Surveying Engineering Slopes Using Ground Penetrating Radar. *International Journal of Geosciences*, 8(3), 296–304. https://doi.org/10.4236/ijg.2017.83014

Jannah, A. N., Faqih, A., Dita, M. S. A., Juliandro, D., Rahayu, H. K., & Lestari, W. (2024). Identifikasi kemenerusan pipa air bawah permukaan menggunakan metode Ground Penetrating Radar (GPR). *Jurnal Geosaintek*, 10(1), 22–29. http://dx.doi.org/10.12962/j25023659.v10i1.19187

Lai, W. W.-L., Dérobert, X., & Annan, P. (2018). A review of Ground Penetrating Radar application in civil engineering: A 30-year journey from Locating and Testing to Imaging and Diagnosis. *NDT & E International*, 96, 58–78. https://doi.org/10.1016/j.ndteint.2017.04.002

Lombardi, F., Podd, F., & Solla, M. (2022). From Its Core to the Niche: Insights from GPR Applications. *Remote Sensing*, 14(13), 3033. https://doi.org/10.3390/rs14133033

Nasution, F., & Nalendra, S. (2017). Characterization of Coal Quality based on Ash Content From M2 Coal-Seam Group, Muara Enim Formation, South Sumatra Basin. *Journal of Geoscience, Engineering, Environment, and Technology*, 2(3), 203–209. https://doi.org/10.24273/jgeet.2017.2.3.292

Putro, A. A., Supriyanto, S., & Rinaldi, A. (2019). Interpretasi bawah permukaan menggunakan metode GPR di amblesan Jalan Ring Road II Kota Samarinda. *Jurnal Geosains Kutai Basin*, 2(1), 1–7. https://doi.org/10.30872/geofisunmul.v2i1.399

Ramadhana, I., Mardiana, U., Muljana, B., & Irvan, H. M. (2022). Fasies Pengendapan Batubara Formasi Muara Enim di Tambang Air Laya, Cekungan Sumatera Selatan. *Padjajaran Geoscience Journal*, 6(4), 994–1006. https://doi.org/10.24198/pgj.v6i4.45245

Rangole, A., De, S., Kuchekar, N., & Raj, A. A. B. (2024). A Comprehensive Review of Ground Penetrating Radar: Techniques, Applications and Future Directions. *International Journal of Engineering Research and Reviews*, 12(3), 30–53. https://doi.org/10.5281/zenodo.13842586

Reynolds, J. M. (1997). *An Introduction to Applied and Environmental Geophysics*. Wiley. www.wiley.com/go/reynolds/introduction2e

Rumansah, R. P. P., Paembonan, A. Y., & Andika, P. P. (2025). Pengembangan Aplikasi "ITERA-VISION-GPR-UI (ITERA Vision System GPR Utilities Inference)" Berbasis Computer Vision dengan Model YOLOv12 untuk Deteksi Utilitas pada Metode Ground Penetrating Radar. *Journal Online of Physics*, 11(1), 120–131.

© 2026 Dept. of Geophysics Hasanuddin University

https://doi.org/10.22437/jop.v11i1.49883

Setiahadiwibowo, A. P. (2017). Analisis Karakteristik Batubara Berdasarkan Rekaman Well Logging Di Daerah Kabupaten Katingan Kalimantan Tengah. *Journal Technology of Civil, Electrical, Mechanical, Geology, Mining, and Urban Design*, 1(2), 81–87. https://doi.org/10.33579/krvtk.v1i2.422

Setiawan, R. A., Adhitya, B., & Amin, S. S. (2025). Analisis Elektrofasies Berdasarkan Data Well Logging Dalam Menentukan Lingkungan Pengendapan Batubara Di Area Pt Bhumi Sriwijaya Perdana Coal, Musi Banyuasin, Sumatra Selatan. *Journal Online of Physics*, 10(2), 21–31. https://doi.org/10.22437/jop.v10i2.41957

Sugiarto, B. J., Junursyah, G. M. L., & Pratomo, I. (2018). Identifikasi objek bawah permukaan menggunakan metode Ground Penetrating Radar di Kompleks Candi Kedaton, Muarojambi. *Jurnal Geologi dan Sumberdaya Mineral*, 19(4), 201–211. https://jgsm.geologi.esdm.go.id/index.php/JGSM/article/view/428

Sujiman, S., & Ramadhani, F. (2023). Analisa Penentuan Kedalaman Dan Ketebalan Lithologi Batuan Menggunakan Data Bor dan Data Logging. *Jurnal Geologi Pertambangan*, 27(2), 38–49. https://ejurnal.unikarta.ac.id/jgp/article/view/1203

Syam, A., Lepong, P., & Supriyanto, S. (2019). Aplikasi Metode Georadar untuk Identifikasi Struktur Geologi di Jalan HM. Ardan Ring Road 1 Samarinda. *Jurnal Geosains Kutai Basin*, 2(1), 1–7. https://jurnal.fmipa.unmul.ac.id/index.php/geofis/article/download/355/160

Wahidah, R., & Basid, A. (2018). Interpretation of coal potential using Ground Penetrating Radar (GPR) method. *Jurnal Neutrino Jurnal Fisika dan Aplikasinya*, 10(1), 23–27. https://doi.org/10.18860/neu.v10i1.4563

Zadhoush, H., & Giannopoulos, A. (2021). Optimizing GPR time-zero adjustment and two-way travel time wavelet measurements using a realistic three-dimensional numerical model. *Near Surface Geophysics*, 20(2), 208–226. https://doi.org/10.1002/nsg.12193

© 2026 Dept. of Geophysics Hasanuddin University

ISSN: 2579-5821 (Print)
ISSN: 2579-5546 (Online)
URL address: http://journal.unhas.ac.id/index.php/geocelebes
DOI: 10.70561/geocelebes.v10i2.50652

Jurnal Geocelebes Vol. 10 No. 2, October 2026, 192 – 216

Aquifer Characterization through Vertical Electrical Sounding (VES), Well Logging, Petrographic Analysis, and Pumping Tests in the Monitoring Well Area, Lampung

Cherly Rizka Susanti, Astrik Rahmi Yati*, Rizka

Geophysical Engineering, Sumatra Institute of Technology, South Lampung, 35365, Indonesia.

*Corresponding author. Email: astrikkrahmi@gmail.com

Manuscript received: 15 April 2026; Received in revised form: 5 June 2026; Accepted: 9 June 2026

Abstract

This study aims to develop a calibrated interpretation framework for aquifer characterization and optimal monitoring well design at the Institut Teknologi Sumatera campus in South Lampung, Indonesia. This study employs the Vertical Electrical Sounding (VES) method using a Schlumberger configuration, with inversion processing performed to obtain a subsurface resistivity model. Dar-Zarrouk parameters were calculated to estimate aquifer hydraulic properties and were supported by well logging data and petrographic analysis for lithological identification, as well as Cooper–Jacob pumping tests for determining hydraulic parameters. The inversion results identify four subsurface layers, with the main aquifer occurring at depths greater than 75 m and characterized by resistivity values ranging from 40.49 to 71.28 Ωm. Based on well logging and petrographic analysis, two productive aquifer zones are identified at depths of 85–90 m and 110–125 m, consisting predominantly of coarse sand with minor gravel content. The Dar-Zarrouk parameter analysis indicates that the hydraulic conductivity, longitudinal conductance, transverse resistance, and transmissivity values reflect aquifer characteristics with moderate to high groundwater potential. Pumping test analysis yields a transmissivity value of 0.0051 m^2/s and a hydraulic conductivity value of 9.30×10^{-5} m/s. The resulting hydrogeological model indicates that the aquifer system in the study area is classified as a confined aquifer. The integrated approach effectively reduces interpretive ambiguity, and well screen installation at depths of 90–120 m is recommended as the optimal interval for groundwater monitoring within volcanic aquifer systems.

Keywords: Aquifer; Electrical Resistivity; Dar-Zarrouk Parameters; Hydrogeological Model.

Citation: Susanti, C. R., Yati, A. R., & Rizka, R. (2026). Aquifer Characterization through Vertical Electrical Sounding (VES), Well Logging, Petrographic Analysis, and Pumping Tests in the Monitoring Well Area, Lampung. *Jurnal Geocelebes*, 10(2): 192–216, doi: 10.70561/geocelebes.v10i2.50652

Introduction

Groundwater level monitoring is an essential component of sustainable groundwater resource management because it provides information on aquifer dynamics and their responses to climate change and anthropogenic activities (Yang et al., 2025). Lampung faces challenges in groundwater management due to rapid regional development. Groundwater levels in this region reportedly vary from approximately 5 to more than 100 meters, reflecting heterogeneous hydrogeological conditions and creating uncertainty in determining monitoring well locations and interpreting groundwater level data (Kumalasari et al., 2025). One area with potential for developing a groundwater monitoring well network is the campus area of Institut Teknologi Sumatera in South Lampung. However, no monitoring wells specifically designed for groundwater level monitoring have yet been established at this site, resulting in limited information regarding aquifer system characteristics, productive aquifer zone depths, and groundwater hydrodynamic behavior in the area. In addition, lithological complexity in sedimentary hydrogeological systems often

© 2026 Dept. of Geophysics Hasanuddin University

creates challenges in accurately identifying aquifers and increases ambiguity in subsurface interpretation (Claprood et al., 2022). Therefore, studies capable of comprehensively characterizing aquifer systems are required to support the development of reliable and sustainable groundwater monitoring systems in Lampung.

Monitoring wells constitute important infrastructure for systematically observing groundwater level fluctuations, drawdown, recovery rates, and aquifer conditions. Accurate groundwater monitoring is crucial for detecting excessive groundwater decline, evaluating pumping impacts, and supporting data-driven groundwater management decisions (Rau et al., 2020). In hydrogeological studies, several investigation methods have been widely applied to characterize subsurface conditions, including geoelectrical Vertical Electrical Sounding (VES), well logging, petrographic analysis, and pumping tests. The VES method is used to map resistivity distributions associated with lithological variations and groundwater occurrence, whereas well logging provides vertical information regarding lithology and aquifer zones. Petrographic analysis helps identify the mineralogical and textural characteristics of rocks that influence aquifer porosity and permeability, while pumping tests provide hydraulic parameters describing aquifer responses to pumping (Rau et al., 2020).

Previous hydrogeological studies conducted in the Institut Teknologi Sumatera campus area and its surroundings have provided an initial understanding of groundwater conditions in this region. Siringoringo et al. (2019) assessed groundwater hydro-geochemistry for drinking purposes in the Institut Teknologi Sumatera (ITERA) campus area and identified dominant hydrogeochemical facies through the integration of Piper diagrams, bivariate ion plots, and Gibbs diagram analysis. Subsequently, Siringoringo & Maulana (2020) investigated unconfined groundwater flow patterns and hydrogeochemical facies changes in Way Huwi Village adjacent to the campus. Their findings indicated that shallow groundwater flows from southwest to northeast following topographic gradients, with six hydrogeochemical facies variation patterns reflecting the influence of local sedimentary lithology. In addition, Rizka & Satiawan (2019) utilized the Vertical Electrical Sounding (VES) method correlated with electrical well logging data to identify aquifer geometry and groundwater potential in the ITERA area. Their results revealed the presence of two main aquifer systems: an unconfined aquifer developed within shallow clay layers at depths of less than 5 meters and a confined aquifer associated with sand layers at depths greater than 75 meters. Collectively, these findings provide an initial framework for understanding aquifer systems developed within the sedimentary geological environment of the ITERA area.

Despite these contributions, several limitations remain that constrain the accuracy and applicability of the existing knowledge for groundwater monitoring purposes. First, the hydrogeochemical studies conducted by Siringoringo et al. (2019) and Siringoringo & Maulana (2020) focused on water quality and shallow groundwater flow patterns but did not address aquifer hydraulic behavior or provide quantitative hydrogeological parameters essential for monitoring well design. Second, the geophysical study conducted by Rizka & Satiawan (2019) was limited to correlations between geoelectrical resistivity data and well logging responses without integrating rock physical properties through petrographic analysis. This ambiguity has not yet been resolved in previous local studies. Third, none of the previous studies incorporated pumping test data to characterize aquifer hydraulic responses, leaving the

© 2026 Dept. of Geophysics Hasanuddin University

productivity and hydrodynamic behavior of the identified aquifer zones poorly constrained. Consequently, the relationships among geoelectrical resistivity values, lithological properties, and aquifer productivity remain poorly defined under the sedimentary geological conditions of this region. Therefore, a research gap persists due to the absence of a calibrated interpretation model integrating geoelectrical, petrographic, well logging, and hydraulic parameter data to improve the accuracy of aquifer identification and monitoring well design in sedimentary hydrogeological systems.

Based on these issues, this study integrates Vertical Electrical Sounding (VES) data, petrographic analysis, well logging, and pumping test data obtained from monitoring wells in the ITERA area to develop a calibrated correlation model among electrical resistivity, petrographic parameters, well logging responses, and hydraulic parameters. The urgency of this research arises from the absence of clear criteria for determining the optimal depth of monitoring wells in Lampung, while subsurface geological complexity often results in high variability in lithology and hydraulic properties, leading to uncertainty in aquifer interpretation. The presence of monitoring wells is essential for obtaining groundwater level data and understanding aquifer dynamics to support sustainable groundwater management (Rau et al., 2020). Therefore, this study aims to establish calibrated interpretation criteria for determining productive aquifer zones and appropriate screen depths for monitoring wells capable of accurately representing groundwater level conditions. This research also contributes by providing a reliable integrated methodology for aquifer characterization through the integration of geophysical and hydrogeological approaches. Specifically, this study integrates geophysical, petrographic, and hydrogeological data to support aquifer identification and monitoring well design.

Materials and Methods

Study Area

This study was conducted at the ITERA in Lampung by integrating the VES geophysical method, well logging, rock petrographic analysis, and pumping tests as the basis for monitoring well planning. VES measurements were conducted at five VES points within the ITERA monitoring well area (Figure 1). VES-1 was designated as the central measurement point and the planned location of the monitoring well, serving as the primary reference for subsurface condition analysis. The other four VES points were systematically positioned around the central point at relatively equal distances of approximately 46 m toward the north, south, west, and east. This arrangement formed a symmetrical configuration that enabled the analysis of lateral subsurface layer variations and the interrelationship among measurement points regarding conditions surrounding the monitoring well.

Each VES point had a maximum current electrode spacing (AB/2) of 200 m, except for VES-03, where the maximum AB/2 distance was 160 m. Meanwhile, the potential electrode spacings (MN/2) used in the measurements were 0.5, 2.5, 8, and 16 m. In the Schlumberger configuration, the effective investigation depth generally ranges from one-quarter to one-third of the total current electrode span (AB) (Roy & Apparao, 1971). With a maximum span of AB/2 = 200 m, the investigation depth was estimated to reach approximately 100–133 m. The deepest layer was modeled as a half-space, representing a homogeneous layer assumed to extend continuously to infinite depth.

© 2026 Dept. of Geophysics Hasanuddin University

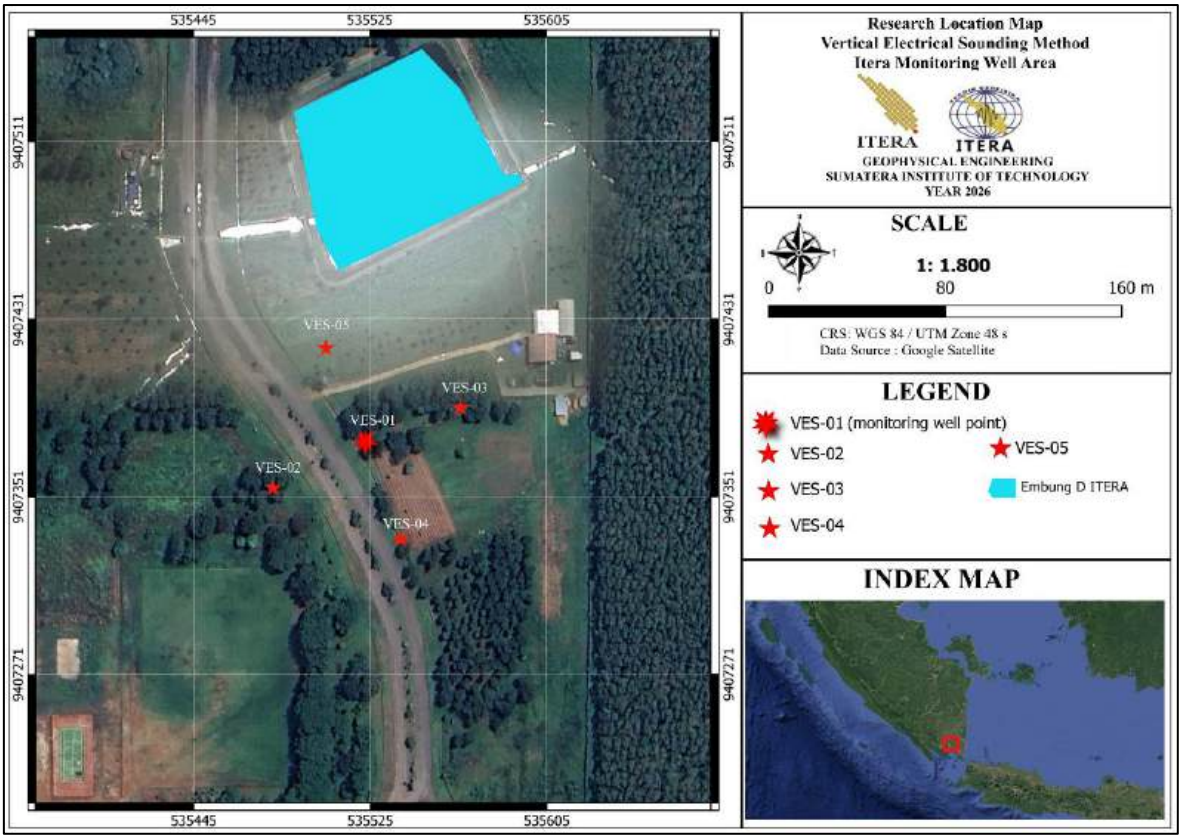


Figure 1. Research area.

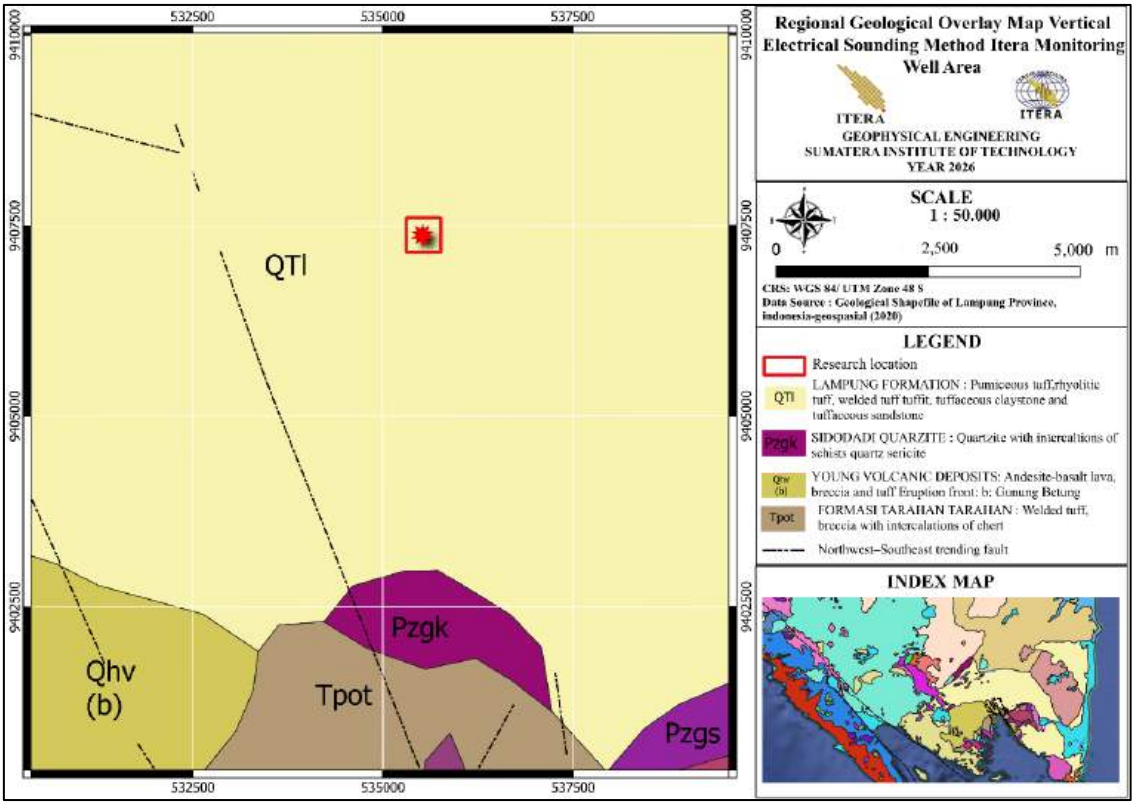


Figure 2. Regional geological map overlay (Mangga et al., 1993).

Geology of the Research Area

This research was conducted at the ITERA campus in Way Huwi, South Lampung. Based on the regional geological map (Figure 2), the study area is located within the Lampung Formation. This formation

© 2026 Dept. of Geophysics Hasanuddin University

consists of Pumiceous tuff, rhyolitic tuff, welded tuff, tuffaceous claystone and tuffaceous sandstone, which are estimated to be of Late Quaternary age (Mangga et al., 1993). The surface rock distribution in the ITERA area is dominated by volcanic rocks formed through volcanic, tectonic, and sedimentary processes. Under certain hydrogeological conditions, tuff can function as an aquifer. Its groundwater flow characteristics are influenced by porosity, permeability, fractures, and hydraulic conductivity. Tuff with well-connected pore spaces and favorable hydraulic conductivity can support effective groundwater flow (Muauz et al., 2025).

Data Acquisition and Processing

The VES measurements were conducted using a Schlumberger array configuration centered around the borehole subjected to the pumping test. The VES data were subsequently interpreted using the curve-fitting method (Nyembwe et al., 2024). An inversion process was then performed to obtain a subsurface resistivity model (Figure 3). Based on the inversion results, the number of layers, resistivity values, and thicknesses of each layer were determined. Furthermore, the resistivity values and thicknesses of each geophysical layer were used to calculate the Dar-Zarrouk parameters (Figure 3), which are commonly applied in aquifer characteristic analysis (Yusuf et al., 2021).

The Dar-Zarrouk parameters were first introduced by Maillet (1947). and consist of longitudinal conductivity (*S*) and transverse resistance (*Tr*). Longitudinal conductivity was calculated using the following Equation 1:

$$S = \sum_i^n \frac{h_i}{\rho_i} \quad (1)$$

where h_i represents the thickness of the i-th layer and ρ_i denotes the resistivity of the i-th layer. Longitudinal conductivity indicates the ability of a layer to conduct electrical current parallel to the layer direction. Higher longitudinal conductivity values generally indicate better aquifer protective capacity.

Meanwhile, transverse resistance was calculated using Equation 2:

$$T = \sum_i^n h_i \rho_i \quad (2)$$

Transverse resistance is obtained by multiplying the thickness of each layer by its resistivity value. This parameter is closely related to aquifer transmissivity and is therefore commonly used as an indicator of groundwater productivity potential (Oli et al., 2022).

The aquifer layer resistivity values obtained from the VES data inversion were used to estimate hydraulic conductivity (K) using the empirical Equation (3) proposed by Heigold et al. (1979):

$$K = (386.40\, R_{rw})^{-0.93283} \quad (3)$$

where R_{rw} is a resistivity parameter associated with groundwater resistivity obtained from resistivity interpretation. To determine the formation water resistivity (*Rw*), Archie's equation is used, which states that the relationship between the resistivity of water-saturated rock, porosity, and fluid resistivity is influenced by the tortuosity factor and the cementation exponent (Archie, 1942), as shown in Equation (4):

$$R_0 = a\, \phi^{-m} R_w \quad (4)$$

where R_0 in Equation (4) represents the resistivity of water-saturated rock derived from geoelectrical inversion results, a is the tortuosity factor assumed to be 1, m is the cementation exponent (typically ranging from 1.3 to 2 for sand), and ϕ is porosity (Archie, 1942). Based on this relationship, the equation for determining formation water resistivity, Equation (5) becomes:

$$R_w = R_0\ \phi^m \quad (5)$$

Subsequently, transmissivity (*T*) was calculated using the Equation (6) proposed by Todd (1980):

© 2026 Dept. of Geophysics Hasanuddin University

$$T = K\,h \;\Leftrightarrow\; \mathrm{K} = \frac{T}{h} \qquad (6)$$

where T denotes transmissivity (m^2/s), K represents hydraulic conductivity (m/s), and h is the saturated thickness of the aquifer (m). This approach provides a quantitative estimate of the aquifer's capacity to transmit water based on the geophysical parameters obtained.

Geophysical models are inherently prone to interpretive ambiguities that may lead to inconsistencies in aquifer data analysis. Therefore, to address this non-uniqueness problem, correlations with monitoring well data were applied (Li et al., 2021). Well drilling was conducted to identify lithological characteristics and aquifer zones vertically using resistivity logs that are sensitive to variations in pore fluids and rock physical properties (Chakraborty et al., 2021).

In this study, short-normal and long-normal resistivity logging were used to obtain resistivity information at different investigation depths, where a resistivity modeling approach has been developed to represent log responses under various geological conditions (Wilkosz, 2022). The short normal method is more sensitive to zones near the borehole and shallow formations, whereas the long normal method better represents the actual formation resistivity, particularly under drilling mud invasion conditions (Wu & Fan, 2021). These differences in investigation depth allow for the evaluation of the effects of drilling mud invasion and subsurface layer heterogeneity that influence the measured resistivity response (Zhou et al., 2023). The combination of these two logs improves the accuracy of lithological interpretation and aquifer identification, as the short normal provides high resolution in zones near the wellbore, while the long normal is more stable against borehole effects and invaded zones (Wilkosz, 2022; Wu & Fan, 2021). The interpretation of well logging data served as the basis for understanding the distribution of petrophysical properties and variations in formation quality at each depth (Amir et al., 2025). In addition, drilling activities enabled the collection of rock samples in the form of cuttings, which were directly analyzed in the laboratory to obtain petrophysical parameters such as porosity, permeability, and mineralogical characteristics (Sanei et al., 2020). The integrated well logging approach has been shown to effectively reduce interpretation uncertainty and provide a more comprehensive representation of subsurface conditions (Wu & Grana, 2017).

Petrographic analysis was conducted to characterize rock types, textures, structures, and mineral compositions. The analyzed rock samples consisted of drill cuttings obtained from boreholes at specific depth intervals based on their correlation with well logging interpretations. The samples were prepared as thin sections and analyzed using a polarizing microscope (Figure 8). The resulting petrographic parameters were subsequently used to evaluate the relationships among rock characteristics, electrical properties, and aquifer potential, as commonly applied in petrographic and hydrogeological studies involving geophysical-geological integration (Nouradine et al., 2024; Putri et al., 2018; Prinaldi et al., 2023; Warsi et al., 2020).

A pumping test is a method used to evaluate well performance and the hydraulic characteristics of the surrounding aquifer (Agussalim et al., 2022). In this study, the pumping test was conducted using a single-well pumping test method without an observation well. Drawdown measurements were taken directly at the pumping well during pumping at a constant discharge rate to determine the hydrogeological parameters of the aquifer. The test was designed to evaluate the aquifer response to hydraulic stress by examining the relationship among pumping rate (Q), time (t), and groundwater level

© 2026 Dept. of Geophysics Hasanuddin University

drawdown (*Sw*), which is also influenced by drawdown changes (*Δs*). The analyzed hydrogeological parameters included transmissivity (T) and hydraulic conductivity (K), which serve as primary indicators of the aquifer's capacity to transmit groundwater.

Transmissivity values were calculated using the Cooper-Jacob method (Cooper & Jacob, 1946), as expressed in Equation (7):

$$T = \frac{2.3Q}{4\pi\Delta s} \quad (7)$$

where T represents transmissivity, Q is the pumping rate, and Δs denotes the drawdown change. Higher transmissivity values indicate greater aquifer capacity to transmit groundwater.

Interpretation of VES data

Vertical Electrical Sounding (VES) data interpretation is performed through an inversion process using a curve-fitting method, in which the apparent resistivity curves obtained from field measurements are fitted to theoretical model curves to obtain a representative subsurface model (Bahri et al., 2022). The inversion process is performed iteratively by adjusting the resistivity and layer thickness parameters until the best fit between the observed data and the calculated model is achieved. The agreement between the field curve and the theoretical curve is evaluated based on the misfit value or Root Mean Square (RMS) error generated during the inversion iteration process (Grandis, 2009). A low RMS error value indicates that the inverted resistivity model has a good level of representation of the actual subsurface conditions (Pinehas & Warsa, 2019). The results of the curve fitting are used to determine the true resistivity distribution and the thickness of each subsurface layer (Oyeyemi et al., 2023). The inverted resistivity and layer thickness parameters are then interpreted to identify lithological characteristics and groundwater-bearing zones in the study area.

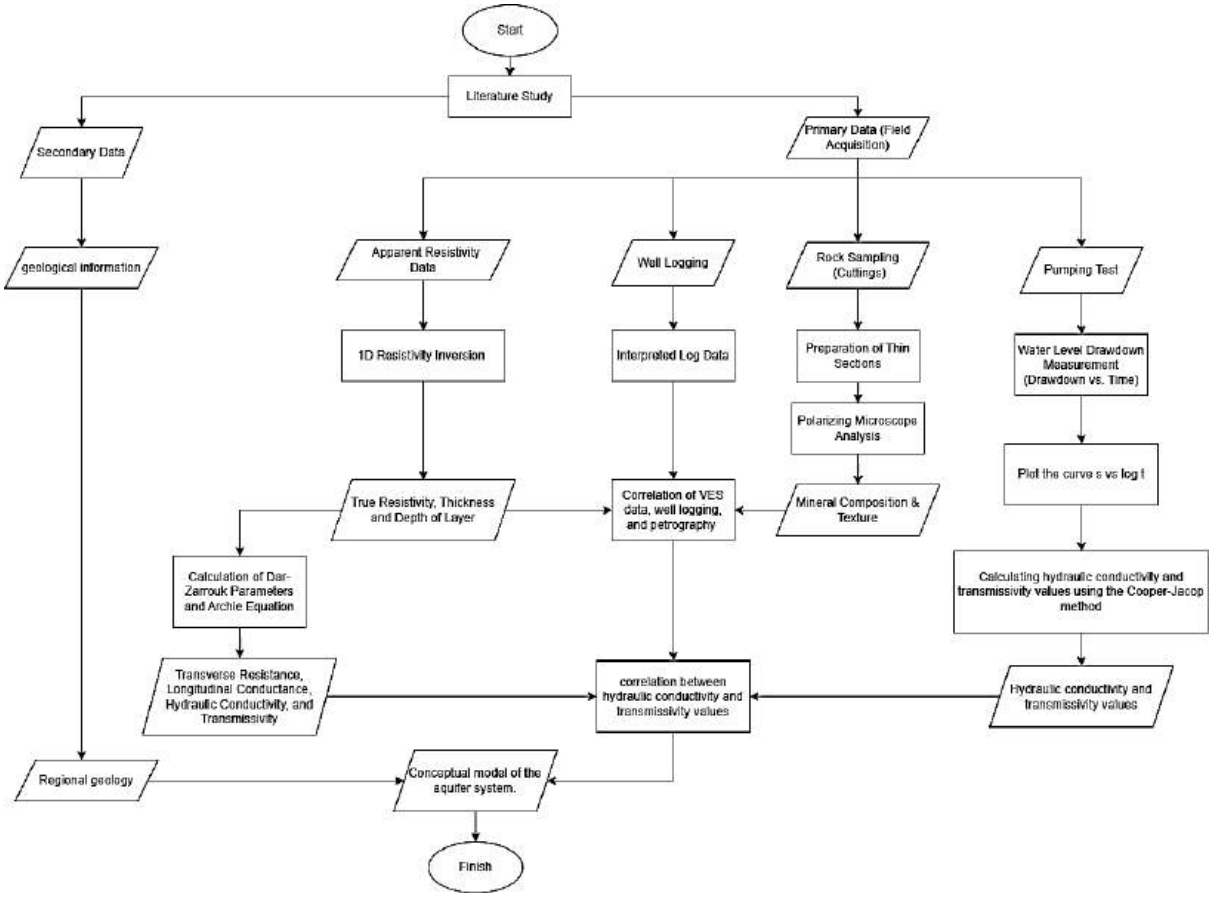


Figure 3. Research methodology workflow.

© 2026 Dept. of Geophysics Hasanuddin University

Results and Discussion

Vertical Electrical Sounding (VES) Analysis

The analysis of VES data based on apparent resistivity (ρ_a) values provides characterization of subsurface layers (Hasani et al., 2023; Syaputri et al., 2024). This characterization is performed through the interpretation of resistivity (ρ) and thickness (h) values for each subsurface layer, thereby enabling the identification of potential aquifer zones at each VES point. The measurement curves (Figure 4) were fitted to the field data to obtain subsurface resistivity cross-section models representing the distribution of subsurface layers according to their resistivity values and thicknesses. The curve patterns obtained at VES point 1 – 5 (Figure 4a – 4e) indicate variations in subsurface resistivity values, with low-resistivity layers situated between layers that have relatively higher resistivity. These patterns indicate differences in lithology and groundwater saturation conditions within the sedimentary formations (Masria et al., 2024) in the study area.

Based on the inversion results of the VES data (Table 1), a four-layer subsurface model with RMS errors ranging from 4% to 11% was obtained. The first layer exhibits resistivity values ranging from 125.14 to 209.41 Ωm with thickness between 2.41 and 4.99 m. This uppermost layer is characterized by relatively high resistivity values. A significant decrease in resistivity is observed in the second layer, where resistivity values range from 2.43 to 9.15 Ωm, with thickness of 7.15–25.32 m. The third layer is characterized by resistivity values between 10.68 and 17.78 Ωm and thicknesses ranging from 51.69 to 70.50 m. The increase in resistivity relative to the overlying layer indicates a lithological transition, particularly toward sandy clay material.

In the deeper part of the model, resistivity values increase further, ranging from 40.49 to 71.28 Ωm. The final layer in the inversion model is interpreted as a half-space layer, meaning that its lower boundary could not be identified because it extends beyond the investigation depth of the measurements. This layer potentially represents an aquifer located at depths greater than 75 m below the surface (Rizka & Satiawan, 2019). In addition, VES point 1 function as the central reference point among the four surrounding VES points.

Dar Zarrouk Parameter

VES data were used to estimate the Dar-Zarrouk parameters, including hydraulic conductivity, longitudinal conductance, transverse resistance, and transmissivity. These parameters are commonly applied to identify aquifer characteristics and groundwater conditions (Muhammad et al., 2023). Based on the Dar-Zarrouk parameter analysis, the values of hydraulic conductivity, longitudinal conductance, transverse resistance, and transmissivity were obtained as presented in Table 2. . In this study, the Dar-Zarrouk parameters were specifically calculated for the fourth resistivity layer (ρ = 40.49–71.28 Ωm), which was identified as the main aquifer unit based on its depth (>75 m), resistivity range consistent with coarse-grained saturated sediments, and correlation with productive zones identified from the well log.

© 2026 Dept. of Geophysics Hasanuddin University

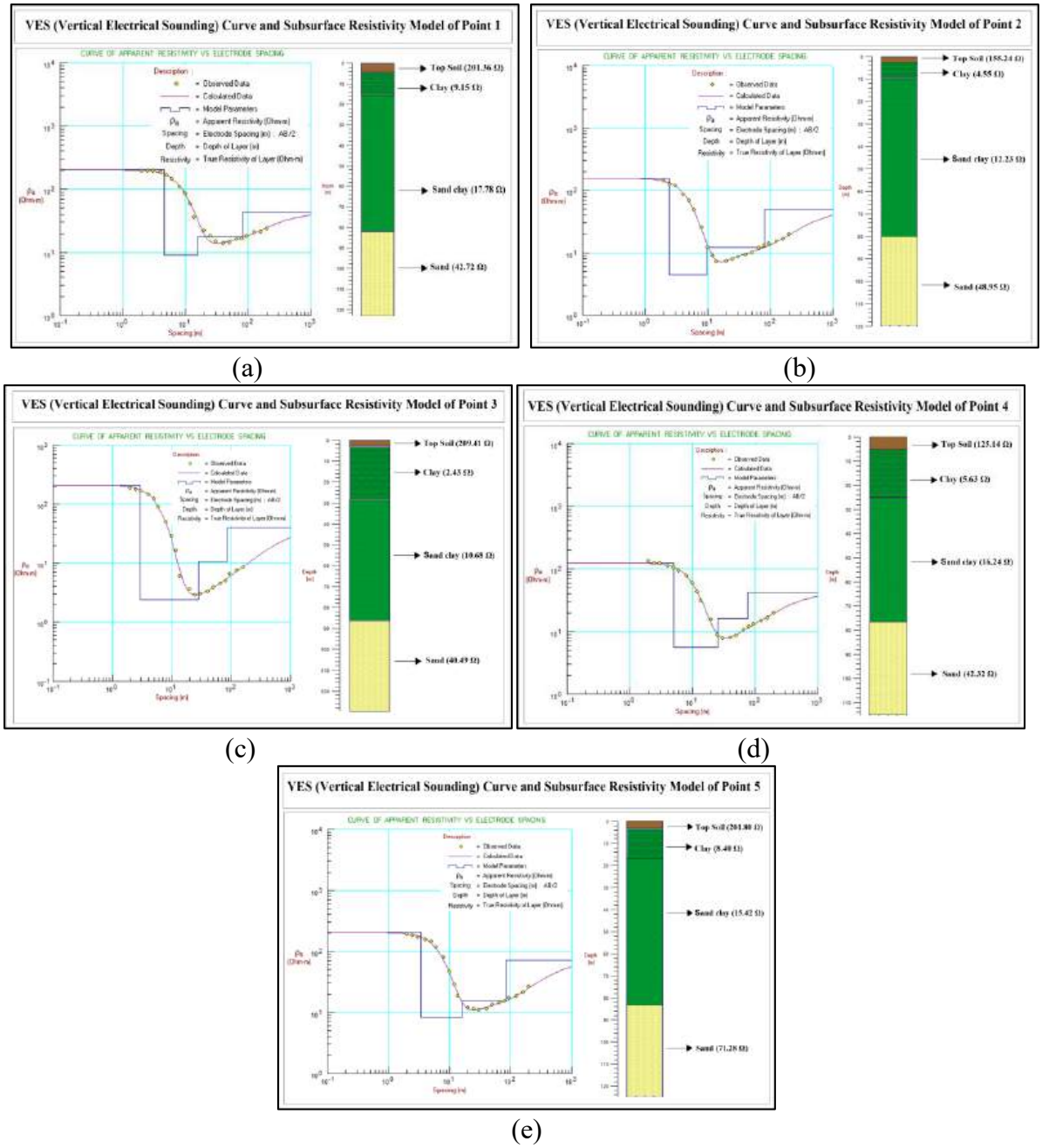


Figure 4. Resistivity curve plots, layer thickness, and lithological interpretation: (a) VES point 1 (b) VES point 2 (c) VES point 3 (d) VES point 4 (e) VES point 5.

Table 1. VES data inversion results in the study area.

VES Point	Latitude (°W)	Longitude (°S)	Electrical Resistivity (Ωm)				Thickness (m)				RMS (%)
			ρ1	ρ2	ρ3	ρ4	h1	h2	h3	h4	
VES 1	105.32062	-5.361414	201.3	9.1	17.7	42.7	4.6	10.8	63	∞	8.367
VES 2	105.32101	-5.361278	155.2	4.5	12.2	48.9	2.4	7.15	70.5	∞	4.032
VES 3	105.32046	-5.361034	209.4	2.4	10.6	40.4	2.9	25.3	58.2	∞	11.18
VES 4	105.32077	-5.361812	125.1	5.6	16.2	42.3	4.9	20.1	51.6	∞	4.366
VES 5	105.32024	-5.361604	201.8	8.4	15.4	71.2	3.4	12.9	66.9	∞	5.604

© 2026 Dept. of Geophysics Hasanuddin University

Table 2. Dar-Zarrouk parameter analysis and estimation of hydrogeological parameters based on VES method and pumping test.

VES Point	Latitude (°W)	Longitude (°S)	Longitudinal conductance (Si)	Transverse Resistance (ohm.m^2)	Hydraulic Conductivity (m/s)	Transmissivity VES (m^2/s)	Transmissivity Pumping (m^2/s)
VES 1	105.32062	-5.361414	1.004	1832.688	0.00155	0.066	0.0051
VES 2	105.32101	-5.361278	0.918	2199.813	0.00136	0.061	
VES 3	105.32046	-5.361034	0.951	1558.460	0.00162	0.063	
VES 4	105.32077	-5.361812	1.138	2037.285	0.00156	0.075	
VES 5	105.32024	-5.361604	0.585	2972.376	0.00096	0.040	

The longitudinal conductance values at the study site range from 0.918 to 1.138 Si, as shown in Figure 5. This parameter was calculated using the thickness and resistivity values of the layers interpreted as aquifers based on the VES inversion results. Longitudinal conductance is commonly used to evaluate groundwater flow characteristics, aquifer transmissivity, and groundwater potential within the Dar-Zarrouk framework (Raju et al., 2023). At VES 1, the longitudinal conductance (S) value of 1.004 indicates adequate aquifer thickness and saturation conditions, suggesting moderate groundwater potential. The values obtained at VES 2 (0.918 Si) and VES 3 (0.951 Si) are relatively similar, indicating fairly uniform aquifer conditions across these locations. Meanwhile, VES 4 exhibits the highest value (1.138 Si), indicating the most favorable aquifer potential among the investigated sites. In contrast, VES 5 shows the lowest value (0.585 Si), suggesting a thinner or less saturated aquifer layer and consequently lower groundwater potential.

In contrast to the longitudinal conductance values, VES 5 exhibits the highest transverse resistance value, reaching 2972.376. This high transverse resistance is influenced by the relatively high resistivity value of 71.28 Ωm recorded at this location. However, elevated resistivity values indicate a reduction in the conductive phase within the rock matrix (Amir et al., 2025). In a hydraulic context, this condition is associated with low effective pore tortuosity and limited hydraulic connectivity among grains, resulting in low hydraulic conductivity (*K*) and transmissivity (*T*) values. Accordingly, VES 5, despite having the highest transverse resistance value, indicates a zone with the potential to store a large volume of static groundwater but with limited groundwater flow and transmissivity, as reflected by its low transmissivity (T = 0.040 m^2/s) and hydraulic conductivity (K = 0.00096 m/s) values. These characteristics indicate an aquifer dominated more by storage capacity than by groundwater flow capacity. Overall, transmissivity values within the study area range from 0.040 to 0.075 m^2/s (Table 2).

Theoretically, transverse resistivity (Tr) and transmissivity (T) exhibit a moderate correlation. The coefficient of determination obtained from the correlation between transverse resistance and transmissivity is 0.6039 (Figure 6), indicating that 60.39% of the transmissivity variation at the study site can be explained by changes in transverse resistance, whereas the remaining 39.61% is influenced by factors outside the model. Zones with high resistivity generally produce large transverse resistance values. Nevertheless, reduced pore connectivity within the rock matrix directly contributes to lower hydraulic conductivity and transmissivity values. This relationship is most evident at VES 5, which recorded the highest transverse resistance value (2972.376 Ωm^2) but the lowest transmissivity value (0.040 m^2/s), indicating an aquifer characterized more by storage than by groundwater flow. In contrast, VES 4, despite having a moderate transverse resistance value, exhibits the most favorable hydraulic performance (T =

© 2026 Dept. of Geophysics Hasanuddin University

0.075 m^2/s). This finding confirms that aquifer prospectivity cannot be interpreted using a single parameter alone but instead requires an integrated evaluation of multiple hydrogeological parameters (Muhammad et al., 2023).

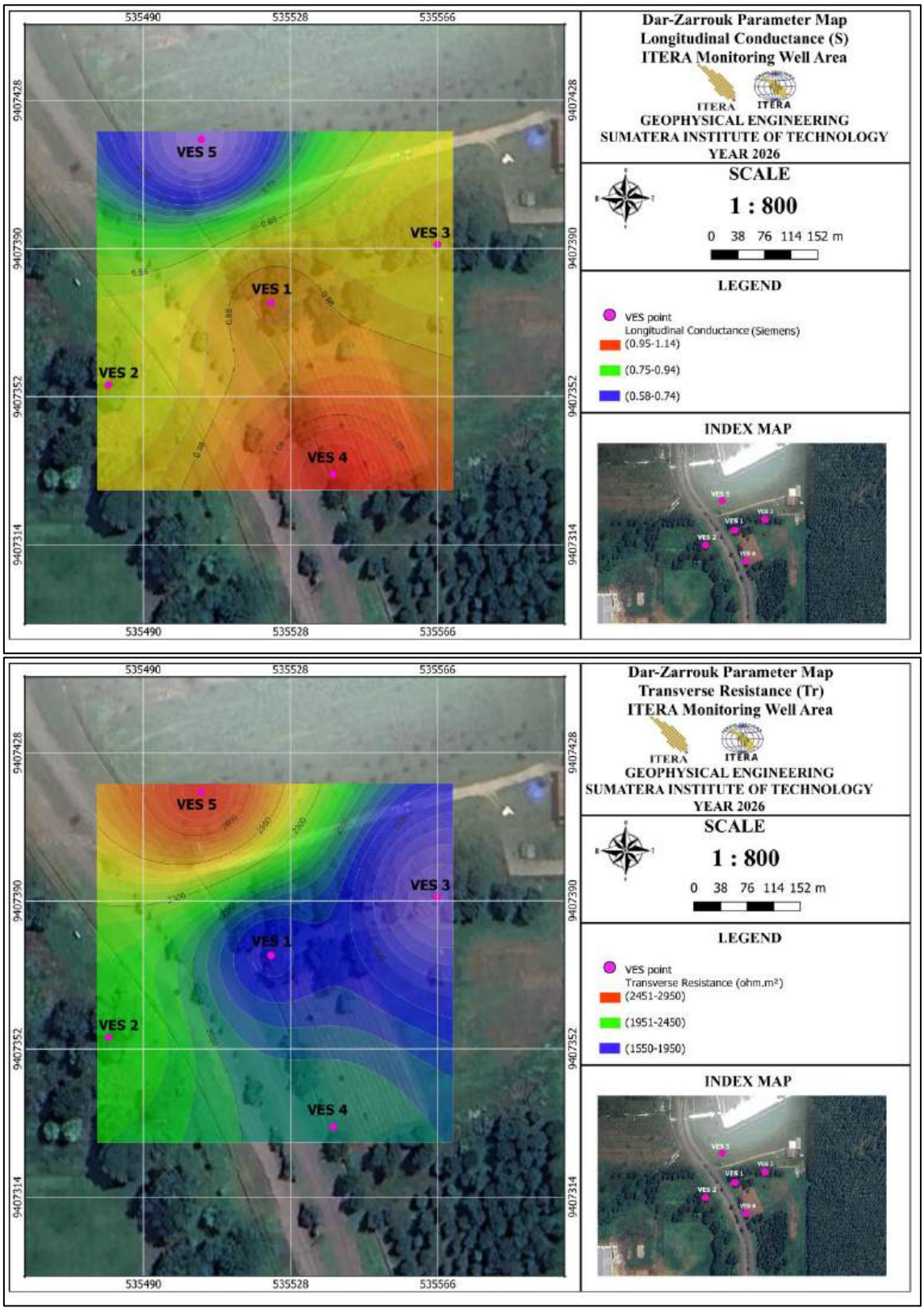


Figure 5. Distribution of longitudinal conductance (S) and transverse resistance (Tr) values based on Dar-Zarrouk parameters.

© 2026 Dept. of Geophysics Hasanuddin University

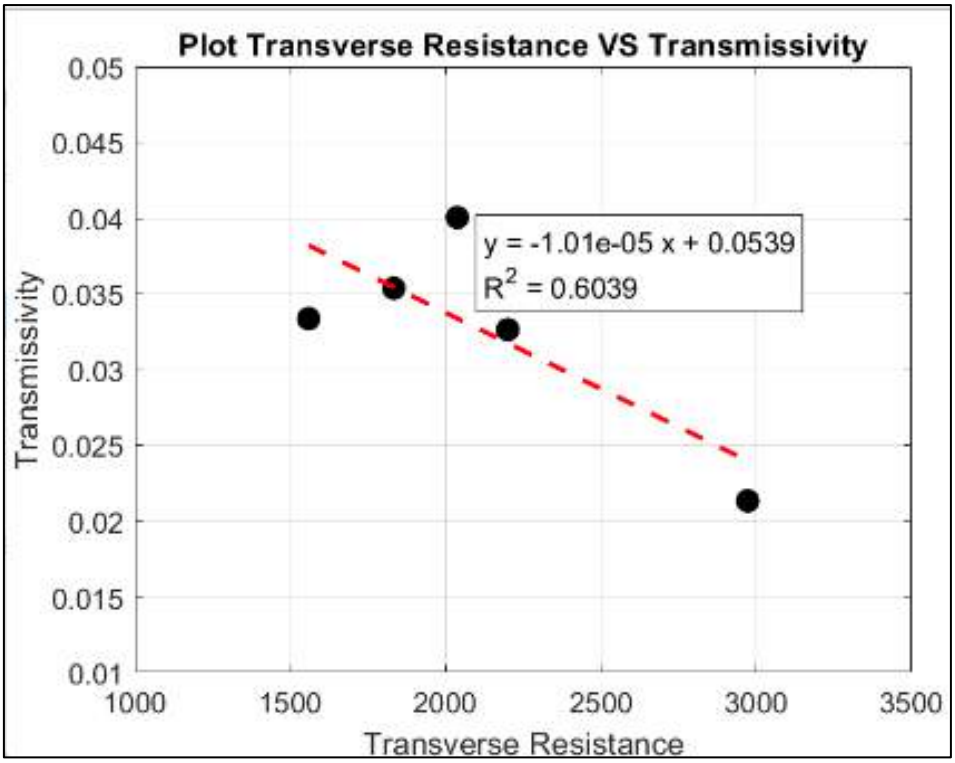


Figure 6. Correlation between transverse resistance (TR) and transmittance (T) based on VES data.

Well logging and Lithology

Resistivity logs provide important information regarding fluid content within rock formations and become more effective when integrated with other geophysical datasets (Al-Mudhafar et al., 2024). Measurements obtained using short- and long-electrode configurations represent invaded zones and true formation zones, respectively (Figure 7a). In general, low resistivity values correspond to sand, sandy clay, clayey sand, and gravelly sand of volcanic origin (Sehah et al., 2024).

At depths shallower than 65 m, the relative resistivity values recorded in the logs are relatively low, causing the log responses to appear less distinct within the display scale presented in Figure 7. The shallow subsurface layers are dominated by clay and volcanic ash, reflecting a typical volcanic depositional environment characterized by low to moderate resistivity values influenced by moisture content, texture, and parent material composition (Juwono et al., 2024). The correlation between resistivity data and lithological information reveals the presence of two main aquifer zones at depths of 85–90 m and 110–125 m. Based on the interpretation of resistivity logs integrated with drilling cutting data, these zones are interpreted to consist predominantly of coarse sand with minor gravel components and are therefore identified as productive aquifer layers (Mohammed et al., 2025).

Geophysical well logging provides a continuous and efficient approach for aquifer characterization and offers significant advantages over conventional methods (Mohammed et al., 2025). Based on the log interpretation, the well construction design incorporates screen installation within productive aquifer intervals and gravel pack placement at depths of 70–125 m to enhance hydraulic flow efficiency. Resistivity-based analysis further supports accurate drilling placement and optimal well design (Sehah et al., 2024). In addition, cement grouting applied at depths of 0–25 m functions to prevent surface contamination because the shallow clay layers act as a natural aquitard

© 2026 Dept. of Geophysics Hasanuddin University

protecting the underlying confined aquifer (Nugraha et al., 2022).

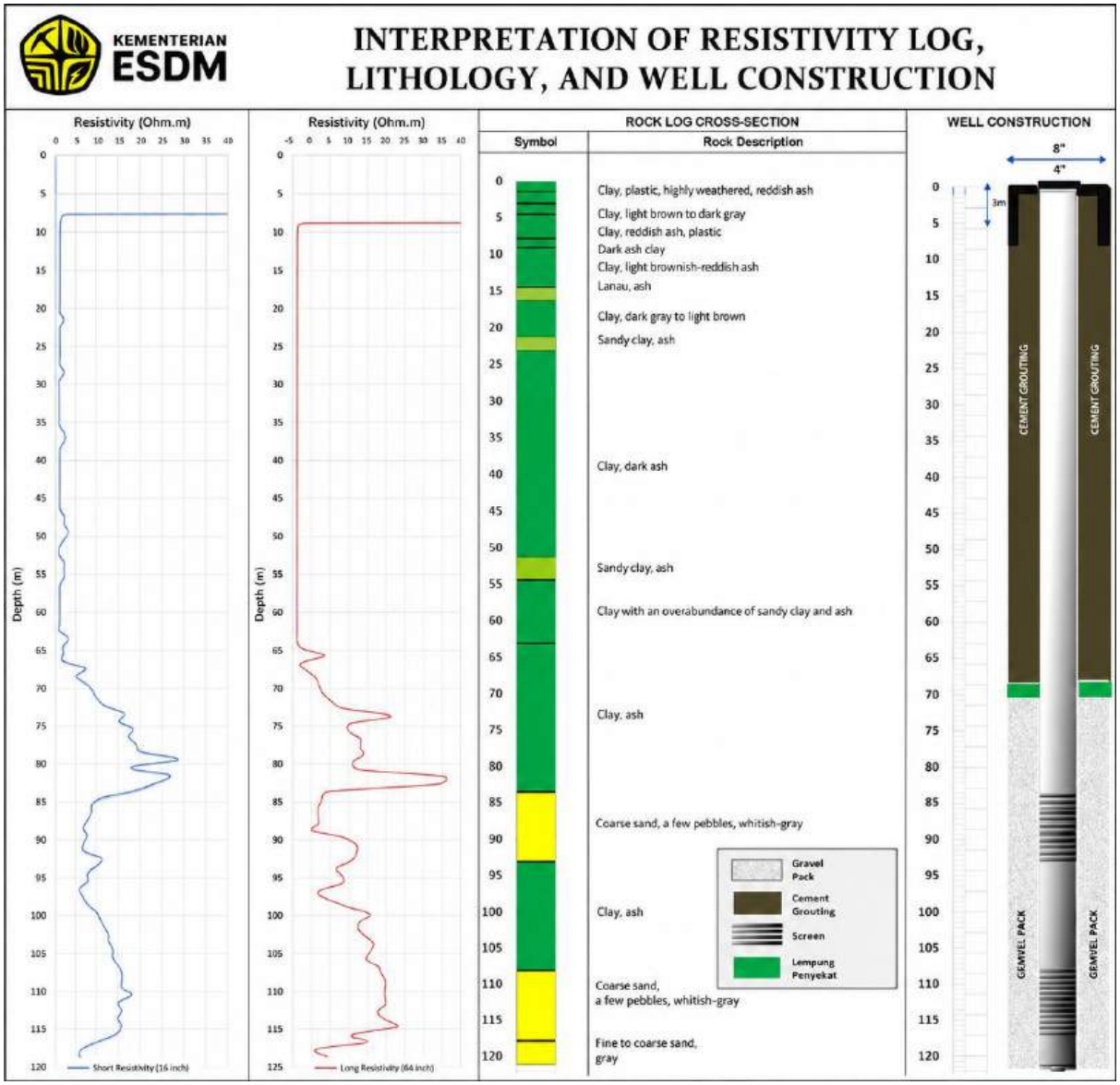


Figure 7. Well logging results and lithological descriptions showing (a) resistivity interpretation and (b) lithological descriptions.

Lithological log interpretation indicates that the subsurface from the ground surface to approximately 85 m depth is dominated by low-permeability clay, silt, and sandy clay layers that collectively function as an aquitard. A transitional zone consisting of coarse sand with minor gravel occurs at depths of 85–95 m, indicating improved porosity and permeability characteristics. The main aquifer is identified at depths of 110–125 m and consists predominantly of coarse-to medium-grained sand with favorable hydraulic properties. Accordingly, the well screen is installed at depths of 90–120 m to optimize groundwater extraction from the productive aquifer interval.

The interbedding of clay, sandy clay, and coarse sand layers observed between depths of 70 and 125 m, as identified from the well log, indicates substantial lithological heterogeneity that is not fully represented in the VES inversion results. This heterogeneity is interpreted as the primary factor contributing to the overestimation of

© 2026 Dept. of Geophysics Hasanuddin University

transmissivity values derived from the Dar-Zarrouk parameters relative to the pumping test results because the geophysical approach assumes lateral continuity and homogeneity within each resistivity layer (Ammar & Kamal., 2019).

Petrographic Analysis

Petrographic analysis was performed on representative thin sections using a polarizing microscope under three observation modes. Plane-polarized light (PPL) was used to identify primary mineral properties, including color, pleochroism, relief, and cleavage (MacKenzie & Guilford, 1980). Cross-polarized light (XPL) was subsequently applied to determine birefringence, interference colors, extinction angles, and crystal twinning, thereby enabling systematic mineral identification (Nesse, 2014). Additionally, a 530 nm gypsum plate (λ-plate) was employed as a retardation compensator to enhance the visibility of low-birefringence minerals and clay alteration products commonly associated with volcanic sequences. This integrated approach facilitated comprehensive characterization of the mineralogical composition and textural properties of the subsurface geological formations.

As shown in Figure 8, petrographic analysis of Samples 22 (22 m), 23 (23 m), 29 (29 m), and 108 (108 m) obtained from drilling cuttings reveals variations in lithology and rock texture characteristics. The thin sections were impregnated with blue-colored resin to enhance the visibility of porosity distribution during microscopic observation. Petrographic interpretation was conducted based on thin-section observations and subsequently correlated with resistivity log data to support the calibration of subsurface lithological identification.

Samples 22, 23, and 29 are dominated by clay matrix material characterized by very fine grain sizes, poor sorting, and matrix-supported fabrics, indicating low porosity and permeability consistent with clay-rich sediments. Sample 22 consists predominantly of clay-sized particles with minor quartz and lithic components, whereas Sample 23 contains limited fine sand fractions but remains matrix-dominated. Sample 29 exhibits similar characteristics with strong matrix dominance and minimal pore space development. In contrast, Sample 108 exhibits a higher proportion of framework grains, including quartz, plagioclase, and lithic fragments, with grain sizes ranging from coarse silt to very fine gravel. The relatively more open grain arrangement and partially grain-supported fabric indicate improved pore space development and suggest a tendency toward sand or conglomeratic lithology.

Overall, the petrographic observations indicate that Samples 22, 23, and 29 predominantly consist of clay-rich sediments characterized by very fine grain sizes, high matrix content, poor sorting, and low porosity. These characteristics indicate low permeability and limited potential as productive aquifer units. In contrast, Sample 108 exhibits relatively coarser grain sizes, higher quartz content, and improved textural maturity, suggesting more favorable reservoir properties than the clay-dominated samples.

From a regional geological perspective, the study area is dominated by tuff, but petrographic analysis indicates a sedimentary/ volcaniclastic character. This is likely due to the reprocessing of pyroclastic material and its subsequent re-deposition by water, which has resulted in a sedimentary texture in the rocks. Additionally, alteration and weathering may cause the original volcanic texture to be less visible in thin sections.

© 2026 Dept. of Geophysics Hasanuddin University

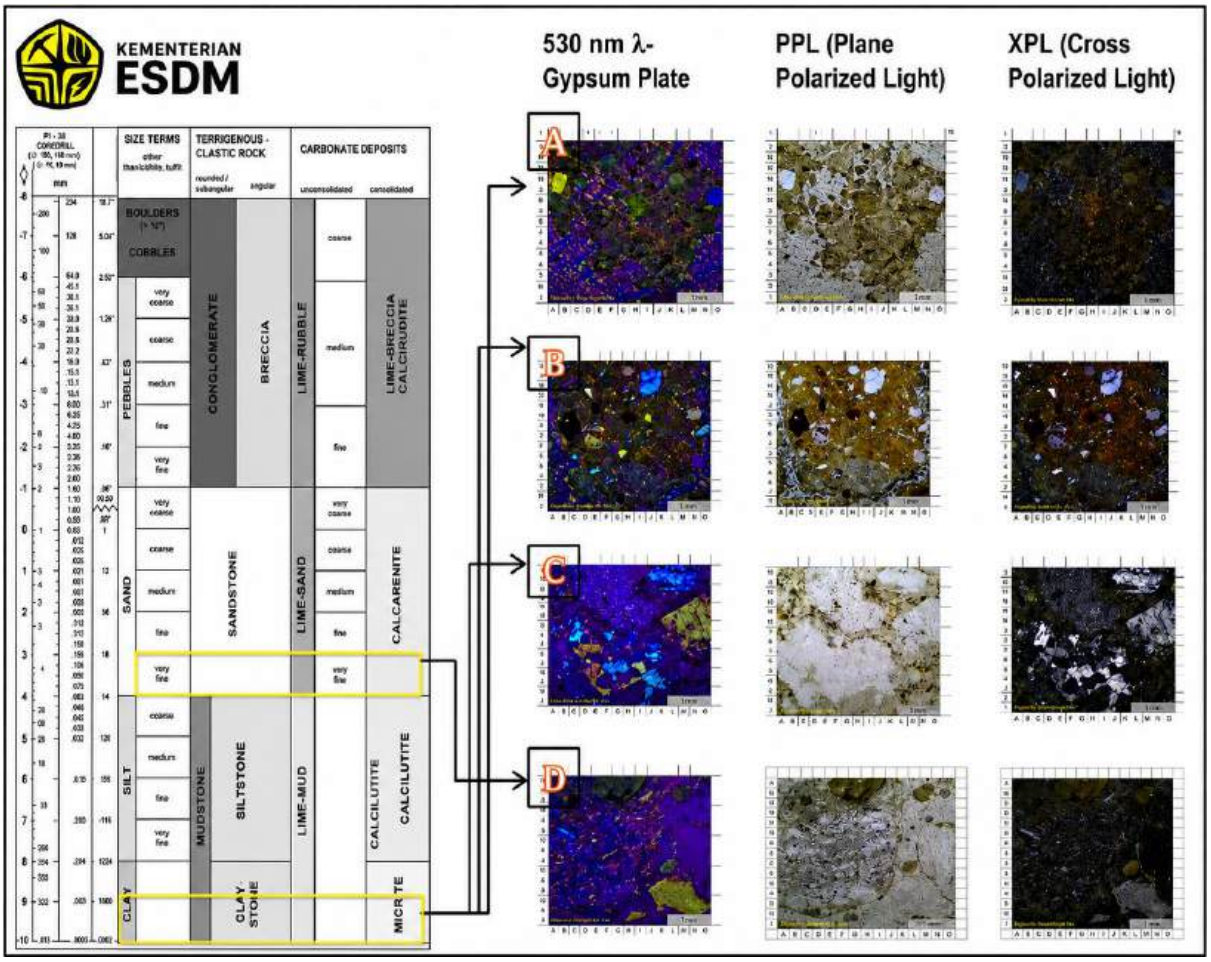


Figure 8. Cutting interpretation for lithological classification: (A) Sample 22, (B) Sample 23, (C) Sample 29, and (D) Sample 108.

Analysis of Pumping Tests

Hydraulic in situ testing requires careful evaluation of procedural assumptions to ensure the reliability of the estimated parameters (Yihdego, 2017). In this study, the Cooper–Jacob method was applied under several assumptions, including confined, homogeneous, and isotropic aquifer conditions; radial groundwater flow; laterally extensive aquifer geometry without boundary effects; and a sufficient pumping duration. Within the context of the study area, the confined aquifer condition is supported by the presence of an overlying low-permeability clay layer identified from the well log at depths of 0–85 m, which functions as a confining unit. Although single-well data inherently limit spatial representativeness, the consistency between the pumping test results and well logging interpretations indicates that these assumptions are reasonably satisfied at the local scale.

The pumping test analysis using the Cooper–Jacob method yields a transmissivity value of 0.0051 m^2/s and a hydraulic conductivity value of 9.30×10^{-5} m/s (Figure 9). These values indicate that the aquifer possesses relatively favorable hydraulic properties and an adequate capacity to transmit groundwater. The relatively high hydraulic conductivity suggests that the aquifer material is predominantly composed of coarse-grained sediments such as sand to gravelly sand. This interpretation is consistent with the borehole log, which identifies coarse sand layers below approximately 85 m depth that represent the primary productive aquifer zone.

© 2026 Dept. of Geophysics Hasanuddin University

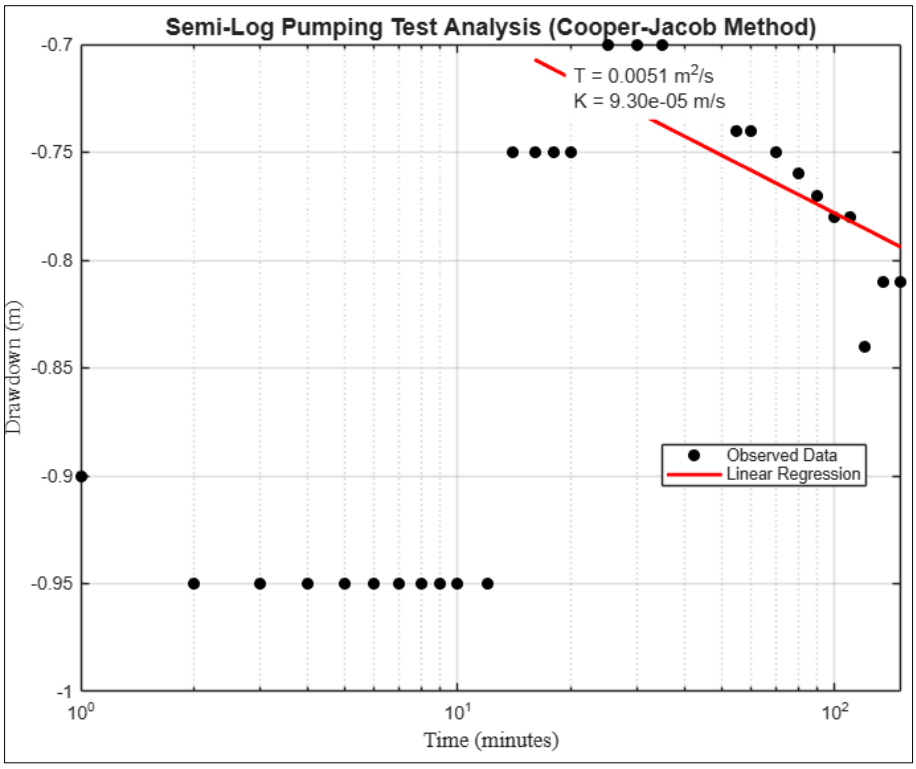


Figure 9. Pumping tests analysis using the Cooper–Jacob method.

It should be noted that the transmissivity and hydraulic conductivity values obtained in this study were derived from a single pumping well, thereby limiting their spatial representativeness at the aquifer scale. Consequently, the reported hydraulic parameters are more appropriately interpreted as point estimates applicable to the immediate vicinity of the monitoring well. Caution is therefore required when extrapolating these values across the broader study area. More comprehensive characterization of aquifer-scale hydraulic properties would require multi-well pumping tests involving additional observation wells.

The agreement between transmissivity estimated from the Dar-Zarrouk parameters (T_{DZ}) and transmissivity obtained from the pumping test ($Tpump$) was evaluated using the ratio (R) presented in Equation (8). This comparison follows the hydrogeophysical validation approach commonly applied to assess the consistency between geoelectrical estimations and field-based hydraulic measurements (Heigold et al., 1979):

$$R = \frac{TDZ}{Tpump} \quad (9)$$

Based on the transmissivity values obtained from the Dar-Zarrouk parameters and the pumping test (Table 2), a ratio of 12.94 was obtained, indicating that the geophysical method produces higher transmissivity estimates than the pumping test. This discrepancy is influenced by differences in measurement scale and by the homogeneity assumptions inherent in the geophysical approach. The VES method represents subsurface conditions over a broader spatial extent, whereas the pumping test primarily reflects localized conditions surrounding the well (Singh & Mondal, 2025). In addition, lithological heterogeneity characterized by alternating clay and sand layers at depths of 70–110 m further influences the effective field permeability values. Therefore, integrating geophysical data with pumping test results is necessary to obtain more representative permeability estimates for sedimentary hydrogeological systems.

Integration of Hydrogeological Models

© 2026 Dept. of Geophysics Hasanuddin University

The conceptual hydrogeological model presented as cross-sections in the west–east and south–north directions demonstrates both lateral continuity and thickness variations among the investigated layers across the study area (Figure 10). The first layer represents the surface soil layer with relatively limited thickness. The second layer exhibits very low resistivity values and is interpreted as clay, a material characterized by low permeability. The third layer consists of sandy clay with moderate resistivity values and functions as a transitional layer. Meanwhile, the fourth layer is located at greater depth and functions as the principal aquifer, consisting predominantly of sand with relatively higher resistivity values (Table 1).

In the west–east section, the aquifer layer exhibits its greatest thickness in the western part of the study area and gradually becomes thinner toward the east, particularly at VES 3. In contrast, the south–north section (VES 1–4–5) shows less significant thickness variation. The southern section at VES 4 exhibits a slightly greater aquifer thickness than the northern section at VES 5. The hydrogeological cross-section (Figure 10) illustrates the vertical and lateral relationships among subsurface strata that control groundwater occurrence and movement within the study area. The subsurface sequence extends to a depth of approximately 125 m and consists of layers with contrasting physical characteristics that influence their hydraulic responses.

The observation well is located at VES 1, which serves as the primary reference point for correlation among measurement locations. Based on the integrated interpretation of VES data, resistivity logging, and lithological information, the groundwater-bearing zone is interpreted to occur at depths of approximately 76–84 m below ground surface. Lateral variations within the groundwater-bearing zone indicate heterogeneity in hydraulic gradients among locations, which may influence groundwater flow directions and flow patterns within the aquifer system. Groundwater flow within the sand layer develops predominantly in the horizontal direction following the hydraulic pressure gradient. The presence of an overlying low-permeability layer causes the groundwater to remain under pressure, thereby supporting its interpretation as a confined aquifer system (Lodh, 2021). The hydrogeological conceptual model presented in Figure 10 illustrates the lateral and vertical relationships among hydrostratigraphic layers, infiltration zones, and groundwater flow directions within the study area. The subsurface sequence extends to a depth of approximately 125 m and consists of layers with contrasting physical characteristics that influence their hydraulic responses. The observation well is located at VES 01, which serves as the primary reference point for correlation among the sounding locations.

Vertically, the study area consists of four main layers. The uppermost layer is topsoil, which functions as an infiltration zone (Dahan, 2020). In this layer, groundwater movement predominantly occurs vertically; however, the downward movement becomes restricted upon reaching the underlying clay layer. This clay layer is relatively impermeable and therefore acts as a barrier to vertical groundwater flow. Beneath the clay layer lies a sandy clay layer with moderate permeability that functions as a transitional zone. The deepest layer consists predominantly of sand and is interpreted as the principal aquifer. The groundwater table is interpreted to occur at depths ranging from 76 to 84 m below the ground surface. Lateral variations in groundwater level indicate differences in hydraulic head that may influence groundwater flow direction within the aquifer system. Groundwater flow within the sand layer develops

© 2026 Dept. of Geophysics Hasanuddin University

predominantly in the horizontal direction following the hydraulic gradient. Because the aquifer layer is confined beneath an impermeable layer and controlled by hydraulic pressure differences, the system is classified as a confined aquifer.

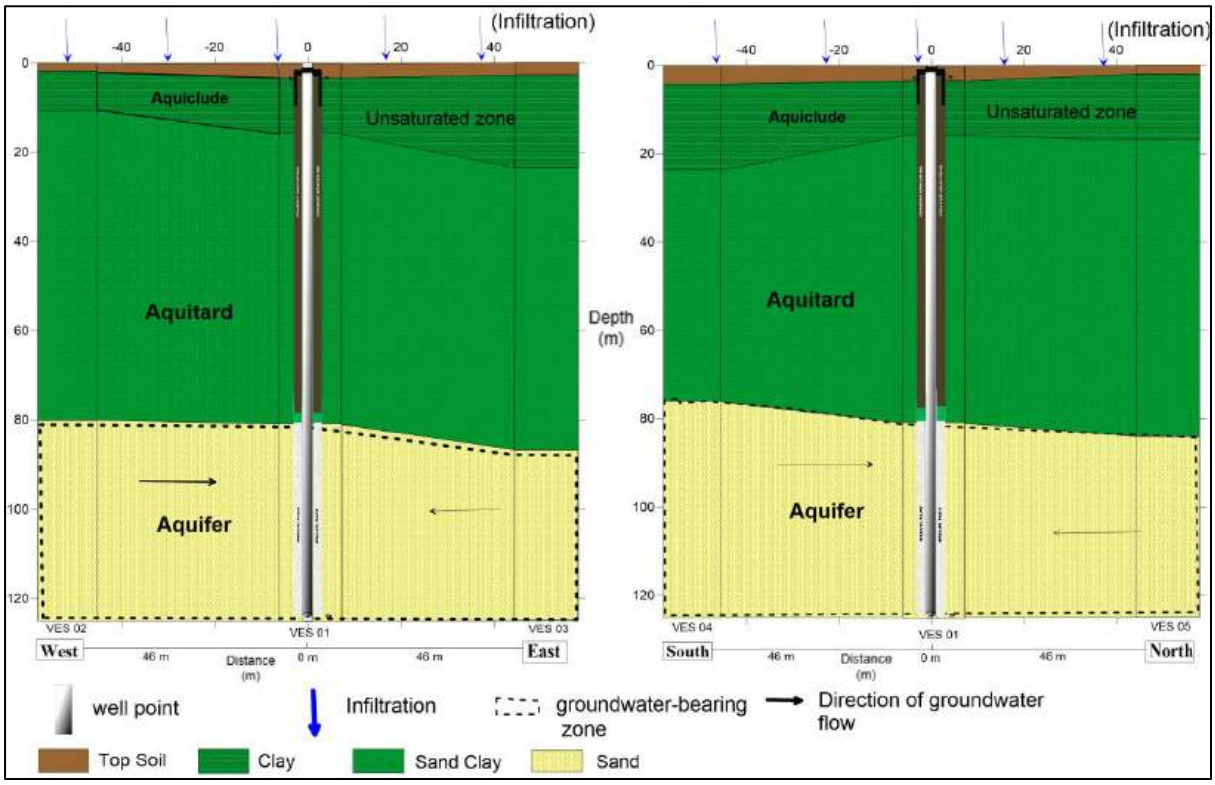


Figure 10. Conceptual hydrogeological model.

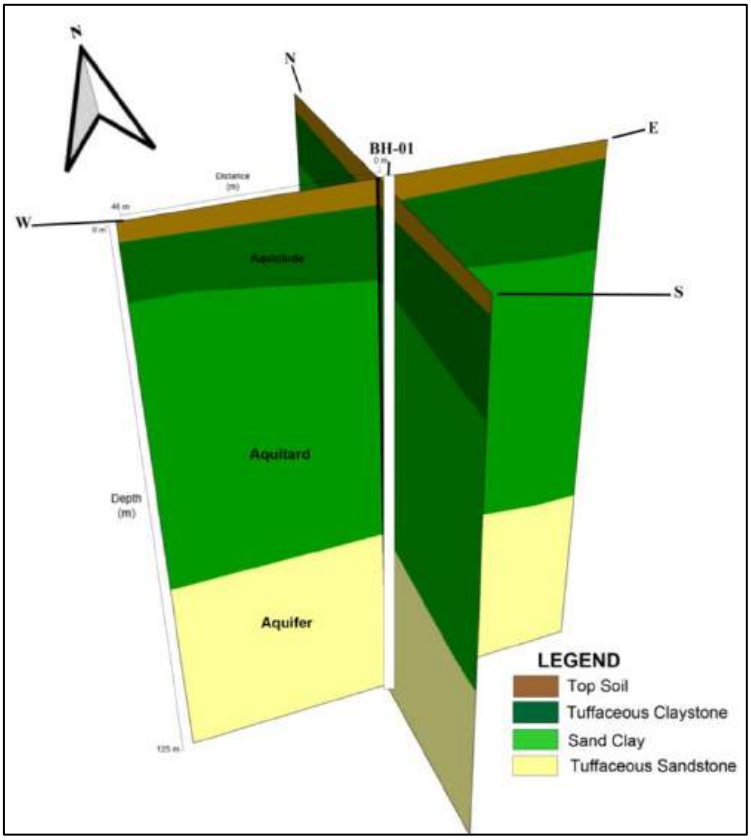


Figure 11. Hydrogeological fence diagram.

© 2026 Dept. of Geophysics Hasanuddin University

The hydrogeological diagram illustrates the subsurface stratification within the study area based on the interpretation of integrated geophysical and borehole data (Figure 11). The identified subsurface units consist of topsoil, clay, sandy clay, and sand layers (Table 3). The topsoil layer functions as an infiltration zone, whereas the clay layer is interpreted as an aquiclude (Vincent et al., 2024). The sandy clay layer functions as an aquitard, while the lowermost sand layer is interpreted as the principal aquifer (Mohamed et al., 2023).

Table 3. Range of resistivity values, lithology, and hydrogeological classification in the ITERA monitoring well area, Lampung.

Resistivity Range	Lithology	Hydrogeological Classification
< 10 Ωm	Clay	Aquiclude
10 – 20 Ωm	Sandy clay	Aquitard
20 – 80 Ωm	Sand	Aquifer

Conclusion

This study successfully achieves its primary objective of developing a calibrated interpretation approach for aquifer identification and determining optimal well construction depths within complex volcanic geological environments. Through the integration of Vertical Electrical Sounding (VES), well logging, petrographic analysis, and pumping test data, a more reliable understanding of the relationships among resistivity values, lithological characteristics, and hydraulic parameters is achieved. The results indicate that the main aquifer occurs at depths greater than 75 m, with two productive zones identified at depths of 85–90 m and 110–125 m. These zones predominantly consist of coarse-grained sand materials with favorable permeability characteristics. The integrated approach effectively reduces the ambiguity commonly associated with resistivity interpretation in volcanic materials, thereby improving the accuracy of aquifer delineation.

The main strength of this study lies in the application of a multidisciplinary approach that integrates geophysical, petrographic, and hydraulic data to produce a more comprehensive and calibrated interpretation. This approach not only enhances the reliability of aquifer identification but also provides a stronger basis for determining the optimal screen depth for monitoring wells. Based on the integrated interpretation results, the recommended screen interval is 90–120 m, representing the most productive aquifer zone within the study area.

Nevertheless, this study has several limitations that introduce uncertainty into the hydrogeological model outputs. The limited vertical resolution of the VES method in detecting thin layers may result in incomplete characterization of transitional zones within the aquifer system. In addition, the pumping test data derived from a single well constrain the spatial representativeness of the hydraulic parameters and introduce uncertainty into aquifer-scale estimates. Furthermore, the assumption of subsurface homogeneity in geophysical interpretation, reflected by the overestimation of Dar-Zarrouk transmissivity by a factor of approximately 12.94 relative to the pumping test results, highlights the inherent limitations of standalone geophysical approaches in heterogeneous sedimentary systems. Collectively, these uncertainties influence the reliability of the proposed hydrogeological model and should therefore be considered when applying the framework to broader areas. From a practical perspective, the findings of this study have significant potential applications in the planning and development of groundwater monitoring systems, particularly for determining the location and design of monitoring wells in volcanic geological environments. In addition, the calibrated interpretation framework developed in this study can be applied to similar hydrogeological

© 2026 Dept. of Geophysics Hasanuddin University

investigations to improve aquifer identification accuracy and support sustainable groundwater resource management.

Future research should focus on validating and expanding the proposed interpretation framework through multi-well pumping tests involving observation wells to better constrain aquifer hydraulic properties at broader spatial scales. Additional long-duration pumping tests would also be beneficial for evaluating boundary effects and confirming steady-state conditions. Furthermore, complementary geophysical surveys, such as Electrical Resistivity Tomography (ERT) and Time-Domain Electromagnetic (TDEM) methods, could improve lateral resolution and reduce interpretation ambiguity, particularly within transitional zones between aquifer and aquitard units.

Acknowledgements

The author would like to thank the Geophysical Engineering Laboratory at the Sumatra Institute of Technology for lending the equipment used for data acquisition. The author would also like to thank the Center for Groundwater and Environmental Geology at the Geological Agency for providing the well logging and pumping test data used in this study, as well as for the opportunity to participate in some of the field measurement activities for the project.

Author Contribution

Cherly Rizka Susanti: Conceptualization (lead); lithological, petrographic, and pumping test analysis (lead); writing and editing (equal). Astrik Rahmi Yati: Methodology (lead); geoelectrical and Dar-Zarrouk analysis (lead); conceptual model development and interpretation (lead); writing—original draft (lead). Rizka: Supervision (lead); validation (lead); writing—review and editing (equal). All authors have read and approved the final version of the manuscript.

Conflict of Interest

The authors report no conflict of interest concerning the publication of this article.

References

Agussalim, A., Djafar, M., & Rizal, A. S. (2022). Analisis potensi debit air tanah melalui pumping test metode step draw down pada sumur bor irigasi di Desa Bonto Rannu, Kecamatan Kajang, Kabupaten Bulukumba, Sulawesi Selatan. *Jurnal Fisika dan Terapannya,* 9(2), 127–137. https://doi.org/10.24252/jft.v9i2.32277

Al-Mudhafar, W. J., Abbas, M. A., & Wood, D. A. (2024). Integration of electromagnetic, resistivity-based and production logging data for validating lithofacies and permeability predictive models with tree ensemble algorithms in heterogeneous carbonate reservoirs. *Petroleum Geoscience,* 30(1), petgeo2023-067. https://doi.org/10.1144/petgeo2023-067

Amir, H. S., Fathy, M., Reda, M., & Mostafa, T. (2025). Integrated core-log petrophysical evaluation of the Sarir Formation reservoir units, southeastern Sirte Basin, Libya. *Journal of Umm Al-Qura University for Applied Sciences.* https://doi.org/10.1007/s43994-025-00295-6

Ammar, A. I., & Kamal, K. A. (2019). Effect of structure and lithological heterogeneity on the correlation coefficient between the electric–hydraulic parameters of the aquifer, Eastern Desert, Egypt. *Applied Water Science*, 9(4), 83. https://doi.org/10.1007/s13201-019-0963-3

© 2026 Dept. of Geophysics Hasanuddin University

Archie, G. E. (1942). The electrical resistivity log as an aid in determining some reservoir characteristics. *Transactions of the AIME*, 146(1), 54–62. https://doi.org/10.2118/942054-G

Bahri, S., Appono, S. V., & Zulfiah. (2022). Global optimization very fast simulated annealing inversion for the interpretation of groundwater potential. *Jurnal Geofisika Eksplorasi*, 8(3), 225–236. https://doi.org/10.23960/jge.v8i3.233

Chakraborty, S., Yadav, A., & Chatterjee, R. (2021). Comprehensive rock physics, petrophysics workflow to correct sonic logs for improved seismic QI: Study using wells of Krishna Godavari Basin. *Journal of Applied Geophysics*, 192, 104394. https://doi.org/10.1016/j.jappgeo.2021.104394

Claprood, M., Gloaguen, E., Béraud, T., Blouin, M., Dupuis, C., Ferron, P., Ouellet, M., Chaussé, M., Martel, R., Paradis, D., & Ballard, J.-M. (2022). A case study using seismic reflection and well logs to reduce and quantify uncertainty during a hydrogeological assessment. *Frontiers in Water*, 3, 779149. https://doi.org/10.3389/frwa.2021.779149

Cooper, H. H., Jr., & Jacob, C. E. (1946). A generalized graphical method for evaluating formation constants and summarizing well-field history. *Eos, Transactions American Geophysical Union*, 27(4), 526–534. https://doi.org/10.1029/TR027i004p00526

Dahan, O. (2020). Vadose zone monitoring as a key to groundwater protection. *Frontiers in Water*, 2, 599569. https://doi.org/10.3389/frwa.2020.599569

Grandis, H. (2009). *Pengantar Pemodelan Inversi Geofisika*. Himpunan Ahli Geofisika Indonesia (HAGI)

Hasani, M. F., Hendrayana, H., & Taufiq, A. (2023). Determination of aquifer system using resistivity method in Pekalongan City and surrounding areas, Central Java, Indonesia. *Proceedings of the 4th International Seminar on Science and Technology* (ISST 2022), 7, 100–108. https://doi.org/10.2991/978-94-6463-228-6_12

Heigold, P. C., Gilkeson, R. H., Cartwright, K., & Reed, P. C. (1979). Aquifer transmissivity from surficial electrical methods. *Groundwater,* 17(4), 338–345. https://doi.org/10.1111/j.1745-6584.1979.tb03326.x

Juwono, A. M., Susilo, A., Hasan, M. F. R., Yunika, N. A., Annabil, A. A., Mujtaba, M. W. H., & Haniyyah, S. (2024). Investigation of groundwater sources in Banyol Hamlet Malang Regency using the geoelectrical resistivity method to overcome drought strategy. *Indonesian Physical Review*, 7(2), 240–248. https://doi.org/10.29303/ipr.v7i2.320

Kumalasari, I. N., Mulyasari, R., Dewanto, O., Mulyatno, B. S., Wibowo, R. C., Maulida, N. H., Hidayatika, A., Hesti, H., Dani, I., & Erfani, S. (2025). Identifikasi akuifer air tanah menggunakan metode geolistrik di Perumahan Gang Jati Baru, Hajimena, Natar, Lampung Selatan. *Jurnal Riset Fisika Indonesia*, 5(2), 71–78. https://doi.org/10.33019/jrfi.v5i2.6504

Li, J., Wang, W., Cheng, D., Li, Y., Wu, P., & Huang, X. (2021). Hydrogeological structure modelling based on an integrated approach using multi-source data. *Journal of Hydrology*, 600, 126435. https://doi.org/10.1016/j.jhydrol.2021.126435

Lodh, A. (2021). Simulating the impact of extended desertification on Indian hydroclimate using ICTP-RegCM4.4.5.10 model. *Journal of Hydrology*, 598, 126405. https://doi.org/10.1016/j.jhydrol.2021.126405

© 2026 Dept. of Geophysics Hasanuddin University

MacKenzie, W. S., & Guilford, C. (1980). *Atlas of Rock-Forming Minerals in Thin Section*. Routledge. https://doi.org/10.4324/9781315837413

Maillet, R. (1947). The fundamental equations of electrical prospecting. *Geophysics*, 12(4), 529–556. https://doi.org/10.1190/1.1437342

Mangga, S. A., Amiruddin. A., Suwarti, T., Gafoer, S., & Sidarto, S. (1993). *Peta geologi lembar Tanjungkarang, Sumatera (Skala 1:250.000).* Pusat Penelitian dan Pengembangan Geologi.

Masria, A., Alshammari, T. O., Ghareeb, M., Seif, A. K., Abd-Elmaboud, M. E., & Ammar, A. I. (2024). 2D and 3D modeling of resistivity and chargeability to identify the type of saturated groundwater for complex sedimentary facies. *Hydrology*, 11(8), 120. https://doi.org/10.3390/hydrology11080120

Mohamed, A., Alarifi, S. S., & Abdelrady, A. (2023). Sedimentary cover and structural trends affecting groundwater flow in the Nubian Sandstone Aquifer System: Inferences from geophysical, field and geochemical data. *Frontiers in Earth Science,* 11, 1173569. https://doi.org/10.3389/feart.2023.1173569

Mohammed, M. A. A., Szabó, N. P., Eltijani, A., & Szűcs, P. (2025). An integrated workflow combining machine learning and wavelet transform for automated characterization of heterogeneous groundwater systems. *Scientific Reports,* 15, 4973. https://doi.org/10.1038/s41598-025-89410-5

Muauz, A., Berehanu, B., & Bedru, H. (2025). An alternative approach using electrical well logging for estimating porosity and hydraulic conductivity in volcanic aquifers of the Upper Awash River Sub-Basin, Ethiopia. Journal of *Hydrology: Regional Studies*, 60, 102547. https://doi.org/10.1016/j.ejrh.2025.102547

Muhammad, S., Khalid, P., Ehsan, M. I., Qureshi, J., & Farooq, S. (2023). Evaluation of aquifer parameters through integrated approach of geophysical investigations, pumping test analysis and Dar-Zarrouk parameters in the central part of Bari Doab, Punjab, Pakistan. *Environmental Monitoring and Assessment,* 195, 1435. https://doi.org/10.1007/s10661-023-12049-0

Nesse, W. D. (2014). *Introduction to Optical Mineralogy* (4th ed.). Oxford University Press. https://global.oup.com/academic/product/introduction-to-optical-mineralogy-9780199846283?cc=my&lang=en&

Nouradine, H., Schamper, C., Valdes, D., Moussa, I., Ramel, D., & Plagnes, V. (2024). Integrating geological, hydrogeological and geophysical data to identify groundwater resources in granitic basement areas (Guéra Massif, Chad). *Hydrogeology Journal*, 32(3), 759–784. https://doi.org/10.1007/s10040-024-02766-2

Nugraha, G. U., Bakti, H., Lubis, R. F., Sudrajat, Y., & Arisbaya, I. (2022). Aquifer vulnerability in the coastal northern part of Lombok Island Indonesia. *Environment, Development and Sustainability,* 24, 1390–1410. https://doi.org/10.1007/s10668-021-01459-0

Nyembwe, I., Nwanosike, A. A., Ndatimana, G., Okot, N., & Muamba, R. T. (2024). Evaluation of aquifer hydraulic properties from resistivity and pumping test data in parts of Gwagwalada, Northcentral Nigeria. *Journal of Groundwater Science and Engineering,* 12(3), 309–320.

© 2026 Dept. of Geophysics Hasanuddin University

https://doi.org/10.26599/JGSE.2024.9280023

Oli, I. C., Opara, A. I., Okeke, O. C., Akaolisa, C. Z., Akakuru, O. C., Osi-Okeke, I., & Udeh, H. M. (2022). Evaluation of aquifer hydraulic conductivity and transmissivity of Ezza/Ikwo area, Southeastern Nigeria, using pumping test and surficial resistivity techniques. *Environmental Monitoring and Assessment*, 194(10), 719. https://doi.org/10.1007/s10661-022-10341-z

Oyeyemi, K. D., Aizebeokhai, A. P., Ukabam, C. S., Kayode, O. T., Olaojo, A. A., & Metwaly, M. (2023). Nonlinear inversion of electrical resistivity sounding data for multi-layered 1-D earth model using global particle swarm optimization (GPSO). *Heliyon*, 9(6), e16528. https://doi.org/10.1016/j.heliyon.2023.e16528

Pinehas, D., & Warsa, W. (2020). Determination of Groundwater Surface using Damped Least-Squares Inversion in the Bekasap Field, Riau. *Jurnal Geofisika*, 17(2), 5–8. https://doi.org/10.36435/jgf.v17i2.414

Prinaldi, D. R., Pratiwi, S. D., & Rosana, M. F. (2023). Karakteristik petrologi dan petrografi satuan batugamping terumbu dan batupasir karbonatan pada Formasi Cibodas daerah Pasiripis dan sekitarnya, Kabupaten Sukabumi, Provinsi Jawa Barat. *Padjadjaran Geoscience Journal,* 7(6), 1749 – 1756. https://jurnal.unpad.ac.id/geoscience/article/view/53360/22344

Putri, S. A., Putra, A., & Abdurrachman, M. (2018). Studi petrografi batuan beku dan sinter silika di Kecamatan Alam Pauh Duo, Kabupaten Solok Selatan. *Jurnal Fisika Unand,* 7(4), 320–327. https://jfu.fmipa.unand.ac.id/index.php/jfu/article/view/371

Raju, B. A., Rao, P. V., & Subrahmanyam, M. (2023). Estimating aquifer transmissivity using Dar-Zarrouk parameters to delineate groundwater potential zones in Alluri Seetharama Raju District, Andhra Pradesh, India. *Journal of Groundwater Science and Engineering,* 11(2), 116–132. https://doi.org/10.26599/JGSE.2023.9280011

Rau, G. C., Cuthbert, M. O., Post, V. E. A., Schweizer, D., Acworth, R. I., Andersen, M. S., Blum, P., Carrara, E., Rasmussen, T. C., & Ge, S. (2020). Future-proofing hydrogeology by revising groundwater monitoring practice. *Hydrogeology Journal,* 28(8), 2963–2969. https://doi.org/10.1007/s10040-020-02242-7

Rizka, R., & Satiawan, S. (2019). Investigasi Lapisan Akuifer Berdasarkan Data Vertical Electrical Sounding (VES) dan Data Electrical Logging; Studi Kasus Kampus ITERA. *Bulletin of Scientific Contribution: Geology,* 17(2), 91–100. https://jurnal.unpad.ac.id/bsc/article/view/22393

Roy, A., & Apparao, A. (1971). Depth of investigation in direct current methods. *Geophysics*, 36(5), 943–959. https://doi.org/10.1190/1.1440226

Sanei, H., Ardakani, O. H., Akai, T., Akihisa, K., Jiang, C., & Wood, J. M. (2020). Core versus cuttings samples for geochemical and petrophysical analysis of unconventional reservoir rocks. *Scientific Reports*, 10(1), 7920. https://doi.org/10.1038/s41598-020-64936-y

Sehah, S., Aziz, A. N., Raharjo, S. A., Buliyanti, S. C., Mubarak, F., Wicaksono, G. F., & Asahi, W. (2024). Study of the Potential of the Purwokerto-Purbalingga Groundwater Basin as a Source of Irrigation using Gravimetric Satellite Data. *Water Conservation and Management,* 8(2), 140–149.

© 2026 Dept. of Geophysics Hasanuddin University

https://doi.org/10.26480/wcm.02.2024.140.149

Singh, S., & Mondal, N. C. (2025). Aquifer hydraulic characteristics using D-Z parameters: A case study of Lohaghat Block, Champawat District, Uttarakhand, India. *Discover Applied Sciences,* 7(11), 1293. https://doi.org/10.1007/s42452-025-06778-9

Siringoringo, L. P., Rizki, R., & Nababan, J. (2019). Hydrogeochemical and groundwater assessment for drinking purpose at ITERA Campus Area and its surroundings. *Journal of Geoscience, Engineering, Environment, and Technology,* 4(1), 40–47. https://doi.org/10.25299/jgeet.2019.4.1.2478

Siringoringo, L. P., & Maulana, S. (2020). Unconfined groundwater flow pattern and facies changes at Way Huwi Village, South Lampung. *RISET Geologi dan Pertambangan, 30*(1), 109–118. https://doi.org/10.14203/risetgeotam2020.v30.1076

Syaputri, T. D., Suhendra, S., Halauddin, H., Lidiawati, L., & Nurhidayah, R. (2024). Groundwater study using vertical electrical sounding (VES) data based on resistivity and porosity of rocks in Kampung Melayu, Bengkulu City. *Jurnal Ilmiah Sains,* 24(1), 38–47. https://doi.org/10.35799/jis.v24i1.54133

Todd, D. K. (1980). *Groundwater hydrology* (2nd ed.). John Wiley & Sons.

Vincent, A., Daigre, C., Fischer, O., Aðalgeirsdóttir, G., Violette, S., Hart, J., Guðmundsson, S., & Pálsson, F. (2024). A hydrogeological conceptual model of aquifers in catchments headed by temperate glaciers. *Hydrology and Earth System Sciences,* 28(14), 3475–3494. https://doi.org/10.5194/hess-28-3475-2024

Warsi, T., Kumar, V. S., Kumar, D., Nandan, M. J., Biswas, G., Sahadevan, D. K., Manikyamba, C., Rao, T. V., Rangarajan, R., Ahmed, S., & Chandrasekhar, V. (2020). Integration of geophysics and petrography for identifying the aquifer and the rock type: A case study from Giddalur, Andhra Pradesh, India. *Journal of Earth System Science,* 129(1), 44. https://doi.org/10.1007/s12040-019-1321-4

Wilkosz, M. (2022). ReMo3D – an open-source Python package for 2D and 3D simulation of normal and lateral resistivity logs. *Geology, Geophysics & Environment*, 48(2), 195–211. https://doi.org/10.7494/geol.2022.48.2.195

Wu, W., & Grana, D. (2017). Integrated petrophysics and rock physics modeling for well log interpretation of elastic, electrical, and petrophysical properties. *Journal of Applied Geophysics*, 146, 54–66. https://doi.org/10.1016/j.jappgeo.2017.09.007

Wu, Y., & Fan, Y. (2021). Fast hierarchical inversion for borehole resistivity measurements in high-angle and horizontal wells using ADNN-AMLM. *Journal of Petroleum Science and Engineering*, 203, 108662. https://doi.org/10.1016/j.petrol.2021.108662

Yang, L., Gao, M., Chen, J., Shi, W., Hou, C., Liu, Z., Luo, C., Yu, J., Yang, X., & Dong, J. (2025). Effects of climate variables and human activities on groundwater level fluctuations in unconsolidated sedimentary aquifers: A data-driven approach. *Hydrology,* 12(8), 215. https://doi.org/10.3390/hydrology12080215

Yihdego, Y. (2017). Hydraulic in situ testing for mining and engineering design: Packer test procedure,

© 2026 Dept. of Geophysics Hasanuddin University

preparation, analysis and interpretation. *Geotechnical and Geological Engineering*, 35(1), 29–44. https://doi.org/10.1007/s10706-016-0112-9

Yusuf, S. N., Ishaku, J. M., & Wakili, W. M. (2021). Estimation of Dar-Zarrouk parameters and delineation of groundwater potential zones in Karlahi, part of Adamawa Massif, Northeastern Nigeria. *Warta Geologi,* 47(2), 103–112. https://doi.org/10.7186/wg472202101

Zhou, F., Giannakis, I., Giannopoulos, A., Holliger, K., & Slob, E. (2023). Extracting mud invasion information using borehole radar—A numerical study. *Geophysics*, 88(2), D69–D83. https://doi.org/10.1190/geo2022-0121

© 2026 Dept. of Geophysics Hasanuddin University

ISSN: 2579-5821 (Print)
ISSN: 2579-5546 (Online)
URL address: http://journal.unhas.ac.id/index.php/geocelebes
DOI: 10.70561/geocelebes.v10i2.50269

Jurnal Geocelebes Vol. 10 No. 2, October 2026, 217 – 240

GIS-Based Flood Susceptibility Mapping Using Weighted Overlay Method in Barabai Sub-District, South Kalimantan, Indonesia

Sandri Erfani*, Nailatussa'adah, Rosna Amaliaatul Ma'rifah, M. Rayya Andisa Putra, Eka Andika, Andri Kurniawan

Department of Geophysical Engineering, Universitas Lampung, Bandar Lampung 35145, Indonesia.

*Corresponding author. Email: sandri.erfani@eng.unila.ac.id

Manuscript received: 12 March 2026; Received in revised form: 26 June 2026; Accepted: 17 July 2026

Abstract

Flooding is a major hydrometeorological hazard in Indonesia. This study assesses flood susceptibility in Barabai Sub-District, Hulu Sungai Tengah Regency, South Kalimantan, using a GIS-based weighted overlay approach. Six flood-conditioning factors were integrated in the analysis, namely slope, elevation, soil texture, rainfall, land use/land cover (LULC), and distance from river networks. The analysis used multi-source geospatial data, including a 30 m SRTM DEM, CHIRPS rainfall (2021–2025), FAO DSMW soil data, ESRI Sentinel-2 LULC data, administrative boundaries, and satellite imagery. The results show that flood susceptibility in Barabai Sub-District is dominated by high and very high classes. High-susceptibility areas cover 26.66 km², equivalent to 70.44% of the study area, whereas very high-susceptibility areas occupy 9.18 km², or 24.25%. In contrast, low and very low susceptibility zones account for only 1.78 km² (4.70%) and 0.23 km² (0.61%), respectively. Overall, 94.69% of the study area falls within the high to very high susceptibility classes. Land cover analysis indicates notable changes between 2021 and 2025, including a reduction in cropland and the emergence of a water body associated with a government-built reservoir for flood mitigation. The spatial pattern of flood susceptibility is mainly controlled by low elevation, proximity to river channels, fine- to medium-textured soils, intensive agricultural and built-up land use, and the dominance of Quaternary alluvial deposits, while high annual rainfall acts as the primary triggering factor. These findings support flood mitigation and land-use planning, while future studies should incorporate field validation and hydrological modeling.

Keywords: Barabai; Geographic Information System; Hydrometeorological Hazard; Land-Cover Dynamics; Multi-Criteria Spatial Analysis; Thematic Mapping.

Citation: Erfani, S., Nailatussa'adah, N., Ma'rifah, R. A., Putra, M. R. A., Andika, E., & Kurniawan, A. (2026). GIS-Based Flood Susceptibility Mapping Using Weighted Overlay Method in Barabai Sub-District, South Kalimantan, Indonesia. *Jurnal Geocelebes*, 10(2): 217–240, doi: 10.70561/geocelebes.v10i2.50269

Introduction

Flooding is among the most frequent and destructive hydrometeorological hazards, affecting both urban and rural areas through damage to communities, infrastructure, agricultural land, and local economies (Dhungana & Liu, 2024; Khan et al., 2025). Flood occurrence is commonly driven by the interaction of intense rainfall, low-lying topography, limited river capacity, and rapid land-use change (Sulaeman et al., 2017; Briantama et al., 2024). As flood impacts continue to increase in many regions, spatially explicit information on flood-conditioning factors has become essential for disaster risk reduction, mitigation planning, and sustainable land management.

In Indonesia, flooding remains the dominant and most frequently recorded hydrometeorological hazard, recurring annually across many regions and showing a significant increasing trend over the past decade (Aji et al., 2025; Ramadhan et al., 2026). Its impacts are often amplified by rapid regional development, particularly

© 2026 Dept. of Geophysics Hasanuddin University

the conversion of permeable land into built-up areas and intensive agricultural land, which reduces water retention capacity and increases surface runoff (Handayani et al., 2020; Fatmala et al., 2023). Beyond direct physical damage to settlements and infrastructure, floods also generate substantial social and economic consequences, especially in areas where communities, infrastructure, and productive land are highly exposed and where the capacity for recovery remains limited (Meng et al., 2022; Rentschler et al., 2022).

Barabai Sub-District, Hulu Sungai Tengah Regency, South Kalimantan, is one of the areas repeatedly affected by flooding. Several major flood events have been recorded, including floods in 2013 and a severe event in 2021 that was regarded as one of the worst floods in the region (Prabowo, 2018; Rizani et al., 2023) (Figure 1). Barabai Sub-District covers approximately 40.71 km² and consists of 18 villages, with a population density of 1,368 people km² (Badan Pusat Statistik Kabupaten Hulu Sungai Tengah, 2024). Physiographically, Barabai is located in a lowland area on the western side of the Meratus Mountains and is crossed by the Barabai River, resulting in a relatively extensive floodplain environment. Geologically, the area forms part of the Barito Basin, a Cenozoic sedimentary basin situated between the Schwaner Complex to the west and the Meratus Complex to the east (Witts et al., 2012). The area is predominantly underlain by alluvial deposits composed of unconsolidated materials such as clay, silt, sand, peat, gravel, and boulders, which generally have low infiltration capacity and increase susceptibility to inundation (Heryanto & Sanyoto, 1994; Pandey et al., 2021) (Figure 2).



Figure 1. Conditions on Murakata Street, one of the worst-hit areas by flooding in Barabai District in 2021 (Poros Kalimantan, 2021).

© 2026 Dept. of Geophysics Hasanuddin University

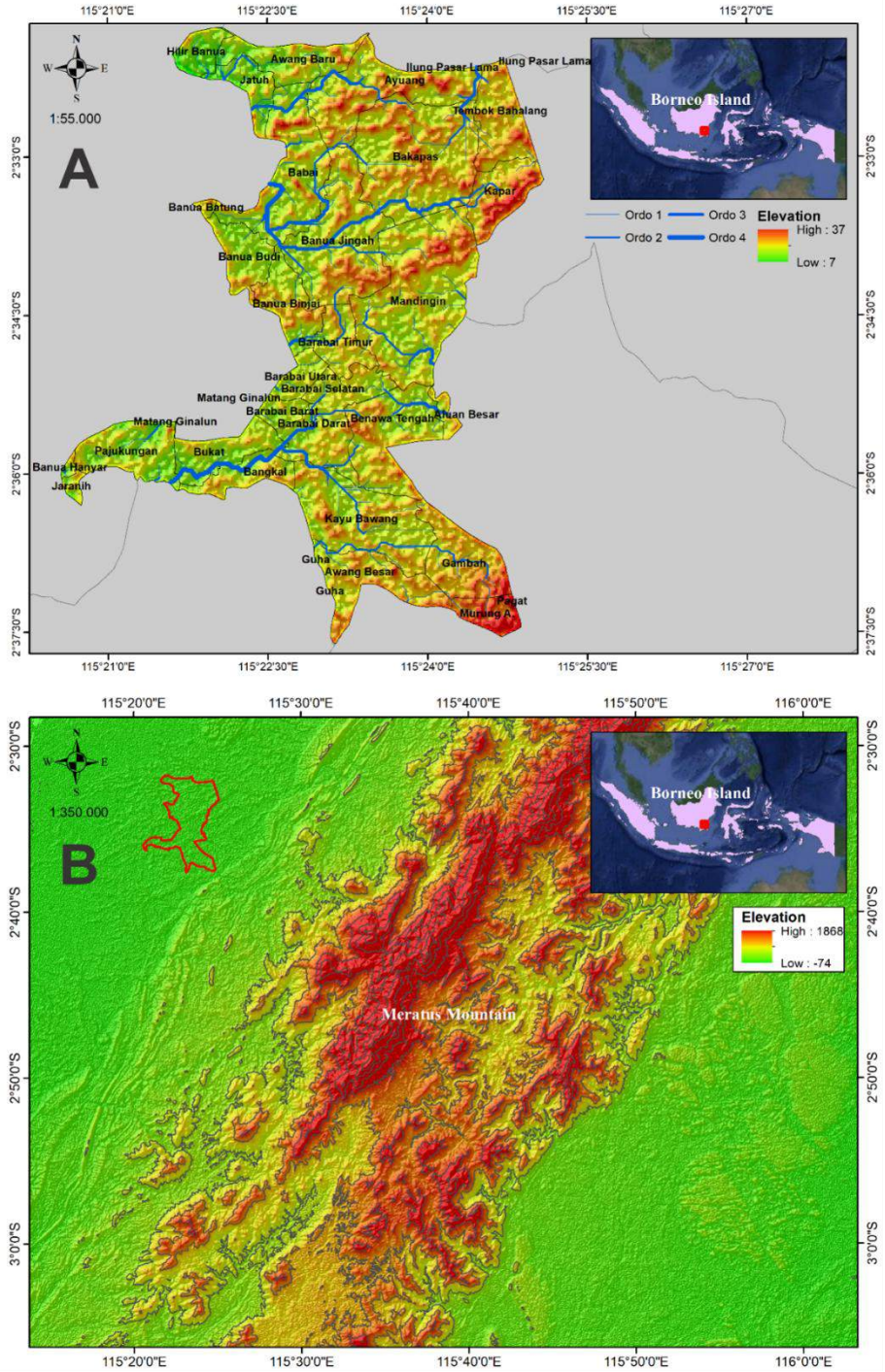


Figure 2. a) Geomorphological map of Barabai Sub-District with a maximum elevation of 37 meters shown in red; b)Topographic of Barabai Sub-District which is located in the western part of the Meratus Mountains.

In addition to its physiographic and geological setting, land-use change has further increased flood susceptibility in Barabai Sub-District. The expansion of residential areas and agricultural land has reduced open and permeable surfaces that previously functioned as water retention and infiltration zones (Handayani et al., 2020; Izzati & Rustandi, 2025). Development along river corridors, including agricultural expansion and settlement growth near riverbanks, may restrict channel capacity and increase the likelihood of overflow during intense rainfall events (Mondal & Patel, 2018; Sapoetra et al., 2024). Moreover, Barabai Sub-District still has limited disaster mitigation infrastructure, including early warning systems, while river maintenance, embankment management, and drainage

© 2026 Dept. of Geophysics Hasanuddin University

normalization remain insufficient in many villages (Badan Pusat Statistik Kabupaten Hulu Sungai Tengah, 2024). These conditions highlight the need for a spatially explicit assessment that can identify areas with different levels of flood susceptibility and support more targeted flood mitigation planning.

Several approaches have been developed to identify and map flood-prone areas, ranging from hydrological and hydraulic modeling to Geographic Information System (GIS)-based spatial analysis (Efraimidou & Spiliotis, 2024; Gasmi & Aly, 2026; Zhou et al., 2021). GIS-based scoring and weighted overlay methods are widely applied because they can integrate multiple flood-conditioning factors in a transparent, reproducible, and relatively simple manner, particularly in areas where detailed hydrological and field-based data are limited (Hanie et al., 2017; Septian et al., 2020; Latue et al., 2023). This approach enables the spatial evaluation of flood susceptibility by considering the relative contribution of topography, rainfall, land cover, soil characteristics, and proximity to river networks.

Although GIS-based flood susceptibility mapping has been widely applied in many regions (Amatebelle et al., 2025), sub-district-scale studies that integrate physical, geological, hydrological, and land-use characteristics remain limited, particularly for Barabai Sub-District. Existing studies and reports have documented flood occurrence in the region; however, spatial information that explicitly delineates flood susceptibility zones and relates them to their controlling factors is still insufficient for local mitigation planning. Therefore, this study aims to develop a GIS-based flood susceptibility map for Barabai Sub-District using a weighted overlay approach. The analysis integrates six flood-conditioning factors: rainfall, slope, elevation, soil texture, land use/land cover, and distance from river networks level.

The main contribution of this study is the development of a sub-district-scale flood susceptibility map that links spatial susceptibility patterns with key environmental and land-use controls. By integrating multi-source geospatial datasets within a GIS-based weighted overlay framework, this study provides practical spatial information for identifying priority areas for flood mitigation, supporting land-use planning, and strengthening disaster risk reduction strategies in Barabai Sub-District.

Materials and Methods

Barabai Sub-District is located in Hulu Sungai Tengah Regency, South Kalimantan, Indonesia, and comprises several villages and urban wards that provide the administrative framework for this spatial analysis. The study area lies in a lowland setting on the western flank of the Meratus Mountains and forms part of a downstream watershed system that receives runoff from surrounding upstream areas. Its relatively flat to gently sloping terrain, combined with the dominance of alluvial deposits and a history of recurrent flooding, makes the area highly susceptible to inundation, particularly during periods of intense rainfall (Indrasari & Rudiarto, 2020; Gultom et al., 2022). In this study, the administrative boundary of Barabai Sub-District was overlaid on high-resolution Google Earth satellite imagery to define the spatial extent of the analysis and to support visual interpretation of the study area, as shown in Figure 3.

Several secondary geospatial datasets were used to derive the flood-conditioning factors in this study, as summarized in Table 1. Topographic parameters, including elevation, slope, and drainage-related variables, were derived from the 30 m Shuttle Radar Topography Mission (SRTM) Digital Elevation Model. The administrative boundary of Barabai Sub-District was obtained from the Indonesia

© 2026 Dept. of Geophysics Hasanuddin University

Geospatial Portal and used to delineate the study area. Rainfall was represented using CHIRPS data for the 2021–2025 period, whereas soil texture information was obtained from the FAO Digital Soil Map of the World (DSMW). Land use/land cover (LULC) data for 2021 and 2025 were extracted from the Esri Sentinel-2 Land Cover Explorer. High-resolution Google satellite imagery was used to support visual interpretation and verification of land cover conditions. In addition, the InaRISK-BNPB flood hazard map was used as an independent reference for comparison with the resulting flood susceptibility map. All datasets were processed and standardized in a GIS environment to ensure consistency in spatial extent, projection, and analysis.

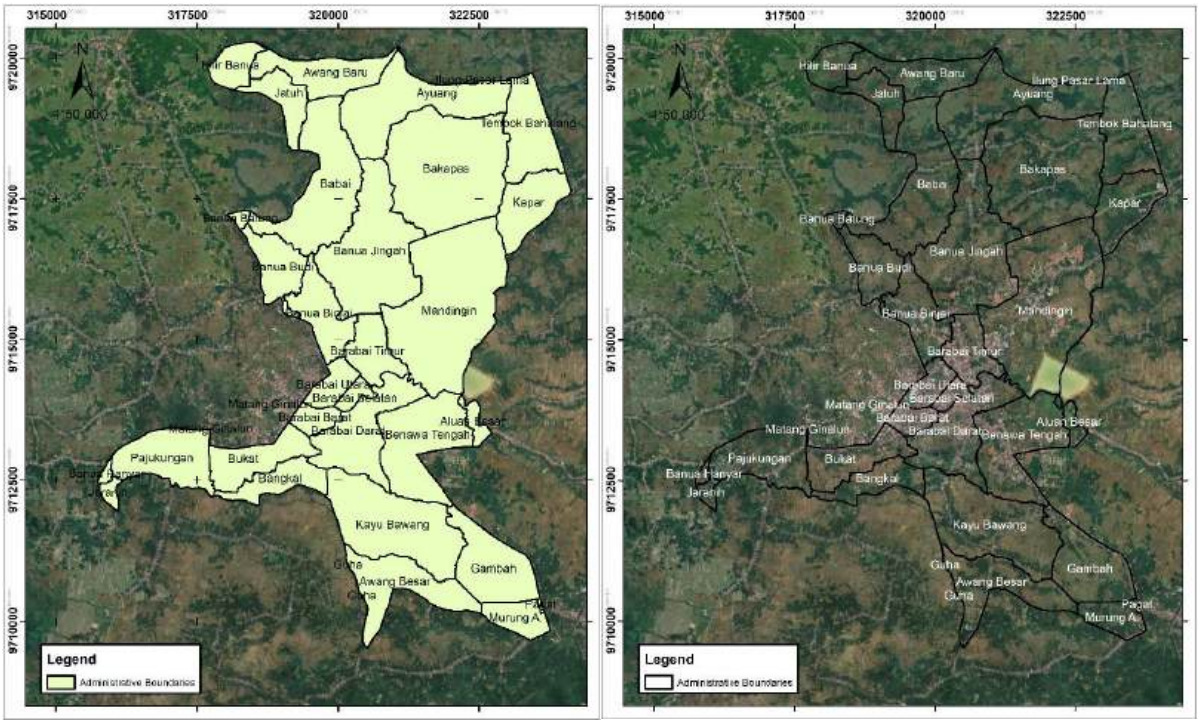


Figure 3. shows the administrative boundaries of Barabai Sub-District displayed on Google Earth satellite imagery. The study area consists of several villages and urban wards (kelurahan/ desa), which provide the spatial framework for flood susceptibility mapping and GIS-based analysis.

Previous spatial flood susceptibility studies have commonly incorporated rainfall, elevation, slope, land cover, soil characteristics, and drainage-related parameters as key flood-conditioning factors (Sihaini et al., 2026; Putri & Triyatno, 2025). Guided by these studies, the analytical framework in this study was designed to integrate six conditioning factors: rainfall, elevation, slope, land use/land cover, soil texture, and distance from river networks. Prior to the weighted overlay analysis, all spatial datasets listed in Table 1 were preprocessed in a GIS environment through coordinate reference system standardization, clipping to the Barabai Sub-District boundary, spatial resolution harmonization, and data format conversion where necessary. These procedures were applied to ensure consistency in spatial extent, projection, and analytical units across all input layers.

After preprocessing, each dataset was processed according to its role in the flood susceptibility analysis. The InaRISK flood hazard data were converted into polygon format to generate a reference flood hazard map. Land use/land cover data for 2021 and 2025 were used to produce LULC maps and to assess land cover changes in Hulu Sungai Tengah Regency and Barabai Sub-District. CHIRPS rainfall data were processed using the Cell Statistics tool and interpolated

© 2026 Dept. of Geophysics Hasanuddin University

using the Inverse Distance Weighting (IDW) method to generate the average annual rainfall distribution map. The DEM was used to derive elevation, slope, and river network parameters through hydrological processing, including sink filling, flow direction, and flow accumulation analysis, followed by the generation of river buffer zones. Soil texture information was extracted from the DSMW dataset to represent the influence of soil properties on infiltration capacity and surface runoff.

Table 1. Research Data Information

Data	Source	Year	Spatial Resolution / Scale	Format	Coordinate Reference System	Purpose in Analysis
SRTM DEM	USGS Earth Explorer (https://earthexplorer.usgs.gov/)	2014	30 m	Raster (GeoTIFF)	WGS 84, UTM Zone 50S	Derivation of elevation, slope, and stream parameters for flood susceptibility analysis
Administrative Boundary of Barabai Regency	Indonesia Geospatial Portal (https://tanahair.indonesia.go.id/)	2017	1:50,000	Vector (Shapefile)	WGS 84, UTM Zone 50S	Delineation of study area boundary
Rainfall Data (CHIRPS)	Climate Hazards Group – CHIRPS	2021 – 2025	0.05° (~5 km)	Raster (Bil/HDR)	WGS 84 Geographic Coordinate System	Rainfall parameter for flood susceptibility analysis
Soil Type Data (DSMW)	Digital Soil Map of the World (FAO)	2007	1:3,000,000	Vector (Shapefile)	WGS 84 Geographic Coordinate System	Soil texture classification for flood susceptibility analysis
Land Cover Data of South Kalimantan	Esri Sentinel-2 Land Cover Explorer (https://livingatlas.arcgis.com/landcoverexplorer/)	2021 & 2025	10 m	Raster	WGS 84 Geographic Coordinate System	Land use/land cover parameter for flood susceptibility analysis
Basemap Imagery	Google Satellite Imagery (Google Maps)	2025	High-resolution imagery	Raster imagery	WGS 84 Web Mercator	Visual interpretation and validation of land cover conditions
Flood Hazard Map	InaRISK-BNPB (https://inarisk.bnpb.go.id/)	2024	30m	Raster	WGS 84 Geographic Coordinate System	Validation and comparison of flood susceptibility results

All derived parameters were then reclassified according to their relative influence on flood occurrence and converted into a common spatial analysis format. Each parameter class was assigned a score, while each parameter was assigned a weight based on its relative contribution to flood susceptibility. In this study, soil

© 2026 Dept. of Geophysics Hasanuddin University

texture was assigned the highest weight of 25%, followed by land use/land cover and slope, each with a weight of 20%. Rainfall was assigned a weight of 15%, whereas elevation and distance from rivers were each assigned a weight of 10%. The weighted scores were then integrated using the weighted overlay method to calculate the flood susceptibility index.

GIS-based multi-criteria approaches have become an effective framework for flood susceptibility and risk assessment by integrating multiple flood-conditioning factors and supporting decision-making for flood mitigation and land-use planning (Efraimidou & Spiliotis 2024).

The final map was evaluated by comparing it with the InaRISK-BNPB flood hazard map and available historical flood records. This comparison was conducted to examine whether areas classified as high and very high susceptibility corresponded to previously reported flood-affected zones. In addition, land use/land cover changes between 2021 and 2025 were analyzed to assess how land cover dynamics may influence flood susceptibility patterns in Hulu Sungai Tengah Regency and Barabai Sub-District. The results of these analyses were used to support the interpretation of flood-controlling factors and to formulate recommendations for flood risk reduction and regional management. The overall workflow of the study is presented in Figure 4.

Results and Discussion

Regional Geology of Barabai Sub-District

Regional geological information indicates that Barabai Sub-District is predominantly underlain by alluvial deposits associated with fluvial and swamp environments (Figure 5). These deposits consist mainly of unconsolidated materials, including kaolinitic clay, silt, sand, peat, gravel, and loose boulders boulder (Heryanto & Sanyoto, 1994). Alluvial deposits commonly develop in low-lying geomorphic settings through the transport and accumulation of sediments by surface runoff and river processes (Vio et al., 2025). Because these materials are generally loose and poorly consolidated, they tend to have limited drainage capacity and are easily reworked during high-flow conditions. Consequently, the dominance of alluvial deposits in Barabai Sub-District supports the formation of floodplain environments and contributes to the area's susceptibility to inundation.

Slope Gradient Classification Results

The slope parameter was classified into six gradient classes adapted from (Fauzi, 2022), and each class was assigned a score according to its relative influence on flood susceptibility, as shown in Table 2. The slope map indicates that Barabai Sub-District is predominantly characterized by flat (0–3%) and gently sloping (3–8%) terrain (Figure 6). These low-gradient areas occupy most of the study area and provide favorable conditions for surface water accumulation during periods of intense rainfall. In contrast, moderately sloping (8–15%) and moderately steep (15–30%) terrain is mainly distributed in the northern part of the study area, where runoff is generally more efficient and surface water is less likely to accumulate. The predominance of flat to gently sloping terrain, together with the low-lying physiography of Barabai Sub-District, reduces runoff velocity and promotes temporary water storage on the land surface. Consequently, these topographic conditions increase the susceptibility of the area to prolonged inundation and flooding, particularly when high-intensity rainfall coincides with limited drainage capacity.

© 2026 Dept. of Geophysics Hasanuddin University

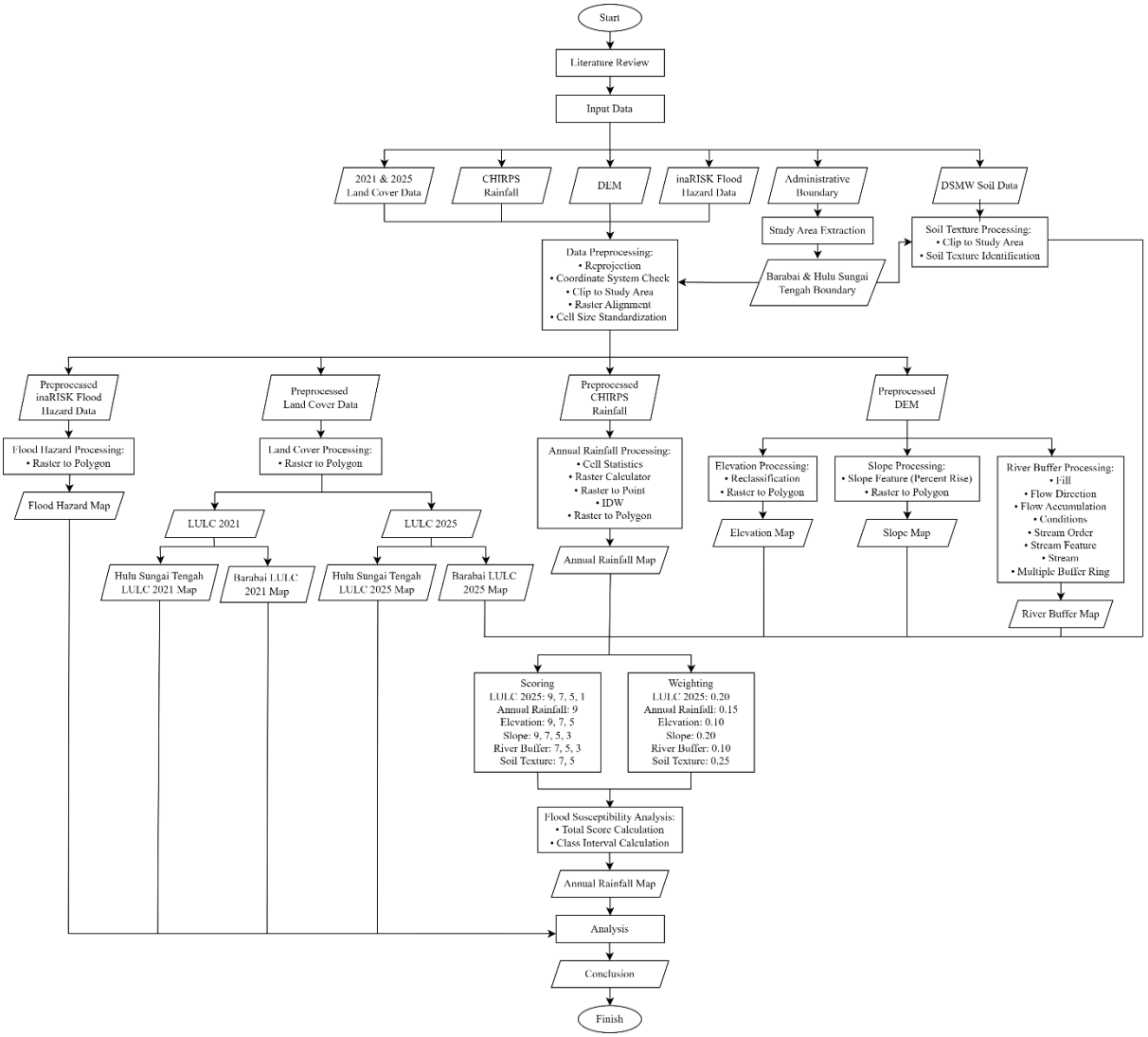


Figure 4. Workflow of the GIS-based flood susceptibility analysis conducted in Barabai Sub-District.

Table 2. Slope Gradient Classification Scoring.

No.	Slope Gradient	Score
1	Flat (0–3%)	9
2	Slightly Slope (3–8%)	7
3	Moderate Slope (8–15%)	5
4	Moderately Steep Slope (15–30%)	3
5	Steep Slope (30–45%)	1
6	Very Steep Slope (>45%)	0

The elevation map and its classification scores are presented in Figure 7 and Table 3, respectively. Elevation was classified into six classes according to its influence on flood susceptibility, with lower elevation classes assigned higher scores because they are generally more prone to inundation. Following the classification adopted from Utama et al., (2021), the elevation classes range from 0–12.5 m to more than 100 m above sea level, with scores decreasing as elevation increases.

The elevation map shows that Barabai Sub-District is dominated by low-lying terrain, particularly elevations between 12.5 m and 25 m above sea level, while the overall elevation ranges from approximately 7 m to 37 m. This low-elevation setting indicates that much of the study area has limited topographic relief, which can reduce natural drainage efficiency and promote surface water accumulation. Low-lying areas are also more likely to receive runoff from surrounding higher terrain, thereby increasing their susceptibility to inundation during intense rainfall events.

© 2026 Dept. of Geophysics Hasanuddin University

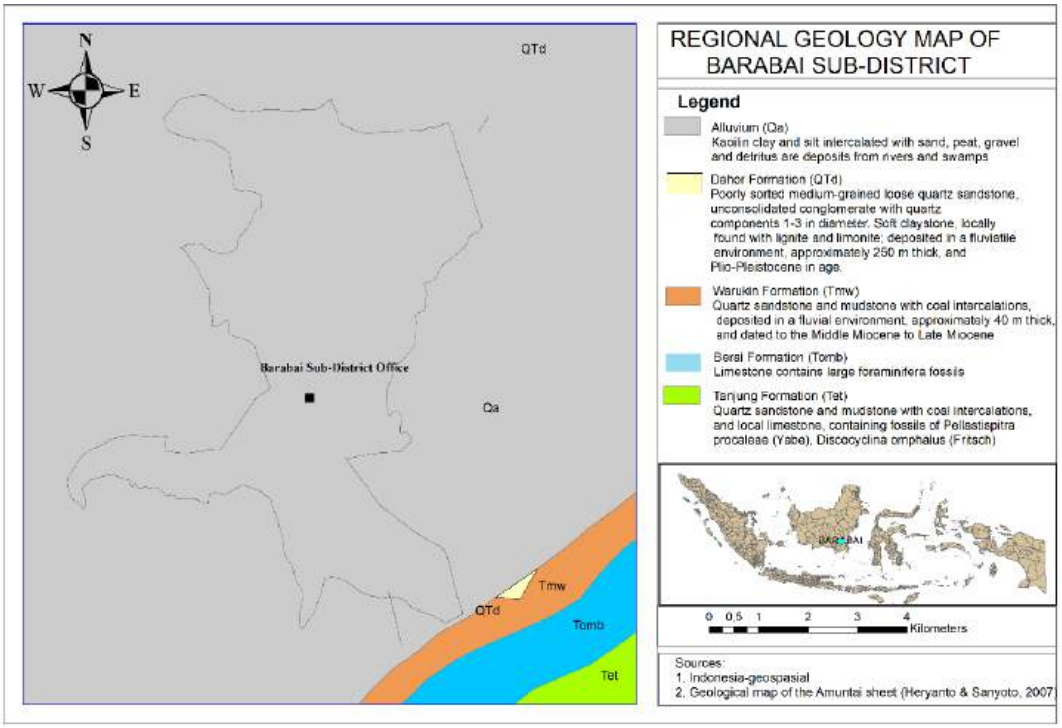


Figure 5. Regional Geological Map of Barabai District showing the dominance of alluvial deposits.

Table 3. Elevation Class Scores (Utama et al., 2021).

No.	Elevation Class (m)	Score
1	0–12.5	9
2	12.5–25	7
3	25–50	5
4	50–75	3
5	75–100	1
6	>100	0

Soil Texture Classification

Soil texture in Barabai Sub-District is dominated by the Sandy Clay Loam (Fine) class, whereas the Loam (Medium) class is mainly distributed in the southeastern part of the study area, particularly around Gambah, Pagat, and Murung A (Figure 8). The dominance of fine-textured soils suggests relatively low infiltration capacity and higher water retention near the surface, which can enhance surface runoff and increase flood susceptibility during intense rainfall events. Soil texture was classified into five classes according to its influence on infiltration capacity and runoff generation, based on the classification framework adopted from (Nkeki et al., 2023). Finer soil textures were assigned higher scores because they generally have lower permeability and are more likely to restrict vertical water movement, whereas coarser textures were assigned lower scores due to their higher infiltration potential (Table 4).

Table 4. Soil Texture Class Scores.

No.	Soil Texture Class	Score
1	Very Fine	9
2	Fine	7
3	Medium	5
4	Coarse	3
5	Very Coarse	1

Land Use/Land Cover (LULC)

Table 5. Land Use/Land Cover (LULC) classes and their assigned scores for the weighted overlay analysis.

No.	Land Cover Class	Score
1	Paddy Fields, Bare Land, Water Body	9
2	Dryland Agriculture, Built Area	7
3	Shrubland, Grassland, Rangeland	5
4	Crops	3
5	Vegetation	1
6	Clouds and Cloud Shadows	1

© 2026 Dept. of Geophysics Hasanuddin University

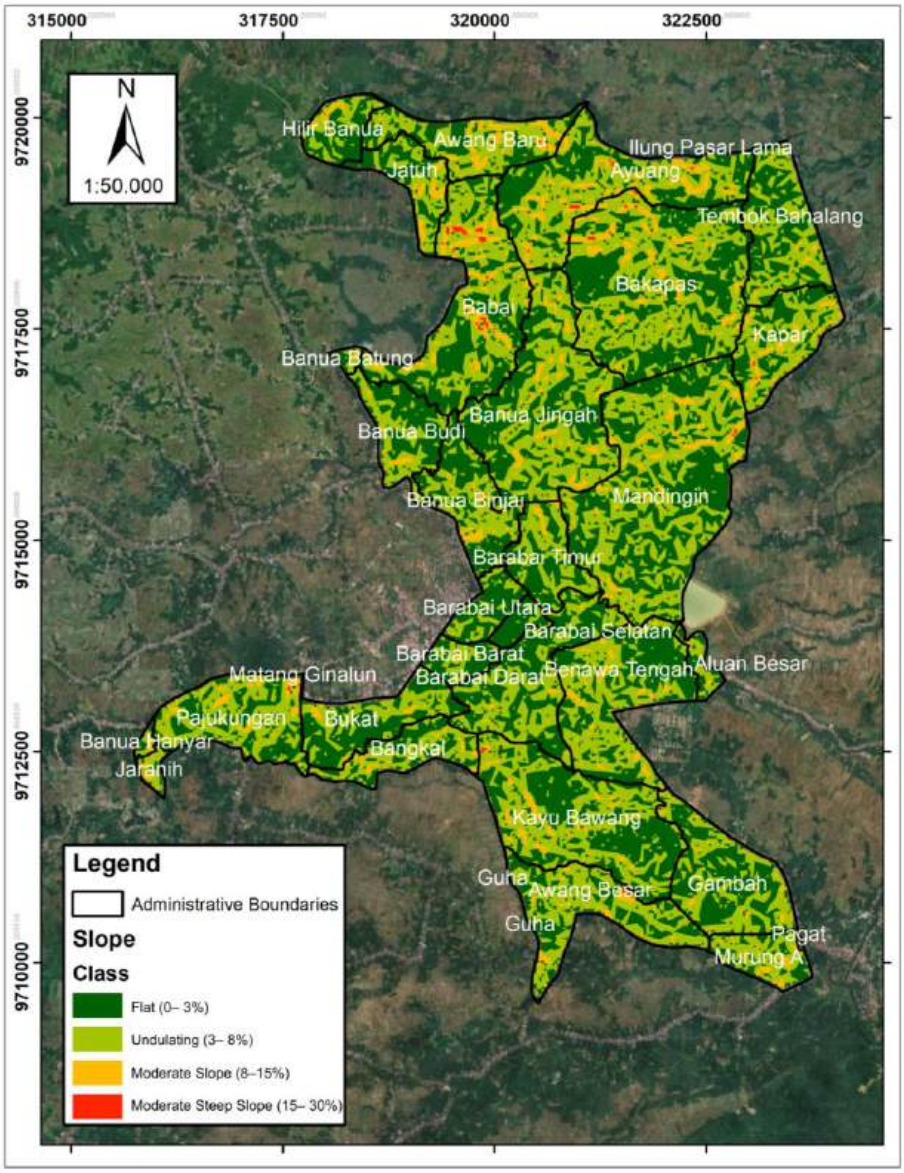


Figure 6. Slope Map of Barabai Sub-District shows variations in slope predominantly characterized by flat (0–3%) and gently sloping or undulating (3–8%) terrain.

Barabai Sub-District experienced noticeable land use and land cover (LULC) changes between 2021 and 2025, although cropland remained the dominant land cover class throughout the study period (Figure 9). Cropland is widely distributed across most villages and urban wards, whereas built-up areas are mainly concentrated in the central part of Barabai, particularly in Barabai Darat, Barabai Timur, Barabai Selatan, and Barabai Utara. Vegetation and rangeland occur as scattered patches, especially in the southern and northeastern parts of the study area. These spatial patterns of land cover can influence infiltration capacity, surface runoff generation, and water retention, thereby affecting flood susceptibility in Barabai Sub-District. A comparison between the 2021 and 2025 LULC maps shows several changes, including the emergence of a water body class in 2025 that was not identified in the 2021 map. This water body corresponds to a reservoir developed as part of the government's flood management initiative, which is expected to improve water retention capacity and support local flood mitigation efforts (Antara Kalsel, 2022). Each land cover class was assigned a score based on its relative influence on flood susceptibility, based on the classification framework adopted from

© 2026 Dept. of Geophysics Hasanuddin University

Irmawati et al. (2023), and was subsequently incorporated into the weighted overlay analysis (Table 5).

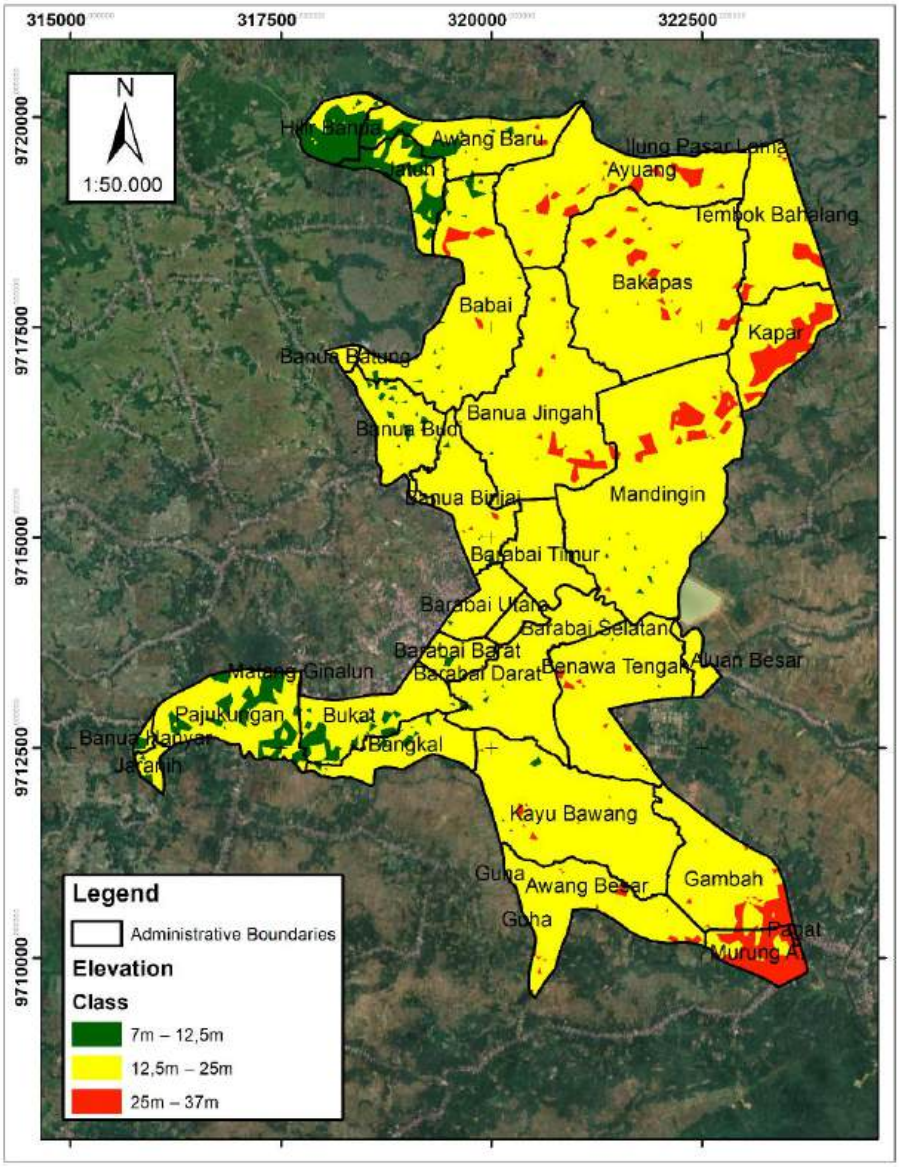


Figure 7. Barabai Sub-District is mainly dominated by elevations of 12.5–25 m, with an overall elevation range of approximately 7–37 m above sea level.

Table 6. Land Use/Land Cover (LULC) Distribution in Barabai Sub-District in 2021

No.	Class	Area (km²)	Percentage (%)
1	Vegetation	1.97	5.02
2	Crops	26.87	68.53
3	Built-up Areas	10.09	25.73
4	Rangeland	0.28	0.71

The Land Use/Land Cover (LULC) distribution in Barabai Sub-District for the years 2021 and 2025 is presented in Tables 6 and 7, respectively. These datasets were used to evaluate changes in land cover and their influence on flood susceptibility. The comparative diagram shown in Figure 10 illustrate the changes in land use and land cover (LULC) between 2021 and 2025 in Barabai Sub-District. Crops remained the dominant land cover class; however, their area decreased from 26.87 km² (68.53%) in 2021 to 24.21 km² (61.76%) in 2025. In contrast, built-up areas increased from 10.09 km² (25.73%) to 10.81 km² (27.58%), indicating ongoing urban development. Rangeland also exhibited a

© 2026 Dept. of Geophysics Hasanuddin University

considerable increase, while vegetation showed a slight decline. In addition, a new water body class covering 0.27 km² (0.69%) was identified in the 2025 LULC map, whereas it was absent in 2021. These changes may alter infiltration capacity and surface runoff patterns, thereby affecting flood susceptibility in the study area.

Table 7. Land Use/Land Cover (LULC) Distribution in Barabai Sub-District in 2025.

No.	Class	Area (km²)	Percentage (%)
1	Water	0.27	0.69
2	Vegetation	1.56	3.98
3	Crops	24.21	61.76
4	Built-up Areas	10.81	27.58
5	Rangeland	2.35	5.99
6	**Total**	**39.20**	**100.00**

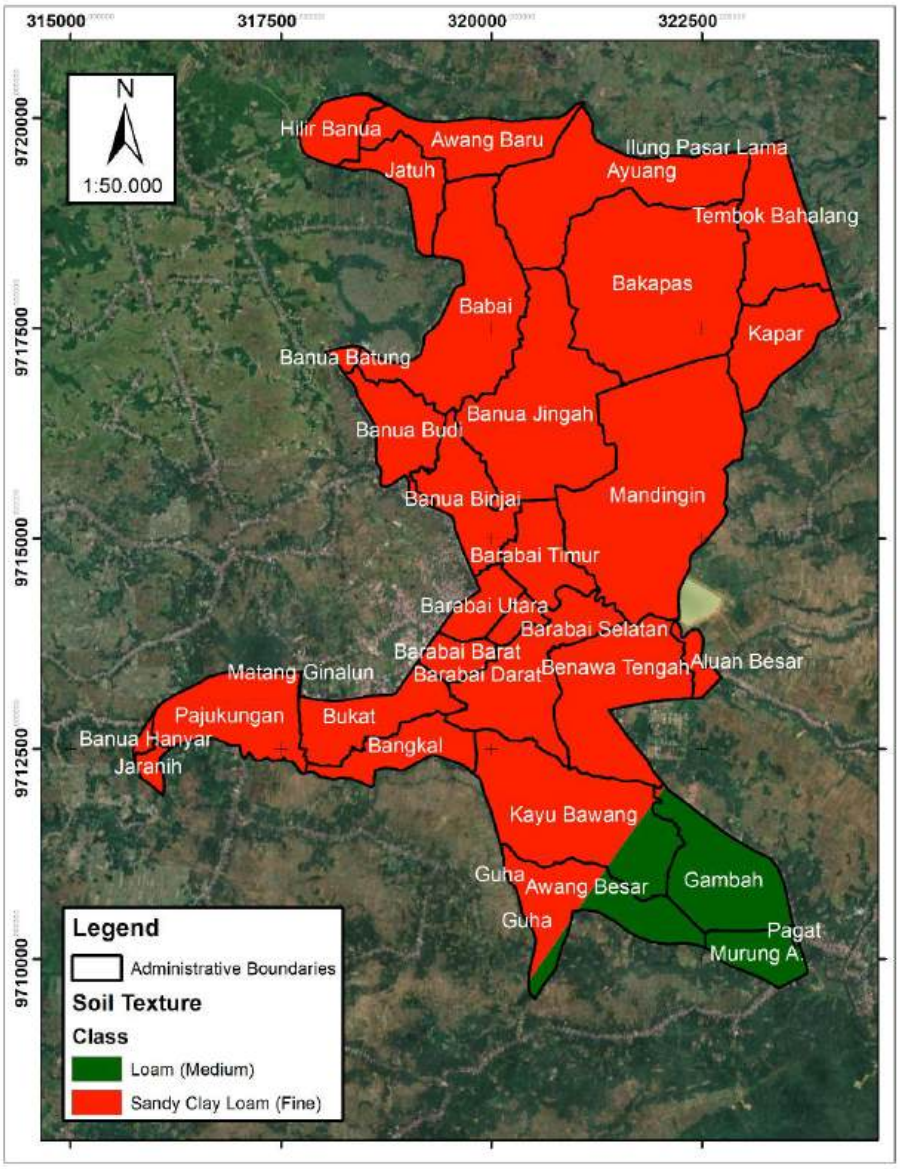


Figure 8. Spatial distribution of soil texture classes in Barabai Sub-District.

To provide a broader perspective, the LULC maps were analyzed for the entire Hulu Sungai Tengah Regency in 2021 and 2025. Figure 11 shows changes in land cover distribution between the two years. Notably, the extent of flooded vegetation decreased in 2025 compared to 2021, indicating a reduction in vegetated areas affected by inundation. Furthermore, the LULC distribution diagram (Figure 12) highlights variations in the area of several land cover classes between 2021 and 2025, expressed in km². These changes indicate shifts in land cover composition across the regency, reflecting ongoing environmental

© 2026 Dept. of Geophysics Hasanuddin University

and land-use dynamics during the study period.

Rainfall Classification Results

Table 8. Rainfall Classification and Scores Used in Flood Susceptibility Analysis (Helmi et al., 2019).

No.	Rainfall Class (mm/year)	Category	Score
1	> 3000	Very Wet	9
2	2501–3000	Wet	7
3	2001–2500	Moderate/Humid	5
4	1501–2000	Dry	3
5	< 1500	Very Dry	1

Rainfall is one of the most important factors influencing flood susceptibility, as it directly affects surface runoff and water accumulation. Table 8 presents the rainfall classification and the corresponding scores used in the weighted overlay analysis. Based on the annual rainfall map derived from CHIRPS data for the 2021–2025 period, Barabai Sub-District is characterized by a single rainfall class ranging from 2501 to 3000 mm/year (Figure 13), which is classified as a wet category. This indicates that the study area receives relatively high annual rainfall, which may increase flood susceptibility.

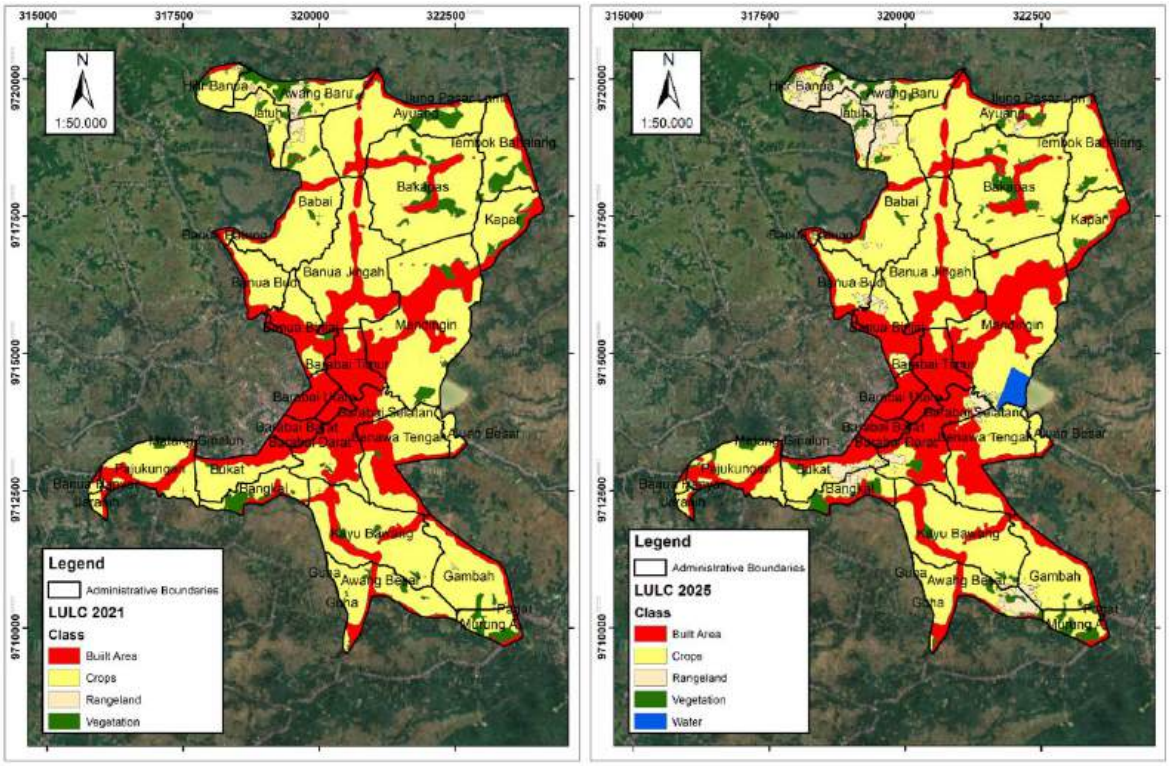


Figure 9. Spatial distribution of Land Use/Land Cover (LULC) classes in Barabai Sub-District for 2025.

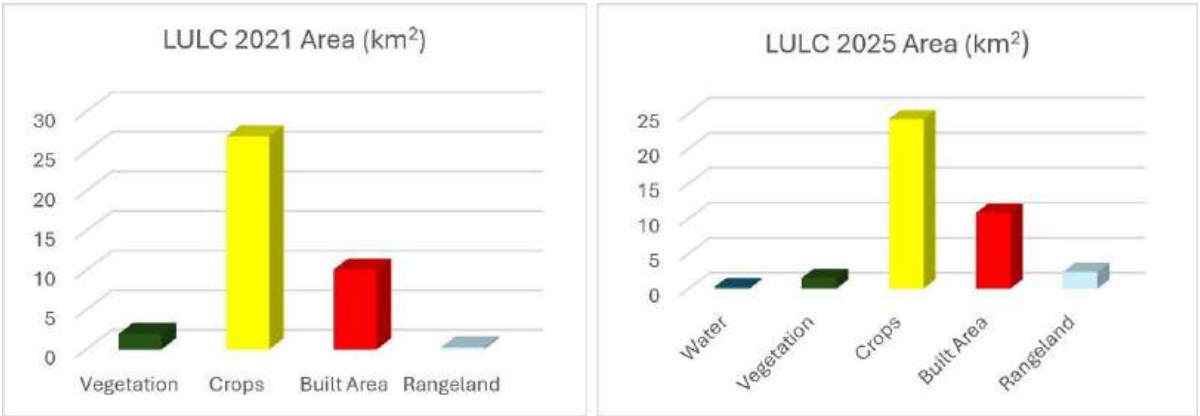


Figure 10. Comparison diagram illustrates the Land Use Land Cover (LULC) area distribution, measured in km², for the years 2021 and 2025.

© 2026 Dept. of Geophysics Hasanuddin University

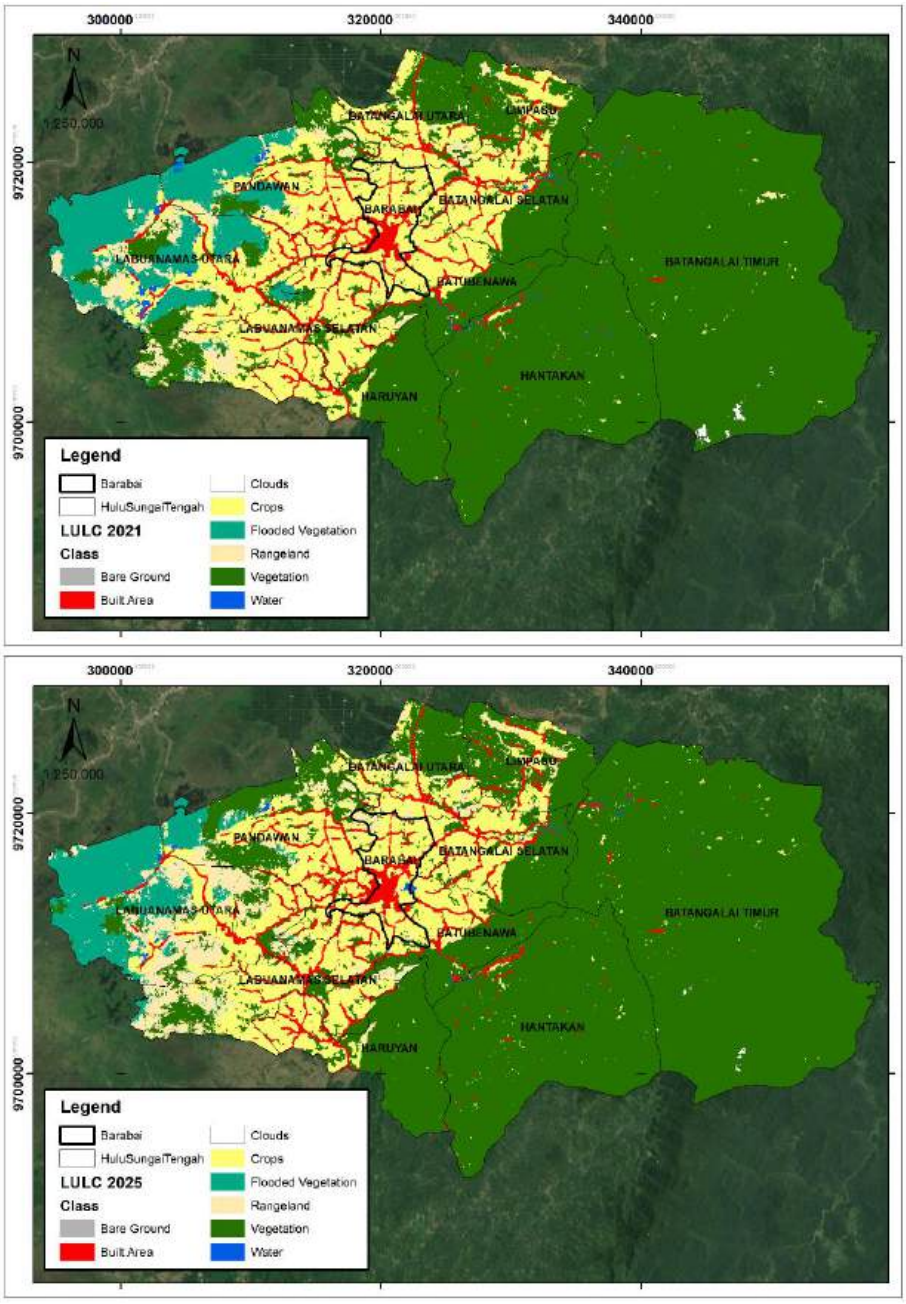


Figure 11. Comparison of Land Use/Land Cover Class Areas in Hulu Sungai Tengah Regency in 2021 and 2025.

River Buffer

Table 9. River Buffer Distance Classification (Utama et al., 2021).

No.	Class	Buffer Distance	Score
1	Very High	0–25 m	7
2	High	>25–100 m	5
3	Moderate	>100–250 m	3

The river network was derived from the Digital Elevation Model (DEM) through a series of hydrological processing steps. The resulting river buffer map was classified into four distance classes to represent the influence of proximity to rivers on flood susceptibility. Table 9 presents the river buffer classification and the corresponding scores used in the weighted overlay analysis. In general, areas located closer to the river receive higher scores because they are more susceptible to flooding, whereas areas farther from the river are assigned lower scores due to their relatively lower flood risk. As shown in Figure 14, several villages and urban wards in Barabai Sub-District, including Barabai Darat, Barabai Utara, Barabai Selatan, Banua Jingah, Awang Baru, Ayuang, and Gambah,

© 2026 Dept. of Geophysics Hasanuddin University

Pajukungan are directly connected to the river network. This condition may increase the likelihood of river overflow during periods of high rainfall, thereby increasing flood susceptibility in these areas.

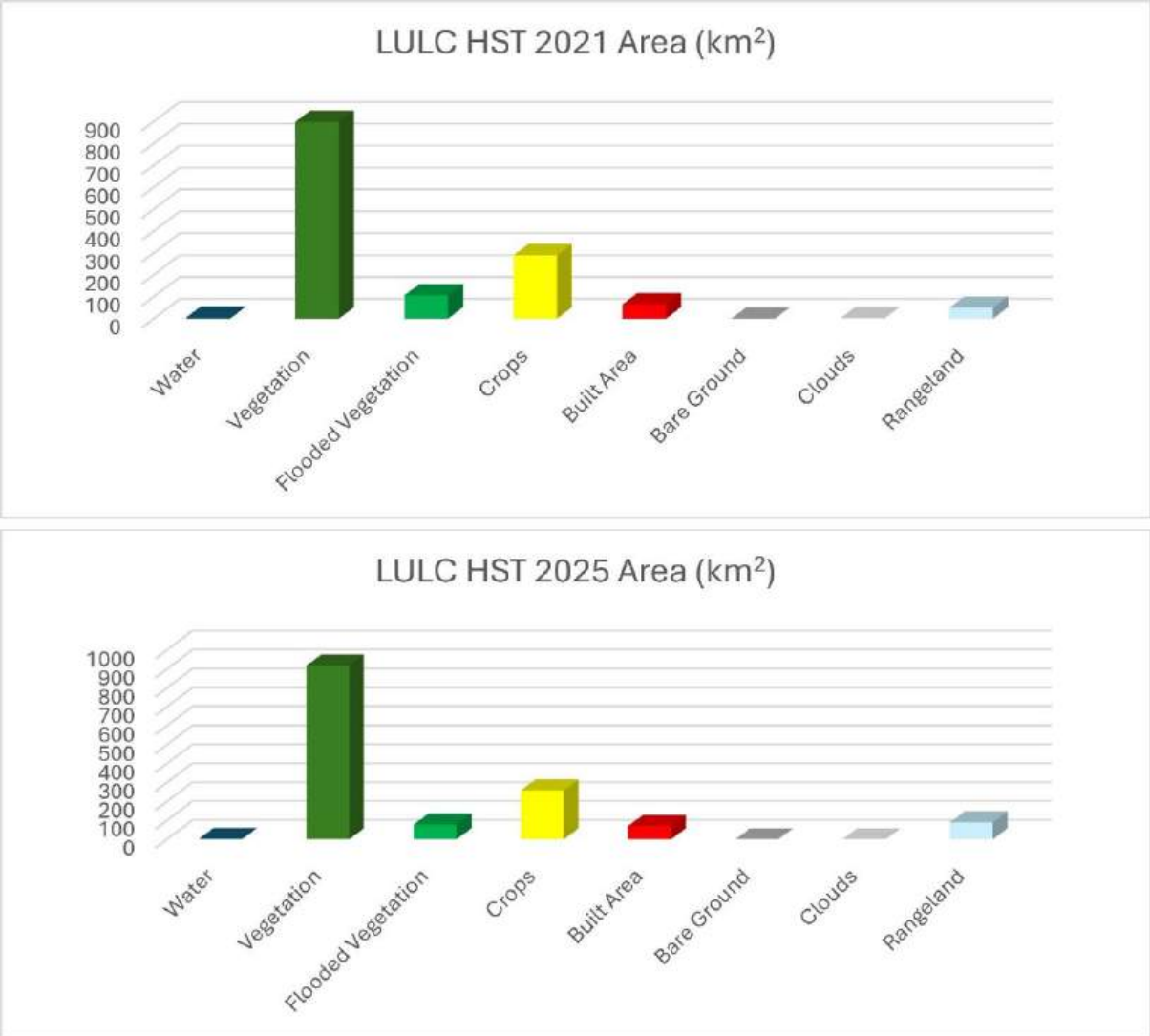


Figure 12. Comparison of LULC class areas in Hulu Sungai Tengah Regency between 2021 and 2025

River Buffer

Table 9. River Buffer Distance Classification (Utama et al., 2021).

No.	Class	Buffer Distance	Score
1	Very High	0–25 m	7
2	High	>25–100 m	5
3	Moderate	>100–250 m	3

The river network was derived from the Digital Elevation Model (DEM) through a series of hydrological processing steps. The resulting river buffer map was classified into four distance classes to represent the influence of proximity to rivers on flood susceptibility. Table 9 presents the river buffer classification and the corresponding scores used in the weighted overlay analysis. In general, areas located closer to the river receive higher scores because they are more susceptible to flooding, whereas areas farther from the river are assigned lower scores due to their relatively lower flood risk. As shown in Figure 14, several villages and urban wards in Barabai Sub-District, including Barabai Darat, Barabai Utara, Barabai Selatan, Banua Jingah, Awang Baru, Ayuang, and Gambah, Pajukungan are directly connected to the river network. This condition may increase the likelihood of river overflow during

© 2026 Dept. of Geophysics Hasanuddin University

periods of high rainfall, thereby increasing flood susceptibility in these areas.

Flood Susceptibility Map Results

Flood susceptibility was assessed by integrating six flood-conditioning factors, namely slope, elevation, soil texture, rainfall, land use/land cover, and distance to river networks, using a GIS-based weighting and scoring approach. Following the general weighted overlay framework applied by Diriba et al. (2024), each reclassified thematic layer was multiplied by its assigned weight and subsequently summed to generate a composite flood susceptibility index. The normalized weights applied to the flood-conditioning factors are presented in Table 10, with their total equal to 1.00. The flood susceptibility index was calculated using Equation (1).

$$K = \sum_{i=1}^{n} (W_i x\, X_i) \quad (1)$$

Where:

K : Flood susceptibility value
W_i : normalized weight assigned to the i-th flood-conditioning factor
X_i : score assigned to the corresponding class of the i-th factor; and
n : total number of flood-conditioning factors

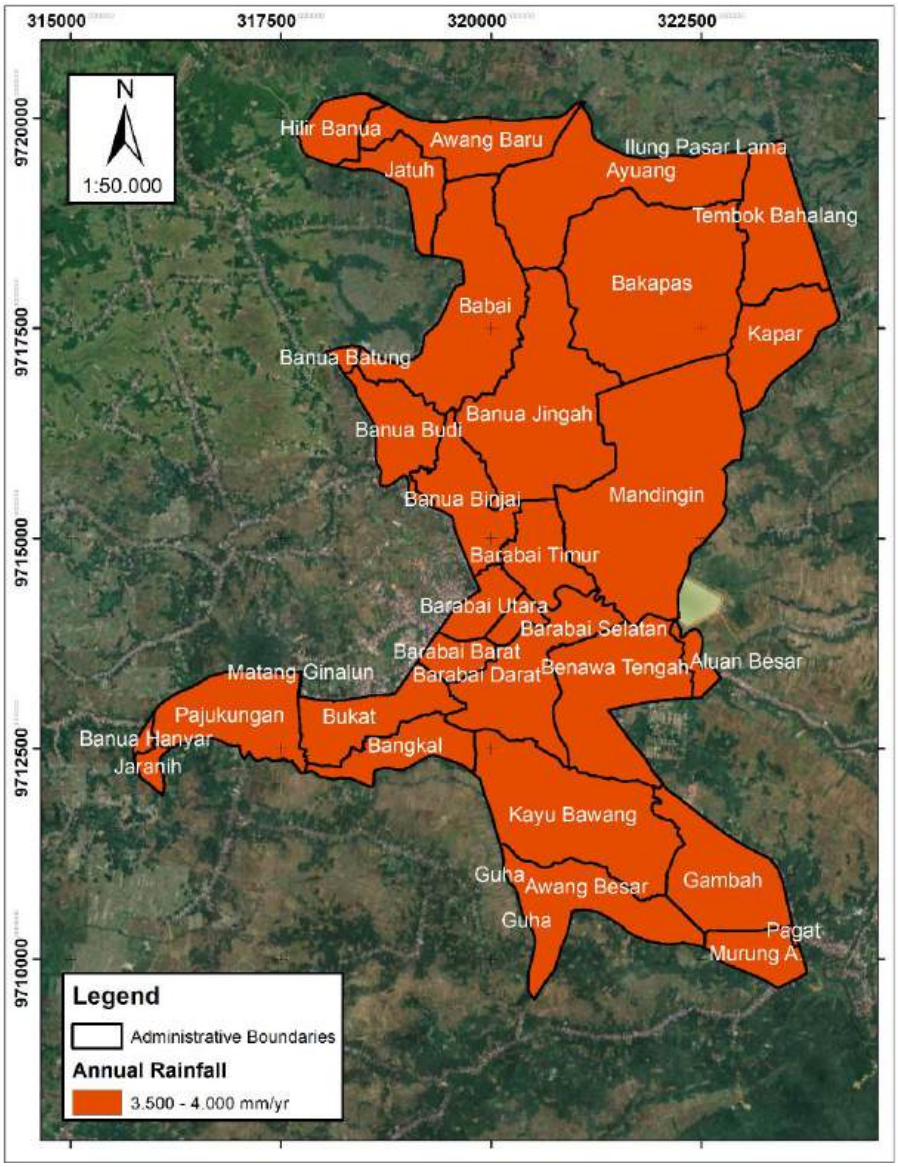


Figure 13. Spatial distribution of average annual rainfall in Barabai Sub-District based on CHIRPS data for the 2021–2025 period.

© 2026 Dept. of Geophysics Hasanuddin University

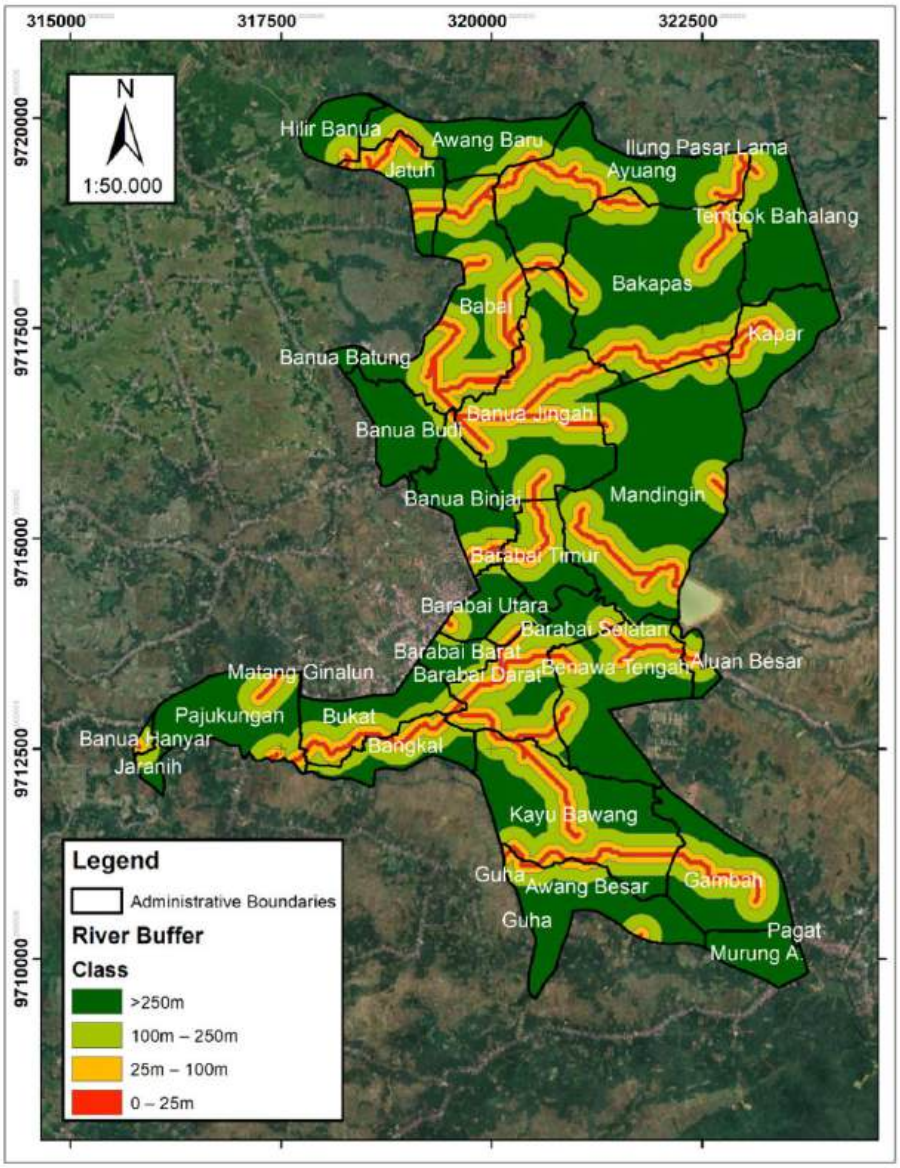


Figure 14. River buffer map of Barabai District derived from DEM data. The widespread distribution of river channels indicates that a large portion of the district is potentially susceptible to flooding, particularly in areas located close to the river network.

The weighted overlay analysis produced flood susceptibility index values ranging from 3.9 to 8.3. These values were classified into four susceptibility classes (Very Low, Low, High, and Very High) using the Equal Interval classification method. This method divides the total range of index values into intervals of equal width (ESRI, 2024). The classified index was subsequently used to generate the final flood susceptibility map of Barabai Sub-District. The class interval width was calculated using Equation (2).

$$i = R/n \qquad (2)$$

Where:

i : class interval width

R : range of the flood susceptibility index, calculated as the difference between the maximum and minimum index values

n : number of flood susceptibility classes

Based on the minimum and maximum flood susceptibility index values of 3.9 and 8.3, respectively, and four predefined susceptibility classes, the calculated class interval width was 1.1. The flood susceptibility map presented in Figure 15

© 2026 Dept. of Geophysics Hasanuddin University

and the corresponding area statistics in Table 11 indicate that the study area is dominated by the High and Very High susceptibility classes.

Table 10. Normalized Weights Assigned to the Flood-Conditioning Factors.

No	Flood-conditioning factor	Weight
1	Slope	0.20
2	Elevation	0.10
3	Soil Texture	0.25
4	Rainfall	0.15
5	Land Use	0.20
6	River Buffer	0.10

Table 11. Area and Percentage of Each Flood Susceptibility Class.

Flood Susceptibility Class	Area (km²)	Percentage (%)
Very Low	0.23	0.61
Low	1.78	4.70
High	26.66	70.44
Very High	9.18	24.25
Total	37.85	100.00

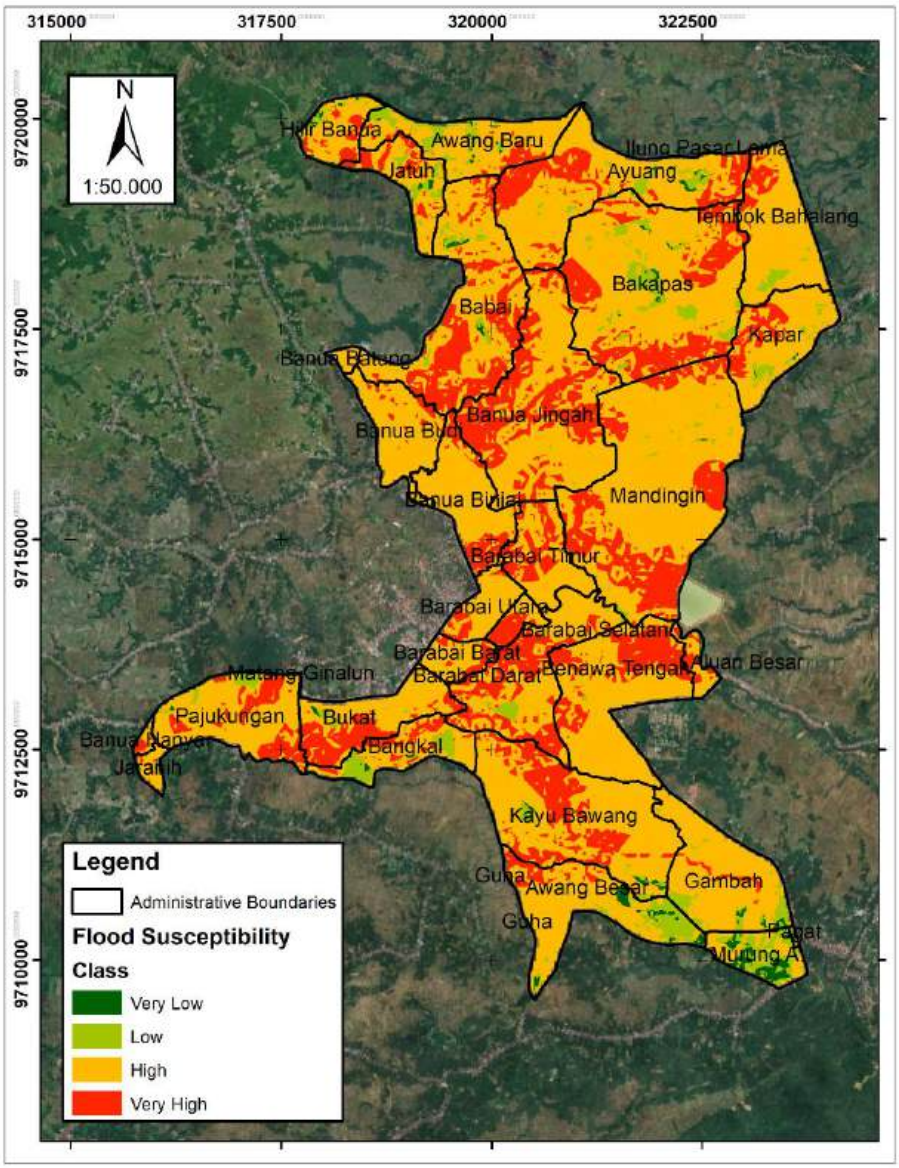


Figure 15. Flood susceptibility map of Barabai District showing the dominance of high and very high susceptibility classes.

© 2026 Dept. of Geophysics Hasanuddin University

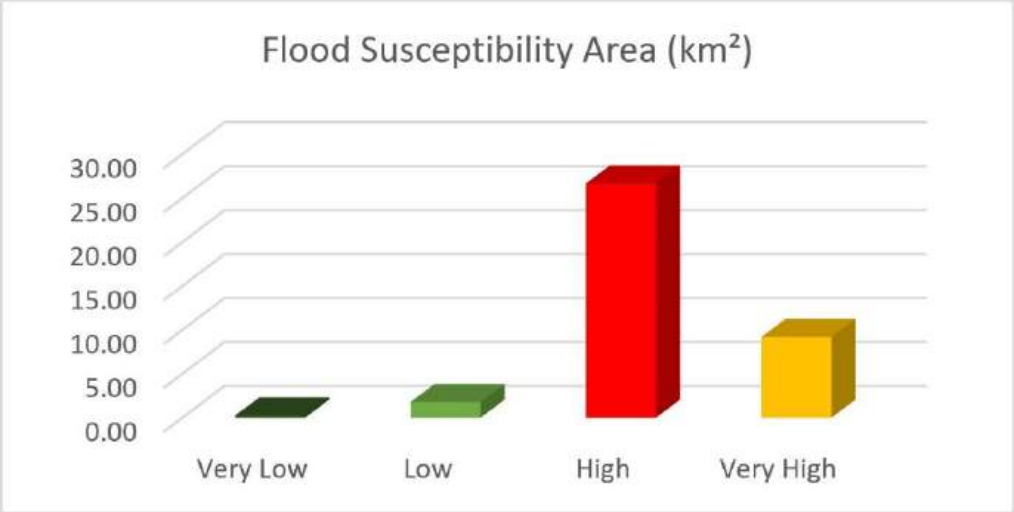


Figure 16. Illustrates the area distribution of flood susceptibility classes, indicating that the study area is predominantly characterized by High and Very High susceptibility levels, which together account for approximately 94.69% of the total area.

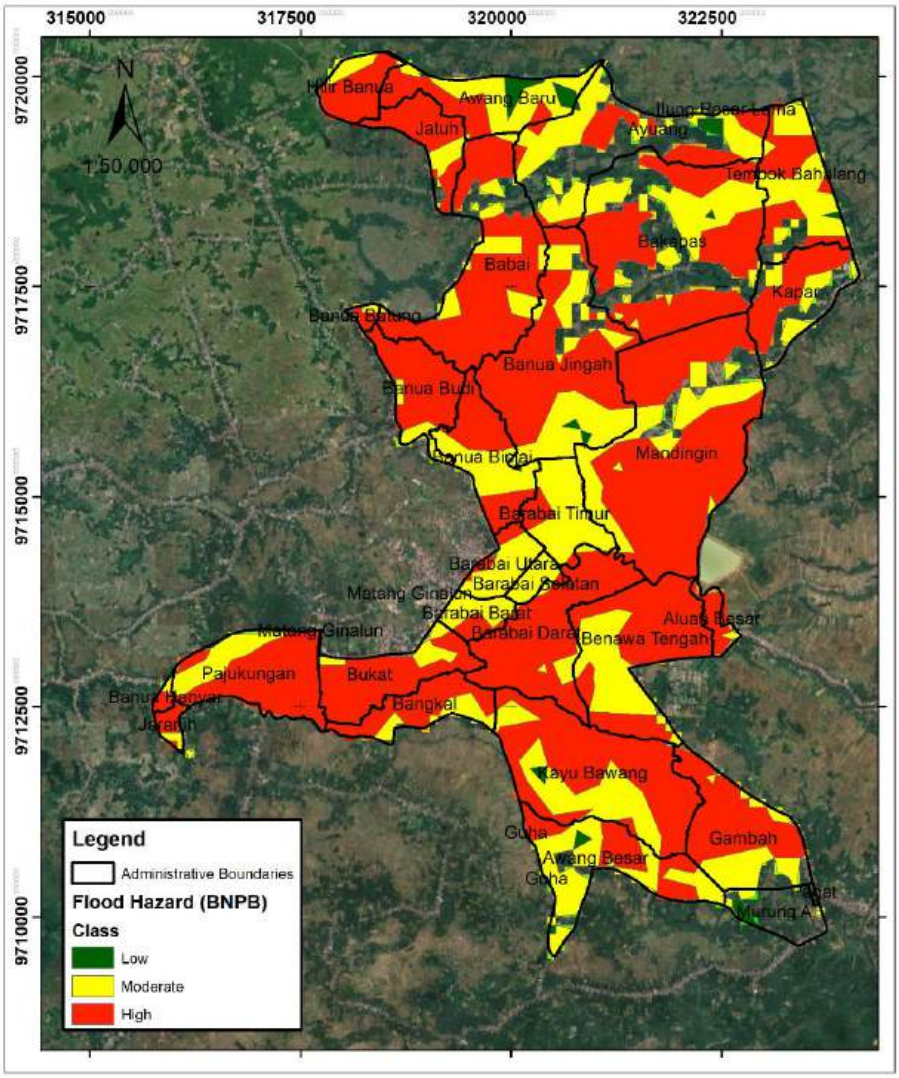


Figure 17. Validation of the flood susceptibility map using BNPB flood hazard data, indicating that most parts of Barabai District fall within moderate to high flood hazard categories.

The flood susceptibility map indicates that Barabai District is dominated by High and

© 2026 Dept. of Geophysics Hasanuddin University

Very High susceptibility classes, covering 26.66 km² and 9.18 km², respectively. Combined, these classes represent approximately 94.69% of the total study area, suggesting a widespread potential for flooding (Figure 16).

Historical flood events in 2021 affected Barabai Darat, Barabai Timur, Barabai Utara, Barabai Selatan, Benawa Tengah, Mandingin, Pajukungan, and Banua Jingah, with inundation depths ranging from 30 to 70 cm (detikNews, 2021). Recent floods reported by Antara Kalsel (2026) also impacted several areas, including Barabai Darat, Barabai Timur, Barabai Selatan, Barabai Utara, Bukat, Mandingin, and Pajukungan, affecting 28–650 houses and 133–1,967 residents, with water depths of 50–85 cm. These records indicate the recurring nature of flood hazards and their significant impacts on local communities within the study area. These areas correspond well with the high-susceptibility zones identified in the present study, providing preliminary evidence of the model's validity. In addition, the resulting flood susceptibility map was compared with the BNPB flood hazard map, which indicates that most parts of Barabai District fall within moderate to high flood hazard categories (Figure 17). The consistency between the susceptibility map, historical flood records, and BNPB hazard data further supports the accuracy of the mapping results.

Conclusions

The integration of six flood-conditioning parameters into a GIS-based weighted overlay model reveals that Barabai Sub-District is overwhelmingly dominated by high to very high flood susceptibility, indicating that the majority of the district faces substantial flood risk. This distribution is largely governed by the combined influence of low-lying, flat terrain, close proximity to river channels, moderately fine-textured soils, Quaternary alluvial deposition, and land dominated by cultivation and built-up areas, while intense rainfall functions as the principal triggering mechanism. The strong correspondence between the model's output and documented flood occurrences in the area lends confidence to the robustness of the approach applied, underscoring the urgency of incorporating these findings into flood mitigation strategies and land-use planning in the region.

From a practical perspective, mitigation efforts should be prioritized in highly susceptible areas, particularly in Barabai Darat, Barabai Timur, Barabai Selatan, Barabai Utara, Bukat, Mandingin, and Pajukungan, which have frequently experienced flood impacts based on both the susceptibility analysis and historical flood records. These measures should include structural approaches such as improving drainage capacity, maintaining river channels, and developing flood control infrastructure. In addition, non-structural measures, including land-use regulation, riverbank protection, and community-based flood preparedness programs, should be implemented to reduce future flood impacts.

This study has several limitations. The resulting map represents flood susceptibility rather than a fully validated flood vulnerability or flood risk assessment, as comprehensive validation using historical flood extent data, field observations, and hydrological simulations was not conducted. Therefore, the results should be interpreted as a preliminary spatial assessment that can support spatial planning and flood management within the study area. Therefore, the results should be interpreted as a preliminary spatial assessment that can support spatial planning and flood management within the study area. Future studies should incorporate historical flood extent data, field observations and hydrological modeling to further improve the accuracy

© 2026 Dept. of Geophysics Hasanuddin University

and reliability of flood susceptibility assessments.

Acknowledgements

This research did not receive any specific grant from funding agencies in the public, commercial, or not-for-profit sectors. The authors gratefully acknowledge the National Digital Elevation Model (DEMNAS) for providing open access the topographic data and Climate Hazards Group InfraRed Precipitation with Station data (CHIRPS) to use in this study. We also thank the journal editor and anonymous reviewers for their constructive comments, which helped improve the quality of this manuscript.

Author Contribution

Sandri Erfani led the research, including conceptualization, methodology design, formal analysis, visualization, and preparation of the initial draft. Nailatussa'adah and Rosna Amaliaatul Ma'rifah contributed to data collection and accuracy, map creation, and weighting. Eka Andika and M. Rayya Andisa Putra assisted in the creation of the geological and topographic maps and editing the manuscript. Andri Kurniawan provided supervision and contributed to the review and editing of the manuscript.

Conflict of Interest

There were no funds or finances exchanged in this study, neither among the authors nor between the parties involved in the research.

References

Aji, S. S., Utami, A. N., & Putri, D. H. (2025). Dampak Eksternalitas Negatif Akibat Bencana Alam Banjir Terhadap Masyarakat. *Jurnal Sosial Humaniora*, 16(2), 128–139. https://doi.org/10.30997/jsh.v16i2.19606

Amatebelle, C. E., Owolabi, S. T., Ogundeji, A. A., & Okolie, C. C. (2025). A systematic analysis of remote sensing and geographic information system applications for flood disaster risk management. *Journal of Spatial Science*, 70(3), 441–467. https://doi.org/10.1080/14498596.2025.2476973

Antara Kalsel. (2022). *Masyarakat HST harapkan segera selesai kolam pengendalian banjir*. AntaraNews. https://kalsel.antaranews.com/berita/336977/masyarakat-hst-harapkan-segera-selesai-kolam-pengendalian-banjir

Antara Kalsel. (2026). *Banjir rendam ribuan rumah warga di HST, tiga kecamatan terdampak*. AntaraNews. https://kalsel.antaranews.com/berita/519547/banjir-rendam-ribuan-rumah-warga-di-hst-tiga-kecamatan-terdampak

Badan Pusat Statistik Kabupaten Hulu Sungai Tengah. (2024). *Kecamatan Barabai dalam Angka 2024*. BPS Kabupaten Hulu Sungai Tengah. https://hulusungaitengahkab.bps.go.id/id/publication/2024/09/26/b6b6ce1d4288e254716d1ed3/kecamatan-barabai-dalam-angka-2024.html

Briantama, R. H., Suhartanto, E., & Sajali, M. A. (2024). Analisis Hidrologi dan Hidrolika Sungai Untuk Pemodelan Banjir Sebagai Upaya Mitigasi Bencana Pada Sungai Kali Surabaya. *Jurnal Teknologi dan Rekayasa Sumber Daya Air*, 4(1), 969–981. https://doi.org/10.21776/ub.jtresda.2024.004.01.082

detikNews. (2021). *6 Kabupaten di Kalsel Banjir, Hulu Sungai Tengah Terdampak Paling Parah*. https://news.detik.com/berita/d-5831272/6-kabupaten-di-kalsel-banjir-hulu-sungai-tengah-terdampak-paling-parah

Dhungana, B., & Liu, W. (2024). Urban–Rural Exposure to Flood Hazard and

© 2026 Dept. of Geophysics Hasanuddin University

Social Vulnerability in the Conterminous United States. *ISPRS International Journal of Geo-Information*, 13(9), 339. https://doi.org/10.3390/ijgi13090339

Diriba, D., Takele, T., Karuppannan, S., & Husein, M. (2024). Flood hazard analysis and risk assessment using remote sensing, GIS, and AHP techniques: a case study of the Gidabo Watershed, main Ethiopian Rift, Ethiopia. *Geomatics, Natural Hazards and Risk*, 15(1), 2361813. https://doi.org/10.1080/19475705.2024.2361813

Efraimidou, E., & Spiliotis, M. (2024). A GIS-Based Flood Risk Assessment Using the Decision-Making Trial and Evaluation Laboratory Approach at a Regional Scale. Environmental Processes, 11(1), 9. https://doi.org/10.1007/s40710-024-00683-w

ESRI. (2024). *Data classification methods*. https://doc.esri.com/en/arcgis-pro/latest/help/mapping/layer-properties/data-classification-methods.html

Fauzi, R. Al. (2022). Analisis tingkat kerawanan banjir Kota Bogor menggunakan metode overlay dan scoring berbasis sistem informasi geografis. *Geomedia Majalah Ilmiah Dan Informasi Kegeografian*, 20(2), 96–107. https://doi.org/10.21831/gm.v20i2.48017

Gasmi, F., & Aly, M. H. (2026). A Comprehensive Systematic Review of Contemporary Geospatial Approaches to Flood Hazard and Risk Assessment. *Urban Science*, 10(5), 271. https://doi.org/10.3390/urbansci10050271

Gultom, N., Badaruddin, B., & Kadir, S. (2022). Analisis Debit Air di Daerah Tangkapan Air (DTA) Barabai Kabupaten Hulu Sungai Tengah. *Jurnal Sylva Scienteae*, 5(5), 711–717. https://doi.org/10.20527/jss.v5i5.6693

Fatmala, I. K., Pratiwi, C. I. B., Setiyono, K. A., Merlina, M., Dewantara, E. J., Fauziyyah, L., Rais, M. L., & Hizbaron, D. R. (2023). Analisis Jasa Ekosistem Pencegahan dan Penanggulangan Bencana Banjir di DAS Blukar Kabupaten Kendal. *Jurnal Ilmu Lingkungan*, 21(4), 965–973. https://doi.org/10.14710/jil.21.4.965-973

Handayani, W., Chigbu, U. E., Rudiarto, I., & Putri, I. H. S. (2020). Urbanization and Increasing Flood Risk in the Northern Coast of Central Java—Indonesia: An Assessment towards Better Land Use Policy and Flood Management. *Land*, 9(10), 343. https://doi.org/10.3390/land9100343

Hanie, M. Z., Tarigan, A. P. M., & Khair, H. (2017). Analisis Mitigasi Banjir di Daerah Aliran Sungai Babura Berbasis Sistem Informasi Geografis (SIG). *Jurnal Dampak*, 14(1), 23–32. https://doi.org/10.25077/dampak.14.1.23-32.2017

Helmi, H., Basri, H., Sufardi, S., & Helmi, H. (2019). Flood vulnerability level analysis as a hydrological disaster mitigation effort in Krueng Jreue Sub-Watershed, Aceh Besar, Indonesia. *Jàmbá Journal of Disaster Risk Studies*, 11(1), a737. https://doi.org/10.4102/jamba.v11i1.737

Heryanto, R., & Sanyoto, P. (1994). *Peta Geologi Lembar Amuntai, Kalimantan*. Pusat Penelitian dan Pengembangan Geologi. https://geologi.esdm.go.id/geomap/pages/preview/peta-geologi-lembar-amuntai-kalimantan

Indrasari, M., & Rudiarto, I. (2020). Kemampuan Kebertahanan Masyarakat pada Permukiman Rawan Banjir di Kecamatan Barabai, Kabupaten Hulu Sungai Tengah. *Jurnal Wilayah dan Lingkungan*, 8(2), 116–129.

© 2026 Dept. of Geophysics Hasanuddin University

https://doi.org/10.14710/jwl.8.2.116-129

Irmawati, V., Cahyono, O., Mujiyo, M., Maro'ah, S., Istiqomah, N. M., & Romadhon, M. R. (2023). Flood Susceptibility Index Analysis Using Overlay Method and GIS-based. *JST (Jurnal Sains dan Teknologi)*, 12(2), 553–561. https://doi.org/10.23887/jstundiksha.v12i2.52737

Izzati, H., & Rustandi, I. (2025). Normalisasi Lanskap Koridor Sungai Mati Citarum Dengan Analisis Hidrologi (Studi Kasus: Desa Rancamanyar, Kabupaten Bandung). *Jurnal Teknik Sipil dan Arsitektur*, 30(1), 32–41. https://doi.org/10.36728/jtsa.v30i1.4153

Khan, T. U., Nabi, G., Ullah, S., Akbar, A., Omifolaji, J. K., Achakzai, J. K., & Iqbal, A. (2025). Mapping flood resilience: a comprehensive geospatial insight into regional vulnerabilities. *Frontiers in Water*, 7, 1465505. https://doi.org/10.3389/frwa.2025.1465505

Latue, P. C., Septory, J. S. I., Somae, G., & Rakuasa, H. (2023). Pemodelan Daerah Rawan Banjir di Kecamatan Sirimau Menggunakan Metode Multi-Criteria Analysis (MCA). *Jurnal Perencanaan Wilayah dan Kota*, 18(1), 10–17. https://doi.org/10.29313/jpwk.v18i1.1964

Meng, M., Dąbrowski, M., Xiong, L., & Stead, D. (2022). Spatial planning in the face of flood risk: Between inertia and transition. *Cities*, 126, 103702. https://doi.org/10.1016/j.cities.2022.103702

Mondal, S., & Patel, P. P. (2018). Examining the utility of river restoration approaches for flood mitigation and channel stability enhancement: a recent review. *Environmental Earth Sciences*, 77(5), 195. https://doi.org/10.1007/s12665-018-7381-y

Nkeki, F. N., Bello, E. I., & Agbaje, I. G. (2023). Is the existing methods sustainable? A hybrid approach to flood risk mapping. *MethodsX*, 11, 102348. https://doi.org/10.1016/j.mex.2023.102348

Pandey, M., Arora, A., Arabameri, A., Costache, R., Kumar, N., Mishra, V. N., Nguyen, H., Mishra, J., Siddiqui, M. A., Ray, Y., Soni, S., & Shukla, U. (2021). Flood Susceptibility Modeling in a Subtropical Humid Low-Relief Alluvial Plain Environment: Application of Novel Ensemble Machine Learning Approach. *Frontiers in Earth Science*, 9, 659296. https://doi.org/10.3389/feart.2021.659296

Poros Kalimantan. (2021). Awal 2021, Banjir Terparah Sepanjang Sejarah di HST. *Poros Kalimantan*. https://poroskalimantan.com/awal-2021-banjir-terparah-sepanjang-sejarah-di-hst/

Prabowo, E. (2018). Studi Pengendalian Banjir di Kota Barabai terkait Rencana Pembangunan Bendungan Pancur Hanau di Sungai Barabai Kabupaten Hulu Sungai Tengah. *Jurnal Teknologi Berkelanjutan*, 7(01), 43–51. https://doi.org/10.20527/jtb.v7i01.114

Putri, A. S. R., & Triyatno, T. (2025). Analisis Bahaya Banjir Beserta Dampaknya pada Hulu Das Batang Sumpur di Kecamatan Lubuk Sikaping Kabupaten Pasaman. *Jurnal Hutan Tropis*, 13(4), 488–499. https://doi.org/10.20527/jht.v13i4.24632

Ramadhan, R., Hanif, M., Marzuki, M., Hashiguchi, H., Harjupa, W., & Yusnaini, H. (2026). Spatio-temporal variability of hydrometeorological disasters in Indonesia based on national disaster risk management data. *International Journal of Disaster*

© 2026 Dept. of Geophysics Hasanuddin University

Risk Reduction, 143, 106256. https://doi.org/10.1016/j.ijdrr.2026.106256

Rentschler, J., Salhab, M., & Jafino, B. A. (2022). Flood exposure and poverty in 188 countries. *Nature Communications*, 13(1), 3527. https://doi.org/10.1038/s41467-022-30727-4

Rizani, M. A., Setiawan, K. P., Sa'dianoor, S., Jarmani, A., Ramadaniar, H. R., Abida, M. R., & Mahasina, D. A. (2023). Analisa Perubahan Tata Guna Lahan Terhadap Ketinggian Banjir di Kota Barabai. *Sebatik*, 27(2), 480–490. https://doi.org/10.46984/sebatik.v27i2.2173

Sapoetra, R., Mustofa, U., Pratomo, R. A., & Hidayat, A. (2024). Arahan Mitigasi Bencana Banjir Pada Kecamatan Balikpapan Timur. *COMPACT: Spatial Development Journal*, 3(1), 167–173. https://doi.org/10.35718/compact.v3i1.1146

Septian, A., Elvarani, A. Y., Putri, A. S., Maulia, I., Damayanti, L., Pahlevi, M. Z., & Aswad, F. H. (2020). Identifikasi Zona Potensi Banjir Berbasis Sistem Informasi Geografis Menggunakan Metode Overlay dengan Scoring di Kabupaten Agam, Sumatera Barat. *Jurnal Geosains dan Remote Sensing*, 1(1), 11–22. https://doi.org/10.23960/jgrs.2020.v1i1.25

Sihaini, E., Supriyono, S., Yunita, M., Alfi, M., & Guntar, D. (2026). Analisis Spasial Tingkat Kerentanan Banjir di Kabupaten Kampar, Provinsi Riau Berdasarkan Sistem Informasi Geografis (SIG). *Dinamika Sosial: Jurnal Pendidikan Ilmu Pengetahuan Sosial*, 5(1), 69–85. https://doi.org/10.18860/dsjpips.v5i1.24940

Sulaeman, A., Suhartanto, E., & Sumiadi, S. (2017). Analisis Genangan Banjir Akibat Luapan Bengawan Solo untuk Mendukung Peta Risiko Bencana Banjir di Kabupaten Bojonegoro. *Jurnal Teknik Pengairan*, 8(2), 146–157. https://doi.org/10.21776/ub.pengairan.2017.008.02.1

Utama, F. P., Setiawan, Y., Vatresia, A., & Sari, J. P. (2021). Flood Vulnerability Analysis using Weighted Overlay. *IT Journal Research and Development*, 6(2), 70–82. https://doi.org/10.25299/itjrd.2022.6193

Vio, D., de Souza, J. O. P., Motta, G. H. M. B., & de Souza, L. C. (2025). Machine learning on alluvial deposit Identification in dryland area. *Revista Contexto Geográfico*, 10(24), 138–182. https://doi.org/10.28998/contegeo.10i.24.18434

Witts, D., Hall, R., Nichols, G., & Morley, R. (2012). A new depositional and provenance model for the Tanjung Formation, Barito Basin, SE Kalimantan, Indonesia. *Journal of Asian Earth Sciences*, 56, 77–104. https://doi.org/10.1016/j.jseaes.2012.04.022

Zhou, Q., Su, J., Arnbjerg-Nielsen, K., Ren, Y., Luo, J., Ye, Z., & Feng, J. (2021). A GIS-Based Hydrological Modeling Approach for Rapid Urban Flood Hazard Assessment. *Water*, 13(11), 1483. https://doi.org/10.3390/w13111483

© 2026 Dept. of Geophysics Hasanuddin University

ISSN: 2579-5821 (Print)
ISSN: 2579-5546 (Online)
URL address: http://journal.unhas.ac.id/index.php/geocelebes
DOI: 10.70561/geocelebes.v10i2.50316

Jurnal Geocelebes Vol. 10 No. 2, October 2026, 241 – 257

Spatial Model of Forest Cover Change using Moisture Index in Kolaka Regency

Septianto Aldiansyah[1,2]*, Amniar Ati[1], Fitriyani Saudi[1]

[1]Department of Geography Education, Faculty of Teacher Training and Education, Universitas Halu Oleo, Kendari 93232, Indonesia.
[2]Department of Geography, Faculty of Mathematics and Natural Sciences, Universitas Indonesia, Depok 16424, Indonesia.

*Corresponding author. Email: septianto.aldiansyah@uho.ac.id

Manuscript received: 15 March 2026; Received in revised form: 14 June 2026; Accepted: 22 June 2026

Abstract

Kolaka Regency plays a crucial role, both ecologically and economically. This study aims to identify long-term changes in forest cover using the Moisture Index, using a collection of Landsat satellite imagery. Forest cover is defined by a threshold: values >0.7 are considered forest cover, while values <0.7 are considered non-forest areas. Forest cover in Kolaka Regency fluctuates. The 2000-2005 period saw the sharpest decline, reaching an unmitigated loss of 404.00 km^2. Although forest cover recovered in subsequent years, it accounted for only a third of the total forest loss, reaching 462.31 km^2. Extractive mining activities and land conversion drive forest loss in this region. A comparison of protected forest areas and the rate of forest loss indicates that legal protection does not automatically guarantee the presence of vegetation cover in the field. Therefore, forest management in Kolaka must shift from an administrative approach to a spatially based, real-time monitoring approach.

Keywords: Forest Cover; Kolaka Regency; Normalized Difference Moisture Index; Remote Sensing.

Citation: Aldiansyah, S., Ati, A., & Saudi, F. (2026). Spatial Model of Forest Cover Change using Moisture Index in Kolaka Regency. *Jurnal Geocelebes*, 10(2): 241–257, doi: 10.70561/geocelebes.v10i2.50316

Introduction

Southeast Sulawesi is a province in the Sulawesi archipelago with the third-highest population, at 9,563 people. However, this province has the highest population growth rate, at 1.65% per year (Badan Pusat Statistik, 2025a). This high growth rate, if not managed properly, can put serious pressure on the environmental carrying capacity. Forests in Sulawesi are reported to continue shrinking under significant pressure, even reaching the edges of protected areas. Sulawesi ranks third after Sumatra and Kalimantan with a forest loss rate of 91,500 ha/year (Santoro et al., 2025). Therefore, the Southeast Sulawesi government continues to conserve biodiversity by monitoring protected areas across its territory. This province has a protected area of 111,756,560 ha, and Nature Reserves and Nature Conservation of 40,707,750 ha (Badan Pusat Statistik, 2025b). Nevertheless, this region requires continuous monitoring to ensure proper forest management. Accurate and reliable forest cover maps play a crucial role in forestry planning, monitoring forest degradation, and developing forest policy and management plans (Tariq et al., 2023).

In Indonesia, the history of forest management is deeply rooted in the Dutch colonial regime, which implemented the Domein Verklaring principle—declaring forest areas as state property primarily for commodity exploitation (Berenschot & Dhiaulhaq, 2025). This highly centralized legacy historically alienated local communities from their traditional living spaces, inadvertently fostering a long-term perception of forests as state-owned

© 2026 Dept. of Geophysics Hasanuddin University

resources that could be freely exploited without sustainability constraints (Bose, 2023). To mitigate the resulting environmental degradation and ongoing social conflicts, the Indonesian government has progressively shifted its paradigm toward collaborative forest management. Formally operationalized through the Social Forestry program, this approach grants legal access rights and management responsibilities to local actors to equitably distribute benefits, foster local stewardship, and optimize conservation performance (Gunawan et al., 2024; Rakatama & Pandit, 2020). Within this collaborative framework, various technical measures are actively deployed to maintain maximum canopy cover and support natural regeneration in highly vulnerable landscapes. These include developing enrichment plantings, enforcing ecosystem restoration, and establishing robust buffer zones around core conservation areas to systematically reduce community dependence on timber extraction while sustainably improving local livelihoods (de Souza et al., 2025).

Remote sensing has become a key alternative for analyzing forest cover changes over the past several years. Numerous methods have been developed to evaluate vegetation and forests. Among various spectral indicators, the Normalized Difference Moisture Index (NDMI) has emerged as one of the most robust and widely adopted frameworks for dense canopy monitoring (Schultz et al., 2018; Shimizu et al., 2019). The deployment of such remote sensing indices is increasingly critical, given that conventional field-based inventory methods are notoriously time-consuming, labor-intensive, and inherently prone to generating outdated baselines in today's rapidly transforming environments (Dragomir et al., 2025). By contrast, NDMI-driven forest monitoring systems leverage advanced sensor capabilities to effectively capture complex land-cover heterogeneities and structural canopy variations. Because it responds directly to cellular water retention rather than superficial greenness, this index is highly sensitive to subtle, long-term degradation trajectories while remaining immensely cost-effective (Nguyen et al., 2025). Therefore, this study aims to identify long-term changes in forest cover, compare local modeling results with Global Forest Watch (GFW) data, and conduct an overlay analysis of land-cover types and forest-area functions. This is done to evaluate the effectiveness of legal protection status in reducing on-the-ground degradation rates, identify area-specific drivers of deforestation, and formulate more targeted collaborative management strategies.

Materials and Methods

Study area

This research was conducted in Kolaka Regency, which is geographically located at 3°36’ – 4°35’ South Latitude and 120°45’ – 121°52’ East Longitude, and spatially located at UTM Zone 51S coordinates using the WGS 84 datum (Figure 1). Kolaka Regency has an area of 2,958.55 km^2. On the east side is a mountainous forest that borders East Kolaka Regency and North Kolaka Regency, with relatively steep terrain, while the coastal area is on the west side, bordering Bone Bay. This area consists of mountains and hills that stretch from north to south, and it has several rivers that provide energy for industrial and household needs, as well as for irrigation and tourism. Kolaka Regency has a strategic position with relatively high mobility and economic activity. The population of Kolaka Regency in 2024 was 257,733 people.

Type and Source of Data

This study uses a remote sensing approach based on Landsat satellite imagery to analyze forest cover dynamics for the period 1990–2025. The primary data used are Landsat Surface Reflectance (SR)

© 2026 Dept. of Geophysics Hasanuddin University

imagery, accessed and processed via the Google Earth Engine (GEE) platform. GEE is a cloud-based computing platform that enables efficient and consistent processing of large-scale geospatial data (Aldiansyah & Saputra, 2023). The datasets used include 5 TM images from before 2015, Landsat 8 Operational Land Imager (OLI) data for 2020, and Landsat 9 OLI data for 2025. The Landsat program was chosen because it has a long-term data archive, 30-meter spatial resolution, and radiometric consistency, which support multi-temporal land-cover change analysis (Demarquet et al., 2023; Donatien et al., 2024). The details of the data used are presented in Table 1.

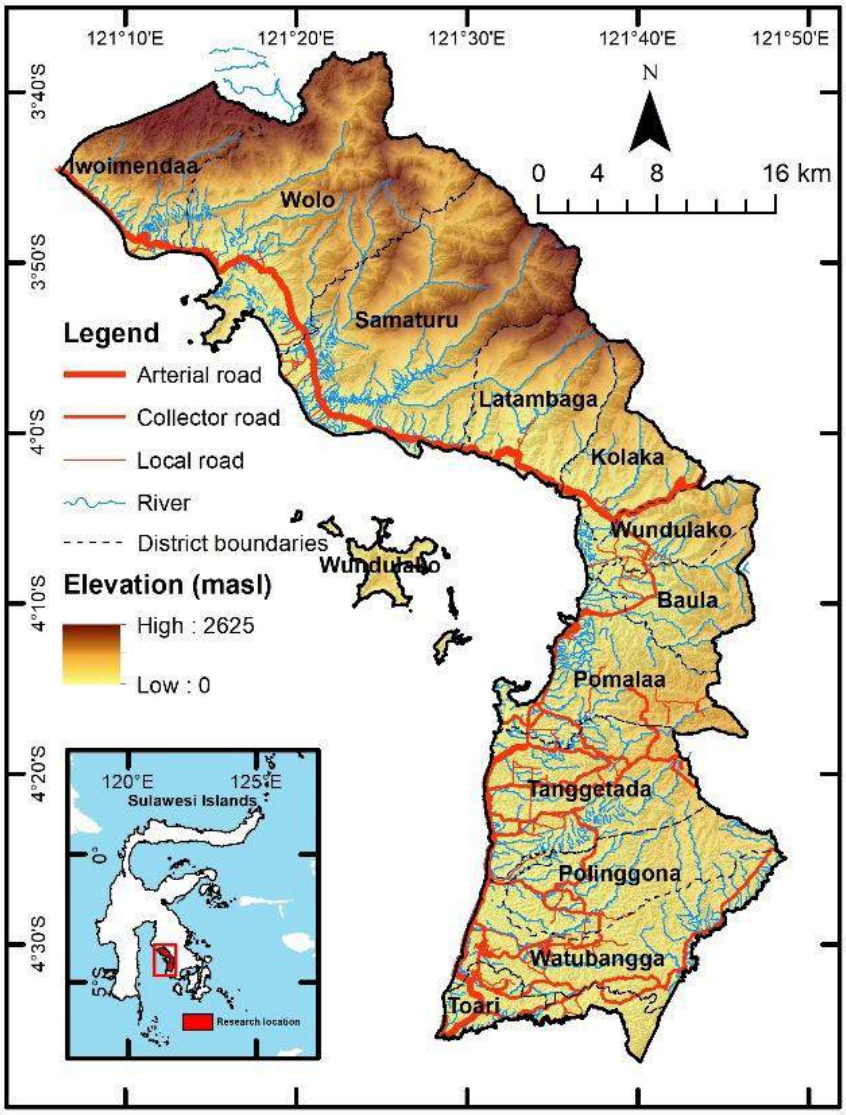


Figure 1. Research Location in Kolaka Regency.

Table 1. Types of satellites used.

Satellite	Sensor	Path/Row	Year	Resolution	Atmospheric correction	Data source
Landsat 5	TM	113/63	1990	30	LEDAPS	USGS
Landsat 5	TM	113/63	1995	30	LEDAPS	USGS
Landsat 5	TM	113/63	2000	30	LEDAPS	USGS
Landsat 5	TM	113/63	2005	30	LEDAPS	USGS
Landsat 5	TM	113/63	2010	30	LEDAPS	USGS
Landsat 5	TM	113/63	2015	30	LEDAPS	USGS
Landsat 8	OLI	113/63	2020	30	LaSRC	USGS
Landsat 9	OLI-2	113/63	2025	30	LaSRC	USGS

© 2026 Dept. of Geophysics Hasanuddin University

Data Collection and Processing

Data collection was conducted using temporal and spatial filtering techniques on USGS Landsat Level-2, Collection 2, Tier 1 image collection at GEE. Temporal filtering was performed by constructing image composites for each target year using three years (year-1 to year+1). To avoid phenological bias and maintain strict interannual consistency, image acquisition was restricted to identical seasonal windows (dry-season months) across all target periods. This approach aims to increase the number of observations and reduce data gaps due to cloud cover, resulting in a more stable representation of annual conditions. Spatial filtering was performed by restricting the imagery to the study area using the boundary filter function. This combination of filters ensured that only temporally and spatially relevant imagery was further processed.

The data processing stage began with cloud and cloud shadow correction (cloud masking) using the pixel quality band (QA_PIXEL) in the Surface Reflectance product. Masking was performed using a bitwise method to remove pixels indicated by clouds, dilated clouds, cloud shadows, and cirrus (specifically for Landsat 8–9). This procedure is crucial for minimizing spectral bias due to atmospheric contamination and improving the accuracy of surface information extraction (Singh et al., 2025). Reflectance values were then converted from digital number scale to surface reflectance using the official Landsat Collection 2 scale factor. Next, cloud-cleared images were composited using the median method for each target year period. The median composite was chosen because it is relatively robust to extreme values and cloud residuals compared to the mean method (Aldiansyah & Saputra, 2023).

Data Analysis

Forest cover analysis was conducted using the Normalized Difference Moisture Index (NDMI), a normalized difference-based spectral index that utilizes the Near-Infrared (NIR) and Shortwave Infrared (SWIR) channels. The NDMI was selected conceptually to distinguish dense, intact forest structures from open or degraded land due to its high sensitivity to vegetation water content, canopy stratification, and cellular leaf structure. This index is calculated using the following equation (Schultz et al., 2018):

$$NDMI = \frac{NIR - SWIR}{NIR + SWIR} \quad (1)$$

where NIR represents the near-infrared band (Landsat TM: Band 4; OLI/OLI-2: Band 5), and SWIR represents the shortwave infrared band (Landsat TM: Band 5; OLI/OLI-2: Band 6).

The NDMI used in this study ranges from -1 to +1, with higher values consistently indicating dense, closed-canopy vegetation. To maintain programmatic consistency across the 35-year monitoring timeline, a pixel-based fixed threshold of NDMI >0.7 was established to classify forest cover, adapting widely accepted empirical baselines for tropical canopy mapping (Choi et al., 2021; Piragnolo et al., 2021). This index was deliberately selected over traditional greenness indices like NDVI because NDMI effectively mitigates spectral saturation issues in dense tropical rainforests and is highly sensitive to canopy logging and perforations, where surface moisture drops rapidly upon tree extraction.

To mitigate the inherent methodological risks of sensor drift and inter-generational variance across multiple Landsat instruments (TM, OLI, and OLI-2), strict pre-processing protocols were enforced. Radiometric normalization and atmospheric comparability were systematically addressed using USGS Landsat Level-2, Collection 2, Tier 1 Surface Reflectance datasets. These products are analysis-ready and have been

© 2026 Dept. of Geophysics Hasanuddin University

cross-calibrated using the LEDAPS (TM) and LaSRC (OLI/OLI-2) (Wulder et al., 2022) atmospheric correction algorithms to ensure surface reflectance stability. Furthermore, temporal harmonization was maintained by targeting cloud-free composites within identical seasonal windows to avoid phenological bias. Lastly, the robustness and sensitivity of the >0.7 threshold were empirically validated through a rigorous chronological accuracy test. This is intended to ensure that the calibrated threshold yields highly reliable, low-bias historical forest area estimates throughout the observation period.

The model's temporal reliability in tracking historical forest cover changes was evaluated using a chronological transition matrix. Instead of validating static land-cover types, this matrix cross-compares the predicted forest-cover year with the observed historical reference years from 1990 to 2025 (Li et al., 2024). The chronological transition matrix is constructed by placing reference classes in rows and classification results in columns. Diagonal values in the matrix indicate the number of correctly classified pixels, while off-diagonal values indicate misclassification. Overall accuracy was calculated by dividing the number of correctly classified pixels by the total number of samples. In addition, producers' and users' accuracies were calculated for each year's class (Rawat et al., 2026). To measure the level of agreement corrected for random chance, the Kappa coefficient (Cohen's Kappa) was used. A Kappa value >0.80 is generally interpreted as very strong agreement, while 0.61–0.80 is categorized as strong agreement (Oo et al., 2026).

To mathematically robustify the historical evaluation, a total of 240 independent validation points were generated across the study area utilizing a stratified random sampling design. The samples were distributed equally to ensure strict chronological balance, with exactly 30 reference points allocated per target observation year. The spatial distribution of these validation points covered the entire study area to eliminate spatial clustering bias.

The ground-truthing verification was performed via high-resolution visual interpretation on Google Earth Pro and historical Landsat composite rollbacks. The temporal matching procedure paired each model output year with reference imagery windows targeted within a ±6-month tolerance of the specific target year. For earlier historical epochs (1990–1995) where sub-meter high-resolution imagery was limited, multi-spectral false-color composites from standalone Landsat archives were utilized as the primary chronological baselines. To maintain strict interpreter consistency, all 240 points were cross-examined using a double-blind consensus interpretation protocol by two independent GIS specialists, who assessed canopy shadow and texture patterns, thereby establishing an inter-rater agreement framework before the final accuracy calculation.

Next, the forest cover model was overlaid with land cover type maps and forest area function maps. Overlay analysis was conducted to identify the spatial distribution of forests across land-use categories and area functions. This approach allows for thematic spatial analysis to understand forest change patterns in the context of spatial planning and forestry policy. To enhance external validity, the forest cover model results were compared with Global Forest Watch (GFW) data, based on the Hansen et al. (2013) dataset on global tree cover change. The GFW dataset provides information on annual tree cover loss at 30 m resolution generated from global Landsat imagery. Comparisons were made by evaluating the correspondence between spatial patterns of forest loss and annual area trends between the research model results and GFW data.

© 2026 Dept. of Geophysics Hasanuddin University

The analysis was conducted by identifying a spatial pattern match. The differences that emerged were analyzed by considering differences in forest definitions, canopy cover thresholds, and classification methods used (Hansen et al., 2013).

Furthermore, the two models were structurally aligned by extracting their spatial extent. A spatial concordance analysis was performed using a confusion matrix to evaluate classification agreement between the local and GFW models at sample points. This process cross-classifies the study area into binary classes: forest and non-forest. The evaluation was conducted using 235 random sample points generated through a stratified random sampling approach. The number of points for each class was adjusted in proportion to each class's percentage of the area.

Four accuracy metrics are calculated from the contingency matrix: Overall Accuracy (OA), Producer's Accuracy (PA), User's Accuracy (UA), and Cohen's Kappa Coefficient. OA Accuracy measures the percentage of sample points correctly classified into both classes (forest and non-forest) across the study area. This formula is calculated using Equation 2 as follows (Foody, 2024):

$$OA = \frac{TP + TN}{TP + TN + FP + FN} \quad (2)$$

where TP, TN, FN, and FP represent True Positives, True Negatives, False Negatives, and False Positives, respectively.

PA Accuracy is used to calculate the proportion of actual forest sample points (based on the GFW reference) that the local model successfully detects. UA Accuracy measures the proportion of points classified as forest by the local model that are forest in the GFW data. Cohen's Kappa Coefficient is used as a more stringent index to evaluate classification agreement between the two models, accounting for chance. The overall workflow of the methodology is presented in Figure 2.

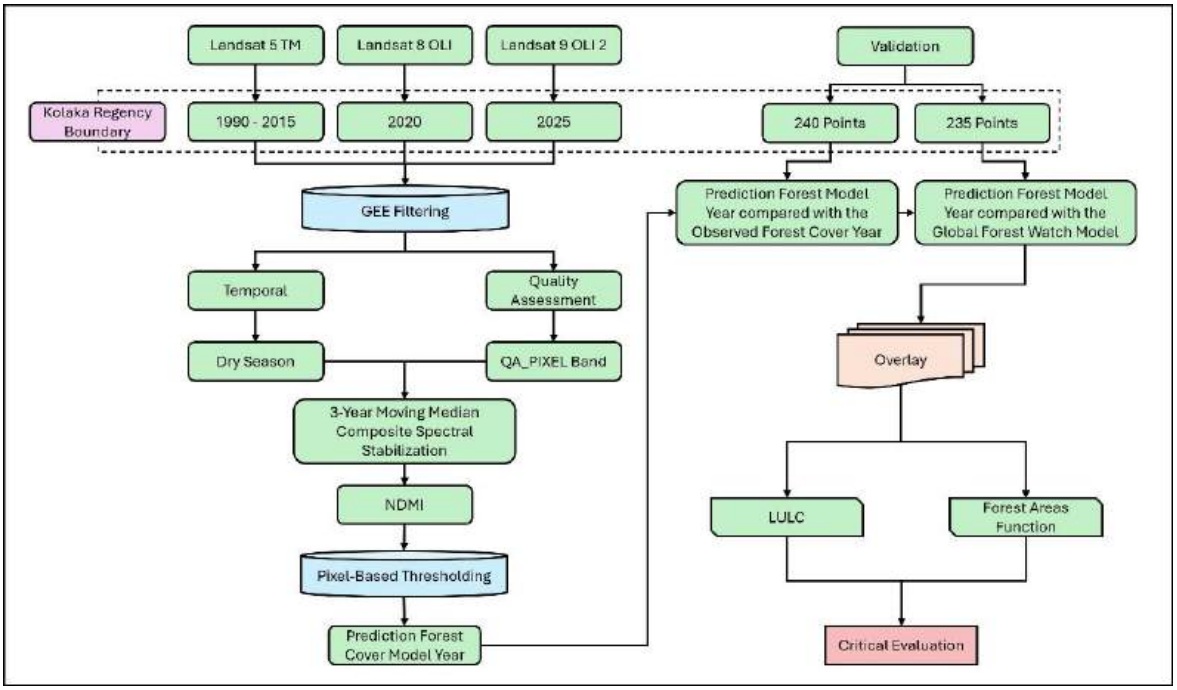


Figure 2. Workflow of the methodology.

Results

Forest cover change

The forest cover change model in Kolaka Regency shows fluctuations throughout the observation period. Forest cover in this

© 2026 Dept. of Geophysics Hasanuddin University

region from 1990 to 2005 continued to decline, with the largest decline occurring from 2000 to 2005, reaching 404,00 km^2. In the following year, forest cover increased to 319,20 km^2. However, a nearly identical decline occurred in the following period, reaching 303,18 km^2. In the following period, forest cover recovered, but only to one-third of the loss. Compared to the baseline period, forest cover in Kolaka Regency had disappeared by 462,31 km^2 (Figure 3). This change demonstrates a dynamic pattern and requires special attention, particularly regarding forest management in this region.

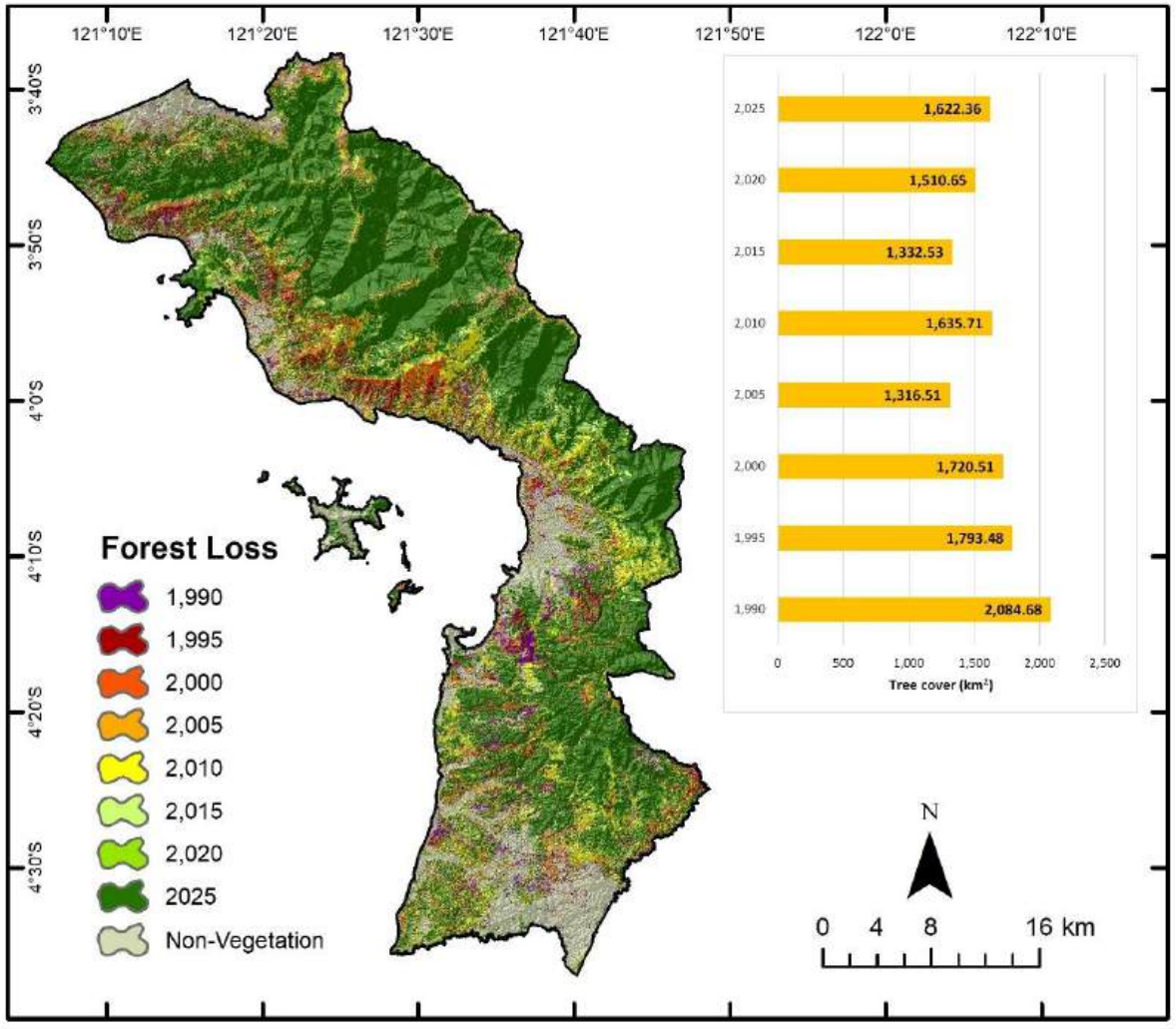


Figure 3. Forest Cover Changes in Kolaka Regency.

Overall, forest cover change in Kolaka Regency indicates an increase in deforestation intensity. Despite efforts to tighten forest governance policies and law enforcement over time, the reality on the ground demonstrates significant challenges in maintaining the region's sustainability. This aligns with the findings of Gunawan et al. (2024), who highlighted that overlapping industrial concessions and protected areas often trigger natural forest loss, resulting in reduced biodiversity and ecosystem function degradation. This study indirectly emphasizes the importance of integrating spatial-temporal data into evidence-based conservation planning to monitor the effectiveness of forest protection policies in affected area.

Accuracy Test

Accuracy testing of forest cover maps from 1990 to 2025 in Kolaka Regency

© 2026 Dept. of Geophysics Hasanuddin University

demonstrated high data reliability. The accuracy test using a confusion matrix yielded an OA value of 80.41% with a Kappa coefficient of 0.77. This value indicates that the forest cover classification generated by the GEE thresholding algorithm exhibits high consistency and is suitable for long-term land-use change analysis.

Specifically, UA accuracy demonstrated impressive performance in the 2025 (100%) and 2020 (93.34%) classifications. This demonstrates that the Landsat 8 OLI and 9 OLI-2 sensors can distinguish forest objects with greater precision than previous-generation sensors. However, PA accuracy varied during the intermediate period (Table 2), particularly in 2005 (68.57%) and 2010 (68.42%). The decrease in accuracy during this period was most likely caused by persistent atmospheric disturbances (cloud cover) in the Mekongga mountain region, as well as the similarity of spectral values between degraded secondary forests and cocoa or clove plantations that began to expand in Kolaka during this period.

Table 2. Forest cover model accuracy test.

Year		Observed forest cover year									
		1990	**1995**	**2000**	**2005**	**2010**	**2015**	**2020**	**2025**	**Total**	**UA**
Predicted forest cover year	**1990**	21	-	-	-	4	-	-	5	30	70
	1995	-	19	-	-	7	2	-	2	30	63.34
	2000	-	-	27	2	-	-	-	1	30	90
	2005	-	-	1	24	1	-	2	2	30	80
	2010	-	-	-	4	26	-	-	-	30	86.67
	2015	-	-	3	5	-	18	2	2	30	60
	2020	-	-	-	-	-	1	28	1	30	93.34
	2025	-	-	-	-	-	-	-	30	30	100
	Total	21	19	31	35	38	21	32	43	240	
	PA	100	100	87.09	68.57	68.42	85.71	87.50	69.77		
OA = 80.41								**Kappa** = 0.77			

Comparative Analysis of Models Against Global Forest Watch

A spatial comparison was conducted between the developed GEE-based vegetation index model and the Global Forest Watch reference data to validate tree-cover loss patterns. Visually, the developed model demonstrated greater accuracy in capturing local-level land-cover dynamics than the GFW data did.

The research model (Figure 4a) identified forest fragmentation and tree loss patterns in hilly areas in greater detail. In contrast, the GFW data (Figure 4b) tended to generalize to areas of vegetation transition. The detected tree loss patterns (marked in orange) showed high location consistency between the two models, particularly in coastal and foothill areas, which are active zones of land conversion. The use of a custom vegetation index in the GEE script enabled more sensitive detection of canopy change in areas with steep topography in Kolaka Regency, where GFW data often suffers from noise due to slope-shadow distortion.

To provide a rigorous validation, a point-based spatial intercomparison analysis was conducted between the two models (Figure 5). The contingency matrix analysis demonstrated an OA of 85.11% across the study area. Focusing on the forest class, the model achieved a PA of 77.42% and a UA of 69.57%. Furthermore, the Cohen's Kappa coefficient was 0.63, indicating a substantial spatial agreement between the local model and the GFW baseline. This strong alignment confirms that the local model successfully captures the distribution of primary forests while maintaining high predictive reliability.

© 2026 Dept. of Geophysics Hasanuddin University

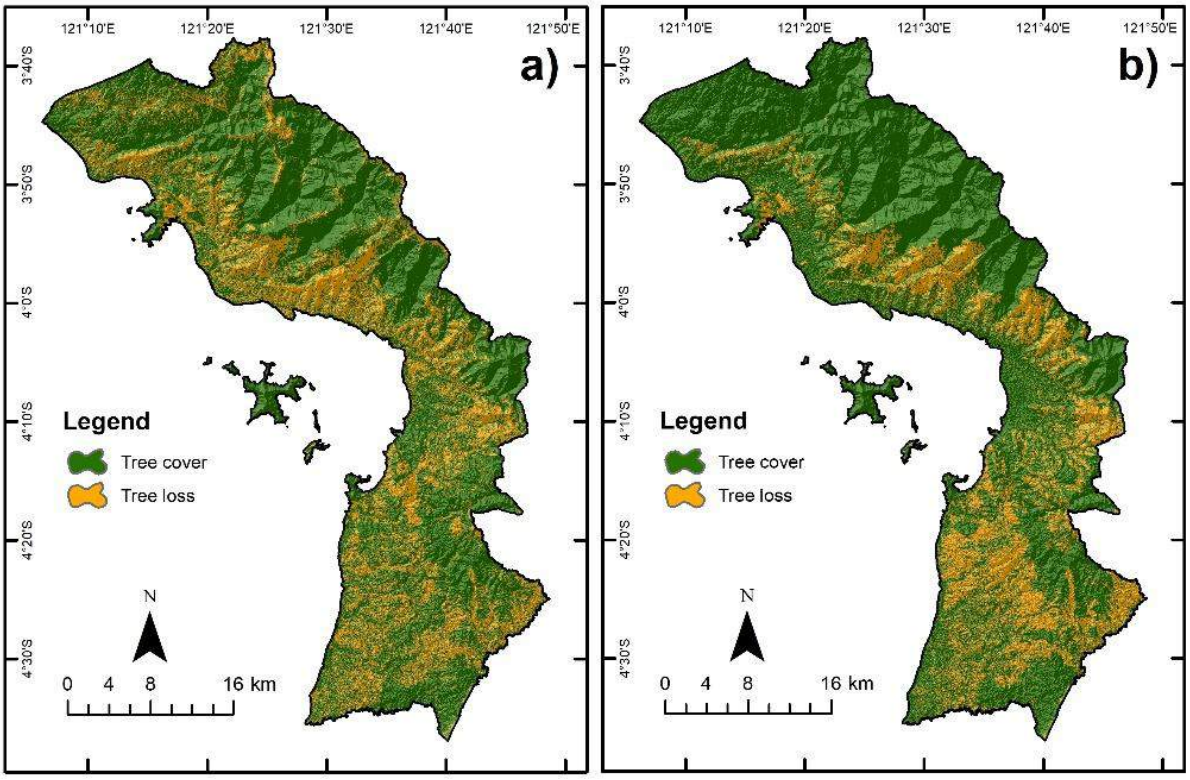


Figure 4. Model comparison between a) the GEE-based forest cover model, and b) the Global Forest Watch model.

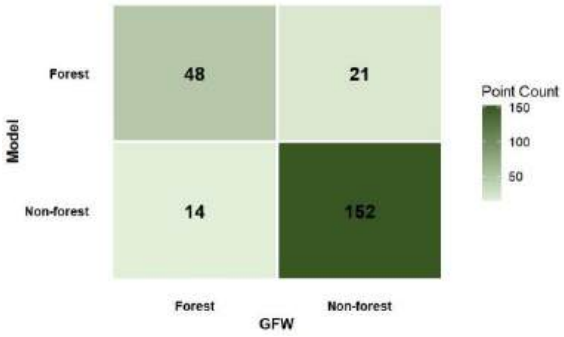


Figure 5. Point-based confusion matrix demonstrating the classification agreement between the vegetation index model and the Global Forest Watch model

Spatial cross-tabulation of forest cover models on land cover and forest area function

To provide rigorous validation and to understand the underlying spatial drivers of forest dynamics, a spatial cross-tabulation matrix analysis was conducted by intersecting the forest model with regional Land Use and Land Cover (LULC) classes (Figure 6) and official Forest Area Functions (Figure 7). This transition framework shifts the interpretation from a purely visual comparison to a robust, analytical evaluation of spatial alignment and localized discrepancies.

The intercomparison with the LULC baseline (Figure 6) demonstrates that, of the 2,638.57 km^2 total reference forest area, the local model confirms a high spatial persistence of 1,876.03 km^2 as stable tree cover. However, a critical structural divergence is uncovered, revealing 762.54 km^2 of tree loss within the designated forest baseline. This substantial discrepancy represents fragmented canopy degradation or secondary forest regrowth that global-scale datasets typically generalize or omit.

Anthropogenic pressures along forest boundaries are quantified, with the model capturing tree-cover extensions into non-forest classes, including built-up areas (47.59 km^2) and crops (29.11 km^2). Conversely, the detection of tree loss overlapping with bare ground (10.64 km^2), built-up clusters (23.14 km^2), and shrublands (26.74 km^2) provides empirical evidence of persistent land clearing and

© 2026 Dept. of Geophysics Hasanuddin University

infrastructure expansion encroaching upon the core forest matrices.

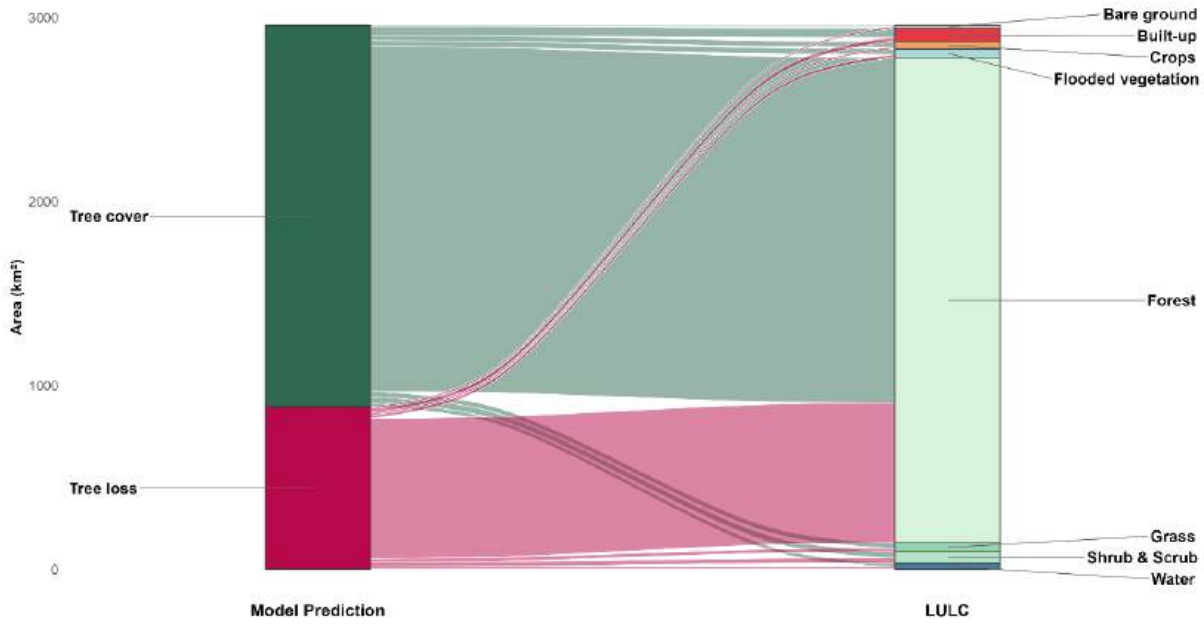


Figure 6. Transition of the local forest cover model illustrating quantitative alignment against baseline LULC.

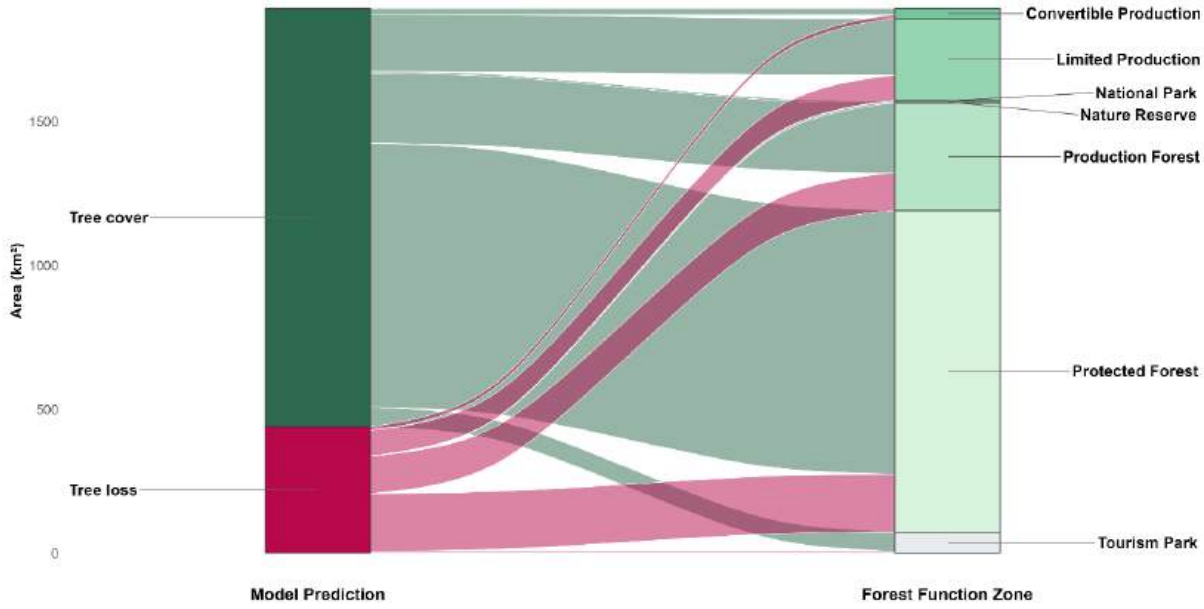


Figure 7. Transition of the local forest cover model illustrating spatial distribution of stable tree cover and localized tree loss across forest function zones

When evaluated against administrative boundaries (Figure 7), the spatial transition reveals critical insights into compliance and management. A total of 916.37 km^2 of stable tree cover is localized within Protected Forests, validating the ecological persistence of the region's core conservation zones. Nevertheless, the overlay successfully identifies a severe environmental hotspot: a total of 200.77 km^2 of tree loss has occurred within these legally protected domains, representing approximately 18% of the protected baseline and placing it under critical threat.

Furthermore, forest extraction dynamics are heavily concentrated within commercial zones, where Production Forests and

© 2026 Dept. of Geophysics Hasanuddin University

Limited Production Forests account for a combined tree loss of 217.79 km^2 (130.08 km^2 and 87.71 km^2, respectively). Because production-related allocations (Production, Limited Production, and Convertible Production Forests) collectively account for over 50% of the managed landscape, the study area exhibits extreme systemic vulnerability to legal canopy modifications through timber utilization permits. The tight spatial overlap between tree loss and bare ground within these production blocks confirms that localized extractive activities, such as mining and agroforestry conversions, are the primary structural drivers creating deforested perforations within the legal forest estate.

Discussion

The long-term multi-decadal forest loss captured in Kolaka Regency indicates a massive landscape transformation. The drastic decline witnessed during the 2000–2005 epoch directly reflects the institutional impacts of the post-decentralization exploitation boom, where the devolution of natural resource management authority often preceded the readiness of regional oversight instruments. The subsequent vegetation recovery phase, which compensated for only one-third of the total historical loss, underscores the low resilience of these dense tropical ecosystems to large-scale, compounded anthropogenic disturbances.

The inability of forests to return to their original state signals an irreversible loss of ecosystem services. This aligns with the findings of Gaveau et al. (2021), which demonstrate that primary forest degradation in Indonesia remains largely permanent, as these areas are immediately converted into industrial plantations or mining sites. Such conversions, particularly in mining sectors, result in irreversible ecological shifts that prevent natural forest regeneration (Giljum et al., 2022). A comparison with the study by Hansen et al. (2013) shows that Sulawesi is characterized by more fragmented deforestation than Kalimantan. This fragmentation increases the risk of extinction for endemic species by reducing habitat connectivity in the Wallacea region (Supriatna et al., 2020). This study indirectly emphasizes the integration of spatial-temporal data in evidence-based forest conservation planning.

An OA value of 80.41% and a Kappa of 0.77 provide scientific evidence that the GEE thresholding algorithm is highly effective for long-term monitoring in complex topographic areas. However, the low PA observed during the 2005–2010 period highlighted the challenge of spectral mixing between degraded secondary forests and agroforestry plantations (cocoa/ cloves). In Kolaka, the expansion of smallholder agriculture often mimics the forest spectral profile in medium-resolution satellite imagery, leading to omission errors. This finding aligns with Escobar-López et al. (2024), who noted that overlapping industrial concessions and complex smallholder landscapes typically complicate automated object discrimination when relying solely on generic passive remote sensing frameworks.

When overlaid with administrative boundaries, the overlay reveals that more than 50% of the study area falls within production-related zones (Limited Production Forest, Production Forest, and Convertible Production Forest), thereby placing the forest ecosystem of Kolaka at high risk of legal canopy modifications (Figure 7). Furthermore, the explicit detection of localized bare-ground perforations clustered within these designated production boundaries structurally signifies the extensive spatial footprint of extractive activities.

While a definitive causal link to corporate boundaries requires decoupled tenure datasets, these bare-ground signatures can be critically contextualized within the

© 2026 Dept. of Geophysics Hasanuddin University

regional footprint of the extractive boom. Historically, the intensity of land clearing in Kolaka exhibits a strong socio-economic alignment with global nickel market dynamics. As a strategic landscape containing one of the largest saprolite ore reserves in the region, local forest extraction trends tend to fluctuate in tandem with the escalating demand for nickel within the global electric vehicle battery supply chain. This structural linkage illustrates a critical, localized green economy paradox, in which global-scale decarbonization efforts are fundamentally offset by severe, irreversible deforestation at the resource frontier.

This contextual trajectory is well supported by Giljum et al. (2022), who argued that industrial mining is the most permanent and destructive driver of forest loss compared with transitional shifts in the agricultural sector. The extractive nature of nickel mining, particularly across the ultrabasic structures of Sulawesi, causes profound disruptions to soil profiles and structural damage, rendering subsequent ecosystem recovery highly protracted and ecologically difficult (D'Alisa & Demaria, 2024). Furthermore, macro-scale observations by Lo et al. (2024) across Indonesia's nickel belt confirm that mining expansion drives systemic fragmentation of forest cover through both direct surface stripping and the cumulative development of supporting transport infrastructure.

The biophysical ramifications of this extractive pressure extend beyond commercial production blocks; they severely compromise core conservation zones. The stark spatial disparity captured between the official legal status of Protected Forests and the high rates of actual canopy loss empirically indicates that an administrative designation does not automatically guarantee vegetation persistence on the ground. Beyond complete canopy removal, the model's successful isolation of extensive transitional Shrub & Scrub areas reflects a substantial accumulation of degraded, idle post-extraction land parcels that have systematically failed to undergo active environmental rehabilitation.

Consequently, these ecological indicators demand an urgent paradigm shift. Forest management in Kolaka must decisively migrate from an archaic, purely administrative compliance approach to a dynamic, real-time spatial monitoring framework. Without stringent law enforcement mechanisms that actively integrate GEE-automated monitoring, the region's remaining core forest cover will continue to be chronically eroded under the guise of expanding forest area through borrow-to-use permits.

Ultimately, this study underscores that high-resolution spatio-temporal data integration must serve as the primary instrument in evidence-based conservation planning. Deploying such localized automated systems is no longer optional, but a vital ecological necessity to prevent the imminent collapse of the hydrological buffering capacity across the critical Mangolo watershed and its surrounding upstream catchments. To bridge the empirical boundaries of this current study with these broader institutional drivers, future investigations must integrate temporal mineral production statistics, commodity pricing models, and spatial mining concession maps into this biophysical remote sensing framework to quantitatively map the direct socio-economic causalities of long-term forest loss.

While the GEE-based localized thresholding framework demonstrated a high operational capacity, several inherent remote sensing constraints must be acknowledged as potential sources of uncertainty propagation within this tropical landscape. First, the 30-meter spatial resolution of the Landsat instruments

© 2026 Dept. of Geophysics Hasanuddin University

naturally introduces the challenge of mixed pixels along highly fragmented forest edges and agroforestry transitions, where sub-pixel combinations of tree canopy, smallholder crops, and bare soil may artificially distort the uniform >0.7 index boundary. Second, despite enforcing strict bitwise logical masking protocols using the QA_PIXEL band, persistent tropical cloud contamination and localized atmospheric haze residuals remain an inevitable source of minor spectral noise across historical annual mosaics (Singh et al., 2025).

Furthermore, the highly complex, rugged topography of the Mekongga Mountains introduces severe shadowing in mountainous terrain. These topographically shaded slopes inherently exhibit reduced surface reflectance, which can lead to local underestimation of canopy density if the spectral index relies solely on visible greenness (Jiang et al., 2019). Lastly, vegetation spectral overlap poses a distinct conceptual challenge in this region; mature commercial agroforestry matrices (such as dense cacao or clove plantations) frequently exhibit near-identical multi-spectral canopy signatures to those of primary or secondary tropical forest estates (Ordway et al., 2017; Pain et al., 2021).

Nevertheless, the propagation of these spectral and spatial uncertainties was successfully constrained and substantially mitigated by our implementation of the 3-year moving-median composite window and strict dry-season temporal filtering, which effectively suppressed ephemeral noise and terrain illumination variability. Empirically, the robustness of the framework is verified by the chronological accuracy assessment (Table 2), where the model maintained high stability. This demonstrates that, despite these structural challenges, the calibrated fixed-threshold approach yields a reliable and chronologically consistent trajectory of long-term forest-cover dynamics.

Conclusion

This study concluded that forest cover in Kolaka Regency experienced significant fluctuations with a progressive degradation trend, with cumulative forest loss reaching 462,31 km^2 since the baseline period. The sharpest decline occurred in the 2000–2005 period, reaching 404,00 km^2. Despite a phase of vegetation recovery, the recovered area only replaced one-third of the total forest loss, indicating a permanent decline in ecosystem function and biodiversity.

Methodologically, the classification model using the thresholding algorithm on the GEE platform proved highly reliable, with an OA value of 80.41% and a Kappa coefficient of 0.77. The use of Landsat 8 and 9 sensors achieved 100% user accuracy by 2024, demonstrating the superiority of this local model in capturing the spatial details of tree loss in steep topographic areas compared to global reference data, while successfully constraining inherent uncertainties such as mixed pixels, cloud residuals, terrain shadowing, and spectral overlap.

Overlay analysis confirms that the primary drivers of deforestation in Kolaka are extractive mining and land conversion, particularly in Production Forest areas, which account for more than 50% of the study area. The presence of bare ground and scrubland within production forest areas underscores their vulnerability to legal deforestation, as evidenced by a substantial accumulation of unrehabilitated, idle post-mining land. Therefore, integrated real-time monitoring and zoning evaluation are needed to protect the remaining 45.61% of the Protected Forest from mining pressures. To fully solidify this framework, future investigations must integrate corporate concession boundaries and temporal production statistics into this biophysical remote sensing model.

Acknowledgements

© 2026 Dept. of Geophysics Hasanuddin University

The authors would like to thank the USGS and NASA for providing Landsat satellite imagery and GEE for serving as a data-processing platform. The authors would like to express their deepest appreciation to the Dean of the Faculty of Teacher Training and Education and the Geography Education Laboratory at Halu Oleo University for providing the necessary facilities for this research.

Author Contribution

Septianto Aldiansyah designed the research method, data analysis, and interpretation of results, drafted the publication manuscript; Amniar Ati conducted data analysis and interpretation of results; and Fitriyani Saudi refined the issues and reviewed the publication manuscript.

Conflict of Interest

The authors declare no conflict of interest.

References

Aldiansyah, S., & Saputra, R. A. (2023). Comparison of Machine Learning Algorithms for Land Use and Land Cover Analysis Using Google Earth Engine (Case Study: Wanggu Watershed). *International Journal of Remote Sensing and Earth Sciences (IJReSES)*, 19(2), 197–210. https://ejournal.brin.go.id/ijreses/article/view/13716

Badan Pusat Statistik. (2025a). *Penduduk, Laju Pertumbuhan Penduduk, Distribusi Persentase Penduduk, Kepadatan Penduduk, Rasio Jenis Kelamin Penduduk Menurut Provinsi, 2025*. Badan Pusat Statistik. https://www.bps.go.id/id/statistics-table/3/V1ZSbFRUY3lTbFpEYTNsVWNGcDZjek53YkhsNFFUMDkjMyMwMDAw/jumlah-penduduk--laju-pertumbuhan-penduduk--distribusi-persentase-penduduk--kepadatan-penduduk--rasio-jenis-kelamin-penduduk-menurut-provinsi.html?year=2025

Badan Pusat Statistik. (2025b). *Luas Kawasan Hutan dan Konservasi Perairan Menurut Kabupaten/Kota (ha) di Provinsi Sulawesi Tenggara, 2023*. Badan Pusat Statistik. https://sultra.bps.go.id/id/statistics-table/1/NDY4MyMx/luas-kawasan-hutan-dan-konservasi-perairan1-menurut-kabupaten-kota-ha-di-provinsi-sulawesi-tenggara-2023.html

Berenschot, W., & Dhiaulhaq, A. (2025). The production of rightlessness: palm oil companies and land dispossession in Indonesia. *Globalizations*, 22(8), 1377–1395. https://doi.org/10.1080/14747731.2023.2253657

Bose, P. (2023). Equitable land-use policy? Indigenous peoples' resistance to mining-induced deforestation. *Land Use Policy*, 129, 106648. https://doi.org/10.1016/j.landusepol.2023.106648

Choi, W.-I., Kim, E.-S., Yun, S.-J., Lim, J.-H., & Kim, Y.-E. (2021). Quantification of One-Year Gypsy Moth Defoliation Extent in Wonju, Korea, Using Landsat Satellite Images. *Forests,* 12(5), 545. https://doi.org/10.3390/f12050545

D'Alisa, G., & Demaria, F. (2024). Accumulation by contamination: Worldwide cost-shifting strategies of capital in waste management. *World Development*, 184, 106725. https://doi.org/10.1016/j.worlddev.2024.106725

de Souza, J. C., Mendes, T. S. G., Bignotto, R. B., de Alcântara, E. H., & Massi, K. G. (2025). Land use dynamics in a tropical protected area buffer zone: is the management plan helping? *Journal of Environmental Studies and Sciences*, 15(1), 156–166. https://doi.org/10.1007/s13412-024-00905-5

Demarquet, Q., Rapinel, S., Dufour, S., & Hubert-Moy, L. (2023). Long-Term Wetland Monitoring Using the

© 2026 Dept. of Geophysics Hasanuddin University

Landsat Archive: A Review. *Remote Sensing*, 15(3), 820. https://doi.org/10.3390/rs15030820

Donatien, L. M. B., Clobite, B. B., & Midel, M. L. M. (2024). Land-use/land-cover change detection using multi-temporal Landsat imagery in the North of the Congo Republic: a case study in the Sangha region. *Geocarto International*, 39(1), 2425184. https://doi.org/10.1080/10106049.2024.2425184

Dragomir, L. O., Popescu, C. A., Herbei, M. V., Popescu, G., Herbei, R. C., Salagean, T., Bruma, S., Sabou, C., & Sestras, P. (2025). Enhancing Conventional Land Surveying for Cadastral Documentation in Romania with UAV Photogrammetry and SLAM. *Remote Sensing*, 17(13), 2113. https://doi.org/10.3390/rs17132113

Escobar-López, A., Castillo-Santiago, M. Á., Mas, J. F., Hernández-Stefanoni, J. L. H., & López-Martínez, J. O. (2024). Identification of coffee agroforestry systems using remote sensing data: a review of methods and sensor data. *Geocarto International*, 39(1), 2297555. https://doi.org/10.1080/10106049.2023.2297555

Foody, G. M. (2024). Ground Truth in Classification Accuracy Assessment: Myth and Reality. *Geomatics,* 4(1), 81–90. https://doi.org/10.3390/geomatics4010005

Gaveau, D. L. A., Santos, L., Locatelli, B., Salim, M. A., Husnayaen, H., Meijaard, E., Heatubun, C., & Sheil, D. (2021). Forest loss in Indonesian New Guinea (2001–2019): Trends, drivers and outlook. *Biological Conservation*, 261, 109225. https://doi.org/10.1016/j.biocon.2021.109225

Giljum, S., Maus, V., Kuschnig, N., Luckeneder, S., Tost, M., Sonter, L. J., & Bebbington, A. J. (2022). A pantropical assessment of deforestation caused by industrial mining. *Proceedings of the National Academy of Sciences*, 119(38), e2118273119. https://doi.org/10.1073/pnas.2118273119

Gunawan, H., Mulyanto, B., Suharti, S., Subarudi, S., Ekawati, S., Karlina, E., Pratiwi, P., Yeny, I., Nurlia, A., Effendi, R., Widarti, A., Martin, E., Kalima, T., Desmiwati, D., Takandjandji, M., Heriyanto, N. M., Garsetiasih, R., Sawitri, R., Rianti, A., Kwatrina, R. T., Sihombing, V. S., Fahmi, S., & Marsandi, F. (2024). Forest land redistribution and its relevance to biodiversity conservation and climate change issues in Indonesia. *Forest Science and Technology*, 20(2), 213–228. https://doi.org/10.1080/21580103.2024.2347902

Hansen, M. C., Potapov, P. V., Moore, R., Hancher, M., Turubanova, S. A., Tyukavina, A., Thau, D., Stehman, S. V., Goetz, S. J., Loveland, T. R., Kommareddy, A., Egorov, A., Chini, L., Justice, C. O., & Townshend, J. R. G. (2013). High-Resolution Global Maps of 21st-Century Forest Cover Change. *Science*, 342(6160), 850–853. https://doi.org/10.1126/science.1244693

Jiang, H., Wang, S., Cao, X., Yang, C., Zhang, Z., & Wang, X. (2019). A shadow-eliminated vegetation index (SEVI) for removal of self and cast shadow effects on vegetation in rugged terrains. *International Journal of Digital Earth,* 12(9), 1013–1029. https://doi.org/10.1080/17538947.2018.1495770

Li, J., Bhatti, U. A., Nawaz, S. A., Huang, M., Ahmad, R. M., & Ghadi, Y. Y. (2024). Remote-Sensing Image Classification: A Comprehensive Review and Applications. In *Deep Learning for Multimedia Processing Applications* (1st Ed., p. 30). CRC

© 2026 Dept. of Geophysics Hasanuddin University

Press. https://doi.org/10.1201/9781032646268-2

Lo, M. G. Y., Morgans, C. L., Santika, T., Mumbunan, S., Winarni, N., Supriatna, J., Voigt, M., Davies, Z. G., & Struebig, M. J. (2024). Nickel mining reduced forest cover in Indonesia but had mixed outcomes for well-being. *One Earth*, 7(11), 2019–2033. https://doi.org/10.1016/j.oneear.2024.10.010

Nguyen, A., Kovyazin, V., & Pham, C. (2025). Application of Remote Sensing and GIS in Monitoring Forest Cover Changes in Vietnam Based on Natural Zoning. *Land*, 14(5), 1037. https://doi.org/10.3390/land14051037

Oo, T. Z., Humphries, U. W., & Mone, M. K. (2026). Remote sensing–derived land use land cover for hydrological modelling of flood hydrographs in the Mun River Basin, Thailand. *Geocarto International*, 41(1), 2620189. https://doi.org/10.1080/10106049.2026.2620189

Ordway, E. M., Asner, G. P., & Lambin, E. F. (2017). Deforestation risk due to commodity crop expansion in sub-Saharan Africa. *Environmental Research Letters*, 12(4), 044015. https://doi.org/10.1088/1748-9326/aa6509

Pain, A., Marquardt, K., Lindh, A., & Hasselquist, N. J. (2021). What is secondary about secondary tropical forest? Rethinking forest landscapes. *Human Ecology,* 49(3), 239–247. https://doi.org/10.1007/s10745-020-00203-y

Piragnolo, M., Pirotti, F., Zanrosso, C., Lingua, E., & Grigolato, S. (2021). Responding to Large-Scale Forest Damage in an Alpine Environment with Remote Sensing, Machine Learning, and Web-GIS. *Remote Sensing,* 13(8), 1541. https://doi.org/10.3390/rs13081541

Rakatama, A., & Pandit, R. (2020). Reviewing social forestry schemes in Indonesia: Opportunities and challenges. *Forest policy and economics*, 111, 102052. https://doi.org/10.1016/j.forpol.2019.102052

Rawat, P., Bagri, D. S., & Kumar, S. (2026). Decadal assessment and future prediction of land use land cover changes in the Upper Yamuna basin using CA-ANN modeling. *Discover Geoscience*, 4(1), 47. https://doi.org/10.1007/s44288-026-00426-4

Santoro, A., Piras, F., & Yu, Q. (2025). Spatial analysis of deforestation in Indonesia in the period 1950–2017 and the role of protected areas. *Biodiversity and Conservation*, 34(9), 3119–3145. https://doi.org/10.1007/s10531-023-02679-8

Schultz, M., Shapiro, A., Clevers, J. G. P. W., Beech, C., & Herold, M. (2018). Forest Cover and Vegetation Degradation Detection in the Kavango Zambezi Transfrontier Conservation Area Using BFAST Monitor. *Remote Sensing,* 10(11), 1850. https://doi.org/10.3390/rs10111850

Shimizu, K., Ota, T., & Mizoue, N. (2019). Detecting Forest Changes Using Dense Landsat 8 and Sentinel-1 Time Series Data in Tropical Seasonal Forests. *Remote Sensing*, 11(16), 1899. https://doi.org/10.3390/rs11161899

Singh, R., Pal, M., & Biswas, M. (2025). Cloud Detection Methods for Optical Satellite Imagery: A Comprehensive Review. *Geomatics*, 5(3), 27. https://doi.org/10.3390/geomatics5030027

Supriatna, J., Shekelle, M., Fuad, H. A. H., Winarni, N. L., Dwiyahreni, A. A., Farid, M., Mariati, S., Margules, C., Prakoso, B., & Zakaria, Z. (2020). Deforestation on the Indonesian island of Sulawesi and the loss of primate habitat. *Global Ecology and*

© 2026 Dept. of Geophysics Hasanuddin University

Conservation, 24, e01205. https://doi.org/10.1016/j.gecco.2020.e01205

Tariq, A., Jiango, Y., Li, Q., Gao, J., Lu, L., Soufan, W., Almutairi, K. F., & Habib-ur-Rahman, M. (2023). Modelling, mapping and monitoring of forest cover changes, using support vector machine, kernel logistic regression and naive bayes tree models with optical remote sensing data. *Heliyon*, 9(2), e13212. https://doi.org/10.1016/j.heliyon.2023.e13212

Wulder, M. A., Roy, D. P., Radeloff, V. C., Loveland, T. R., Anderson, M. C., Johnson, D. M., Healey, S., Zhu, Z., Scambos, T. A., Pahlevan, N., Hansen, M., Gorelick, N., Crawford, C. J., Masek, J. G., Hermosilla, T., White, J. C., Belward, A. S., Schaaf, C., Woodcock, C. E., Huntington, J. L., Lymburner, L., Hostert, P., Gao, F., Lyapustin, A., Pekel, J.-F., Strobl, P., & Cook, B. D. (2022). Fifty years of Landsat science and impacts. *Remote Sensing of Environment*, 280, 113195. https://doi.org/10.1016/j.rse.2022.113195

© 2026 Dept. of Geophysics Hasanuddin University

ISSN: 2579-5821 (Print)
ISSN: 2579-5546 (Online)
URL address: http://journal.unhas.ac.id/index.php/geocelebes
DOI: 10.70561/geocelebes.v10i2.50394

Jurnal Geocelebes Vol. 10 No. 2, October 2026, 258 – 268

Calcareous Nannofossils from Bojongsana River, Purbalingga Regency: Implication for Identifying the Age of Tapak Formation

Akmaluddin[1], Efrilia Mahdilah Nurhidayah[2]*

[1]Department of Geological Engineering, Faculty of Engineering, Universitas Gadjah Mada, Jl. Grafika No. 2, Yogyakarta 55281, Indonesia.
[2]Department of Geological Engineering, Faculty of Engineering, Jenderal Soedirman University, Jl. Raya Mayjen Sungkono No.KM 5, Purbalingga, Jawa Tengah 53371, Indonesia

*Corresponding author. Email: efrilia.nurhidayah@unsoed.ac.id

Manuscript received: 27 March 2026; Received in revised form: 19 June 2026; Accepted: 14 July 2026

Abstract

Calcareous nannofossils are widely used in Cenozoic biostratigraphy due to their rapid evolution and wide geographic distribution. Their biostratigraphic significance provides a useful basis for resolving age uncertainties in sedimentary successions. In this context, the lower Tapak Formation exposed along the Bojongsana River section in the Banyumas Basin, Central Java, represents an important stratigraphic unit whose depositional age remains poorly constrained. This study aims to determine the depositional age of the lower Tapak Formation using calcareous nannofossil biostratigraphy. A 61 m-thick stratigraphic section was systematically measured, and 24 samples were collected at 2–5 m intervals for analysis. The nannofossil assemblages showed moderate to good preservation, with abundances ranging from rare to abundant. A total of 24 nannofossil species from 10 genera were identified. Biostratigraphic analysis revealed two partial distribution zones: the *Discoaster berggrenii* Zone (CNM17) and the *Nicklithus amplificus* Zone (CNM18), indicating a Late Miocene age (equivalent to zone NN11). The First Occurrence (FO) of *Nicklithus amplificus* was used to define the lower boundary of the CNM18 zone, whereas the upper boundary could not be determined because no additional biodatum or bioevent was recorded in the upper part of the section. Reworked taxa indicate sediment input from older Middle Miocene units but do not affect age interpretation. This finding demonstrates that the lower Tapak Formation in the Bojongsana River section represents a Late Miocene interval. Stratigraphically constrained biostratigraphic data are therefore essential for refining the regional chronostratigraphic framework of the Banyumas Basin.

Keywords: Banyumas Basin; Late Miocene; Nannofossils; Tapak Formation.

Citation: Akmaluddin, A., & Nurhidayah, E. M. (2026). Calcareous Nannofossils from Bojongsana River, Purbalingga Regency: Implication for Identifying the Age of Tapak Formation. *Jurnal Geocelebes*, 10(2): 258–268, doi: 10.70561/geocelebes.v10i2.50394

Introduction

Calcareous nannofossils are a group of unicellular marine phytoplankton that are highly abundant and widely distributed, both in the geological past and in modern oceans (Balch, 2018; Gastaldello et al., 2023; Karatsolis et al., 2026), and their application has also been widely implemented in various sedimentary basins in Indonesia (Rendy et al., 2021; Supardi & Rahmawati, 2022; Ratumanan et al., 2023; Nurhidayah et al., 2024; Choiriah et al., 2025). Calcareous nannofossils represent the principal microfossil groups used in Cenozoic marine biostratigraphic studies (Agnini et al., 2014; 2017; Puentes-Jorge et al., 2025). These characteristics make them particularly useful for improving the resolution and consistency of stratigraphic interpretation (Raffi & Backman, 2022).

The Banyumas Basin, located in Central Java, is considered a Neogene sedimentary basin with hydrocarbon potential and records complex interactions between

© 2026 Dept. of Geophysics Hasanuddin University

tectonics, sedimentation, and sea-level changes (Purwasatriya et al., 2019; Permana et al., 2024). One of its key stratigraphic units, the Tapak Formation, has been widely studied, including its potential as a hydrocarbon reservoir (Rizal et al., 2018; Tampubolon & Rizal, 2019). The Tapak Formation is generally characterised by clastic marine deposits, including interbedded coarse sandstone and marl, greenish sand, conglomerate and andesitic breccia (Tampubolon & Rizal, 2019). Establishing a reliable depositional age for this formation is therefore essential for refining its stratigraphic position and improving regional correlations within the basin.

Previous studies have attempted to constrain the age of the Tapak Formation using planktonic and benthic foraminifera, suggesting an Early to Late Pliocene age, corresponding to zones N18–N21 (Novandaru et al., 2025). Meanwhile, calcareous nannofossil studies from other parts of the basin indicate an Early Pliocene age based on zones NN14–NN15 (Dwijaya et al., 2021). Although these studies provide valuable biostratigraphic information, calcareous nannofossil data from the lower Tapak Formation in the Bojongsana River section remain limited. Given this limitation, calcareous nannofossil analysis from a systematically measured stratigraphic section is needed to provide additional biostratigraphic evidence for the lower Tapak Formation and to refine the Neogene chronostratigraphic framework of the Banyumas Basin (Wolfgring et al., 2026).

In the Bojongsana River section, which represents the outcrop marine sediment of the lower Tapak Formation (Djuri et al., 1996) (Figure 1), the depositional age has not yet been evaluated using a stratigraphically constrained nannofossil approach.

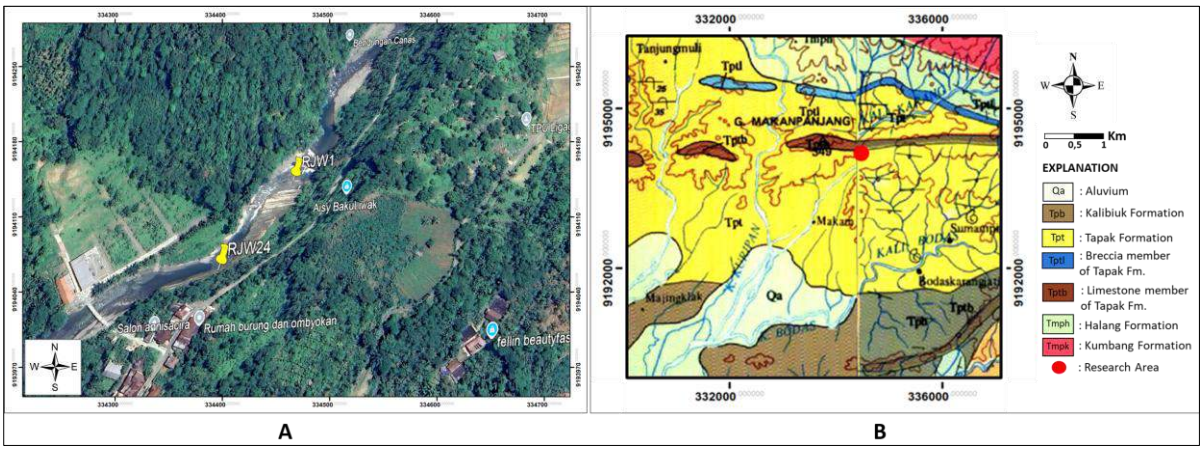


Figure 1. Location of the research area along the Bojongsana River, Purbalingga Regency, Central Java. (A) Google Earth satellite image (2026) showing the measured stratigraphic section and sampling points. (B) Regional geological map of the Purwokerto–Tegal (Djuri et al., 1996) sheets, with the research area marked by a red dot within the Tapak Formation.

To address this issue, this study applies calcareous nannofossil biostratigraphy to a systematically measured stratigraphic section in the Bojongsana River area. This study aims to establish the depositional age of the lower Tapak Formation and to provide a more consistent age interpretation by integrating nannofossil data within a well-constrained stratigraphic framework. The results are expected to improve the chronostratigraphic framework of the Tapak Formation and contribute to a better understanding of basin evolution in the Banyumas Basin.

Regional Geology

Physiographically, the Banyumas Basin is subdivided into the South Serayu and North Serayu Zones (Husein et al., 2013). The tectonic framework of the region was

© 2026 Dept. of Geophysics Hasanuddin University

established by Cenozoic subduction along the southern margin of Java. This tectonic evolution also controlled the present basin architecture, in which the Banyumas Basin is subdivided into the Majenang and Citanduy sub-basins, separated by the Cipari Anticline (Hidayat et al., 2020), and is characterised by northwest–southeast strike-slip faults and east–west basement highs (Setiadi, 2017).

Stratigraphically, the Banyumas Basin in the North Serayu Zone begins with the Rambatan Formation (Figure 2). The Rambatan Formation was deposited during the N13–N19 interval in a deep-marine setting (Astuti et al., 2019). Above it, the Halang Formation, deposited in the Late Miocene to Early Pliocene (Adam et al., 2025), is composed primarily of marl and turbiditic sandstone (Purwasatriya et al., 2021). The Tapak Formation, deposited during the Pliocene (Djuri et al., 1996). This unit comprises calcareous sandstone, calcarenite, and marl, with abundant shallow-marine fossils. Stratigraphically, the Tapak Formation lies conformably above the Halang Formation and reflects a shift in depositional environment toward shallower (Rohmana et al., 2019).

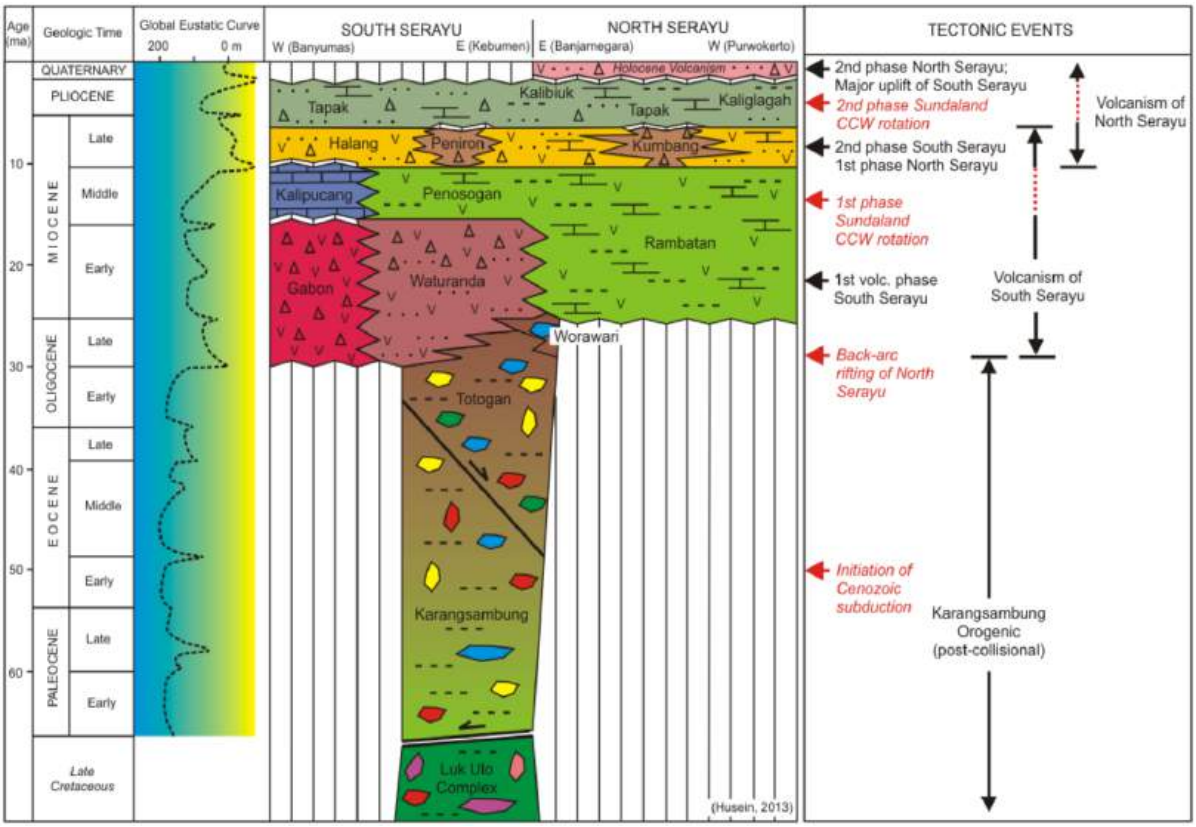


Figure 2. Cenozoic tectonostratigraphy of the Serayu Zone (Husein et al., 2013).

Materials and Methods

Data collection was conducted using stratigraphic measurements and systematic rock sampling. In this study, a 61 m thick stratigraphic section was measured in the Bojongsana River area, Purbalingga Regency, Central Java. A total of 24 samples were collected at 2–5 m intervals for calcareous nannofossil analysis (Figure 3).

Calcareous nannofossil slide preparation was conducted using the drop technique, producing smear slides suitable for microscopic examination. This modification allowed an even distribution of sediment on the coverslip without additional dilution steps.

© 2026 Dept. of Geophysics Hasanuddin University



Figure 3. Outcrop of the Tapak Formation exposed along the Bojongsana River, Purbalingga Regency, Central Java Province. Numbers 1–4 indicate representative nannofossil sampling points.

Species abundance was assessed semi-quantitatively following, using the following categories: A (abundant; >10 specimens per field of view), C (common; 2–10 specimens per field of view), F (few; 1 specimen per 1–5 fields of view), R (rare; 1 specimen per 6–10 fields of view), and VR (very rare; 1 specimen in >10 fields of view). Nannofossil identification was performed based on morphological criteria compiled in Nannotax3 (Young et al., 2023). Biostratigraphic zonation follows the standard scheme of Agnini et al. (2014) and is correlated with previous zonations by Okada & Bukry (1980) and Martini (1971). The First Occurrence (FO) and Last Occurrence (LO) of marker nannofossil species also follow the latest geochronological framework (Agnini et al., 2017; Blair et al., 2017).

Results

Diversity and Systematic Taxonomy of Nannofossils

Nannofossil analysis of 24 samples indicates moderate to good preservation, with abundances ranging from rare to abundant. The nannofossils identified in the study area generally exhibit good preservation. Biodatum ages were determined using several established references, and detailed analysis identified 24 species across 10 genera. The taxonomic identification and nomenclature of all calcareous nannofossil species follow the Nannotax database (Young et al., 2023). A taxonomic summary of the identified species is presented in Table 1, and selected species from the Bojongsana River area are presented in Figure 4.

Table 1. Resume of the taxonomic ranks of calcareous nannofossil in research area.

Group	Order	Family	Genus	Species
Heterococcoliths	Coccolithales	Coccolithaceae	*Coccolithus*	*Coccolithus pelagicus*
		Calcidiscaceae	*Calcidiscus*	*Calcidiscus leptoporus*
			Umbilicosphaera	*Umbilicosphaera jafari*
				Umbilicosphaera rotula
	Isochrysidales	Noelaerhabdaceae	*Cyclicargolithus*	*Cyclicargolithus floridanus*
			Reticulofenestra	*Reticulofenestra haqii* (
				Reticulofenestra pseudoumbilicus
				Reticulofenestra rotaria
	Zygodiscales	Helicosphaeraceae	*Helicosphaera*	*Helicosphaera carteri*
				Helicosphaera princei
		Pontosphaeraceae	*Pontosphaera*	*Pontosphaera discopora*
Nannoliths	Discoasterales	Ceratolithaceae	Amaurolithus	*Nicklithus amplificus*
		Discoastersceae	*Discoaster*	*Discoaster deflandrei*
				Discoaster berggrenii
				Discoaster brouweri
				Discoaster calcaris
				Discoaster neorectus
				Discoaster pentaradiatus
				Discoaster musicus
				Discoaster quinqueramus
				Discoaster variabilis
		Sphenolithaceae	*Sphenolithus*	*Sphenolithus abies*
				Sphenolithus moriformis
				Sphenolithus neoabies

© 2026 Dept. of Geophysics Hasanuddin University

Biostratigraphy

Based on measured stratigraphic sections, the Tapak Formation outcrops show vertical lithological variations. The lower part consists mainly of thick, light grey, coarse-grained sandstone with parallel bedding. Towards the upper part of the section, the lithology becomes predominantly interbedded calcareous mudstone and sandstone (Figure 5).

A total of 24 nannofossil species were successfully identified (Figure 3 & 6), including several biostratigraphically significant taxa as biodatum, namely *Discoaster berggrenii* and *Nicklithus amplificus*. Based on the first and last occurrences of these taxa (Figure 3 & 5), the studied interval is subdivided into two biozones, arranged from oldest to youngest as follows:

1. *Discoaster berggrenii* Partial Range Zone (CNM17 zone)

The *Discoaster berggrenii* Zone (CNM17) is defined as a partial range zone marked by the first occurrence (FO) of *Nicklithus amplificus* in the upper part of the interval (sample RJW 18), while its lower boundary could not be determined because no diagnostic bioevent was recorded at the base of the studied interval.

This zone is assigned to the CNM17 zone of Agnini et al. (2014) and is broadly correlated with Zone NN11 of Martini (1971) and Zones CN9b of Okada & Bukry (1980). Chronostratigraphically, the interval is interpreted as Late Miocene in age and is recorded within the 0–50 m stratigraphic interval.

In addition, the occurrence of *Cyclicargolithus floridanus* within this interval is interpreted as a reworked fossil derived from Middle Miocene or older deposits. Therefore, this taxon is not used as an indicator of the depositional age of the lower Tapak Formation, but is interpreted as evidence of sediment input or erosion from older stratigraphic units exposed in the source area.

2. *Nicklithus amplificus Partial Range Zone (CNM18 zone or younger)*

The *Nicklithus amplificus* Zone (CNM18 zone or younger) is a partial range zone. The base of the *Nicklithus amplificus* Zone is defined by the First Occurrence (FO) of *Nicklithus amplificus* in sample RJW 18, recorded at the 51 m stratigraphic interval. However, the upper boundary of this zone could not be determined because no additional biodatum or bioevent was recorded in the upper part of the studied section. Therefore, the interval from 51 to 60.5 m is tentatively assigned to CNM18 of Agnini et al. (2014), or possibly younger.

This interval is broadly comparable to the upper part of NN11 of Martini (1971) and approximately to CN9b of Okada & Bukry (1980). Chronostratigraphically, the occurrence of N. amplificus supports a Late Miocene age interpretation. The occurrences of *Discoaster deflandrei* and *Discoaster musicus* are interpreted as reworked material from older Middle Miocene to Late Miocene deposits and are therefore not used as primary indicators of depositional age.

Discussion

Biostratigraphic analysis of calcareous nannofossils from the lower Tapak Formation indicates a Late Miocene age for the studied section. This interpretation is supported not only by the recognition of the *Discoaster berggrenii* Zone (CNM17) and the *Nicklithus amplificus* Zone (CNM18) or younger of Agnini et al. (2014), which broadly correlate with the NN11 Zone of Martini (1971) and the CN9b interval of Okada & Bukry (1980), but also by the occurrence of other Late Miocene nannofossil taxa. These taxa include *Discoaster quinqueramus*, *Discoaster calcaris*, *Reticulofenestra rotaria*, and *Discoaster neorectus*, which provide additional biostratigraphic support for the

© 2026 Dept. of Geophysics Hasanuddin University

Late Miocene age interpretation. Although several reworked taxa were recorded, they are interpreted as derived from older stratigraphic units and do not affect the Late Miocene age interpretation of the studied interval.

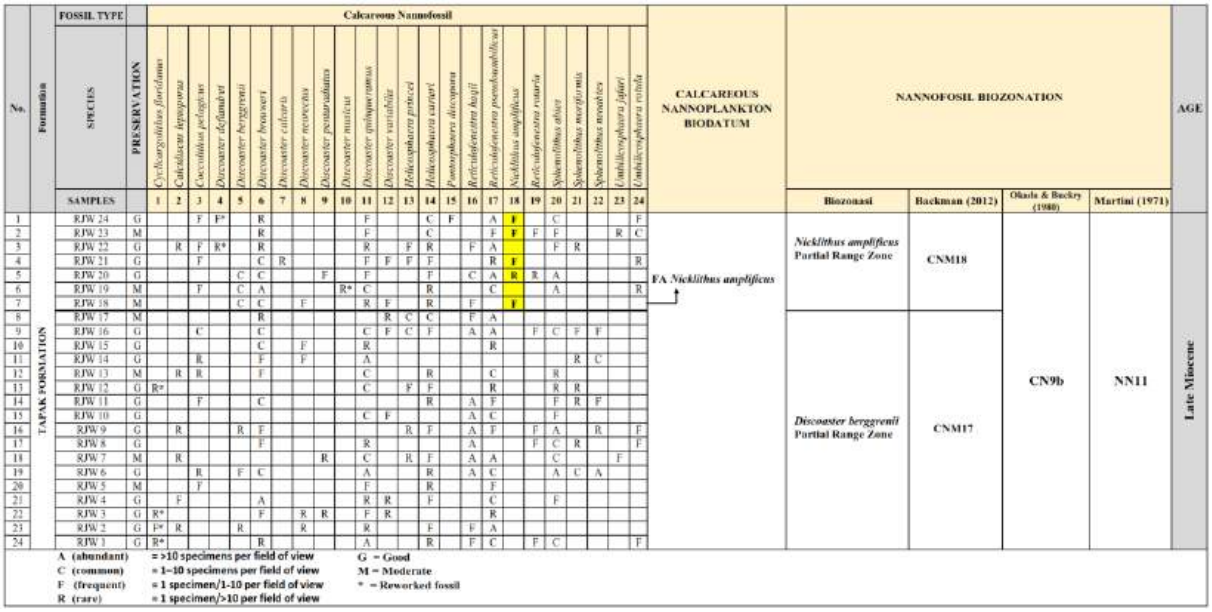


Figure 4. Distribution chart of calcareous nannofossil in the Bojongsana River area.

The Late Miocene age obtained in this study provides a more detailed nannofossil-based constraint for the lower Tapak Formation in the Bojongsana River section. Previous foraminiferal data from the lower Tapak Formation suggested an Early Pliocene to Late Pliocene age corresponding to zones N18–N21 (Novandaru et al., 2025), whereas nannofossil data from other parts of the Banyumas Basin indicated an Early Pliocene age based on zones NN14–NN15 (Dwijaya et al., 2021). This difference is likely due to differences in sampling locations and stratigraphic positions. Compared with the regional geological framework of Djuri et al. (1996), in which the Tapak Formation was generally assigned to the Pliocene, the Late Miocene age obtained in this study suggests that the lower part of the formation may be older than previously generalised. This difference may reflect the broader scale of regional mapping compared with the higher-resolution biostratigraphic data from the measured section.

Overall, the lower Tapak Formation in the Bojongsana River section is interpreted to have been deposited during the Late Miocene, while younger Pliocene ages reported from other sections may represent higher stratigraphic levels within the formation.

Conclusion

Based on calcareous nannofossil analysis, the Tapak Formation within the studied interval contains 24 species, with abundances ranging from rare to abundant, indicating deposition in an open-marine setting with favourable preservation conditions. Biostratigraphic evaluation establishes the *Discoaster berggrenii* zone (CNM17) and *Nicklithus amplificus* zone (CNM18), indicating a Late Miocene age. The boundary between these zones is defined by the First Occurrence (FO) of *Nicklithus amplificus*, which serves as a reliable datum for regional stratigraphic correlation.

Acknowledgements

© 2026 Dept. of Geophysics Hasanuddin University

The authors gratefully acknowledge the Department of Geological Engineering, Faculty of Engineering, Universitas Gadjah Mada, for providing financial support for this research in FY 2025. The authors also gratefully acknowledge Muhammad Rafly Siregar for his valuable assistance with the preparation of calcareous nannofossil samples at the Paleontology Laboratory, Universitas Gadjah Mada.

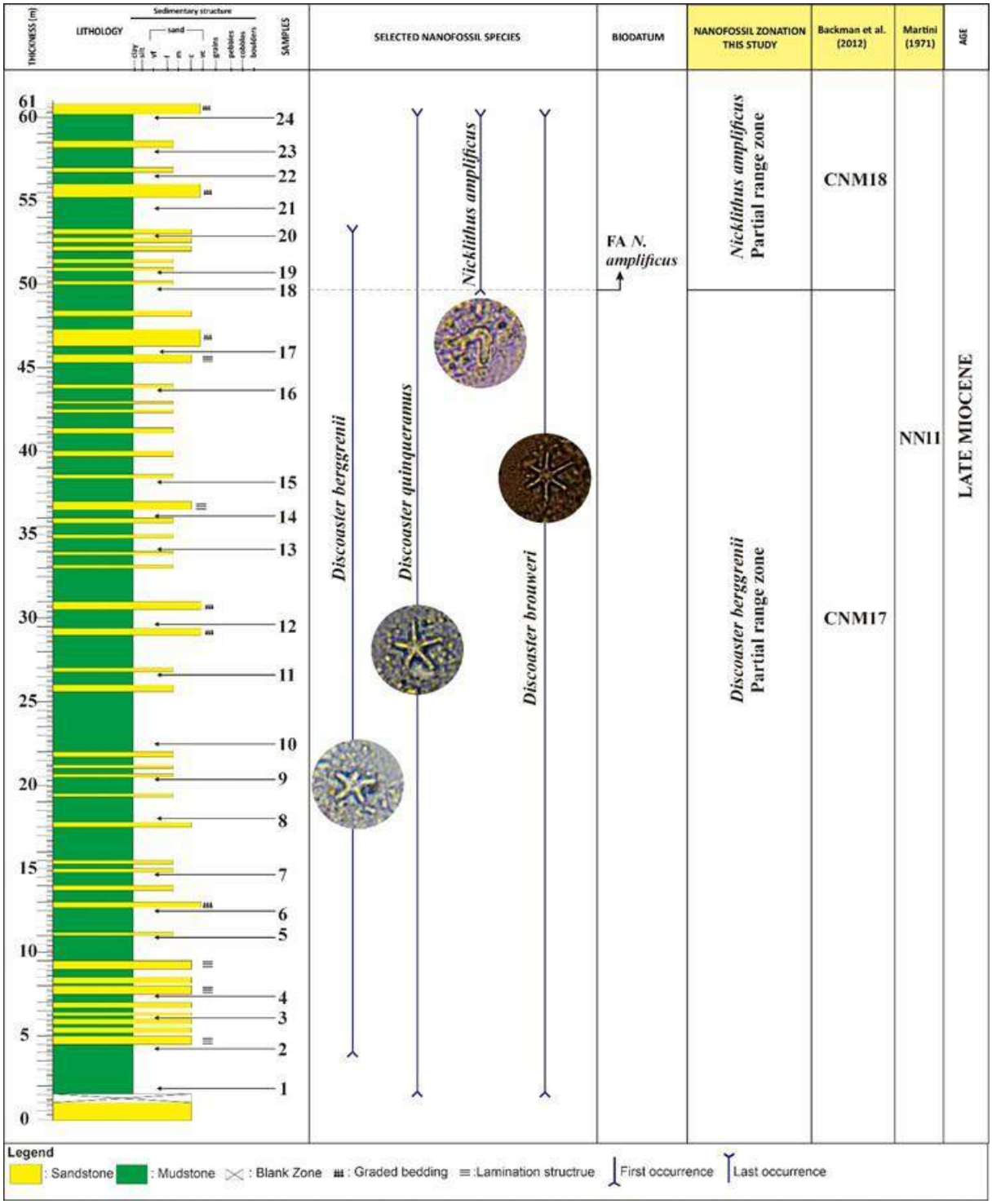


Figure 5. Stratigraphic column and biostratigraphic zones of the research area in the Bojongsana River area, Purbalingga.

© 2026 Dept. of Geophysics Hasanuddin University

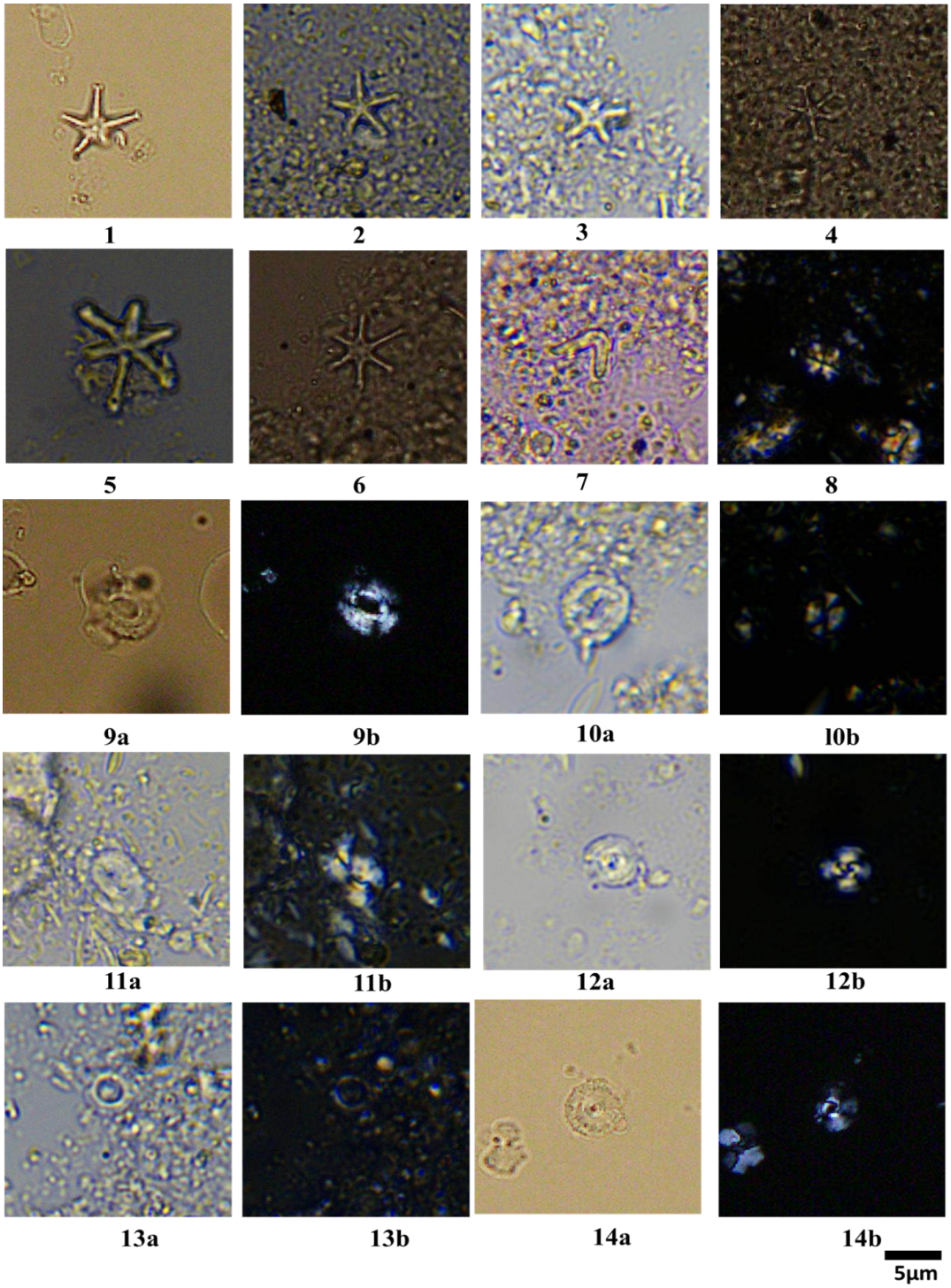


Figure 6. Selected image of a nannofossil species in this research. PPL view (a) and XPL view (b). (1) *Discoaster pentaradiatus* (sample RJW7), (2) *Discoaster quinqueramus* (sample RJW16), (3) *Discoaster bergrenii* (sample RJW2), (4) *Discoaster variabilis* (sample RJW18), (5) *Discoaster neorectus* (sample RJW18), (6) *Discoaster brouweri* (sample RJW18), (7) *Nicklithus amplificus* (sample RJW18), (8) *Sphenolithus moriformis* (sample RJW24), (9) *Reticulofenestra pseudoumbilicus* (sample RJW12), (10) *Coccolithus pelagicus* (sample RJW14), (11) *Helicosphaera carteri* (sample RJW20), (12) *Cyclicargolithus floridanus* (sample RJW3), (13) *Umbilicosphaera rotula* (sample RJW23), (14) *Calcidiscus leptoporus* (sample RJW4)

Author Contribution

Akmaluddin was responsible for conceptualization, methodology, investigation, data curation, supervision, and contribution to the original draft, review, and editing of the manuscript. Efrilia Mahdilah Nurhidayah contributed to

© 2026 Dept. of Geophysics Hasanuddin University

methodology and investigation, performed the formal analysis, prepared the visualizations, and contributed to the original draft, review, and editing of the manuscript.

Conflict of Interest

All authors state that they have no financial or personal interests that may have affected the outcomes of this research.

References

Adam, I., Saadjad, A., Isliko, R., & Umagapi, R. (2025). Reconstruction of Geological History Based on Stratigraphic Analysis in the Gombong Region, North Serayu Basin. *Jurnal Geologi Dan Sumberdaya Mineral*, 26(1), 29–37. https://doi.org/10.33332/jgsm.geologi.v26i1.922

Agnini, C., Fornaciari, E., Raffi, I., Catanzariti, R., Pälike, H., Backman, J., & Rio, D. (2014). Biozonation and biochronology of Paleogene calcareous nannofossils from low and middle latitudes. *Newsletters on Stratigraphy*, 47(2), 131–181. https://doi.org/10.1127/0078-0421/2014/0042

Agnini, C., Monechi, S., & Raffi, I. (2017). Calcareous nannofossil biostratigraphy: historical background and application in Cenozoic chronostratigraphy. *Lethaia*, 50(3), 447–463. https://doi.org/10.1111/let.12218

Astuti, B. S., Isnaniawardhani, V., Abdurrokhim, A., & Sudradjat, A. (2019). Sedimentation Process of Rambatan Formation in Larangan Brebes, North Serayu Range, Central Java. *Indonesian Journal on Geoscience*, 6(2), 141–151. https://doi.org/10.17014/ijog.6.2.141-151

Balch, W. M. (2018). The Ecology, Biogeochemistry, and Optical Properties of Coccolithophores. *Annual Review of Marine Science*, 10, 71–98. https://doi.org/10.1146/annurev-marine-121916-063319

Blair, S., Bergen, J. A., de Kaenel, E., Browning, E., & Boesiger, T. M. (2017). Upper Miocene-Lower Pliocene taxonomy and stratigraphy in the circum North Atlantic Basin: radiation and extinction of Amauroliths, Ceratoliths and the D. quinqueramus lineage. *Journal of Nannoplankton Research*, 37(2-3), 113–144. https://doi.org/10.58998/jnr2018

Choiriah, S. U., Yudiantoro, D. F., & Kapid, R. (2025). Nannofossil Diversity and Climate Change of Rembang Zone, North East Java Basin. *International Journal on Advanced Science, Engineering and Information Technology*, 15(1), 215–222. https://doi.org/10.18517/ijaseit.15.1.20103

Djuri, M., Samodra, H., Amin, T. C., & Gafoer, S. (1996). *Peta Geologi Lembar Purwokerto dan Tegal*. Pusat Survei Geologi. https://geologi.esdm.go.id/geomap//pages/preview/peta-geologi-lembar-tuban-jawa

Dwijaya, B. A., Prabowo, R. E., Waluyo, G., Prayitno, I., & Ramdhani, A. (2021). Paleoproduktivitas Formasi Tapak Banyumas Berdasarkan Bukti Mikrofosil. *Syntax Idea*, 3(2), 246–262. https://doi.org/10.46799/syntax-idea.v3i2.1001

Gastaldello, M. E., Agnini, C., Westerhold, T., Drury, A. J., Sutherland, R., Drake, M. K., Lam, A. R., Dickens, G. R., Dallanave, E., Burns, S., & Alegret, L. (2023). The Late Miocene-Early Pliocene Biogenic Bloom: An Integrated Study in the Tasman Sea. *Paleoceanography and Paleoclimatology*, 38(4), e2022PA004565.

© 2026 Dept. of Geophysics Hasanuddin University

https://doi.org/10.1029/2022PA004565

Hidayat, H., Subagio, S., & Praromadani, Z. S. (2020). Interpretasi Struktur Geologi Bawah Permukaan Berdasarkan Updating Data Gaya Berat Cekungan Banyumas, Jawa Tengah. *Jurnal Geologi dan Sumberdaya Mineral*, 21(3), 111–118. https://doi.org/10.33332/jgsm.geologi.v21i3.524

Husein, S., Jyalita, J., & Nursecha, M. A. Q. (2013). Kendali Stratigrafi dan Struktur Gravitasi pada Rembesan Hidrokarbon Sijenggung, Cekungan Serayu Utara. *Prosiding Seminar Nasional Kebumian Ke-6,* Yogyakarta, 2013, 474–489. https://doi.org/10.13140/RG.2.1.4987.7200

Karatsolis, B.-T., Asanbe, J. D., & Henderiks, J. (2026). Coccolithophore signatures across the termination of the late Miocene to early Pliocene biogenic bloom in the Atlantic and Indian oceans. *Journal of Micropalaeontology*, 45(1), 475–486. https://doi.org/10.5194/jm-45-475-2026

Martini, E. (1971) Standard Tertiary and Quaternary Calcareous Nannoplankton Zonation. *Proceedings of the 2nd Planktonic Conference*, Roma, 1970, 739–785.

Novandaru, N., Maryunani, K. A., Ardi, R. D. W., & Nurhidayah, E. M. (2025). Biostratigrafi dan Analisis Paleobatimetri berdasarkan Kumpulan Foraminifera di Daerah Cirahab, Banyumas, Jawa Tengah. *Bulletin of Geology*, 9(1), 28–41. https://doi.org/10.5614/bull.geol.2025.9.1.3

Nurhidayah, E. M., Akmaluddin, A., Barianto, D. H., Husein, S., & Saripudin, A. (2024). Nannofossil Biostratigraphy from Banggai-Sula Basin, Central Sulawesi. *Journal of Tropical Biodiversity and Biotechnology*, 9(1), jtbb85308. https://doi.org/10.22146/jtbb.85308

Okada, H., & Bukry, D. (1980). Supplementary Modification and Introuction of Code Number to the Low-Latitude Coccolith Biostratigraphic Zonation (Bukry, 1973; 1975). *Marine Micropaleontology*. 5(3), 321–325. https://doi.org/10.1016/0377-8398(80)90016-X

Permana, A. K., Setiawan, R., Marjiyono, M., Junursyah, G. M. L., Hidayat, H., Yurnaldi, D., Patriani, E. Y., & Setiawan, A. (2024). Review of Geological Framework and Hydrocarbon Potential of the Banyumas Basin. *Jurnal Geologi Dan Sumberdaya Mineral*, 25(4), 249–257. https://doi.org/10.33332/jgsm.geologi.v25i4.872

Puentes-Jorge, X., Del Gaudio, A. V., Piller, W. E., De Vleeschouwer, D., Lyu, J., Hechemer, T., & Auer, G. (2025). Middle to Late Miocene integrated biostratigraphy and biozonation for the mid-latitude Indian Ocean (ODP Site 752). *Newsletters on Stratigraphy*, 58(3), 343–371. https://doi.org/10.1127/nos/2025/0887

Purwasatriya, E. B., Surjono, S. S., & Amijaya, D. H. (2019). Sejarah Geologi Pembentukan Cekungan Banyumas Serta Implikasinya Terhadap Sistem Minyak dan Gas Bumi. *Jurnal Dinamika Rekayasa*, 15(1), 25–34. https://doi.org/10.20884/1.dr.2019.15.1.242

Purwasatriya, E. B., Gibran, A. K., Aditama, M. R., & Waluyo, G. (2021). Sedimentologi dan Tektonostratigrafi Formasi Halang di Cekungan Banyumas serta Potensinya untuk Reservoir Hidrokarbon. *Jurnal Geologi Dan Sumberdaya Mineral*, 22(3), 153–163. https://doi.org/10.33332/jgsm.geologi.v22i3.640

© 2026 Dept. of Geophysics Hasanuddin University

Raffi, I., & Backman, J. (2022). The role of calcareous nannofossils in building age models for Cenozoic marine sediments: a review. *Rendiconti Lincei. Scienze Fisiche e Naturali*, 33, 25–38. https://doi.org/10.1007/s12210-022-01048-x

Ratumanan, R. C. F., Isnaniawardhani, V., & Muljana, B. (2023). Middle Eocene Nannofossil Assemblages Responding to Depositional Dynamics of the Elat Formation, Maluku. *Jurnal Geocelebes*, 7(2), 138–153. https://doi.org/10.20956/geocelebes.v7i2.25371

Rendy, R., Suzuki, H., Chiyonobu, S., Sato, T., Syavitri, D., Widianto, E., Burhanudinnur, M., Putra, T. E., & Raguwanti, R. (2021). Cenozoic Basin History of the Cepu Area Based on Calcareous Nannofossil Biostratigraphy in Eastern Java, Indonesia. *International Journal on Advanced Science, Engineering and Information Technology*, 11(5), 2071–2081. https://doi.org/10.18517/ijaseit.11.5.14225

Rizal, Y., Santoso, W. D., Rudyawan, A., Tampubolon, R. A., & Nurfarhan, A. A. (2018). Sedimentary Facies and Hydrocarbon Reservoir Potential of Sand Flat in The Upper Part of Tapak Formation in Banyumas Area, Central Java. *RISET Geologi Dan Pertambangan*, 28(2), 251–263. https://doi.org/10.14203/risetgeotam2018.v28.835

Rohmana, R. C., Achmad, A., & Suyoto, S. (2019). Analisis Sedimentologi dan Stratigrafi untuk Rekonstruksi model Paleogeografi: Mengungkap Proses Pembentukan Formasi Tapak, Sub-Cekungan Banyumas. *Jurnal Geosains dan Teknologi*, 2(3), 126-134. https://doi.org/10.14710/jgt.2.3.2019.126-134

Setiadi, I. (2017). Basement Configuration and Delineation of Banyumas Subbasin based on Gravity Data Analysis. *Jurnal Geologi Dan Sumberdaya Mineral*, 18(2), 67–76. https://doi.org/10.33332/jgsm.geologi.v18i2.237

Supardi, N., & Rahmawati, S. A. (2022). Biostratigraphy of Limestone based on Large Foraminifera in the Donggala Region, Central Sulawesi. *Jurnal Geocelebes*, 6(1), 47–55. https://doi.org/10.20956/geocelebes.v6i1.19949

Tampubolon, R. A., & Rizal, Y. (2019). Sedimentary Facies of the Upper Part of Tapak Formation in Banyumas Area, Central Java. *Berita Sedimentologi*, *44*(1), 5–10. https://journal.iagi.or.id/index.php/FOSI/article/view/64

Wolfgring, E., Petrizzo, M. R., & Watkins, D. K. (2026). Albian integrated foraminiferal and calcareous nannofossil biostratigraphy in the southern high latitudes (IODP Site U1513, Indian Ocean) across OAE 1d, and correlation to low latitudes. *Cretaceous Research*, 184, 106355. https://doi.org/10.1016/j.cretres.2026.106355

Young, J. R., Bown, P. R., & Lees, J. A. (2023). *Nannotax3 Website*. https://www.mikrotax.org/Nannotax3/

© 2026 Dept. of Geophysics Hasanuddin University

ISSN: 2579-5821 (Print)
ISSN: 2579-5546 (Online)
URL address: http://journal.unhas.ac.id/index.php/geocelebes
DOI: 10.70561/geocelebes.v10i2.48409

Jurnal Geocelebes Vol. 10 No. 2, October 2026, 269 – 286

Tidal Wave Transformation in the Mahakam Delta: Integrating Observations and Machine Learning

Muhammad Riza*, Nanda Khoirunisa, Zetsaona Sihotang, Idris Mandang

[1]Department of Geophysics, Mulawarman University, Samarinda, 75123, Indonesia.

*Corresponding author. Email: Muhammad.riza@fmipa.unmul.ac.id

Manuscript received: 19 November 2025; Received in revised form: 30 June 2026; Accepted: 27 July 2026

Abstract

Tidal dynamics in tropical estuaries have made it difficult to predict water level variations and to understand the interaction between river discharge and ocean forcing. This study investigated tidal wave propagation, attenuation, and asymmetry in the Mahakam Delta, East Kalimantan, Indonesia. The objective was to quantify tidal wave transformation along the estuary-upstream transect and to evaluate the capability of machine learning to reproduce key hydrodynamic parameters. Water level time series with a 10-minute interval, collected from 12 July to 4 August 2018 at an estuary station and an upstream station, were analysed. A Random Forest regression model with temporal lag features predicted upstream water level with a coefficient of determination (R-squared) of 0.883 and a mean absolute error of 0.150 m; the most informative lag was 60 minutes. Analysis of 34 tidal cycles showed a mean attenuation coefficient of 0.76, indicating hyposynchronous conditions dominated by friction. A machine learning model for attenuation coefficient prediction reached an R-squared of 0.968 and a mean absolute error of 0.084, with estuary peak water level as the most influential predictor. The delta exhibited flood-dominant tidal asymmetry and negligible phase lag between estuary and upstream peaks. These findings demonstrated that the integration of data-driven modelling and hydrodynamic analysis can improve the prediction of water levels and support flood risk assessment in tropical deltaic systems.

Keywords: Deltaic Hydrodynamics; Hyposynchronous Estuary; Mahakam Delta; Random Forest Regression; Tidal Wave Propagation.

Citation: Riza, M., Khoirunisa, N., Sihotang, Z., & Mandang, I. (2026). Tidal Wave Transformation in the Mahakam Delta: Integrating Observations and Machine Learning. *Jurnal Geocelebes*, 10(2): 269–286, doi: 10.70561/geocelebes.v10i2.48409

Introduction

Tidal dynamics in tropical estuaries provide considerable obstacles for forecasting water level fluctuations and comprehending intricate hydrodynamic interactions. Efficient management of water resources, flood prediction, and coastal defense requires comprehension of the propagation, attenuation, and transformation of tidal waves as they move from estuaries to upstream river segments. The Mahakam Delta in East Kalimantan, Indonesia, illustrates these challenges as an extensive tropical river–estuary system whose hydrodynamics are governed by the combined effects of ocean tides, river flow, and complex channel geometry (Van et al., 2020).

The metamorphosis of tidal waves in estuaries is regulated by two opposing physical forces. The geometric convergence of estuary morphology may enhance tidal energy, producing hypersynchronous systems characterized by higher waves, while bottom friction reduces tidal energy, resulting in smaller waves in hyposynchronous systems (Khojasteh et al., 2023). These changes in tidal-wave propagation can also generate tidal asymmetry, expressed as unequal flood and ebb durations and current intensities. Such asymmetry regulates

© 2026 Dept. of Geophysics Hasanuddin University

residual sediment transport and sediment redistribution among branching estuarine channels, with implications for channel siltation, tidal-flat accretion, and longer-term morphological change (Zhou et al., 2025). Seasonal fluctuations in river flow markedly affect tidal propagation by changing effective friction due to alterations in depth and the balance between pressure-gradient and frictional forces (Tenorio-Fernandez et al., 2019).

Classical harmonic analysis has limited ability to reproduce non-stationary estuarine water levels because tidal amplitudes and phases are modified by nonlinear interactions among river discharge, tidal forcing, water depth, and channel geometry. Although process-based hydrodynamic models can explicitly represent these interactions, they generally require detailed boundary conditions and extensive model configuration (Gan et al., 2024). Such modelling challenges are pronounced in the Mahakam Delta because of its complex channel network, variable topography, and interacting riverine and marine forcing across the river–delta–sea continuum (Van et al., 2020). Traditional models fail to accurately represent nonlinear tidal dynamics and demand significant computing resources. Recent advancements in machine learning, specifically Random Forest and deep learning frameworks, present promising alternatives by identifying nonlinear relationships within tidal systems while offering computational efficiency benefits for real-time forecasting (Zhou et al., 2025; Lim & Zohren, 2021). Temporal lag characteristics in machine learning models have shown significant effectiveness in predicting tides by integrating historical data at different time intervals, which represent wave velocity and propagation distance via estuarine systems (Han et al., 2024). Interpretability approaches like SHAP (SHapley Additive exPlanations) facilitate comprehension of black-box models by pinpointing the factors that most substantially affect tidal dynamics (Kim et al., 2023; Lundberg & Lee, 2017).

Hydrodynamic processes and tidal dynamics within the Mahakam river-lake-delta system have been extensively modeled using multi-scale, finite-element simulations and hydraulic geometry frameworks (de Brye et al., 2011; Sassi et al., 2011; Van et al., 2016). Research has also successfully quantified how upstream river flow controls tidal propagation and water level profiles within the system's freshwater reaches (Sassi & Hoitink, 2013). More recent data-driven studies have applied neural-network architectures to tidal rivers and estuaries, including long short-term memory and feed-forward neural networks that incorporate river discharge to improve non-stationary tidal water-level predictions (Zhang et al., 2023). Within the Mahakam system, other recent studies have focused on the morphometric evolution and sediment infilling of the upstream Mahakam Lakes (Jati et al., 2026) or localized sediment dynamics (Rasimeng et al., 2019), a critical gap remains. Specifically, the integration of contemporary, modern machine learning methodologies has yet to be comprehensively explored for quantitative tidal analysis in the delta.

This study fills the gap by combining high-resolution observational data with machine learning methods to quantify tidal attenuation coefficients and their temporal variations, examine spatial and temporal patterns of tidal asymmetry, create predictive models for upstream water levels utilizing temporal lag features, and determine key factors influencing tidal wave propagation through feature importance evaluation. This study seeks to increase scientific comprehension and predictive accuracy of tidal dynamics in tropical deltaic systems by integrating extensive tidal cycle research with modern machine learning, hence offering improved

© 2026 Dept. of Geophysics Hasanuddin University

instruments for water resource management and flood prediction.

Methods

Research Location

This study was conducted in the Mahakam Delta, located on the eastern coast of Borneo Island, East Kalimantan, Indonesia (Figure 1). The delta occupies the low-lying coastal plain along the lower reach of the Mahakam River, bounded approximately by longitudes 117.15°E–117.68°E and latitudes 1.01°S–0.27°S. This area is characterized by a dense network of distributary channels, tidal creeks, and coastal wetlands that are strongly influenced by both river discharge and tidal forcing from the adjacent Makassar Strait.

Two tidal datasets were used to represent the upstream and downstream boundaries of the study domain. The upstream boundary is defined by an observed tide station (field observation site) located in the upper delta at approximately 0.57746°S, 117.2747°E, capturing water-level variability in the fluvial-tidal transition zone. The downstream boundary is specified using modeled water-level data derived from tidal surge predictions provided by the Geospatial Information Agency (BIG), representing conditions near the estuary mouth at approximately 0.695061°S, 117.627144°E, where marine tidal influence is dominant. The modeled dataset was converted into a continuous time series using only records with valid timestamps and was used as a proxy for offshore tidal dynamics. Validation of the BRIN-associated tidal model against in situ observations in Indonesian coastal settings showed good agreement, with reported Willmott Skill Score 0.652 (Sufyan et al., 2023). These validation results indicate the model reproduces the main tidal variability with reasonable accuracy and can serve as a regional offshore tidal boundary signal rather than a direct substitute for estuarine point observations.

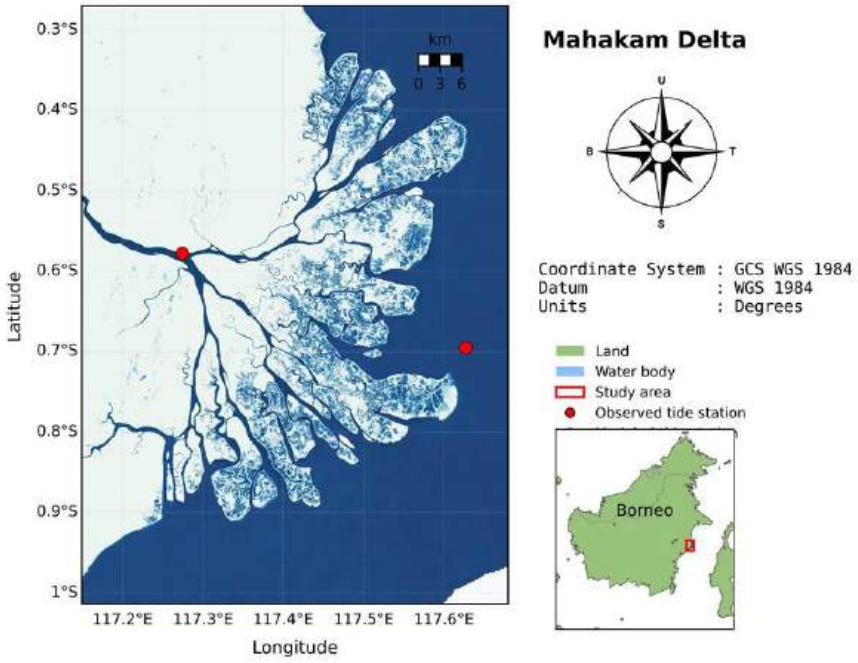


Figure 1. Research location in Mahakam Delta, East Kalimantan, Indonesia.

Data and Pre-processing

This study uses two water level (WL) time series:

1. Water Level at the Estuary Mouth

a. Source: Model outputs from tidal surge predictions from BIG (Geospatial Information Agency).
b. Format: Each row contains *longitude, latitude, date, time*, and *elevation* (m).

© 2026 Dept. of Geophysics Hasanuddin University

Only rows with complete date patterns (YYYY-MM-DD HH:MM:SS) are read and stored as a time series wl_estuary with a time index.

2. Water Level Upstream (Upper Delta)

a. Source: Data logger tidal station at Anggana.
b. Format: Data recorded in the data logger with 2-minute intervals.

Both time series are subsequently processed as follows:

a. Resampled to 10-minute resolution (RESAMPLE_RULE = "10min").
   - wl_estuary is linearly interpolated with respect to time.
   - wl_upstream is averaged within each 10-minute interval.
b. Inner-joined so that only time points with complete data at both the mouth and upstream are retained (Hu et al., 2024).

Dataset Assembly and Lag Feature Engineering

To model upstream water level as a response to conditions at the estuary mouth, lag features are constructed from the estuarine water level with $\eta_e(t)$ is qater level at the estuary mouth at time t.

The use of estuarine-mouth water levels as predictors is physically reasonable because tidal signals propagate from the estuary mouth toward upstream locations with a measurable phase delay. The magnitude of this delay may vary spatially because of channel geometry, bathymetry, bottom friction, river discharge, and tidal forcing (Iglesias et al., 2019). Previous water-level observations also contain important information about the temporal evolution of hydrological systems and can therefore be used as lagged input variables in data-driven water-level models (Liu et al., 2022; Gan et al., 2024).

Accordingly, the program generates the following lagged features from the estuarine water-level series:

$$X(t) = \eta_e(t),\ \eta_e(t - 10\ \text{min}),\ \eta_e(t - 20\ \text{min}),\ \ldots,\ \eta_e(t - 60\ \text{min}) \quad (1)$$

Lagged water-level features were constructed from antecedent estuarine water levels because historical water-level observations contain information on the temporal dependence of estuarine hydrodynamics and can improve short-term prediction performance (Gan et al., 2024).

Each lagged variable represents the water level observed at the estuary mouth at a particular time before the corresponding upstream observation. These variables allow the model to identify delayed relationships between changes occurring at the estuary mouth and the subsequent response of the upstream water level. Such lagged representations are particularly useful because water-level time series commonly exhibit temporal dependence and autocorrelation, meaning that current water-level conditions are partly related to previous observations (Gan et al., 2024).

Generating lagged variables through temporal shifting produces missing values in the first six observations because complete historical records are not available for these initial timestamps. Therefore, samples containing NaN values resulting from the shifting operation are removed. The remaining complete observations are then assembled into the final modelling dataset

Extraction of Tidal Cycles and Hydrodynamic Metrics

1. Tidal Peak Detection

After resampling and temporal synchronization, the two water-level time series were denoted as wl_estuary and wl_upstream. The variable wl_estuary represents the water level at the estuary mouth, whereas wl_upstream represents the water level at the upstream station. Both series were expressed in meters and

© 2026 Dept. of Geophysics Hasanuddin University

recorded at synchronized 10-minute intervals (Palmer et al., 2023).

a. The estuary water level (wl_estuary) is smoothed using a rolling maximum with a window of 5 steps (±50 minutes).
b. A time point (t_{est}) is designated as a tidal peak at the estuary mouth if:

$$\eta_e(t_{\text{est}}) = \max_{t\in[t_{\text{est}}-25\text{ min},t_{\text{est}}+25\text{ min}]}\eta_e(t) \quad (2)$$

High-water turning points were identified using a peak-based approach in which a tidal peak corresponds to a local maximum within a predefined temporal neighborhood (Palmer et al., 2023).

c. For each estuary peak (t_{est}), an upstream peak (t_{up}) is identified as the time of maximum wl_upstream within a 3-hour window following the estuary peak:

$$t_{\text{up}} = \arg\max_{t\in[t_{\text{est}},t_{\text{est}}+3\text{ hours}]}\eta_u(t) \quad (3)$$

where $\eta_u(t)$ is the upstream water level. This procedure represents the landward propagation of tidal waves, which may experience changes in amplitude and timing because of friction, channel geometry, water depth, and river discharge (Hoitink & Jay, 2016). For each estuarine high-water peak, the corresponding upstream peak was defined as the maximum upstream water level occurring within the subsequent three-hour search window. The window length was selected as a study-specific criterion to accommodate the expected landward propagation time.

2. Tidal Attenuation (Coefficient K)

Peak heights at the estuary mouth and upstream are defined as:

$$H_{\text{est}} = \eta_e(t_{\text{est}}), \quad H_{\text{up}} = \eta_u(t_{\text{up}}) \quad (4)$$

Tidal attenuation (attenuation coefficient) is defined as the ratio:

$$K = \frac{H_{\text{up}}}{H_{\text{est}}} \quad (5)$$

Cases where $H_{\text{est}} = 0$ are eliminated to avoid division by zero (Khojasteh et al., 2021; Xie & Wang, 2021).

3. Phase Lag

Phase lag between upstream and estuary mouth responses is measured as the time difference between the estuary peak and upstream peak, in minute:

$$\Delta\varphi = \frac{t_{\text{up}} - t_{\text{est}}}{60\text{ seconds/minute}}\ [\text{minutes}] \quad (6)$$

The high-water propagation lag was calculated as the difference between the occurrence time of the upstream and estuarine high-water peaks, expressed in minutes (Iglesias et al., 2019).

Flood-Ebb Asymmetry (FE)

To characterize the asymmetry between rising (flood) and falling (ebb) phases at upstream, a 12-hour segment is constructed around the upstream peak (Yu et al., 2020):

$$\text{segment} = \left[t_{\text{up}} - 6\text{ hours}, t_{\text{up}} + 6\text{ hours}\right] \quad (7)$$

A 12-hour analysis window centered on each upstream high-water peak was used as a study-specific approximation of one semidiurnal tidal cycle. Within this window, the preceding and subsequent low-water turning points were identified (Yu et al., 2020; Wünsche et al., 2024). Within this segment, the following are identified:

a. $(t_{\text{min}}^{\text{before}})$: time of minimum water level before the peak (flood phase onset).
b. $(t_{\text{min}}^{\text{after}})$: time of minimum water level after the peak (ebb phase end).

Flood duration is defined as the period from the preceding low water to the following high water, whereas ebb duration is the period from high water to the following low water (Wünsche et al., 2024):

$$T_f = t_{\text{up}} - t_{\text{min}}^{\text{before}}, \quad T_e = t_{\text{min}}^{\text{after}} - t_{\text{up}} \quad (8)$$

© 2026 Dept. of Geophysics Hasanuddin University

(both in minutes). Flood-ebb asymmetry is defined as (Wünsche et al., 2024):

$$\mathrm{FE} = \frac{T_f}{T_e} \quad (9)$$

If $T_e \leq 0$ or is undefined, the cycle is excluded (marked as NaN) This ratio represents the inequality between the rising and falling tidal durations (Guo et al., 2018; Hu et al., 2024).

Local Tidal Range at the Estuary Mouth

For the same cycle, the local tidal range at the estuary mouth is computed within the 12-hour segment:

$$\mathrm{TR_{est}} = \max\left(\eta_e(t)\right) - \min\left(\eta_e(t)\right) \in \left[t_{\mathrm{up}} - 6\ \mathrm{hours}, t_{\mathrm{up}} + 6\ \mathrm{hours}\right] \quad (10)$$

Local tidal range was defined as the difference between the maximum and minimum water levels within the identified tidal cycle (Khojasteh et al., 2021; Palmer et al., 2023). The 12-hour segment is used as a study-specific approximation for capturing one semidiurnal tidal cycle. Additionally, for each cycle:

a. Hour of day at estuary peak:

$$\mathrm{hour_of_day} = \mathrm{hour}(t_{\mathrm{est}}) \quad (11)$$

The hour of day was extracted from the timestamp of each estuarine high-water peak and was included as an operational temporal predictor.

b. Estuary peak level: estuary_peak_level = H_{est} (Sandbach et al., 2018; Xie & Wang, 2021).

Filtering of Tidal Cycles (Hydro Cycles Clean)

To focus on physically realistic and relevant cycles, the following filtering criteria are applied:

a. Minimum tidal range at estuary mouth:

$$\mathrm{TR_{est}} \geq 1.0\ \mathrm{m}$$

Cycles with an estuarine tidal range below 1.0 m were excluded using a study-specific threshold intended to remove weak or poorly resolved tidal cycles.

b. Realistic tidal attenuation:

$$0 < K \leq 3.0$$

Positive tidal-range ratios were retained, while extremely large ratios were treated as potential peak-matching or data-quality outliers. The upper threshold was selected empirically and evaluated through sensitivity analysis.

c. Reasonable phase lag:

$$0 \leq \Delta\varphi \leq 60\ \mathrm{minutes}$$

Only non-negative peak lags of up to 60 minutes were retained. The upper limit was selected as a study-specific criterion based on station spacing, temporal resolution, and the expected order of high-water propagation times reported for shallow estuarine systems (Iglesias et al., 2019).

d. Removal of entire cycles with missing values (NaN) in attenuation_K or phase_lag_min.

This criterion ensures that the upstream tidal peak occurs after the estuary peak, consistent with the landward propagation of tidal waves (Iglesias et al., 2019). The maximum phase lag of 60 minutes is applied as a study-specific threshold based on the expected hydrodynamic response between the two stations.

Machine Learning Modeling of Upstream Water Level

To evaluate how far estuarine dynamics can explain upstream water level variations at the 10-minute scale, a Random Forest Regression model is employed with the following framework. Random Forest has been widely applied to hydrological water-level forecasting because it can represent complex and nonlinear relationships between predictor and response variables (Atashi et al., 2022; Nhu et al., 2020). Historical water-level observations can also provide relevant predictors for short-term

© 2026 Dept. of Geophysics Hasanuddin University

estuarine water-level modeling because water-level time series exhibit temporal dependence (Gan et al., 2024).

a. Model Structure

Target:

$$y(t) = \eta_u(t) \text{ (upstream water level)} \quad (12)$$

Features:

$$\mathrm{x}(t) = [\eta_e(t), \eta_e(t - 10 \text{ min}), \ldots, \eta_e(t - 60 \text{ min})] \quad (13)$$

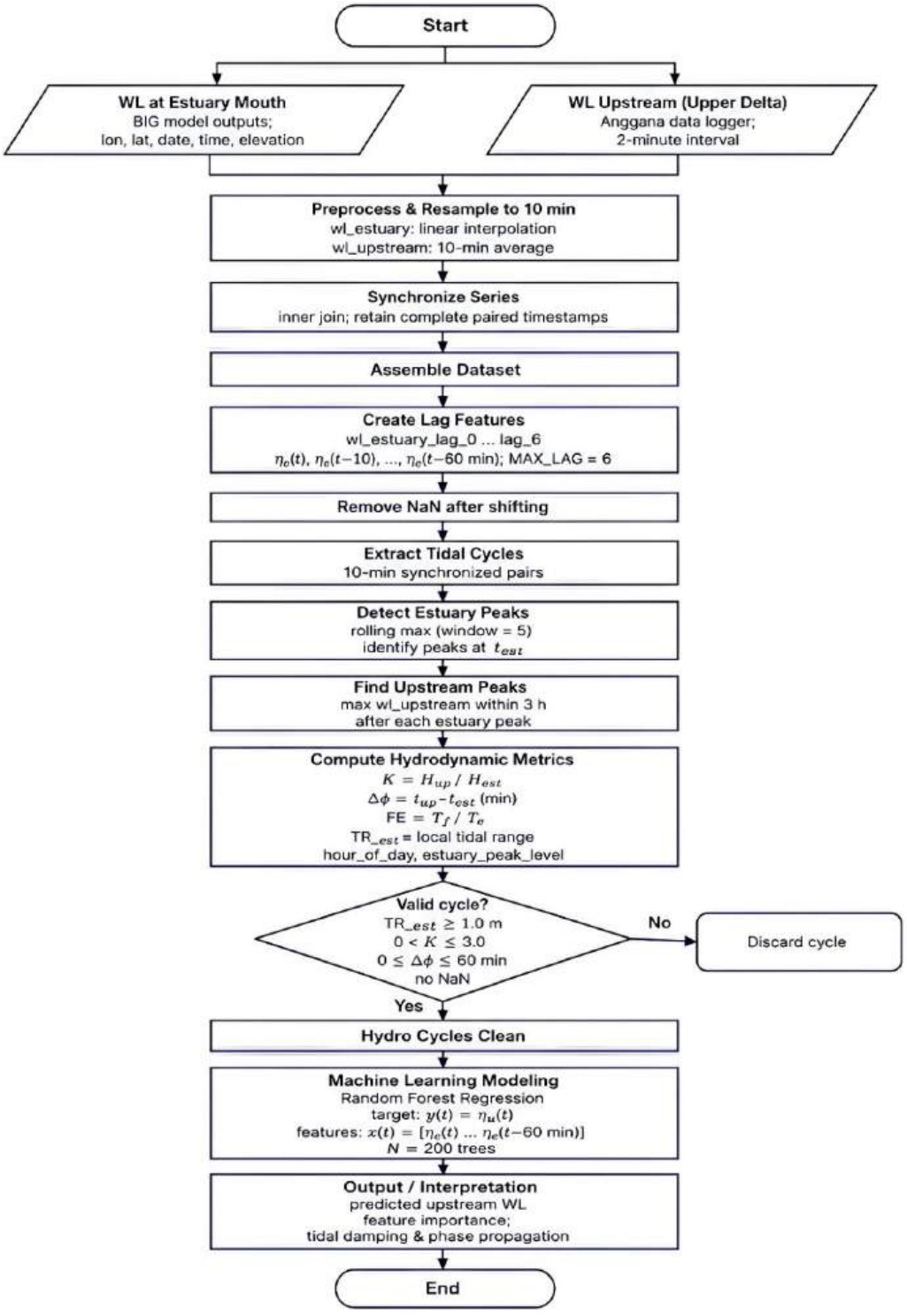


Figure 2. Data processing and machine learning workflow for estuarine and upstream tidal water level analysis.

© 2026 Dept. of Geophysics Hasanuddin University

The use of lagged water-level observations as model inputs is consistent with previous machine-learning studies showing that antecedent water levels can contribute substantially to subsequent water-level prediction (Nhu et al., 2020; Gan et al., 2024). The Random Forest model learns a non-linear function (James et al., 2021):

$$\hat{y}(t) = f\big(\mathrm{x}(t)\big) \tag{14}$$

computed as the average prediction from N regression decision trees ($N = 200$):

$$\hat{y}(t) = \frac{1}{N}\sum_{i=1}^{N} f_i\left(\mathrm{x}(t)\right) \tag{15}$$

where f_i is the i-th tree (James et al., 2021; Hosseinzadeh et al., 2023).

b. Hydrodynamic Interpretation

The ensemble approach provides robust predictions while permitting interpretation of feature importance. Lagged estuarine water levels serve as proxies for wave propagation and tidal signal transmission through the estuary-delta system. The model implicitly captures the phase relationships and tidal damping effects that characterize the hydrodynamics of the study region (Zhou et al., 2025).

Figure 2 illustrates the workflow used to develop a machine-learning model for predicting upstream water level from downstream observations (Sarafanov et al., 2020). Water-level data from the estuary mouth and upper-delta stations are first processed resampled to 10-minute intervals, and synchronized using matched timestamps. The combined dataset is then used to generate lagged downstream water-level features, after which tidal cycles are identified and screened using physically plausible hydrodynamic criteria, including tidal range, time lag, and the absence of missing values. For each valid cycle, upstream peak water level and associated hydrodynamic metrics are calculated. Finally, these clean tidal-cycle data are used to train a Random Forest regression model, enabling prediction of upstream water-level peaks and supporting the interpretation of tidal damping and propagation along the estuary (Zounemat-Kermani et al., 2020).

Results and Discussion

Tidal Data Characteristics

This research analyzed tidal data with a temporal resolution of 10 minutes, gathered from July 12 to August 4, 2018, yielding a total of 3,303 observations in the Mahakam Delta estuary and upstream. The water levels in the Mahakam Delta estuary fluctuated between -0.970 and 1.355 m, whereas at the Mahakam Delta upstream, they varied between -0.488 and 1.690 m (Table 1). Figure 3 illustrates that the water levels at both sites exhibited a distinct semidiurnal tidal pattern throughout time.

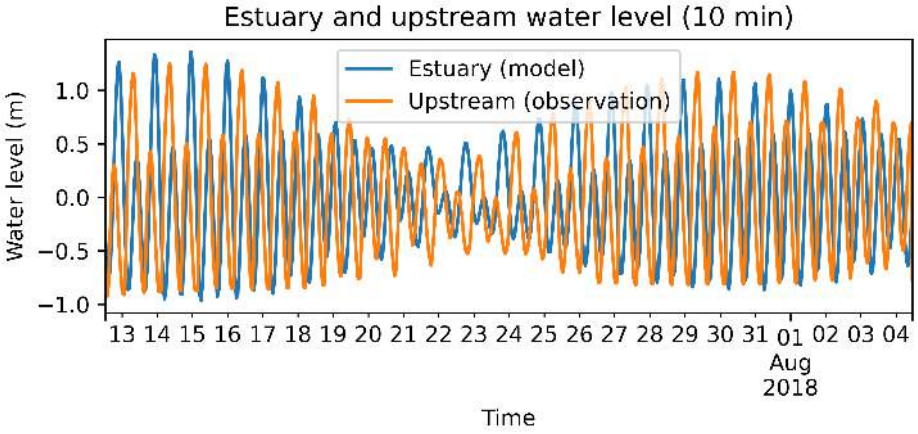


Figure 3. Timeseries estuary and upstream.

© 2026 Dept. of Geophysics Hasanuddin University

The Pearson correlation value between estuary and upstream water levels was -0.072, indicating a negligible relationship. This indicates a negligible direct linear correlation between the two locations. The scatter plot (Figure 4) illustrates that the data is distributed in a complex and non-linear manner. The data concentration exhibits an elliptical pattern that aligns with the tidal cycle.

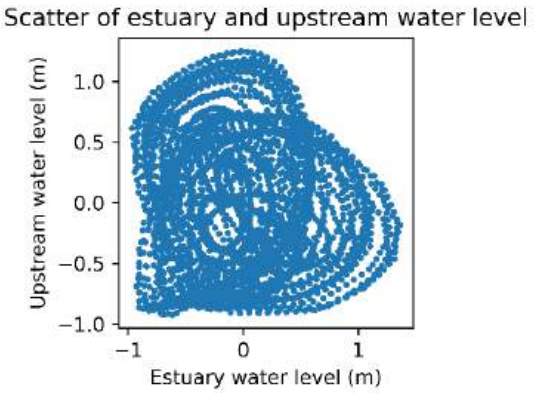


Figure 4. Scatter estuary and upstream.

Machine Learning Prediction with Temporal Lag

Table 1. Summary of Tidal Dynamics Research Results at Mahakam Delta Estuary and Upstream.

Parameter	Value
Temporal data resolution	10 minutes
Study period	July 12 - August 4, 2018
Number of observations	3,303 samples
Water level range at Mahakam Delta estuary	-0.970 to 1.355 m
Water level range at upstream Mahakam Delta	-0.488 to 1.690 m
R^2 model	0.883
MAE model	0.150 m
Optimal temporal lag	60 minutes (6 intervals)
Number of tidal cycles analyzed	34 cycles
Mean attenuation coefficient (K)	0.762 ± 0.651
Mean tidal range at estuary	1.571 ± 0.342 m
Mean phase lag	0 minutes
Mean tidal asymmetry (Fe)	0.632 ± 0.599

The machine learning model using temporal lag characteristics achieved a coefficient of determination (R^2) of 0.883 and a Mean Absolute Error (MAE) of 0.150 m (Table 1). An R^2 value over 0.85 indicates that the model accounts for 88.3% of the variations in upstream Mahakam Delta water levels by using estuarine Mahakam Delta data with a temporal. This performance parallels experiments using a multilayer perceptron to forecast tides in estuaries, achieving R^2 values as high as 0.97 (Guillou & Chapalain, 2021).

The optimal time lag identified was 60 minutes (comprising 6 periods of 10 minutes), indicating that it takes about one hour for the tidal signal to propagate from the Mahakam Delta estuary to the upstream Mahakam Delta. Machine learning methodologies, particularly Recurrent Neural Networks (RNN) and hybrid systems, are the most promising approach to modeling complex physical processes in tidal rivers and estuaries. The efficacy of the lag-feature model confirms a substantial time-dependent link between tidal dynamics at the Mahakam Delta estuary and the resultant reactions at the upstream Mahakam Delta.

Tidal Cycle Analysis and Attenuation

An analysis of 34 tidal cycles revealed important characteristics of tidal wave propagation in the studied Mahakam Delta system. The tidal attenuation coefficient (K) exhibited a mean value of 0.762 ± 0.651, however its distribution varied significantly (Figure 5).

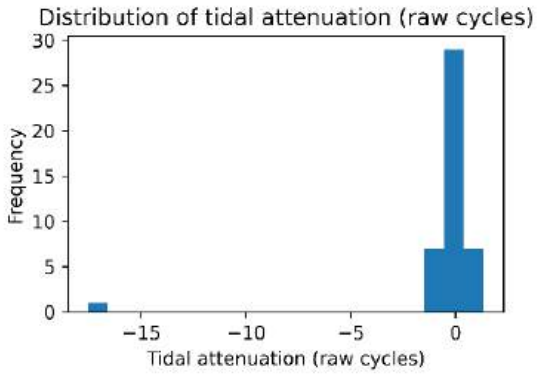


Figure 5. Distribution of tidal attenuation (raw cycles).

The histogram distribution indicates that the majority of cycles (about 43) had little attenuation (K around 0). The majority of

© 2026 Dept. of Geophysics Hasanuddin University

cycles have low K values, indicating a hyposynchronous condition. This indicates that frictional effects surpass the geometric convergence of the estuary, resulting in the attenuation of tidal waves as they propagate from the estuary to the upstream Mahakam Delta. In hyposynchronous deltas, bottom friction and riverbank resistance are the primary factors influencing tidal amplitude decrease in inland areas (Khojasteh et al., 2021). In hypersynchronous systems, geometric convergence dominates, leading to tidal amplification. The mean tidal range of the Mahakam Delta estuary was 1.571 ± 0.342 m, indicating that the region was in a mesotidal condition (Khojasteh et al., 2021). The alteration in tidal range results from the spring-neap cycles prevalent in semidiurnal tidal systems (Garel et al., 2021; Xie & Wang, 2021).

Phase Lag and Tidal Asymmetry

The research indicated that the mean phase lag between tidal maxima in the Mahakam Delta estuary and the upstream Mahakam Delta was 0 minutes for all cycles studied. This result suggests that the dominant belief that tidal wave propagation requires measurable travel time may need reconsideration. In the higher reaches of tidal rivers, river discharge may entirely govern incoming tidal attenuation. In some instances, river flow may postpone or alter tidal effects (Sassi & Hoitink, 2013). The mean tidal asymmetry value (Fe) was 0.632 ± 0.599, indicating that the Mahakam Delta system analyzed had a greater propensity for flooding than for ebbing. Flood-dominant tidal asymmetry is characterized by a reduced flood duration compared to ebb length, resulting in heightened peak currents during the flood phase. Shallow-water impacts, friction, and/or inadequate exchange between deep channels and intertidal zones may asymmetrically affect tidal timing and amplitude (Spicer et al., 2023). Flood dominance often transports material into interior regions (upstream of the Mahakam Delta) during periods of slow to moderate river flow (Friedrichs & Aubrey, 1994). Nonetheless, seasonal variations in river flow may significantly influence tidal asymmetry. For instance, elevated discharge during wet seasons may amplify tidal amplitudes in the lower reaches due to non-linear effects, while concurrently diminishing tidal amplitudes in the upstream Mahakam Delta due to increased friction damping (Yu et al., 2020).

Feature Importance in Water Level Prediction

The machine learning model for forecasting water levels in the upstream Mahakam Delta indicated that temporal lag elements derived from estuary data are crucial for identifying tidal propagation patterns. Figure 6 illustrates the outcomes of a feature importance study conducted using the Random Forest model. The characteristic with the greatest relevance value is lag 6 (60 minutes), at 0.508, followed by lag 0 (present observation), at 0.309. These two primary characteristics together account for 81.8% of the overall model relevance. Historical data with the greatest lag and real-time estuary data from the Mahakam Delta are important for forecasting upstream water level conditions (Anggraini et al., 2024). These findings align with previous studies indicating that including temporal lag factors can improve prediction accuracy in systems with complex temporal dynamics (Liu et al., 2025).

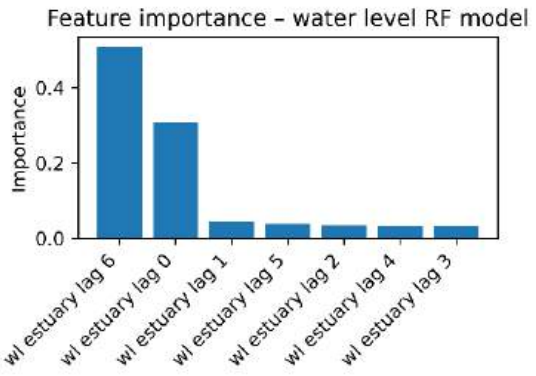


Figure 6. Feature importance-water level random forest model.

Tidal Attenuation Coefficient Modeling

© 2026 Dept. of Geophysics Hasanuddin University

The development of a machine learning model to predict the tidal attenuation coefficient yielded exceptional results, with a R^2 value of 0.968 and a mean absolute error (MAE) of 0.084 (Table 2). The precision of this forecast indicates that the model effectively simulated the movement of tidal waves from the Mahakam Delta estuary to the upstream Mahakam Delta.

The histogram of filtered attenuation distribution (Figure 7) exhibits a more concentrated pattern compared to the raw histogram. The majority of tidal cycles have attenuation coefficients ranging from 0 to 0.5, indicating that the Mahakam Delta experiences very hyposynchronous circumstances. Figure 8 presents a scatter plot depicting the relationship between attenuation and estuary tidal range. This indicates that the two variables are intricately connected. Generally, increased attenuation occurs more often when the tidal range is reduced, particularly within the 1.0–1.5 m interval. Conversely, attenuation varies significantly at greater tidal ranges (> 2.0 m). This pattern indicates that the attenuation coefficient in the Mahakam Delta system is influenced by factors outside the tidal amplitude of the estuary. The interaction of river bottom topography, friction, and discharge also influences it (Khojasteh et al., 2023; Su & Jiang, 2023).

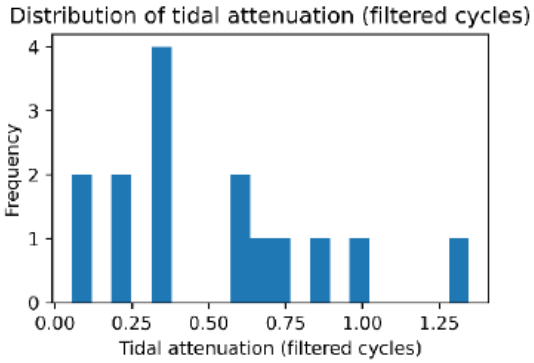


Figure 7. Distribution of tidal attenuation (filtered cycles).

Table 2. Performance of machine learning models for predicting tidal hydrodynamic parameters at Mahakam Delta.

Parameter	Model	R^2	MAE	RMSE
Water level (upstream)	Regression with lag features	0.883	0.150 m	—
Attenuation coefficient (K)	Random Forest	0.968	0.084	0.114
Tidal asymmetry (Fe)	Random Forest	0.786	0.318	0.114
Phase lag (minutes)	Classifier	0.0	—	—

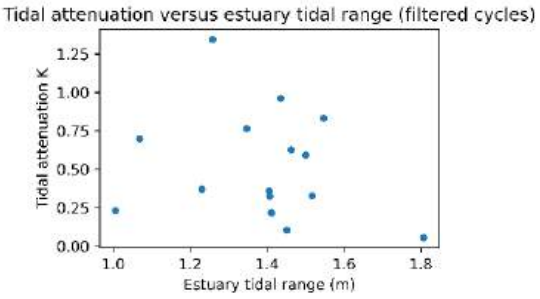


Figure 8. Tidal attenuation and estuary tidal range (filtered cycles)

Figure 9 illustrates an examination of feature importance for predicting attenuation. The paramount characteristic is the highest water level in the Mahakam Delta estuary, which has a significance value of 0.776. This element is far more critical than the others, indicating that the local tidal amplitude at the estuary is the primary determinant influencing the magnitude of attenuation as waves propagate upwards. This conclusion aligns with studies demonstrating that peak water levels substantially affect the degree of shallow-water distortion and friction experienced by tidal waves (Su & Jiang, 2023).

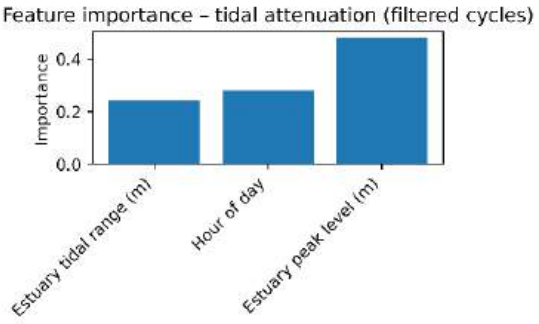


Figure 9. Feature importance-tidal attenuation.

© 2026 Dept. of Geophysics Hasanuddin University

Figure 9 presents the Random Forest feature-importance analysis for predicting the tidal attenuation coefficient. Estuary peak water level was identified as the most important predictor, with a feature-importance value of 0.776. This value was substantially higher than those of the other predictors, indicating that water-level conditions at the estuary boundary strongly influenced the landward transmission of the tidal signal. This interpretation is physically plausible because tidal propagation and attenuation in estuarine channels depend on the magnitude of tidal forcing and its interaction with bottom friction, river discharge, and channel geometry (Wang et al., 2021; Wu et al., 2022). This conclusion aligns with studies demonstrating that peak water levels substantially affect the degree of shallow-water distortion and friction experienced by tidal waves (Su et al., 2023).

Influence of Tidal Range on Attenuation

Table 3. Attenuation characteristics based on large tide vs. small tide groups at Mahakam Delta Estuary.

Characteristic	Large Tide	Small Tide
Number of cycles	24	10
Mean tidal range (m)	1.718 ± 0.236	1.218 ± 0.055
Median attenuation coefficient	0.379	0.956
Mean attenuation coefficient	0.625 ± 0.562	1.088 ± 0.771

The investigation, categorized by tidal range size (Table 3), revealed significant disparities in attenuation characteristics between large and small tides. The median attenuation coefficient was 0.379, whereas the mean was 0.625 during times of significant tidal fluctuations, with a mean range of 1.718 m (n=24 cycles). Conversely, during times of minor tides with a mean range of 1.218 m (n=10 cycles), the median attenuation coefficient increased to 0.956, while the mean reached 1.088. This indicates that damping was more pronounced during periods of reduced tidal amplitude. There are scientific explanations for this peculiar phenomenon that first seem illogical. During high tide, the energy of the tidal wave increases, resulting in relatively significant amplitudes in the upstream reach despite the presence of friction. Conversely, during times of low tides, diminished wave amplitudes render friction effects comparatively more significant, resulting in elevated attenuation coefficients (Su & Jiang, 2023). This conclusion highlights the importance of data stratification based on spring-neap circumstances in the examination of complex tidal dynamics.

Phase Lag and Tidal Asymmetry Models

Presents a study of the significance of each feature in predicting phase lag. All characteristics have significance values around zero, aligning with empirical estimates indicating a mean phase lag of 0 minutes for all examined cycles. This indicates that certain circumstances in the Mahakam Delta during the research period resulted in simultaneous tidal maxima occurring at the estuary and upstream, despite the temporal delay of physical wave transmission (Zhou et al., 2025). The tidal asymmetry prediction model (Fe) performed adequately, although not as well as the attenuation model. The model exhibited a R^2 of 0.786 and a mean absolute error (MAE) of 0.318 (Table 2). The asymmetry model yields more varied predictions due to several variables influencing tidal asymmetry, including non-linear interactions among various tidal components, changes in bottom topography, and fluctuations in river flow. These results highlight the relative robustness of the attenuation model in capturing local tidal characteristics and their hydrodynamic implications. The attenuation model ($R^2 = 0.968$) outperforms the asymmetry prediction model ($R^2 = 0.786$), indicating that local tidal parametric properties provide more precise predictions of attenuation coefficients. This concerns the deterministic properties of tidal wave

© 2026 Dept. of Geophysics Hasanuddin University

propagation governed by continuity and momentum equations (Niesten et al., 2024).

Tidal asymmetry arises from complex overtide interactions and non-linear constituent interactions. This complicates predictions using linear or semi-linear data-driven models (Kim et al., 2024). The comprehensive synthesis of studies reveals that the Mahakam Delta system exhibits hydrodynamic characteristics typical of expansive tropical hyposynchronous estuaries. The significant influence of estuary tidal amplitude on attenuation coefficients indicates that bottom friction is the primary component governing this system (Khojasteh et al., 2023). As tidal waves go upstream, they dissipate energy due to friction, and their morphology alters as a result of shallow-water phenomena. This exacerbates the imbalance of flood dominance (Su & Jiang, 2023).

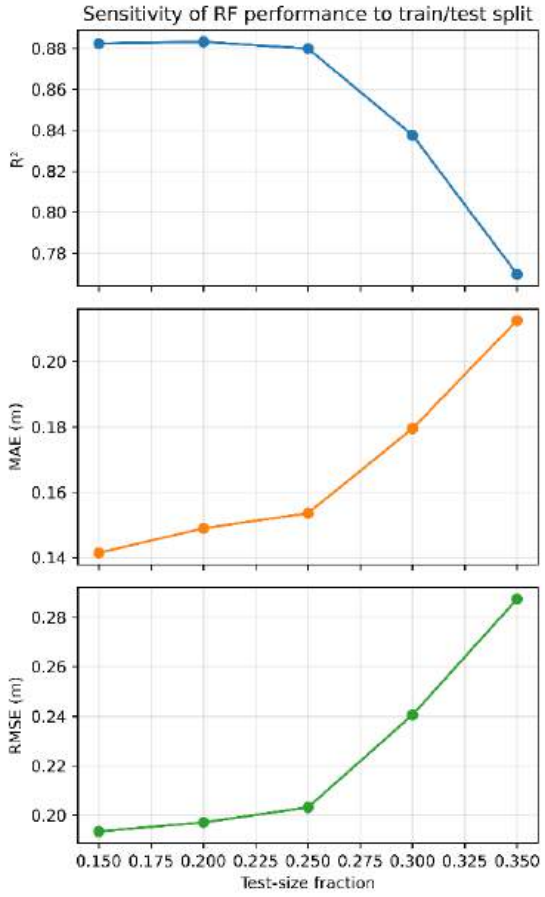


Figure 10. Sensitivity of Random Forest performance to different train/test split.

Figure 10 shows the sensitivity of the Random Forest model to different train/test partitions. The model achieved the highest performance at smaller test fractions, with R^2 values of 0.882, 0.883, and 0.880 for test fractions of 0.15, 0.20, and 0.25, respectively, and still remained relatively strong at a test fraction of 0.30 with R^2 = 0.838. However, performance declined further when the test fraction increased to 0.35, where R^2 dropped to 0.770, while MAE and RMSE increased from 0.142 m and 0.194 m at the 0.15 split to 0.207 m and 0.286 m at the 0.35 split, respectively.

These variations indicate that the estimated predictive performance was sensitive to the amount of data allocated to training and testing. In time-series forecasting, performance estimates can vary across testing periods because observations are temporally dependent and may exhibit non-stationary behavior; therefore, evaluation procedures should preserve temporal order and, where possible, examine performance across multiple testing periods (Bergmeir et al., 2018; Cerqueira et al., 2020). The relatively consistent performance across test fractions of 0.15–0.30 reduces, although does not eliminate, concern that the reported model skill resulted from a single favorable partition. Moreover, the simultaneous evaluation of R^2, MAE, and RMSE provides a more comprehensive assessment than reliance on R^2 alone, because a high coefficient of determination does not necessarily imply low forecast error or reliable predictive performance (Hewamalage et al., 2023). Therefore, Figure 10 provides evidence of the model's temporal robustness within the observed study period, while also showing that its predictive accuracy was not uniform across all train/test partitions.

Conclusion

This study successfully integrated high-resolution observational data with machine learning techniques to investigate tidal wave propagation and attenuation in the

© 2026 Dept. of Geophysics Hasanuddin University

Mahakam Delta, East Kalimantan, Indonesia. The Mahakam Delta exhibits strongly hyposynchronous characteristics, with a mean attenuation coefficient of 0.762 ± 0.651, indicating that frictional effects dominate over geometric convergence as tidal waves propagate upstream. The Random Forest model achieved exceptional predictive accuracy (R^2 = 0.883, MAE = 0.150 m) for upstream water level prediction using temporal lag features, with the optimal lag identified at 60 minutes. The attenuation coefficient prediction model (R^2 = 0.968, MAE = 0.084) identified estuary peak water level as the dominant factor controlling tidal wave energy dissipation, accounting for 77.6% of feature importance. The result that median attenuation is higher during small tides (0.956) than during large tides (0.379) indicates a non-linear interaction between wave energy and friction. Additionally, the Mahakam Delta exhibits flood-dominant tidal asymmetry (Fe = 0.632 ± 0.599) with a mean phase lag of zero minutes between estuary and upstream tidal peaks.

These findings advance our understanding of tropical deltaic hydrodynamics and demonstrate the efficacy of machine learning for complex tidal systems. The integration of temporal lag features with feature importance analysis provides interpretable insights into physical wave propagation mechanisms while maintaining predictive power. The developed models offer practical applications for water resource management, flood forecasting, and navigation safety in the Mahakam Delta and comparable tropical estuarine systems. Future research should incorporate seasonal variations in river discharge, explore deep learning architectures for extended forecasting horizons, and validate model performance across multiple years to capture climate variability impacts. Enhanced understanding and predictive capabilities will support adaptive coastal management in regions highly vulnerable to tidal flooding and climate change impacts.

Acknowledgements

Thanks to Geospatial Information Agency of Indonesia (BIG) for the open access data, so the authors can use it in this research. We also express our gratitude to who contributed to this research.

Author Contribution

Muhammad Riza conceptualized the research, performed data collection, designed the methodology, supervised the overall study, and led the manuscript writing and revision. Nanda Khoirunisa pre-processing, and analysis, prepared the figures and tables, and contributed to drafting the manuscript. Zetsaona Sihotang supported data acquisition and curation, conducted the literature review, assisted in interpreting the results, and contributed to manuscript editing. Idris Mandang provided scientific supervision, contributed to refining the research design, critically reviewed the results, and offered substantial suggestions during manuscript revision.

Conflict of Interest

The authors declare no conflict of interest.

References

Anggraini, A. P. K., Trismadi, T., & Supriyadi, A. A. (2024). Predicting Water Levels from Environmental Parameters Using Random Forest Models. *International Journal of Engeineering Continuity*, 4(1), 39–53. https://doi.org/10.58291/ijec.v4i1.314

Atashi, V., Gorji, H. T., Shahabi, S. M., Kardan, R., & Lim, Y. H. (2022). Water level forecasting using deep learning time-series analysis: A case study of Red River of the North. *Water*, 14(12), 1971. https://doi.org/10.3390/w14121971

Bergmeir, C., Hyndman, R. J., & Koo, B.

© 2026 Dept. of Geophysics Hasanuddin University

(2018). A note on the validity of cross-validation for evaluating autoregressive time series prediction. *Computational Statistics & Data Analysis*, 120, 70–83. https://doi.org/10.1016/j.csda.2017.11.003

Cerqueira, V., Torgo, L., & Mozetič, I. (2020). Evaluating time series forecasting models: An empirical study on performance estimation methods. *Machine Learning*, 109(11), 1997–2028. https://doi.org/10.1007/s10994-020-05910-7

de Brye, B., Schellen, S., Sassi, M., Vermeulen, B., Kärnä, T., Deleersnijder, E., & Hoitink, T. (2011). Preliminary results of a finite-element, multi-scale model of the Mahakam Delta (Indonesia). *Ocean Dynamics*, 61(8), 1107–1120. https://doi.org/10.1007/s10236-011-0410-y

Friedrichs, C. T., & Aubrey, D. G. (1994). Tidal propagation in strongly convergent channels. *Journal of Geophysical Research*, 99(C2), 3321–3336. https://doi.org/10.1029/93JC03219

Gan, M., Chen, Y., Pan, S., Lai, X., Pan, H., Wen, Y., & Xia, M. (2024). An improved machine learning-based model to predict estuarine water levels. *Ocean Modelling*, 190, 102376. https://doi.org/10.1016/j.ocemod.2024.102376

Garel, E., Zhang, P., & Cai, H. (2021). Dynamics of fortnightly water level variations along a tide-dominated estuary with negligible river discharge. *Ocean Science*, 17(6), 1605–1621. https://doi.org/10.5194/os-17-1605-2021

Guillou, N., & Chapalain, G. (2021). Machine learning methods applied to sea level predictions in the upper part of a tidal estuary. *Oceanologia*, 63(4), 531–544. https://doi.org/10.1016/j.oceano.2021.07.003

Guo, L., Brand, M., Sanders, B. F., Foufoula-Georgiou, E., & Stein, E. D. (2018). Tidal asymmetry and residual sediment transport in a short tidal basin under sea level rise. *Advances in Water Resources*, 121, 1–8. https://doi.org/10.1016/j.advwatres.2018.07.012

Han, H., Kang, N., Yoon, J., & Hwang, S. (2024). Utilizing deep learning algorithm and high-resolution precipitation product to predict water level variability. *Journal of Korea Water Resources Association*, 57(7), 471–479. https://doi.org/10.3741/JKWRA.2024.57.7.471

Hewamalage, H., Ackermann, K., & Bergmeir, C. (2023). Forecast evaluation for data scientists: Common pitfalls and best practices. *Data Mining and Knowledge Discovery*, 37, 788–832. https://doi.org/10.1007/s10618-022-00894-5

Hoitink, A. J. F., & Jay, D. A. (2016). Tidal river dynamics: Implications for deltas. *Reviews of Geophysics*, 54(1), 240–272. https://doi.org/10.1002/2015RG000507

Hosseinzadeh, P., Nassar, A., Boubrahimi, S. F., & Hamdi, S. M. (2023). ML-based streamflow prediction in the Upper Colorado River Basin using climate variables time series data. *Hydrology*, 10(2), 29. https://doi.org/10.3390/hydrology10020029

Hu, S., Zhang, P., Cai, H., Ou, S., Liu, F., Lin, J., & Yang, Q. (2024). Long-term evolution and controlling factors of tidal duration asymmetry in the mainstream of the Zhujiang River Estuary, China. *Ocean & Coastal Management*, 256, 107289. https://doi.org/10.1016/j.ocecoaman.2024.107289

© 2026 Dept. of Geophysics Hasanuddin University

Iglesias, I., Avilez-Valente, P., Bio, A., & Bastos, L. (2019). Modelling the main hydrodynamic patterns in shallow water estuaries: The Minho case study. *Water*, 11(5), 1040. https://doi.org/10.3390/w11051040

James, G., Witten, D., Hastie, T., & Tibshirani, R. (2021). *An introduction to statistical learning: With applications in R*. Springer. https://doi.org/10.1007/978-1-0716-1418-1

Jati, S. N., Irawan, D. E., Wijaya, D. D., & Puradimaja, D. J. (2026). Declining volume development index precedes basin infilling in Mahakam Lakes, Indonesia. *Frontiers in Earth Science*, 14, 1818351. https://doi.org/10.3389/feart.2026.1818351

Khojasteh, D., Chen, S., Felder, S., Heimhuber, V., & Glamore, W. (2021). Estuarine tidal range dynamics under rising sea levels. *PLoS ONE*, 16(9), 1–25. https://doi.org/10.1371/journal.pone.0257538

Khojasteh, D., Felder, S., Heimhuber, V., & Glamore, W. (2023). A global assessment of estuarine tidal response to sea level rise. *Science of the Total Environment*, 894, 165011. https://doi.org/10.1016/j.scitotenv.2023.165011

Kim, D., Handayani, M. P., Lee, S., & Lee, J. (2023). Feature Attribution Analysis to Quantify the Impact of Oceanographic and Maneuverability Factors on Vessel Shaft Power Using Explainable Tree-Based Model. *Sensors*, 23(3), 1072. https://doi.org/10.3390/s23031072

Kim, S. I., Seo, J. Y., Park, J.-H., Kim, P. J., Kim, I. G., Kim, K. M., & Ha, H. K. (2024). Imbalance of sediment transport in a meso-tidal bay: effect of tidal pumping and residual circulation. *Frontiers in Marine Science*, 11, 1362583. https://doi.org/10.3389/fmars.2024.1362583

Lim, B., & Zohren, S. (2021). Time-series forecasting with deep learning: a survey. *Philosophical Transactions of the Royal Society A,* 379(2194), 20200209. https://doi.org/10.1098/rsta.2020.0209

Liu, C.-H., Yang, T.-H., & Wijaya, O. T. (2022). Development of an Artificial Neural Network Algorithm Embedded in an On-Site Sensor for Water Level Forecasting. *Sensors*, 22(21), 8532. https://doi.org/10.3390/s22218532

Liu, Z., Lu, Z., Zhu, W., Yuan, J., Cao, Z., Cao, T., Liu, S., Xu, Y., & Zhang, Z. (2025). Comparison of machine learning methods for predicting ground-level ozone pollution in Beijing. *Frontiers in Environmental Science*, 13, 1561794. https://doi.org/10.3389/fenvs.2025.1561794

Lundberg, S. M., & Lee, S.-I. (2017). A Unified Approach to Interpreting Model Predictions. *31st Conference on Neural Information Processing Systems*, 1–10. https://doi.org/10.48550/arXiv.1705.07874

Nhu, V.-H., Shahabi, H., Nohani, E., Shirzadi, A., Al-Ansari, N., Bahrami, S., Miraki, S., Geertsema, M., & Nguyen, H. (2020). Daily water level prediction of Zrebar Lake (Iran): A comparison between M5P, random forest, random tree and reduced error pruning trees algorithms. *ISPRS International Journal of Geo-Information*, 9(8), 479. https://doi.org/10.3390/ijgi9080479

Niesten, I., Huismans, Y., & Hoitink, A. J. F. (2024). Ebb-Dominant Mixing Increases the Seaward Sediment Flux in a Stratified Estuary. *Journal of Geophysical Research: Oceans*, 129(12), e2024JC021201. https://doi.org/10.1029/2024JC021201

Palmer, K., Watson, C. S., Hunter, J. R.,

© 2026 Dept. of Geophysics Hasanuddin University

Hague, B. S., & Power, H. E. (2023). An improved method for computing tidal datums. *Coastal Engineering*, 184, 104354. https://doi.org/10.1016/j.coastaleng.2023.104354

Rasimeng, S., Mandang, I., & S. (2019). Identification of eroded sediment layer thickness and depth of {Mahakam} River at Tenggarong Bridge Area, Kutai Kartanegara East Kalimantan using Ground Penetrating Radar Method. *IOP Conf. Series: Earth and Environmental Science*, 279, 012040. https://doi.org/10.1088/1755-1315/279/1/012040

Sandbach, S. D., Nicholas, A. P., Ashworth, P. J., Best, J. L., Keevil, C. E., Parsons, D. R., Prokocki, E. W., & Simpson, C. J. (2018). Hydrodynamic modelling of tidal-fluvial flows in a large river estuary. *Estuarine, Coastal and Shelf Science*, 212, 176–188. https://doi.org/10.1016/j.ecss.2018.06.023

Sarafanov, M., Kazakov, E., & Borisova, Y. (2020). Modeling water level using downstream river water level observations and machine learning methods. *E3S Web of Conferences*, 163, 01009. https://doi.org/10.1051/e3sconf/202016301009

Sassi, M. G., Hoitink, A. J. F., de Brye, B., Vermeulen, B., & Deleersnijder, E. (2011). Tidal impact on the division of river discharge over distributary channels in the Mahakam Delta. *Ocean Dynamics*, 61(12), 2211–2228. https://doi.org/10.1007/s10236-011-0473-9

Sassi, M. G., & Hoitink, A. J. F. (2013). River flow controls on tides and tide-mean water level profiles in a tidal freshwater river. *Journal of Geophysical Research: Oceans*, 118(9), 4139–4151. https://doi.org/10.1002/jgrc.20297

Spicer, P., Yang, Z., Wang, T., & Deb, M. (2023). Tidal energy extraction modifies tidal asymmetry and transport in a shallow, well-mixed estuary. *Frontiers in Marine Science*, 10, 1268348. https://doi.org/10.3389/fmars.2023.1268348

Su, Y., & Jiang, X. (2023). Prediction of tide level based on variable weight combination of LightGBM and CNN-BiGRU model. *Nature*, 13, 9. https://doi.org/10.1038/s41598-022-26213-y

Sufyan, A., Risandi, J., & Akhwady, R. (2023). Observasi Pasang Surut dan Arus di Muara Porong untuk Mendukung Pengembangan Pulau Lusi: Observation of Tide and Current in Muara Porong to Support Lusi Island Development. *Jurnal Teknologi Lingkungan*, 24(2), 200–206. https://doi.org/10.55981/jtl.2023.986

Tenorio-Fernandez, L., Zavala-Hidalgo, J., & Olvera-Prado, E. R. (2019). Seasonal variations of river and tidal flow interactions in a tropical estuarine system. *Continental Shelf Research*, 188, 103965. https://doi.org/10.1016/j.csr.2019.103965

Van, C. P., Gourgue, O., Sassi, M., Hoitink, A. J. F., Deleersnijder, E., & Soares-Frazão, S. (2016). Modelling fine-grained sediment transport in the Mahakam land–sea continuum, Indonesia. *Journal of Hydro-Environment Research*, 13, 103–120. https://doi.org/10.1016/j.jher.2015.04.005

Wang, J., de Swart, H. E., & Dijkstra, Y. M. (2021). Dependence of tides and river water transport in an estuarine network on river discharge, tidal forcing, geometry and sea level rise. *Continental Shelf Research*, 225, 104476. https://doi.org/10.1016/j.csr.2021.104476

Wu, Y., Hannah, C., Matte, P., O'Flaherty-Sproul, M., Mo, R., Wang, X., & MacAulay, P. (2022). Tidal

© 2026 Dept. of Geophysics Hasanuddin University

propagation in the Lower Fraser River, British Columbia, Canada. *Estuarine, Coastal and Shelf Science*, 264, 107695. https://doi.org/10.1016/j.ecss.2021.107695

Wünsche, A., Becker, M., Fritzsch, R., Kelln, J., & Winter, C. (2024). The sensitivity of tidal asymmetry descriptors in the Ems estuary. O*cean Dynamics*, 74, 613–627. https://doi.org/10.1007/s10236-024-01622-x

Xie, D., & Wang, Z. B. (2021). Seasonal Tidal Dynamics in the Qiantang Estuary: The Importance of Morphological Evolution. *Frontiers in Earth Science*, 9, 782640. https://doi.org/10.3389/feart.2021.782640

Yu, X., Zhang, W., & Hoitink, A. J. F. (2020). Impact of river discharge seasonality change on tidal duration asymmetry in the Yangtze River Estuary. *Scientific Reports*, 10, 6304. https://doi.org/10.1038/s41598-020-62432-x

Zhang, Z., Zhang, L., Yue, S., Wu, J., & Guo, F. (2023). Correction of nonstationary tidal prediction using deep-learning neural network models in tidal estuaries and rivers. *Journal of Hydrology*, 622, 129686. https://doi.org/10.1016/j.jhydrol.2023.129686

Zhou, J., Chen, L., Hu, T., Lu, H., Shi, Y., & Chen, L. (2025). The comparative study of machine learning agent models in flood forecasting for tidal river reaches. *Scientific Reports*, 15, 19130. https://doi.org/10.1038/s41598-025-04633-w

Zounemat-Kermani, M., Matta, E., Cominola, A., Xia, X., Zhang, Q., Liang, Q., & Hinkelmann, R. (2020). Neurocomputing in surface water hydrology and hydraulics: A review of two decades retrospective, current status and future prospects. *Journal of Hydrology*, 588, 125085. https://doi.org/10.1016/j.jhydrol.2020.125085

© 2026 Dept. of Geophysics Hasanuddin University

ISSN: 2579-5821 (Print)
ISSN: 2579-5546 (Online)
URL address: http://journal.unhas.ac.id/index.php/geocelebes
DOI: 10.70561/geocelebes.v10i2.51240

Jurnal Geocelebes Vol. 10 No. 2, October 2026, 287 – 305

Analysis Distribution and Deformation Changes of Mount Dukono in 2024 using the SBAS – InSAR Method

Nova Triyani Siagian, Erlangga Ibrahim Fattah*

Department of Geophysics Engineering, Sumatera Institute of Technology, Lampung Selatan 35365, Indonesia

*Corresponding author. Email: erlangga.fattah@tg.itera.ac.id

Manuscript received: 19 May 2026; Received in revised form: 24 June 2026; Accepted: 10 August 2026

Abstract

Mount Dukono in Halmahera is one of the most active volcanoes in Indonesia, with nearly continuous eruptive activity since 1933. The high frequency of these eruptions makes the dynamics of the magmatic system complex and difficult to understand through visual observation alone. This situation limits the ability to identify changes in magma pressure, which play a crucial role in volcanic disaster mitigation. Therefore, a surface deformation-based approach is needed to quantitatively represent the volcano's internal conditions. This study employs the Small Baseline Subset Interferometric Synthetic Aperture Radar (SBAS-InSAR) method using Sentinel-1 data to analyze the spatial and temporal surface deformation of Mount Dukono throughout 2024. A total of 21 Sentinel-1 images from February 2024 to January 2025 were processed to generate interferograms, unwrapped phase, cumulative deformation (LOS), and deformation time series. The SBAS-InSAR method successfully mapped surface deformation of Mount Dukono during the period from February 2024 to January 2025. The analysis results show that surface deformation ranged from approximately −30 mm to +25 mm along the line of sight (LOS), with a tendency toward uplift in the central to northeastern sectors of the volcanic edifice. Time series analysis indicates a correlation between deformation and eruption activity, where increased eruption activity tends to occur during the uplift phase of deformation. These deformation characteristics suggest changes in pressure within the magmatic system and demonstrate the potential of the SBAS-InSAR method to support the continuous monitoring of volcanic deformation at Mount Dukono.

Keywords: Deformation; Magmatic uplift; Mount Dukono; SBAS-InSAR; Sentinel-1.

Citation: Siagian, N. T., & Fattah, E. I. (2026). Analysis Distribution and Deformation Changes of Mount Dukono in 2024 using the SBAS – InSAR Method. *Jurnal Geocelebes*, 10(2): 287–305, doi: 10.70561/geocelebes.v10i2.51240

Introduction

Mount Dukono is one of the most active volcanoes in Indonesia. That showing in Figure 1, Mount Dukono located in North Halmahera, North Maluku, with nearly continuous eruptive activity since 1933 (Smithsonian Institution Global Volcanism Program (GVP), 2025). This persistent activity makes Mount Dukono a volcanic system with complex magmatic dynamics, so it is difficult to understand solely through visual observations at the surface. In the context of disaster mitigation, the limited understanding of changes in magma pressure is an important issue because it is directly related to the ability to identify potential increases in volcanic activity earlier.

In geophysical terms, the dynamics of this magmatic system can be represented through surface deformation in the form of uplift and subsidence, which reflect changes in pressure within the magma reservoir (Segall, 2010). Therefore, deformation analysis is a crucial approach for understanding the internal conditions of active volcanoes.

Various methods have been used to monitor surface deformation, such as GPS, EDM,

© 2026 Dept. of Geophysics Hasanuddin University

and leveling, which offer high precision but are spatially limited and difficult to apply in areas with complex geographical conditions. As an alternative, Interferometric Synthetic Aperture Radar (InSAR) technology, specifically the Small Baseline Subset (SBAS-InSAR) method, enables high-precision spatial and temporal deformation analysis and can mitigate decorrelation effects in multi-temporal data (Yunjun et al., 2019). This method has been successfully applied to various active volcanoes worldwide to identify magma pressure dynamics and magmatic fluid migration (Biggs et al., 2026; Pepe & Calò, 2017).

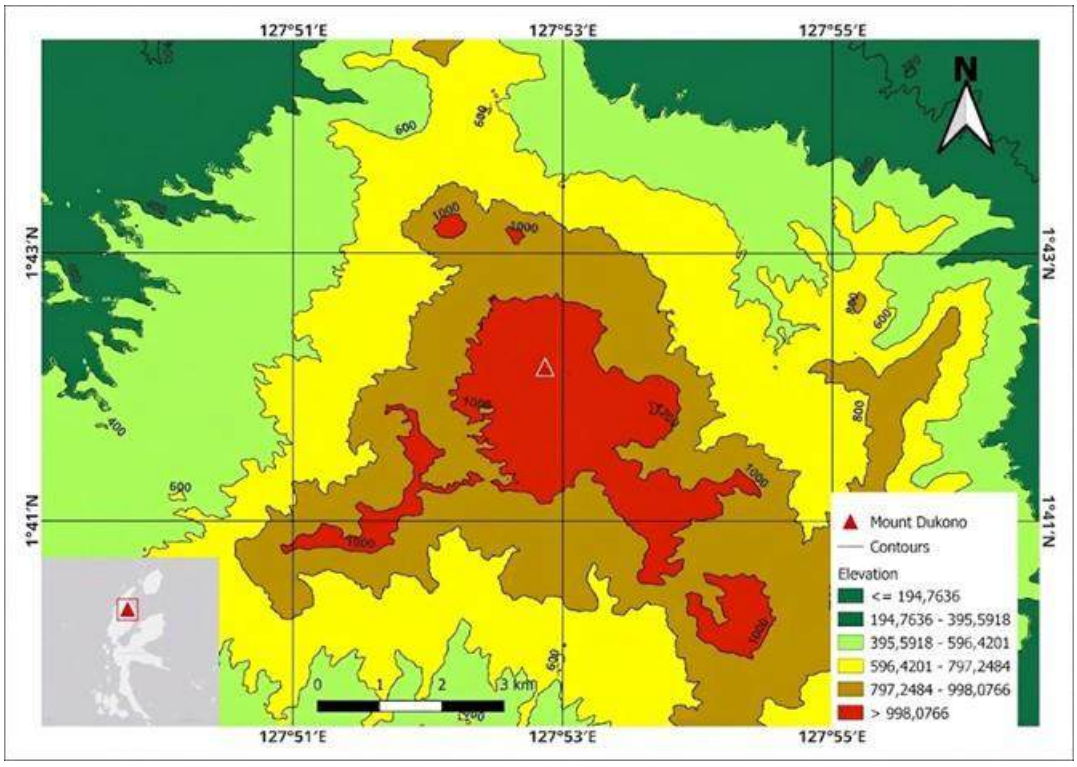


Figure 1. Research location.

Nevertheless, the deformation characteristics of each volcano cannot be generalized because they are strongly influenced by local geological conditions and the evolving magmatic system (Ebmeier et al., 2018).

At Mount Dukono, previous research has identified deformation patterns for the 2021–2023 period using the SBAS - InSAR method and demonstrated a shift from a subsidence phase to an uplift phase (Adiwijaya et al., 2025). However, the evolution of deformation during the 2024 period, which coincided with persistent eruptive activity, has not yet been studied in detail. Additionally, the correlation between surface deformation, volcanic seismic activity, and eruptive activity has not yet been analyzed in an integrated manner, so understanding of the dynamics of Mount Dukono's magmatic system remains limited.

Based on these conditions, this study aims to analyze the spatial distribution and temporal evolution of surface deformation at Mount Dukono during February 2024–January 2025 using the SBAS-InSAR method based on Sentinel-1 data. This study also correlates deformation results with seismic and eruption activity data to examine the correlation between changes in deformation and volcanic activity and to gain a more comprehensive understanding of the dynamics of Mount Dukono's magmatic system. The results of this study are expected to provide information

© 2026 Dept. of Geophysics Hasanuddin University

regarding the potential of deformation as an indicator of changes in volcanic activity and to support the development of remote sensing-based volcano monitoring for disaster mitigation.

Materials and Methods

Method

The Halmahera region is a complex tectonic system formed by the convergent interaction of the Pacific, Philippine, and Eurasian plates, resulting in an active double volcanic arc. Subduction activity in this region has created crustal deformation, fault systems, and fractures that play a role in controlling the migration of magma toward the surface. In geological terms, this region is dominated by basaltic–andesitic volcanic rocks and pyroclastic deposits, reflecting complex magma evolution and the influence of geological structures on volcanic activity.

The data used consists of Sentinel-1A Level-1 Single Look Complex (SLC) data obtained from the Alaska Satellite Facility (ASF) in GeoTIFF format. The data were acquired using the Interferometric Wide Swath (IW) mode with VV polarization and descending orbits during the period from February 2024 to January 2025, comprising a total of 21 images. The temporal and perpendicular baseline network of the selected image pairs is shown in Figure 2.

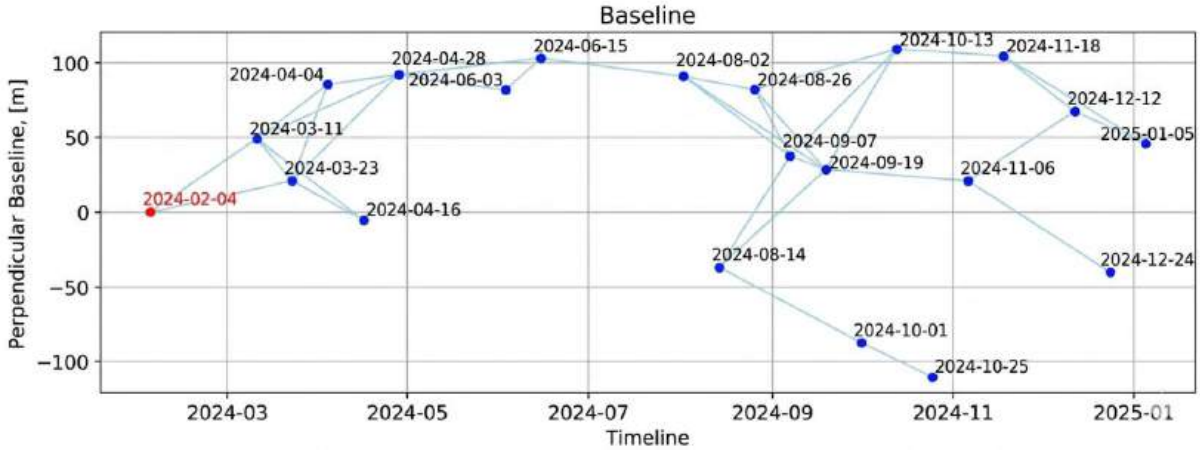


Figure 2. Temporal baseline and Perpendicular baseline pairs in the SBAS-InSAR interferogram

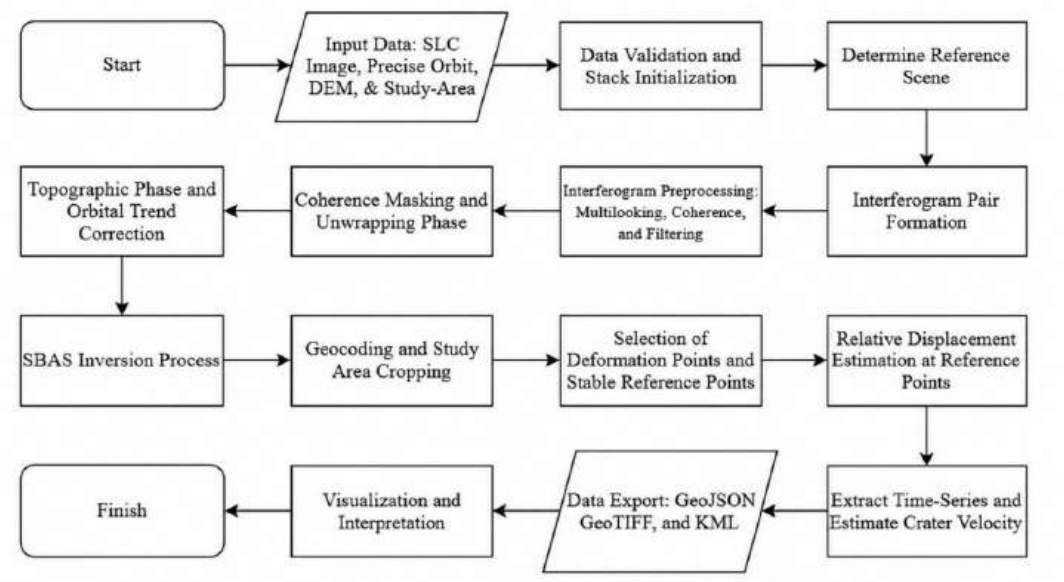


Figure 3. Workflow processing Sentinel-1 data using the SBAS-IN SAR method.

© 2026 Dept. of Geophysics Hasanuddin University

The selection of Sentinel-1 and the orbital direction was based on high temporal resolution and continuous data availability, enabling the creation of a stable interferogram network for multi-temporal deformation analysis using the processing workflow shown in Figure 3. Additionally, a 30-meter resolution Copernicus Digital Elevation Model (DEM) was used for topographic correction.

The crater of Mount Dukono, located at coordinates 127.877182° E and 1.698985° N, were used as the main observation target, while reference points for deformation estimation were selected in stable areas. Data processing was performed using the GMTSAR-based Python library on the Google Colab platform.

Data processing was performed using the SBAS-InSAR method to analyze multi-temporal surface deformation on Mount Dukono, with a coverage area corresponding to the Sentinel-1 footprint and a grid resolution of approximately 100 m. The data used consisted of co-registered Sentinel-1 SLC images, with interferogram grids formed using a 48-day temporal baseline and an 80 m perpendicular baseline to maintain coherence and minimize decorrelation in multi-temporal radar data. Based on these criteria, an interferogram network was generated as shown in Figure 2, which provides sufficient temporal connectivity for SBAS time-series analysis.

The interferometry process includes topographic correction using a DEM, filtering with the Goldstein method to reduce noise with a wavelength of 60 km to eliminate large-scale regional variations while preserving local deformation signals associated with volcanic activity (Goldstein & Werner, 1998), and phase unwrapping using SNAPHU to eliminate 2π phase ambiguities and produce a continuous phase distribution. The multi-looking technique is performed with a target surface resolution of approximately 400 m and a smoothing factor of 1.4, resulting in larger, more homogeneous pixels that reduce speckle noise while preserving the deformation signal.

Data quality selection was performed using a coherence threshold of 0.75 to retain reliable pixels for deformation analysis (Chaussard et al., 2013). The relatively low coherence observed in some parts of the study area is influenced by dense vegetation cover, high rainfall, frequent changes in surface moisture, and persistent volcanic activity, which generally cause temporal decorrelation under tropical environmental conditions.

No explicit atmospheric correction was applied in this study. However, the multi-temporal SBAS approach helps reduce the influence of temporally uncorrelated atmospheric signals through the integration of multiple interferograms and time-series inversion. As a result, part of the atmospheric contribution is expected to be suppressed in the final deformation estimates, although residual atmospheric artifacts may still remain.

To ensure representative deformation results, reference points were selected in relatively stable areas with cumulative deformation criteria approaching zero ($|LOS| < 2$ mm) and high coherence values (> 0.6). The selected reference areas were assumed to remain stable during the observation period and were located outside the main deformation zones to minimize bias in relative deformation estimates. Subsequently, SBAS inversion was performed to obtain deformation along the LOS in the form of cumulative deformation and time series, which were used for spatial and temporal analysis of magmatic system dynamics.

Principles of SAR Interferometry

© 2026 Dept. of Geophysics Hasanuddin University

Interferometric Synthetic Aperture Radar (InSAR) is a remote sensing technique used to measure changes in the distance between the sensor and the Earth's surface based on differences in radar wave phase. The phase interferogram is obtained from the phase difference between two SAR images (Dogru et al., 2023):

$$\Delta\phi = \phi_2 - \phi_1 \quad (1)$$

where $\Delta\phi$ is the interferogram phase, ϕ_1 and ϕ_2 are the phases of the SAR images at different times. The interferogram phase correction consists of several components that can be represented as (Dogru et al., 2023):

$$\Delta\phi = \Delta\phi_{def} + \Delta\phi_{topo} + \Delta\phi_{atm} + \Delta\phi_{orbit} + \Delta\phi_{noise} \quad (2)$$

where each component represents the correction of deformation, topography, atmosphere, orbit, and noise. The separation of these components forms the basis for deformation analysis using the InSAR technique.

Principles of the Small Baseline Subset (SBAS-InSAR) Method

The Small Baseline Subset (SBAS-InSAR) method is a multi-temporal InSAR technique that uses image pairs with a small baseline to maintain coherence and improve the stability of deformation estimates and also been demonstrated through automated processing frameworks developed for large-scale deformation monitoring (Lazeckỳ et al., 2020). The connection between the interferogram phase and deformation can be expressed as (Manunta et al., 2019):

$$\Delta\phi_i = \frac{4\pi}{\lambda}[d(t_{k+1}) - d(t_k)] + \varepsilon_i \quad (3)$$

with $\Delta\phi_i$ as the interferogram phase, $d(t_k)$ as the phase at a specific time, and ε as the measurement error. The resulting interferogram pattern allows for the reconstruction of deformation as a function of time through a system of linear equations.

The Relation Between Phase and Deformation

Radar phase changes are directly related to distance changes between the satellite sensor and the Earth's surface along the satellite's line of sight (LOS), as stated by (Pepe, 2021):

$$\Delta d = \frac{4\pi}{\lambda}\,\Delta\phi \quad (4)$$

which is Δd the LOS deformation, λ is the radar wavelength, For Sentinel-1 (λ ≈ 5.6 cm), a phase change of 2π corresponds to a distance change of approximately 2.8 cm.

Inversion and Time Series of Deformation

Deformation reconstruction is performed by inverting a system of equations using the least squares method or Singular Value Decomposition (SVD) (Pepe, 2021):

$$A \cdot x = \Delta\phi \quad (5)$$

which is A the time of matrix, x is the deformation vector, and $\Delta\phi$ is the interferogram phase vector. The results of the inversion are the cumulative deformation and the deformation time series.

Results and Discussion

Result

Surface deformation data processing was performed using the SBAS-InSAR method with 21 Sentinel-1 images from February 2024 to January 2025. The main parameters used include a 100 m resolution, a 48-day temporal baseline, an 80 m spatial baseline, and a coherence threshold of 0.75, which is adjusted for tropical conditions to maintain signal quality.

The processing results consist of deformations along the Line of Sight (LOS), represented as cumulative deformation and deformation time series to illustrate spatial and temporal changes in deformation. Deformation visualization uses a color scheme, where yellow–red indicates uplift, while green–blue indicates

© 2026 Dept. of Geophysics Hasanuddin University

subsidence or deformation approaching zero.

Unwrapped Phase

An interferogram is the initial result of the interferometry process, depicting the phase difference between two SAR images taken at different times. The phase patterns in the interferogram are still a combination of deformation, topography, atmospheric effects, and noise, so they cannot be directly interpreted as surface deformation. Therefore, phase unwrapping is performed to eliminate 2π phase ambiguities and produce a continuous phase that can be converted into deformation along the Line of Sight (LOS).

The unwrapped phase results in Figure 4 show a more structured deformation distribution compared to the raw interferogram, enabling clearer spatial analysis. Generally, deformation tends to be positive (relative uplift) in the central to northeastern sectors of Mount Dukono, with approximately from +5 mm to +15 mm. In contrast the northwestern sector shows small deformation with an irregular pattern, generally ranging from -5 mm to +5 mm, indicating a stronger influence of noise and lower coherence.

This difference reflects variations in coherence quality, where areas with clearer patterns have better signal quality. Nevertheless, the unwrapped phase results still contain noise and represent only specific interferogram pairs, so the deformation patterns obtained are indicative and not yet temporally integrated. Therefore, the interpretation of deformation at this stage requires confirmation through cumulative LOS and time-series analysis.

Cumulative LOS

Cumulative LOS is the result of integrating interferograms within the SBAS-InSAR framework, representing the total surface deformation over the observation period consequently, it is more stable than the unwrapped phase, which is still based on image pairs. The results in Figure 5. indicate that deformation of Mount Dukono generally has a small magnitude, with cumulative LOS values ranging from approximately −30 mm to +25 mm. Most areas show limited deformation, generally between −10 mm and +10 mm throughout the observation period.

Nevertheless, there is a relative uplift trend in the central to northeastern sectors that consistently emerges as a deformation zone, with cumulative uplift values reaching approximately +15 mm to +25 mm. The deformation pattern in the cumulative LOS appears clearer and more stable compared to the unwrapped phase, suggesting that the multi-temporal approach may reduce part of the interferometric noise and enhance the consistency of the deformation signal.

Conversely, the northwest sector shows relatively small to near-zero deformation, generally ranging from approximately -5 mm to -15 mm with a less stable pattern indicating the influence of low coherence and noise dominance. However, the consistency of patterns between the unwrapped phase and cumulative LOS suggests that part of the detected signal may represent gradual surface changes rather than isolated interferometric artifacts. Nevertheless, the observed deformation pattern should be interpreted with caution because several areas are still affected by low coherence and residual noise, which may influence the reliability of the deformation estimates.

© 2026 Dept. of Geophysics Hasanuddin University

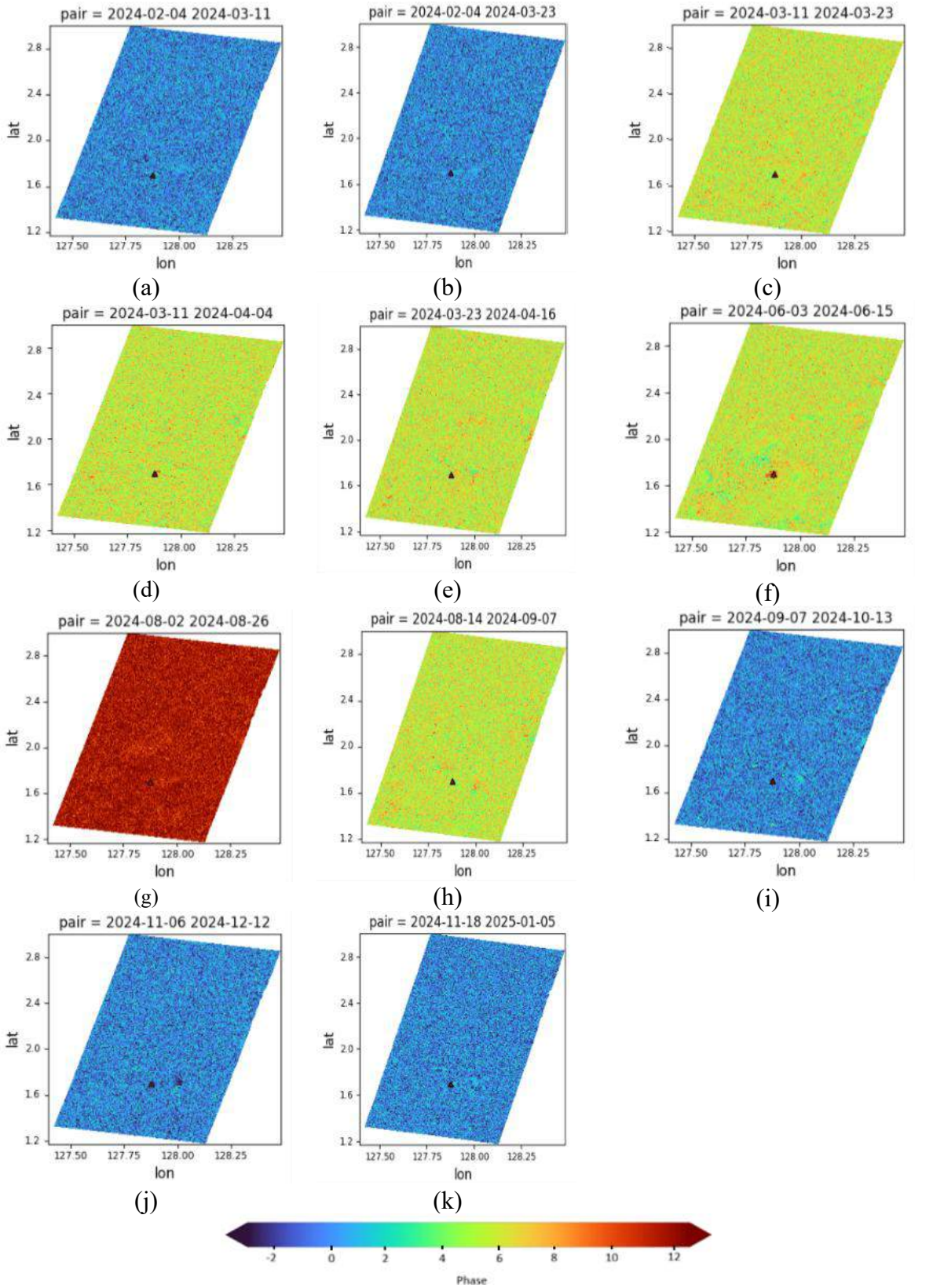


Figure 4. Results of the Unwrapped Phase with relatively clearer deformation patterns in ((c), (d), (e), (f), and (h)).

© 2026 Dept. of Geophysics Hasanuddin University

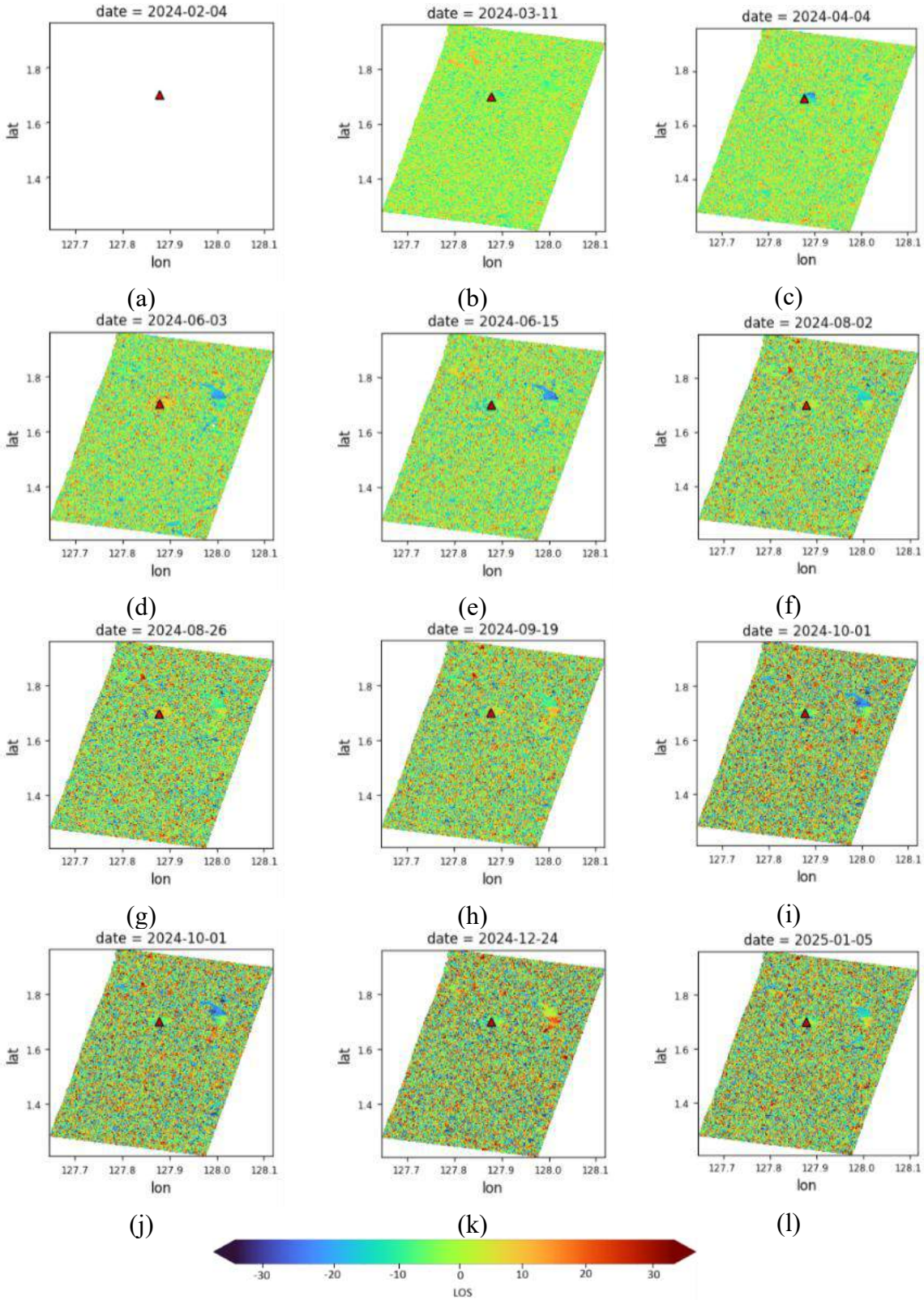


Figure 5. Results of Cumulative LOS with the phase of increasing deformation marked by the appearance of more contrasting value variations in (g), (h), (i), and (j)).

© 2026 Dept. of Geophysics Hasanuddin University

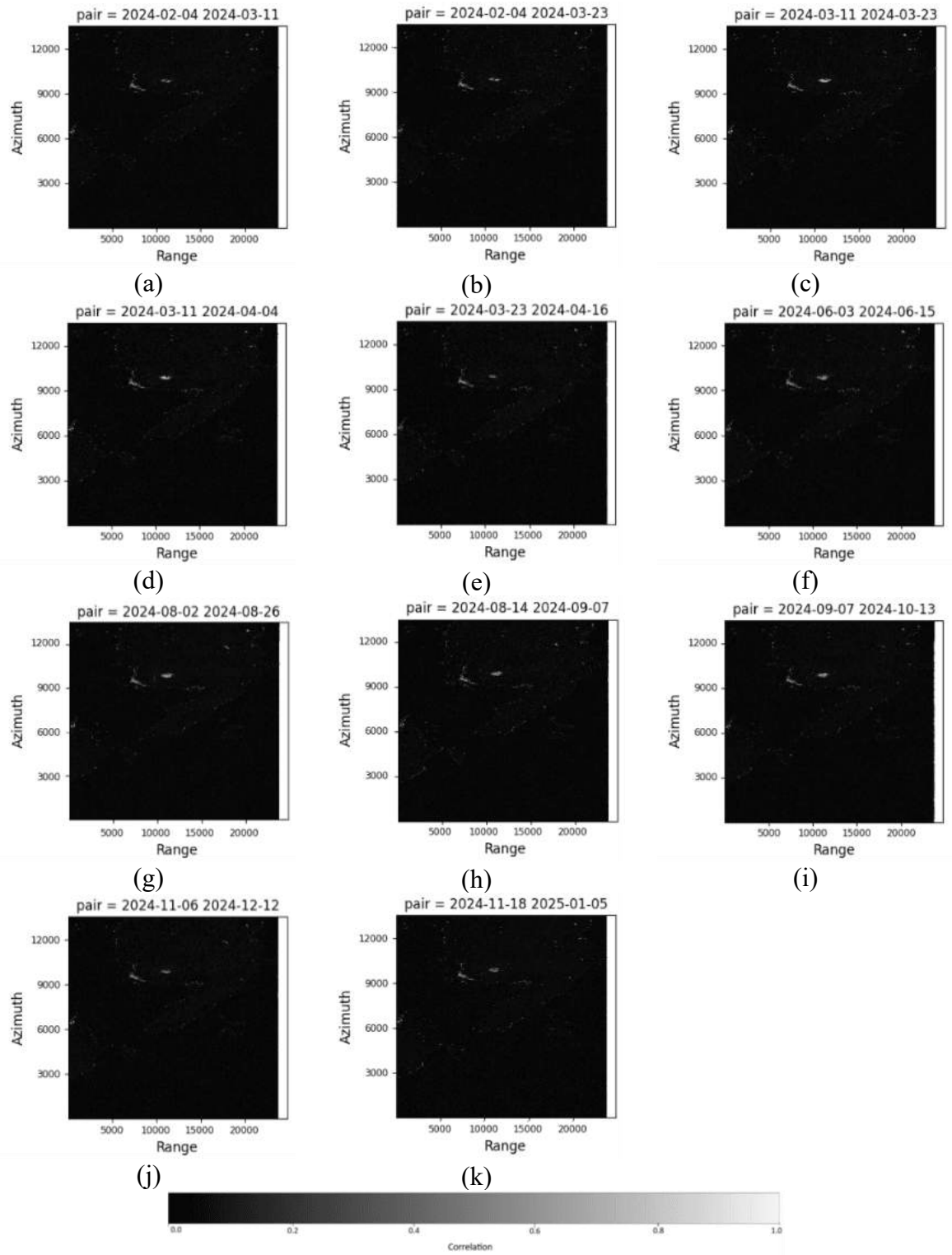


Figure 6. Coherence results with relatively phase of locally increasing coherence that begins to show signal stability in ((c), (d), (e), (f), and (h)).

Validation of Results for Coherence

Validation of the deformation results in Figure 6 was performed through interferogram coherence analysis as an indicator of InSAR data quality. The coherence value reflects the degree of signal alignment between images with higher values indicating more reliable deformation results. The results show that coherence in the Mount Dukono region is generally low to moderate due to the influence of dense vegetation, continuous

© 2026 Dept. of Geophysics Hasanuddin University

eruptive activity, and dynamic tropical atmospheric conditions, which cause temporal decorrelation. Frequent rainfall, variations in surface moisture, vegetation growth, and continuous deposition of volcanic ash can alter radar backscattering characteristics between acquisition times, thereby reducing coherence values and increasing uncertainty in deformation measurements.

Areas with higher coherence, particularly in the central to northeastern sectors exhibit clearer and more consistent deformation patterns in both the unwrapped phase and cumulative LOS. Conversely, the northwest sector with low coherence tends to be dominated by noise, making the deformation patterns difficult to interpret with confidence. Therefore, deformation interpretation is focused primarily on areas with relatively better coherence. Nevertheless, uncertainty associated with low-coherence regions should be considered when evaluating the spatial distribution of deformation.

Time Series

The time-series deformation graph in Figure 7 shows fluctuations in the surface deformation of Mount Dukono from February 2024 to January 2025 relative to the reference point. The deformation values initially tended to be positive, then decreased in the middle of the period and increased again toward the end of the period indicating a nonlinear pattern.

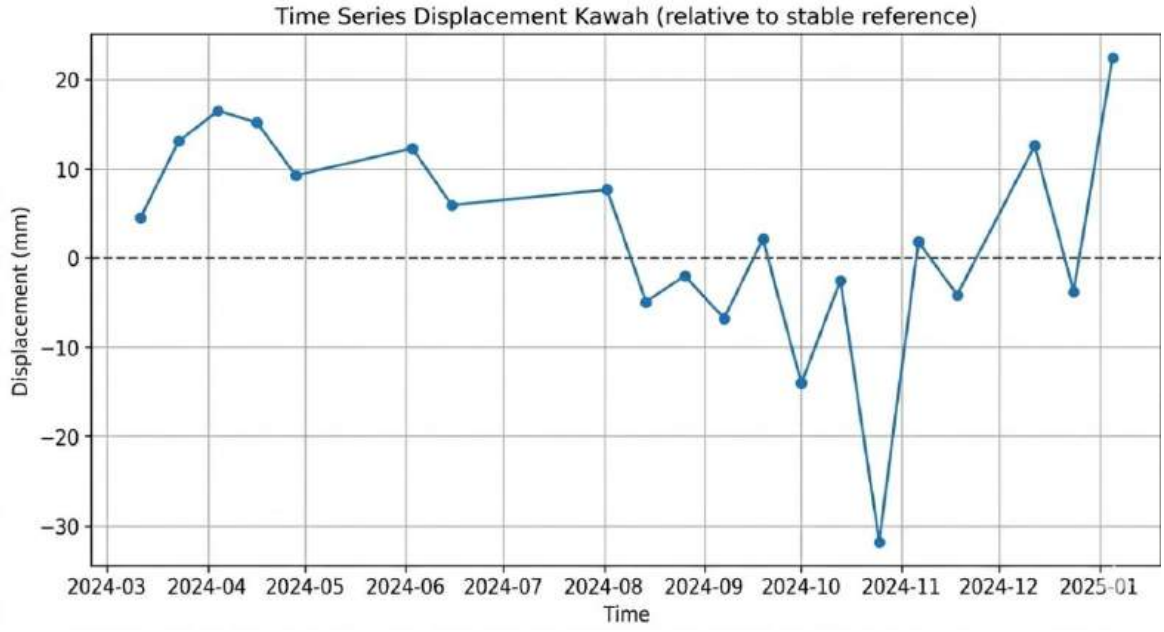


Figure 7. Time series deformation.

These fluctuations indicate that deformation does not develop consistently in a single direction but is influenced by changing dynamics, including sharp variations within specific time intervals. The observed deformation fluctuates within a range of approximately −32 mm to +23 mm throughout the observation period. However, no clear long-term upward or downward trend is observed, indicating that the deformation remains relatively small over time.

The consistency between the time series results and the cumulative LOS suggests that the detected deformation is relatively weak and gradual. However, considering the generally low-to-moderate coherence conditions in parts of the study area, the observed temporal variations should be interpreted cautiously because residual noise may contribute to some of the recorded fluctuations.

Velocity Maps

© 2026 Dept. of Geophysics Hasanuddin University

The velocity map in Figure 8 represents the annual rate of surface deformation based on the average deformation over the observation period. In general, deformation velocity values are dominated by values close to zero, which are distributed throughout the study area as indicated by the predominance of green to yellow colors on the map. This suggests that the deformation rates are relatively small and did not undergo significant changes throughout the observation period. The predominance of near-zero velocity values is consistent with the cumulative LOS results, which show deformation generally limited to approximately −30 mm to +25 mm, indicating gradual surface displacement during the observation period.

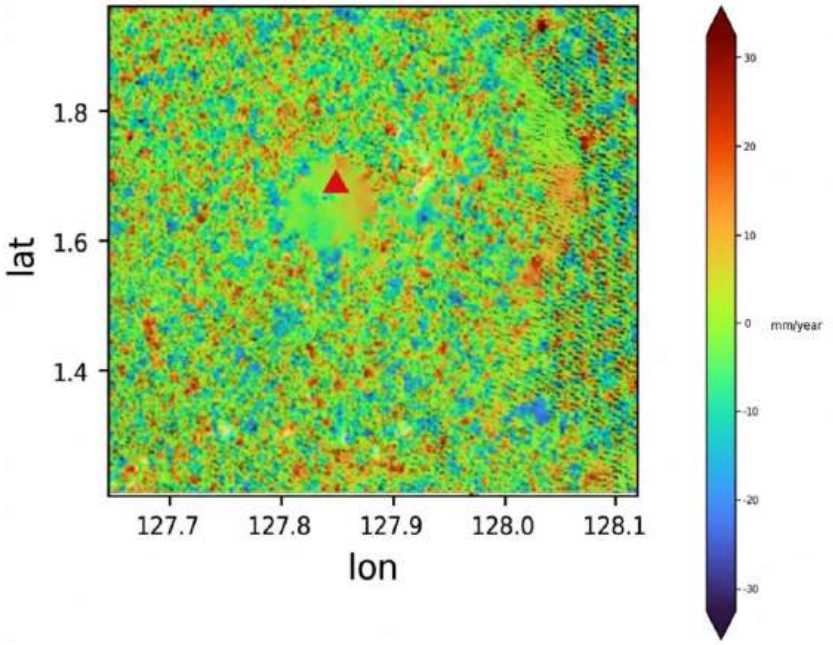


Figure 8. Velocity maps.

Although local variations in uplift and subsidence are observed, the resulting patterns appear diffuse and spatially scattered without clear concentrations of deformation. Therefore, no clearly defined spatially dominant deformation zone can be confidently identified from the velocity map. The observed variations may reflect both actual surface deformation and residual interferometric noise associated with low coherence conditions in tropical environments. Therefore, the velocity map indicates that deformation is slow, weak, and does not undergo significant acceleration, and is consistent with the results of the unwrapped phase, cumulative LOS, and time series.

Discussion

The Small Baseline Subset Interferometric Synthetic Aperture Radar (SBAS-InSAR) approach is an effective method for analyzing volcanic deformation because it can reconstruct multitemporal surface changes with high precision. This method uses a network of interferograms with small temporal and spatial baselines to maintain coherence and produce stable long-term deformation estimates (Manunta et al., 2019). The multitemporal approach also allows for the detection of small deformations that cannot be identified in a single interferogram, making it effective for monitoring pressure dynamics within complex magmatic systems (Crosetto et al., 2016; Pepe, 2021).

The other study has shown that SBAS-InSAR is capable of recording deformation trends before and after eruptions of active

© 2026 Dept. of Geophysics Hasanuddin University

volcanoes. At Mount Etna, the detected inflationary deformation was associated with shallow magma intrusions that increased reservoir pressure prior to eruption. Another study showed that deformation at Mount Etna is nonlinear and follows an inflation–deflation cycle due to the interaction between magma supply and pressure release (Cigna et al., 2019). Similar pre-eruptive deformation has also been observed at Agung Volcano, Indonesia, where high-resolution InSAR detected localized crater uplift associated with magma and hydrothermal fluid migration prior to the 2017 eruption (Bemelmans et al., 2023). At Kilauea, small changes in the deformation time series have been shown to represent changes in magma system conditions prior to eruption making deformation an important indicator of a volcano's internal dynamics (Poland & Zebker, 2022). Similar deformation behaviour prior to eruptive activity has also been documented at Agung Volcano using Sentinel-1 SBAS-InSAR time-series observations (Albino et al., 2020). In addition, deformation may reflect pressure release processes during deflationary phases and pressure increases during inflationary phases.

The application of SBAS-InSAR in tropical regions faces challenges due to low coherence caused by vegetation and atmospheric conditions. However, through multitemporal integration, this method remains capable of identifying significant deformation patterns even though their spatial distribution is diffuse and affected by noise (Chaussard et al., 2013; Gündüz et al., 2023). The atmospheric effects on the interferometric phase can also be minimized so that actual deformation remains well represented. Nevertheless, atmospheric artifacts and decorrelation effects cannot be completely eliminated and should be considered when interpreting deformation results (Kalavrezou et al., 2024).

In the context of Mount Dukono, previous research indicates that the observed deformation is generally of small magnitude, not localized, and fluctuating in nature, reflecting gradual pressure dynamics within the magmatic system (Adiwijaya et al., 2025). These characteristics are associated with Mount Dukono's activity as a volcano with an open magmatic system.

According to a PVMBG report, Mount Dukono exhibits sustained eruptive activity with relatively stable intensity and no extreme increases prior to eruption (Pusat Vulkanologi dan Mitigasi Bencana Geologi (PVMBG), 2024). In such systems, pressure may be released gradually through recurring eruptive activity, limiting the accumulation of pressure within shallow magma reservoirs.

Consequently, surface deformation is expected to remain relatively small compared with volcanoes characterized by closed magmatic systems (Sabrian et al., 2023). Differences in deformation magnitude and spatial patterns among volcanoes are strongly controlled by magma storage geometry, crustal properties, and the dynamics of magma transport (Montgomery-Brown et al., 2024). This interpretation is consistent with previous research indicating that surface deformation is one of the key parameters for identifying changes in the state of a volcanic system. Therefore, the interpretation of deformation will be more comprehensive when combined with other monitoring parameters, such as seismic activity (Biggs & Pritchard, 2017).

The deformation time series obtained in this study indicates that deformation variations occurred during the observation period, particularly between August and late October 2024, when deformation values decreased to approximately −30 mm. This decrease may represent a relative reduction in LOS displacement values during the

© 2026 Dept. of Geophysics Hasanuddin University

observation period and could be associated with changes in subsurface pressure conditions. Similar decreases have been documented in volcanic environments undergoing changes in subsurface conditions associated with degassing, cooling, crystallization, or magma migration processes (Segall, 2010). However, considering that the deformation magnitude observed in this study remains relatively small and that several sectors are characterized by low to moderate coherence, the observed decrease cannot be interpreted as direct evidence of magma reservoir contraction. Instead, it is more appropriate to regard this pattern as a possible indication of changing conditions within the volcanic system.

After reaching a minimum value, deformation rapidly shifted to positive values from November until just before the eruption. This increase may indicate a transition from a relative deflationary trend to a relative inflationary trend and could be associated with changes in subsurface pressure conditions within the volcanic system (Caricchi et al., 2021; Rinamu & Saepuloh, 2026). Similar deformation behavior has been observed in other volcanic systems and is commonly interpreted as reflecting pressure redistribution or magma migration processes (Crozier et al., 2023). However, the available InSAR observations are insufficient to confirm magma recharge directly. Therefore, the observed increase should be interpreted as a possible indication of evolving volcanic conditions rather than conclusive evidence of new magma intrusion. This pattern suggests that the magmatic system of Mount Dukono may have undergone temporal variations in pressure conditions during the observation period, although the underlying processes cannot be determined with certainty from the available dataset.

In the lead-up to the eruption on December 24, 2024, deformation showed fluctuations characterized by a rapid shift from negative to positive values. These observations indicate that the volcanic system underwent dynamic variations over time during the final months of the observation period. The deformation pattern does not show a clear long-term trend or significant acceleration, consistent with LOS results and cumulative velocity, which indicate relatively weak and spatially dispersed deformation. Nevertheless, the occurrence of pronounced fluctuations suggests that measurable changes are taking place within the volcanic system during the same period.

Deformation patterns in Figure 9 showing characterized by a decrease followed by an increase in displacement prior to eruptive activity have been reported in various volcanic systems (Reath et al., 2019). Similar temporal pattern was observed at Mount Dukono, where deformation data show a transition from lower to higher displacement values prior to the December 2024 eruption. Although this pattern is consistent with conceptual models of volcanic deformation associated with changes in subsurface pressure conditions, available observations are insufficient to confirm specific magmatic processes. However, the temporal correlation between deformation changes and volcanic activity suggests that the observed deformation likely reflects evolving conditions within the volcanic system.

Unlike volcanoes with closed magmatic systems, deformation at Mount Dukono did not develop into significant inflation. This behavior is consistent with an open volcanic system interpretation, where pressure may be released continuously through repeated eruptive activity. Consequently, pressure variations may occur without generating large-amplitude deformation signals, causing surface deformation to remain relatively small despite ongoing volcanic activity. This interpretation is consistent with the small deformation magnitudes, weak velocity

© 2026 Dept. of Geophysics Hasanuddin University

patterns, and scattered spatial distribution observed in this study.

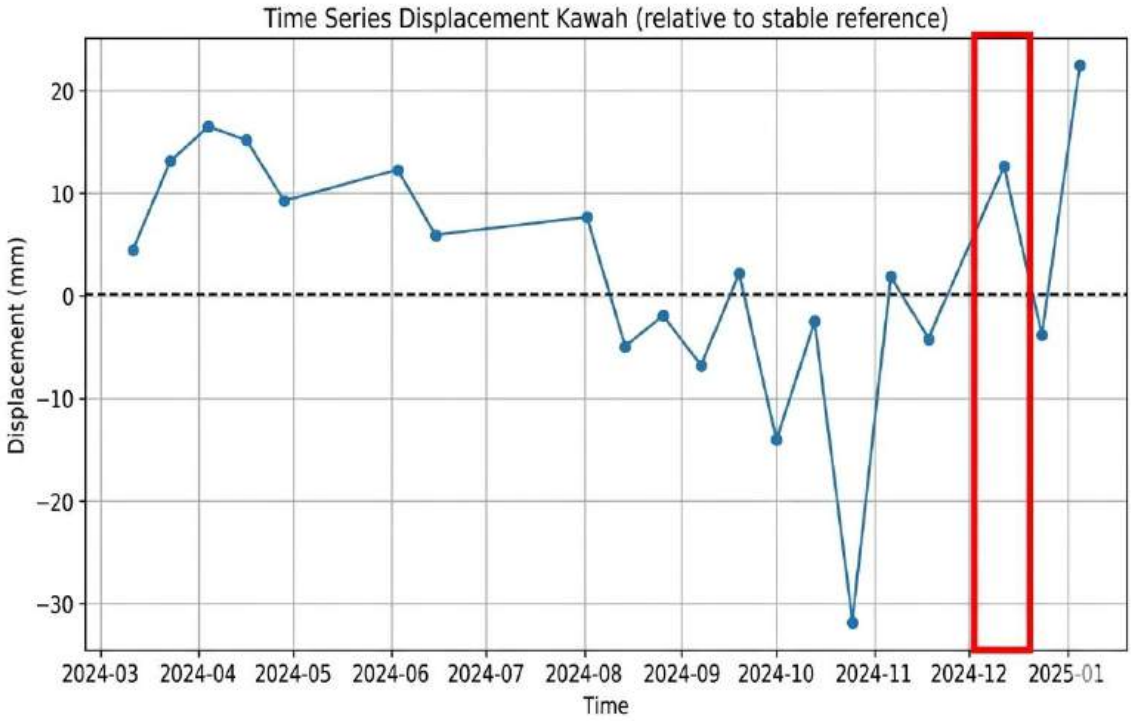


Figure 9. Time series plot with eruption times during the observation period.

The seismicity data used in this study were obtained from daily volcanic activity reports published by PVMBG during February 2024–January 2025. Earthquake events were classified according to the PVMBG classification system and compiled into monthly event frequencies. The seismic dataset was temporally aligned with the SBAS-InSAR deformation time series to analyze the relationship between variations in seismic activity and surface deformation during the observation period.

To support the interpretation of deformation derived from time-series analysis, earthquake event data were analyzed using temporal histograms in Figure 10. The histogram results indicate that most of the observation period was characterized by a relatively low number of earthquake events. This implies that seismic activity generally remained at a low level and did not show a sustained increase throughout the observation period.

Additional information was obtained from the occurrence of Volcanic-Tectonic A (VTA) earthquakes during several intervals. VTA earthquakes are generally associated with rock fracturing processes caused by stress changes within the volcanic system and are frequently observed during periods of volcanic instability. The increase in VTA earthquake frequency toward the end of 2024 indicates that volcanic activity remained active during the same period when deformation changes were observed.

The temporal consistency between the increase in VTA activity and the observed deformation variations reinforces the interpretation that Mount Dukono was experiencing evolving subsurface conditions by the end of 2024. The consistency among these independent observations increases confidence that the deformation patterns identified by SBAS-InSAR analysis reflect actual volcanic processes, rather than merely the result of measurement noise or processing artifacts.

© 2026 Dept. of Geophysics Hasanuddin University

However, the available dataset does not allow for the direct determination of the specific magmatic mechanisms responsible for these observations.

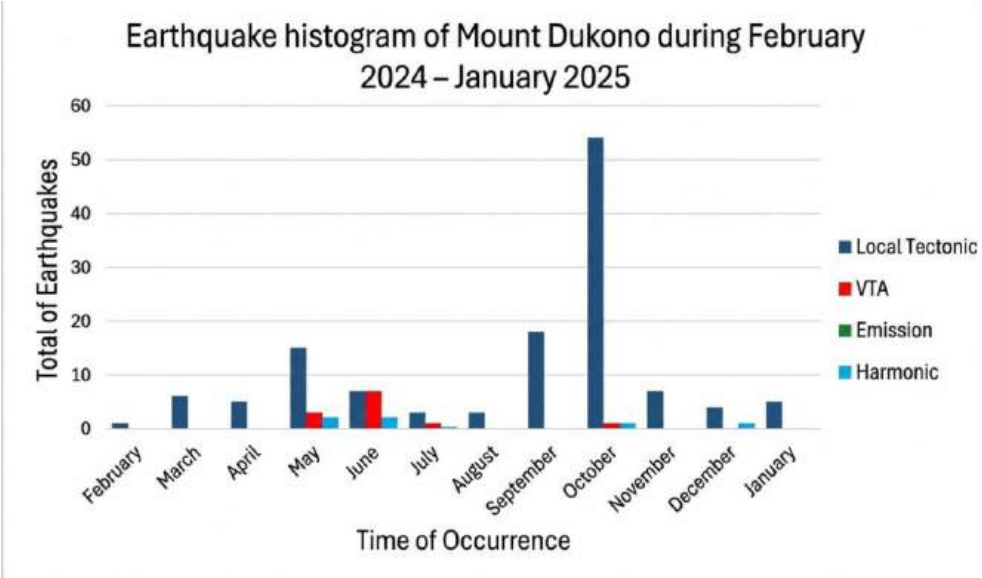


Figure 10. Earthquake Histogram of Mount Dukono from February 2024 to January 2025.

The combination of fluctuating deformation and the occurrence of VTA earthquakes indicates that Mount Dukono remained dynamically active throughout the observation period. The observed deformation patterns, characterized by relatively small magnitudes and a dispersed spatial distribution, are also consistent with the behavior of an open volcanic system where pressure may be released repeatedly through persistent eruptive activity.

Overall, the deformation anomalies identified in this study indicate that Mount Dukono experienced measurable temporal variations in surface deformation during 2024. Decreases followed by increases in deformation values, along with the occurrence of VTA earthquakes prior to eruptions, suggest changes within the volcanic system consistent with variations in subsurface pressure conditions. Although the relatively small magnitude of deformation and low-to-moderate coherence limit the level of certainty that can be achieved, the temporal alignment between deformation, seismic activity, and eruptive activity suggests that the observed deformation likely reflects actual volcanic processes occurring within the magmatic system of Mount Dukono during the period leading up to the 24 December 2024 eruption.

The results of this study show that the SBAS-InSAR method is capable of detecting small-magnitude surface deformation associated with temporal variations in volcanic activity, even though coherence conditions in tropical environments are relatively low (Dogru et al., 2023). The temporal consistency between changes in deformation, the occurrence of VTA earthquakes, and eruptive activity suggests that the deformation data obtained can provide insight into changes in the state of the volcanic system.

Therefore, SBAS-based deformation results -InSAR can provide valuable information for monitoring volcanic activity and offer a more comprehensive understanding of subsurface dynamics when interpreted in conjunction with seismic data, in line with operational volcanic monitoring approaches that integrate deformation products derived from InSAR with seismic observations to improve the quality of interpretation (Poland & Zebker, 2022; Wei et al., 2024).

© 2026 Dept. of Geophysics Hasanuddin University

Conclusion

The main issue in this study is the lack of identification of the spatial and temporal characteristics of surface deformation at Mount Dukono, meaning that the interpretation of magmatic activity remains limited when based solely on visual observations. To address this, a Sentinel-1-based SBAS-InSAR method was employed, capable of detecting multi-temporal deformation with high sensitivity to small changes.

The results of the study indicate that surface deformation has a small magnitude with a scattered distribution and a fluctuating temporal pattern, showing no significant long-term deformation trends or acceleration. The observed deformation characteristics indicate that Mount Dukono experienced relatively smooth surface displacement changes during the observation period, consistent with the behavior of an active volcanic system characterized by continuous eruptive activity (Camejo-Harry et al., 2023; Hanif et al., 2024).

The temporal consistency between deformation variations, the occurrence of VTA earthquakes, and eruptive activity indicates that the detected deformation reflects ongoing volcanic processes at Mount Dukono. These findings demonstrate that the SBAS-InSAR method is capable of detecting small deformation signals in tropical volcanic environments and provides valuable information for monitoring volcanic activity. When interpreted in conjunction with seismic data, these deformation results provide a more comprehensive understanding of the temporal evolution of the magmatic system and the dynamics of volcanic activity at Mount Dukono.

Acknowledgements

The author would like to express sincere gratitude to all parties who contributed to this research. Special appreciation is given to the academic supervisors for their guidance and constructive suggestions throughout the research process. The author also acknowledges the Alaska Satellite Facility (ASF) for providing Sentinel-1 data and the Center for Volcanology and Geological Hazard Mitigation (PVMBG) for supporting volcanic activity data.

Author Contribution

Nova Triyani Siagian contributed to conceptualization, methodology, data processing, formal analysis, visualization, and writing of the original draft. Erlangga Ibrahim Fattah contributed to supervision, validation, interpretation of results, and review and editing of the manuscript.

Conflict of Interest

The authors declare that there are no conflicts of interest, either financial or personal that could influence the conduct of the research, data analysis, interpretation of results, or the preparation and publication of this article.

References

Adiwijaya, R. F., Kriswati, E., & Rafli, M. F. (2025). Deformation of Mt Dukono in 2021-2024 from InSAR Observation. *IOP Conference Series: Earth and Environmental Science*, 1551(1), 012023. https://doi.org/10.1088/1755-1315/1551/1/012023

Albino, F., Biggs, J., Yu, C., & Li, Z. (2020). Automated Methods for Detecting Volcanic Deformation Using Sentinel-1 InSAR Time Series Illustrated by the 2017–2018 Unrest at Agung, Indonesia. *Journal of Geophysical Research: Solid Earth*, 125(2), e2019JB017908. https://doi.org/10.1029/2019JB017908

Bemelmans, M. J. W., Biggs, J., Poland, M., Wookey, J., Ebmeier, S. K.,

© 2026 Dept. of Geophysics Hasanuddin University

Diefenbach, A. K., & Syahbana, D. (2023). High-Resolution InSAR Reveals Localized Pre-Eruptive Deformation Inside the Crater of Agung Volcano, Indonesia. *Journal of Geophysical Research: Solid Earth*, 128(5), e2022JB025669. https://doi.org/10.1029/2022JB025669

Biggs, J., & Pritchard, M. E. (2017). Global Volcano Monitoring: What Does It Mean When Volcanoes Deform?. *Elements*, 13(1). 17–22. https://doi.org/10.2113/gselements.13.1.17

Biggs, J., Anantrasirichai, N., Anderson, K. R., Cayol, V., Dualeh, E. W., Dumont, Q., Ebmeier, S. K., Froger, J. L., Gaddes, M., Galetto, F., Gonzalez, P. J., Hamling, I., Hooper, A., Lazecky, M., Lizama, C. N., & Pritchard, M. E. (2026). Advances in volcano monitoring driven by the first decade of Sentinel-1 observations. *Remote Sensing of Environment*, 339, 115377. https://doi.org/10.1016/j.rse.2026.115377

Camejo-Harry, M., Pascal, K., Euillades, P., Grandin, R., Hamling, I., Euillades, L., Contreras-Arratia, R., Ryan, G. A., Latchman, J. L., Lynch, L., & Jo, M. (2023). Monitoring volcano deformation at La Soufrière, St Vincent during the 2020–21 eruption with insights into its magma plumbing system architecture. In: R.E.A. Robertson, E.P. Joseph, J. Barclay, and R.S.J. Sparks. *The 2020–21 Eruption of La Soufrière Volcano, St Vincent*. *Geological Society of London*. Collection. https://doi.org/10.1144/SP539-2022-270

Caricchi, L., Townsend, M., Rivalta, E., & Namiki, A. (2021). The build-up and triggers of volcanic eruptions. In *Nature Reviews Earth and Environment,* 2(7), 458–476. https://doi.org/10.1038/s43017-021-00174-8

Chaussard, E., Amelung, F., & Aoki, Y. (2013). Characterization of open and closed volcanic systems in Indonesia and Mexico using InSAR time series. *Journal of Geophysical Research: Solid Earth*, 118(8), 3957–3969. https://doi.org/10.1002/jgrb.50288

Cigna, F., Tapete, D., Garduño-Monroy, V. H., Muñiz-Jauregui, J. A., García-Hernández, O. H., & Jiménez-Haro, A. (2019). Wide-Area InSAR Survey of Surface Deformation in Urban Areas and Geothermal Fields in the Eastern Trans-Mexican Volcanic Belt, Mexico. *Remote Sensing*, 11(20), 2341. https://doi.org/10.3390/rs11202341

Crosetto, M., Monserrat, O., Cuevas-González, M., Devanthéry, N., & Crippa, B. (2016). Persistent Scatterer Interferometry: A review. *ISPRS Journal of Photogrammetry and Remote Sensing*, 115, 78–89. https://doi.org/10.1016/j.isprsjprs.2015.10.011

Crozier, J., Karlstrom, L., Montgomery-Brown, E., Angarita, M., Cayol, V., Bato, M. G., Wang, T. A., Grapenthin, R., Shreve, T., Anderson, K., Astort, A., Bodart, O., Cannavò, F., Currenti, G., Dabaghi, F., Erickson, B. A., Garg, D., Head, M., Iozzia, A., Kim, Y. C., Le Mével, H., Lizama, C. N., Rucker, C., Silverii, F., Trasatti, E., & Zhan, Y. (2023). Understanding the drivers of volcano deformation through geodetic model verification and validation. *Bulletin of Volcanology*, 85, 74. https://doi.org/10.1007/s00445-023-01687-4

Dogru, F., Albino, F., & Biggs, J. (2023). Weather model based atmospheric corrections of Sentinel-1 InSAR deformation data at Turkish volcanoes. *Geophysical Journal International*, 234(1), 280–296. https://doi.org/10.1093/gji/ggad070

Ebmeier, S. K., Andrews, B. J., Araya, M. C., Arnold, D. W. D., Biggs, J., Cooper, C., Cottrell, E., Furtney, M.,

© 2026 Dept. of Geophysics Hasanuddin University

Hickey, J., Jay, J., Lloyd, R., Parker, A. L., Pritchard, M. E., Robertson, E., Venzke, E., & Williamson, J. L. (2018). Synthesis of global satellite observations of magmatic and volcanic deformation: implications for volcano monitoring & the lateral extent of magmatic domains. *Journal of Applied Volcanology*, 7, 2. https://doi.org/10.1186/s13617-018-0071-3

Goldstein, R. M., & Werner, C. L. (1998). Radar interferogram filtering for geophysical applications. *Geophysical Research Letters*, 25(21), 4035–4038. https://doi.org/10.1029/1998GL900033

Gündüz, H. İ., Yılmaztürk, F., & Orhan, O. (2023). An Investigation of Volcanic Ground Deformation Using InSAR Observations at Tendürek Volcano (Turkey). *Applied Sciences (Switzerland)*, 13(11), 6787. https://doi.org/10.3390/app13116787

Hanif, M., Apichontrakul, S., & Razi, P. (2024). Multi-Temporal InSAR analysis for monitoring the ground deformation of Mount Sinabung. *Asia-Pacific Journal of Science and Technology*, 29(05), APST–29. https://doi.org/10.14456/apst.2024.83

Kalavrezou, I.-E., Castro-Melgar, I., Nika, D., Gatsios, T., Lalechos, S., & Parcharidis, I. (2024). Application of Time Series INSAR (SBAS) Method Using Sentinel-1 for Monitoring Ground Deformation of the Aegina Island (Western Edge of Hellenic Volcanic Arc), *Land*, 13(4), 485. https://doi.org/10.3390/land13040485

Lazecký, M., Spaans, K., González, P. J., Maghsoudi, Y., Morishita, Y., Albino, F., Elliott, J., Greenall, N., Hatton, E., Hooper, A., Juncu, D., McDougall, A., Walters, R. J., Watson, C. S., Weiss, J. R., & Wright, T. J. (2020). LiCSAR: An Automatic InSAR Tool for Measuring and Monitoring Tectonic and Volcanic Activity. *Remote Sensing*, 12(15), 2430. https://doi.org/10.3390/rs12152430

Manunta, M., De Luca, C., Zinno, I., Casu, F., Manzo, M., Bonano, M., Fusco, A., Pepe, A., Onorato, G., Berardino, P., De Martino, P., & Lanari, R. (2019). The Parallel SBAS Approach for Sentinel-1 Interferometric Wide Swath Deformation Time-Series Generation: Algorithm Description and Products Quality Assessment. *IEEE Transactions on Geoscience and Remote Sensing*, 57(9), 6229–6281. https://doi.org/10.1109/TGRS.2019.2904912

Montgomery-Brown, E. K., Anderson, K. R., Johanson, I. A., Poland, M. P., & Flinders, A. F. (2024). *Ground Deformation and Gravity for Volcano Monitoring*. United States Scientific Investigations Report 2024-5062, USGS Volcano Science Center. https://doi.org/10.3133/sir20245062D

Pepe, A., & Calò, F. (2017). A review of interferometric synthetic aperture RADAR (InSAR) multi-track approaches for the retrieval of Earth's Surface displacements. *Applied Sciences (Switzerland)*, 7(12), 1264. https://doi.org/10.3390/app7121264

Pepe, A. (2021). Multi-temporal small baseline interferometric sar algorithms: Error budget and theoretical performance. *Remote Sensing*, 13(4), 557. https://doi.org/10.3390/rs13040557

Poland, M. P., & Zebker, H. A. (2022). Volcano geodesy using InSAR in 2020: the past and next decades. *Bulletin of Volcanology*, 84, 27. https://doi.org/10.1007/s00445-022-01531-1

Pusat Vulkanologi dan Mitigasi Bencana Geologi (PVMBG). (2024). *Laporan Aktivitas Gunung Dukono Tahun 2024*. https://magma.esdm.go.id/v1/gunung-api/laporan-harian

Reath, K., Pritchard, M., Poland, M., Delgado, F., Carn, S., Coppola, D.,

© 2026 Dept. of Geophysics Hasanuddin University

Andrews, B., Ebmeier, S. K., Rumpf, E., Henderson, S., Baker, S., Lundgren, P., Wright, R., Biggs, J., Lopez, T., Wauthier, C., Moruzzi, S., Alcott, A., Wessels, R., Griswold, J., Ogburn, S., Loughlin, S., Meyer, F., Vaughan, G., & Bagnardi, M. (2019). Thermal, Deformation, and Degassing Remote Sensing Time Series (CE 2000–2017) at the 47 most Active Volcanoes in Latin America: Implications for Volcanic Systems. *Journal of Geophysical Research: Solid Earth*, 124(1), 195–218. https://doi.org/10.1029/2018JB016199

Rinamu, M. S. R., & Saepuloh, A. (2026). Observing Volcanic Activity at Mt. Merapi 2018-2023 with An Advanced InSAR Time – Series Method. *OPHIOLITE: Jurnal Geologi Terapan*, 7(3), 133–139. https://doi.org/10.56099/ophi.v7i3.p133-139

Sabrian, P. G., Saepuloh, A., Koike, K., Septyandy, M. R., Pratama, H. B., Kriswati, E., Haerani, N. (2024). Geostatistical multitemporal InSAR method and elastic deformation model for detailed characterizations of topographic change and magma reservoirs: Application to the Tangkuban Parahu Volcano, Indonesia. *Journal of Volcanology and Geothermal Research*, 445, 107964. https://doi.org/10.1016/j.jvolgeores.2023.107964

Smithsonian Institution Global Volcanism Program (GVP). (2025). *Dukono*. Smithsonian Institution. https://volcano.si.edu/volcano.cfm?vn=268010

Wei, L., Sun, Y., Pan, X., Liu, G., Trasatti, E., Tolomei, C., Ventura, G., Bignami, C., Ao, M., & Liu, S. (2024). Dynamics of the 2021 unrest at Changbaishan Tianchi volcano from ALOS-2/PALSAR-2 and seismic data. International Journal of Applied *Earth Observation and Geoinformation*, 128, 103775. https://doi.org/10.1016/j.jag.2024.103775

Yunjun, Z., Fattahi, H., & Amelung, F. (2019). Small baseline InSAR time series analysis: Unwrapping error correction and noise reduction. *Computers and Geosciences*, 133, 104331. https://doi.org/10.1016/j.cageo.2019.104331

© 2026 Dept. of Geophysics Hasanuddin University

ISSN: 2579-5821 (Print)
ISSN: 2579-5546 (Online)
URL address: http://journal.unhas.ac.id/index.php/geocelebes
DOI: 10.70561/geocelebes.v10i2.51982

Jurnal Geocelebes Vol. 10 No. 2, October 2026, 306 – 321

Physically Consistent Peak Ground Acceleration Prediction in Bali Using Ensemble Machine Learning

Rayhan Irfan Hielmy, Muzli*

Geophysics Department, State College of Meteorology Climatology and Geophysics (STMKG)
Tangerang City, Banten 15221, Indonesia

*Corresponding author. Email: muzli@bmkg.go.id

Manuscript received: 12 June 2026; Received in revised form: 5 August 2026; Accepted: 11 August 2026

Abstract

Bali faced significant seismic risks from the Java Trench and back-arc thrust faults, making accurate Peak Ground Acceleration (PGA) prediction crucial. While traditional empirical models struggled with complex, non-linear site effects, machine learning offered a robust alternative. This study aimed to develop and compare Random Forest and XGBoost algorithms, utilizing moment magnitude (Mw), hypocentral distance (Rhypo), and local site conditions (Vs30) as primary inputs, to predict PGA in the Bali region. The research utilized 1,000 strong-motion records from 287 earthquakes (Mw > 4.0) recorded between 2018 and 2025. Following rigorous quality control, we applied logarithmic transformations and hyperparameter optimization via Randomized Search with 3-fold cross-validation. Expanding upon our preliminary model evaluations, this comprehensive analysis demonstrated that the Random Forest architecture outperformed XGBoost by maintaining superior predictive stability, yielding a Coefficient of Determination of 0.741, a Mean Absolute Error of 0.340, and a highly constrained residual standard deviation of 0.434. Furthermore, feature importance analysis revealed that Random Forest was physically consistent with seismological principles. It correctly identified hypocentral distance as the dominant ground-motion attenuation predictor, whereas XGBoost exhibited an overfitted bias toward local site conditions. Ultimately, the Random Forest algorithm provided a highly reliable model for PGA prediction, effectively supporting the development of Probabilistic Seismic Hazard Analysis maps and rapid real-time ShakeMaps in Indonesia.

Keywords: Attenuation relationship; Ensemble learning; Hyperparameter tuning; Seismic hazard assessment; Strong-motion records.

Citation: Hielmy, R. I., & Muzli, M. (2026). Physically Consistent Peak Ground Acceleration Prediction in Bali Using Ensemble Machine Learning. *Jurnal Geocelebes*, 10(2): 306–321, doi: 10.70561/geocelebes.v10i2.51982

Introduction

Bali is a major tourism destination in Indonesia that faces high seismic risks from the Java Trench subduction zone and northern back-arc thrust faults. Accurate prediction of Peak Ground Acceleration (PGA) is essential for seismic hazard assessment because it estimates the maximum ground shaking during an earthquake. These predictions, which fundamentally depend on the rapid determination of initial earthquake parameters (Hielmy et al., 2025a), are vital for comprehensive seismic hazard assessments and rapid ShakeMap generation (Monterrubio-Velasco et al., 2024), which have traditionally relied on standard empirical Ground Motion Prediction Equations (Hielmy & Rajagukguk, 2025; Khosravikia & Clayton, 2021; Parker et al., 2022) to model regional site effects.

However, traditional GMPEs often struggle to capture complex, non-linear site effects without requiring extensive regional calibration. Recent studies show that GMPEs fail to model non-linear seismic wave attenuation, which drives the shift toward machine learning architectures like Support Vector Machines and tree-based

© 2026 Dept. of Geophysics Hasanuddin University

ensembles (Bojórquez et al., 2025; Zhu et al., 2023). Tree-based models, such as Random Forests, perform better on global datasets by capturing multidimensional predictors and overcoming the rigid assumptions of GMPEs (Somala et al., 2024; Ziar & Basari, 2025). Furthermore, compared to Support Vector Machines and the opaque nature of Artificial Neural Networks, ensemble tree architectures like Random Forest and XGBoost were specifically selected for this study because they offer superior robustness against overfitting on skewed tabular data and provide transparent feature importance metrics essential for physical validation. Therefore, Machine Learning (ML) has emerged as a powerful, data-driven alternative for modeling ground motion (Khosravikia & Clayton, 2021; Kubo et al., 2020).

Recent applications in active subduction zones, like southern Sumatra, show that ensemble algorithms can extract non-linear patterns from historical records to improve predictive accuracy (Lisa et al., 2026). Globally, tree-based ensemble models also show better performance in ground motion prediction compared to classical numerical simulations (Sun et al., 2023). Similar studies in West Java have proven the potential of ML to support early warning systems (Rachmadan et al., 2025). Despite this progress, there is still a lack of comparative studies evaluating the physical consistency and precision of algorithms like Random Forest and XGBoost for the unique site conditions (Vs30) in Bali.

Evaluating these ML algorithms against physical attenuation laws can provide a robust approach to fill this research gap. Building significantly upon our preliminary extended abstract (Hielmy & Muzli, 2026), this comprehensive manuscript introduces rigorous cross-validation and evaluates the models' strict adherence to physical wave attenuation principles. Therefore, this study aims to develop and compare Random Forest and XGBoost models to accurately predict PGA in the Bali region. The research uses 1,000 strong-motion records partitioned into a 70:30 training-testing split, applying data preprocessing, logarithmic transformations, and hyperparameter tuning; evaluating a search space of 100 to 1,000 estimators and maximum tree depths from 10 to 50 (including no limit); with a 3-fold cross-validation method. Ultimately, this study offers a reliable and physically consistent model for PGA prediction, which supports better seismic hazard assessment and resilient infrastructure planning in Indonesia.

Materials and Methods

Study Area and Geological Setting

The research area encompasses Bali and its surrounding regions, which are characterized by a highly active and complex tectonic framework. A robust understanding of this local setting is essential for accurate ground motion modeling, similar to studies on the Sumedang and Baribis faults in West Java or the Palu-Koro fault in Sulawesi (Muzli et al., 2026). Bali is highly susceptible to seismic activity driven primarily by the Java Trench subduction zone to the south, where the Indo-Australian plate subducts beneath the Eurasian plate. Additionally, the region is continually affected by back-arc thrust faulting located to the north of the island.

Figure 1 illustrates the spatial distribution of earthquake epicenters and strong-motion sensor stations, focusing specifically on the Bali region delineated by the red bounding box. The map explicitly displays the seismicity profile, where earthquake epicenters are scaled by magnitude and color-coded by hypocentral depth. As observed, shallow earthquakes (red to yellow circles, < 50 km depth) are predominantly concentrated along the Java Trench and local thrust faults. In contrast,

© 2026 Dept. of Geophysics Hasanuddin University

deeper earthquakes (green to blue circles) are distributed further north, and their ground motions are captured by 17 well-distributed accelerometer stations marked as purple triangles.

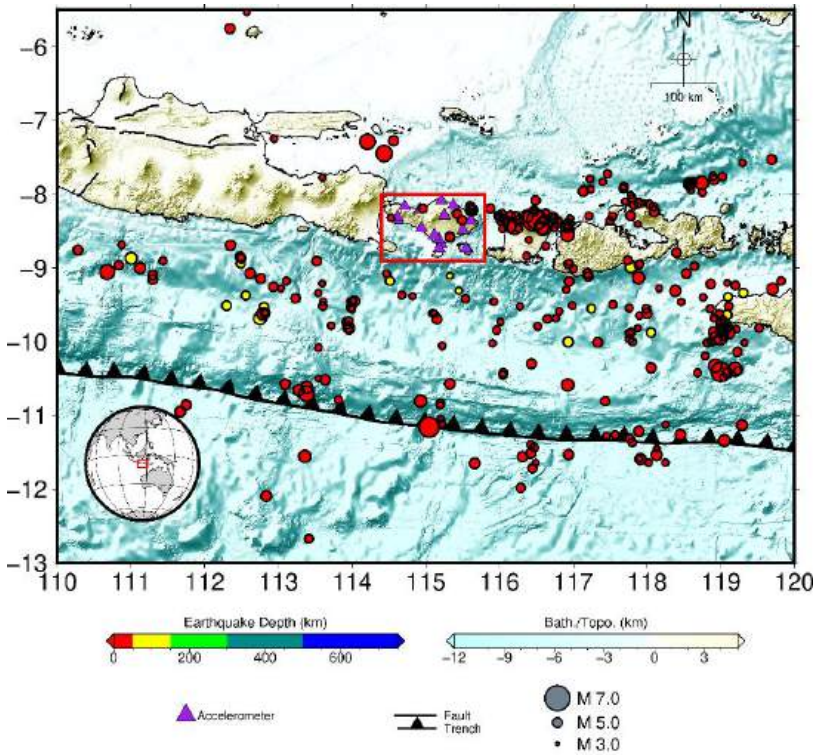


Figure 1. Map of the study area showing earthquake epicenters and sensor stations distributed across Bali and nearby regions. The map is projected using the WGS 84 coordinate reference system. The spatial distribution reveals a high concentration of shallow seismic events (depth < 50 km) dominating the Java Trench and northern back-arc thrust faults, which are comprehensively captured by the localized accelerometer network.

Dataset and Quality Control

This study utilized a strong-motion dataset comprising 1,000 earthquake records obtained from the Agency for Meteorology, Climatology, and Geophysics (BMKG). The collected data covered the period from 2018 to 2025, recording 287 distinct earthquake events across 17 regional seismic stations. To ensure data homogeneity, all recorded earthquake magnitudes were standardized and converted to Moment Magnitude (Mw). This standardization adhered to the guidelines of the 2024 National Center for Earthquake Studies (PuSGeN, 2024) and the framework by the Team for Revision of Seismic Hazard Maps of Indonesia (Irsyam et al., 2010).

Prior to extracting the PGA values, the raw waveforms underwent uniform baseline correction and bandpass filtering to eliminate instrumental noise, after which only quality-controlled events with a magnitude of Mw > 4.0 and a hypocentral distance (Rhypo) of less than 500 km were retained for modeling. Furthermore, for stations where local measurements were unavailable, the time-averaged shear-wave velocity (Vs30) was estimated using a global model based on topographic slope (Allen & Wald, 2009; Heath et al., 2020; Thompson et al., 2014; Wald & Allen, 2007), though we explicitly acknowledge that this proxy introduces inherent uncertainties and potential biases in regions where surface topography does not fully capture complex local geological anomalies. The resulting earthquake frequency distribution is presented in Figure 2, while Figure 3 depicts the spatial distribution of the 17 seismic stations categorized by their site class conditions (Badan Standardisasi Nasional, 2019).

© 2026 Dept. of Geophysics Hasanuddin University

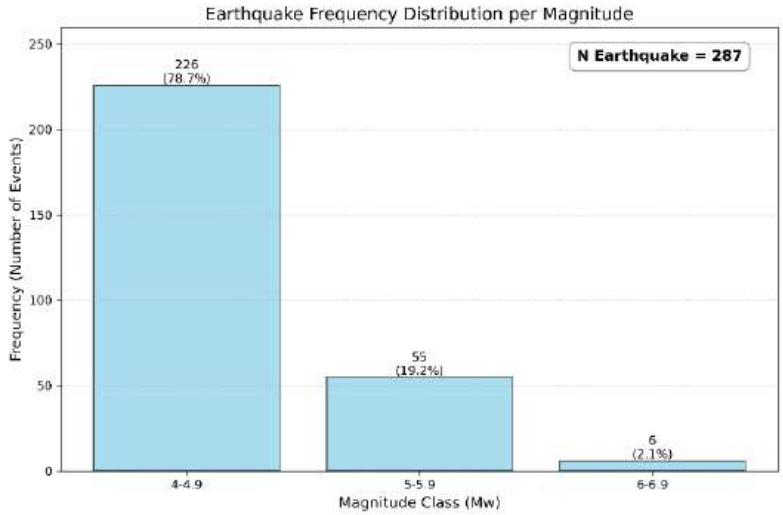


Figure 2. Earthquake frequency distribution per magnitude class (Mw). The dataset is heavily dominated by moderate seismic events (Mw 4.0–4.9), which account for nearly 79% of the catalog, highlighting the highly skewed distribution of the regional seismicity.

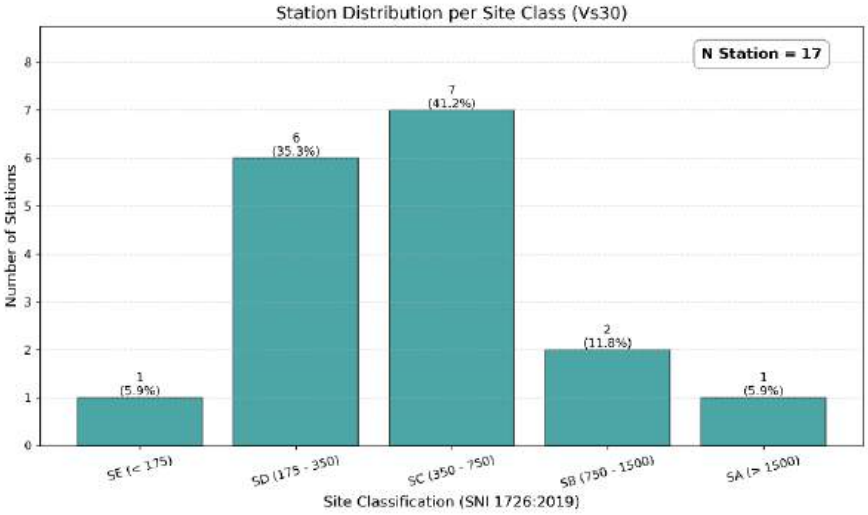


Figure 3. Station distribution per site classification (Vs30). The majority of the recording stations are situated on medium to stiff soil classes (SD and SC), which fundamentally influence the non-linear local ground motion amplification.

Exploratory Data Analysis (EDA)

Before training the models, Exploratory Data Analysis (EDA) was conducted to evaluate the data distribution and feature relationships. This analysis revealed significant non-linear relationships between the target variable and the input predictors. As a result, a Base-10 Logarithmic (Log10) transformation was applied to the Peak Ground Acceleration (PGA), hypocentral distance (Rhypo), magnitude (Mw), and site class conditions (Vs30). This logarithmic transformation is a fundamental procedure in ground motion modeling because it stabilizes residual variance and perfectly matches the log-normal attenuation behavior of seismic waves (Baumann & Dalguer, 2014).

The resulting feature correlation heatmap (Figure 4) shows that Log10_PGA has a strong inverse correlation with logarithmic hypocentral distance (-0.5657) and a positive correlation with magnitude (0.3016). Conversely, the local site condition (Vs30) demonstrates a relatively weak negative correlation (-0.1054) with the target variable. Furthermore, the empirical attenuation behavior is clearly visualized in the hexbin distribution plot of PGA against hypocentral distance (Figure

© 2026 Dept. of Geophysics Hasanuddin University

5). This plot of 1,000 data points reveals a distinct physical trend where ground acceleration exponentially decays as distance increases, with the highest concentration of events occurring beyond 100 km.



Figure 4. Correlation heatmap showing the relationships between predictor variables and target variables. Positive values indicate direct correlations, whereas negative values indicate inverse relationships. The analysis reveals that logarithmic hypocentral distance (Log10_Rhypo) has the strongest inverse correlation (-0.5657) with ground motion intensity, establishing it as the most critical predictor.

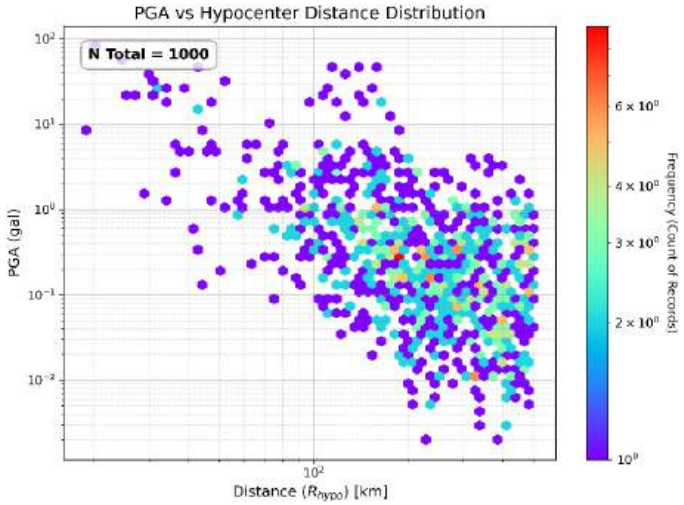


Figure 5. Distribution of Peak Ground Acceleration (PGA) against hypocentral distance (Rhypo). The data concentration clearly visualizes the physical principle of empirical attenuation, demonstrating that ground shaking intensity decays exponentially as distance from the seismic source increases.

Machine Learning Approach

To predict PGA, two distinct ensemble machine learning algorithms were implemented and compared: Random Forest and XGBoost. Random Forest is a bagging method that builds multiple decision trees during training and averages their outputs to reduce variance and prevent overfitting (Probst et al., 2019). This algorithm outperforms conventional linear regression methods in geospatial sciences, especially when handling complex spatial datasets with uncertainties (Apriliansyah et al., 2026). Additionally, random forest architectures are highly recommended for modern seismological tasks due to their strong resilience against overfitting on complex earthquake records (Kong et al., 2019; Mousavi & Beroza, 2022).

Conversely, XGBoost (eXtreme Gradient Boosting) is a highly scalable sequential tree boosting system that iteratively minimizes residual errors (Chen & Guestrin, 2016). Gradient boosting machines are proficient at modeling non-linear relationships in sparse data, making them effective for rapid and physics-consistent peak acceleration estimations (Feng et al., 2025; Ramadan et al., 2026). The conceptual comparison of these methodologies is illustrated in Figure 6, which highlights the architectural differences between the two models. As

© 2026 Dept. of Geophysics Hasanuddin University

depicted, Random Forest uses a parallel approach to train independent trees using bootstrap samples, whereas XGBoost uses a sequential mechanism where each new tree corrects the residual errors of the previous one.

The complete analytical workflow proceeded sequentially: (1) data preprocessing including Log10 transformations, (2) model training via data partitioning, (3) hyperparameter optimization using Randomized Search, and (4) robust model validation. To ensure optimal predictive performance, hyperparameter optimization was conducted using Randomized Search (Moon et al., 2024). Asdetailed in the optimization module of Figure 6, the dataset was initially partitioned into a 70% training set and a 30% testing set, with the training portion paired with a 3-fold cross-validation strategy. This approach was deliberately chosen over 5-fold or 10-fold methods to iteratively evaluate hyperparameter combinations while ensuring each validation fold retained a statistically robust sample (~233 records) of the highly skewed ground motion distribution. The search space ranged from 100 to 1000 for the number of estimators and from None to 50 for the maximum tree depth, ensuring both models successfully avoided data overfitting.

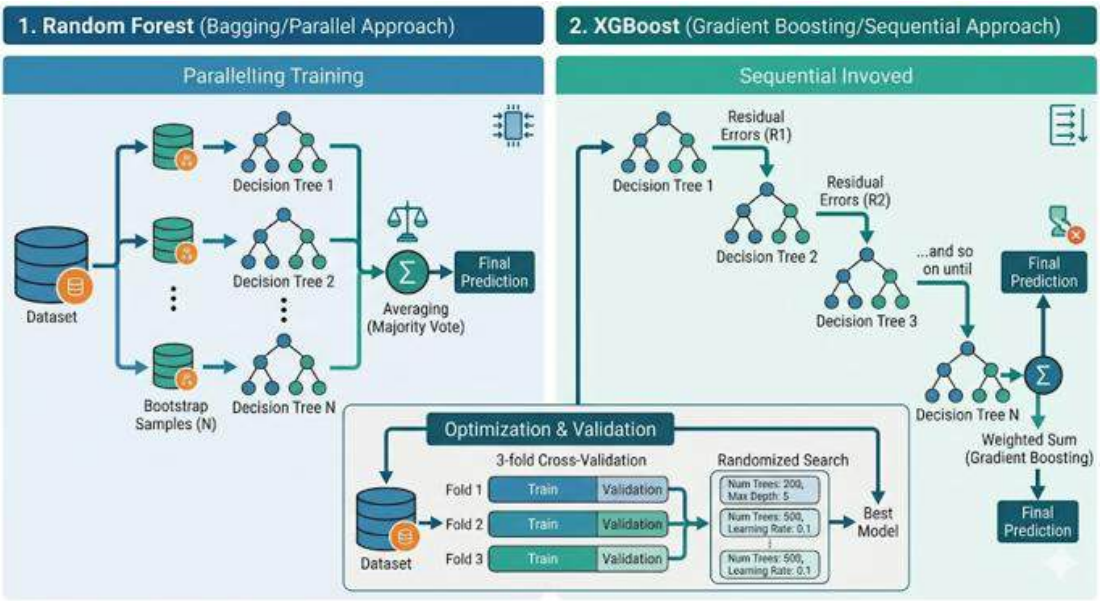


Figure 6. The sequential analytical workflow, illustrating the parallel training of Random Forest, the sequential approach of XGBoost, and the progression from initial data handling through to the hyperparameter optimization process. This rigorous cross-validation strategy ensures optimal model tuning while effectively preventing data overfitting (Adapted from Khan et al., 2021; Mohammadi et al., 2023).

Results and Discussion

Predictive Performance Metrics

The two machine learning models were evaluated based on their ability to accurately predict Peak Ground Acceleration (PGA) after rigorous hyperparameter tuning. The Random Forest model achieved its best performance using 1000 trees (n_estimators = 1000) with a maximum depth of 10. In contrast, the XGBoost model reached its optimal setup with 500 trees (n_estimators = 500) and no maximum depth limit. Quantitative evaluation showed that Random Forest outperformed XGBoost across all key metrics, as summarized in the bar chart comparison (Figure 7).

Specifically, Random Forest achieved a higher Coefficient of Determination (R^2) of 0.741 and a lower Mean Absolute Error (MAE) of 0.340, whereas XGBoost yielded a slightly lower R^2 of 0.715 and an MAE of

© 2026 Dept. of Geophysics Hasanuddin University

0.344. Although the numerical difference in the aggregate MAE appears modest, this performance gain is structurally significant due to Random Forest's significantly tighter error variance; it effectively minimizes extreme prediction outliers and yields a noticeably lower residual standard deviation (0.434) compared to XGBoost (0.456). Figure 8 illustrates the observed versus predicted Log10 PGA values for both of these tuned models. The scatter plots show that Random Forest predictions (Figure 8a) tightly follow the ideal 1:1 reference line, whereas XGBoost predictions (Figure 8b) display a wider dispersion with noticeable errors.

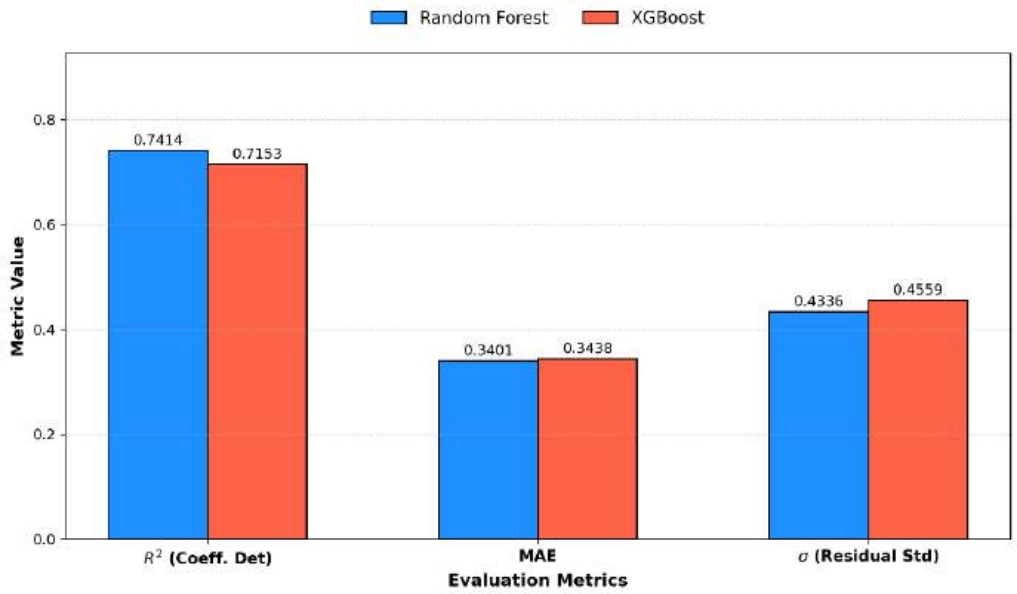


Figure 7. Quantitative performance comparison between the machine learning models. Random Forest consistently outperforms XGBoost across all metrics, achieving a higher Coefficient of Determination (R^2= 0.741) and a lower residual standard deviation (σ = 0.434), which demonstrates its superior predictive stability.

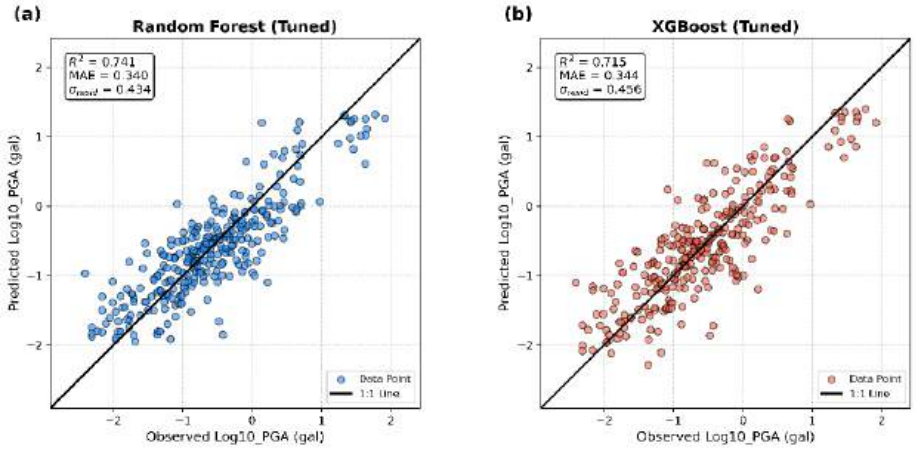


Figure 8. Comparison of observed versus predicted PGA values for (a) Random Forest and (b) XGBoost. The Random Forest predictions (a) cluster more tightly along the ideal 1:1 reference line, indicating higher precision and fewer extreme prediction outliers compared to the wider error dispersion seen in the XGBoost model (b).

Residual Analysis

To further evaluate model precision, we conducted a comprehensive residual analysis. The results showed that the residual standard deviation for Random Forest was 0.434. This value was noticeably lower than the standard deviation of 0.456 recorded for the XGBoost model. This clear difference in error variance between the two models is visually depicted in the residual distribution density plot (Figure 9).

© 2026 Dept. of Geophysics Hasanuddin University

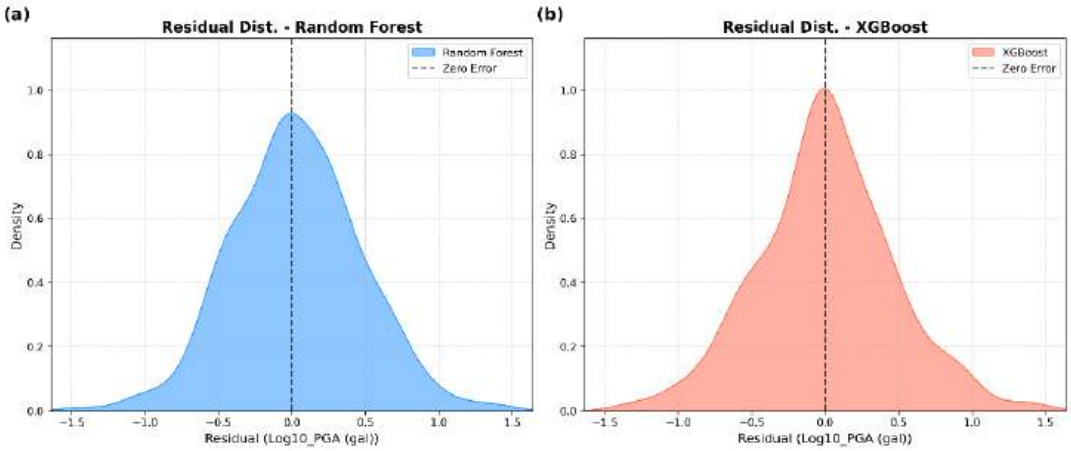


Figure 9. Residual distribution density plot for (a) Random Forest and (b) XGBoost. The Random Forest model produces a highly constrained, symmetrical error distribution, whereas XGBoost exhibits wider tails associated with higher prediction uncertainty and extreme outliers.

The plot reveals that while XGBoost residuals (Figure 9b) are slightly denser at the zero-error line, they exhibit wider tails that indicate more extreme prediction errors. In contrast, the Random Forest model (Figure 9a) forms a more proportional bell curve with narrower tails and fewer extreme outliers. To further investigate this behavior across key earthquake parameters, the prediction residuals were plotted against hypocentral distance (Figures 10a and 10b), local site conditions or Vs30 (Figures 11a and 11b), and moment magnitude or Mw (Figures 12a and 12b). These scatter plots demonstrate that both models, particularly Random Forest (Figures 10a, 11a, and 12a), maintain a well-distributed and unbiased error variance across the entire parameter space, with the majority of data points falling within the ± 1 standard deviation threshold and showing no systemic distance, site, or magnitude-dependent trends. This statistical behavior proves that Random Forest provides higher precision and stability across varying earthquake distances and magnitudes. This stability is consistent with recent comparative studies, which emphasize the adaptive learning capacity and robust residual patterns of Random Forest across diverse site conditions (Taya et al., 2026).

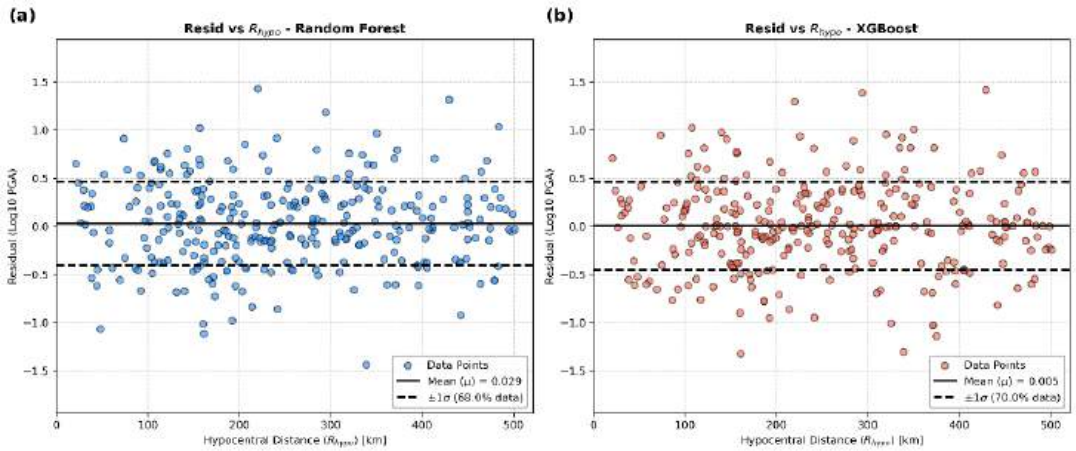


Figure 10. Scatter plots of prediction residuals against hypocentral distance (Rhypo) for (a) Random Forest and (b) XGBoost, highlighting the ± 1 standard deviation error bounds. Both models maintain stable error variances across varying distances without systemic bias, proving their robustness in capturing regional attenuation.

© 2026 Dept. of Geophysics Hasanuddin University

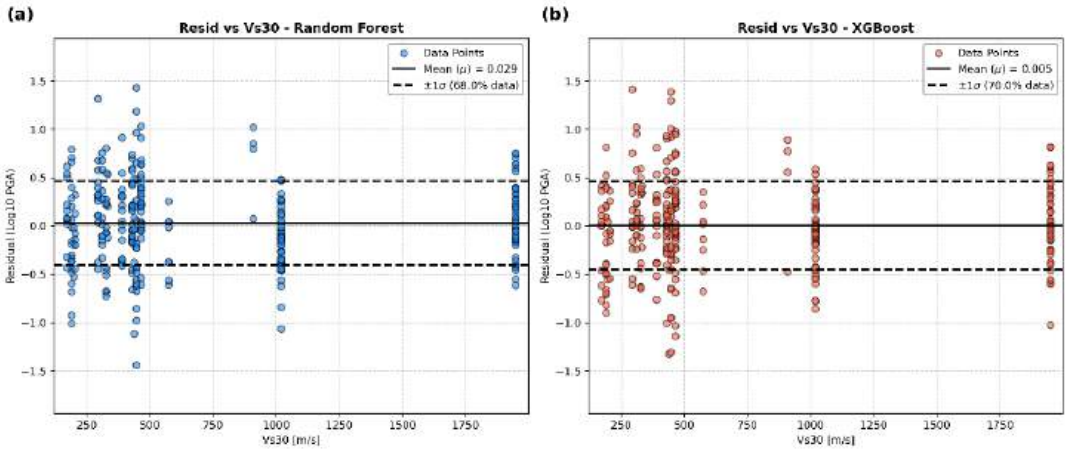


Figure 11. Scatter plots of prediction residuals against time-averaged shear-wave velocity (Vs30) for (a) Random Forest and (b) XGBoost. The Random Forest model demonstrates robust stability across diverse site classifications without overfitting to localized ground responses.

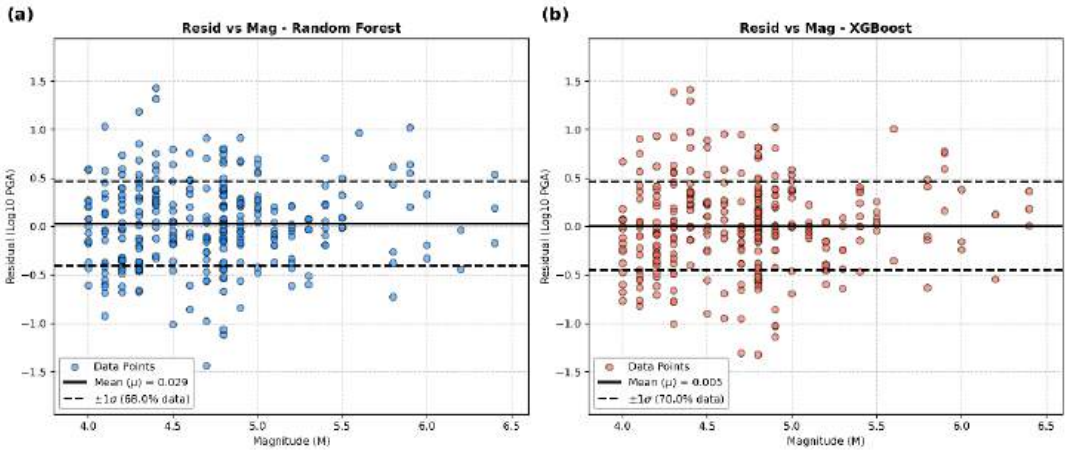


Figure 12. Scatter plots of prediction residuals against moment magnitude (Mw) for (a) Random Forest and (b) XGBoost. The uniform spread of residuals confirms an unbiased error distribution irrespective of earthquake size, validating the models' reliability for both moderate and large events.

Feature Importance and Physical Consistency

A critical aspect of modeling ground motion is ensuring that data-driven algorithms follow established seismological principles. Feature importance metrics were extracted from both models to quantitatively understand which input variables drove the predictions. The Random Forest model (Figure 13a) correctly identified Hypocentral Distance (Log10_Rhypo) as the dominant predictor with a relative importance of 0.533, followed by Magnitude (0.237) and local site conditions (Log10_Vs30) at 0.230. This hierarchical order perfectly aligns with standard physical attenuation laws, where distance is the primary factor of shaking decay.

Recent machine learning evaluations strongly support this finding, showing that distance is a highly reliable predictor for regional co-seismic impacts (Shi et al., 2024). Conversely, the XGBoost model (Figure 13b) exhibited an unexpected and physically incorrect bias. It assigned the highest relative importance to local site conditions (Log10_Vs30) at 0.427. At the same time, it reduced Magnitude (0.291) and Hypocentral Distance (0.282) to secondary and tertiary roles. This prioritization fundamentally violates the established seismological principle of exponential decay, wherein seismic energy dissipates primarily as a function of geometric spreading and anelastic attenuation over distance. While local site conditions (Vs30) certainly contribute to localized amplification, the overarching

© 2026 Dept. of Geophysics Hasanuddin University

decay of ground motion is unequivocally driven by source-to-site distance, rendering XGBoost's feature hierarchy physically inconsistent with empirical attenuation laws.

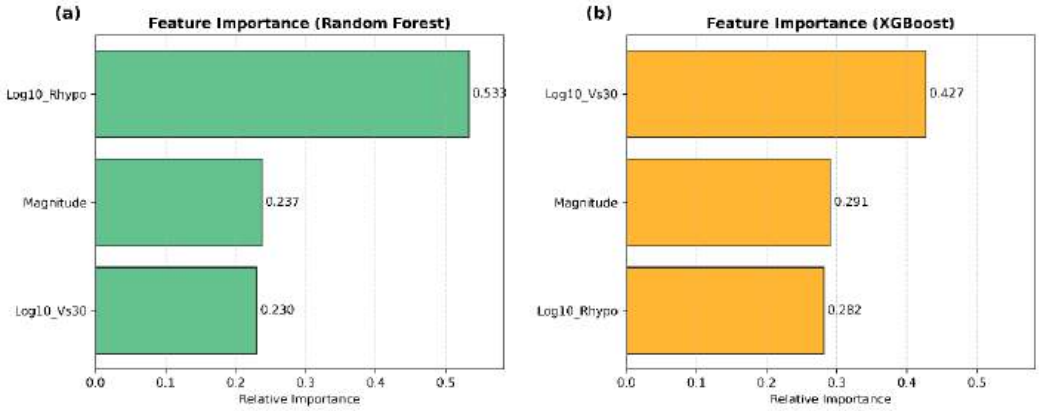


Figure 13. Feature importance chart showing (a) hypocentral distance as the dominant predictor for Random Forest, whereas (b) XGBoost prioritizes site class (Vs30). The feature hierarchy of Random Forest is physically consistent with established empirical attenuation laws, unlike the physically counterintuitive, localized overfitting observed in the XGBoost model.

Discussion

The results of this study clearly demonstrate that Random Forest provides a more accurate, precise, and physically consistent model for predicting PGA in Bali compared to XGBoost. The superiority of Random Forest is attributed to its parallel bagging architecture, which is robust against noise and prevents overfitting on complex geological data (Probst et al., 2019). However, it is important to acknowledge that XGBoost remains a highly potent algorithm in different seismological contexts. While its sequential gradient boosting approach was susceptible to overfitting the localized site conditions in our specific regional dataset, XGBoost typically excels when applied to massive, high-dimensional global catalogs (such as the NGA-West2 database). In such large-scale environments, its ability to iteratively minimize complex residual errors allows it to capture highly intricate, non-linear feature interactions more effectively than Random Forest, provided that extensive regularization is employed. Most importantly, the feature importance analysis reveals that Random Forest aligns seamlessly with empirical ground-motion attenuation laws. In traditional seismology, ground shaking intensity decreases mainly as a function of distance from the seismic source due to geometric spreading and anelastic attenuation.

The combined effect of geometric spreading and anelastic damping dictates that hypocentral distance fundamentally controls the decay of seismic waves (Kramer & Stewart, 2024). By prioritizing hypocentral distance over site conditions, Random Forest successfully captures these physical attenuation principles. On the other hand, XGBoost tends to prioritize Vs30, which indicates potential overfitting to local site responses at the expense of regional attenuation behavior. These overall findings represent a significant step forward from traditional Ground Motion Prediction Equations (GMPEs).

As noted in previous studies, traditional GMPEs deployed in Bali often struggle to handle the non-linear effects of local geology without extensive calibration (Hielmy, 2024; Hielmy, et al., 2026; Hielmy & Rajagukguk, 2025). The Random Forest model in this study overcomes this limitation by learning complex interactions directly from recent strong-motion records to produce a robust localized model. The ability of ensemble models to capture complex seismic

© 2026 Dept. of Geophysics Hasanuddin University

relationships addresses the limitations of empirical equations and earlier neural network designs (Leema et al., 2025). Once optimized, these data-driven approaches provide well-calibrated predictions that can be directly evaluated against engineering thresholds to assess structural damage risks (Shokrgozar-Yatimdar & Chen, 2025).

The application of such advanced algorithms has proven effective in solving complex seismological problems, from aftershock decay estimation to ground motion prediction (Withers et al., 2020). This success aligns with recent advancements in neighboring areas like West Java, where ML has successfully enhanced predictive capabilities (Rachmadan et al., 2025). The implementation of this highly accurate Random Forest model has substantial practical applications for disaster mitigation. For long-term planning, a reliable PGA model is crucial to develop Probabilistic Seismic Hazard Analysis (PSHA) maps, which dictate national building codes in vulnerable areas like Bali.

Such robust hazard mapping is essential for regional earthquake mitigation, similar to vulnerability assessments used to identify high-risk zones across Indonesia (Ningrum et al., 2022). Translating these technical models into community preparedness is also vital, as shown by school mitigation simulations that rely on accurate seismic risk data (Hielmy et al., 2026; Hielmy et al., 2025b). For rapid response, integrating ML algorithms into seismic networks significantly improves the generation of real-time ShakeMaps by BMKG (Jozinović et al., 2020). Recent deployments of such hybrid workflows have demonstrated reduced prediction errors and significant lead time gains, which strengthen the overall effectiveness of early warning systems (Zhang et al., 2026).

Conclusion

This study successfully evaluated and compared the predictive capabilities of Random Forest and XGBoost algorithms for estimating Peak Ground Acceleration in the highly seismic region of Bali. The results demonstrated that the parallel bagging architecture of Random Forest provides a more accurate and stable prediction model than the sequential boosting approach of XGBoost. This statistical superiority is clearly evidenced by a higher Coefficient of Determination and significantly lower overall error metrics. Beyond pure statistical performance, a major advantage of the Random Forest model is its strong adherence to physical consistency.

The model successfully captured geometric spreading and anelastic attenuation by correctly identifying hypocentral distance as the primary driver of ground shaking. By prioritizing distance, the model effectively avoided the overfitting to local site conditions that was observed in XGBoost. Although constrained by the available training data, this data-driven approach overcomes the limitations of traditional empirical equations in modeling non-linear site effects. Ultimately, this accurate model establishes a fundamental precedent for developing Probabilistic Seismic Hazard Analysis maps, enhancing real-time ShakeMaps, and supporting proactive structural risk mitigation in Indonesia (Nemutlu et al., 2025).

Acknowledgements

The authors express their sincere gratitude to the Agency for Meteorology, Climatology, and Geophysics (BMKG) and the State College of Meteorology, Climatology, and Geophysics (STMKG). These institutions generously provided the extensive strong-motion datasets and the computational facilities required to successfully conduct this research.

Author Contribution

© 2026 Dept. of Geophysics Hasanuddin University

Rayhan Irfan Hielmy: Conceptualization, Methodology, Software, Formal analysis, Visualization, Writing - Original Draft. Muzli Muzli: Supervision, Validation, Writing - Review & Editing.

Conflict of Interest

The authors declare that they have no known competing financial interests or personal relationships that could have appeared to influence the work reported in this paper.

References

Allen, T. I., & Wald, D. J. (2009). On the Use of High-Resolution Topographic Data as a Proxy for Seismic Site Conditions (VS30). *Bulletin of the Seismological Society of America*, 99(2A), 935–943. https://doi.org/10.1785/0120080255

Apriliansyah, F., Nuha, M. U., Atmojo, A. T., Setiawan, K. T., & Syafnur, A. (2026). Comparative Accuracy of Satellite-Derived Bathymetry Using Random Forest, Multiple Linear Regression, and Van Hengel and Spitzer Algorithm. *Jurnal Geocelebes*, 48–68. https://doi.org/10.70561/geocelebes.v10i1.43582

Badan Standardisasi Nasional. (2019). *SNI 1726:2019: Tata Cara Perencanaan Ketahanan Gempa untuk Struktur Bangunan Gedung dan Nongedung*. Badan Standardisasi Nasional. https://sitaba.pu.go.id/publikasi/6977fb4f-d02f-4fd0-a857-65219c38f24e

Baumann, C., & Dalguer, L. A. (2014). Evaluating the Compatibility of Dynamic Rupture-Based Synthetic Ground Motion with Empirical Ground-Motion Prediction Equation. *Bulletin of the Seismological Society of America*, 104(2), 634–652. https://doi.org/10.1785/0120130077

Bojórquez, E., Payán-Serrano, O., Bojórquez, J., Rodríguez-Castellanos, A., Ruiz, S. E., Reyes-Salazar, A., & Velarde, F. (2025). Support Vector Machines to Propose a Ground Motion Prediction Equation for the Particular Case of the Bojorquez Intensity Measure INp. *AI*, 6(10), 254. https://doi.org/10.3390/ai6100254

Chen, T., & Guestrin, C. (2016). XGBoost : A Scalable Tree Boosting System. *Proceedings of the 22nd ACM SIGKDD International Conference on Knowledge Discovery and Data Mining*, 785–794. https://doi.org/10.1145/2939672.2939785

Feng, Y., Li, Y., Wang, F., & Yang, L. (2025). Hybrid CNN-GRU-Attention-XGBoost Model for Rapid and Accurate Prediction of Peak Acceleration and Trigger Time in Dam Safety Monitoring. In *2025 5th International Conference on Artificial Intelligence, Big Data and Algorithms (CAIBDA)*, 1245–1251. https://doi.org/10.1109/CAIBDA65784.2025.11183451

Heath, D. C., Wald, D. J., Worden, C. B., Thompson, E. M., & Smoczyk, G. M. (2020). A global hybrid VS30 map with a topographic slope–based default and regional map insets. *Earthquake Spectra*, 36(3), 1570–1584. https://doi.org/10.1177/8755293020911137

Hielmy, R. I. (2024). Perbandingan Metode Davenport, Milne, dan McGuirre dalam Penentuan Nilai Percepatan Tanah Maksimum di Pulau Bali. *Buletin Meteorologi, Klimatologi Dan Geofisika*, 4(5), 9–16. https://balai2bmkg.id/index.php/buletin_mkg/article/view/133

Hielmy, R. I., Pranata, B., Wijayanto, & Daryono. (2025a). Performance Evaluation of Automated and Manual Seismic Phase Picking for Rapid Earthquake Parameter. *Jurnal Meteorologi Dan Geofisika*, 26(2), 89–107. https://doi.org/10.31172/jmg.v26i2.11

© 2026 Dept. of Geophysics Hasanuddin University

89

Hielmy, R. I., Aritonang, B. H., Sijabat, N. A., An-nizami, M. S., Setyowati, P. R., Wijaya, A., Adzan, M. A., Aji, T. W., Kristianto, A., Rachmawardani, A., & Sianipar, D. S. J. (2025b). Sosialisasi Mitigasi Bencana Gempa Bumi , Tsunami, dan Hidrometeorologi di SMAN 6. *To Maega | Jurnal Pengabdian Masyarakat*, 8(3), 607–616. https://doi.org/10.35914/hk0rn065

Hielmy, R. I., Kean, F. A. C., Gosi, M. F. Al, Syifa, F., Daraman, M. A., Lala, R. Y., Sianipar, D. S. J., Justicea, A. A., Suardi, I., Muzli, Karyono, Harahap, D., Adi, S. P., Wandono, & Peera, F. (2026). Evaluasi Efektivitas Simulasi Mitigasi Bencana Gempa Bumi di Sekolah An-Nisaa' Izada, Tangerang Selatan. *To Maega | Jurnal Pengabdian Masyarakat*, 9(1), 1–12. https://doi.org/10.35914/4gqdgn87

Hielmy, R. I., & Muzli, M. (2026). Comparative Analysis of Random Forest and XGBoost for Peak Ground Acceleration Prediction in Bali, Indonesia. *Proceedings of the 8th Asia Pacific Meeting on Near Surface Geoscience & Engineering,* 2026(1), 1–4. European Association of Geoscientists & Engineers. https://www.earthdoc.org/content/papers/10.3997/2214-4609.202671070

Hielmy, R. I., & Rajagukguk, M. L. (2025). Analisis Probabilistik Bahaya Seismik di Denpasar dan Sekitarnya Berdasarkan Pendekatan PSHA. *Journal Online of Physics*, 11(1), 21–28. https://doi.org/10.22437/jop.v11i1.47825

Hielmy, R. I., Santoso, E., Muzli, M., Pramono, S., & Prayoedhie, S. (2026). Machine learning-based ground motion prediction models for Indonesia: A performance evaluation of XGBoost and Random Forest against conventional GMPE. *Jurnal Meteorologi dan Geofisika*, 27(1), 51–67. https://doi.org/10.31172/jmg.v27i1.1233

Irsyam, M., Sengara, W., Aldiamar, F., Widiyantoro, S., Triyoso, W., Hilman, D., Kertapati, E., Meilano, I., Suhardjono, Asrurifak, M., & Ridwan, M. (2010). *Ringkasan Hasil Studi Tim Revisi Peta Gempa Indonesia 2010*. Kementerian Pekerjaan Umum Republik Indonesia.

Jozinović, D., Lomax, A., Štajduhar, I., & Michelini, A. (2020). Rapid Prediction of Earthquake Ground Shaking Intensity Using Raw Waveform Data and a Convolutional Neural Network. *Geophysical Journal International*, 222(2), 1379–1389. https://doi.org/10.1093/gji/ggaa233

Khan, M. Y., Qayoom, A., Nizami, M. S., Siddiqui, M. S., Wasi, S., & Raazi, S. M. K.-u.-R. (2021). Automated Prediction of Good Dictionary EXamples (GDEX): A Comprehensive Experiment with Distant Supervision, Machine Learning, and Word Embedding-Based Deep Learning Techniques. *Complexity*, 2021(1), 2553199. https://doi.org/10.1155/2021/2553199

Khosravikia, F., & Clayton, P. (2021). Machine learning in ground motion prediction. *Computers and Geosciences*, 148, 104700. https://doi.org/10.1016/j.cageo.2021.104700

Kong, Q., Trugman, D. T., Ross, Z. E., Bianco, J., Meade, B. J., & Gerstoft, P. (2019). Machine Learning in Seismology : Turning Data into Insights. *Seismological Research Letters*, 90(1), 3–14. https://doi.org/10.1785/0220180259

Kramer, S. L., & Stewart, J. P. (2024). *Geotechnical Earthquake Engineering*. CRC Press. https://doi.org/10.1201/9781003512011

Kubo, H., Kunugi, T., Suzuki, W., Suzuki, S., & Aoi, S. (2020). Hybrid predictor

© 2026 Dept. of Geophysics Hasanuddin University

for ground-motion intensity with machine learning and conventional ground motion prediction equation. *Scientific Reports*, 10(1), 1–12. https://doi.org/10.1038/s41598-020-68630-x

Leema, A., Balakrishnan, P., Kiruba, G. G., Rajarajan, G., Goel, S., & Aggarwal, P. (2025). SeismoQuakeGNN: A Hybrid Framework for Spatio-Temporal Earthquake Prediction with Transformer-Enhanced Models. *Frontiers in Artificial Intelligence*, 8, 1690476. https://doi.org/10.3389/frai.2025.1690476

Lisa, A., Refrizon, R., & Samdara, R. (2026). The Earthquake Prediction in the Southern Part of Sumatra Using Deep Learning (Long Short-Term Memory) Models. *Jurnal Geocelebes*, 1–11. https://doi.org/10.70561/geocelebes.v10i1.42958

Mohammadi, A., Karimzadeh, S., Banimahd, S. A., Ozsarac, V., & Lourenço, P. B. (2023). The potential of region-specific machine-learning-based ground motion models: Application to Turkey. *Soil Dynamics and Earthquake Engineering*, 172, 108008. https://doi.org/10.1016/j.soildyn.2023.108008

Monterrubio-Velasco, M., Callaghan, S., Modesto, D., Carrasco, J. C., Badia, R. M., Pallares, P., Vázquez-Novoa, F., Quintana-Ortí, E. S., Pienowska, M., & de la Puente, J. (2024). A machine learning estimator trained on synthetic data for real-time earthquake ground-shaking predictions in Southern California. *Communications Earth & Environment*, 5(1), 258. https://doi.org/10.1038/s43247-024-01436-1

Moon, Y., Lee, Y., Hwang, Y., & Jeong, J. (2024). Long Short-Term Memory Autoencoder and Extreme Gradient Boosting-Based Factory Energy Management Framework for Power Consumption Forecasting. *Energies*, 17(15), 3666. https://doi.org/10.3390/en17153666

Mousavi, S. M., & Beroza, G. C. (2022). Deep-learning Seismology. *Science*, 377(6607), eabm4470. https://doi.org/10.1126/science.abm4470

Muzli, M., Lythgoe, K. H., Hielmy, R. I., Triyono, R., & Wei, S. (2026). Aftershock Characteristics of the 2018 Palu Earthquake: Implications for Supershear Rupture Segment. *Indonesian Physical Review*, 9(2), 374–385. https://doi.org/10.29303/ipr.v9i2.666

Nemutlu, Ö. F., Özçelik, S. T. A., & Freeshah, M. (2025). A Machine Learning Framework for Regional Damage Assessment Using Multi-Station Seismic Parameters: Insights from the 2023 Kahramanmaraş Earthquakes. *Buildings*, 15(18), 3326. https://doi.org/10.3390/buildings15183326

Ningrum, R. W., Amelia, R. N., Taib, S., Achmad, R., & Aswan, M. (2022). Pemetaan Potensi Kerentanan Seismik sebagai Mitigasi Bencana Gempa di Morotai Selatan. *Jurnal Geocelebes*, 37–46. https://doi.org/10.20956/geocelebes.v6i1.19150

Parker, G. A., Stewart, J. P., Boore, D. M., Atkinson, G. M., & Hassani, B. (2022). NGA-subduction global ground motion models with regional adjustment factors. *Earthquake Spectra*, 38(1), 456-493. https://doi.org/10.1177/87552930211034889

Probst, P., Wright, M. N., & Boulesteix, A.-L. (2019). Hyperparameters and tuning strategies for random forest. *Wiley Interdisciplinary Reviews: Data Mining and Knowledge Discovery*, 9(3), e1301. https://doi.org/10.1002/widm.1301

PuSGeN. (2024). *Buku Peta Sumber dan*

© 2026 Dept. of Geophysics Hasanuddin University

Bahaya Gempa Indonesia Tahun 2024. Kementerian Pekerjaan Umum Republik Indonesia. https://ciptakarya.pu.go.id/admin/assets/upload/galeri/gempa/2026/02/10/887359_0.%20Final_BUKU_PETA_SUMBER_DAN_BAHAYA_GEMPA_2024_Publish.pdf

Rachmadan, A., Koeshidayatullah, A., & Kaka, S. L. I. (2025). Developing ground motion prediction models for West Java: A machine learning approach to support Indonesia's earthquake early warning system. *Applied Computing and Geosciences*, 25, 100212. https://doi.org/10.1016/j.acags.2024.100212

Ramadan, F., Nissen-Meyer, T., Koelemeijer, P., & Fry, B. (2026). PGVnet: a Machine Learning Framework for the Generation of Rapid, Physics-Consistent PGV Maps. *Geophysical Journal International*, 244(3), 1–14. https://doi.org/10.1093/gji/ggag008

Shi, Y., Zhang, Z., Xue, C., & Feng, Y. (2024). Machine Learning Prediction of Co-Seismic Landslide with Distance and Azimuth Instead of Peak Ground Acceleration. *Sustainability*, 16(19), 8332. https://doi.org/10.3390/su16198332

Shokrgozar-Yatimdar, E., & Chen, P. (2025). Explainable Deep Learning for Real-Time Prediction of Uniform Hazard Spectral Acceleration for On-Site Earthquake Early Warning. *Geophysical Journal International*, 243(2), 1–18. https://doi.org/10.1093/gji/ggaf345

Somala, S. N., Chanda, S., Alhamaydeh, M., & Mangalathu, S. (2024). Explainable XGBoost–SHAP Machine-Learning Model for Prediction of Ground Motion Duration in New Zealand. *Natural Hazards Review*, 25(2), 4024005. https://doi.org/10.1061/NHREFO.NHENG-1837

Sun, R., Qi, W., Zheng, T., & Qi, J. (2023). Explainable Machine-Learning Predictions for Peak Ground Acceleration. *Applied Sciences*, 13(7), 4530. https://doi.org/10.3390/app13074530

Taya, R., Mittal, H., Saini, A., & Kumar, R. (2026). Comparative Evaluation of Machine-Learning Models and Recalibrated GMPEs for Ground-Motion Prediction. *EGU General Assembly 2026*, Vienna, Austria, 3–8 May 2026, EGU26-17735, https://doi.org/10.5194/egusphere-egu26-17735

Thompson, E. M., Wald, D. J., & Worden, C. B. (2014). A V_{S30} Map for California with Geologic and Topographic Constraints. *Bulletin of the Seismological Society of America*, 104(5), 2313–2321. https://doi.org/10.1785/0120130312

Wald, D. J., & Allen, T. I. (2007). Topographic slope as a proxy for seismic site conditions and amplification. *Bulletin of the Seismological Society of America*, 97(5), 1379–1395. https://doi.org/10.1785/0120060267

Withers, K. B., Moschetti, M. P., & Thompson, E. M. (2020). A machine learning approach to developing ground motion models from simulated ground motions. *Geophysical Research Letters*, 47(6), e2019GL086690. https://doi.org/10.1029/2019GL086690

Zhang, H., Liu, Q., Jin, X., Cai, H., Chen, Z., & Wang, S. (2026). Hybrid Approach of Real-Time Ground Motion Prediction for Earthquake Early Warning. *Seismica*, 5(1), 1–18. https://doi.org/10.26443/seismica.v5i1.2194

Zhu, C., Cotton, F., Kawase, H., & Nakano, K. (2023). How Well Can We Predict Earthquake Site Response So Far? Machine Learning vs Physics-Based Modeling. *Earthquake Spectra*, 39(1),

© 2026 Dept. of Geophysics Hasanuddin University

478–504. https://doi.org/10.1177/87552930221116399

Ziar, A., & Basari, E. (2025). Accurate Prediction of Peak Ground Acceleration Using Random Forests: A Data-Driven Approach with PEER Updated NGA-WEST2 Ground Motion Records. *Archives of Advanced Engineering Science*, 0(0), 1–9. https://doi.org/10.47852/bonviewAAES52026930

© 2026 Dept. of Geophysics Hasanuddin University

ISSN: 2579-5821 (Print)
ISSN: 2579-5546 (Online)
URL address: http://journal.unhas.ac.id/index.php/geocelebes
DOI: 10.70561/geocelebes.v10i2.52334

Jurnal Geocelebes Vol. 10 No. 2, October 2026, 322 – 342

Characteristics of Land–Sea Breeze Circulation along the West Coast of West Sumatra Using Observations and WRF-ARW Simulations

Reinal Taruna Wahyu Halawa*, Latifah Nurul Qomariyatuzzamzami, Yosafat Donni Haryanto, Avrionesti

Meteorology Study Program, School of Meteorology Climatology and Geophysics, Tangerang, 15119, Indonesia.

*Corresponding author. Email: reinaltaruna.25@gmail.com

Manuscript received: 26 February 2026; Received in revised form: 3 August 2026; Accepted: 24 August 2026

Abstract

Land–sea breeze circulation is an important mesoscale atmospheric phenomenon in tropical coastal areas, yet its behavior and interaction with complex topography remain insufficiently understood along the west coast of West Sumatra. This study examined land–sea breeze characteristics and atmospheric dynamics during the 2025 dry season using Automatic Weather Station (AWS) observations and Weather Research and Forecasting (WRF) simulations with the Advanced Research WRF (WRF-ARW) dynamical core. Events were identified using a modified Six Filters method, and three representative cases were selected for numerical simulation and detailed atmospheric analysis. Model performance was evaluated against surface observations, while horizontal, vertical, and time–height analyses examined circulation evolution and structure. A total of 51 events were identified at AWS Digi Minangkabau. Sea-breeze circulation generally developed between 02 and 03 UTC and reached its mature phase between 06 and 09 UTC. WRF-ARW reproduced the observed evolution of near-surface temperature and wind fields and captured the main circulation characteristics. Marine air penetrated inland toward the foothills of the Bukit Barisan, where strong convergence and upward motion occurred. The circulation was mainly confined to the lower troposphere, with a typical depth of 1–2 km and a defined return flow aloft. These findings indicate that land–sea breeze evolution is influenced by differential land–sea heating and topographic modulation by the Bukit Barisan.

Keywords: Atmospheric Dynamics; Coastal Circulation; Land–Sea Breeze; West Sumatra; WRF-ARW.

Citation: Halawa, R. T. W., Qomariyatuzzamzami, L. N., Haryanto, Y. D., & Avrionesti, A. (2026). Characteristics of Land–Sea Breeze Circulation along the West Coast of West Sumatra Using Observations and WRF-ARW Simulations. *Jurnal Geocelebes*, 10(2): 322–342, doi: 10.70561/geocelebes.v10i2.52334

Introduction

Land–sea breeze circulation is one of the most important mesoscale atmospheric phenomena in coastal regions and represents a major source of diurnal variability in the lower atmosphere. The circulation plays a critical role in regulating heat and moisture transport, boundary-layer development, convergence, and convective activity, thereby influencing local weather and climate conditions. Beyond the characteristic reversal of coastal winds, land–sea breeze systems contribute to the redistribution of energy and water vapor between the ocean and adjacent land areas, affecting cloud formation, precipitation development, and air–sea interactions. These processes are particularly important in tropical coastal environments, where strong daytime heating and abundant low-level moisture favor active land–atmosphere coupling and the development of thermally driven circulations (Zhu et al., 2017; Drobinski et al., 2018; Park et al., 2020).

Previous studies have demonstrated that land–sea breeze circulation exhibits substantial variability in timing, duration,

© 2026 Dept. of Geophysics Hasanuddin University

inland penetration, and vertical extent across different coastal environments. Along the west coast of Sumatra, North et al. (2025) showed that sea-breeze circulations occur almost daily and constitute a dominant component of the regional low-level wind system. Similar studies conducted in Seoul, China, and other tropical coastal regions have reported that sea-breeze circulations commonly extend tens of kilometers inland and are typically confined within the lowest 1–2 km of the atmosphere (Park & Chae, 2018; Jia et al., 2022; Muppa et al., 2012). In addition to modifying near-surface winds, these circulations play an important role in transporting moist marine air inland, thereby influencing atmospheric instability and convective development (Davis et al., 2019; Zhu et al., 2017). Collectively, these studies indicate that land–sea breeze circulation is a key mechanism governing coastal atmospheric dynamics, although its characteristics remain strongly dependent on local geographical and meteorological conditions.

Among the factors controlling land–sea breeze evolution, topography is recognized as one of the most important modifiers of circulation structure and intensity. Coastal mountain ranges can alter inland penetration, redistribute convergence zones, modify circulation depth, and enhance vertical motion through interactions between sea-breeze flow and slope circulations (Miao et al., 2003; He et al., 2021). Numerical and observational studies have shown that such interactions may strengthen or weaken sea-breeze development depending on terrain configuration and ambient atmospheric conditions (Allouche et al., 2023). The west coast of West Sumatra provides a particularly interesting environment for investigating these processes because the Bukit Barisan Mountain range lies in close proximity to the Indian Ocean coastline. This geographical setting creates a unique natural laboratory where coastal thermal forcing and topographic forcing interact over a relatively short spatial scale, potentially exerting a strong influence on the horizontal and vertical evolution of land–sea breeze circulation.

Despite increasing interest in tropical coastal circulations, detailed investigations of land–sea breeze dynamics along the west coast of West Sumatra remain limited. Previous studies in Sumatra have primarily focused on near-surface characteristics of coastal wind reversals and seasonal variability (North et al., 2025), while the coupled horizontal and vertical evolution of the circulation has received comparatively little attention. Furthermore, studies integrating surface observations and numerical simulations remain scarce, particularly in coastal regions characterized by complex terrain. As a result, the role of the Bukit Barisan topography in modulating inland penetration, convergence, circulation depth, and vertical atmospheric structure remain insufficiently understood. A comprehensive description of the atmospheric evolution of land–sea breeze circulation from its onset to mature phase is therefore still lacking for this region.

Accordingly, this study aims to (1) identify the characteristics of land–sea breeze circulation along the west coast of West Sumatra during the 2025 dry season using observations from Automatic Weather Stations (AWS), and (2) evaluate the capability of the Weather Research and Forecasting model with the Advanced Research WRF dynamical core (WRF-ARW) in reproducing the observed circulation and its vertical structure. By integrating surface observations and high-resolution numerical simulations, this study characterizes the horizontal and vertical evolution of land–sea breeze circulation and examines the influence of the Bukit Barisan topography on convergence, moisture transport, and vertical motion. The results contribute to an improved

© 2026 Dept. of Geophysics Hasanuddin University

understanding of coastal atmospheric dynamics in tropical mountainous environments and provide a regional reference for future observational and modeling studies of land–sea breeze systems.

Materials and Methods

Study Area

The study was conducted along the west coast of West Sumatra, Indonesia, a region directly facing the Indian Ocean and characterized by complex coastal and mountainous terrain (Figure 1). The study area is bounded by a narrow coastal plain and the Bukit Barisan Mountain range, which extends parallel to the western coastline of Sumatra. This geographical setting provides favorable conditions for the development of land–sea breeze circulation and its interaction with topographic forcing (Nayak, 2017).

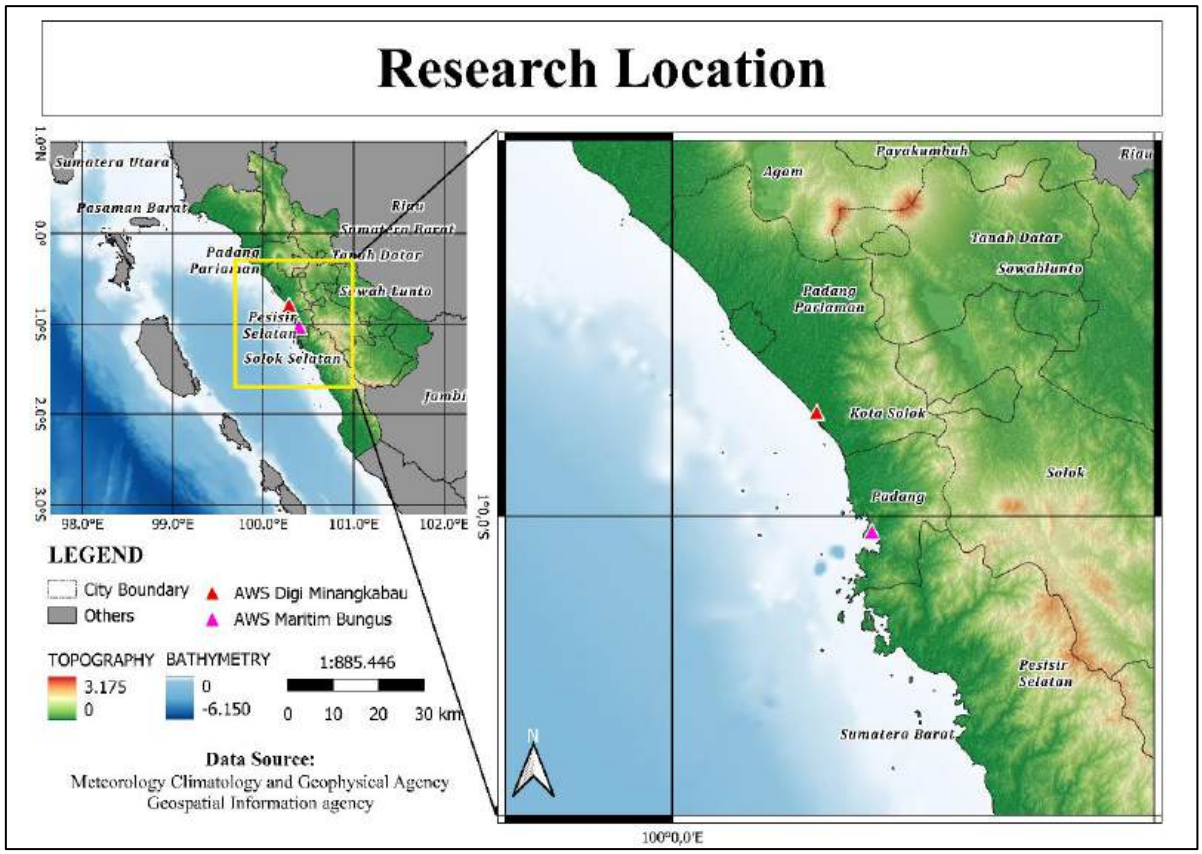


Figure 1. Study area and AWS locations.

Two Automatic Weather Stations (AWS) operated by the Meteorology, Climatology, and Geophysics Agency (BMKG) were used in this study. The first station, AWS Digi Stamet Minangkabau (0.789° S, 100.287° E), is located on the coastal plain and represents inland atmospheric conditions influenced by sea-breeze penetration. The second station, AWS Maritim Bungus (1.030° S, 100.396° E), is situated near the coastline and represents the marine–coastal environment. The combination of these stations enables the investigation of land–sea breeze evolution from the coastal zone toward inland areas.

The analysis focused on the dry-season period from May to September 2025, when land–sea thermal contrasts are typically more pronounced and local mesoscale circulations are less frequently disrupted by widespread rainfall. The proximity of the Bukit Barisan Mountain range to the coastline makes the region particularly suitable for examining the interaction between coastal thermal forcing and topographic influences on land–sea breeze

© 2026 Dept. of Geophysics Hasanuddin University

development (BMKG, 2025; Liang & Wang, 2017).

Observational Data

This study utilized surface meteorological observations from two Automatic Weather Stations (AWS) operated by the Meteorology, Climatology, and Geophysics Agency (BMKG): AWS Digi Minangkabau and AWS Maritim Bungus (Figure 1). The observation period covered the 2025 dry season from May to September. The characteristics of the observational datasets employed in this study are presented in Table 1.

Table 1. Observational datasets used in this study.

Station	Latitude (°)	Longitude (°)	Temporal Resolution	Variables
AWS Digi Minangkabau	0.789° S	100.287° E	10 min	Wind speed, wind direction, air temperature, relative humidity, pressure, rainfall, solar radiation
AWS Maritim Bungus	1.030° S	100.396° E	1 min*	Wind speed, wind direction, air temperature, relative humidity, pressure, rainfall

*AWS Maritim Bungus observations were aggregated to hourly values for analysis.

Meteorological variables used in this study included wind speed, wind direction, air temperature, relative humidity, atmospheric pressure, rainfall, and solar radiation. These observations were employed for land–sea breeze identification, characterization of circulation properties, and validation of WRF-ARW simulations. Data quality control was conducted prior to analysis to identify missing observations and ensure data reliability. Days with excessive missing data were excluded from subsequent analyses.

The AWS observations were further used to determine the onset time, duration, dominant wind direction, and wind speed associated with land–sea breeze circulation. In addition, observations from AWS Digi Minangkabau were used to evaluate the performance of WRF-ARW simulations through comparisons of near-surface temperature and wind fields.

Identification of Land–Sea Breeze Events

Land–sea breeze events were identified using a six-step filtering framework developed by integrating objective identification criteria proposed in previous land–sea breeze studies (Borne et al., 1998; Hwang et al., 2020; Coulibaly et al., 2021; Guo et al., 2023; McCabe & Freedman, 2023). Rather than adopting a single published algorithm, the framework combines complementary criteria describing wind reversal, wind persistence, thermodynamic conditions, precipitation, and solar heating. The resulting procedure was subsequently adapted to the geographical characteristics of the west coast of West Sumatra and the temporal resolution of the AWS observations. The overall workflow used for event identification is illustrated in Figure 2.

The identification process consisted of six sequential steps. First, quality control was applied to remove days with excessive missing observations. Second, potential sea-breeze events were identified based on wind direction, wind speed, and predefined daytime time windows representing onshore flow conditions. Third, potential land-breeze events were detected using corresponding nighttime offshore-flow criteria. Fourth, sea-breeze and land-breeze occurrences were paired to identify complete daily circulation cycles. Fifth,

© 2026 Dept. of Geophysics Hasanuddin University

rainfall-based filtering was applied to exclude days affected by significant precipitation that could disrupt thermally driven circulations. Finally, sunshine-duration filtering was performed to ensure sufficient daytime solar heating for sea-breeze development.

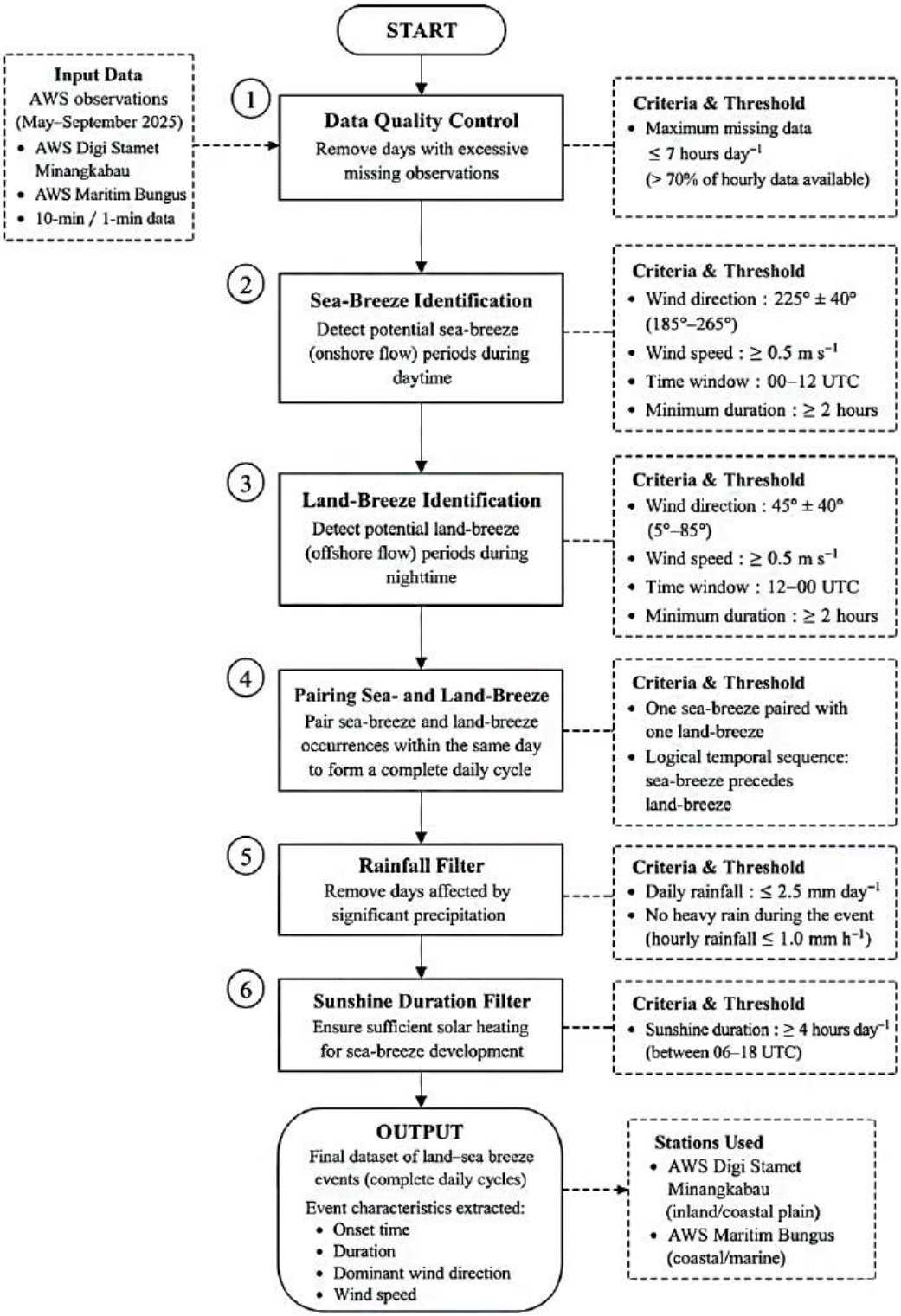


Figure 2. Workflow of the land–sea breeze identification procedure based exclusively on AWS observations using the modified Six Filters approach.

© 2026 Dept. of Geophysics Hasanuddin University

The modified criteria were adjusted to account for the geographical characteristics of the west coast of West Sumatra and the temporal resolution of the AWS observations. Event characteristics, including onset time, duration, dominant wind direction, and wind speed, were subsequently derived from all identified land–sea breeze events. The resulting event database was then used to characterize circulation properties and to select representative cases for detailed numerical simulation and atmospheric analysis.

Representative Event Selection

Following the identification of land–sea breeze events, all identified cases were considered as candidate events for numerical simulation. A total of 54 land–sea breeze events were identified during the study period, comprising 51 events at AWS Digi Minangkabau and three events at AWS Maritim Bungus (Table 2).

Candidate events were ranked based on five meteorological characteristics: sea-breeze duration (30%), land-breeze duration (20%), mean sea-breeze wind speed (20%), sunshine duration (20%), and daily rainfall (10%). Each parameter was normalized using min–max normalization before calculating the ranking score. The ten highest-ranked candidate events are presented in Table 3.

Table 2. Identified land–sea breeze events during the May–September 2025 study period

Month	AWS Digi Minangkabau	AWS Maritim Bungus
May	5, 6, 7, 9, **18**, 19, 20, 21, 23, 24, 26, **27**, 28	-
June	**2**, 3, 12, 13, 14, 21, 22, 24, 25, 26, 27, 29, 30	-
July	1, 2, 3, 4, 9, 10, 12, 16, 17, 18, 19, 21, 22, 24, 28	-
August	5, 11, 26, 27, 30	13, 15, 26
September	1, 7, 12, 25, 26	-

*Bold dates indicate representative WRF simulation cases

The representative cases were selected from the ten highest-ranked candidate events to encompass a broader range of land–sea breeze characteristics for model evaluation. Among the highest-ranked candidates, the events on 27 May and 6 May exhibited very similar land–sea breeze characteristics. To avoid selecting two representative cases with nearly identical atmospheric conditions, the 18 May event was chosen instead because it exhibited stronger sea-breeze intensity and provided a more distinct circulation pattern. This selection was intended to maximize the diversity of the representative validation cases while retaining only high-ranked candidate events.

Table 3. Top ten ranked candidate land–sea breeze events used for representative case selection.

Rank	Date	SB Onset (UTC)	SB Duration (h)	LB Onset (UTC)	LB Duration (h)	Mean SB Speed ($m\ s^{-1}$)	Selected for WRF
1	2025-06-02	02:00	9	13:00	10	4,09	✓
2	2025-05-27	03:00	9	12:00	12	2,78	✓
3	2025-05-06	01:00	10	13:00	11	2,44	
4	2025-06-03	03:00	10	13:00	9	2,77	
5	2025-05-28	02:00	10	12:00	12	1,73	
6	2025-05-18	02:00	7	12:00	12	3,51	✓
7	2025-05-26	02:00	8	12:00	12	2,87	
8	2025-06-27	02:00	10	13:00	10	2,19	
9	2025-07-17	03:00	9	12:00	11	2,36	
10	2025-07-22	02:00	7	12:00	12	3,14	

© 2026 Dept. of Geophysics Hasanuddin University

Accordingly, the three representative events selected for WRF-ARW simulations were 18 May, 27 May, and 2 June 2025.

WRF-ARW Configuration

The simulations were initialized using the Global Data Assimilation System Final Analysis (GDAS-FNL) dataset with a spatial resolution of 0.25° as the initial and lateral boundary conditions, while static geographical fields were generated through the WRF Preprocessing System (WPS). A three-level nested domain configuration with horizontal resolutions of 9 km, 3 km, and 1 km was adopted to represent mesoscale and local-scale atmospheric processes along the west coast of West Sumatra (Yoon et al., 2021). The model domains and the cross-section transect used for the vertical analyses are shown in Figure 3.

Table 4 summarizes the configuration of the WRF-ARW model (version 4.6.1) used in this study. The selected physical parameterization schemes were adopted based on previous studies demonstrating good performance in simulating sea-breeze circulation and mesoscale atmospheric processes over tropical coastal environments (Yoon et al., 2021; Reddy et al., 2022; McCabe & Freedman, 2025).

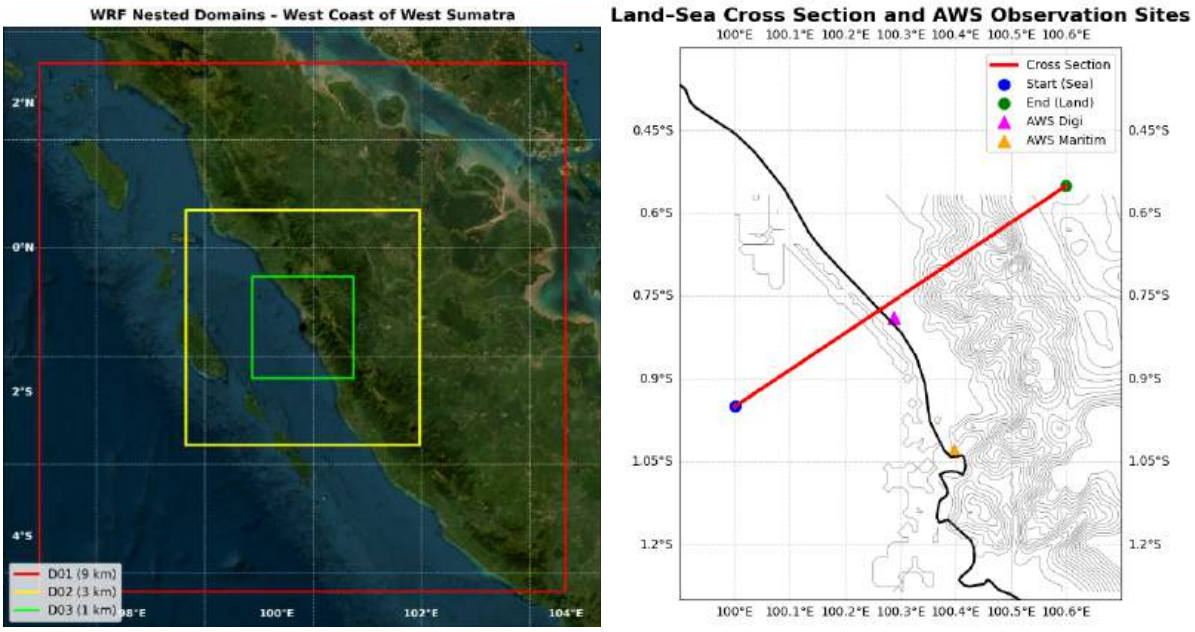


Figure 3. WRF-ARW nested domains and cross-section transect (Sea–Land) used in this study.

In particular, the combination of the MYNN2 planetary boundary layer scheme, Noah-MP land surface model, and RRTMG longwave and shortwave radiation schemes was selected following Yoon et al. (2021), who reported improved numerical prediction of sea-breeze circulation using this configuration. The urban canopy model was disabled following McCabe & Freedman. (2025), who showed that urban parameterizations can overestimate the land–sea thermal contrast in coastal simulations. The Kain–Fritsch cumulus parameterization was applied only in the outermost domain, following the default configuration adopted by Yoon et al. (2021), while convection was explicitly resolved in the convection-permitting inner domains. Other model settings followed the default Tropical Suite configuration. The complete model configuration is presented in Table 4.

Hourly model outputs included both near-surface meteorological variables and three-dimensional atmospheric fields. The near-surface variables were used for comparison with AWS observations during model validation, whereas the three-dimensional fields were used to investigate the

© 2026 Dept. of Geophysics Hasanuddin University

horizontal circulation, vertical atmospheric structure, and temporal evolution of land–sea breeze events.

Table 4. WRF-ARW model configuration used in this study

Configuration	Domain 1	Domain 2	Domain 3	Reference
Horizontal resolution	9 km	3 km	1 km	Yoon et al., 2021
Grid points (e_we × e_sn)	100 × 100	91 × 91	82 × 82	-
Vertical levels	45	45	45	-
Parent grid ratio	1	3	3	-
Microphysics		WSM6		Tropical Suite
Longwave radiation		RRTMG		Yoon et al., 2021
Shortwave radiation		RRTMG		Yoon et al., 2021
Land surface model		Noah-MP		Reddy et al., 2022
Surface Layer Scheme		MYNN		Yoon et al., 2021
Urban Scheme		OFF		McCabe & Freedman., 2025
PBL scheme		MYNN2		Yoon et al., 2021
Cumulus parameterization	Kain-Fritsch	OFF	OFF	Yoon et al., 2021
Simulation output interval		1 h		-

The AWS observations and WRF-ARW simulations served complementary roles in this study. AWS observations were used to identify land–sea breeze events and to provide reference measurements for model validation, whereas the WRF-ARW simulations were used to reproduce the selected events and examine their spatial evolution and three-dimensional atmospheric structure.

Model Validation

The performance of the WRF-ARW model was evaluated by comparing simulated variables with observations from AWS Digi Minangkabau for the three selected land–sea breeze events. The validation focused on 2-m air temperature (T2), 10-m wind speed (WS), and 10-m wind direction (WD). Statistical metrics were used to quantify the agreement between simulations and observations.

Model performance for temperature and wind speed was evaluated using the Root Mean Square Error (RMSE), Mean Absolute Error (MAE), Mean Bias Error (MBE), and Pearson correlation coefficient (r). These metrics are defined as (Arrillaga et al., 2016; McCabe et al., 2025):

$$RMSE = \sqrt{\frac{1}{n}\sum_{i=1}^{n}(S_i - O_i)^2} \quad (1)$$

$$MAE = \frac{1}{n}\sum_{i=1}^{n}|S_i - O_i| \quad (2)$$

$$MBE = \frac{1}{n}\sum_{i=1}^{n}(S_i - O_i) \quad (3)$$

$$r = \frac{\sum_{i=1}^{n}(S_i - S)(O_i - O)}{\sqrt{\sum_{i=1}^{n}(S_i - S)^2}\sqrt{\sum_{i=1}^{n}(O_i - O)^2}} \quad (4)$$

Where S_i and O_i represent simulated and observed values, respectively, S and O denote their means, and (n) is the number of paired observations.

Because wind direction is a circular variable, its performance was evaluated using Circular Root Mean Square Error (CRMSE) and Normalized Root Mean Square Error (NRMSE). Circular error was calculated by considering the minimum angular difference between simulated and observed wind directions (Arrillaga et al., 2016; McCabe et al., 2025).

$$CRMSE = \sqrt{\frac{1}{n}\sum_{i=1}^{n}(\Delta\theta_i)^2} \quad (5)$$

$$NRMSE = \frac{CRMSE}{180} \times 100 \quad (6)$$

© 2026 Dept. of Geophysics Hasanuddin University

Where $\Delta\theta_i$ is the minimum angular difference between simulated and observed wind directions.

Atmospheric Analysis

Atmospheric dynamics associated with land–sea breeze circulation were investigated using WRF-ARW output from the three selected events. Horizontal analyses were performed using 2-m air temperature (T2), 10-m wind vectors, surface convergence, and Planetary Boundary Layer Height (PBLH) to examine the evolution of thermal gradients, circulation patterns, convergence zones, and boundary-layer development. These analyses were used to identify the initiation, mature phase, and transition stages of the land–sea breeze circulation.

To evaluate the vertical atmospheric structure, cross-sectional analyses were conducted along the A–B transect shown in Figure 3. The analyses included wind fields, virtual potential temperature, mixing ratio, vertical velocity, and U–W circulation. In addition, time–height cross sections were generated at AWS Digi Minangkabau and AWS Maritim Bungus to examine the temporal evolution of wind structure and vertical motion throughout the circulation cycle. The combination of horizontal, vertical, and time–height analyses was used to characterize the development of land–sea breeze circulation and its interaction with the Bukit Barisan topography.

Results and Discussion

Characteristics of Land-Sea Breeze Events

A total of 51 land–sea breeze events were identified at AWS Digi Minangkabau during the May–September 2025 dry season, whereas only three events satisfied all identification criteria at AWS Maritim Bungus (Table 5). The large difference in the number of detected events indicates that the occurrence of complete land–sea breeze cycles was considerably more consistent at the inland station than at the coastal station. This result suggests that local environmental conditions at Bungus, including complex coastline geometry, surrounding terrain, and the influence of larger-scale atmospheric forcing, may have reduced the frequency of clearly detectable land–sea breeze signatures.

Table 5. Characteristics of Identified Land–Sea Breeze Events over the West Coast of West Sumatra

Parameter	AWS Digi Minangkabau	AWS Maritim Bungus
Number of identified events	51	3
Mean sea-breeze onset (UTC)	02-03	03–04
Sea-breeze onset range (UTC)	01-06	01-07
Mean sea-breeze duration (h)	7.35	6.67
Mean sea-breeze direction (°)	238.13	195.68
Mean sea-breeze speed (m s^{-1})	2.62	1.95
Mean land-breeze onset (UTC)	12–13	15–16
Mean land-breeze duration (h)	8.57	3.00
Mean land-breeze direction (°)	55.97	348.96
Mean land-breeze speed (m s^{-1})	0.90	0.52

The identified events exhibited relatively consistent onset times throughout the study period. At AWS Digi, sea-breeze onset generally occurred between 02 and 03 UTC, with a wider onset range of 01–06 UTC. A similar pattern was observed at AWS Maritim, where sea-breeze onset typically occurred between 03 and 04 UTC. The occurrence of sea-breeze onset during the morning hours is consistent with the development of land–sea thermal contrasts following solar heating over land. As the land surface warms more rapidly than the adjacent ocean, a horizontal pressure

© 2026 Dept. of Geophysics Hasanuddin University

gradient is established, initiating the onshore flow characteristic of sea-breeze circulation (Allouche et al., 2025).

The duration of sea-breeze circulation was also relatively stable. Mean sea-breeze duration reached 7.35 h at AWS Digi and 6.67 h at AWS Maritim. These values indicate that once established, the sea-breeze circulation persisted for a substantial portion of the daytime period. The longer duration observed at AWS Digi suggests that inland penetration of marine air remained active even after the initial onset near the coastline. Such behaviour is consistent with the continued maintenance of thermal and pressure gradients between land and ocean during daytime conditions.

Differences between the two stations were more evident in wind direction. The mean sea-breeze direction at AWS Digi was 238.13°, indicating a southwesterly to westerly onshore flow, whereas AWS Maritim recorded a more southerly direction (195.68°). These differences reflect the influence of coastline orientation and the Bukit Barisan topography on the inland penetration of marine air (Miao et al., 2003; He et al., 2021).

Sea-breeze circulation was consistently stronger than land-breeze circulation at both stations. Mean sea-breeze wind speeds reached 2.62 m s^{-1} at AWS Digi and 1.95 m s^{-1} at AWS Maritim, compared with only 0.90 and 0.52 m s^{-1} during the land-breeze phase. This asymmetry indicates stronger daytime thermal forcing than nocturnal cooling during the dry season.

Land-breeze circulation exhibited greater variability than sea-breeze circulation. At AWS Digi, offshore flow generally developed between 12 and 13 UTC and persisted for about 8.6 h, whereas AWS Maritim showed a later onset (15–16 UTC) and a much shorter duration (3 h). This contrast suggests that nocturnal offshore flow was more susceptible to local topographic effects and background atmospheric conditions. Unlike AWS Digi, AWS Maritim is located within Bungus Bay, where the narrow coastal plain is immediately bounded by the Bukit Barisan Mountains. Such geographical conditions favor interactions between land-breeze circulation, mountain–valley winds, and background synoptic forcing, which can weaken or interrupt nocturnal offshore flow and shorten its persistence (Miao et al., 2015; Allouche et al., 2023). Furthermore, the irregular coastal geometry of Bungus Bay likely modifies local airflow and wind direction, resulting in land-breeze characteristics that reflect the local geographical setting rather than an idealized land–sea-breeze circulation (Lim & Lee, 2021). This interpretation is also supported by the markedly different mean land-breeze direction observed at AWS Maritim (348.96°), indicating a stronger influence of local terrain on the nighttime circulation than at AWS Digi.

Overall, the observational analysis indicates three characteristic features of land–sea breeze circulation along the west coast of West Sumatra: (1) a relatively consistent morning sea-breeze onset with a duration of approximately 6–8 h, (2) stronger and more persistent sea-breeze circulation than land breeze, and (3) clear spatial differences between the inland and coastal stations, highlighting the influence of complex coastal topography and local atmospheric forcing on the development and persistence of land–sea breeze circulation. These observations provide the basis for evaluating the capability of WRF-ARW to reproduce the identified events and their associated atmospheric dynamics.

Performance of WRF-ARW in Simulating Land–Sea Breeze Circulation

The performance of WRF-ARW was evaluated by comparing simulated atmospheric variables with observations from AWS Digi Minangkabau during the three selected land–sea breeze events. Validation was conducted for near-surface

© 2026 Dept. of Geophysics Hasanuddin University

air temperature (T2), wind speed (WS), and wind direction (WD). Statistical metrics were calculated using 24 hourly observation–simulation pairs (00–23 UTC) for each event day, while each WRF simulation was initialized at 06 UTC on the preceding day to provide an 18-hour spin-up period. The results are summarized in Table 6.

Table 6. Validation Statistics of WRF-ARW Simulations for Selected Land–Sea Breeze Events.

Parameter	Variable	RMSE	MAE	MBE	r	NRMSE (%)
18 May 2025	T2	1.470	1.270	-0.361	0.961	-
	WS	0.519	0.419	0.177	0.929	-
	WD	73.465	-	-	-	40.814
27 May 2025	T2	1.446	1.206	-0.560	0.966	-
	WS	0.504	0.416	0.189	0.903	-
	WD	44.195	-	-	-	24.553
2 June 2025	T2	1.828	1.548	-1.435	0.928	-
	WS	1.473	1.119	-0.018	0.600	-
	WD	69.080	-	-	-	38.378

Overall, the model demonstrated good skill in reproducing the temporal evolution of near-surface temperature throughout the study period. Temperature simulations exhibited high correlation coefficients ranging from 0.928 to 0.966, indicating that WRF-ARW successfully captured the observed diurnal temperature variability associated with the development of land–sea thermal contrasts. RMSE values varied between 1.446 and 1.828 °C, while MAE values ranged from 1.206 to 1.548 °C. In all cases, the model produced negative MBE values, suggesting a systematic tendency to underestimate near-surface air temperature. The strongest temperature performance was obtained during the 27 May 2025 event, which yielded the highest correlation coefficient (r = 0.966) and the lowest RMSE (1.446 °C). These results indicate that WRF-ARW was able to reproduce the thermal forcing responsible for the initiation and maintenance of land–sea breeze circulation with a high degree of accuracy.

Wind speed simulations also showed generally satisfactory performance, particularly during the 18 May and 27 May events. Correlation coefficients exceeded 0.90 in both cases, accompanied by relatively low RMSE values of approximately 0.5 ms^{-1}. Positive MBE values indicate a slight tendency for the model to overestimate wind speed during these events. The ability of WRF-ARW to reproduce the observed wind-speed variability suggests that the model adequately represented the strength of the sea-breeze circulation and its inland penetration during periods characterized by well-defined local forcing.

A notable reduction in model performance was observed during the 2 June 2025 event. Although temperature simulations remained highly correlated with observations (r = 0.928), wind-speed performance deteriorated substantially, as indicated by the increased RMSE (1.473 ms^{-1}) and reduced correlation coefficient (r = 0.600). This decline suggests that atmospheric conditions during this event were influenced by additional processes that were not represented as effectively by the model. Similar interactions between local sea-breeze circulations and larger-scale atmospheric forcing have been documented in monsoon-affected coastal regions (Jayakrishnan et al., 2021; Allouche et al., 2025). The reduced skill may reflect stronger interactions between local land–sea breeze circulation and larger-scale atmospheric forcing, resulting in a more complex wind field than those observed during the other two cases.

© 2026 Dept. of Geophysics Hasanuddin University

The accuracy of simulated wind direction was assessed using normalized circular root mean square error (NRMSE) to account for the circular nature of directional data. Among the three events, the 27 May case produced the lowest directional error, with an NRMSE of 24.55%, indicating the best agreement between simulated and observed wind directions. The 18 May and 2 June events exhibited higher NRMSE values of 40.81% and 38.38%, respectively, suggesting greater directional variability and larger discrepancies between model output and observations. Nevertheless, the model successfully reproduced the primary transition from offshore to onshore flow and the subsequent reversal associated with the land–sea breeze cycle.

Taken together, the validation results demonstrate that WRF-ARW was capable of reproducing the principal characteristics of land–sea breeze circulation along the west coast of West Sumatra. The model consistently captured the evolution of near-surface temperature and wind fields, particularly during the 18 May and 27 May events, which exhibited the strongest agreement with observations. Although model performance declined during the 2 June event, the overall results provide sufficient confidence to use the simulations for investigating the horizontal and vertical atmospheric dynamics associated with the selected land–sea breeze cases, as discussed in the following section.

Atmospheric Dynamics of Representative Land–Sea Breeze Events

1. Atmospheric Evolution during the 18 May 2025 Event

The 18 May 2025 event represents a typical land–sea breeze circulation case over the west coast of West Sumatra. The circulation developed following daytime heating over land, which generated a land–sea thermal contrast and induced onshore flow from the Indian Ocean. Similar thermally driven mechanisms have been widely recognized as the primary driver of sea-breeze formation in tropical coastal regions (Allouche et al., 2025).

Although Figure 5 presents the representative horizontal evolution of the circulation for 27 May 2025, a comparable development was also observed on 18 May. Marine air penetrated inland toward the foothills of the Bukit Barisan, where convergence became increasingly organized. The displacement of convergence away from the coastline suggests a strong interaction between the sea breeze and local topography. Similar topographically induced convergence has been reported in coastal mountainous environments where sea-breeze flow interacts with terrain barriers and slope circulations (Miao et al., 2003; He et al., 2021).

© 2026 Dept. of Geophysics Hasanuddin University

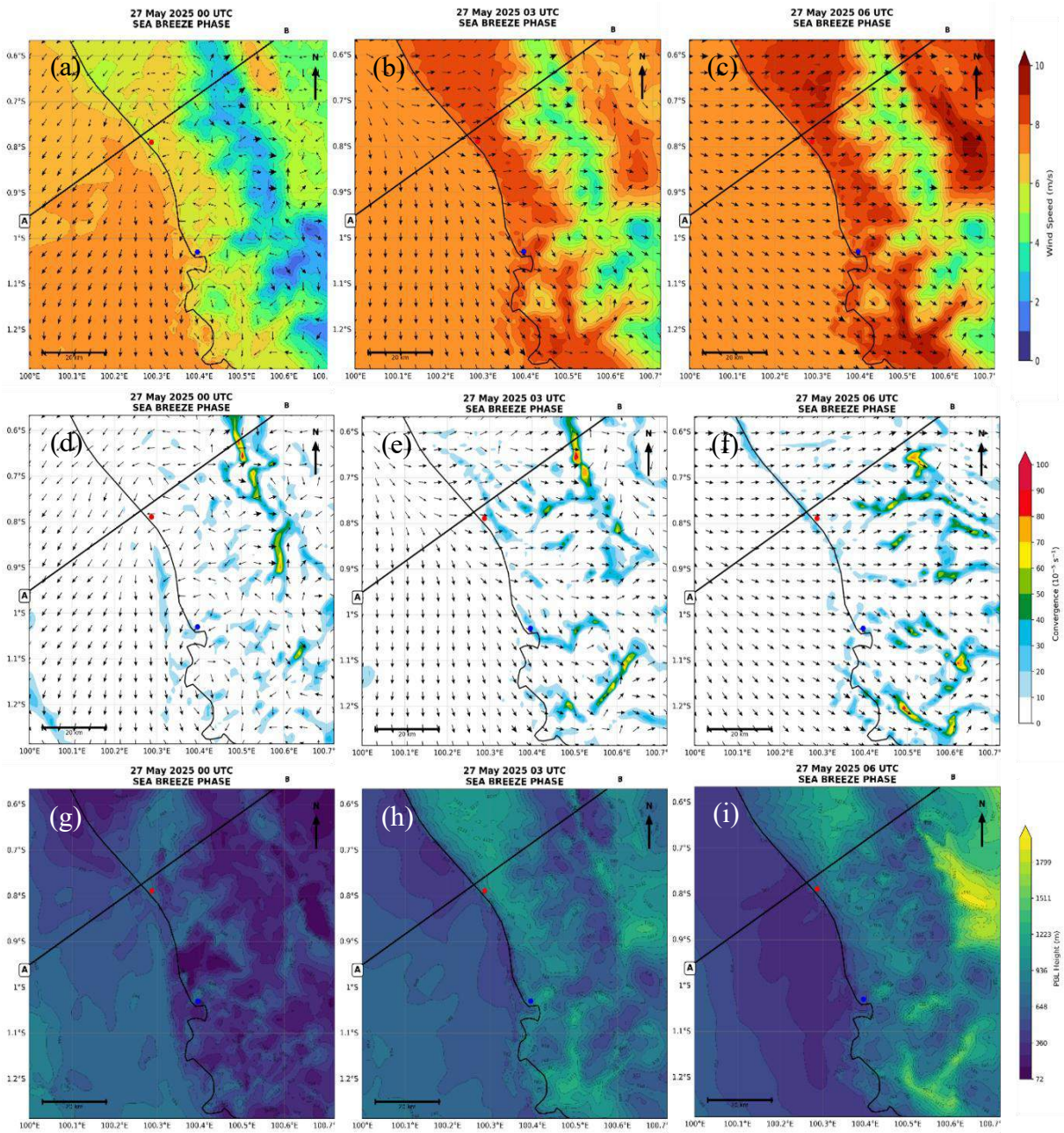


Figure 5. Horizontal evolution of land–sea breeze circulation on 27 May 2025: (a–c) Near-surface air temperature (T2; shaded) and 10-m wind vectors at 03, 06, and 09 UTC, respectively; (d–f) Surface convergence (shaded) at 03, 06, and 09 UTC, respectively; (g–i) Planetary Boundary Layer Height (PBLH; shaded) at 03, 06, and 09 UTC, respectively.

The vertical structure of the circulation was characterized by low-level onshore flow, moisture transport toward inland regions, and enhanced upward motion over the foothills. As illustrated by the representative vertical structure in Figure 6, the circulation extended through approximately 1–2 km of the lower troposphere. Comparable circulation depths have been reported in several coastal regions, indicating that sea-breeze circulations are generally confined to the lower atmosphere (Park & Chae, 2018; Jia et al., 2022). Overall, the 18 May event demonstrates a well-organized land–sea breeze circulation strongly influenced by both thermal forcing and topographic modulation.

2. Atmospheric Evolution during the 27 May 2025 Event

© 2026 Dept. of Geophysics Hasanuddin University

The 27 May 2025 event exhibited the most persistent land–sea breeze circulation among the three selected cases and corresponded to the best overall model performance. The horizontal evolution of the circulation is shown in Figure 5. A pronounced thermal gradient between land and ocean promoted the rapid development of onshore flow, followed by inland penetration of marine air toward the foothills of the Bukit Barisan.

As the circulation intensified, convergence became concentrated over inland regions, while planetary boundary layer development remained active throughout much of the daytime period. The sustained transport of marine moisture inland indicates favourable conditions for maintaining the circulation after its initial formation. Similar relationships between boundary-layer growth, moisture transport, and sea-breeze persistence have been documented in tropical coastal environments (Jia et al., 2022; Yoo et al., 2025).

The mature circulation structure is illustrated in Figure 6. A well-defined onshore flow occupied the lower troposphere, while compensating return flow developed aloft, forming a classical sea-breeze circulation cell. Strong upward motion over the foothill region coincided with maximum convergence, indicating efficient coupling between coastal thermal forcing and topographic effects. Similar topographically induced convergence has been reported in coastal mountainous environments (Miao et al., 2003; He et al., 2021). These characteristics suggest that the interaction between land–sea thermal gradients and the Bukit Barisan topography was particularly effective during this event, resulting in the most persistent circulation observed in this study.

3. Atmospheric Evolution during the 2 June 2025 Event

The 2 June 2025 event displayed a more complex circulation structure than the previous cases. Although a clear land–sea breeze cycle was identified, the horizontal and vertical organization of the circulation was comparatively weaker. The event also corresponded to reduced model performance for wind-related variables, suggesting the influence of additional atmospheric processes.

Despite these differences, marine air still penetrated inland and generated convergence over both coastal and inland regions. Such dual convergence patterns have been reported in other coastal environments where sea-breeze circulations interact with local terrain and evolving background flows (He et al., 2021; Zhu et al., 2017). Compared with the representative circulation shown in Figures 5 and 6, the 2 June event exhibited a less coherent distribution of convergence, vertical motion, and moisture transport.

Nevertheless, the fundamental characteristics of land–sea breeze circulation remained evident. Onshore flow dominated the lower atmosphere during the daytime period, while upward motion developed over inland regions and foothills. The circulation depth remained within approximately 1–2 km of the lower troposphere, although the cell was less symmetrical and less persistent than in previous events. This depth aligns with observations from Seoul and other coastal regions, where sea-breeze circulation is largely confined to the lower troposphere (Park & Chae, 2018; Jia et al., 2022). These findings suggest that local thermal forcing remained important, but its influence was partly modulated by larger-scale atmospheric conditions—a behavior also documented in monsoon-influenced coastal environments (Jayakrishnan et al., 2021; Allouche et al., 2025).

© 2026 Dept. of Geophysics Hasanuddin University

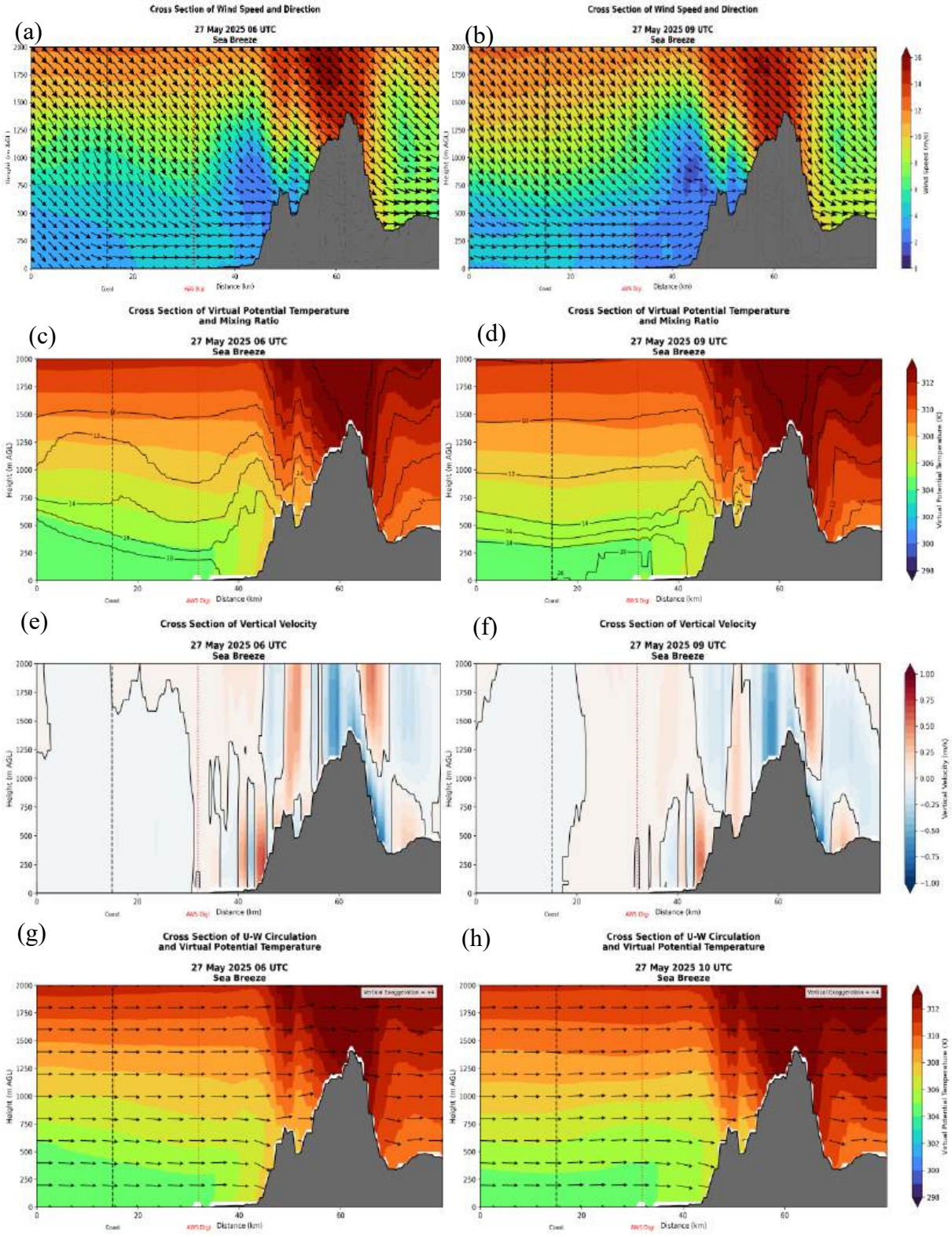


Figure 6. Vertical structure of land–sea breeze circulation during the mature phase of the 27 May 2025 event: (a–b) Cross-sections of wind speed and wind vectors at 06 and 09 UTC, respectively; (c–d) Cross-sections of virtual potential temperature (θ_v; shaded) and mixing ratio (contours) at 06 and 09 UTC, respectively; (e–f) Cross-sections of vertical velocity at 06 and 09 UTC, respectively; (g–h) U–W circulation cross-sections at 06 and 10 UTC, respectively.

Comparative Characteristics of the Three Events

Although all three events exhibited the fundamental characteristics of thermally

© 2026 Dept. of Geophysics Hasanuddin University

driven land–sea breeze circulation, substantial differences were observed in their spatial organization, persistence, and vertical structure (Table 7). The similarities among the events include a relatively consistent sea-breeze onset between 02 and 03 UTC and a mature phase occurring between 06 and 09 UTC. This consistency suggests that the initiation and development of land–sea breeze circulation along the west coast of West Sumatra are strongly controlled by the diurnal cycle of surface heating, which establishes a recurring land–sea thermal contrast during the dry season.

Table 7. Comparative characteristics of three selected land–sea breeze events.

Characteristic	18 May 2025	27 May 2025	2 June 2025
Sea-breeze onset (UTC)	02	03	02
Sea-breeze duration (h)	7	9	9
Mature phase (UTC)	06–09	06–09	06–09
Surface convergence	Strong and organized	Widespread and fragmented	Strong and relatively organized
PBL development	Rapid and intensive	More persistent	Extensive and organized
Moisture transport	Intensive	Continuous	Intensive and continuous
Upward motion	Concentrated over mountain slopes	Widespread and persistent	Strong and sustained until transition phase
U–W circulation structure	Well-defined	Relatively weak but persistent	Most complete
Dominant characteristic	Strong circulation organization	High circulation persistence	Most complete land–sea breeze cycle

The 18 May 2025 event was characterized by the strongest circulation organization. Surface convergence developed as a coherent zone extending from the coastal plain toward the foothills of the Bukit Barisan, while ascending motion remained concentrated over the eastern portion of the study area. The U–W circulation pattern was clearly identifiable, indicating efficient coupling between low-level onshore flow and compensating return flow aloft. These characteristics suggest that the interaction between thermal forcing and topographic effects produced a highly organized mesoscale circulation structure.

In contrast, the 27 May 2025 event exhibited the greatest circulation persistence. Although the convergence pattern appeared more spatially fragmented than in the 18 May case, moisture transport from the ocean remained active for a longer period and the sea-breeze circulation persisted throughout much of the daytime cycle. The prolonged development of the planetary boundary layer and the sustained presence of upward motion indicate that the thermally driven circulation remained active for an extended duration. This behavior suggests that atmospheric conditions on 27 May were particularly favorable for maintaining the sea-breeze system after its initial formation.

The 2 June 2025 event displayed the most complete land–sea breeze cycle among the three cases. Strong and relatively organized convergence was observed during the mature stage of the circulation, while upward motion remained active until the transition toward the evening land-breeze phase. Unlike the previous events, the circulation evolution captured both the mature sea-breeze stage and the subsequent transition toward offshore flow. The resulting U–W circulation structure was the most complete among the selected cases, indicating a well-developed coupling between daytime onshore flow and nighttime offshore circulation.

The time–height analysis further reveals several common characteristics shared by all events. The sea-breeze circulation was generally confined to the lower troposphere and rarely extended above approximately 1–2 km altitude. The strongest onshore flow was consistently observed below 1

© 2026 Dept. of Geophysics Hasanuddin University

km, while ascending motion developed above regions affected by convergence and topographic lifting. These recurring features indicate that the land–sea breeze circulation along the west coast of West Sumatra is primarily a shallow mesoscale phenomenon whose vertical extent is strongly influenced by both coastal thermal gradients and the nearby Bukit Barisan topography.

Overall, the comparison demonstrates that differences among the three events are primarily associated with the degree of circulation organization, persistence, and completeness rather than with the fundamental mechanisms governing their development. Despite variations in intensity and structure, all events consistently show the combined influence of differential land–sea heating and topographic forcing, confirming that these two processes constitute the primary controls on land–sea breeze evolution in the study region.

General Characteristics of Land–Sea Breeze Circulation along the West Coast of West Sumatra

The observational and numerical analyses indicate that land–sea breeze circulation is a recurrent mesoscale phenomenon along the west coast of West Sumatra during the dry season. Despite variations among the selected events, the circulation exhibited relatively consistent onset times between 02 and 03 UTC and generally reached its mature phase between 06 and 09 UTC. Similar diurnal behavior has been reported along the west coast of Sumatra and other tropical coastal regions, where the evolution of sea-breeze circulation is primarily controlled by differential heating between land and ocean surfaces (North et al., 2025; Allouche et al., 2025).

A key characteristic identified in this study is the strong influence of topography on circulation development. Rather than remaining confined to the coastline, marine air consistently penetrated inland toward the foothills of the Bukit Barisan Mountain range. The strongest convergence and upward motion were frequently observed over inland and foothill regions, indicating that the interaction between coastal thermal gradients and mountainous terrain plays a major role in regulating circulation evolution. Similar topographic modulation of sea-breeze circulation has been documented in coastal mountainous environments, where terrain influences convergence patterns, penetration distance, and circulation intensity (Miao et al., 2003; He et al., 2021).

The vertical structure of the circulation was characterized by low-level onshore flow, compensating return flow aloft, and a circulation depth of approximately 1–2 km. Time–height and cross-sectional analyses revealed that the strongest sea-breeze influence remained confined to the lower troposphere, consistent with observations reported in other coastal regions (Park & Chae, 2018; Jia et al., 2022). These results indicate that land–sea breeze circulation along the west coast of West Sumatra develops as a shallow but well-organized mesoscale system.

The WRF-ARW simulations successfully reproduced the principal characteristics of the observed circulation, including the timing of sea-breeze development, inland penetration of marine air, convergence patterns, and vertical circulation structure. Collectively, the results demonstrate that the evolution of land–sea breeze circulation in the study region is governed by the combined effects of differential land–sea heating and topographic modulation by the Bukit Barisan Mountain range. This interaction represents the dominant mechanism controlling coastal atmospheric dynamics along the west coast of West Sumatra.

Conclusion

© 2026 Dept. of Geophysics Hasanuddin University

This study characterized land–sea breeze circulation along the west coast of West Sumatra during the 2025 dry season using AWS observations and WRF-ARW simulations. A total of 54 land–sea breeze events were identified during the study period, comprising 51 events from AWS Digi Minangkabau and three events from AWS Maritim Bungus. The results indicate that sea-breeze circulation generally developed between 02 and 03 UTC, reached its mature phase between 06 and 09 UTC, and typically persisted for 7–9 h. Horizontal, vertical, and time–height analyses consistently showed that marine air penetrated inland toward the foothills of the Bukit Barisan, where enhanced surface convergence, planetary boundary-layer development, and upward motion led to the development of a well-organized circulation cell extending to approximately 1–2 km above ground level. These findings indicate that the evolution of land–sea breeze circulation in the study area is jointly controlled by differential land–sea heating and topographic modulation associated with the Bukit Barisan Mountain range.

Model validation demonstrated that WRF-ARW reproduced the observed land–sea breeze characteristics with consistently good performance for near-surface temperature (correlation coefficients of 0.93–0.97 and MAE of 1.21–1.55 °C), although wind-speed performance exhibited greater variability among events (correlation coefficients of 0.60–0.93). The model also successfully captured the timing of sea-breeze development, inland penetration of marine air, the evolution of convergence and boundary-layer growth, and the vertical circulation structure. Overall, the findings demonstrate that WRF-ARW provides a reliable framework for investigating mesoscale coastal circulations over complex tropical terrain while providing new insight into the interaction between coastal thermal forcing and the Bukit Barisan topography along the west coast of West Sumatra.

Acknowledgements

The authors would like to express their sincere gratitude to the Meteorological Station Minangkabau and the Maritime Meteorological Station Teluk Bayur, Indonesian Agency for Meteorology, Climatology, and Geophysics (BMKG), for providing the observational data used in this study. The authors also gratefully acknowledge all individuals and institutions whose support, technical assistance, and constructive discussions contributed to the completion of this research.

Author Contribution

Reinal Taruna Wahyu Halawa: Conceptualization, data curation, formal analysis, investigation, methodology, software, visualization, writing—original draft, and correspondence. Latifah Nurul Qomariyatuzzamzami: Conceptualization, supervision, validation, methodology, writing—review and editing. Yosafat Donni Haryanto: Validation, supervision, and writing—review and editing. Avrionesti: Validation, supervision, and writing—review and editing.

Conflict of Interest

The authors declare no conflict of interest.

References

Allouche, M., Bou-Zeid, E. & Iipponen, J. (2023) The influence of synoptic wind on land–sea breezes. *Quarterly Journal of the Royal Meteorological Society*, 149(757), 3198–3219. https://doi.org/10.1002/qj.4552

Allouche, M., Iipponen, J., & Bou-Zeid, E. (2025). Unsteady land-sea breeze circulations in the presence of a synoptic pressure forcing. *Journal of Geophysical Research: Atmospheres*, 130, e2023JD040708. https://doi.org/10.1029/2023JD040708

© 2026 Dept. of Geophysics Hasanuddin University

Arrillaga, J. A., Yagüe, C., Sastre, M., & Román-Cascón, C. (2016). A characterisation of sea-breeze events in the eastern Cantabrian coast (Spain) from observational data and WRF simulations. *Atmospheric Research,* 181, 265–280. https://doi.org/10.1016/j.atmosres.2016.06.021

BMKG. (2025). *Buku pemutakhiran prediksi musim kemarau 2025 (Update Juni 2025)*. Badan Meteorologi, Klimatologi, dan Geofisika (BMKG). https://content.bmkg.go.id/wp-content/uploads/Buku-Update-PMK25-20250601.pdf

Borne, K., Chen, D., & Nunez, M. (1998). A method for finding sea breeze days under stable synoptic conditions and its application to the Swedish west coast. *International Journal of Climatology,* 18(8), 901–914. https://doi.org/10.1002/(SICI)1097-0088(19980630)18:8<901::AID-JOC295>3.0.CO;2-F

Coulibaly, A., Omotosho, B. J., Sylla, M. B., Diallo, Y., & Ballo, A. (2021). Numerical simulation of land and sea-breeze (LSB) circulation along the Guinean Coast of West Africa. *Modeling Earth Systems and Environment,* 7(3), 2031–2045. https://doi.org/10.1007/s40808-020-00953-0

Davis, S. R., Farrar, J. T., Weller, R. A., Jiang, H., & Pratt, L. J. (2019). The Land–Sea Breeze of the Red Sea: Observations, Simulations, and Relationships to Regional Moisture Transport. *Journal of Geophysical Research: Atmospheres*, 124(24), 13803–13825. https://doi.org/10.1029/2019JD031007

Drobinski, P., Bastin, S., Arsouze, T., Béranger, K., Flaounas, E., & Stéfanon, M. (2018). North-western Mediterranean Sea-breeze circulation in a regional climate system model. *Climate Dynamics*, 51, 1077–1093. https://doi.org/10.1007/s00382-017-3595-z

Guo, Z., Cao, L., Guo, J., Shang, M., & Guo, X. (2023). On three types of sea breeze in Qingdao of East China: An observational analysis. *Frontiers in Environmental Science,* 11*,* 1188952. https://doi.org/10.3389/fenvs.2023.1188952

He, G., Yuan, G., Liu, Y., Jiang, Y., Liu, Y., Shu, Z., Ma, X., Li, Y., & Huo, Z. (2021). The Effects of Topography and Urban Agglomeration on the Sea Breeze Evolution over the Pearl River Delta Region. *Atmosphere*, 13(1), 39. https://doi.org/10.3390/atmos13010039

Hwang, H., Eun, S.-H., Kim, B.-G., Park, S.-J., & Park, G.-M. (2020). Occurrence characteristics of sea breeze in the Gangneung region for 2009–2018. *Atmosphere,* 30(3), 221–236. https://doi.org/10.14191/Atmos.2020.30.3.221

Jayakrishnan, P. R., Sivaprasad, P., Chenoli, S. N., Babu, C. A., Samah, A. A., & Mohammedali, N. P. (2021). Sea breeze characteristics over a coastal station in peninsular Malaysia. *Journal of Earth System Science*, 130, 126. https://doi.org/10.1007/s12040-021-01632-z

Jia, D., Xin, J., Wang, Z., Wang, W., Wang, X., Xiao, H., Liu, C., Zhou, J., Tong, L., Sun, Y., Zhao, D., Wu, F., & Wang, L. (2022). The dynamic, thermal and material structures of sea-land breeze circulation at the coastal of Ningbo, East China Sea. *Atmospheric Research*, 283, 106540. https://doi.org/10.1016/j.atmosres.2022.106540

Liang, Z., & Wang, D. (2017). Sea breeze and precipitation over Hainan Island. *Quarterly Journal of the Royal Meteorological Society,* 143(702), 137–151. https://doi.org/10.1002/qj.2952

© 2026 Dept. of Geophysics Hasanuddin University

Lim, H.-J., & Lee, Y.-H. (2021). High-Resolution Modeling of Mesoscale Circulation in the Atmospheric Boundary Layer over a Complex Coastal Area. *Atmosphere*, 12(12), 1649. https://doi.org/10.3390/atmos12121649

McCabe, E. J., & Freedman, J. M. (2023). Development of an Objective Methodology for Identifying the Sea-Breeze Circulation and Associated Low-Level Jet in the New York Bight. *Weather and Forecasting*, 38(4), 571–589. https://doi.org/10.1175/WAF-D-22-0119.1

McCabe, E. J., & Freedman, J. M. (2025). Quantifying the Uncertainty in the Weather Research and Forecasting Model under Sea Breeze and Low-Level Jet Conditions in the New York Bight: Importance to Offshore Wind Energy. *Weather and Forecasting*, 40(3), 425–450. https://doi.org/10.1175/WAF-D-24-0086.1

Miao, J.-F, Kroon, L. J. M., de Arellano, J. V.-G., & Holtslag, A. A. M. (2003). Impacts of topography and land degradation on the sea breeze over eastern Spain. *Meteorology and Atmospheric Physics*, 84, 157–170. https://doi.org/10.1007/s00703-002-0579-1

Miao, Y., Liu, S., Zheng, Y., Wang, S., & Chen, B. (2015). Numerical study of the effects of topography and urbanization on the local atmospheric circulations over the Beijing-Tianjin-Hebei, China. *Advances in Meteorology,* 2015(1), 397070. https://doi.org/10.1155/2015/397070

Muppa, S. K., Anandan, V. K., Kesarkar, K. A., Rao, S. V. B., & Reddy, P. N. (2012). Study on deep inland penetration of sea breeze over complex terrain in the tropics. *Atmospheric Research*, 104–105, 209–216. https://doi.org/10.1016/j.atmosres.2011.10.007

Nayak, S. (2017). Coastal zone management in India − present status and future needs. *Geo-Spatial Information Science*, 20(2), 174–183. https://doi.org/10.1080/10095020.2017.1333715

North, R., Schumacher, C., Epifanio, C. C., Deranadyan, G., Putra, A. W., & Adiyasa, A. (2025). The Land–Sea Breeze Circulation over the West Coast of Sumatra. *Monthly Weather Review*, 153(11), 2295–2312. https://doi.org/10.1175/MWR-D-25-0020.1

Park, M.-S., & Chae, J.-H. (2018). Features of sea–land-breeze circulation over the Seoul Metropolitan Area. *Geoscience Letters,* 5(1), 28. https://doi.org/10.1186/s40562-018-0127-6

Park, J. M., van den Heever, S. C., Igel, A. L., Grant, L. D., Johnson, J. S., Saleeby, S. M., Miller, S. D., & Reid, J. S. (2020). Environmental Controls on Tropical Sea Breeze Convection and Resulting Aerosol Redistribution. *Journal of Geophysical Research: Atmospheres*, 125(6), e2019JD031699. https://doi.org/10.1029/2019JD031699

Reddy, B. R., Srinivas, C. V., & Venkatraman, B. (2022). Observational analysis and numerical simulation of sea breeze using WRF model over the Indian southeast coastal region. *Meteorology and Atmospheric Physics,* 134(1), 57. https://doi.org/10.1007/s00703-022-00891-9

Yoo, J.-W., Park, S.-Y., Kim, J., Chae, D., Moon, J., Kim, C.-H., Park, J., Kim, T.-H., & Lee, S.-H. (2026). Understanding the mechanisms of coastal PM2.5 formation driven by land–sea breeze recirculation and ship emissions. *Environmental Pollution,* 390, 127483. https://doi.org/10.1016/j.envpol.2025.

© 2026 Dept. of Geophysics Hasanuddin University

127483

Yoon, J. W., Lim, S., & Park, S. K. (2021). Combinational optimization of the WRF physical parameterization schemes to improve numerical sea breeze prediction using micro-genetic algorithm. *Applied Sciences,* 11(23), 11221. https://doi.org/10.3390/app112311221

Zhu, L., Meng, Z., Zhang, F., & Markowski, P. M. (2017). The influence of sea- and land-breeze circulations on the diurnal variability in precipitation over a tropical island. Atmospheric Chemistry and Physics, 17(21), 13213–13232. https://doi.org/10.5194/acp-17-13213-2017

© 2026 Dept. of Geophysics Hasanuddin University

ISSN: 2579-5821 (Print)
ISSN: 2579-5546 (Online)
URL address: http://journal.unhas.ac.id/index.php/geocelebes
DOI: 10.70561/geocelebes.v10i2.52563

Jurnal Geocelebes Vol. 10 No. 2, October 2026, 343 – 358

Multi-Attribute Analysis and Probabilistic Neural Network (PNN) Method for Predicting Carbonate Volume and Water Saturation in Biogenic Gas Reservoir: A Case Study of the Nias Basin, North Sumatra

Chikita Mery Yuliani[1], Renita Dwi Vadila[1], Mokhammad Puput Erlangga[1]*, Harnanti Y. Hutami[1], Egie Wijaksono[2]

[1]Geophysical Engineering, Faculty of Industrial Technology, Sumatra Institute of Technology, Lampung 35365, Indonesia.
[2]Oil and Gas Testing Center, Lemigas Office, Kebayoran Lama, South Jakarta 12230, Indonesia.

*Corresponding author. Email: mokhammad.erlangga@tg.itera.ac.id

Manuscript received: 6 July 2026; Received in revised form: 28 August 2026; Accepted: 31 August 2026

Abstract

Carbonate reservoirs frequently exhibit high heterogeneity, complicating the lateral prediction of petrophysical properties from sparse well log data. This study evaluates the hydrocarbon potential of a biogenic gas-bearing carbonate reservoir in the 'RC' Field, Nias Basin, by integrating well log and 2D seismic data. A multi-attribute analysis was conducted to identify seismic attributes sensitive to reservoir properties, which were subsequently used as input to a Probabilistic Neural Network (PNN) algorithm to predict the lateral distribution of Carbonate Volume (Vcr) and Water Saturation (Sw). Results identify a prospective gas-bearing carbonate zone in Well S-1 at depths of 4990 – 5693 ft, characterized by favorable reservoir quality and water saturation values predicted by the PNN model, with an average 0.4 (v/v). The PNN model significantly improved prediction accuracy, achieving correlation coefficients of 0.88 for Carbonate Volume and 0.83 for Water Saturation. These findings demonstrate that the PNN method effectively captures non-linear relationships between seismic attributes and petrophysical parameters, providing a robust framework for mapping prospective biogenic gas zones and optimizing future exploration planning in the Nias Basin.

Keywords: Biogenic Gas; Carbonate Reservoir; Carbonate Volume; Probabilistic Neural Network; Water Saturation.

Citation: Yuliani, C. M., Vadila, R. D., Erlangga, M. P., Hutami, H. Y., & Wijaksono, E. (2026). Multi-Attribute Analysis and Probabilistic Neural Network (PNN) Method for Predicting Carbonate Volume and Water Saturation in Biogenic Gas Reservoir: A Case Study of the Nias Basin, North Sumatra. *Jurnal Geocelebes*, 10(2): 343–358, doi: 10.70561/geocelebes.v10i2.52563

Introduction

In response to increasing energy demand and declining conventional hydrocarbon production, this study aims to evaluate the potential of hydrocarbon resources in the Nias Basin, North Sumatra. This situation encourages ongoing exploration efforts to discover new hydrocarbon resources.

Evaluating the hydrocarbon potential of carbonate reservoirs containing biogenic gas in the "RC" Field in the Nias Basin presents an exploration challenge. Carbonate reservoirs generally exhibit high levels of heterogeneity due to depositional processes, diagenesis, and porosity development. Consequently, the lateral distribution of petrophysical properties is difficult to characterize accurately with limited well data.

To address these challenges, well-log and seismic data were integrated to obtain a more representative distribution of reservoir properties and better characterize lateral reservoir variability. Water Saturation (Sw) and Carbonate Volume distributions were predicted using a multi-attribute seismic analysis with the

© 2026 Dept. of Geophysics Hasanuddin University

Probabilistic Neural Network (PNN) algorithm. Previous research by Khan et al. (2025) and Durrani et al. (2020) shows that the Probabilistic Neural Network (PNN) method provides more accurate predictions of petrophysical properties and characterizes reservoir heterogeneity more effectively than conventional approaches, making it well-suited for complex carbonate reservoirs.

Characterizing carbonate reservoirs in forearc settings, such as the Nias Basin in North Sumatra, remains a significant challenge due to the complex nature of carbonate diagenesis and the inherent heterogeneity of the rocks. Although previous studies, such as Rifai et al. (2019), have successfully characterized reservoir properties in this region using conventional seismic inversion methods, this approach is often limited in its ability to map heterogeneity within carbonate systems. Deterministic inversion techniques generally produce overly smoothed models that often fail to capture the complex nonlinear relationships between seismic attributes and petrophysical parameters, leading to estimates that overlook local variations in these carbonate features. This study addresses this gap by applying the Probabilistic Neural Network (PNN) method. By minimizing prediction bias in highly heterogeneous reservoir zones, this method improves the accuracy of carbonate volume and water saturation predictions, thereby providing better spatial resolution for identifying exploration targets (Ardinda & Riyanto, 2020).

Materials and Methods

This study comprises four main processing stages to estimate the spatial distribution of reservoir petrophysical properties. The first stage involves reservoir marker identification through well-log sensitivity analysis using crossplot log, which defines the target reservoir intervals based on the relationships among petrophysical parameters. The second stage involves calculating Water Saturation (Sw) and Carbonate Volume from well-log data to quantify reservoir properties within the identified intervals. These results provide the reference data for subsequent seismic-based prediction. The third stage consists of multi-attribute analysis to identify the seismic attributes most sensitive to the target petrophysical parameters. The selected attributes are evaluated for their correlation with well-log data to determine the optimal attribute combination for predicting reservoir properties. Probabilistic Neural Network (PNN) was trained using the selected seismic attributes and the corresponding log-derived Water Saturation (Sw) and Carbonate Volume values from Wells S-1 and T-1. During training, the PNN learned the nonlinear relationship between the seismic attributes and the log-derived reservoir properties. Model performance was evaluated by comparing the PNN-predicted log values with the corresponding measured well-log values using linear regression. The reported correlation coefficients were calculated from the regression of the predicted on the measured reservoir properties and were used to assess the predictive capability of the PNN model. Finally, a multi-attribute Probabilistic Neural Network (PNN) is applied to predict the lateral distribution of Water Saturation and Carbonate Volume across the seismic sections. By integrating seismic attributes with well-log data, the PNN models the complex relationship between seismic responses and petrophysical properties, enabling reliable prediction of reservoir properties in areas lacking well control (Sinaga et al., 2019). The workflow of the present study is illustrated in Figure 1.

Geological Setting

The Nias Basin is part of the Sumatran forearc basin within the Sunda subduction system and developed from the Early Eocene to the Late Pleistocene. The basin plays a significant geomorphological and

© 2026 Dept. of Geophysics Hasanuddin University

tectonic role as the rear boundary of compressional deformation associated with subduction processes, while forming the structural and geomorphological transition between uplifted and subsiding regions. Several major fault systems, such as the Batee and Mentawai Faults, cross the Nias Basin. These faults developed as a result of the oblique subduction of the northward-moving Indo-Australian Plate beneath the Eurasian Plate (Wibowo et al., 2024).

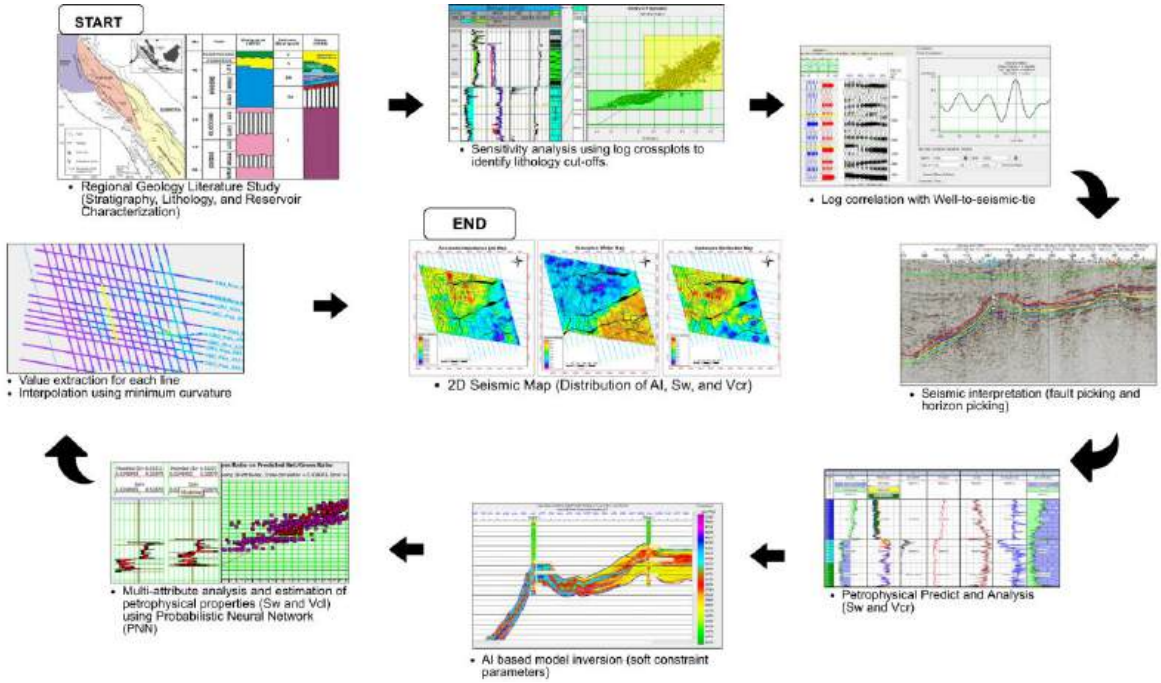


Figure 1. Research Workflow.

The regional geological structure is dominated by northwest–southeast trending extensional and transtensional faults that control the development of sub-basins, sedimentation patterns, and structural deformation within the Nias Basin. On a regional scale, basin deformation is also influenced by the Betee Fault and the Mentawai Fault Zone, which developed parallel to the Sunda subduction zone and are characterized by dextral strike-slip movement (Wibowo et al., 2024). As part of the forearc basin system, the location of the Nias Basin between Sumatra Island and the Indian Ocean contribute to a relatively low geothermal gradient, with an average shallow heat flow of approximately 1.2 HFU (Haris et al., 2020).

According to the Geological Map of Nias, the study area belongs to the Gomo Formation. These formations are composed of claystone, marl, sandstone, limestone with tuff, tuff and peat inserts. Based on the fossil content, the age of this formation is Early Miocene to Middle Pliocene (Rifai et al., 2019). The stratigraphic framework of the study area is presented in Figure 2.

The stratigraphy of the study area is shown in Table 1 and ranges in age from Middle Miocene to Early Pleistocene.

Biogenic Gas

Biogenic gas is commonly found in deltaic environments and is typically trapped within Quaternary sedimentary rocks. This type of gas is predominantly methane, produced through microbial activity under relatively low temperatures (Astawa et al., 2016). The biogenic gas formation process begins with the decomposition of organic material by bacteria, which then produces gas dissolved in pore water (Dewanto et al., 2020). When the dissolved gas concentration exceeds the saturation limit, the gas migrates and forms biogenic gas accumulations (Astawa et al., 2016).

© 2026 Dept. of Geophysics Hasanuddin University

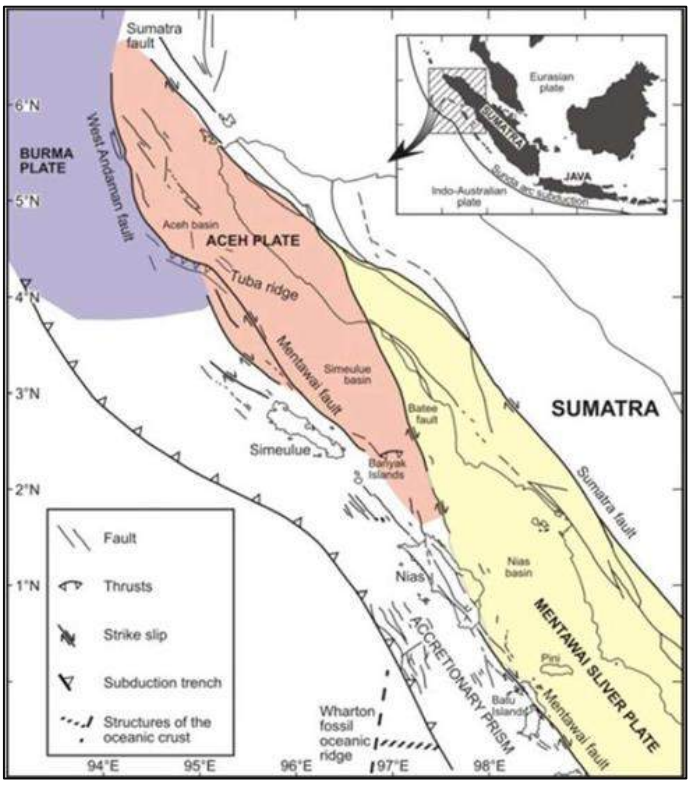
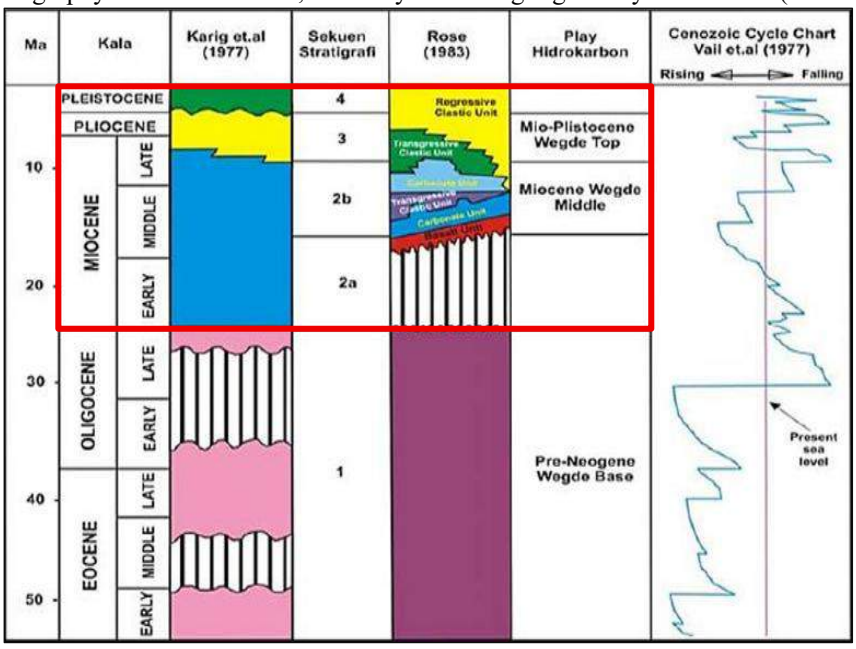


Figure 2. Geological setting modifed by Haris et al., (2020) and Base Map 2D Seismic Lines.

Table 1. Stratigraphy of the Nias Basin, the study area is highlighted by the red box (Rifai et al., 2019).



Acoustic Impedance Inversion

Seismic inversion is fundamentally influenced by several key factors, such as the quality of the well-to-seismic tie, the accuracy of horizon picking, the results of wavelet extraction, and the initial model used (Abdulaziz, 2020). In this study, a model-based seismic inversion method was applied to estimate Acoustic Impedance (AI) by integrating an initial low-frequency impedance model with seismic reflection data to produce a high-resolution AI model consistent with both well-log and seismic data (Shakir et al., 2024). The creation of the initial impedance model and the determination of parameters are based on

© 2026 Dept. of Geophysics Hasanuddin University

subsurface conditions that reflect variations in rock lithology (Lestari et al., 2023). A statistical wavelet extraction method was employed to generate a representative seismic wavelet for the inversion process. The extracted wavelet has a dominant frequency of 23 Hz, corresponding to an estimated wavelength of approximately 200 ft within the target interval. The quality of the well-to-seismic tie was evaluated prior to inversion. For Well S-1, the synthetic and seismic traces achieved a correlation coefficient of 0.639 with a 0-time shift, whereas Well T-1 yielded 0.566 with a 0-time shift. These correlation values indicate an acceptable match between the synthetic and seismic data.

The Acoustic Impedance (AI) was calculated using the Equation (1):

$$AI = V_p \cdot \rho \qquad (1)$$

where AI is acoustic impedance (g/cc)·(ft/s), ρ is density (g/cc), and Vp is P-Wave velocity (ft/s) (Erryansyah et al., 2020).

The results of this acoustic impedance measurement will later be used as an external attribute in the Probabilistic Neural Network (PNN) method.

Probabilistic Neural Network (PNN)

Reservoir parameter predictions are made by integrating well-log interpretations with both internal and external seismic attributes using the Probabilistic Neural Network (PNN) method illustrated in Figure 3. The functional equation of the PNN algorithm proposed by Wenando et al. (2023) is given in Equation (2).

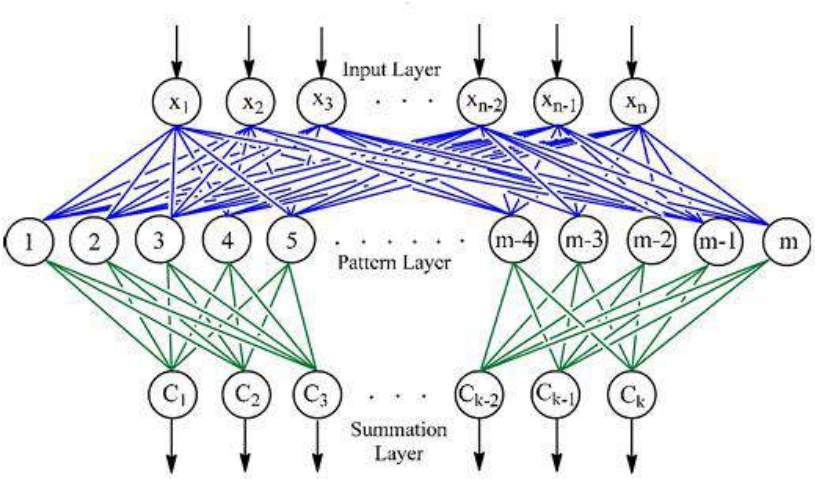


Figure 3. Illustration of the Probabilistic Neural Network (PNN) working mechanism (Ahangarani et al., 2022).

$$f_i(x) = g_i(x) = \frac{1}{(2\pi)^{\frac{\rho}{2}}(\sigma^{\rho})} \cdot \frac{1}{M_i} \sum_{j=i}^{M_i} \left[exp\left(-\frac{\left((x - x_{ij})^T \cdot (x - x_{ij})\right)}{2 \cdot \sigma^2} \right) \right] \qquad (2)$$

The functions $f_i(x)$or $g_i(x)$are used to represent the probability response for each $i\text{-}th$ class, where $i = 1,2, \dots, K$. In this equation, T denotes the transpose operation. The index $i$represents the number of analyzed classes, while the index j indicates the number of samples or data points within each class. The variable X_{ij} refers to the $j\text{-}th$ training data vector belonging to the $i\text{-}th$ class, whereas $x$represents the test data vector to be predicted, such as seismic attribute data at a specific location. Furthermore, $M_i$denotes the number of training samples in the $i\text{-}th$ class, and ρrepresents the dimensionality of a vector x, which is generally associated with the number of attributes used in the analysis. The parameter σ is the smoothing

© 2026 Dept. of Geophysics Hasanuddin University

parameter that controls the spread of the probability function, thereby influencing the model's sensitivity to data variations. In this study, the smoothing parameter (σ), which controls the spread of the Gaussian function and the sensitivity of the PNN to the training data, was determined during the PNN training process. The optimal smoothing value was selected by maximizing the correlation coefficient from linear regression while minimizing the prediction error between PNN-predicted and log-derived reservoir properties (Mohebali et al., 2020).

This study utilized a dataset comprising 27 post-stack time-migrated 2D seismic lines and two wells (S-1 and T-1) from the study area. The seismic basemap, showing the distribution of the seismic lines and well locations, is presented in Figure 2. The Probabilistic Neural Network (PNN) algorithm consists of several components: the input layer, the pattern layer, and the summation layer. During training, the PNN learns the relationship between well-log data and seismic attributes around the well, which is then used to estimate the distribution of reservoir parameters in data-free areas (Abdulaziz, 2020). During training, the PNN algorithm performs several trials to determine the optimal combination of seismic attributes, which is evaluated using the correlation coefficient between the predicted results and well-log data. The combination with the highest correlation and lowest error is selected as the best model (Joshi & Sain, 2021). This approach enables the lateral mapping of porosity, water saturation, and carbonate volume distribution on 2D seismic data, thereby providing a more comprehensive picture of subsurface reservoir characteristics.

Petrophysics Evaluation

Petrophysical evaluation is carried out to characterize the reservoir's physical properties using parameters such as shale volume (VSH), porosity, water saturation (Sw), and Carbonate Volume (Vcr).

The calculation of shale volume (Vsh) in this study was performed using Gamma Ray (GR) logs with the Gamma Ray Index (IGR) approach, as shown in Equation (3). This method was used as the basis for estimating shale content by utilizing the GR response as the primary indicator of lithology (Jassam et al., 2023).

$$VSG = IGR = \frac{GR_{log} - GR_{min}}{GR_{max} - GR_{min}} \quad (3)$$

The total porosity (ϕ_T) values within the reservoir zone were calculated based on density log (RHOB) data using the Equation (4) by Saadu & Nwankwo (2018):

$$\phi_T = \frac{\rho_{matrix} - \rho_{log}}{\rho_{matrix} - \rho_{fluid}} \quad (4)$$

To obtain effective porosity, an approach is used that corrects total porosity for the influence of shale, as shown in Equation (5) (Tariq et al., 2023):

$$\phi eff = \phi_T \cdot (1 - Vshale) \quad (5)$$

Water saturation (Sw) is a petrophysical parameter that measures the proportion of pore space occupied by water in the rock matrix. This parameter plays a crucial role in reservoir evaluation, as it is directly related to the presence of hydrocarbons. In this study, water saturation was determined using the Equation (6) (Schön, 2015) as shown below:

$$S_w = \frac{1}{2} \cdot \frac{R_w}{\phi^m} \left[\sqrt{\frac{4\phi^m}{R_w \cdot R_t} + \left(\frac{V_{sh}}{R_{sh}}\right)^2} - \frac{V_{sh}}{R_{sh}} \right] \quad (6)$$

The parameters used in this calculation include porosity (ϕ), formation resistivity (R_t), formation water resistivity (R_w), shale volume (V_{sh}), shale resistivity (R_{sh}), and the cementation exponent (m), which represents the relationship between

© 2026 Dept. of Geophysics Hasanuddin University

porosity and the electrical resistivity response of the rock matrix.

Furthermore, the Carbonate Volume (Vcr) is a parameter that describes the proportion of rock that is relatively clean of shale. This parameter is used to identify the distribution of rocks that have the potential to function as reservoirs, as increasing shale content is generally associated with decreased reservoir quality due to lower porosity and effective permeability. The calculation of Carbonate Volume (Vcr) is given by Equation (7).

$$Vcr = 1 - Vshale \quad (7)$$

Result and Discussion

The Time Structure Map (TSM) at Well S-1 as shown in Figure 4 indicates that the well is located within a carbonate buildup structure at a two-way travel time of approximately 1520 ms. The high-relief contours surrounding Well S-1 are interpreted as potential hydrocarbon accumulation zones. Furthermore, the structural relief variations observed on the TSM reflect the relatively complex geological setting of the study area, which is likely to influence the subsurface distribution of reservoir properties. Petrophysical analysis was subsequently conducted to evaluate the distribution of Water Saturation (Sw) and Carbonate Volume within the study area.

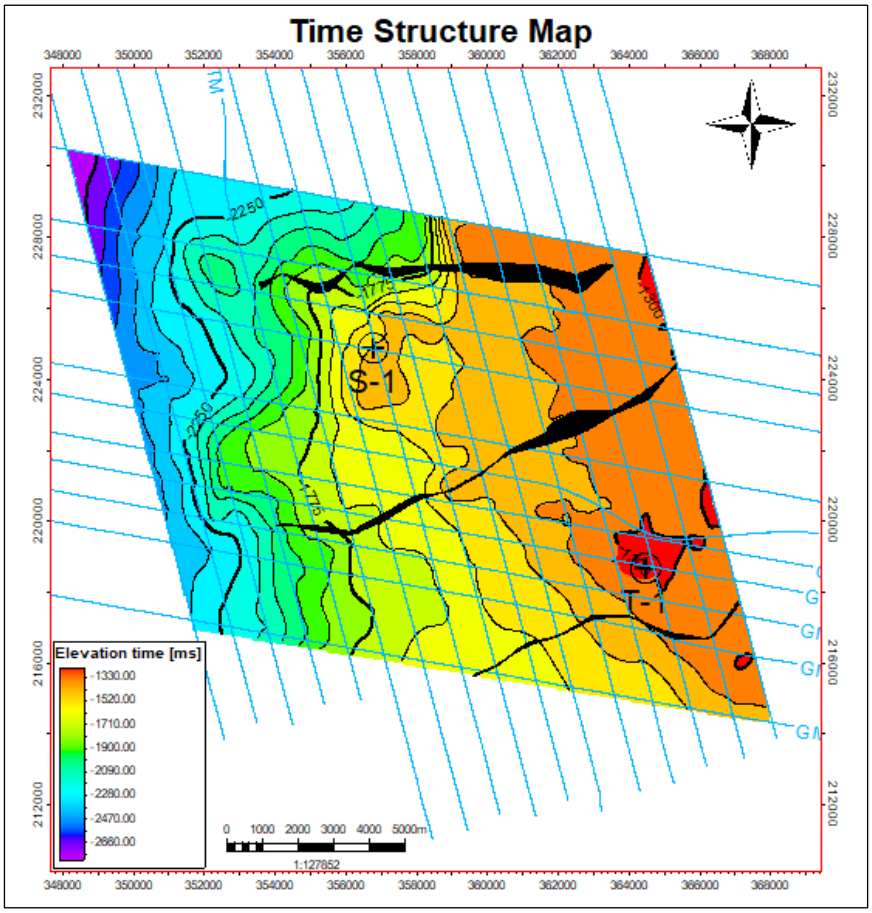


Figure 4. Time structure map at Nias Basin.

© 2026 Dept. of Geophysics Hasanuddin University

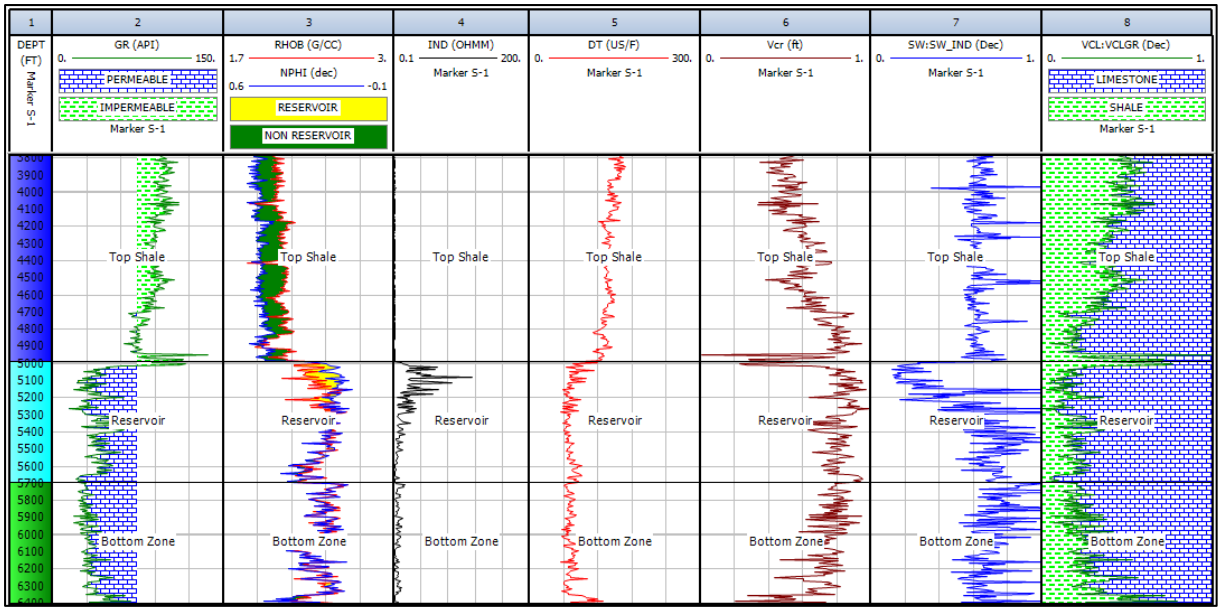


Figure 5. Petrophysical Log Interpretation of Well S-1: Carbonate Volume (*Vcr*), Water Saturation (S_w) and Shale Volume (V_{sh}).

Petrophysical analysis of reservoir intervals in the target area revealed contrasting reservoir characteristics between Wells S-1 and T-1. Well S-1 4990–5693 ft, exhibited several hydrocarbon indicators, including an RHOB–NPHI crossover and high resistivity values. The log-derived petrophysical analysis indicates a high Carbonate Volume of 0.76 (v/v) and a relatively low Water Saturation (S_w) of 0.4 (v/v) in the Top Reservoir. These characteristics indicate the presence of porous carbonate rocks with pore spaces partially filled with hydrocarbons, as shown in Figure 5 for Well S-1.

In contrast, based on log-derived petrophysical analysis, Well T-1 4280–4864 ft exhibited higher Water Saturation (S_w) values 0.9 (v/v), lower resistivity, and no NPHI–RHOB crossover, indicating that the reservoir is largely saturated with water, as shown in Figure 6 for Well T-1

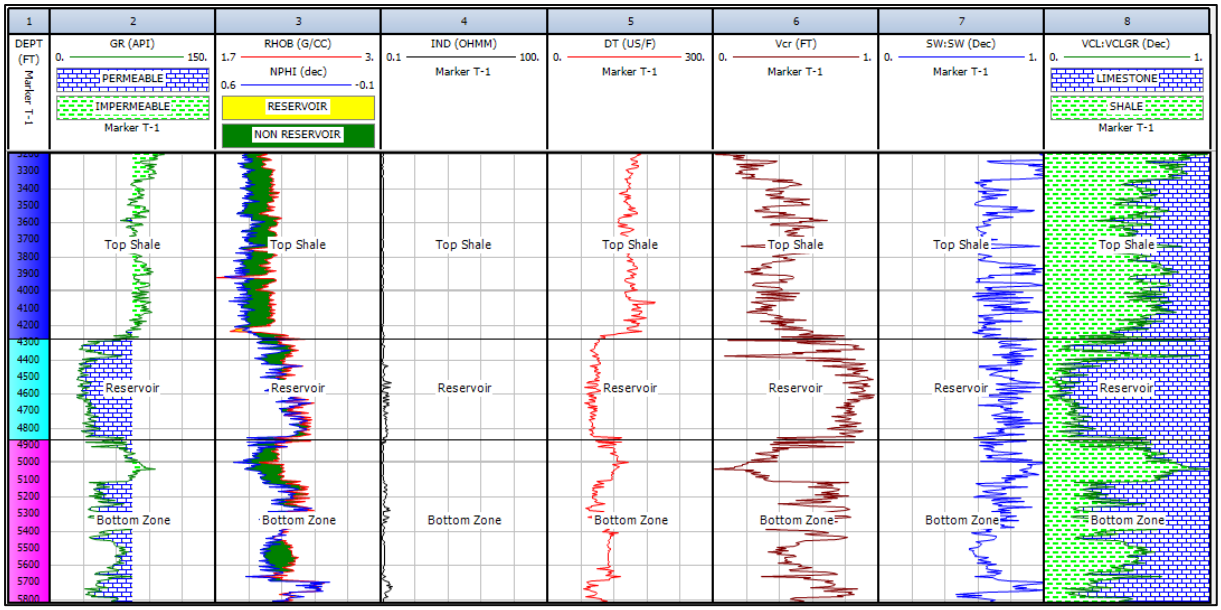
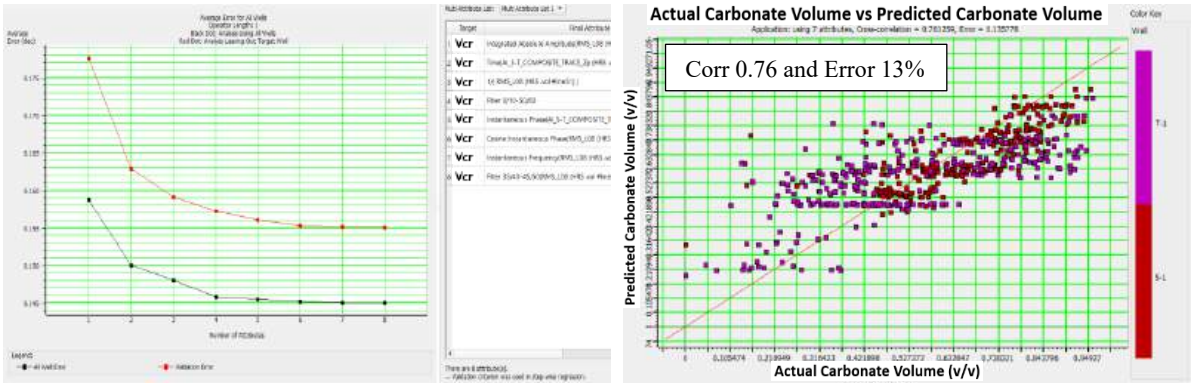


Figure 6. Petrophysical Log Interpretation of Well T-1: Carbonate Volume (Vcr), Water Saturation (S_w) and Shale Volume (V_{sh}).

© 2026 Dept. of Geophysics Hasanuddin University



a) b)

Figure 7. Carbonate Volume Prediction with Multi-Attribute Analysis; a) Attribute Training Curve of Vcr Prediction with 8 Attributes and b) Crossplot Actual Vcr (v/v) vs Predicted Vcr (v/v) using 7 Attributes.

Before applying the Probabilistic Neural Network (PNN) to reservoir property prediction, attribute training and multi-attribute analysis were conducted to identify the seismic attributes most sensitive to Water Saturation (Sw) and Carbonate Volume. Each seismic attribute was evaluated based on its correlation with well-log data, and the seven most effective attributes, including amplitude, frequency, phase, and external acoustic impedance, were selected. The significant prediction error obtained by using acoustic impedance indicates that it helps distinguish different lithologies and provides a more accurate characterization of carbonate reservoirs. The selected attribute combination provided a stronger representation of carbonate rock properties than individual attributes, yielding a correlation coefficient of 0.76 and an error of 13% for Carbonate Volume prediction as shown in Figure 7. Since multi-attribute analysis is based on linear regression, its ability to capture the complex nonlinear relationship between seismic attributes and reservoir properties is limited. Therefore, the Probabilistic Neural Network (PNN) was employed to improve prediction accuracy. The PNN model produced more accurate predictions of Carbonate Volume and Water Saturation and generated a laterally continuous distribution that more effectively represents reservoir characteristics across the seismic section as shown in Figure 8.

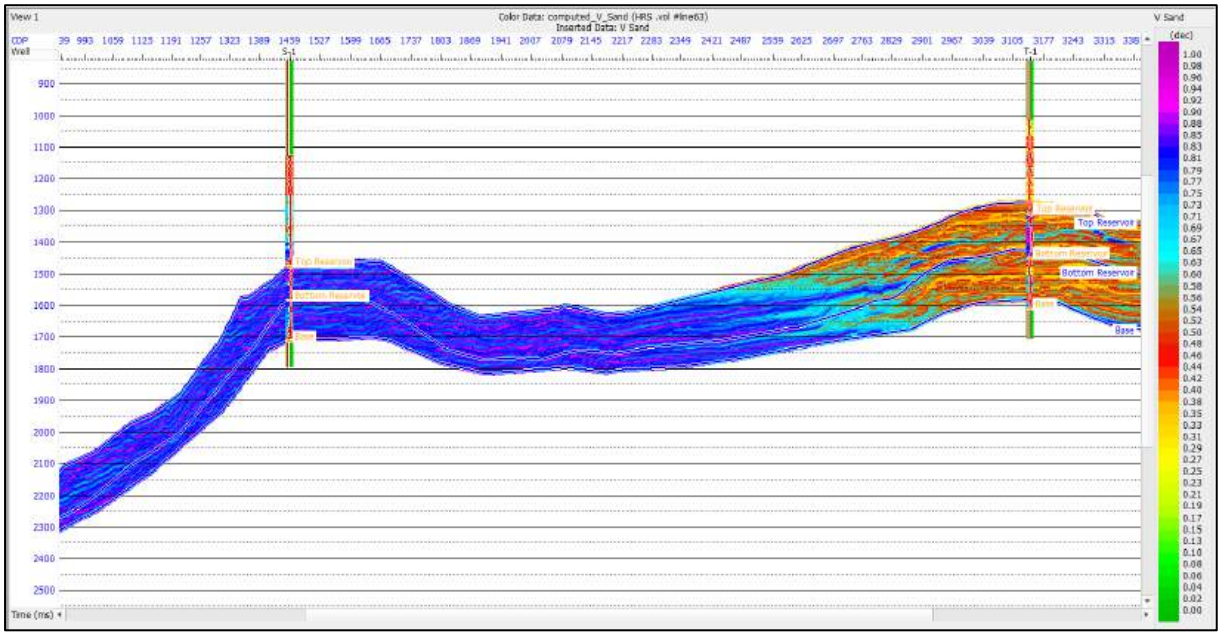
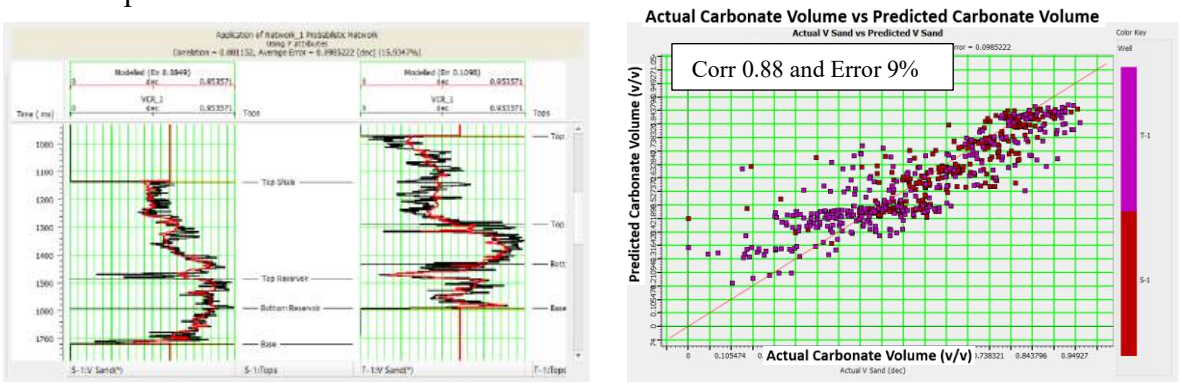


Figure 8. Carbonate Volume cross-section predicted using the PNN method.

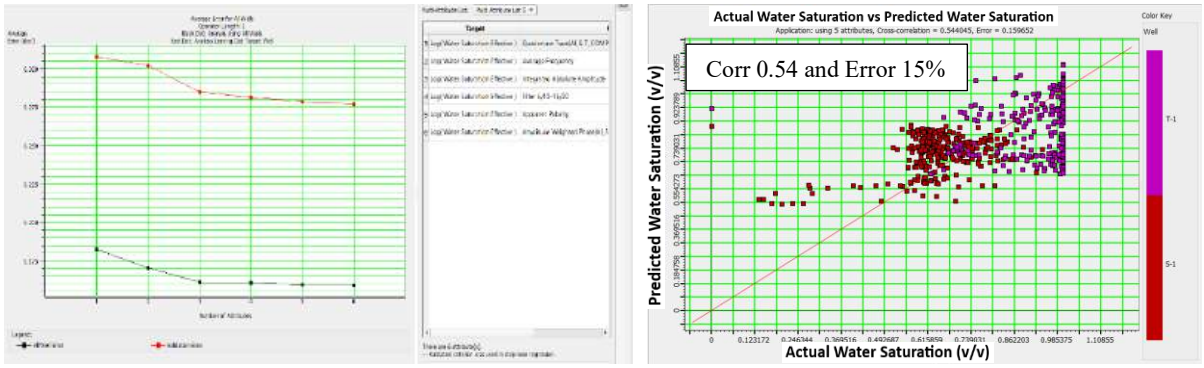
© 2026 Dept. of Geophysics Hasanuddin University

The result shown in Figure 8 indicates that the application of the Probabilistic Neural Network (PNN) method improved the prediction accuracy of Carbonate Volume compared to the multi-attribute analysis. The validation error and crossplot results presented in Figure 8 show that the correlation coefficient increased to 0.88, while the prediction error decreased to 9%. These improvements indicate that the PNN model can better capture the nonlinear relationship between seismic attributes and Carbonate Volume, resulting in predictions that are closer to the well-log data. The higher correlation coefficient and lower error demonstrate that the model accurately represents the Carbonate Volume distribution, with only minor deviations from the actual data. Therefore, the validation results confirm that the PNN model is reliable for predicting the spatial distribution of Carbonate Volume within the study area.



a) b)

Figure 9. Carbonate Volume Prediction with Multi-Attribute Analysis; a) Attribute Training Curve of Vcr Prediction with 8 Attributes and b) Crossplot Actual Vcr (v/v) vs Predicted Vcr (v/v) using 7 Attributes.



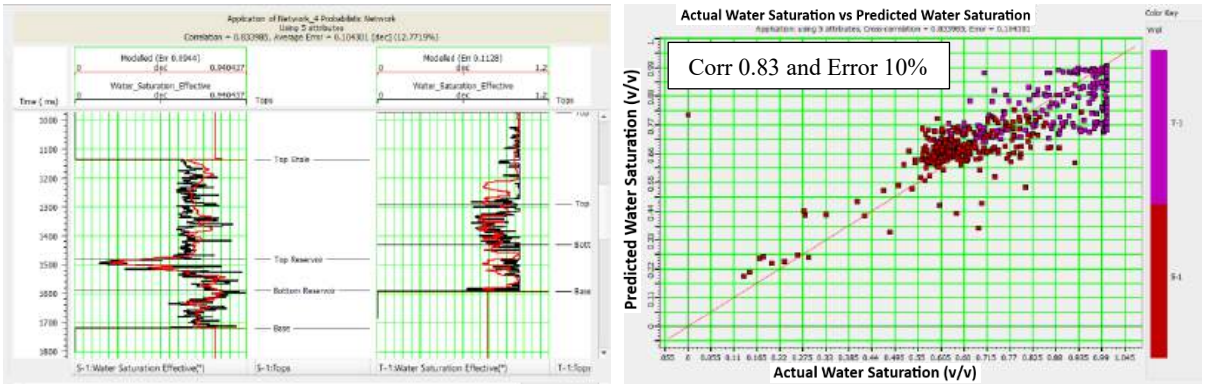
a) b)

Figure 10. Water Saturation Prediction with Multi-Attribute Analysis; a) Attribute Training Curve of Sw Prediction with 6 Attributes and b) Crossplot Actual Sw (v/v) vs Predicted Sw (v/v) using 5 Attributes.

The estimation of Water Saturation (Sw) followed the same workflow as the Carbonate Volume prediction, beginning with attribute training and multi-attribute analysis, and then applying the Probabilistic Neural Network (PNN). Attribute training was carried out to identify the seismic attributes most sensitive to Water Saturation. Based on the results shown in Figure 10(a), five optimal attributes were selected. These attributes were then used as input for the multi-attribute analysis to establish the relationship between the seismic attributes and Water Saturation. The results of the multi-attribute analysis, presented in Figure 10(b), yielded a correlation coefficient of 0.54 and an error of 15%, indicating that the relationship between the seismic attributes and Water Saturation remained relatively limited.

© 2026 Dept. of Geophysics Hasanuddin University

These results suggest that the regression-based approach was insufficient to accurately capture the spatial variation in Water Saturation across the study area. This limitation indicates that the relationship between seismic responses and Water Saturation is nonlinear and cannot be adequately represented using a regression-based approach alone. Therefore, the Probabilistic Neural Network (PNN) was applied to capture these nonlinear relationships, resulting in improved prediction accuracy and a Water Saturation distribution that better represents the reservoir conditions throughout the study area.



a) b)

Figure 11. Water Saturation Prediction with Probabilistic Neural Network (PNN) Analysis; a) Attribute Training Curve of Sw Prediction with 6 Attributes and b) Crossplot Actual Sw (v/v) vs Predicted Sw (v/v) using 5 Attributes.

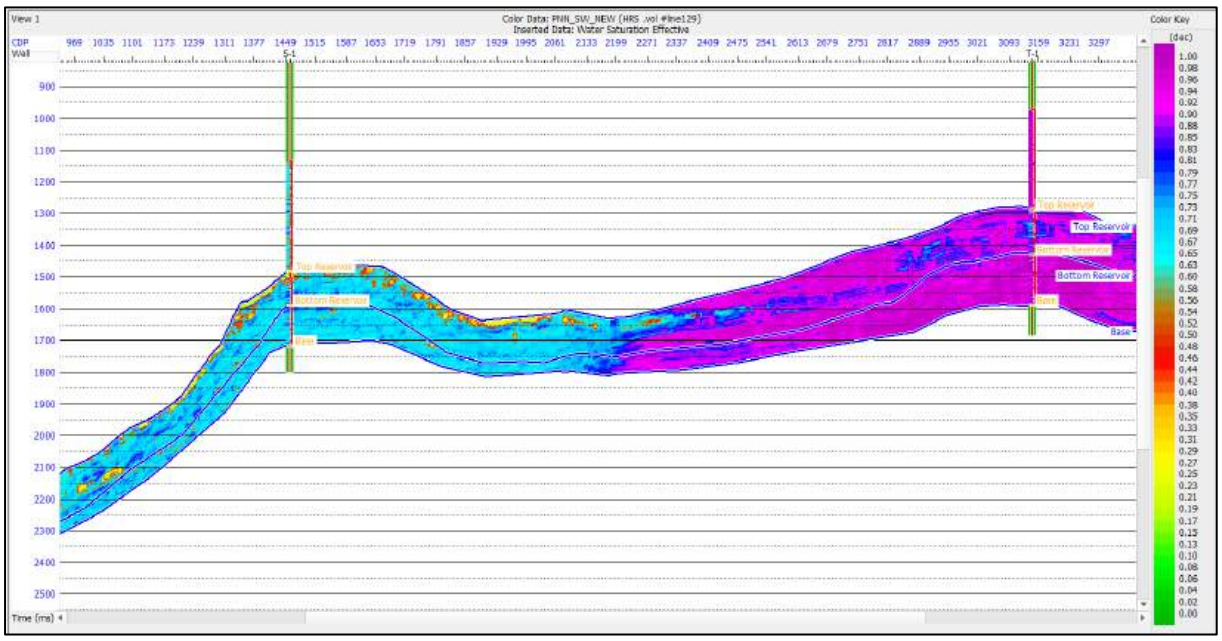


Figure 12. Water Saturation cross-section predicted using the PNN method.

Following the application of the Probabilistic Neural Network (PNN), the prediction accuracy of Water Saturation (Sw) improved compared with the results obtained from the multi-attribute analysis. The validation error and crossplot results presented in Figure 11 show that the correlation coefficient increased from 0.54 to 0.83, while the error value decreased from 15% to 10%. These improvements indicate that the PNN model is more effective in capturing the nonlinear relationship between the seismic attributes and Water Saturation, resulting in predictions that are in closer agreement with the well-log data. The higher correlation

© 2026 Dept. of Geophysics Hasanuddin University

coefficient and lower error further demonstrate that the PNN model provides a reliable estimation of Water Saturation within the target interval. The Water Saturation prediction generated from the five selected attributes yielded a distribution that is more representative of subsurface conditions. The predicted results indicate that Water Saturation is more dominant around Well T-1 than Well S-1 as shown in Figure 12, suggesting that the area surrounding Well T-1 is predominantly saturated with water. Therefore, the application of the PNN method not only improved prediction accuracy compared with multi-attribute analysis but also produced a laterally continuous Water Saturation distribution that better represents the reservoir characteristics in the study.

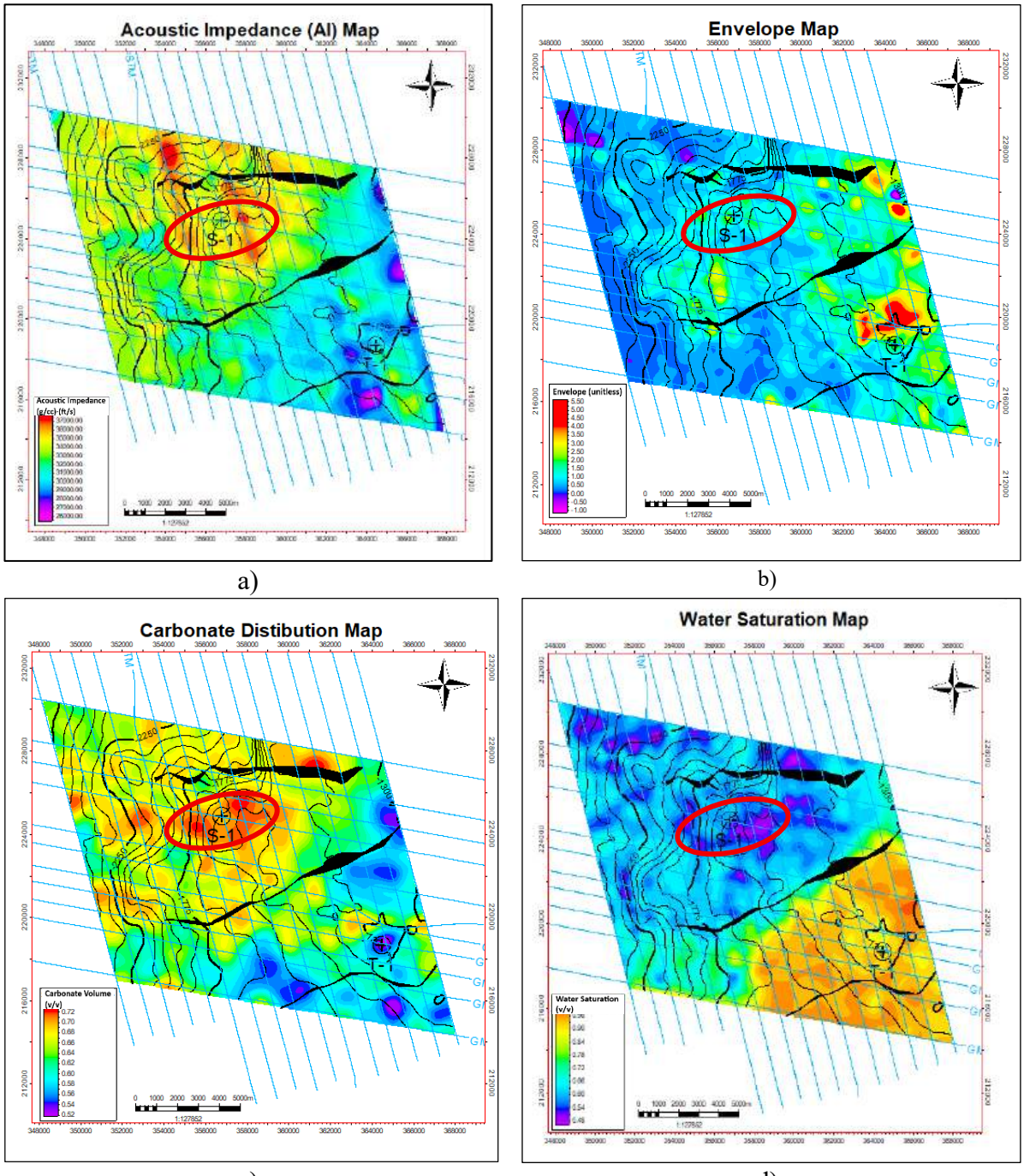


Figure 13. Distribution of variations value on the 2D seismic surface map, including a) Acoustic Impedance Map, b) Envelope Attribute Map, c) Carbonate Volume, and d) Water Saturation.

© 2026 Dept. of Geophysics Hasanuddin University

As shown in Figure 13(a), the Acoustic Impedance (AI) distribution indicates that AI values around Well S-1 range from 32,000 to 35,000 (g/cc)·(ft/s), whereas those around Well T-1 range from 28,000 to 31,000 (g/cc)·(ft/s), with a northwest–southeast orientation. According to the cutting samples data in the PPPGL (2018) report, the higher AI values observed around Well S-1 are attributed to the presence of pyrite within the reservoir interval. Because pyrite has a relatively high density, its presence increases the rock's bulk density, resulting in higher Acoustic Impedance values. In addition, carbonate lithologies generally exhibit higher Acoustic Impedance than clastic sedimentary rocks due to their higher density and more compact rock framework.

In the case of biogenic gas reservoirs in the Nias Basin, high envelope anomalies associated with low acoustic impedance values do not necessarily indicate the presence of hydrocarbons as shown in Figure 13(b). This interpretation is supported by well data from around Well T-1, which show water saturation (Sw) values close to 1 dec and relatively low Carbonate Volume values, indicating that the reservoir interval is predominantly occupied by formation water. Conceptually, the envelope attribute represents the magnitude of the reflection amplitude, regardless of signal polarity. Therefore, both positive and negative reflection amplitudes generated by interlayer acoustic contrast can produce high envelope responses. Consequently, strong impedance contrasts caused by lithological variations, porosity changes, or thin carbonate layers can produce high envelope anomalies that are not directly related to hydrocarbon accumulation. These anomalies are then interpreted as indicators of significant contrasts in rock physical properties, and the hydrocarbon interpretation must be supported by additional petrophysical parameters.

As shown in Figure 13(c), the predicted Carbonate Volume distribution indicates that the area surrounding Well S-1 exhibits better reservoir quality than Well T-1. Based on the PNN model, the average Carbonate Volume was predicted to be 0.76 (v/v) around Well S-1, whereas the average Carbonate Volume around Well T-1 was 0.50 (v/v). The relatively higher Carbonate Volume values in Well S-1 indicate a greater proportion of effective reservoir intervals, dominated by clean carbonate rocks with low shale content. In contrast, the lower Carbonate Volume values observed around Well T-1 are associated with lithologies such as claystone and calcilutite, which contain higher shale content and consequently reduce reservoir quality. This interpretation is consistent with the higher acoustic impedance values observed in the Well S-1 area, indicating denser, cleaner carbonate rocks with more favourable reservoir characteristics for hydrocarbon accumulation.

The results in Figure 13(d) show variations in Water saturation (Sw) along the southeast–northwest trend reveal contrasting reservoir conditions within the study area. The PNN model predicted a high average Water Saturation (Sw) of 0.9 (v/v) for Well T-1, whereas the average predicted Water Saturation for Well S-1 was 0.4 (v/v). Although both wells are dominated by limestone lithology, the difference in Sw values is attributed to stratigraphic geometry, specifically the development of carbonate stacking structures in the S-1 area that are absent in T-1. This interpretation is supported by the higher Acoustic Impedance (AI) values observed in Well S-1, which reflect differences in rock elastic properties between facies. Structurally, a northeast–southwest-trending fault is interpreted to have controlled hydrocarbon migration towards Well S-1. Therefore, the relatively low water saturation anomaly observed in S-1 suggests the presence of fluids other than formation water, most likely hydrocarbons, controlled by a

© 2026 Dept. of Geophysics Hasanuddin University

combination of stratigraphic and structural factors.

This interpretation is further supported by the Drill Stem Test (DST) results from Well S-1, which confirm the occurrence of biogenic gas within the study interval. The gas is predominantly composed of methane (98.95%), consistent with the characteristic composition of biogenic gas (PPPGL, 2018), as shown in Table 2.

Table 2. Gas Composition Results from the Drill Stem Test (DST) of Well S-1 (PPPGL, 2018).

Gas Composition	S-1 (Late Miocene) Water Depth: 196 ft	
	DST 2 (%) 5198 – 5216 ft	DST 3 (%) 5034 – 5090 ft
Carbon Dioxide	0.29	0.23
Nitrogen	0.56	0.61
Ethane	0.18	0.19
Methane	**98.95**	**98.96**
Propane	0.02	0.01
Oxygen	0	0
Total	100	100

Conclusion

Based on the Probabilistic Neural Network (PNN) results, the estimated distribution of petrophysical properties within the carbonate reservoir of the Nias Basin demonstrates higher prediction accuracy than conventional multi-attribute analysis, particularly in reservoirs with complex heterogeneity. The PNN model achieved a correlation coefficient of 0.83 with a 10% error for Water Saturation (Sw), and a correlation coefficient of 0.88 with a 9% error for Carbonate Volume. The predicted distributions of Carbonate Volume and Water Saturation indicate that hydrocarbon accumulation is concentrated around Well S-1, which is characterized by high Carbonate Volume and resistivity, along with low Water Saturation. These results suggest that biogenic gas accumulation is localized around Well S-1, whereas the inferred hydrocarbon migration is controlled by the regional geological setting and the subsurface structural framework.

This study recommends incorporating the frequency-based attribute Amplitude Versus Frequency (AVF) as an external attribute, as its spectral sensitivity has the potential to improve the prediction of petrophysical properties in heterogeneous carbonate reservoirs when integrated with the Probabilistic Neural Network (PNN) approach.

Acknowledgements

The authors gratefully acknowledge the reviewers and editors for their constructive comments and insightful suggestions, which have significantly improved this manuscript. The authors also thank Jurnal Geocelebes for providing a platform to disseminate the findings of this study and contribute to the development of geoscientific knowledge. The authors sincerely appreciate the support and contributions of all individuals and institutions involved throughout the research process.

Author Contribution

The authors' contributions to this manuscript are as follows: **Chikita Mery Yuliani** and **Renita Dwi Vadila** contributed to conceptualization, formal analysis, and writing of the original draft. **Mokhammad Puput Erlangga** and **Harnanti Y. Hutami** were responsible for supervision, formal analysis, and validation. **Egie Wijaksono** contributed to the resources and data curation. All authors have read and approved the final version of the manuscript.

Conflict of Interest

The authors declare that there are no conflicts of interest regarding the publication of this manuscript.

References

Abdulaziz, A. M. (2020). The effective seismic attributes in porosity

© 2026 Dept. of Geophysics Hasanuddin University

prediction for different rock types: Some implications from four case studies. *Egyptian Journal of Petroleum*, 29(1), 95–104. https://doi.org/10.1016/j.ejpe.2019.12.001

Ahangarani, M. L., Mojeddifar, S., & Chegeni, M. H. (2022). Reservoir characterization and porosity classification using a probabilistic neural network (PNN) based on single and multi-smoothing parameters. *International Journal of Mining and Geo-Engineering*, 56(4), 383–390. https://doi.org/10.22059/IJMGE.2022.287780.594822

Ardinda, F., & Riyanto, A. (2020). Seismic Multi-Attribute Analysis for Petrophysics Reservoir Prediction with Probabilistic Neural Network in "FA" Field. *E3S Web of Conferences*, 200, 06010. https://doi.org/10.1051/e3sconf/202020006010.

Astawa, I. N., Setiady, D., Wijaya, P. H., Hermansyah, G. M., & Saputra, M. D. (2016). Indikasi Gas Biogenik Di Perairan Delta Mahakam, Provinsi Kalimantan Timur. *Jurnal Geologi Kelautan*, 14(2), 103–114. https://doi.org/10.32693/jgk.14.2.2016.354

Dewanto, O., Maulina, M., & Nainggolan, T. B. (2020). Identification of biogenic gas reservoir zone using log, petrophysics and geochemical data in S-1 well of Nias basin, North Sumatera. *Journal of Physics: Conference Series*, 1572(1), 012037. https://doi.org/10.1088/1742-6596/1572/1/012037

Durrani, M. Z. A., Talib, M., Ali, A., Sarosh, B., & Naseem, N. (2020). Characterization and probabilistic estimation of tight carbonate reservoir properties using quantitative geophysical approach: a case study from a mature gas field in the Middle Indus Basin of Pakistan. *Journal of Petroleum Exploration and Production Technology*, 10(7), 2785–2804. https://doi.org/10.1007/s13202-020-00942-0

Erryansyah, M., Nainggolan, T. B., & Manik, H. M. (2020). Acoustic impedance model-based inversion to identify target reservoir: a case study Nias Waters. *IOP Conference Series: Earth and Environmental Science*, 429(1), 012033. https://doi.org/10.1088/1755-1315/429/1/012033

Haris, N. A., Saphira, N., Fathkhurozak, M., Rifai, Y., Zulivandama, S. R., & Aswad, S. (2020). Biogenic Gas Reservoir Distribution Analysis Using AI Inversion and Seismic Attributes in The Nias Basin, North Sumatra. *Proceedings of the Indonesian Petroleum Association*, 14–17 September 2020. Indonesian Petroleum Association. https://doi.org/10.29118/IPA20-SG-164

Jassam, S. A., AL-Fatlawi, O., & Canbaz, C. H. (2023). Petrophysical Analysis Based on Well Logging Data for Tight Carbonate Reservoir: The SADI Formation Case in Halfaya Oil Field. *Iraqi Journal of Chemical and Petroleum Engineering*, 24(3), 55–68. https://doi.org/10.31699/ijcpe.2023.3.6

Joshi, A. K., & Sain, K. (2021). Subsurface porosity estimation: A case study from the Krishna Godavari offshore basin, eastern Indian margin. *Journal of Natural Gas Science and Engineering*, 89, 103866. https://doi.org/10.1016/j.jngse.2021.103866

Khan, M., Bery, A. A., Bashir, Y., Sharoni, S. M. H., Gnapragasan, J., & Imran, Q. S. (2025). Optimizing petrophysical property prediction in fluvial-deltaic reservoirs: A multi-seismic attribute transformation and probabilistic neural network approach. *Journal of Petroleum Exploration and Production Technology*, 15, 29.

© 2026 Dept. of Geophysics Hasanuddin University

https://doi.org/10.1007/s13202-024-01912-6

Lestari, I., Ekawati, G. M., & Firdaus, R. (2023). Analisis Kuantitatif Seismik Inversi Impedansi Akustik dan Porositas Pada Zona Target Lapangan "II." *Jurnal Geofisika Eksplorasi*, 9(1), 61–82. https://doi.org/10.23960/jge.v9i1.238

Mohebali, B., Tahmassebi, A., Meyer-Baese, A., & Gandomi, A. H. (2020). Chapter 14 - Probabilistic neural networks: a brief overview of theory, implementation, and application. *Handbook of Probabilistic Models*, 347–367. Butterworth-Heinemann. https://doi.org/10.1016/B978-0-12-816514-0.00014-X

PPGL. (2018). *Report Penelitian gas methana Cekungan Nias. Bandung, Indonesia*. Lemigas.

Rifai, F. Y., Bernhard Nainggolan, T., & Munandar Manik, H. (2019). Reservoir Characterization Using Acoustic Impedance Inversion and Multi-Attribute Analysis in Nias Waters, North Sumatra. *Bulletin of the Marine Geology*, 34(1), 51–62. https://doi.org/10.32693/bomg.34.1.2019.637

Saadu, Y. K., & Nwankwo, C. N. (2018). Petrophysical evaluation and volumetric estimation within Central swamp depobelt, Niger Delta, using 3-D seismic and well logs. *Egyptian Journal of Petroleum*, 27(4), 531–539. https://doi.org/10.1016/j.ejpe.2017.08.004

Schön, J. H. (2015). *Basic Well Logging and Formation Evaluation*. Bookboon the E-Book Company,

Shakir, U., Ali, A., Hussain, M., Radwan, A. E., & Aal, A. A. El. (2024). PNN Enhanced Seismic Inversion for Porosity Modeling and Delineating the Potential Heterogeneous Gas Sands via Comparative Inversion Analysis in the Lower Indus Basin. *Pure and Applied Geophysics*, 181, 2801–2821 (2024). https://doi.org/10.1007/s00024-024-03562-5

Sinaga, T. M., Rosid, M. S., & Wahdanadi Haidar, M. (2019). Porosity Prediction Using Neural Network Based on Seismic Inversion and Seismic Attributes. *E3S Web of Conferences*, 125, 15006. https://doi.org/10.1051/e3sconf/201912515006

Tariq, Z., Gudala, M., Yan, B., Sun, S., & Mahmoud, M. (2023). A fast method to infer Nuclear Magnetic Resonance based effective porosity in carbonate rocks using machine learning techniques. *Geoenergy Science and Engineering*, 222, 211333. https://doi.org/10.1016/j.geoen.2022.211333

Wenando, F. A., Fatma, Y., Ulfa, A., & Suroya Taurin, J. (2023). Aplikasi dan Kerentanan Algoritma Probabilistic Neural Network (PNN): Systematic Literature Review. *Jurnal CoSciTech (Computer Science and Information Technology)*, 4(2), 491–499. https://doi.org/10.37859/coscitech.v4i3.5676

Wibowo, R., Setiadi, I., Firdaus, Y., & Rahardiawan, R. (2024). Gravity Modeling of Subsurface Structures and Reservoir Characterization Using Seismic Inversion in the Nias Basin. *Bulletin of the Marine Geology*, 39(2), 69–84. https://doi.org/10.32693/bomg.39.2.2024.890

© 2026 Dept. of Geophysics Hasanuddin University

ISSN: 2579-5821 (Print)
ISSN: 2579-5546 (Online)
URL address: http://journal.unhas.ac.id/index.php/geocelebes
DOI: 10.70561/geocelebes.v10i2.53140

Jurnal Geocelebes Vol. 10 No. 2, October 2026, 359 – 370

Multi-Sensor Remote Sensing and GIS for Potential CO_2 Leakage Mapping in Gundih CCUS Field

Tirta Khayru Putra, Ridwan Rahmanto*, Syahrbanu

Department of Geological Engineering, Universitas Pertamina, Jakarta 12220, Indonesia.

*Corresponding author. Email: ridwan.rahmanto@universitaspertamina.ac.id

Manuscript received: 31 July 2026; Received in revised form: 6 September 2026; Accepted: 9 September 2026

Abstract

Geological caprock integrity is critical for preventing gas migration to the surface in carbon sequestration sites. This study evaluated surface gas escape pathways by integrating multi-sensor spatial datasets in the Gundih area, Central Java. Lineament networks were extracted from national digital elevation models (DEMNAS) to calculate Fault Fracture Density (FFD), representing structural conduits. Surface conditions and thermal anomalies were assessed independently using the Normalized Difference Vegetation Index (NDVI) and Land Surface Temperature (LST) derived from satellite imagery. Rather than relying on weighted overlay modeling, a qualitative spatial correlation approach was utilized to evaluate the interplay between structural deformation, vegetation cover, and thermal behavior. The results indicate that high-density FFD zones predominantly align along Northwest–Southeast and Northeast–Southwest structural trends. Spatial cross-analysis reveals that localized thermal anomalies (elevated LST) coincide with high-FFD fracture zones, even in areas characterized by dense vegetation (high NDVI), potentially indicating that localized thermal responses are associated with subsurface structural pathways rather than land-surface solar exposure. These findings demonstrate that integrating FFD, NDVI, and LST without arbitrary weighting provides an objective preliminary screening baseline for prioritizing caprock containment monitoring zones in subsurface storage projects.

Keywords: Caprock Integrity; Fault Fracture Density; Land Surface Temperature; Spatial Correlation; Vegetation Index.

Citation: Putra, T. K., Rahmanto, R., & Syahrbanu, S. (2026). Multi-Sensor Remote Sensing and GIS for Potential CO_2 Leakage Mapping in Gundih CCUS Field. *Jurnal Geocelebes*, 10(2): 359–370, doi: 10.70561/geocelebes.v10i2.53140

Introduction

Ensuring caprock containment security against buoyant gas migration remains a critical technical challenge in subsurface carbon sequestration projects (Zhang et al., 2020), such as the Gundih Carbon Capture, Utilization, and Storage (CCUS) field in Central Java (Tsuji et al., 2014; Santoso et al., 2019; Sule et al., 2019). Structural discontinuities, particularly fault networks and localized fracture systems within caprock formations, act as primary fluid conduits facilitating vertical gas escape toward the surface (Zhang et al., 2020). Consequently, identifying potential surface leakage pathways and evaluating high-density fracture zones are essential prerequisites for establishing containment baselines and mitigating environmental risks in ongoing geological storage operations (Chen et al., 2019; Thiruchittampalam et al., 2022).

Conventionally, caprock integrity and structural leakage risks are evaluated using 3D seismic horizon interpretation, well-log fracture characterization, and subsurface geomechanical modeling (Tsuji et al., 2013; Bohloli et al., 2018). While these subsurface techniques provide high vertical resolution at depth, their spatial coverage across regional scales is often limited and economically prohibitive for continuous

© 2026 Dept. of Geophysics Hasanuddin University

surface monitoring (Garain et al., 2019). To address this, satellite remote sensing approaches such as Fault Fracture Density (FFD) derived from digital elevation models have been increasingly utilized to map regional structural conduits (Inoh et al., 2023; Rafiq et al., 2025). Furthermore, Land Surface Temperature (LST) and Normalized Difference Vegetation Index (NDVI) extracted from satellite imagery offer valuable surface proxies for detecting localized thermal and environmental anomalies (Avdan & Jovanovska, 2016; Gemitzi et al., 2021). In addition, microwave remote sensing and polarimetric Synthetic Aperture Radar (SAR) decomposition provide complementary insights into physical surface roughness and structural lineament detection (Zahratunnisa et al., 2025).

Despite these advancements, remote sensing-based leakage monitoring has commonly focused on individual surface responses, such as vegetation stress or spectral alteration, or on specific structural and thermal indicators. Thiruchittampalam et al. (2022), for example, evaluated remote-sensing techniques for detecting CO_2 leakage primarily through vegetation stress, while Chen et al. (2019) reviewed the use of remote sensing for monitoring vegetation responses to CO_2 leakage at Carbon Capture and Storage (CCS) sites. Zhang et al. (2020) further reviewed a broad range of remote sensing techniques for CCS leakage monitoring, including the deployment of Raman lidar for surface CO_2 leak detection (Kim et al., 2018). These studies demonstrate the potential of remote sensing for leakage detection but also highlight the complexity of distinguishing leakage-related surface responses from other environmental effects. Although structural density and surface thermal anomalies have also been investigated as indicators of subsurface fluid pathways in other geological settings (Hidayat et al., 2023; Iqbal & Juliarka, 2020), their spatial relationship with vegetation conditions has not been explicitly evaluated for the Gundih CCUS field within a unified, non-weighted framework. Therefore, assessing the spatial coincidence of high FFD, elevated LST, and vegetation conditions may provide an additional basis for identifying potential leakage pathways in the study area.

To address this research gap, this study aims to identify potential CO_2 leakage pathways in the Gundih CCUS field through a qualitative spatial correlation analysis integrating DEMNAS-derived FFD, Landsat-derived LST, and NDVI. The analysis evaluates the spatial coincidence between high fracture density and localized thermal anomalies while considering vegetation conditions to distinguish potential subsurface thermal responses from land-surface environmental effects. This approach provides a non-weighted spatial framework for assessing potential leakage-prone zones and supporting caprock integrity monitoring in geological carbon storage projects.

Materials and Methods

Study Area and Geological Setting

This study was conducted in the Gundih CCUS field, Central Java, Indonesia. Gundih was selected as the study area because it represents an important site for the development of geological carbon storage in Indonesia and was investigated as the location of the country's first CCS pilot project. The field was selected based on the availability of CO_2 resources, potential storage conditions, existing facilities, and the potential to convert an existing well into a CO_2 injection well (Marbun et al., 2019). The Gundih field produces CO_2-rich natural gas, with reported CO_2 concentrations of up to approximately 21%, making CO_2 management and geological storage directly relevant to the area (Marbun et al., 2019). The geographical location and regional geological setting of the study area are presented in Figure 1. The summary of

© 2026 Dept. of Geophysics Hasanuddin University

geological and operational characteristics of the Gundih CCUS field is presented in Table 1.

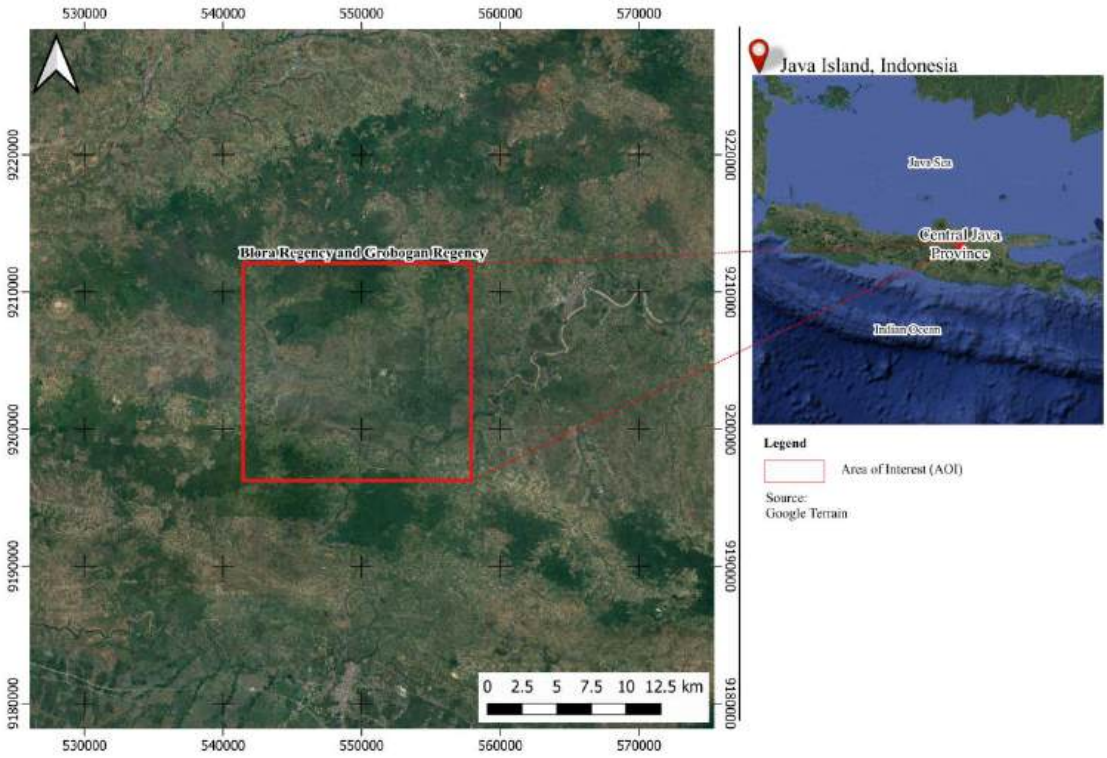


Figure 1. Geographic map and administrative location of the Gundih CCUS study area in Central Java, Indonesia. The red box delineates the primary Area of Interest (AOI), with the inset map showing its regional position on Java Island.

Table 1. Geological and operational characteristics of the Gundih CCUS field.

Parameter	Geological Specification	References
Regional Setting	Randublatung Sub-Basin (Kendeng Thrust Belt – Rembang Zone)	Sribudiyani et al. (2003)
Target Storage Reservoir	Middle Miocene Ngrayong Formation (Quartzose Sandstone)	Tsuji et al. (2014)
Primary Caprock Seal	Late Miocene Wonocolo & Pliocene Ledok Formations (Marine Claystone)	Tsuji et al. (2013)
Target Injection Depth	830 – 1,100 m True Vertical Depth Subsea (TVDSS)	Tsuji et al. (2014)
Trapping Mechanism	Anticlinal structural trapping with hydrodynamic sealing	Tsuji et al. (2013)
Primary Containment Risk	Reactivated strike-slip faults creating vertical fracture conduits	Tsuji et al. (2014)

Geologically, the Gundih field is located within the East Java Basin and the Randublatung Sub-Basin. The main storage target is the Miocene Ngrayong Formation, which consists predominantly of sandstone and has been investigated as a potential CO_2 injection reservoir (Tsuji et al., 2014). At the JPN-1 well, the proposed CO_2 injection interval is located at approximately 854–862 m depth within the Ngrayong Formation (Marbun et al., 2019). The Ngrayong Formation is overlain by the low-permeability Wonocolo Formation, which has been considered a sealing formation for the storage system (Tsuji et al., 2014). The regional stratigraphic succession of the study area is summarized in Table 1.

© 2026 Dept. of Geophysics Hasanuddin University

The structural setting is also important because faults and fractures may influence subsurface fluid migration and therefore need to be considered when evaluating CO_2 containment. The selection of Gundih is further supported by documented well-integrity concerns. Previous investigation of the JPN-1 well identified gas leakage and casing-integrity problems that needed to be addressed before the well could be converted into a CO_2 injector (Marbun et al., 2019). These conditions highlight the importance of evaluating potential pathways that may facilitate subsurface fluid migration. Therefore, spatial screening of surface indicators can provide a complementary baseline assessment of areas potentially associated with subsurface CO_2 migration. In this study, FFD, LST, and NDVI are integrated to evaluate their spatial coincidence and identify areas that may indicate potential leakage pathways.

Data Sets and Processing Framework

To evaluate potential surface leakage pathways without introducing subjective weighting bias, spatial parameters were extracted independently from multi-sensor remote sensing imagery and national digital elevation models. Topographic lineaments were extracted using the high-resolution Digital Elevation Model Nasional (DEMNAS) with an 8.27 m spatial resolution (Badan Informasi Geospasial, 2018). Optical and thermal bands were acquired from Landsat 8/9 Operational Land Imager (OLI) and Thermal Infrared Sensor (TIRS) satellite imagery. The multi-sensor spatial datasets utilized in this study are detailed in Table 2.

Table 2. Multi-sensor spatial datasets and derived parameters utilized in this study.

Dataset / Sensor	Resolution / Spec	Primary Application
DEMNAS	0.27" (~8.1 m) Raster DEM	Topographic lineament & Raster DEM multi-azimuth hill-shades
Landsat 8/9 TIRS	30 m	Land Surface Temperature (Surface thermal anomaly identification)
Landsat 8/9 OL	30 m Multispectral	NDVI calculation (surface modifier proxy)

Fault Fracture Density (FFD) Extraction

Regional structural lineaments were extracted automatically and manually verified using DEMNAS raster imagery (Badan Informasi Geospasial, 2018). Lineament networks were processed to calculate FFD, defined as the total lineament length per unit surface area (km/km^2) (Inoh et al., 2023; Rafiq et al., 2025). The spatial calculation is governed by Equation (1):

$$FFD = \frac{\sum_i^n L_i}{A} \quad (1)$$

where $\sum_i^n L_i$ is the total cumulative length of extracted structural lineaments within a given grid cell (km), A is the area of the evaluation grid cell (km^2), and FFD represents the fault fracture density expressed in km/km^2, Lineament density was computed using a continuous moving window with an evaluation grid cell size of 100 m × 100 m and a search radius of 1 km.

Normalized Difference Vegetation Index (NDVI)

Surface vegetation density was mapped using optical bands from Landsat 8/9 OLI satellite imagery. NDVI was calculated to characterize land-surface cover conditions and serve as an environmental mask for thermal analysis (Xue & Su, 2017; Chen et al., 2019), following Equation (2):

$$NDVI = \frac{\rho_{NIR} - \rho_{Red}}{\rho_{NIR} + \rho_{Red}} \quad (2)$$

where ρ_{NIR} represents the surface reflectance of Band 5 (Near-Infrared, 0.85–0.88 μm) and ρ_{Red} corresponds to Band 4 (Red, 0.64–0.67 μm) acquired from Landsat 8/9 OLI.

© 2026 Dept. of Geophysics Hasanuddin University

Land Surface Temperature (LST) Calculation

Surface thermal responses were quantified using the Thermal Infrared Sensor (TIRS) Band 10 of Landsat 8/9 (Avdan & Jovanovska, 2016; Gemitzi et al., 2021). The processing sequence involved converting digital numbers (DN) to Top of Atmosphere (TOA) spectral radiance, calculating brightness temperature (TB), and correcting for land surface emissivity (ε) based on NDVI proportions, as expressed in Equation (3) (Avdan & Jovanovska, 2016; Gemitzi et al., 2021):

$$LST = \frac{T_B}{1 + \left(\frac{\lambda \cdot T_B}{\rho}\right) \ln(\varepsilon)} \quad (3)$$

where TB is the satellite brightness temperature (K), λ is the effective wavelength of emitted radiance (10.8 μm for TIRS Band 10), ρ = h · c / σ = 1.438 × 10^{-2} m·K (derived from Planck's constant h, velocity of light c, and Boltzmann constant σ), and ε is the unitless land surface emissivity calculated from fractional vegetation cover (Pv). The final temperature was converted to Celsius (°C) by subtracting 273.15.

Qualitative Spatial Correlation Analysis

Rather than converting continuous rasters into discrete reclassified categories or applying subjective weighted overlays, this study preserves the continuous spatial values of FFD, NDVI, and LST datasets to maintain high spatial resolution. Localized thermal anomalies were isolated by identifying LST values exceeding the statistical threshold of mean plus 1.5 standard deviations (μ + 1.5σ) (Hidayat et al., 2023). Direct spatial overlay was conducted to evaluate whether high FFD fracture networks directly coincide with surface thermal hotspots under dense vegetation canopy. A quantitative summary of these spatial parameters is presented in Table 3.

Table 3. Quantitative summary of spatial parameters used in the qualitative spatial correlation analysis.

Parameter	Data Type	Value Range / Representation	Interpretation
FFD	Continuous Raster	0 to > 2.5 km/km²	Spatial density of structural fracture networks
NDVI	Continuous Raster	-1.0 to +1.0	Surface vegetation density and canopy cover condition
LST	Continuous / Threshold	Real Temperature (°C) / Anomaly (> μ + 1.5σ)	Surface thermal baseline and localized thermal anomalies

The complete methodological workflow illustrated in Figure 2.

Results and Discussion

Structural Lineament and Fault Fracture Density (FFD) Analysis

Lineament extraction from DEMNAS reveals marked structural heterogeneity across the Gundih field, with FFD values reaching > 2.5 km/km^2. High-density anomalies (≥ 1.5 km/km^2) cluster predominantly within the eastern and southwestern sectors along dominant NW–SE and NE–SW orientations (Figure 3). This localized clustering aligns with the regional compressional deformation and strike–slip fault dynamics near the Kendeng–Rembang boundary zone (Tsuji et al., 2014; Dhara et al., 2022).

© 2026 Dept. of Geophysics Hasanuddin University

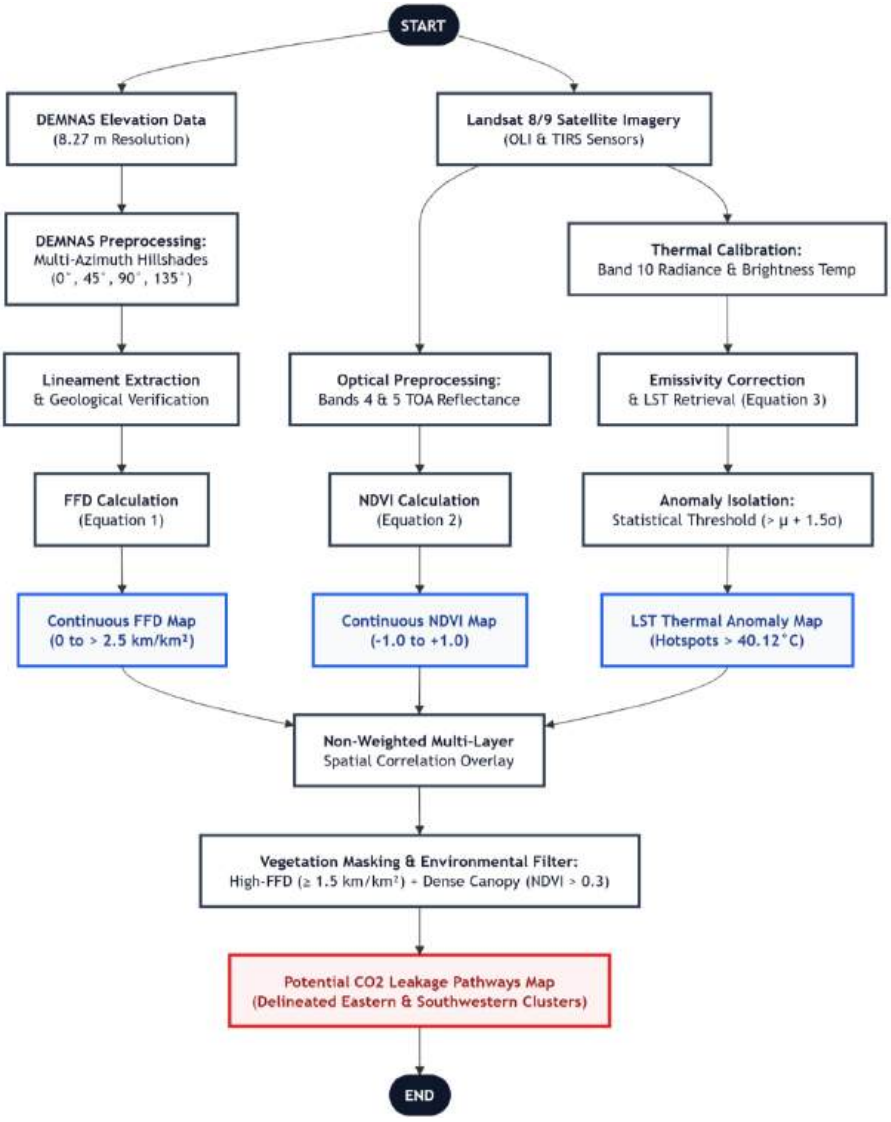


Figure 2. Methodological flowchart illustrating multi-sensor data extraction, continuous parameter processing, and non-weighted qualitative spatial correlation for potential CO2 leakage pathway mapping in the Gundih CCUS field.

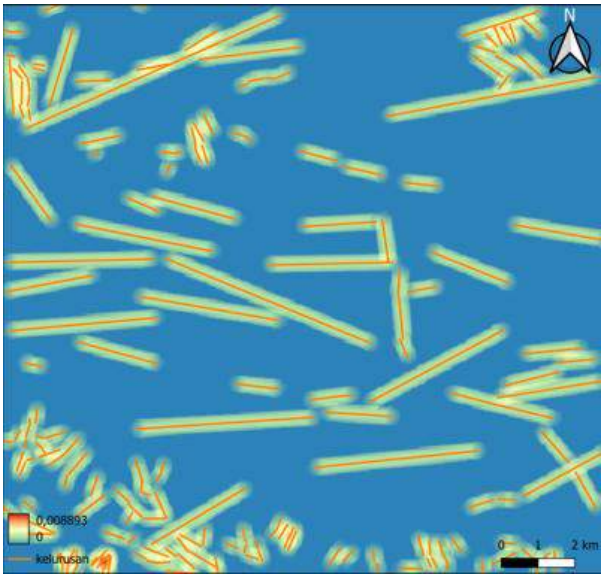


Figure 3. Continuous FFD distribution map derived from DEMNAS automatically extracted structural lineaments in the Gundih field.

© 2026 Dept. of Geophysics Hasanuddin University

In caprock integrity assessment, elevated surface lineament density highlights zones of potential mechanical weakness and secondary permeability above the target Ngrayong reservoir. However, because FFD maps surface-expressed discontinuities, these clusters represent structural susceptibility baselines rather than definitive proof of active subsurface CO_2 migration.

Surface Vegetation Canopy Assessment (NDVI)

To distinguish subsurface thermal anomalies from solar-induced ground heating, the vegetation canopy was mapped using Landsat-derived NDVI (Xue & Su, 2017; Chen et al., 2019) NDVI values ranged from -1.0 to +1.0. Densely vegetated agricultural and forested zones (NDVI > 0.3) covered the majority of the area, while areas with low NDVI (< 0.2) represented bare soil, roads, and riverbeds (Figure 4).

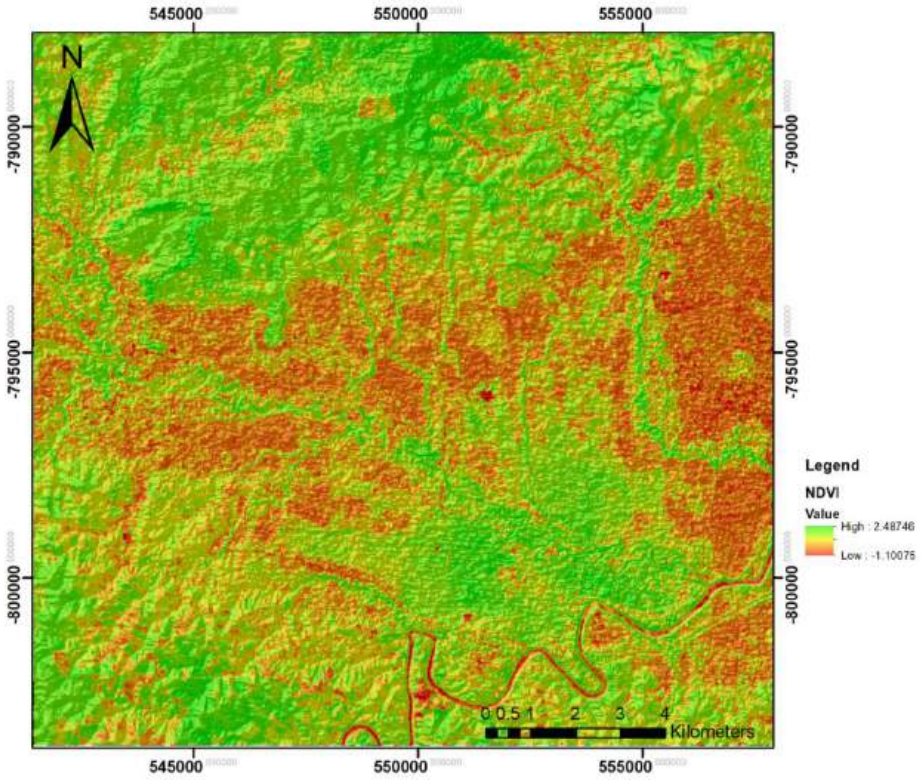


Figure 4. Continuous NDVI map representing surface canopy density across the study area.

In the context of potential CO_2 leakage assessment, vegetation information is useful as a surface-condition constraint rather than as direct evidence of leakage. Elevated soil CO_2 concentrations can affect vegetation condition, but vegetation responses may also result from non-CO_2 factors such as water availability, nutrient conditions, and land management (Chen et al., 2019). Therefore, areas with dense and relatively healthy vegetation provide an important context for interpreting thermal anomalies because elevated surface temperature in such areas is less likely to be explained simply by exposed bare ground. In this study, NDVI is consequently used together with FFD and LST to evaluate whether localized thermal anomalies occur within structurally complex areas while accounting for vegetation cover.

Land Surface Temperature (LST) and Thermal Anomaly Isolation

The spatial distribution of LST in the Gundih CCUS field ranged from 29.52 °C to 45.41 °C, with a mean (μ) of 36.28 °C and a standard deviation (σ) of 2.56 °C (Avdan & Jovanovska, 2016). By applying

© 2026 Dept. of Geophysics Hasanuddin University

the statistical anomaly threshold (> μ + 1.5σ), localized thermal hotspots exceeding 40.12 °C were isolated (Hidayat et al., 2023). These thermal anomalies manifested as discrete spatial clusters concentrated within the eastern and southwestern sectors (Figure 5).

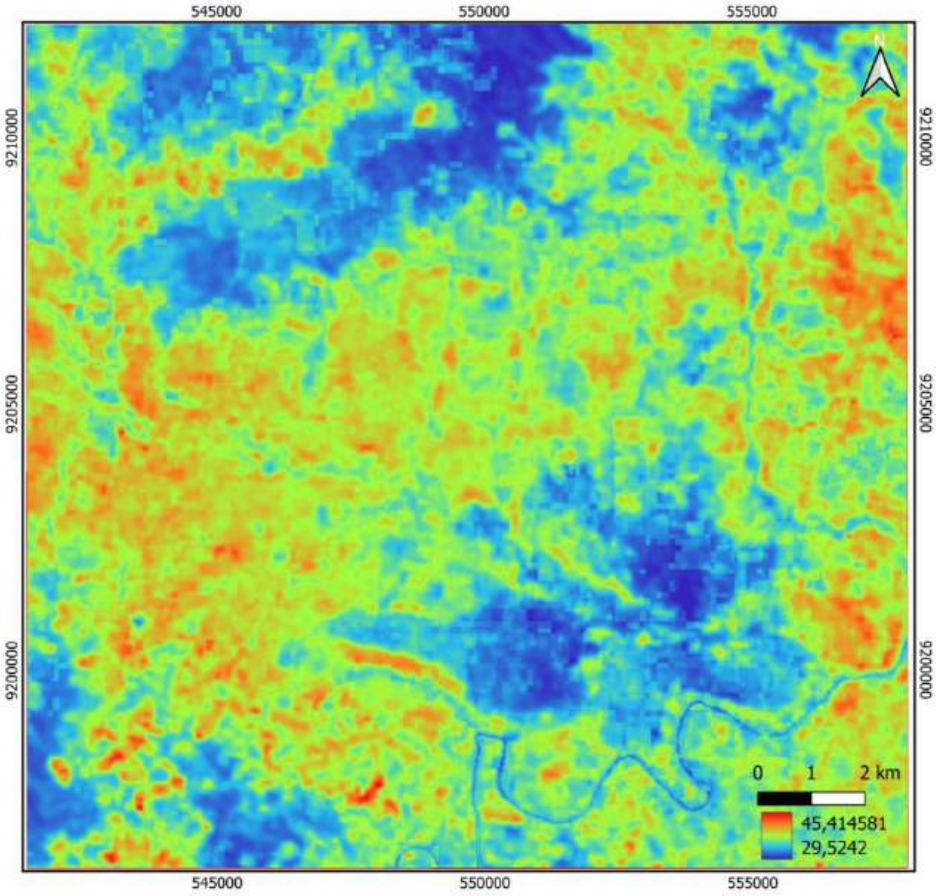


Figure 5. LST map integrated with isolated thermal anomaly outlines (> 40.12 °C).

In geological carbon storage settings, localized surface thermal anomalies along structural corridors typically reflect advective heat transport driven by ascending deep fluids or localized geothermal flux variations along permeable fault conduits (Thiruchittampalam et al. 2022). When formation fluids or gases migrate upward through breached seal zones, they create subtle temperature contrasts relative to surrounding ambient terrain. However, because surface thermal responses are not uniquely diagnostic of CO_2 leakage and can be influenced by solar insolation and surface moisture, their presence alone is insufficient to confirm leakage. Therefore, the spatial concentration of these thermal anomalies warrants direct cross-comparison with structural discontinuity networks (high-FFD zones) to evaluate potential leakage pathways without overstating unverified subsurface migration.

Integrated Qualitative Spatial Correlation for Potential CO_2 Leakage Pathways

The integrated spatial correlation overlays DEMNAS-derived FFD, Landsat LST anomalies, and NDVI canopy constraints to evaluate structural containment risks above the Gundih CCUS complex without applying subjective weighting schemes. The rationale for the selected parameter thresholds is grounded in empirical statistical separation. The FFD threshold of ≥ 1.5 km/km^2 isolates the upper quartile of structural deformation, capturing intense fracture corridors associated with reactivated fault zones. The LST anomaly

© 2026 Dept. of Geophysics Hasanuddin University

threshold (> μ + 1.5σ, exceeding 40.12 °C) delineates discrete thermal hotspots that deviate significantly from the regional background mean of 36.28 °C. Furthermore, the NDVI threshold of > 0.3 defines closed and semi-closed canopy cover, effectively masking solar-induced heating artifacts typically found in exposed bare soils, roads, and riverbeds. Spatial cross-analysis demonstrates that delineated thermal anomalies in the eastern and southwestern sectors directly coincide with high-FFD fracture corridors, as delineated in Figure 6.

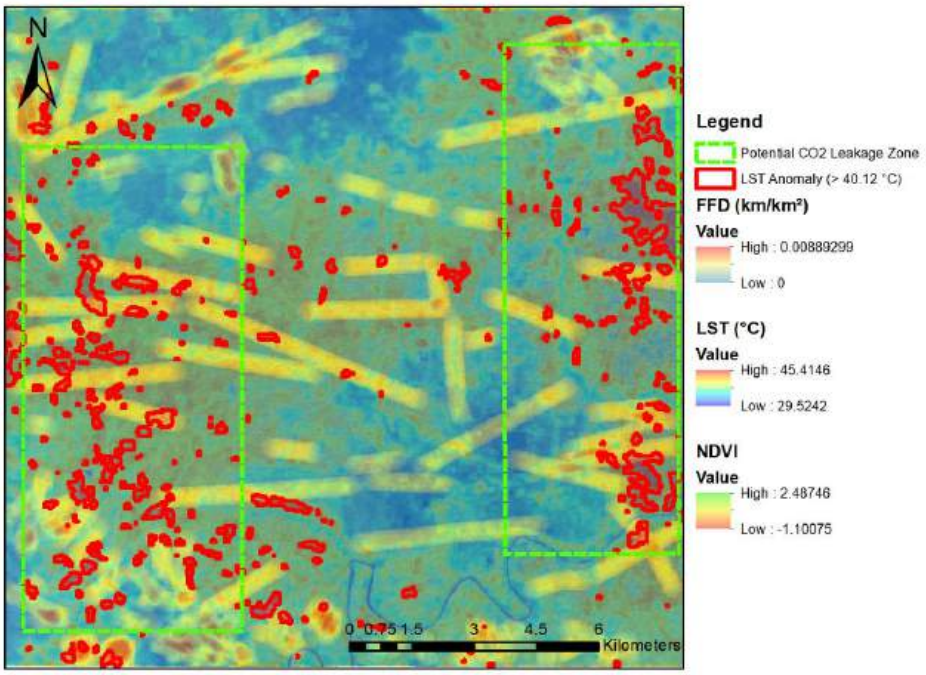


Figure 6. Qualitative spatial correlation map integrating FFD, LST anomalies, and NDVI over DEMNAS hillshade, delineating potential CO_2 leakage pathways in the Gundih field.

The spatial coincidence between high FFD and elevated LST under dense vegetation cover is geologically significant when evaluated against the subsurface architecture of the Gundih field. The target storage reservoir within the Middle Miocene Ngrayong Sandstone is situated at depths of 830–1,100 m TVDSS, overlain by the marine claystones of the Wonocolo Formation acting as the primary regional seal. Structurally, the delineated NW–SE and NE–SW anomaly trends align with reactivated strike-slip fault corridors characteristic of the Kendeng–Rembang boundary zone. In this setting, localized fracture clustering may compromise the mechanical integrity of the overlying Wonocolo mudstones, creating secondary vertical permeability networks that facilitate advective fluid or geothermal heat transport toward the surface.

Nevertheless, remotely sensed surface thermal responses cannot be uniquely attributed to subsurface CO_2 seepage. Non-geological environmental factors, including localized soil moisture deficits, agricultural variations, and seasonal insolation, can also produce elevated surface temperatures. Consequently, the delineated spatial clusters represent structural susceptibility pathways and prioritization screening targets rather than confirmed active CO_2 leakages. These findings establish a baseline for subsequent field monitoring campaigns, wherein direct in-situ soil-gas CO_2 concentration profiling, geochemical flux measurements, and shallow geophysical surveys are required to validate actual fluid migration along these structural corridors.

Conclusion

© 2026 Dept. of Geophysics Hasanuddin University

This study demonstrates a non-weighted, multi-sensor spatial screening framework integrating Fault Fracture Density (FFD), Land Surface Temperature (LST), and the Normalized Difference Vegetation Index (NDVI) to delineate potential structural leakage pathways in the Gundih CCUS field. DEMNAS-derived lineament extraction identified concentrated high-FFD corridors (≥ 1.5 km/km²) trending primarily NW–SE and NE–SW, conforming to the regional compressional and strike–slip fault patterns near the Kendeng–Rembang boundary zone. Independent satellite thermal processing isolated discrete statistical hotspots (> 40.12 °C) that spatially coincide with these dense fracture networks in the eastern and southwestern sectors, even beneath dense vegetation canopies (NDVI > 0.3).

From a caprock integrity perspective, these spatial overlaps highlight zones where secondary fracture permeability may compromise the mechanical sealing capability of the marine claystones of the Wonocolo Formation above the target Middle Miocene Ngrayong Sandstone reservoir (injection depth: 830–1,100 m TVDSS). However, because satellite remote sensing provides indirect surface observations that can be influenced by meteorological variations and soil moisture dynamics, these indicators cannot independently confirm active subsurface CO_2 escape. Consequently, the delineated anomalies serve as preliminary structural susceptibility pathways and prioritization baselines for future monitoring campaigns. Direct ground-truthing including in-situ soil-gas CO_2 concentration profiling, geochemical flux surveys, and high-resolution shallow geophysics remains imperative to validate actual fluid migration along these prioritized structural corridors (Kim et al., 2018).

Acknowledgements

The authors express their sincere gratitude to the Geospatial Information Agency (BIG) of Indonesia for providing the DEMNAS datasets, as well as NASA and the U.S. Geological Survey (USGS) for making the Landsat satellite imagery publicly accessible. Special thanks are extended to the Department of Geological Engineering, Universitas Pertamina for providing spatial analysis facilities, software support, and academic guidance throughout this research. The authors would also like to thank colleagues and technical supporters who contributed valuable insights during data analysis and manuscript preparation.

Author Contribution

Tirta Khayru Putra: Conceptualization, Methodology, Software, Formal Analysis, Investigation, Data Curation, Writing – Original Draft, Writing – Review & Editing, Visualization. **Ridwan Rahmanto**: Conceptualization, Validation, Writing – Review & Editing, Supervision. **Syahrbanu**: Software, Investigation, Data Curation, Writing – Original Draft, Writing – Review & Editing.

Conflict of Interest

The authors declare that there is no conflict of interest regarding the publication of this article.

References

Avdan, U., & Jovanovska, G. (2016). Algorithm for Automated Mapping of Land Surface Temperature Using LANDSAT 8 Satellite Data. *Journal of Sensors*, 2016(1), 1–10. https://doi.org/10.1155/2016/1480307

Badan Informasi Geospasial. (2018). *Petunjuk teknis pengolahan dan pemanfaatan Data Digital Elevation Model Nasional (DEMNAS)*. Pusat Pemetaan Rupabumi dan Toponim, BIG. https://tanahair.indonesia.go.id/portal

© 2026 Dept. of Geophysics Hasanuddin University

-web/

Bohloli, B., Bjørnarå, T. I., Park, J., & Rucci, A. (2018). Can we use surface uplift data for reservoir performance monitoring? A case study from In Salah, Algeria. *International Journal of Greenhouse Gas Control*, 76, 200–207. https://doi.org/10.1016/j.ijggc.2018.06.024

Chen, Y., Guerschman, J. P., Cheng, Z., & Guo, L. (2019). Remote sensing for vegetation monitoring in carbon capture storage regions: A review. *Applied Energy*, 240, 312–326. https://doi.org/10.1016/j.apenergy.2019.02.027

Dhara, M., Baisantry, M., & Prusty, G. (2022). Automatic extraction and analysis of lineament features using ASTER and Sentinel 1 SAR data. *Journal of Earth System Science*, 131(2), 111. https://doi.org/10.1007/s12040-022-01851-y

Garain, S., Mitra, D., & Das, P. (2019). Detection of hydrocarbon microseepage-induced anomalies by spectral enhancements of Landsat 7 ETM+ images in part of Assam-Arakan Fold Belt, India. *Journal of Petroleum Exploration and Production Technology*, 9(4), 2573–2582. https://doi.org/10.1007/s13202-019-00747-w

Gemitzi, A., Dalampakis, P., & Falalakis, G. (2021). Detecting geothermal anomalies using Landsat 8 thermal infrared remotely sensed data. *International Journal of Applied Earth Observations and Geoinformation*, 96, 102283. https://doi.org/10.1016/j.jag.2020.102283

Hidayat, M. R., Marin, J., Abdurrahman, R. B., Devienna, S. N., & Fatimah, I. N. (2023). Analisis Land Surface Temperature (LST) dan Fault Fracture Density (FFD) di daerah geotermal Bukit Kili-Gunung Talang, Sumatra Barat. *Journal of Aceh Physics Society*, 12(2), 25–31. https://doi.org/10.24815/jacps.v12i2.31160

Inoh, H. A, Tayebi, M. A., & Rajji, A. A. (2023). A comparative analysis of lineaments extracted from Landsat 8 OLI & ASTER-GDEM data, in Talmakent area, Western High Atlas, Morocco. *Iraqi Geological Journal*, 56(1F), 303-315. https://doi.org/10.46717/igj.56.1F.20ms-2023-6-28

Iqbal, M., & Juliarka, B. R. (2020). Identification of permeability level by using fault fracture density analysis and Landsat 8 OLI at Ulubelu geothermal area. *IOP Conference Series: Earth and Environmental Science*, 537, 012016. https://doi.org/10.1088/1755-1315/537/1/012016

Kim, D., Kang, H., Ryu, J.-Y., Jun, S.-C., Yun, S.-T., Choi, S., Park, S., Yoon, M., & Lee, H. (2018). Development of Raman Lidar for Remote Sensing of CO_2 Leakage at an Artificial Carbon Capture and Storage Site. *Remote Sensing*, 10(9), 1439. https://doi.org/10.3390/rs10091439

Marbun, B. T. H., Prasetyo, D. E., Prabowo, H., Susilo, D., Firmansyah, F. R., Palilu, J. M., Silamba, I. C., Santoso, D., Kadir, W. G. A., Sule, R., Kardani, I., Saprudin, W., & Andhika, B. (2019). Well integrity evaluation prior to converting a conventional gas well to CO_2 injector well—Gundih CCS pilot project in Indonesia (phase 1). *International Journal of Greenhouse Gas Control*, 88, 447–459. https://doi.org/10.1016/j.ijggc.2019.06.006

Rafiq, J., Abu-Mahfouz, I. S., Chavanidis, K., & Soupios, P. (2025). Integrated structural analysis for geothermal exploration: A new protocol combining remote sensing and aeromagnetic geophysical data.

© 2026 Dept. of Geophysics Hasanuddin University

MethodsX, 14, 103189. https://doi.org/10.1016/j.mex.2025.103189

Santoso, D., Tirza, A., Wahyudi, E. J., Alawiyah, S., Kadir, W. G. A., & Sule, R. M. (2019). An application of gravity method to estimate a storage capacity of Ngrayong Formation for Carbon Capture and Storage (CCS) Pilot Project of Gundih Field, East Java, Indonesia. *Proceedings of the 14th International Conference on Greenhouse Gas Control Technologies* (GHGT-14). https://doi.org/10.2139/ssrn.3365938

Sule, R., Kadir, W. G. A., Matsuoka, T., Prabowo, H., & Sidemen, G. S. (2019). Gundih CCS pilot project: Current status of the first carbon capture and storage project in South and Southeast Asia regions. *Proceedings of the 14th International Conference on Greenhouse Gas Control Technologies* (GHGT-14). https://doi.org/10.2139/ssrn.3366415

Sribudiyani, Muchsin, N., Ryacudu, R., Kunto, T., Astono, P., Prasetya, I., Sapiie, B., Asikin, S., Harsolumakso, A. H., & Yulianto, I. (2003). The collision of East Java Microplate and its implication for hydrocarbon occurrences in the East Java Basin. *Proceedings of the Indonesian Petroleum Association (IPA)*, 29th Annual Convention, 1–12. https://www.ipa.or.id/en/publications/the-collision-of-the-east-java-microplate-and-its-implication-for-hydrocarbon-occurrences-in-the-east-java-basin

Thiruchittampalam, S., Raval, S. A., Glenn, N. F., & Hussain, F. (2022). Indirect remote sensing techniques for long term monitoring of CO_2 leakage in geological carbon sequestration: A review. *Journal of Natural Gas Science and EngiAneering*, 100, 104488. https://doi.org/10.1016/j.jngse.2022.104488

Tsuji, T., Khakim, M. Y. N., Kitamura, K., Yamada, Y., Matsuoka, T., Onishi, K., Asikin, A. R., Ariadji, T., Kadir, W. G. A., & Gundih CCS Project Team. (2013). CCS project in Gundih gas field, Indonesia (Part 2): Reservoir characterization and simulation. *Proceedings of the 129th SEGJ Conference*, 1–4.

Tsuji, T., Matsuoka, T., Kadir, W. G. A., Hato, M., Takahashi, T., Sule, M. R., Kitamura, K., Yamada, Y., Onishi, K., Widarto, D. S., Sebayang, R. I., Prasetyo, A., Priyono, A., Ariadji, T., Sapiie, B., Widianto, E., Asikin, A. R., & Gundih CCS Project Team. (2014). Reservoir characterization for site selection in the Gundih CCS project, Indonesia. *Energy Procedia*, 63, 6335–6343. https://doi.org/10.1016/j.egypro.2014.11.666

Xue, J., & Su, B. (2017). Significant Remote Sensing Vegetation Indices: A Review of Developments and Applications. *Journal of Sensors*, 2017(1), 1353691. https://doi.org/10.1155/2017/1353691

Zahratunnisa, Z., Hapsari, T., Joyontono, P., Rangkuti, N. S., & Wiguna, H. S. (2025). Karakterisasi zona geotermal menggunakan pendekatan dekomposisi polarimetrik Yamaguchi pada citra SAR. *Jurnal Geosains Kutai Basin*, 8(2), 69–78. https://doi.org/10.30872/s384n096

Zhang, T., Zhang, W., Yang, R., Liu, Y., & Jafari, M. (2020). CO_2 capture and storage monitoring based on remote sensing techniques: A review. *Journal of Cleaner Production*, 281, 124409. https://doi.org/10.1016/j.jclepro.2020.124409

© 2026 Dept. of Geophysics Hasanuddin University

ISSN: 2579-5821 (Print)
ISSN: 2579-5546 (Online)
URL address: http://journal.unhas.ac.id/index.php/geocelebes
DOI: 10.70561/geocelebes.v10i2.53080

Jurnal Geocelebes Vol. 10 No. 2, October 2026, 371 – 396

ENSO and IOD Teleconnection with Sumbawa Rainfall: Seasonal Predictability Beyond Monthly Lag Structure

Romi Aprianto[1]*, Akbar Tawaqqal[2], Syaharuddin[3]

[1]Physics Education Study Program, University of Samawa, Sumbawa, West Nusa Tenggara 84315, Indonesia.
[2]Industrial Engineering Study Program, University of Mataram, Mataram, West Nusa Tenggara 83115, Indonesia.
[3]Mathematics Education Study Program, Muhammadiyah University of Mataram, Mataram 83225, West Nusa Tenggara, Indonesia.

*Corresponding author. Email: romi.aprianto@samawa-university.ac.id

Manuscript received: 29 July 2026; Received in revised form: 5 October 2026; Accepted: 8 October 2026

Abstract

Cross-correlation analysis is the standard tool for quantifying how the El Niño-Southern Oscillation (ENSO) and the Indian Ocean Dipole (IOD) influence Indonesian rainfall, and it routinely yields an "optimal time lag" offered as operational lead time. For Sumbawa Regency (West Nusa Tenggara) we show that this lag structure is an artefact. Using 44 years of NASA POWER precipitation (1982-2025; 528 months) with the SOI, Niño 3.4 and Dipole Mode Index from NOAA PSL, the conventional cross-correlation function returns significant coefficients at non-causal negative lags (rainfall leading the index), with the naive maximum for Niño 3.4 falling at a negative lag. After Box-Jenkins pre-whitening the structure collapses: only the concurrent SOI signal survives ($r = 0.239$), while the concurrent oceanic coefficients also fall to zero, so the reported "climate memory" is predictor persistence. Predictability exists at seasonal aggregation. Using June-August index means to forecast September-November (SON) rainfall across 43 years under leave-one-year-out cross-validation, a LASSO model attains an out-of-sample R^2 of 0.405 and an RMSE skill score of +0.247 against climatology, and predicts the wet-season onset month with a skill score of +0.219. Skill is carried almost entirely by the JJA-mean SOI; the IOD contributes nothing detectable here, and a random forest does not outperform linear regression. As a categorical warning for below-normal SON rainfall the forecast reaches a critical success index of 0.53 against chance 0.20. Usable lead time therefore comes from seasonal aggregation, not monthly lag structure, and reported optimal lags in the regional literature should be re-examined.

Keywords: Forecast verification; Pre-whitening; Southern Oscillation Index; Warning skill; Wet-season onset.

Citation: Aprianto, R., Tawaqqal, A., & Syaharuddin, S. (2026). ENSO and IOD teleconnection with Sumbawa rainfall: Seasonal predictability beyond monthly lag structure. *Jurnal Geocelebes*, 10(2): 371–396, doi: 10.70561/geocelebes.v10i2.53080

Introduction

Sumbawa Regency, in West Nusa Tenggara, lies in one of the driest and most climatically exposed parts of the Indonesian Maritime Continent. Its rainfall is strongly monsoonal: most annual precipitation falls between December and March, while core dry-season totals can approach zero. The regional economy rests on rainfed dryland agriculture, so the timing of the wet-season onset, rather than the annual total, most directly governs planting, water allocation and crop outcomes. A delayed or failed onset propagates within one season into water scarcity and food insecurity, and Nusa Tenggara in particular is projected to become drier and to experience longer dry spells under continued warming (Ghosh & Shepherd, 2023; Hariadi et al., 2024; Kurniadi et al., 2024).

© 2026 Dept. of Geophysics Hasanuddin University

Interannual rainfall variability here is dominated by two coupled ocean-atmosphere modes, ENSO and the IOD. The classification of Indonesian rainfall into monsoonal, equatorial and local regimes, with southern Indonesia in the monsoonal class (Aldrian & Susanto, 2003), is long established, as is the finding that ENSO modulates seasonal rainfall and extremes most strongly during the dry season and the dry-to-wet transition and only weakly during the peak wet season (As-syakur et al., 2014; Kurniadi et al., 2021; Marzuki et al., 2025; Supari et al., 2018). The two flavours of ENSO leave distinct rainfall signatures across Southeast Asia (Nguyen-Thanh et al., 2023), and the teleconnection propagates into hydrological regimes such as Java stream-flow (Nugroho et al., 2022). ENSO and IOD exert partially independent effects on Indonesian extremes (Kurniadi et al., 2021), their co-occurrence can delay onset and extend dry conditions for several months (Hidayat et al., 2025; Sulaiman et al., 2023), and the teleconnection is projected to intensify and shift eastward under warming (Chen et al., 2023; Chen et al., 2025). The background state is itself changing: the Pacific Walker circulation shows contested multi-decadal trends (Heede & Fedorov, 2023; Kosovelj & Zaplotnik, 2023; Watanabe et al., 2023) whose longer-term weakening is increasingly attributed to anthropogenic forcing (Watanabe et al., 2024; Wu et al., 2024), ENSO variability is projected to intensify (Cai et al., 2023), while IOD-related sea surface temperature variability is projected to increase this century (Wang et al., 2024a) before reversing to a reduction after 2100 (Wang et al., 2024c); the 2023 El Niño was a recent demonstration across the archipelago (Zehri et al., 2025). The existence and seasonality of this teleconnection are well established and are the point of departure for this study, not its result.

What remains unresolved, and what motivates this study, are three problems that sit between this established physical picture and its operational use at district scale.

First, a methodological problem. Much regional and district-scale work in Indonesia quantifies the teleconnection by applying a cross-correlation function (CCF) to deseasonalised monthly anomalies, reporting an "optimal lag" plus a tail of significant coefficients extending several months, interpreted as short-term climate memory (Wei & Yuan, 2024). This carries a well-known pitfall. The SOI, Niño 3.4 and Dipole Mode Index (DMI) are themselves strongly autocorrelated at monthly resolution (lag-1 typically 0.85-0.95). If a predictor X influences rainfall Y only concurrently, the expected cross-correlation at lag k is still approximately $r_0 \cdot \rho_x(k)$, the predictor's own autocorrelation. A slowly decaying tail of "significant" lagged correlations is therefore the null expectation, not evidence of atmospheric memory; without pre-whitening both the lag structure and its significance are inflated (Box et al., 2016; Bretherton et al., 1999; Ebisuzaki, 1997). To our knowledge no published assessment for the Lesser Sunda Islands has tested whether a reported lag structure survives this correction.

Second, and more consequentially, an inferential problem: the leap from correlation to operational lead time. Teleconnection coefficients in this literature typically fall in $|r| = 0.2$-0.6, that is 4-36% of explained variance, yet are routinely presented as justifying early warning and dynamic crop scheduling. Three distinctions are collapsed in that move. An in-sample correlation is not out-of-sample skill; predictive skill is meaningful only against a climatological baseline, since a model can correlate positively with observations yet perform worse than a forecast of the long-term mean; and skill on a continuous target is not

© 2026 Dept. of Geophysics Hasanuddin University

skill at issuing the categorical warning a decision-maker consumes. Warning metrics such as probability of detection (POD), false alarm ratio (FAR), critical success index (CSI) and Peirce skill score (PSS) can remain near zero where a continuous correlation is nominally significant. The caution is not new: the limited predictability of Indonesian wet-season rainfall was shown two decades ago (Haylock & McBride, 2001). Yet district-scale Indonesian studies almost never report climatology-referenced, out-of-sample skill, so the operational value of the teleconnection at this scale remains effectively unquantified.

Third, a specification problem. Work in the Lesser Sunda Islands has frequently examined ENSO in isolation, even though ENSO and IOD co-occur and their September-November impacts are partially collinear (Amirudin et al., 2020; Hidayat et al., 2025; Kurniadi et al., 2021; Wang et al., 2024b). Attributing rainfall variability to ENSO without partialling out the DMI risks double-counting a shared signal. Relatedly, claims that the teleconnection has "strengthened" in recent decades are common but seldom tested: comparing correlation coefficients between two epochs requires a formal test of the difference, and comparisons based on Niño 3.4 anomalies referenced to a long, fixed base period are additionally confounded by the secular warming trend in tropical Pacific Sea surface temperature.

This study addresses these three problems for Sumbawa Regency over 1982-2025 using entirely open data and a fully reproducible pipeline. Its objectives are: (i) to quantify the ENSO-IOD-rainfall association using both a naive CCF, for comparability with the existing literature, and a pre-whitened CCF with effective-degrees-of-freedom and phase-randomisation significance testing, and thereby to determine whether any true lagged signal survives; (ii) to isolate the independent contributions of ENSO and IOD by partial correlation; (iii) to evaluate, strictly out of sample, whether June-August (JJA) mean values of the SOI, Niño 3.4 and DMI carry usable predictive skill for two decision-relevant targets: the September-November (SON) rainfall total and the wet-season onset month, each relative to a climatological baseline; and (iv) to translate that skill into categorical warning metrics for below-normal SON rainfall, and to test formally whether the teleconnection differs between 1982-2003 and 2004-2025.

Three falsifiable hypotheses follow. H1: after pre-whitening, significant cross-correlation is confined to lag 0, and the multi-month climate memory reported in the literature is an artefact of predictor persistence. H2: notwithstanding H1, seasonal aggregation (JJA predictors, SON target) yields genuine and non-trivial out-of-sample skill, because a three-month mean integrates the concurrent coupling and delivers a real operational lead time of one to three months. H3: continuous skill overstates warning skill: the critical success index for below-normal SON rainfall will be substantially lower than the correlation coefficient alone would suggest.

This work therefore contributes a decision-relevant quantification of how much lead information the teleconnection contains at district scale, rather than a new claim for the teleconnection itself, together with a transparent, executable pipeline that other Indonesian districts can reuse. This is consistent with a broader shift in the machine-learning weather and climate literature from accuracy metrics in isolation toward operational utility, interpretability and verification (Camps-Valls et al., 2025; Gibson et al., 2021; Materia et al., 2024; Price et al., 2025; Yang et al., 2024; Zhou & Zhang, 2023).

Materials and Methods

Study area

© 2026 Dept. of Geophysics Hasanuddin University

Sumbawa Regency (approximately 8.2-9.1°S, 116.7-118.4°E) occupies the western half of Sumbawa Island in West Nusa Tenggara Province. Analyses are anchored on a representative point at 8.50°S, 117.42°E, close to the regency capital Sumbawa Besar. The regency falls within the monsoonal rainfall regime of southern Indonesia (Aldrian & Susanto, 2003), with a single pronounced wet season centred on December-February and a severe dry season from June to September. Agriculture is predominantly rainfed. The location of the regency and the analysis point is shown in Figure 1, and the complete analytical workflow in Figure 2.

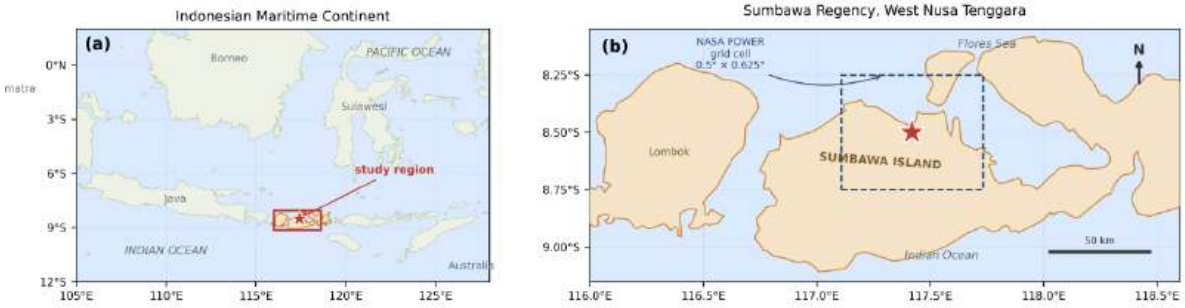


Figure 1. Study area. (a) Location of West Nusa Tenggara (orange) within the Indonesian Maritime Continent; the red box marks the extent of panel (b) and the star the analysis point. (b) Sumbawa Regency on Sumbawa Island, with the analysis point at 8.50°S, 117.42°E near Sumbawa Besar and the 0.5° × 0.625° NASA POWER grid cell from which precipitation is drawn. Coastlines are from Natural Earth (1:10 m).

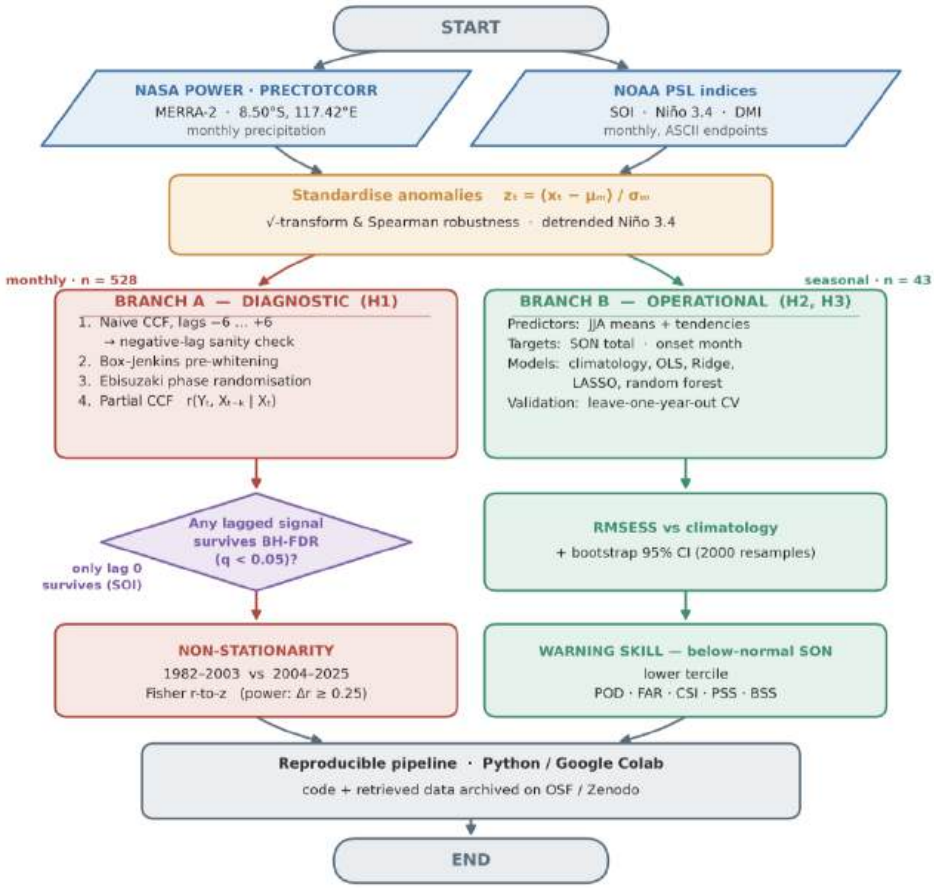


Figure 2. Analytical workflow. Branch A (red) is the diagnostic analysis at monthly resolution and tests hypothesis H1. Branch B (green) is the operational analysis at seasonal resolution, which uses one sample per year and is therefore structurally free of the autocorrelation artefact examined in Branch A; it tests H2 and H3.

Rainfall data

Monthly precipitation was obtained from the NASA Prediction of Worldwide Energy

© 2026 Dept. of Geophysics Hasanuddin University

Resources (POWER) project, parameter PRECTOTCORR (bias-corrected total precipitation), for January 1982 to December 2025, giving 528 monthly values spanning 44 complete calendar years, with no missing months. Data were retrieved on 14 July 2026 through the POWER REST API for the point (-8.50°, 117.42°); the same series is accessible through the nasapower client (Sparks, 2018). POWER meteorological parameters derive from NASA's MERRA-2 reanalysis (Gelaro et al., 2017) on a 0.5° × 0.625° grid, with near-real-time values appended from GEOS-IT. POWER reports monthly precipitation as a mean daily flux (mm day^{-1}); values were multiplied by the number of days in each calendar month to obtain monthly totals.

Three limitations of this product are carried through to interpretation. First, POWER is a reanalysis, not a gauge record: over tropical basins it reproduces climatology and rain-day occurrence reasonably but underestimates totals and especially extremes (Madushan et al., 2025; Tan et al., 2023; Tayyeh et al., 2023), with skill uneven across variables and regions (Khalid et al., 2024); satellite products such as GSMaP show comparable difficulties over the Maritime Continent (Ramadhan et al., 2023), and POWER is nonetheless widely used as an operational input for data-driven rainfall models (Saleh et al., 2024). Second, the native cell is coarse relative to Sumbawa's topography and contains a substantial marine fraction, so the series is a grid-cell areal estimate, not a point observation, and orographic contrasts are unresolved. Third, NASA recommends ending climate analyses roughly two months behind real time because of the GEOS-IT append, so the series is truncated at December 2025; the retrieval date is reported above because POWER is periodically reprocessed.

Because the inferences concern the relative association between large-scale indices and local anomalies rather than absolute magnitudes, these biases are unlikely to reverse the sign or seasonality of the teleconnection, though they place a ceiling on achievable skill; the skill reported in the subsection “Seasonal aggregation recovers genuine, cross-validated skill” should be read as an upper bound for a single grid cell. The POWER series is validated against the CHIRPS observational product in the subsection “Validation of the rainfall series and grid-cell representativeness”, which also shows the single grid cell to be representative of regional interannual variability; direct validation against multi-decadal BMKG gauge records, whose access requires an institutional data agreement, remains a next step before operational use (see the subsection “Limitations”).

Climate indices

Three monthly indices covering 1982-2025 were obtained from the NOAA Physical Sciences Laboratory (PSL) archive: the Southern Oscillation Index (SOI; standardised Tahiti minus Darwin sea-level pressure anomaly), the Niño 3.4 sea surface temperature series (5°N-5°S, 170°W-120°W), and the Dipole Mode Index (DMI), which represents the IOD as the difference in SST anomaly between the western and south-eastern tropical Indian Ocean. The DMI is a new predictor relative to earlier versions of this analysis and is included because ENSO and IOD forcing of southern Indonesian rainfall is partially independent (Hidayat et al., 2025; Kurniadi et al., 2021; Wang et al., 2024b). Satellite and reanalysis rainfall products have well-documented regional biases over Indonesia (As-syakur et al., 2013), reinforcing the need for the validation reported in the subsection “Validation of the rainfall series and grid-cell representativeness”. All files are distributed as fixed-width ASCII (one row per year, twelve monthly values, with a sentinel missing-value code) and are parsed programmatically at run time. Endpoints are listed in Table 1.

© 2026 Dept. of Geophysics Hasanuddin University

Two data notes are important for reproducibility. The PSL SOI series has a sample standard deviation of 1.61 over 1982-2025 and a range of -6.0 to +4.8, and is therefore not identical in scaling to the standardised SOI distributed by the NOAA Climate Prediction Center; because all series are subsequently standardised by calendar month (see the subsection "Anomaly construction and transformation"), this leaves every correlation reported here unchanged, though the specific product must be stated. The PSL DMI is HadISST-based and terminates in April 2025, leaving eight missing months at the end of the record; this excludes 2025 from the seasonal analysis (see the subsection "Out-of-sample seasonal predictability experiment") but does not affect the monthly diagnostics.

Table 1. Data sources and endpoints.

Variable	Product / index	Source endpoint	Notes
Precipitation (mm month^{-1})	NASA POWER PRECTOTCORR (MERRA-2 / GEOS-IT, bias-corrected)	power.larc.nasa.gov →/api/temporal/monthly/ point (lat -8.50, lon 117.42)	Served in mm day^{-1}; converted to monthly totals. 0.5° × 0.625° grid cell. Retrieved 14 Jul 2026.
SOI	Standardised Tahiti-Darwin SLP anomaly	psl.noaa.gov/data/ correlation/soi.data	Positive = La Niña-like state. σ = 1.61 (not CPC scaling).
Niño 3.4 SST (°C)	ERSSTv5-based, 5°N-5°S / 170°W-120°W	psl.noaa.gov/data/correlation/ nina34.data	Anomalies computed in-house; detrended variant used for the epoch comparison.
DMI - IOD (°C)	Dipole Mode Index (west minus south-east tropical Indian Ocean SST anomaly)	psl.noaa.gov/gcos/wgsp/Timeseries/ Data/dmi.had.long.data	HadISST-based; ends April 2025 (8 missing months).
Precipitation - validation (mm day^{-1})	CHIRPS v2 (gauge-blended satellite; Funk et al., 2015)	developers.google.com/earth-engine/ datasets/catalog/UCSB-CHG_CHIRPS_DAILY (via Google Earth Engine)	0.05° grid; independent observational reference used to validate POWER (see the subsection "Validation of the rainfall series and grid-cell representativeness").
Precipitation - station (attempted)	NOAA ISD/GSOD daily, WMO 97260 (Sumbawa Besar)	ncei.noaa.gov/data/ global-summary-of-the-day	Digitised record too incomplete over 1982-2025 (26.6% of days) for interannual validation (see the subsection "Validation of the rainfall series and grid-cell representativeness").

Anomaly construction and transformation

For each variable, the monthly climatological mean μ_m and standard deviation σ_m (m = 1…12) were computed over the full 44-year record, and standardised anomalies were formed, following Wilks (2019), as

$$z_t = \frac{x_t - \mu_m}{\sigma_m} \quad (1)$$

Dividing by σ_m, rather than subtracting μ_m alone, is essential in a monsoonal regime. The interannual standard deviation of rainfall in January is one to two orders of magnitude larger than in August, so a mean-only anomaly series remains strongly heteroscedastic and allows a small number of wet-season months to dominate any pooled Pearson correlation. This is a material departure from the common

© 2026 Dept. of Geophysics Hasanuddin University

practice of subtracting the monthly mean only.

Because monthly rainfall in this regime is strongly right-skewed and contains near-zero values (Figure 6b), two robustness variants are carried through the entire analysis: rainfall is additionally analysed after a square-root transform, and Spearman's ρ is computed alongside Pearson's r wherever a correlation is quoted. Conclusions are reported only where they are stable across all three variants.

Cross-correlation: naive and pre-whitened

For comparability with the existing literature, the conventional cross-correlation function (Box et al., 2016) was computed for lags k = -6 to +6 months, where a positive lag denotes the index leading rainfall (Box et al., 2016):

$$r_{XY}(k) = corr(y_t, x_{t-k}) \qquad (2)$$

Negative lags are included deliberately as a diagnostic rather than as a physical hypothesis. Since no mechanism allows rainfall over Sumbawa to force the Pacific or Indian Ocean basins, any apparent significance at negative lags is direct evidence that the significance test is contaminated by serial correlation.

The pre-whitened cross-correlation, our primary analysis, follows the Box-Jenkins procedure (Box et al., 2016), an ARIMA(p, d, q) model was fitted to each predictor series by minimising AICc; the fitted filter was then applied to both the predictor and the rainfall series, and the CCF was computed between the two residual series. Under the null hypothesis of no relationship, the pre-whitened cross-correlations are approximately mutually independent with standard error 1/√n, so the conventional ±1.96/√n significance bounds are valid, which is precisely what is not true of the naive CCF.

Two further significance procedures are reported alongside. An effective-sample-size correction (Bretherton et al., 1999) is applied to the naive coefficients,

$$N_{eff} = N \frac{1 - \rho_X(1)\rho_Y(1)}{1 + \rho_X(1)\rho_Y(1)} \qquad (3)$$

which adjusts the degrees of freedom for the serial dependence of both series; and a nonparametric phase-randomisation test (Ebisuzaki, 1997) with 1000 surrogates is used to construct an empirical null distribution. Because phase randomisation preserves the power spectrum, and hence the autocorrelation function, of each series, it provides a significance test valid without any parametric model of the serial dependence. It should be noted, however, that this test establishes only that $r \neq 0$ in the presence of autocorrelation; it does not by itself distinguish a lag-0 signal from a lagged one.

A partial cross-correlation tests explicitly whether lagged predictors carry information beyond the concurrent one; the partial correlation $r(Y_t, X_{t-k} \mid X_t)$ was computed for k = 1…6. A lag is treated as genuine only if this partial correlation remains significant after correction for multiple comparisons. Together, pre-whitening and partial cross-correlation render hypothesis H1 falsifiable: a real lagged signal would survive both.

Separating the ENSO and IOD signals

Because the DMI and Niño 3.4 covary, particularly during SON, partial correlations r(Y, Niño3.4 | DMI) and r(Y, DMI | Niño3.4) were computed so that each mode's independent contribution can be reported. Variance inflation factors (VIF) were computed for the multiple-predictor models described in the subsection "Out-of-sample seasonal predictability experiment"; all remained below 4 (maximum 3.53 for the JJA Niño 3.4 mean), and collinearity was in any case handled by regularisation.

© 2026 Dept. of Geophysics Hasanuddin University

Out-of-sample seasonal predictability experiment

This experiment is the operational core of the study, and it is constructed so as to be structurally immune to the autocorrelation artefact described in the subsection "Cross-correlation: naive and pre-whitened", because it uses one sample per year, giving 43 effectively independent observations rather than 528 serially dependent ones. Predictors are issued at the end of August, giving a genuine operational lead time of one to three months: the June-August means of the SOI, the Niño 3.4 anomaly and the DMI, together with the within-season tendency (August minus June) of each index, which captures the developing rather than the mature phase of an event.

Two targets are used. T1 is the SON rainfall total (September + October + November, in mm), which conditions water availability at the start of the growing season. T2 is the wet-season onset month, defined at monthly resolution as the first month from September onward in which rainfall reaches at least 100 mm and the following month also reaches at least 100 mm; thresholds of 75 mm and 125 mm were tested as sensitivity variants.

Four models are compared. M0 is a climatological baseline that predicts the mean of the target, and every other model must beat it. M1 is a multiple linear regression on the JJA predictors. M2 is a regularised regression (ridge and LASSO), appropriate given n = 43 and collinear predictors. M3 is a nonlinear benchmark (random forest, 500 trees, minimum leaf size 3), included to test whether the ENSO-IOD-rainfall relationship is materially nonlinear at seasonal scale; the same predictor-target framing underlies CMIP-based assessments of Indonesian rainfall drivers (Kurniadi et al., 2023).

Validation uses leave-one-year-out cross-validation. All preprocessing, namely standardisation, feature selection and hyperparameter choice, is performed inside each training fold, so that no information leaks from the held-out year, following recommended practice for climate-forecast verification (Risbey et al., 2022). Skill is reported as RMSE, MAE and out-of-sample R^2, and, decisively, as the RMSE skill score relative to climatology (Wilks, 2019),

$$RMSESS = 1 - \frac{RMSE_{model}}{RMSE_{clim}} \qquad (4)$$

A model that correlates positively with the observations but returns RMSESS ≤ 0 has no operational value, and this quantity, not the correlation coefficient, is the figure on which the practical claims of this paper stand or fall. Ninety-five per cent confidence intervals for all skill scores are obtained by bootstrapping years (2000 resamples).

Warning skill

The continuous forecasts are converted into a categorical warning for below-normal SON rainfall, defined as the lower tercile of the observed distribution. From the 2 × 2 contingency table we compute POD, FAR, CSI and PSS, testing CSI against a permutation null (5000 permutations preserving the forecast rate). For probabilistic forecasts from a leave-one-year-out logistic regression on the same predictors, the Brier skill score is computed against a climatological base-rate forecast (Wilks, 2019). Continuous and categorical skill are reported separately, since a system can be accurate in the mean-square sense yet of little use for warning; this decision-threshold view follows recent guidance (Loveday et al., 2024; Necker et al., 2024).

Non-stationarity

The record is divided into two equal epochs, 1982-2003 and 2004-2025. Rather than compare correlations descriptively, differences are tested with Fisher's r-to-z transform. With roughly 264 months per epoch the design has about 80% power to

© 2026 Dept. of Geophysics Hasanuddin University

detect only $\Delta r \gtrsim 0.25$; smaller differences are not resolvable and will not be read as change. Anomalies are recomputed within each epoch and the linearly detrended Niño 3.4 series is used, so the comparison is not confounded by the secular warming of tropical Pacific SST.

Control of multiple comparisons

The diagnostic analysis involves 99 hypothesis tests across three predictors, thirteen lags and four testing procedures. Reporting an uncorrected maximum coefficient selected from such a family would materially overstate both its magnitude and its significance. All p-values in the Results are therefore adjusted using the Benjamini-Hochberg false discovery rate procedure at $q = 0.05$ (Benjamini & Hochberg, 1995), and both raw and adjusted values are archived with the code.

Software and reproducibility

All analyses were performed in Python 3.12 on Google Colab using pandas, NumPy, statsmodels (ARIMA, CCF), scikit-learn (regularised regression, ensemble models, cross-validation), SciPy and Matplotlib. The rainfall series and the climate indices are retrieved at run time directly from the NASA POWER REST API and the NOAA PSL ASCII endpoints, so no data files are redistributed and the analysis is exactly reproducible. The notebook, retrieved series, figure code and the full table of 99 tests are archived at https://doi.org/10.5281/zenodo.21636374 (Aprianto et al., 2026a). The revised archive additionally includes the CHIRPS validation, inter-cell coherence and skill re-run code (see the subsection "Validation of the rainfall series and grid-cell representativeness"), the station-audit notebook, and all article figures, and is available as a new version at https://doi.org/10.5281/zenodo.21636373 (Aprianto et al., 2026b). Hypotheses H1-H3, the model set, the validation scheme and the skill metrics were specified before the analysis was run.

Results

Validation of the rainfall series and grid-cell representativeness

POWER was compared against CHIRPS v2 (0.05°, gauge-blended satellite; Funk et al., 2015), an observational product independent of the MERRA-2 lineage of POWER, over 1982-2025 at the analysis point. The two series share the monsoonal annual cycle with matched phase, both peaking in January and reaching their minimum in August; POWER is drier in the wettest months (January climatology 244.6 versus 362.5 mm) but nearly identical in the dry season (August 6.1 versus 8.2 mm). The distinction between magnitude and co-variation is explicit in the correlation structure: on raw monthly totals the products agree at $r = 0.899$, inflated by the shared seasonal cycle; on standardised monthly anomalies the agreement is $r = 0.721$, and for the interannual SON total the products correlate at $r = 0.889$ (Spearman 0.877; 95% CI 0.81-0.94) (Figure 4). The interannual variability ratio is $\alpha = 1.10$ (CI 0.93-1.28) and the mean ratio $\beta = 0.91$ (SON PBIAS -8.8%), giving KGE = 0.83 (CI 0.68-0.87). POWER therefore reproduces the interannual SON variability the seasonal analysis uses with high fidelity while underestimating totals modestly; because Pearson correlation is invariant to a linear magnitude bias, the teleconnection inferences are unaffected (Figure 3, Table 2). A direct comparison against the co-located station (WMO 97260, Sumbawa Besar/ WADS) was attempted through the NOAA ISD/GSOD archive, but the digitised daily record is too incomplete over 1982-2025 (26.6% of days present; only three SON seasons with fewer than four missing days) to support interannual validation. Direct validation against the multi-decadal BMKG gauge record, whose access requires an institutional data

© 2026 Dept. of Geophysics Hasanuddin University

agreement, remains the appropriate next step (see the subsection “Limitations”).

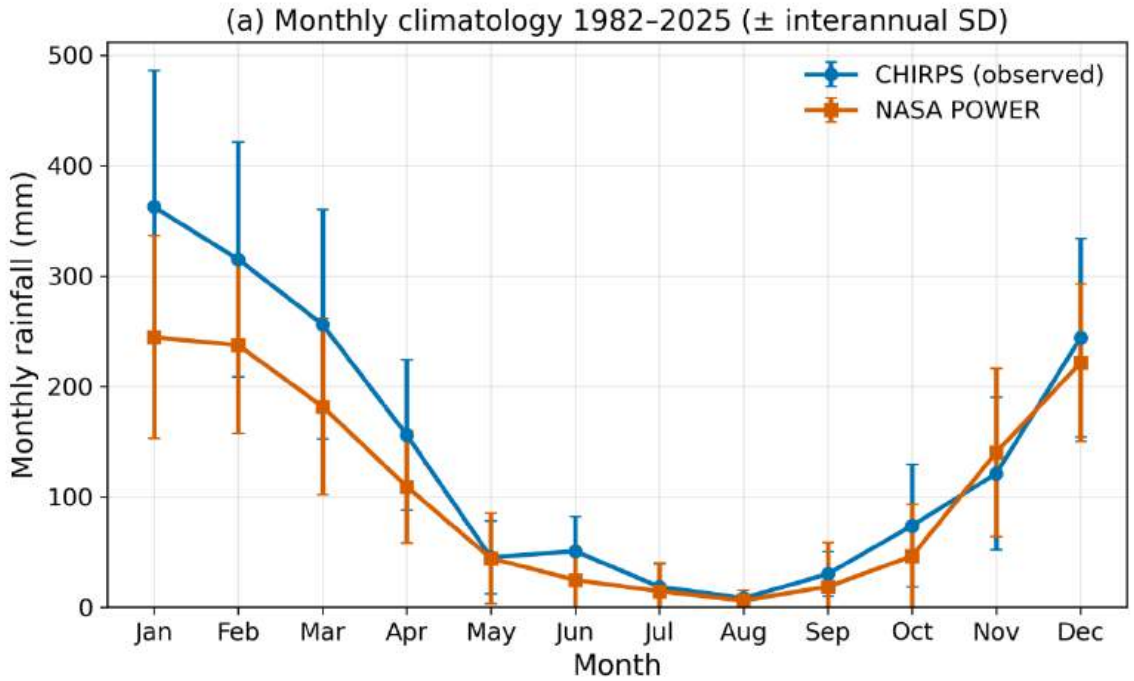


Figure 3. Monthly rainfall climatology at the analysis point, 1982–2025, for NASA POWER and CHIRPS; error bars show interannual standard deviation.

Table 2. Agreement between NASA POWER and CHIRPS rainfall at the analysis point, 1982–2025.

Metric	All months	SON
Pearson r (raw monthly)	0.899	-
Pearson r (standardised anomaly)	0.721	0.889
Spearman ρ (anomaly)	0.711	0.877
Variability ratio α	-	1.10
Mean ratio β	-	0.91
PBIAS	-	−8.8%
RMSE / MAE (mm)	-	63.8 / 53.0
KGE	-	0.83

To test whether the single cell represents the regency, the interannual SON anomaly of the analysis cell was correlated with the eight surrounding POWER cells spanning Sumbawa Regency. The mean SON total varies substantially across the block (166-261 mm), reflecting spatial heterogeneity in absolute rainfall associated with topography, elevation and coast; the interannual anomalies, however, are highly coherent (correlations 0.88-1.00, median 0.92; all eight ≥ 0.87). Interannual variability is thus spatially coherent across the regency even where climatological totals differ with position (Haylock & McBride, 2001; Moron et al., 2009). The single cell is representative of the regional interannual variability the analysis uses; it is not claimed to resolve intra-regency contrasts in totals (Figure 5).

Finally, the leave-one-year-out SON experiment (see the subsection “Out-of-sample seasonal predictability experiment”) was repeated with CHIRPS as the rainfall target in place of POWER, using identical predictors and validation. The out-of-sample skill is essentially unchanged (LASSO out-of-sample R^2 = 0.407, RMSESS = +0.248, 95% CI +0.12 to +0.35), statistically indistinguishable from the POWER-based result reported in the subsection “Seasonal aggregation recovers genuine, cross-validated skill”. The seasonal predictability therefore does not depend on the reanalysis product; an independent, gauge-informed observational dataset yields the same skill.

© 2026 Dept. of Geophysics Hasanuddin University

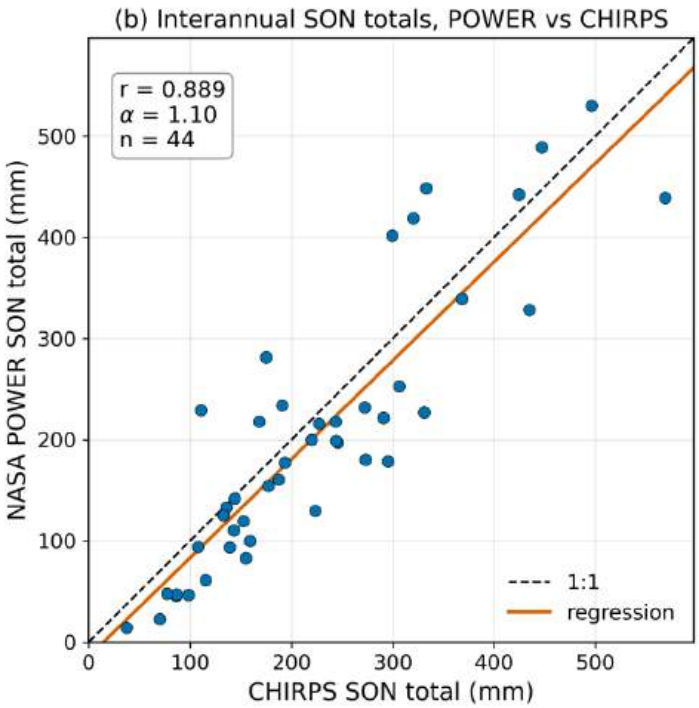


Figure 4. Interannual SON totals, NASA POWER versus CHIRPS (n = 44); dashed line 1:1, solid line least-squares fit. r = 0.889, α = 1.10.

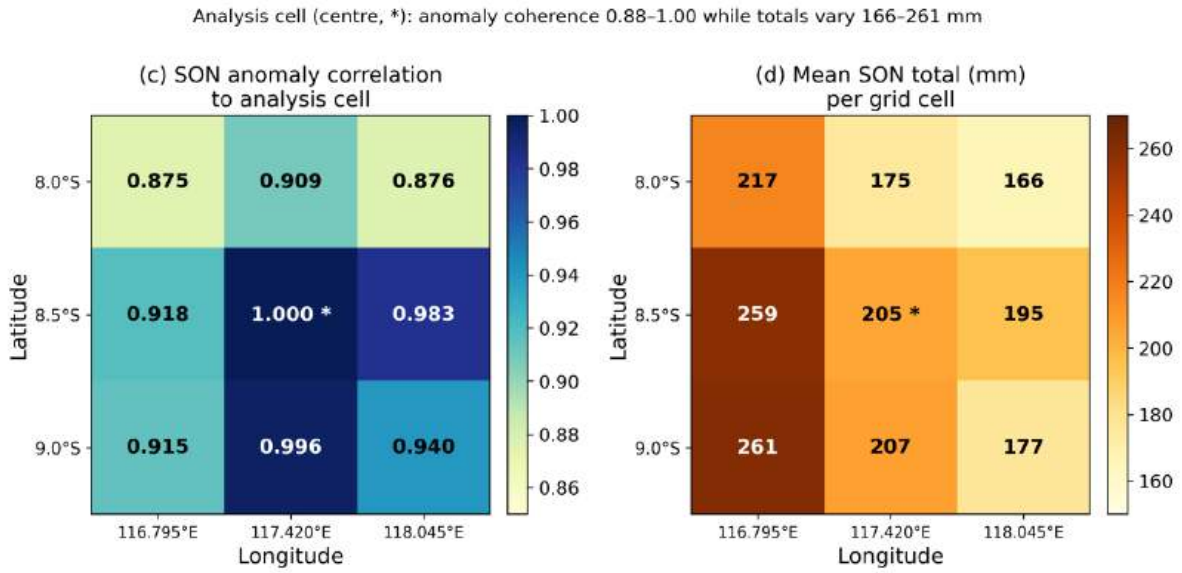


Figure 5. Representativeness of the analysis cell (centre, *): (a) correlation of interannual SON anomalies with the eight surrounding NASA POWER cells; (b) mean SON total per cell. Anomalies are coherent (0.88–1.00) while totals vary (166–261 mm).

Data characteristics and the autocorrelation problem

The NASA POWER series for the Sumbawa grid cell reproduces the expected monsoonal regime (Figure 6). Mean monthly rainfall over 1982-2025 is 107.5 mm with a standard deviation of 107.1 mm, and the climatology ranges from 244.6 mm in January to 6.1 mm in August; the wettest month is January 1990 (428.4 mm) and the driest September 2007 (0.3 mm). The near-equality of mean and standard deviation and the pronounced right skew (median 77.3 mm against a mean of 107.5 mm) reflect the extreme intra-annual contrast and are why anomalies are standardised by month rather than merely centred.

© 2026 Dept. of Geophysics Hasanuddin University

The critical quantity for what follows is the lag-1 autocorrelation of each series (Table 3). The two oceanic indices are highly persistent (Niño 3.4 ρ_1 = 0.952, DMI 0.795), whereas the atmospheric SOI is markedly less so (0.665) and the rainfall anomaly series is almost serially independent (0.132). The effective sample size for the Niño 3.4-rainfall pair is about 410 rather than 528, a reduction of only 22%: the effective-degrees-of-freedom correction alone, the most common remedy in the applied literature, is far too weak to remove the artefact demonstrated below.

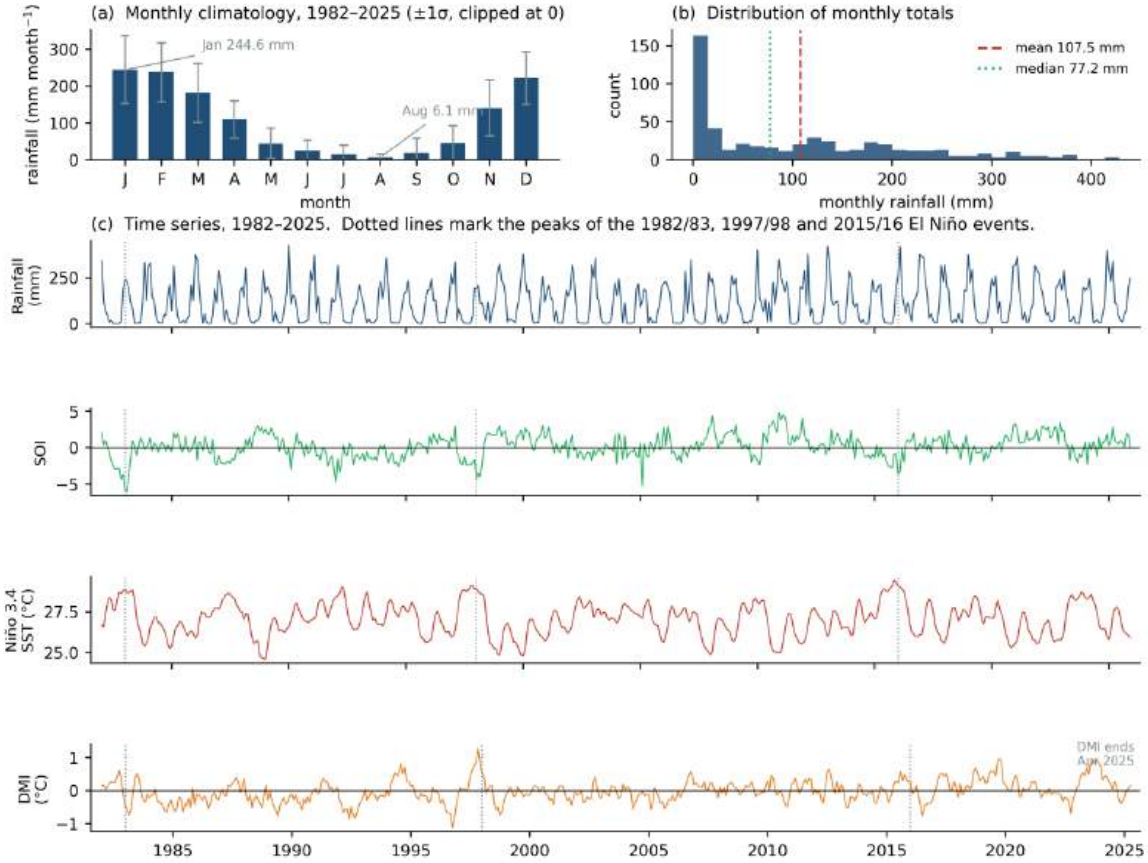


Figure 6. Characteristics of the analysed series. (a) Monthly rainfall climatology with interannual standard deviation, clipped at zero since negative rainfall is not admissible. (b) Distribution of monthly totals, showing the strong right skew that motivates the square-root and Spearman robustness checks. (c) Time series of rainfall, SOI, Niño 3.4 SST and the DMI, 1982-2025; dotted lines mark the peaks of the 1982/83, 1997/98 and 2015/16 El Niño events. The DMI record terminates in April 2025.

Table 3. Lag-1 autocorrelation of the standardised anomaly series.

Series	ρ_1	Character
Rainfall (NASA POWER)	0.132	Effectively serially independent
SOI	0.665	Atmospheric; retains month-to-month variability
Niño 3.4 SST	0.952	Oceanic; variance almost entirely low-frequency
DMI (IOD)	0.795	Oceanic; strongly persistent

The naive cross-correlation function fails a physical sanity check

Computed conventionally on standardised monthly anomalies, the CCF reproduces the pattern reported throughout the regional literature: a positive association with the SOI peaking at lag 0 (r = 0.364) and a negative association with Niño 3.4, both decaying slowly and remaining nominally significant for several months. Had the analysis stopped there, we would have reported an SOI signal significant to lag 5 and a Niño 3.4 signal significant to lag 3, and interpreted the tail as short-term climate memory.

© 2026 Dept. of Geophysics Hasanuddin University

The lags below zero refute that interpretation. A negative lag places rainfall ahead of the index, which no mechanism permits: convection over Sumbawa cannot force central-Pacific Sea surface temperature two months later. Yet the naive CCF, even after the effective-sample-size correction and Benjamini-Hochberg adjustment, returns significant coefficients at every negative lag from -6 to -1 for both the SOI and Niño 3.4 (Figure 7, top row; Table 4). For Niño 3.4 the naive maximum in the window falls not at lag 0 (r = -0.241) but at a non-causal negative lag (lag -2, r = -0.249), a value statistically indistinguishable from lag -1 (r = -0.248; difference 0.001), so no distinct two-month lead is implied; taken at face value the method would make Sumbawa rainfall the better predictor of the Pacific. The method, not the physics, is at fault.

Table 4. Naive cross-correlation coefficients with effective-sample-size correction. Asterisks denote significance after Benjamini-Hochberg FDR correction (q < 0.05).

Lag (months)	SOI	Niño 3.4	DMI	Interpretation
-6	0.177 *	-0.164 *	0.123 *	Non-causal (rainfall leads index)
-5	0.198 *	-0.205 *	0.069	Non-causal (rainfall leads index)
-4	0.236 *	-0.224 *	0.048	Non-causal (rainfall leads index)
-3	0.238 *	-0.238 *	-0.015	Non-causal (rainfall leads index)
-2	0.256 *	-0.249 *	-0.044	Non-causal (tied with lag −1)
-1	0.193 *	-0.248 *	-0.092	Non-causal (rainfall leads index)
0	0.364 *	-0.241 *	-0.139 *	Concurrent
1	0.266 *	-0.230 *	-0.148 *	Apparent lead
2	0.221 *	-0.193 *	-0.087	Apparent lead
3	0.217 *	-0.151 *	-0.040	Apparent lead
4	0.141 *	-0.112	0.005	-
5	0.118 *	-0.070	0.019	-
6	0.046	-0.013	0.062	-

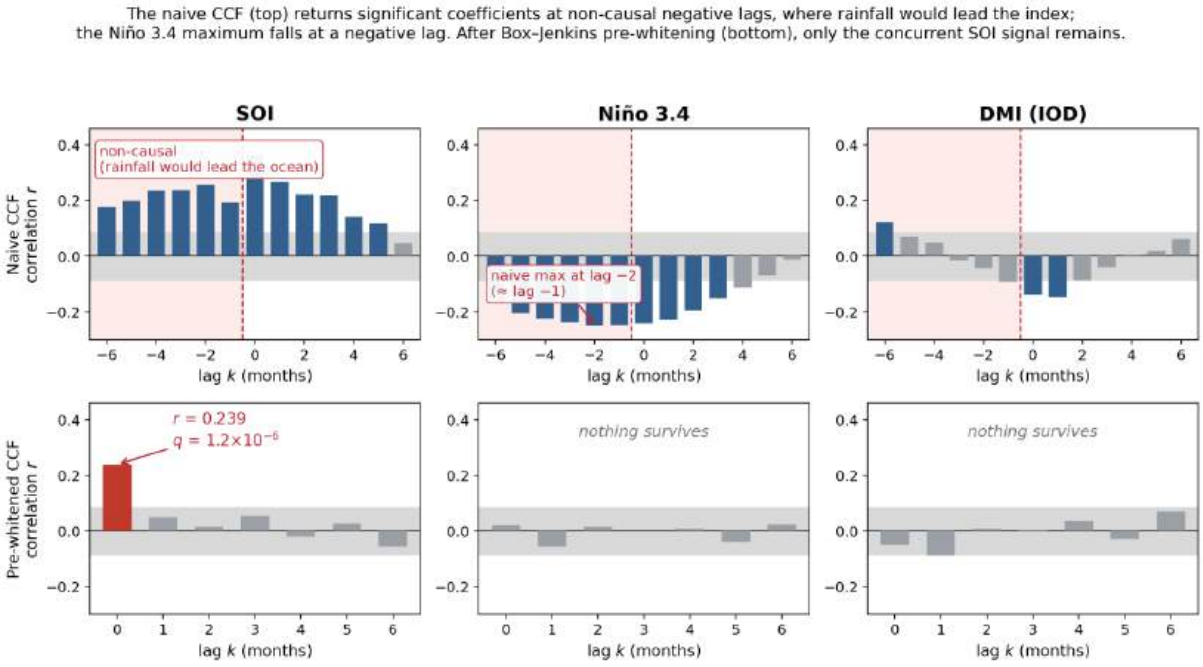


Figure 7. Naive (top) and pre-whitened (bottom) cross-correlation between the climate indices and Sumbawa rainfall anomalies, 1982-2025. Coloured bars are significant after BH-FDR correction; the shaded band is the ±1.96/√n bound. The red panel at the left of each upper plot marks negative lags, at which significance would be non-causal (rainfall leading the index).

© 2026 Dept. of Geophysics Hasanuddin University

Figure 8 makes the mechanism explicit. If a predictor X influences rainfall Y only concurrently, the expected cross-correlation at lag k is nevertheless $r_0 \cdot \rho_x(k)$. Plotted against the observed CCF, this null accounts for the observed lagged correlations in full: for the SOI the two curves are almost indistinguishable, and for Niño 3.4 and the DMI the observed correlations decay faster than the null, so at every lag the observed coefficient is equal to, or weaker than, what persistence alone would generate. At no lag, for any index, does the observed correlation exceed the concurrent-only expectation. The decaying tail of "significant" lagged coefficients is therefore what persistence produces in the absence of any lagged mechanism.

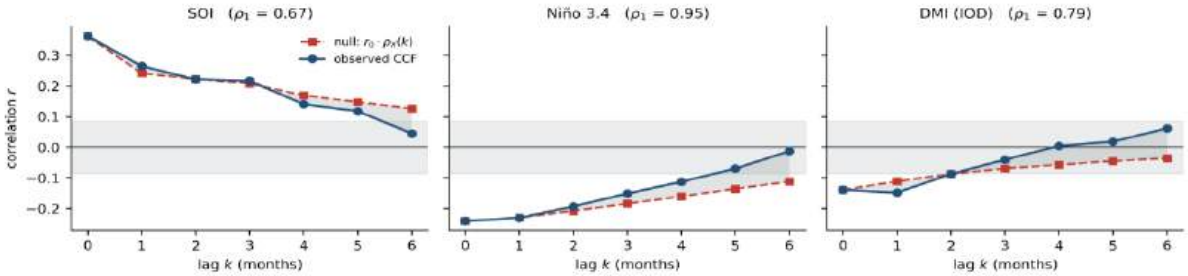


Figure 8. Observed lagged correlations (blue) against the concurrent-only null expectation $r_0 \cdot \rho_x(k)$ (red); the shaded area is the difference. At every lag and for every index the observed correlation is equal to, or weaker than, the null. No lagged coefficient exceeds what the predictor's own persistence alone would produce.

After pre-whitening, only the concurrent SOI signal survives

ARIMA models were fitted to each index and the same filter applied to the rainfall series, so that the cross-correlations of the residuals are approximately independent with standard error $1/\sqrt{n} = 0.043$ and a 95% bound of ±0.085. The result is unambiguous (Table 5, Figure 7 bottom row). Of the twenty-one pre-whitened coefficients tested, exactly one survives FDR correction: the SOI at lag 0, r = 0.239 ($q = 1.2 \times 10^{-6}$). Every coefficient at lags 1 through 6 falls inside the noise band for all three predictors.

Two features of this result stand out. First, the entire multi-month climate memory reported by the naive method disappears. Second, and this was not anticipated, the concurrent coefficients for Niño 3.4 (r = 0.023) and DMI (r = -0.048) also collapse to zero. At monthly resolution, once the shared low-frequency component is removed, the oceanic indices carry no information about Sumbawa rainfall anomalies at all. Only the SOI does. The physical reading of this asymmetry is developed in the Discussion, in the subsection "Why the ocean indices carry no monthly signal".

Table 5. Pre-whitened cross-correlation coefficients. Significance bound = ±0.085 (95%).

Lag (months)	SOI	Niño 3.4	DMI
0	0.239 *	0.023	-0.048
1	0.050	-0.056	-0.087
2	0.015	0.016	0.009
3	0.055	0.000	-0.001
4	-0.020	0.008	0.035
5	0.028	-0.038	-0.028
6	-0.055	0.024	0.069

* $q = 1.2 \times 10^{-6}$ (BH-FDR). No other coefficient is significant.

The partial cross-correlation $r(Y_t, X_{t-k} \mid X_t)$ reaches the same conclusion: no lagged predictor is significant at lags 1-5 for any index. Two lag-6 coefficients are formally significant (Niño 3.4, r = 0.114, q = 0.027; DMI, r = 0.104, q = 0.049) but both carry the wrong sign (positive, where the mechanism requires a negative association) and a six-month lag is half the annual cycle; we read these as aliasing of the semi-annual harmonic, not teleconnection. Hypothesis H1 is accepted.

Seasonal aggregation recovers genuine, cross-validated skill

© 2026 Dept. of Geophysics Hasanuddin University

The seasonal experiment uses one sample per year and is therefore structurally free of the autocorrelation artefact. Over 43 independent years, the June-August mean SOI correlates with the SON rainfall total at r = +0.643 ($p < 0.0001$) and with the wet-season onset month at r = -0.663. The corresponding coefficients for the JJA Niño 3.4 mean are -0.563 and +0.575, and for the JJA DMI mean only -0.223 ($p = 0.15$) and +0.295 ($p = 0.054$).

Under leave-one-year-out cross-validation, a LASSO model achieves an out-of-sample R^2 of 0.405 for the SON total and an RMSE skill score of +0.247 against a climatological baseline, with a bootstrap 95% confidence interval of [+0.109, +0.353] that excludes zero (Table 6, Figure 9). For the onset month the skill score is +0.219 with a confidence interval of [+0.128, +0.338]. Hypothesis H2 is accepted: a real operational lead time of one to three months exists.

Table 6. Out-of-sample skill (leave-one-year-out, 43 years). RMSESS is referenced to climatology; a value ≤ 0 indicates no operational value.

Model	r	R^2 (oos)	RMSESS	95% CI	Skill?
Target T1: SON rainfall total (mm)					
M0 Climatology	-	-	0.000	-	-
M1 OLS	+0.607	0.345	+0.209	[+0.034, +0.347]	Yes
M2 Ridge	+0.615	0.378	+0.230	[+0.108, +0.326]	Yes
M2 LASSO	+0.638	0.405	+0.247	[+0.109, +0.353]	Yes
M3 Random forest	+0.502	0.235	+0.146	[-0.003, +0.282]	No
Target T2: wet-season onset month					
M0 Climatology	-	-	**0.000**	-	-
M1 OLS	+0.569	0.286	+0.175	[-0.035, +0.328]	No
M2 Ridge	+0.592	0.350	+0.212	[+0.090, +0.334]	Yes
M2 LASSO	+0.610	0.361	+0.219	[+0.128, +0.338]	Yes
M3 Random forest	+0.602	0.356	+0.216	[+0.092, +0.362]	Yes

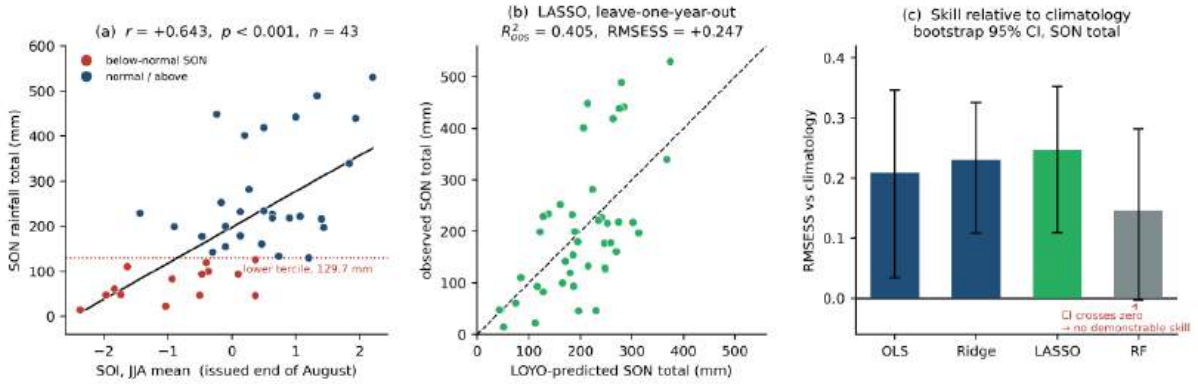


Figure 9. (a) JJA-mean SOI against SON rainfall total; red points fall in the lower tercile. (b) Observed versus leave-one-year-out predicted SON total (LASSO); the dashed line is the 1:1 reference. (c) Skill relative to climatology with bootstrap 95% confidence intervals. The vertical axis extends below zero so that the random-forest interval, whose lower bound is -0.003, can be seen to cross it.

Two secondary results follow. First, the random forest does not outperform regularised linear regression on either target, and for the SON total its confidence interval includes zero. The seasonal ENSO-rainfall relationship in Sumbawa is, to the resolution of a 43-year record, linear; the additional flexibility of a nonlinear learner buys nothing and costs variance.

Second, the model is radically parsimonious. LASSO eliminates the JJA Niño 3.4 mean, the JJA DMI mean and the DMI tendency entirely, retaining only the

© 2026 Dept. of Geophysics Hasanuddin University

JJA SOI (standardised coefficient +54.3 mm), the Niño 3.4 tendency (-28.5 mm) and the SOI tendency (+20.9 mm). A model using the JJA-mean SOI alone attains RMSESS = +0.218 for the SON total and +0.233 for the onset month, equal to, and for onset better than, the full six-predictor model. The operationally relevant information in this system is contained in a single number.

On the multicollinearity raised for the two ENSO indices: the JJA-mean SOI and Niño 3.4 are strongly anti-correlated (r = -0.78), which is exactly why a single joint regression would be unstable; nonetheless all variance inflation factors remain below 4 (maximum 3.53), and collinearity is handled by design through regularisation. That LASSO retains the SOI rather than Niño 3.4 is physical, not arbitrary: the SOI is an atmospheric index carrying sub-seasonal Walker-circulation variability whereas Niño 3.4 is a slowly varying oceanic index, and the two carry distinct information at monthly resolution. Consistently, an SOI-only model matches the full six-predictor model (RMSESS +0.218 for the SON total, +0.233 for onset), confirming that the operational information resides in a single atmospheric index.

The forecast translates into usable, but incomplete, warning skill

Below-normal SON rainfall was defined as the lower tercile of the 1982-2024 distribution (129.7 mm; base rate 0.326) and the continuous forecasts were converted into categorical warnings. Contrary to hypothesis H3, warning skill does not collapse. The Ridge model attains a critical success index of 0.53 against a permutation-derived chance value of 0.20 (p = 0.0002), with a probability of detection of 0.57, a false alarm ratio of 0.11 and a Peirce skill score of +0.54 (Table 7, Figure 10). A probabilistic version of the forecast achieves a Brier skill score of +0.422 against a climatological forecast equal to the base rate. Hypothesis H3 is rejected.

Table 7. Warning skill for below-normal SON rainfall (lower tercile, threshold 129.7 mm, base rate 0.326, n = 43).

Model	POD	FAR	CSI	PSS	Permutation p (CSI)
M1 OLS	0.57	0.27	0.47	+0.47	0.0030
M2 Ridge	0.57	0.11	0.53	+0.54	0.0002
M2 LASSO	0.57	0.20	0.50	+0.50	0.0014
M3 Random forest	0.64	0.25	0.53	+0.54	0.0006
Chance (permutation mean)	—	—	0.20	0.00	—

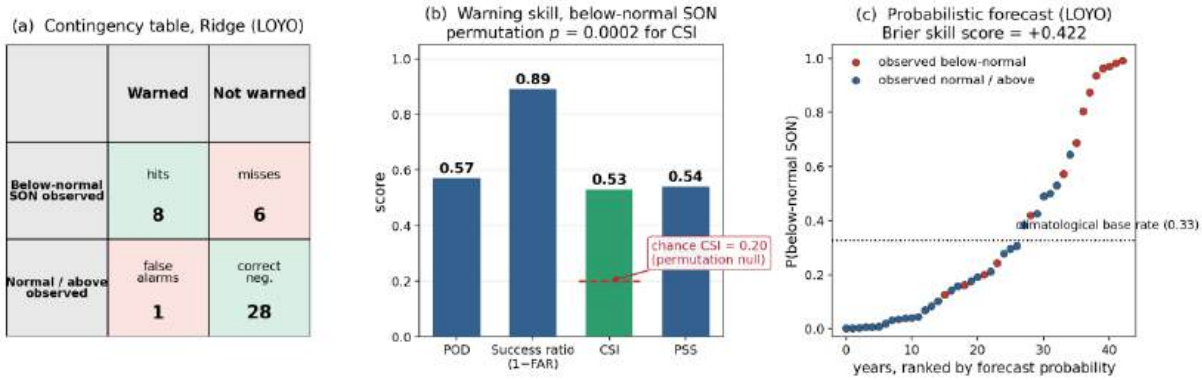


Figure 10. (a) Contingency table for the Ridge forecast under leave-one-year-out validation. (b) Warning scores; the success ratio is 1-FAR. The dashed reference marks the permutation-derived chance value of the CSI (0.20) and applies to the CSI bar only. (c) Leave-one-year-out probabilistic forecasts, ranked; red points are the observed below-normal seasons.

© 2026 Dept. of Geophysics Hasanuddin University

The operational reading is nevertheless sober. A probability of detection of 0.57 means that six of the fourteen below-normal seasons in the record would not have been warned. The system is decision-relevant, but it is not a safety net, and it should be communicated as a probabilistic shift in the odds rather than as a deterministic alert.

No detectable change between epochs

Correlations were recomputed for 1982-2003 and 2004-2025 using within-epoch anomalies and the detrended Niño 3.4 series. The concurrent SOI correlation moves from 0.328 to 0.368 and detrended Niño 3.4 from -0.229 to -0.256, but neither difference, nor any of ten others, is significant: all twelve Fisher r-to-z tests give $p \geq 0.199$. With about 264 months per epoch the design resolves only $\Delta r \gtrsim 0.25$, so this indicates absence of detectable change, not stability. These data give no evidence of intensification, and descriptive epoch comparisons of correlations should not be reported without a formal test of the difference.

Discussion

Why the ocean indices carry no monthly signal

After pre-whitening, the Niño 3.4 and DMI coefficients fall to zero even at lag 0 ($r = 0.023$ and $r = -0.048$), while the SOI keeps a clear concurrent signal ($r = 0.239$). This does not contradict the established physics; it locates where each index holds its variance. Niño 3.4 has a lag-1 autocorrelation of 0.952, so almost all of its variance sits at interannual and longer periods. Pre-whitening strips that component and leaves only month-to-month residuals in a slowly evolving sea surface temperature field, and those residuals have no physical route to change convection over Sumbawa inside the same month.

The SOI behaves differently because it measures the atmosphere rather than the ocean. As the standardised Tahiti-minus-Darwin pressure difference it carries real sub-seasonal variability (lag-1 autocorrelation 0.665) that tracks the instantaneous Walker circulation, and that variability couples to local convection within the month. The monthly rainfall-SST correlations reported across the region are therefore the monthly footprint of an interannual co-variation, not evidence of a month-scale ocean-to-rainfall mechanism. This is the sense in which "climate memory" applies here (Wei & Yuan, 2024): the memory sits in the ocean index, not in the local rainfall response, which also bears on which flavour of ENSO a predictor represents (Nguyen-Thanh et al., 2023).

Stated dynamically, the coupling is direct. During El Niño and negative-SOI conditions the ascending branch of the Walker circulation shifts east and subsidence strengthens over the Maritime Continent; low-level divergence weakens the convergence of water vapour over Sumbawa and suppresses deep convection, and rainfall drops. La Niña and positive-SOI conditions reverse the sign, strengthening convergence and convection. Because this bridge acts through the atmosphere within a single month, the index that retains a concurrent signal is the SOI, which measures the pressure gradient driving it, and not the oceanic indices, whose sub-monthly residuals carry no such information once pre-whitened (As-syakur et al., 2014; Chen et al., 2023; Supari et al., 2018).

One consequence is worth stating plainly. The Darwin pole of the SOI lies inside the Maritime Continent, so the lag-0 SOI-rainfall correlation reads more naturally as a concurrent diagnostic of one coupled state than as a signal travelling from the Pacific to Sumbawa in under a month. Calling it a fast teleconnection, as is common, attaches a causal story the data do not require.

© 2026 Dept. of Geophysics Hasanuddin University

Which lag results survive, and which do not

The negative-lag result is the most portable finding here, so it is worth being exact about what it shows. Cross-correlating a highly persistent index against a weakly autocorrelated local series always produces a decaying tail of nominally significant lagged coefficients (Table 4), and that tail imitates climate memory. Every significant coefficient at a negative lag is an artefact of serial correlation and predictor persistence, not a physical finding; we report these coefficients only to expose the failure of the naive test, and the concurrent-only null $r_0 \cdot \rho_X(k)$ reproduces them in full (Figure 8). The signal that survives is the concurrent SOI correlation alone ($r = 0.239$). The negative seasonal correlation between Niño 3.4 and SON rainfall ($r = -0.563$) is a real in-sample association, but we do not present it as predictive skill: the operational claims of this paper rest only on the cross-validated, climatology-referenced scores reported in the subsection "Seasonal aggregation recovers genuine, cross-validated skill", never on a correlation coefficient.

The check that catches the artefact costs nothing. Compute the negative lags; if they are significant, the significance test is contaminated and the reported optimal lag cannot be trusted. Running this check, together with pre-whitening or an equivalent correction, before quoting a lag structure would alter the conclusions of several district-scale Indonesian teleconnection studies, and their published lags should be revisited on that basis.

The same logic reaches into data-driven modelling. Supplying a network with lagged copies of an index (SOI at t-2, SST at t-3) as separate predictors, as an earlier version of this work did, adds collinear and largely redundant features once the index is strongly autocorrelated, and the partial cross-correlations show those lags carry nothing beyond the concurrent value. The seasonal experiment agrees: the random forest does not beat regularised linear regression, and LASSO keeps three of six predictors. Models that now reach real skill in ENSO and weather forecasting (Price et al., 2025; Zhou & Zhang, 2023) draw it from large, physically meaningful state vectors, and recent multivariate rainfall models improve on the same principle rather than on autocorrelated lags (El Hafyani et al., 2024; Fredyan & Kusuma, 2022; Wani et al., 2024).

The IOD leaves no footprint here

The DMI contributes nothing detectable to Sumbawa rainfall at either time scale (JJA DMI against the SON total, $r = -0.223$, $p = 0.15$; dropped by LASSO). This is a substantive result, not a null to be explained away. The contrast with Sumatra is instructive: there a positive IOD coinciding with El Niño can delay onset and extend the dry season by several months (Hidayat et al., 2025), and peatland groundwater has served as an IOD-sensitive alert variable in the western archipelago (Sulaiman et al., 2023). Sumbawa lies far from the eastern pole of the dipole in the south-eastern tropical Indian Ocean, and the IOD footprint over Indonesia weakens eastward from Sumatra (Amirudin et al., 2020; Hanifa & Wiratmo, 2024). For the Lesser Sunda Islands, the Pacific dominates, and reporting that the IOD adds nothing locally is more useful than carrying a predictor with no local information. The IOD is itself a partially predictable mode whose seasonal skill peaks in JJA-SON (Ling et al., 2022; Zhang et al., 2024), so its negligible local footprint reflects Sumbawa's position rather than a limit on the mode's own predictability.

What the skill means operationally for Sumbawa

The operational content is small and specific. The June-August mean SOI, one publicly available number, explains about 40% of the out-of-sample variance in SON rainfall and predicts the onset month with a

© 2026 Dept. of Geophysics Hasanuddin University

skill score near 0.22 against climatology. The same skill appears when CHIRPS replaces NASA POWER as the target (see the subsection "Validation of the rainfall series and grid-cell representativeness"), so the result is a property of the rainfall itself, not of the reanalysis. Issued at the end of August, the forecast gives one to three months of lead before the planting decision (Moron et al., 2009). For a rainfed economy, anticipating eight of the fourteen below-normal seasons in the record with one false alarm in twenty-nine normal seasons beats a fixed climatological calendar, and it stays inside the predictability limits established for Indonesian wet-season rainfall two decades ago (Haylock & McBride, 2001). Comparable seasonal-regression benchmarks confirm that skill varies by season and that simple regularised models remain competitive (Shravankumar et al., 2026).

The limits belong with the claim. Six of the fourteen below-normal seasons would have gone unwarned. The forecast supports shifting the odds, moving planting windows, staging water reserves and pre-positioning drought contingency, not triggering irreversible action, and it should be issued as a probability rather than a yes-or-no alert. We had expected warning skill to fall well short of the continuous accuracy (hypothesis H3), and it did not: the critical success index reaches 0.53 against a chance value of 0.20. Even so, the distance between a correlation of 0.64 and a detection rate of 0.57 is exactly where a forecast that looks strong can still fail the people relying on it, which is why we report the contingency table rather than the correlation alone.

Limitations

Four limitations bound these conclusions. First, the rainfall series is a NASA POWER reanalysis grid cell, not a gauge record. POWER reproduces tropical climatology and rain-day occurrence acceptably but underestimates extremes (Madushan et al., 2025; Tan et al., 2023), and the 0.5° × 0.625° cell contains a substantial marine fraction and does not resolve orographic contrast within the regency. The POWER series has now been validated against the CHIRPS observational product (see the subsection "Validation of the rainfall series and grid-cell representativeness"): the interannual SON anomalies of the two products correlate at $r = 0.889$ with KGE = 0.83, and the SON seasonal skill is reproduced when CHIRPS replaces POWER as the target, so the operational conclusions do not depend on the reanalysis. A direct comparison with the co-located station (WMO 97260) via NOAA ISD/GSOD was attempted but its daily record is too incomplete (26.6% of days) for interannual validation; multi-decadal BMKG gauge validation, which requires an institutional data agreement, remains outstanding, and the reported skill should be read as an upper bound for a single grid cell.

Second, the onset definition is coarse. At monthly resolution, twenty-three of forty-three onsets fall in November, which compresses the target and probably understates achievable onset skill. A daily POWER retrieval with the BMKG dekadal criterion (three consecutive dekads of at least 50 mm) is the appropriate refinement, and is the most promising avenue for improving the operational product.

Third, the DMI series available from NOAA PSL is HadISST-based and terminates in April 2025, which excludes 2025 from the seasonal analysis. Since the IOD proved to be a non-contributor at this location, this leaves the conclusions unchanged, though a real-time operational implementation would require an OISST-based dipole index.

Fourth, the record is 43 to 44 years. The epoch comparison can resolve only $\Delta r \gtrsim 0.25$, and the bootstrap confidence intervals

© 2026 Dept. of Geophysics Hasanuddin University

on the skill scores are correspondingly wide. Claims about non-stationarity of this teleconnection, in either direction, are not supportable at this sample size, and we make none.

Conclusion

For Sumbawa Regency, the multi-month optimal time lags that a conventional cross-correlation analysis reports between ENSO indices and local rainfall do not exist. The naive method attributes significance to non-causal negative lags, where rainfall would lead the index, and places the naive Niño 3.4 maximum at a negative lag; after Box-Jenkins pre-whitening, only the concurrent SOI signal survives ($r = 0.239$), and the concurrent oceanic signals disappear along with the lagged ones. The apparent climate memory of these indices is the persistence of the indices themselves.

Predictability nevertheless exists, at seasonal aggregation rather than in monthly lag structure. The June-August mean SOI forecasts SON rainfall with an out-of-sample R^2 of 0.405 and a skill score of +0.247 against climatology, predicts the onset month with a skill score of +0.219, and supports a categorical warning for below-normal rainfall with a critical success index of 0.53 against a chance value of 0.20 and a Brier skill score of +0.422. A single index, issued at the end of August, carries almost all of this information; Niño 3.4 and the IOD add nothing, and a nonlinear learner does not outperform linear regression. No change in teleconnection strength between 1982-2003 and 2004-2025 is detectable.

Two recommendations follow. Operationally, regional meteorological and agricultural agencies in West Nusa Tenggara can construct a defensible seasonal outlook for Sumbawa from the JJA-mean SOI alone, communicated as a probabilistic shift in the odds of a below-normal wet-season onset, with the explicit caveat that roughly two in five dry seasons will be missed. Methodologically, cross-correlation studies of climate teleconnections at district scale should report the negative-lag diagnostic and apply pre-whitening as a matter of routine; where they have not, their reported optimal lags, and any machine-learning feature sets built upon them, should be treated as unverified.

Acknowledgements

The authors gratefully acknowledge the NASA POWER project and the NOAA Physical Sciences Laboratory for providing open access to the precipitation and climate-index data used in this study, and colleagues at LPPM Universitas Samawa for their support. No specific external funding.

Author Contribution

This work is reported following the CRediT taxonomy. Romi Aprianto: Conceptualization, Methodology, Software, Formal analysis, Data curation, Visualization, Writing - original draft. Akbar Tawaqqal: Investigation, Writing – review & editing. Syaharuddin: Validation, Supervision, Writing - review & editing. All authors have read and agreed to the submitted version of the manuscript.

Conflict of Interest

The authors declare no conflict of interest.

References

Aldrian, E., & Susanto, R. D. (2003). Identification of three dominant rainfall regions within Indonesia and their relationship to sea surface temperature. *International Journal of Climatology,* 23(12), 1435–1452. https://doi.org/10.1002/joc.950

Amirudin, A. A., Salimun, E., Tangang, F., Juneng, L., & Zuhairi, M. (2020). Differential influences of teleconnections from the Indian and Pacific Oceans on rainfall variability

© 2026 Dept. of Geophysics Hasanuddin University

in Southeast Asia. *Atmosphere,* 11(9), 886. https://doi.org/10.3390/atmos11090886

Aprianto, R., Tawaqqal, A., & Syaharuddin. (2026a). ENSO and IOD teleconnection with Sumbawa rainfall: Reproducible pipeline and data (Version 1) [Data set]. Zenodo. https://doi.org/10.5281/zenodo.21636374

Aprianto, R., Tawaqqal, A., & Syaharuddin. (2026b). ENSO and IOD teleconnection with Sumbawa rainfall: Reproducible pipeline and data (revised version) [Data set]. Zenodo. https://doi.org/10.5281/zenodo.21636373

As-syakur, A. R., Tanaka, T., Osawa, T., & Mahendra, M. S. (2013). Indonesian rainfall variability observation using TRMM multi-satellite data. *International Journal of Remote Sensing,* 34(21), 7723–7738. https://doi.org/10.1080/01431161.2013.826837

As-syakur, A. R., Adnyana, I. W. S., Mahendra, M. S., Arthana, I. W., Merit, I. N., Kasa, I. W., Ekayanti, N. W., Nuarsa, I. W., & Sunarta, I. N. (2014). Observation of spatial patterns on the rainfall response to ENSO and IOD over Indonesia using TRMM Multisatellite Precipitation Analysis (TMPA). *International Journal of Climatology,* 34(15), 3825–3839. https://doi.org/10.1002/joc.3939

Benjamini, Y., & Hochberg, Y. (1995). Controlling the False Discovery Rate: A Practical and Powerful Approach to Multiple Testing. *Journal of the Royal Statistical Society: Series B,* 57(1), 289–300. https://doi.org/10.1111/j.2517-6161.1995.tb02031.x

Box, G. E. P., Jenkins, G. M., Reinsel, G. C., & Ljung, G. M. (2016). *Time series analysis: Forecasting and control* (5th ed.). Wiley.

Bretherton, C. S., Widmann, M., Dymnikov, V. P., Wallace, J. M., & Bladé, I. (1999). The effective number of spatial degrees of freedom of a time-varying field. *Journal of Climate,* 12(7), 1990–2009. https://doi.org/10.1175/1520-0442(1999)012<1990:TENOSD>2.0.CO;2

Cai, W., Ng, B., Geng, T., Jia, F., Wu, L., Wang, G., Liu, Y., Gan, B., Yang, K., Santoso, A., Lin, X., Li, Z., Liu, Y., Yang, Y., Jin, F.-F., Collins, M., & McPhaden, M. J. (2023). Anthropogenic impacts on twentieth-century ENSO variability changes. *Nature Reviews Earth & Environment,* 4(6), 407–418. https://doi.org/10.1038/s43017-023-00427-8

Camps-Valls, G., Fernández-Torres, M. Á., Cohrs, K.-H., Höhl, A., Castelletti, A., Pacal, A., Robin, C., Martinuzzi, F., Papoutsis, I., Prapas, I., Pérez-Aracil, J., Weigel, K., Gonzalez-Calabuig, M., Reichstein, M., Rable, M., Giuliani, M., Mahecha, M. D., Popescu, O.-I., Pellicer-Valero, O. J., Ouala, S., Salcedo-Sanz, S., Sippel, S., Kondylatos, S., Happé, T., & Williams, T. (2025). Artificial intelligence for modeling and understanding extreme weather and climate events. *Nature Communications,* 16, 1919. https://doi.org/10.1038/s41467-025-56573-8

Chen, C., Sahany, S., Moise, A. F., Chua, X. R., Hassim, M. E., Lim, G., & Prasanna, V. (2023). ENSO-rainfall teleconnection over the Maritime Continent enhances and shifts eastward under warming. *Journal of Climate,* 36(14), 4635–4663. https://doi.org/10.1175/JCLI-D-23-0036.1

Chen, Y., Teo, F. Y., Wong, S. Y., Chan, A., Weng, C., & Falconer, R. A.

© 2026 Dept. of Geophysics Hasanuddin University

(2025). Monsoonal extreme rainfall in Southeast Asia: A review. *Water,* 17(1), 5. https://doi.org/10.3390/w17010005

Ebisuzaki, W. (1997). A Method to Estimate the Statistical Significance of a Correlation When the Data Are Serially Correlated. *Journal of Climate,* 10(9), 2147–2153. https://doi.org/10.1175/1520-0442(1997)010<2147:AMTETS>2.0.CO;2

El Hafyani, M., El Himdi, K., & El Adlouni, S. E. (2024). Improving monthly precipitation prediction accuracy using machine learning models: A multi-view stacking learning technique. *Frontiers in Water,* 6, 1378598. https://doi.org/10.3389/frwa.2024.1378598

Fredyan, R., & Kusuma, G. P. (2022). Spatiotemporal convolutional LSTM with attention mechanism for monthly rainfall prediction. *Communications in Mathematical Biology and Neuroscience,* 2022, 105. https://doi.org/10.28919/cmbn/7761

Funk, C., Peterson, P., Landsfeld, M., Pedreros, D., Verdin, J., Shukla, S., Husak, G., Rowland, J., Harrison, L., Hoell, A., & Michaelsen, J. (2015). The climate hazards infrared precipitation with stations—a new environmental record for monitoring extremes. *Scientific Data,* 2, 150066. https://doi.org/10.1038/sdata.2015.66

Gelaro, R., McCarty, W., Suárez, M. J., Todling, R., Molod, A., Takacs, L., Randles, C. A., Darmenov, A., Bosilovich, M. G., Reichle, R., Wargan, K., Coy, L., Cullather, R., Draper, C., Akella, S., Buchard, V., Conaty, A., da Silva, A. M., Gu, W., Kim, G.-K., Koster, R., Lucchesi, R., Merkova, D., Nielsen, J. E., Partyka, G., Pawson, S., Putman, W., Rienecker, M., Schubert, S. D., Sienkiewicz, M., & Zhao, B. (2017). The Modern-Era Retrospective Analysis for Research and Applications, Version 2 (MERRA-2). *Journal of Climate,* 30(14), 5419–5454. https://doi.org/10.1175/JCLI-D-16-0758.1

Ghosh, R., & Shepherd, T. G. (2023). Storylines of Maritime Continent dry period precipitation changes under global warming. *Environmental Research Letters,* 18(3), 034017. https://doi.org/10.1088/1748-9326/acb788

Gibson, P. B., Chapman, W. E., Altinok, A., Monache, L. D., DeFlorio, M. J., & Waliser, D. E. (2021). Training machine learning models on climate model output yields skillful interpretable seasonal precipitation forecasts. *Communications Earth & Environment,* 2, 174. https://doi.org/10.1038/s43247-021-00225-4

Hanifa, R., & Wiratmo, J. (2024). ENSO and IOD Influence on Extreme Rainfall in Indonesia: Historical and Future Analysis. Agromet, 38(2), 78–87. https://doi.org/10.29244/j.agromet.38.2.78-87

Hariadi, M. H., van der Schrier, G., Steeneveld, G.-J., Sutanto, S. J., Sutanudjaja, E., Ratri, D. N., Sopaheluwakan, A., & Tank, A. K. (2024). A high-resolution perspective of extreme rainfall and river flow under extreme climate change in Southeast Asia. *Hydrology and Earth System Sciences,* 28(9), 1935–1956. https://doi.org/10.5194/hess-28-1935-2024

Haylock, M. R., & McBride, J. (2001). Spatial coherence and predictability of Indonesian wet season rainfall. *Journal of Climate,* 14(18), 3882–3887. https://doi.org/10.1175/1520-0442(2001)014<3882:SCAPOI>2.0.CO;2

© 2026 Dept. of Geophysics Hasanuddin University

Heede, U. K., & Fedorov, A. V. (2023). Colder eastern equatorial Pacific and stronger Walker circulation in the early 21st century: Separating the forced response from natural variability. *Geophysical Research Letters,* 50(3), e2022GL101020. https://doi.org/10.1029/2022GL101020

Hidayat, R., Apip, A., Dasril, A. P., Taufik, M. (2025). Climate teleconnection triggers prolonged dry season in tropical maritime continent. *Theoretical and Applied Climatology,* 156, 626. https://doi.org/10.1007/s00704-025-05852-x

Khalid, M. R., Ahmed, S., & Abdullah, A. (2024). Assessing NASA-POWER precipitation product in predicting surface flow: Lower Jhelum River case study. *Air, Soil and Water Research,* 17, 11786221241280753. https://doi.org/10.1177/11786221241280753

Kosovelj, K., & Zaplotnik, Ž. (2023). Indices of Pacific Walker circulation strength. *Atmosphere,* 14(2), 397. https://doi.org/10.3390/atmos14020397

Kurniadi, A., Weller, E., Min, S.-K., & Seong, M.-G. (2021). Independent ENSO and IOD impacts on rainfall extremes over Indonesia. *International Journal of Climatology,* 41(6), 3640–3656. https://doi.org/10.1002/joc.7040

Kurniadi, A., Weller, E., Kim, Y.-H., & Min, S.-K. (2023). Evaluation of Couplled Model Intercomparison Project Phase 6 model-simulated extreme precipitation over Indonesia. *International Journal of Climatology*, 43(1), 174-196. https://doi.org/10.1002/joc.7744

Kurniadi, A., Weller, E., Salmond, J., & Aldrian, E. (2024). Future projections of extreme rainfall events in Indonesia. *International Journal of Climatology,* 44(1), 160–182. https://doi.org/10.1002/joc.8321

Ling, F., Luo, J. J., Li, Y., Tang, T., Bai, L., Ouyang, W., & Yamagata, T. (2022). Multi-task machine learning improves multi-seasonal prediction of the Indian Ocean Dipole. *Nature Communications*, 13(1), 7681. https://doi.org/10.1038/s41467-022-35412-0

Loveday, N., Taggart, R., & Khanarmuei, M. (2024). A user-focused approach to evaluating probabilistic and categorical forecasts. *Weather and Forecasting*, 39(8), 1163-1180. https://doi.org/10.1175/WAF-D-23-0201.1

Madushan, H., Jayaratne, C., & Wijemannage, A. (2025). Evaluation of NASA POWER daily rainfall products against ground observations in Sri Lanka. *Remote Sensing in Earth Systems Sciences,* 8, 264–272. https://doi.org/10.1007/s41976-024-00173-5

Marzuki, M., Ramadhan, R., Yusnaini, H., Vonnisa, M., Muharsyah, R., Nugraha, Y., Sari, A. Y., & Erajalita, A. (2025). Long-term spatial-temporal variability, trends and extreme rainfall events over Indonesia based on 43 years of CHIRPS data. *International Journal of Climatology,* 45(14), e70107. https://doi.org/10.1002/joc.70107

Materia, S., García, L. P., van Straaten, C., O, S., Mamalakis, A., Cavicchia, L., Coumou, D., de Luca, P., Kretschmer, M., & Donat, M. (2024). Artificial intelligence for climate prediction of extremes: State of the art, challenges, and future perspectives. *WIREs Climate Change,* 15(6), e914. https://doi.org/10.1002/wcc.914

Moron, V., Robertson, A. W., & Boer, R. (2009). Spatial coherence and seasonal predictability of monsoon onset over Indonesia. *Journal of Climate,* 22(3), 840–850.

© 2026 Dept. of Geophysics Hasanuddin University

https://doi.org/10.1175/2008JCLI2435.1

Necker, T., Wolfgruber, L., Kugler, L., Weissmann, M., Dorninger, M., & Serafin, S. (2024). The fractions skill score for ensemble forecast verification. *Quarterly Journal of the Royal Meteorological Society*, 150(764), 4457–4477. https://doi.org/10.1002/qj.4824

Nguyen-Thanh, H., Ngo-Duc, T., & Herrmann, M. (2023). The distinct impacts of the two types of ENSO on rainfall variability over Southeast Asia. *Climate Dynamics,* 61(5), 2155–2172. https://doi.org/10.1007/s00382-023-06673-2

Nugroho, A. R., Tamagawa, I., & Harada, M. (2022). Spatiotemporal analysis on the teleconnection of ENSO and IOD to the stream flow regimes in Java, Indonesia. *Water,* 14(2), 168. https://doi.org/10.3390/w14020168

Price, I., Sanchez-Gonzalez, A., Alet, F., Andersson, T. R., El-Kadi, A., Masters, D., Ewalds, T., Stott, J., Mohamed, S., Battaglia, P., Lam, R., & Willson, M. (2025). Probabilistic weather forecasting with machine learning. *Nature,* 637(8044), 84–90. https://doi.org/10.1038/s41586-024-08252-9

Ramadhan, R., Marzuki, M., Yusnaini, H., Muharsyah, R., Suryanto, W., Sholihun, S., & Vonnisa, M. (2023). A preliminary assessment of the GSMaP version 08 products over Indonesian Maritime Continent against gauge data. *Remote Sensing,* 15(4), 1115. https://doi.org/10.3390/rs15041115

Risbey, J. S., Squire, D. T., Baldissera Pacchetti, M., Black, A. S., Chapman, C. C., Dessai, S., Irving, D. B., Matear, R. J., Monselesan, D. P., Moore, T. S., Richardson, D., Sloyan, B. M. & Tozer, C. R. (2022). Common issues in verification of climate forecasts and projections. *Climate,* 10(6), 83. https://doi.org/10.3390/cli10060083

Saleh, A., Tan, M. L., Yaseen, Z. M., & Zhang, F. (2024). Integrated machine learning models for enhancing tropical rainfall prediction using NASA POWER meteorological data. *Journal of Water and Climate Change,* 15(12), 6022–6042. https://doi.org/10.2166/wcc.2024.719

Shravankumar, S.M., Paliwal, V., & Lavanya, B. (2026). Evaluating Seasonal Variability in Rainfall Forecast Accuracy Using Comparative Regression Modelling Approaches. *Water Resources Management*, 40(9), 401. https://doi.org/10.1007/s11269-026-04597-0

Sparks, A. H. (2018). nasapower: A NASA POWER global meteorology, surface solar energy and climatology data client for R. *Journal of Open Source Software,* 3(30), 1035. https://doi.org/10.21105/joss.01035

Sulaiman, A., Osaki, M., Takahashi, H., Yamanaka, M. D., Susanto, R. D., Shimada, S., Kimura, K., Hirano, T., Wetadewi, R. I., Sisva, S., Kato, T., Kozan, O., Kubo, H., Awaluddin, A., & Tsuji, N. (2023). Peatland groundwater level in the Indonesian maritime continent as an alert for El Niño and moderate positive Indian Ocean Dipole events. *Scientific Reports,* 13, 939. https://doi.org/10.1038/s41598-023-27393-x

Supari, S., Tangang, F., Salimun, E., Aldrian, E., Sopaheluwakan, A., & Juneng, L. (2018). ENSO modulation of seasonal rainfall and extremes in Indonesia. *Climate Dynamics,* 51(7-8), 2559–2580. https://doi.org/10.1007/s00382-017-4028-8

Tan, M. L., Armanuos, A. M., Ahmadianfar, I., Demir, V., Heddam, S., Al-Areeq, A. M., Abba, S. I.,

© 2026 Dept. of Geophysics Hasanuddin University

Halder, B., Lilinc, H. C., & Yaseen, Z. M. (2023). Evaluation of NASA POWER and ERA5-Land for estimating tropical precipitation and temperature extremes. *Journal of Hydrology,* 624, 129940. https://doi.org/10.1016/j.jhydrol.2023.129940

Tayyeh, H. K., & Mohammed, R. (2023). Analysis of NASA POWER reanalysis products to predict temperature and precipitation in Euphrates River basin. *Journal of Hydrology*, 619, 129327. https://doi.org/10.1016/j.jhydrol.2023.129327

Wang, G., Cai, W., & Santoso, A. (2024a). Simulated thermocline tilt over the tropical Indian Ocean and its influence on future sea surface temperature variability. *Geophysical Research Letters,* 48(6), e2020GL091902. https://doi.org/10.1029/2020GL091902

Wang, G., Cai, W., Santoso, A., Abram, N., Ng, B., Yang, K., Geng, T., Doi, T., Du, Y., Izumo, T., Ashok, K., Li, J., Li, T., McKenna, S., Sun, S., Tozuka, T., Zheng, X., Liu, Y., Wu., L., Jia, F., Hu, S., & Li, X. (2024b). The Indian Ocean Dipole in a warming world. *Nature Reviews Earth & Environment,* 5(8), 588–604. https://doi.org/10.1038/s43017-024-00573-7

Wang, G., Cai, W., & Santoso, A. (2024c). Variability of the Indian Ocean Dipole post-2100 reverses to a reduction despite persistent global warming. *Nature Communications,* 15, 5023. https://doi.org/10.1038/s41467-024-49401-y

Wani, O. A., Mahdi, S. S., Yeasin, M., Kumar, S. S., Gagnon, A. S., Danish, F., Al-Ansari, N., El-Hendawy, S. & Mattar, M. A. (2024). Predicting rainfall using machine learning, deep learning, and time series models across an altitudinal gradient in the North-Western Himalayas. *Scientific Reports,* 14, 27876. https://doi.org/10.1038/s41598-024-77687-x

Watanabe, M., Iwakiri, T., Dong, Y., & Kang, S. M. (2023). Two competing drivers of the recent Walker circulation trend. *Geophysical Research Letters,* 50(23), e2023GL105332. https://doi.org/10.1029/2023GL105332

Watanabe, M., Kang, S. M., Collins, M., Hwang, Y.-T., McGregor, S., & Stuecker, M. F. (2024). Possible shift in controls of the tropical Pacific surface warming pattern. *Nature,* 630(8016), 315–324. https://doi.org/10.1038/s41586-024-07452-7

Wei, Z., & Yuan, N. (2024). Identifying climate memory impacts on climate network analysis: A new approach based on fractional integral techniques. *Climate Dynamics,* 62(5), 3465–3476. https://doi.org/10.1007/s00382-023-07076-z

Wilks, D. S. (2019). *Statistical methods in the atmospheric sciences* (4th ed.). Elsevier. https://doi.org/10.1016/C2017-0-03921-6

Wu, M., Li, C., Collins, M., Li, H., Chen, X., Zhou, T., & Zhang, Z. (2024). Early emergence and determinants of human-induced Walker circulation weakening. *Nature Communications,* 15, 9161. https://doi.org/10.1038/s41467-024-53509-6

Yang, R., Hu, J., Li, Z., Mu, J., Yu, T., Xia, J., Li, X., Dasgupta, A., & Xiong, H. (2024). Interpretable machine learning for weather and climate prediction: A review. *Atmospheric Environment,* 338, 120797. https://doi.org/10.1016/j.atmosenv.2024.120797

© 2026 Dept. of Geophysics Hasanuddin University

Zhang, Y., Li, J., Diao, Y., Wang, Q., Wu, R., Liu, T., Jin, Y., Hou, Z., & Wang, H. (2024). Reconciling roles of the South China Sea summer monsoon and ENSO in prediction of the Indian Ocean dipole. *Environmental Research Letters*, 19(1), 014041. https://doi.org/10.1088/1748-9326/ad122a

Zehri, S., Yulihastin, E., Marpaung, F., Adiputra, A., Mushoddik, M., Purwadani, N. N., & Gammamerdianti. G. (2025). Diverse impact of 2023 El Niño on weather patterns over the Indonesian Maritime Continent. *Journal of Southern Hemisphere Earth System Science,* 75(2), ES25005. https://doi.org/10.1071/ES25005

Zhou, L., & Zhang, R.-H. (2023). A self-attention-based neural network for three-dimensional multivariate modeling and its skillful ENSO predictions. *Science Advances,* 9(10), eadf2827. https://doi.org/10.1126/sciadv.adf2827

© 2026 Dept. of Geophysics Hasanuddin University

ISSN: 2579-5821 (Print)
ISSN: 2579-5546 (Online)
URL address: http://journal.unhas.ac.id/index.php/geocelebes
DOI: 10.70561/geocelebes.v10i2.52311

Jurnal Geocelebes Vol. 10 No. 2, October 2026, 397 – 412

Estimation of Meteorological Drought in West Kalimantan Using the Random Forest Model

Nurputri, Muhammad Ishak Jumarang*, Andi Ihwan

Geophysics Study Program, Tanjungpura University, Pontianak 78124, Indonesia.

*Corresponding author. Email: ishakjumarang@physics.untan.ac.id

Manuscript received: 25 June 2026; Received in revised form: 7 October 2026; Accepted: 9 October 2026

Abstract

West Kalimantan is highly vulnerable to meteorological drought driven by global climate variability, particularly El Niño–Southern Oscillation (ENSO). This study aims to estimate the Standardized Precipitation Index (SPI) using a Random Forest (RF) model and to analyze the spatio-temporal patterns of meteorological drought across West Kalimantan. Monthly ERA5 reanalysis precipitation data (resolution ±0.25°) for 1995–2024 were used as the primary dataset; the model was trained on 1995–2018 data and tested on 2019–2024 data. Model performance was evaluated using the coefficient of determination (R^2) and Root Mean Square Error (RMSE). The RF model achieved R^2 = 0.997 and RMSE = 0.052 during training, and R^2 = 0.968 and RMSE = 0.176 during testing, demonstrating excellent generalization capability. Spatial analysis of four representative El Niño years (1997, 2009, 2019, 2023) revealed that El Niño consistently triggers dry conditions across the province, with drought intensity scaling with ENSO strength and peak dryness occurring in July–August. The most severe drought was recorded during the Very Strong El Niño of 1997, which caused extreme dryness across most of the province, while Weak and Strong El Niño events of 2019 and 2023 produced less extensive but still significant mid-year drying. These findings demonstrate that the RF model is effective for spatio-temporal drought estimation under varying El Niño intensities and has strong potential to support drought early warning system development in West Kalimantan.

Keywords: Drought; ENSO; Random Forest; SPI; West Kalimantan.

Citation: Nurputri, N., Jumarang, M. I., & Ihwan, A. (2026). Estimation of Meteorological Drought in West Kalimantan Using the Random Forest Model. *Jurnal Geocelebes*, 10(2): 397–412, doi: 10.70561/geocelebes.v10i2.52311

Introduction

Drought is one of the most recurring hydrometeorological disasters, occurring when precipitation falls below the climatological mean over a sustained period, leading to declining river discharge, depleted groundwater reserves, and disrupted food and water security (Mukherjee et al., 2018). Meteorological drought—defined as a prolonged deficit in precipitation relative to the climatological normal—is considered an early indicator of drought onset in Indonesia (Irawan & Komori, 2025). Strong El Niño events, including the Very Strong 1997–1998 event, were associated with severe drought and massive wildfires in Borneo (Taufik et al., 2017; Ihwan et al., 2019). The impacts of drought include declining river discharge, reduced groundwater availability, and threats to food and water security (Widyastuti, 2020). Although Indonesia is generally recognized as a high-rainfall country, precipitation is unevenly distributed spatially and seasonally. In West Kalimantan, the June–September period is generally drier than other months, while El Niño events can substantially reduce monthly precipitation, contributing to periodic moisture deficits (Carlson et al., 2014).

© 2026 Dept. of Geophysics Hasanuddin University

West Kalimantan, situated on the equatorial belt at 2°05'N–3°05'S and 108°30'–114°10'E, exhibits a humid tropical climate with year-round high rainfall. Nevertheless, the region is particularly susceptible to meteorological drought during El Niño phases, when El Niño-related anomalous circulation over the Maritime Continent reduces moisture transport toward Indonesia (Supari et al., 2018). The regional consequences of dry conditions are also reflected in the historical occurrence of forest and land fires. In Kubu Raya Regency, West Kalimantan, a total of 342 forest and land fire cases were recorded during 2015–2019, with an average of approximately 60 cases per year (Muharrama & Widjonarko, 2023). These recurrent fire events provide quantitative evidence of the vulnerability of the region to fire during periods of dry conditions.

Prolonged precipitation deficits dry out peatlands, heightening the risk of land and forest fires, which in turn generate transboundary haze and serious public-health consequences (Qonita et al., 2019). Despite the acknowledged risk, spatially resolved and temporally continuous drought monitoring in West Kalimantan remains limited.

Meteorological drought—the earliest manifestation of drought along the hydrological cascade—is most commonly quantified by the Standardized Precipitation Index (SPI), developed by McKee et al. (1993). SPI requires only precipitation data, is applicable at multiple time scales, and produces standardized values that allow cross-regional comparison (Yuningsih et al., 2022). However, computing SPI for every grid cell across a large domain demands efficient computational approaches. Machine learning methods, particularly ensemble algorithms, have shown strong capability in modeling complex non-linear hydroclimatic relationships (Roihan et al., 2020).

Effective drought mitigation in West Kalimantan requires accurate spatial data to guide targeted policy responses, yet existing studies leave critical gaps unaddressed. Previous studies have demonstrated the effectiveness of Random Forest (RF) for drought classification and prediction in Indonesia. Ayuningtyas & Prasetyo (2020) reported an accuracy of 99.91% for drought classification in Yogyakarta, while Heo et al. (2023) achieved over 80% accuracy using RF integrated with climate projections in Kalimantan. Silvianugroho et al. (2019) reported an accuracy of 75.07% in Central Java, with SAVI identified as the dominant predictor, while Rezaei et al. (2025) demonstrated further improvement using a hybrid RF–SVR approach. However, these studies have primarily focused on drought classification, risk mapping, or prediction using satellite-derived vegetation indices, climate projections, or other drought-related predictors rather than continuous, grid-scale SPI estimation across West Kalimantan. ENSO classification based on the Oceanic Niño Index (ONI) enables systematic differentiation of drought intensities across El Niño and La Niña phases (BMKG, 2026). However, the application of RF for continuous, grid-scale SPI estimation across the entire West Kalimantan province using ERA5 reanalysis data has received limited attention. Furthermore, the extent to which RF can accurately reproduce drought patterns during neutral ENSO conditions—driven primarily by internal monsoon seasonality—remains insufficiently explored. Addressing these gaps is essential for developing a robust, province-wide drought estimation system.

This study therefore estimates monthly SPI-1 values at every ERA5 grid point in West Kalimantan for the period 1995–2024 using an RF model trained on feature-engineered hydroclimatic variables, and evaluates model performance systematically across six representative

© 2026 Dept. of Geophysics Hasanuddin University

ENSO phases ranging from Very Strong El Niño to Strong La Niña, including a neutral-phase year. SPI-1 was selected because the primary objective of this study is to characterize short-term, monthly precipitation deficits and their spatial variability across West Kalimantan. A one-month accumulation period is particularly suitable for identifying rapid changes in meteorological moisture conditions and their responses to seasonal and ENSO-related precipitation variability. Longer accumulation periods, such as SPI-3, SPI-6, or SPI-12, are more appropriate for assessing medium- to long-term hydrological and agricultural drought conditions, but they can smooth short-term precipitation anomalies. Therefore, SPI-1 was selected to maintain the monthly temporal resolution required for examining drought variability across different ENSO phases. The specific objectives are: (1) to evaluate the accuracy and generalization capability of the RF model in estimating SPI-1 across West Kalimantan, and (2) to characterize the spatio-temporal patterns of meteorological drought as reproduced by the model under different ENSO intensities. The resulting spatio-temporal drought maps are expected to provide a science-based foundation for drought early warning and hydrometeorological disaster risk management in West Kalimantan.

Materials and Methods

Study Area and Data

The study area covers the entire province of West Kalimantan, Indonesia (2°05'N–3°05'S; 108°30'–114°10'E) as shown in Figure 1. Monthly total precipitation data were obtained from the ERA5 reanalysis product (European Centre for Medium-Range Weather Forecasts Reanalysis v5), available via the Climate Data Store (CDS) at https://cds.climate.copernicus.eu, with a spatial resolution of ±0.25° and covering the period January 1995 to December 2024 (360 months). ERA5 was selected because its 0.25° × 0.25° spatial resolution provides spatially continuous precipitation information suitable for regional drought analysis (Keune et al., 2025). A total of 195 ERA5 grid cells at a spatial resolution of 0.25° × 0.25° were located within the West Kalimantan administrative boundary and included in the analysis. ENSO phase and intensity were classified using the Oceanic Niño Index (ONI) obtained from the NOAA Climate Prediction Center (CPC), defined as the three-month running mean of SST anomalies in the Niño 3.4 region.

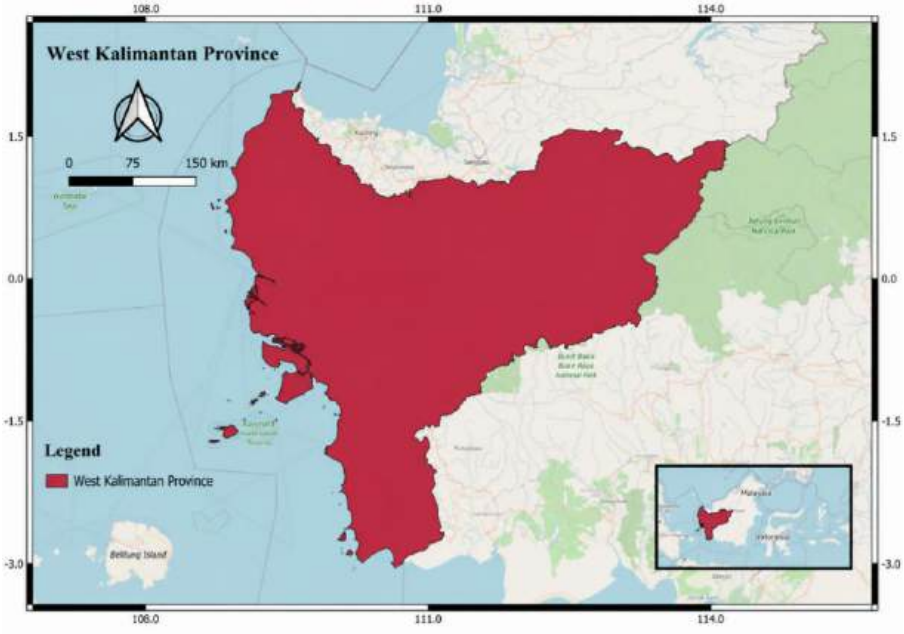


Figure 1. Study location.

© 2026 Dept. of Geophysics Hasanuddin University

SPI Calculation

The one-month Standardized Precipitation Index (SPI-1) was calculated independently for each of the 195 ERA5 grid cells using its corresponding 360-month precipitation time series. Prior to SPI computation, the precipitation time series for each grid cell were checked for missing values. No missing values were identified in the 360-month ERA5 precipitation records; therefore, no imputation or interpolation was required The Gamma distribution parameters were estimated separately for each grid cell rather than from the pooled dataset, thereby preserving the local precipitation characteristics of each grid location. The SPI computation was implemented in Python on Google Colab (Alfarizi et al., 2023), following the procedure of McKee et al. (1993). SPI is widely used because it requires only precipitation data, is applicable across multiple timescales, and allows spatial comparison between regions with different climatic characteristics (Saidah et al., 2017). For each ERA5 grid cell, non-zero monthly precipitation values were fitted to a two-parameter Gamma distribution (McKee, 1993; Saidah et al., 2017), with the probability density function given in Equation (1):

$$g(x) = \frac{1}{\beta^{\alpha}\Gamma(\alpha)} x^{\alpha-1} e^{-x/\beta}, x > 0 \quad (1)$$

where α and β are the shape and scale parameters, respectively. The parameters were estimated separately for each grid cell using the sample mean and the mean of the natural logarithm of non-zero precipitation values, as exspressed in Equations (2)-(4) (McKee, 1993; Widyastuti, 2020):

$$A = \ln(\bar{x}) - \frac{1}{n}\sum \ln(x_i) \quad (2)$$

$$\alpha = \frac{1 + \sqrt{1 + \frac{4A}{3}}}{4A} \quad (3)$$

$$\beta = \frac{\bar{x}}{\alpha} \quad (4)$$

where $\bar{x}$ is the mean of non-zero precipitation and n is the number of non-zero observations. Because the Gamma distribution is undefined at x = 0, the probability of zero precipitation (q = m/n, where m is the count of zero-precipitation months) is incorporated into the cumulative probability as given in Equation (5) (McKee, 1993):

$$H(x) = q + (1 - q)G(x) \quad (5)$$

where G(x) is the Gamma cumulative distribution function. The cumulative probability H(x) was then transformed to the standard normal distribution to obtain SPI-1 using Equation (6) (McKee, 1993) where Φ^{-1} is the inverse of the standard normal cumulative distribution function:

$$\text{SPI} = \Phi^{-1}[H(x)] \quad (6)$$

The resulting SPI values were classified according to McKee et al. (1993), as summarized in Table 1.

Table 1. SPI classification scheme.

SPI Value	Classification
≥ 2.0	Extremely wet
1.50 to 1.99	Very wet
1.00 to 1.49	Moderately wet
-0.99 to 0.99	Near normal
-1.00 to -1.49	Moderately dry
-1.50 to -1.99	Severely dry
≤ -2.0	Extremely dry

Feature Engineering and Random Forest Model

After computing SPI-1 for each grid cell, a feature dataset was constructed for model training. The overall research workflow is summarized in Figure 2. Feature engineering produced the following predictor variables: (1) monthly precipitation (rain), the primary driver of SPI; (2) three-month and six-month rolling mean precipitation (rain_roll3, rain_roll6), capturing accumulated moisture memory; (3) lagged SPI values at one, two, and three months (lag_1, lag_2, lag_3), representing temporal autocorrelation in drought

© 2026 Dept. of Geophysics Hasanuddin University

dynamics. SPI lag variables (lag-1, lag-2, and lag-3) were included to represent the temporal persistence of drought conditions. These variables were derived exclusively from preceding months and were used to capture short-term temporal dependence in SPI. Thus, the lagged predictors provide information available prior to the target month rather than contemporaneous information from the target month.; (4) seasonal cyclic variables using sine and cosine transformations of the calendar month (month_sin, month_cos); and (5) geographic coordinates (latitude, longitude), capturing spatial heterogeneity in climate characteristics across the province.

The dataset was split chronologically: 1995–2018 (approximately 80%) for training and 2019–2024 (approximately 20%) for independent testing. The dataset comprised 221,875 samples, with 176,875 samples (79.72%) used for training and 45,000 samples (20.28%) used for independent testing. The RF model was implemented using Random Forest Regressor from Scikit-learn (Breiman, 2001) with the following hyperparameters: n_estimators = 600, max_features = sqrt, max_samples = 0.8, random_state = 42. These settings were selected to provide a sufficiently large ensemble, introduce randomness among individual trees, and reduce the risk of overfitting while maintaining computational efficiency. Random Forest hyperparameter tuning is the process of finding the best combination of parameters for the Random Forest algorithm to ensure the model delivers optimal predictions while minimizing the risk of overfitting or underfitting (Lujan-Moreno et al., 2018). The training objective is to learn a mapping f(·) from the feature vector Xi to the target SPI value $\hat{y}_i = f(Xi)$, where f aggregates predictions from 600 decision trees through ensemble averaging.

Model Evaluation

Model performance was assessed using two complementary metrics, the coefficient of determination (R^2) and root mean square error (RMSE). R^2 was used to evaluate the proportion of SPI variance explained by the model, while RMSE was used to quantify the magnitude of prediction errors in SPI units. These two metrics were selected to assess both the explanatory performance and prediction error of the Random Forest model. Both R^2 and RMSE were calculated using pooled observations from all grid cells within the study area for the respective training and testing periods, resulting in a single overall value for each metric rather than separate values for individual grid cells. Following Hair et al. (2020), an $R^2 \geq 0.75$ is classified as a very strong relationship. The R^2 and RMSE metrics were calculated using the complete set of observations in the training and testing datasets, combining all grid cells and time steps. Therefore, the reported metrics represent the overall model performance across the study domain rather than performance calculated separately for each grid cell.

The coefficient of determination (R^2) measures the proportion of SPI variance explained by the model as given in Equation (7) (Chicco et al., 2021):

$$R^2 = 1 - \frac{\sum(y_i - \hat{y}_i)^2}{\sum(y_i - \bar{y})^2} \qquad (7)$$

Root Mean Square Error (RMSE) quantifies mean prediction deviation in SPI units, as given in Equation (8) (Hodson, 2022) where n is the total number of observations:

$$\text{RMSE} = \sqrt{\frac{1}{n}\sum(y_i - \hat{y}_i)^2} \qquad (8)$$

© 2026 Dept. of Geophysics Hasanuddin University

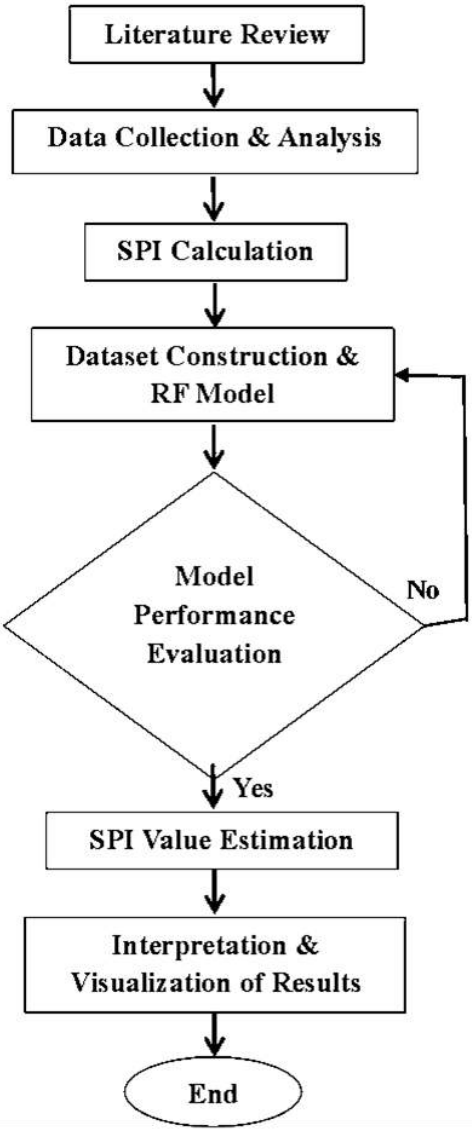


Figure 1. Research flowchart.

Results and Discussion

Results

Analysis of area-averaged SPI-1 across West Kalimantan for 1995–2024 (Figure 3) reveals high interannual variability driven primarily by ENSO. Extremely dry conditions (SPI ≤ −2.0) affected approximately 11.6% of grid-month observations in 1997 (SPI ranging from −4.75 to 2.12) and 9.5% in 2015 (SPI ranging from −4.12 to 2.95), coinciding with strong-to-very-strong El Niño events, with the 1997 peak descending below −3.0 in several grid cells. Conversely, extremely wet conditions (SPI ≥ 2.0) affected approximately 0.5% of grid-month observations in 2010 (SPI ranging from −1.73 to 2.78) and during 2021–2022, corresponding to La Niña phases.

The RF model trained on 1995–2018 data (Figure 4) achieved R^2 = 0.997 and RMSE = 0.052, demonstrating that the model explains 99.7% of SPI-1 variability with minimal average deviation. On the independent test set (2019–2024, Figure 5), performance remained high with R^2 = 0.968 and RMSE = 0.176, indicating strong generalization to unseen data. Feature importance analysis (Figure 10) showed that monthly precipitation (rain) contributed 60.1%, followed by rain_roll3 (12.8%), month_cos (7.2%), longitude (4.2%), latitude (3.3%), rain_roll6 (3.1%), and lagged SPI variables collectively (6.9%).

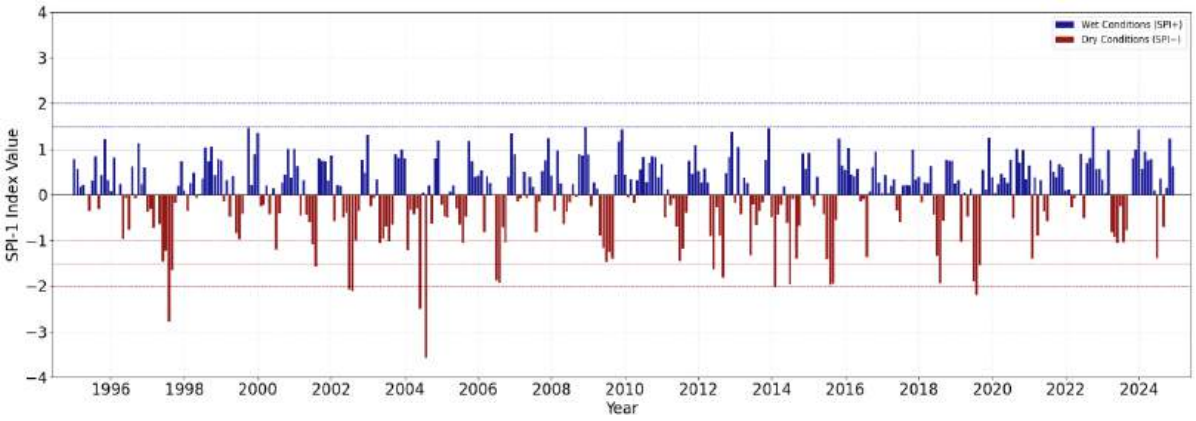


Figure 2. Temporal SPI-1 Time Series for West Kalimantan, 1995–2024.

© 2026 Dept. of Geophysics Hasanuddin University

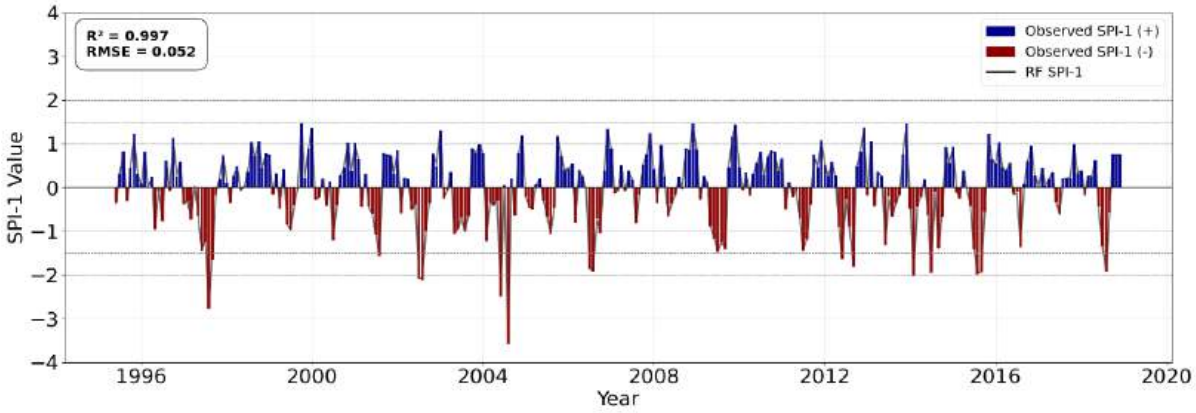


Figure 4. Random Forest Model Estimation on Training Data (1995–2018).

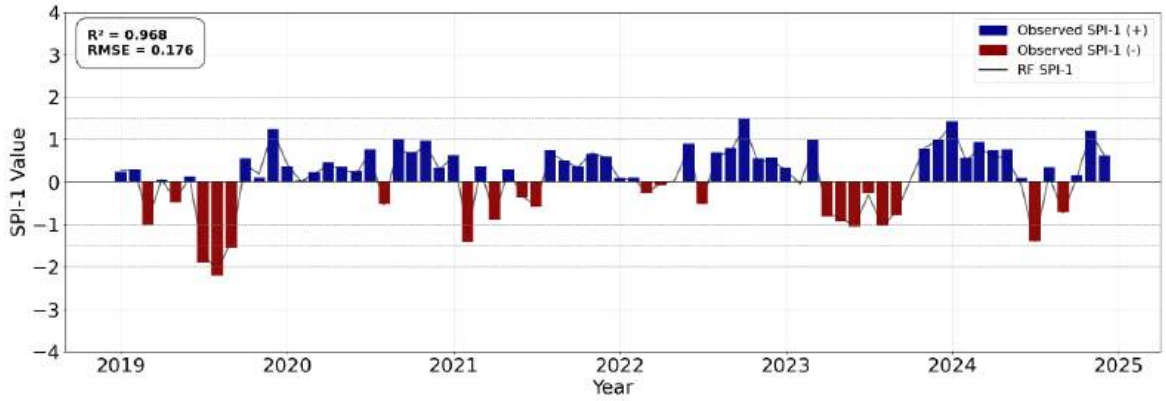


Figure 5. Random Forest Model Estimation on Testing Data (2019–2024).

Model performance evaluated across four representative El Niño years (1997, 2009, 2019, and 2023) is presented in Table 2. The highest R^2 was recorded during Moderate El Niño 2009 ($R^2 = 0.998$), while the lowest was during Strong El Niño 2023 ($R^2 = 0.969$), which belongs to the test set. All R^2 values exceeded 0.96 across all phases. For each year, R^2 and RMSE were computed from all 195 ERA5 grid cells across the 12 months of that year, yielding a sample size of n = 2,340 monthly grid-cell observations per year (Table 2).

Table 2. Comparison of R^2 and RMSE values.

Year	ENSO Phase	R^2	RMSE	n
1997	Very strong El Niño	0.997	0.062	2.340
2009	Moderate El Niño	0.998	0.051	2.340
2019	Weal El Niño	0.974	0.189	2.340
2023	Strong El Niño	0.969	0.175	2.340

Spatial distributions of actual SPI-1 (panel A) and RF estimates (panel B) for each representative year are shown in Figures 6–9. During the Very Strong El Niño of 1997 (Figure 6), extremely dry conditions dominated nearly the entire province in July–August, with the most severe deficit concentrated in the southern and southwestern regions. For Moderate El Niño 2009 (Figure 7), a more structured, gradual drought development was observed from May to August, followed by a swift recovery. Weak El Niño 2019 (Figure 8) and Strong El Niño 2023 (Figure 9) both showed clear mid-year drying, though less extensive than 1997, with rapid October recovery.

© 2026 Dept. of Geophysics Hasanuddin University

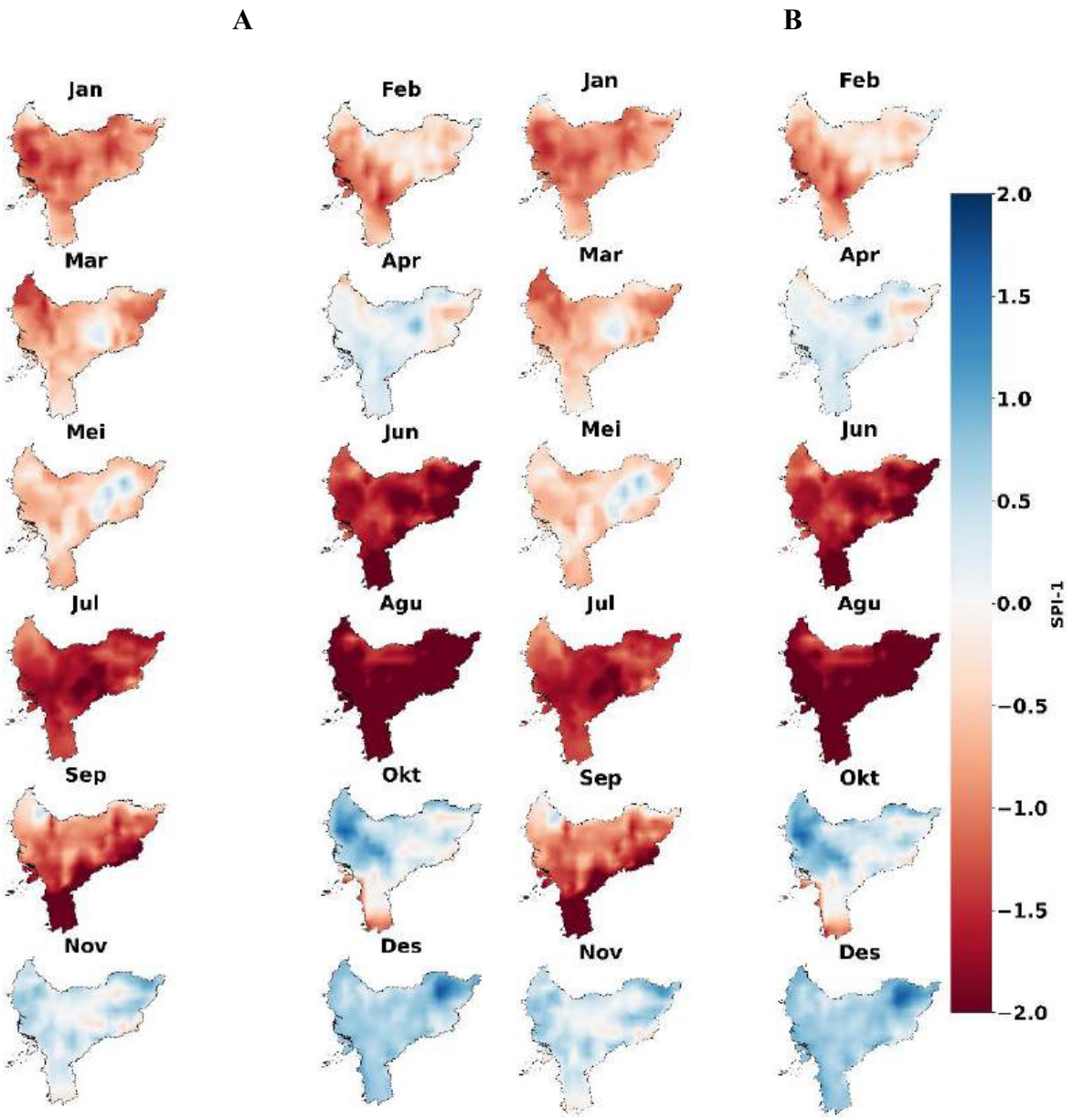


Figure 6. Spatial Distribution of Actual SPI (A) and Random Forest SPI (B) During the Very Strong El Niño Event (Year 1997).

© 2026 Dept. of Geophysics Hasanuddin University

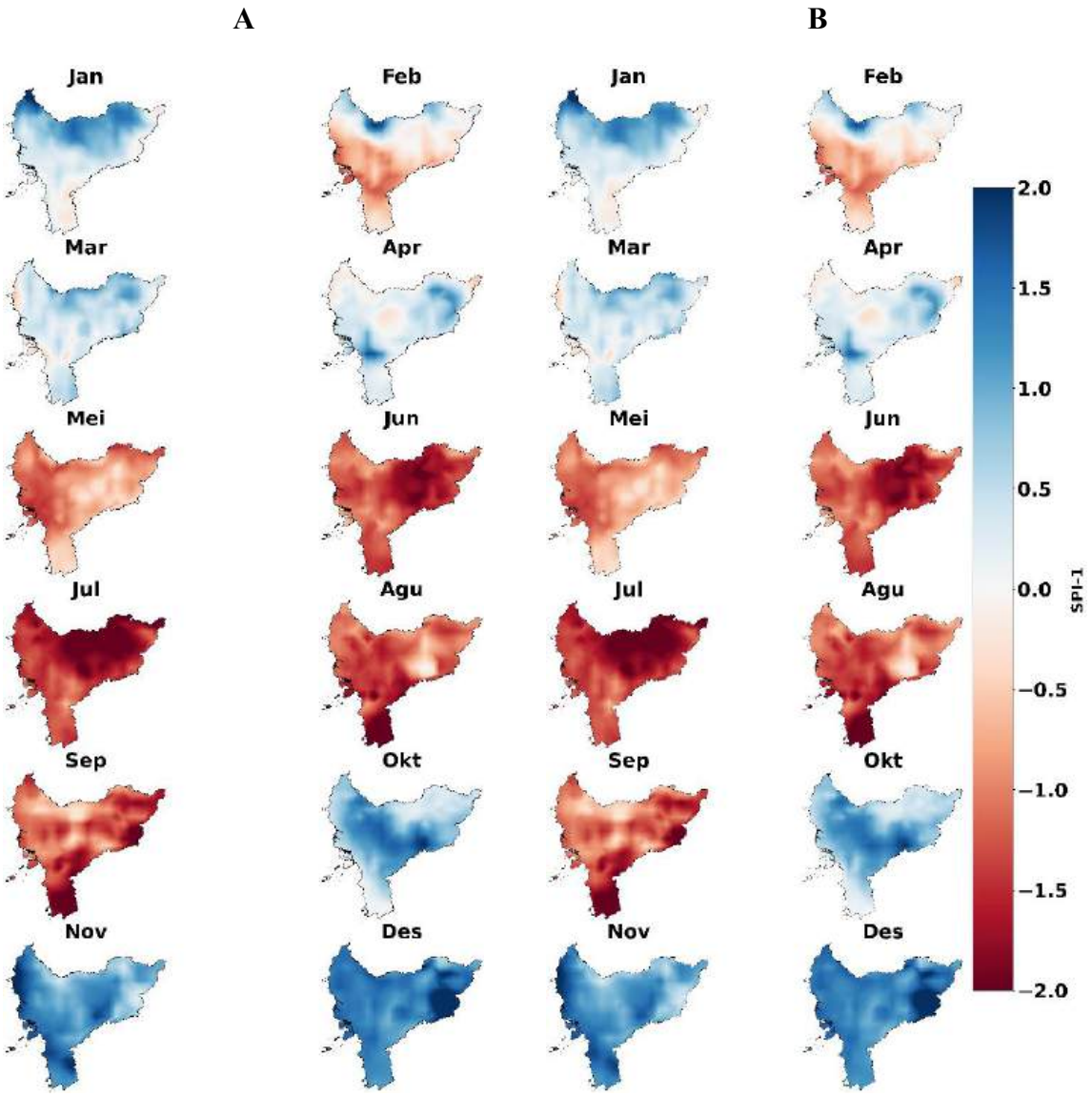


Figure 7. Spatial Distribution of Actual SPI (A) and Random Forest SPI (B) During the Moderate El Niño Event (Year 2009).

© 2026 Dept. of Geophysics Hasanuddin University

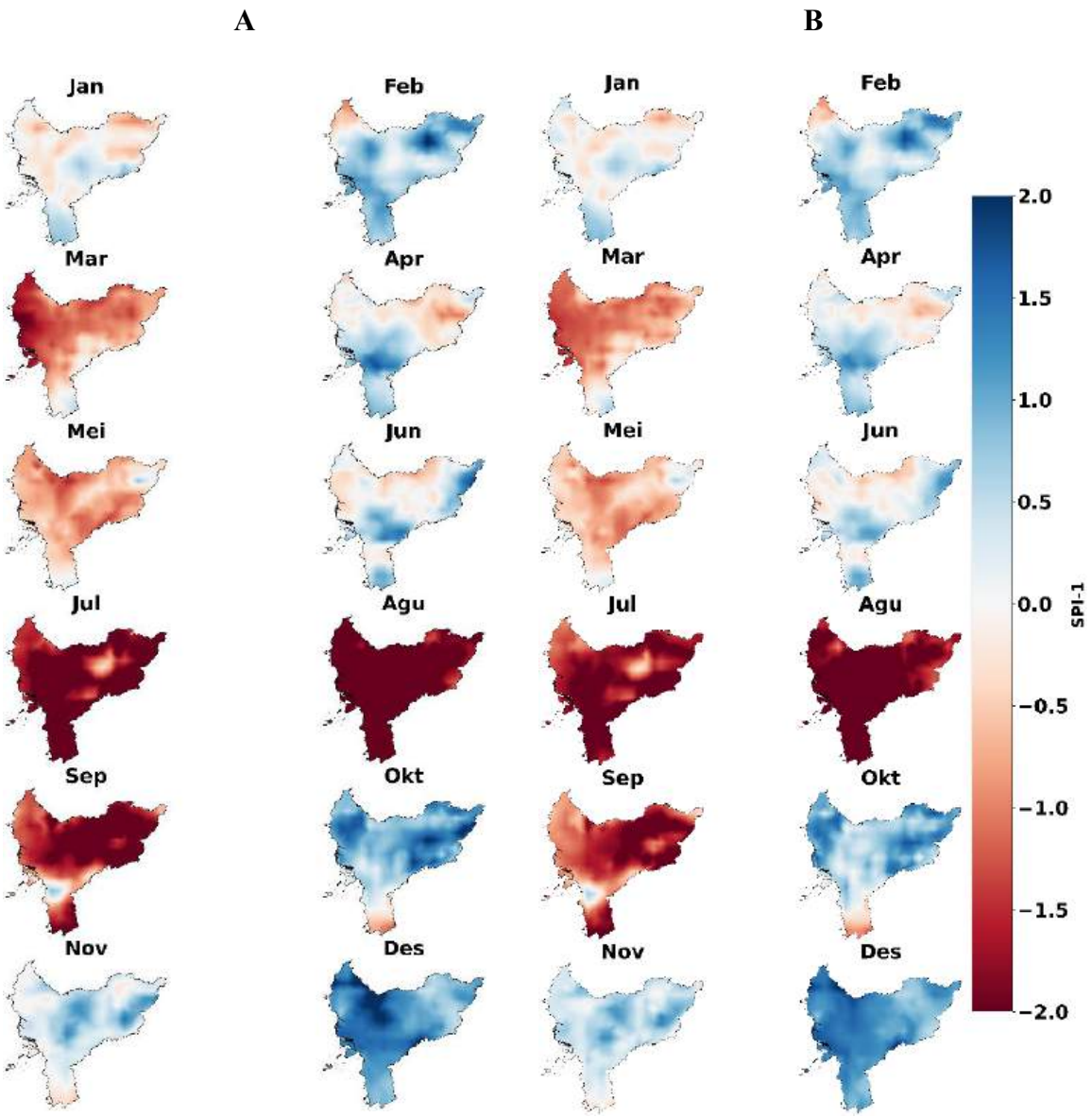


Figure 8. Spatial Distribution of Actual SPI (A) and Random Forest SPI (B) During the Weak El Niño Event (Year 2019).

© 2026 Dept. of Geophysics Hasanuddin University

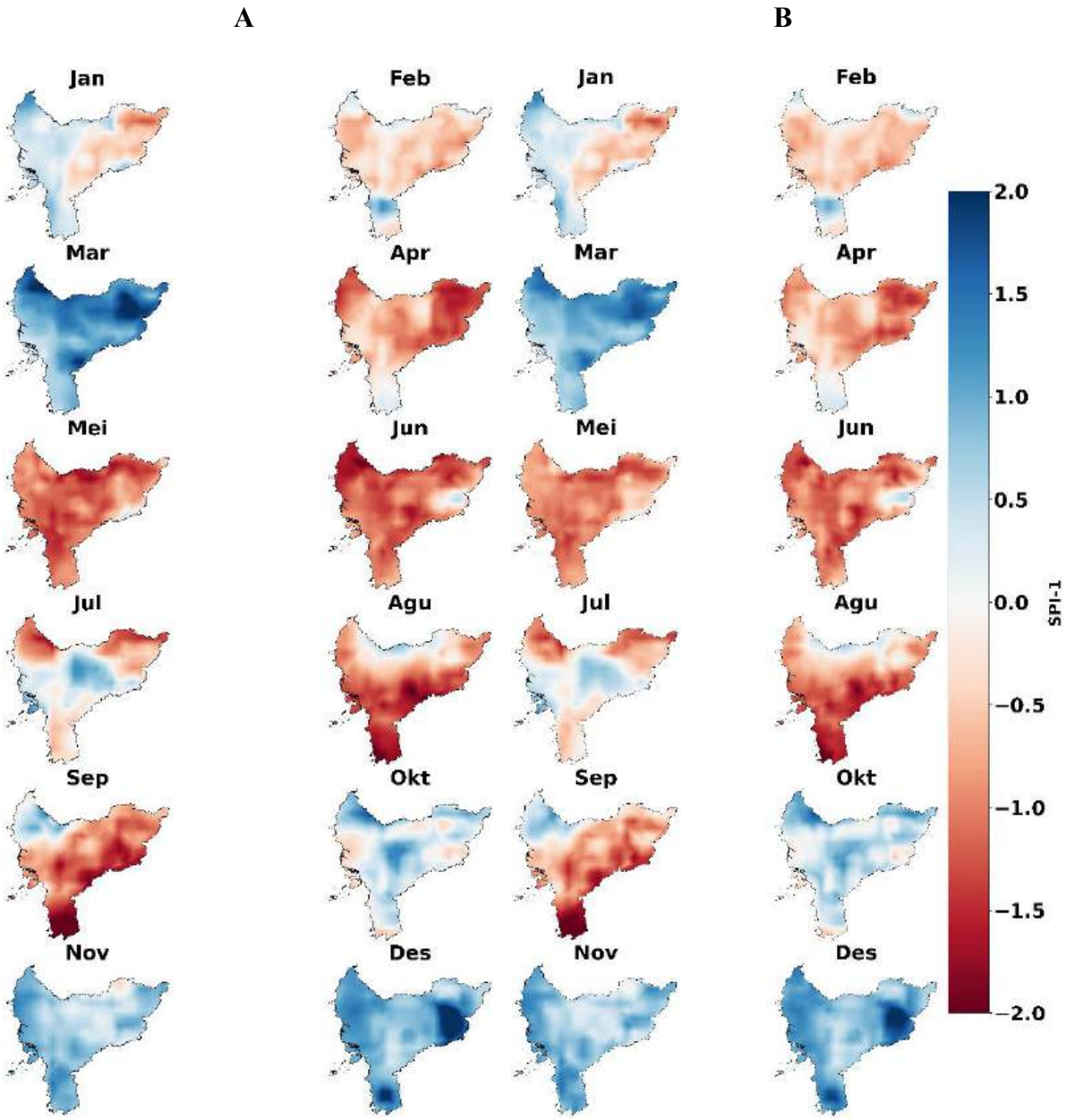


Figure 9. Spatial Distribution of Actual SPI (A) and Random Forest SPI (B) During the Strong El Niño Event (Year 2023).

© 2026 Dept. of Geophysics Hasanuddin University

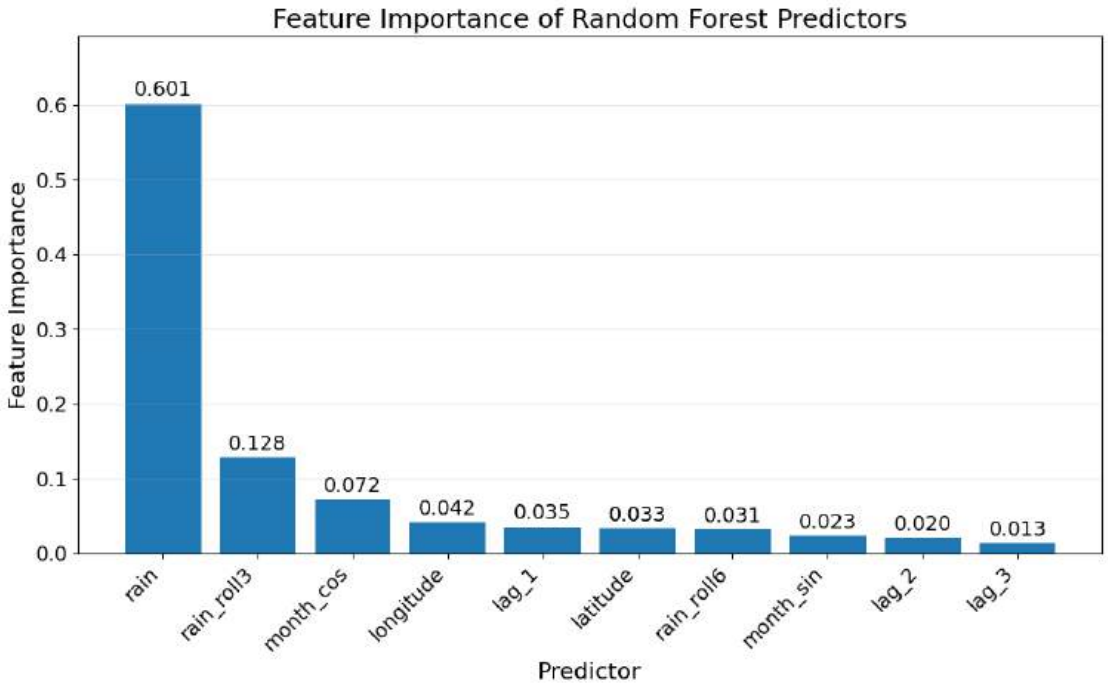


Figure 10. Relative Importance of Predictor Variables in the Random Forest Model for SPI-1 Estimation.

Discussion

The temporal SPI-1 pattern (Figure 3) confirms a strong ENSO–drought coupling in West Kalimantan. The extreme drought of 1997 aligns with one of the strongest El Niño events on record; according to Supari et al. (2018), El Niño suppresses seasonal rainfall over most of Indonesia. This is consistent with Taufik et al. (2017), who linked strong El Niño years to widespread hydrological drought and wildfires in Borneo, asconfirmed by Maulida et al. (2025) for the Kalimantan region.

The RF model's strong performance—R^2 = 0.997 during training and R^2 = 0.968 during testing—demonstrates that ensemble learning effectively captures the non-linear hydroclimatic relationships governing SPI dynamics at the grid scale. The modest R^2 decrease from training to testing (Δ = 0.029) indicates excellent generalization, consistent with the inherent overfitting resistance of RF through bootstrap aggregation (Breiman, 2001). These results compare favorably with previous RF-based drought studies; Ayuningtyas & Prasetyo (2020) achieved 99.91% accuracy in Yogyakarta and Heo et al. (2023) exceeded 80% for multi-hazard risk mapping in Kalimantan, though both used classification rather than continuous SPI estimation. Because those studies report classification accuracy while the present study reports regression-based R^2 and RMSE for a continuous SPI-1 target, these figures are not directly comparable in a strict numerical sense; the comparison above is intended only to indicate that RF-based approaches generally perform well for drought-related estimation in Indonesia, not to claim superiority on a common metric. This constitutes a limitation of the present study: because no shared regression-based benchmark for RF-based drought estimation currently exists in the Indonesian literature, classification accuracy and continuous SPI regression performance cannot be placed on a single comparative scale, and the high R^2 obtained here should not be interpreted as evidence of superior model skill relative to these prior classification-based studies. The slight underestimation of extreme SPI values in the test set reflects the well-known smoothing effect of ensemble averaging (Rezaei et al., 2025), whereby the mean prediction across many trees regresses toward central values during anomalous conditions.

© 2026 Dept. of Geophysics Hasanuddin University

Feature importance results confirm the fundamental role of precipitation in determining SPI: monthly precipitation alone accounts for 60.1% of the model importance, while the 12.8% contribution of the three-month rolling mean (rain_roll3) reflects accumulated moisture memory. The dominant contribution of precipitation is expected because SPI is directly derived from precipitation and therefore should not be interpreted as a novel finding by itself. Instead, these results confirm that the model captures the expected relationship between precipitation variability and meteorological drought. The contribution of rain_roll3 further indicates that accumulated precipitation information provides additional temporal context for SPI estimation, consistent with the nature of SPI as a transformed precipitation anomaly (McKee, 1993). The combined 6.9% contribution of three lag-SPI variables corroborates the temporal autocorrelation of drought, where past drought conditions influence present ones. Spatial coordinates contribute 7.5% in total, reflecting the heterogeneous climate gradient across the province documented by Putri et al. (2024), who found spatially varying trends in precipitation extremes across Kalimantan.

Spatial comparisons between actual (panel A) and RF-estimated (panel B) SPI-1 maps reveal consistently high agreement across all four El Niño phases. During the 1997 Very Strong El Niño (Figure 6), estimated maps faithfully reproduced the spatial extent and intensity of extreme dryness (R^2 = 0.997), particularly the intensification in southern and southwestern areas. This spatial concentration of drought in southern and southwestern West Kalimantan may be related to the seasonal distribution of rainfall and the regional response to El Niño. During El Niño events, the eastward displacement of the Walker circulation suppresses convection and reduces moisture availability over the Indonesian Maritime Continent, particularly during the dry season. The southern and southwestern parts of West Kalimantan may therefore experience greater rainfall deficits when seasonal moisture supply is reduced, resulting in stronger negative SPI anomalies. Local geographic and topographic characteristics may further modulate rainfall distribution and contribute to the observed spatial differences in drought intensity. For Moderate El Niño 2009 (Figure 7), the model achieved its highest R^2 (0.998), suggesting that moderate-intensity El Niño signals produce more spatially coherent drought patterns that are easier to learn. For the two test-set years—Weak El Niño 2019 (Figure 8, R^2 = 0.974) and Strong El Niño 2023 (Figure 9, R^2 = 0.969)—the spatial agreement remained high, with only moderate underestimation of peak dry intensities attributable to the smoothing effect of ensemble averaging (Rezaei et al., 2025). The pattern that drought intensity scales with El Niño strength, as evidenced across all four years, corroborates Qonita et al. (2019) finding that ENSO is the primary driver of drought distribution in West Kalimantan.

Conclusion

This study demonstrates that a Random Forest model trained on ERA5 reanalysis data can estimate SPI-1 with high accuracy across West Kalimantan (R^2 = 0.997, RMSE = 0.052 training; R^2 = 0.968, RMSE = 0.176 testing), maintaining consistent performance across all El Niño intensity phases. Meteorological drought in West Kalimantan is predominantly governed by ENSO, with El Niño triggering widespread dry anomalies that peak in July–September and intensify with increasing ENSO strength. The most severe drought episode occurred during the Very Strong El Niño of 1997, which produced extreme dryness across most of the province, while Moderate El Niño 2009, Weak El Niño 2019, and Strong El Niño 2023 exhibited progressively varying drought extents

© 2026 Dept. of Geophysics Hasanuddin University

consistent with their respective ENSO intensities. The spatial agreement between actual and RF-estimated SPI maps was consistently high ($R^2 > 0.96$) across all four representative El Niño years, confirming the model's effectiveness for spatio-temporal drought characterization. These findings provide a methodological foundation for developing grid-scale drought early warning systems in West Kalimantan and demonstrate the broader potential of ERA5-driven RF models for drought monitoring in data-sparse tropical regions.

The results of this study have practical implications for drought monitoring and early warning in West Kalimantan. The Random Forest model provides continuous SPI-1 estimates by integrating precipitation, temporal SPI persistence, rainfall memory, seasonal, and spatial information. This approach can support the identification of emerging drought conditions and their spatial development before they reach more severe categories. In particular, the observed drought patterns during El Niño years indicate that SPI-based monitoring can be used to identify areas that are more susceptible to rainfall deficits during ENSO events.

The model outputs could be incorporated into an operational drought monitoring framework by updating the predictor variables as new precipitation observations become available and generating spatial SPI estimates at regular intervals. Areas showing increasingly negative SPI values could then be prioritized for closer monitoring and early intervention. Such information may support relevant agencies in planning water-resource management, agricultural preparedness, and drought-response measures. However, operational implementation would require continuous data updates, independent validation under different climatic conditions, and integration with other indicators such as soil moisture, temperature, and reservoir or river conditions.

Acknowledgements

The authors would like to thank the European Centre for Medium-Range Weather Forecasts (ECMWF) for providing the ERA5 reanalysis data through the Copernicus Climate Data Store (CDS), and NOAA for making the Oceanic Niño Index (ONI) data publicly available. The authors also express sincere gratitude to the reviewers and editors for their constructive comments and suggestions that improved the quality of this manuscript.

Author Contribution

Nurputri: Conceptualization, Methodology, Software, Data Curation, Formal Analysis, Writing – Original Draft, Visualization. Muhammad Ishak Jumarang: Supervision, Conceptualization, Writing – Review & Editing, Validation. Andi Ihwan: Supervision, Writing – Review & Editing, Validation, Resources.

Conflict of Interest

The authors declare no conflict of interest.

References

Alfarizi, M. R. S., Al-farish, M. Z., Taufiqurrahman, M., Ardiansah, G., & Elgar, M. (2023). Penggunaan Python Sebagai Bahasa Pemrograman untuk Machine Learning dan Deep Learning. *Karimah Tauhid*, 2(1), 1–6. https://ojs.unida.info/karimahtauhid/article/view/7518

Ayuningtyas, F., & Prasetyo, S. Y. J. (2020). Pemanfaatan Teknologi Machine Learning Untuk Klasifikasi Wilayah Risiko Kekeringan di Daerah Istimewa Yogyakarta Menggunakan Citra Landsat 8 Operational Land Imager (OLI). *Jurnal Transformatika*, 18(1), 13–24. https://doi.org/10.26623/transformati

© 2026 Dept. of Geophysics Hasanuddin University

ka.v18i1.2140

BMKG. (2026). *ENSO (El Niño–Southern Oscillation)*, Badan Meteorologi Klimatologi dan Geofisika. https://iklim.bmkg.go.id/id/enso/

Breiman, L. (2001). Random Forests. *Machine Learning*, 45, 5–32. https://doi.org/10.1023/A:1010933404324

Carlson, K. M., Curran, L. M., Ponette-González, A. G., Ratnasari, D., Ruspita, Lisnawati, N., Purwanto, Y., Brauman, K. A. & Raymond, P. A. (2014). Influence of watershed-climate interactions on stream temperature, sediment yield, and metabolism along a land use intensity gradient in Indonesian Borneo. *Journal of Geophysical Research: Biogeosciences*, 119(6), 1110–1128. https://doi.org/10.1002/2013JG002516

Chicco, D., Warrens, M. J., & Jurman, G. (2021). The coefficient of determination R-squared is more informative than SMAPE, MAE, MAPE , MSE and RMSE in regression analysis evaluation. PeerJ Computer Science, 7, e623. https://doi.org/10.7717/peerj-cs.623

Hair Jr., J. F., Black, W. C., Babin, B. J.,& Anderson, R. E. (2020). *Multivariate Data Analysis*. Pearson Education Limited.

Heo, S., Park, S., & Lee, D. K. (2023). Multi-hazard exposure mapping under climate crisis using random forest algorithm for the Kalimantan Islands, Indonesia. *Scientific Reports*, 13(1), 13472. https://doi.org/10.1038/s41598-023-40106-8

Hodson, T. O. (2022). Root-mean-square error (RMSE) or mean absolute error (MAE): when to use them or not. Geoscientific Model Development, 15(14), 5481–5487. https://doi.org/10.5194/gmd-15-5481-2022

Ihwan, A., Pawitan, H., Hidayat, R., Latifah, A. L., & Taufik, M. (2019). Analisis Karakteristik Kekeringan DAS Kapuas Kalimantan Barat Berdasarkan Luaran Global Climate Model. *Positron*, 9(2), 74–80. https://jurnal.untan.ac.id/index.php/jpositron/article/view/35072/0

Irawan, A. N. R., & Komori, D. (2025). Long term variability of agricultural drought's characteristic in Indonesia. *Journal of Agricultural Meteorology*, 81(4), 203–213. https://doi.org/10.2480/agrmet.D-24-00024

Keune, J., Di Giuseppe, F., Barnard, C., da Costa, E. D., & Wetterhall, F. (2025). *ERA5–Drought: Global drought indices based on ECMWF reanalysis*. Scientific Data, 12, 616. https://doi.org/10.1038/s41597-025-04896-y

Lujan-Moreno, G. A., Howard, P. R., Rojas, O. G., & Montgomery, D. C. (2018). Design of experiments and response surface methodology to tune machine learning hyperparameters, with a random forest case-study. *Expert Systems with Applications*, 109, 195–205. https://doi.org/10.1016/j.eswa.2018.05.024

Maulida, N. P., Ariska, M., Suhadi, S., & Akhsan, H. (2025). Rainfall Characteristics in Kalimantan Island During ENSO and IOD Phases: Insights from Composite Analysis. *Jurnal Ilmu Fisika | Universitas Andalas*, 17(1), 88–100. https://doi.org/10.25077/jif.17.1.88-100.2025

McKee, T. B., Doesken, N. J., & Kleist, J. (1993). The relationship of drought frequency and duration to time scales. *Proceedings of the 8th Conference on Applied Climatology*, 179–183. https://www.droughtmanagement.info/literature/AMS_Relationship_Drought_Frequency_Duration_Time_Scales_1993.pdf

Muharrama, D., & Widjonarko, W. (2023).

© 2026 Dept. of Geophysics Hasanuddin University

Risiko Bencana Kebakaran Hutan dan Lahan Gambut di Kabupaten Kubu Raya, Provinsi Kalimantan Barat. *Teknik PWK (Perencanaan Wilayah Kota)*, 12(2), 160–170. https://doi.org/10.14710/tpwk.2023.32816

Mukherjee, S., Mishra, A., & Trenberth, K. E. (2018). Climate Change and Drought: a Perspective on Drought Indices. *Current Climate Change Reports*, 4(2), 145–163. https://doi.org/10.1007/s40641-018-0098-x

Putri, J. K., Irfan, M., Akhsan, H., Suhadi, S., & Iskandar, I. (2024). Oberved trend of precipitation extreme in Kalimantan. *Global NEST Journal*, 26(9), 06543. https://doi.org/10.30955/gnj.06543

Qonita, I. R., Putra, Y. S., & Kushadiwijayanto, A. A. (2019). Pola Distribusi Kekeringan Menggunakan Metode Standardized Precipitation Index (SPI) di Kalimantan Barat. *Prisma Fisika*, 7(2), 139–142. https://doi.org/10.26418/pf.v7i2.35574

Rezaei, M., Moghaddam, M. A., Piri, J., Azizyan, G., & Shamsipour, A. A. (2025). Drought prediction using advanced hybrid machine learning for arid and semi-arid environments. *KSCE Journal of Civil Engineering*, 29(4), 100025. https://doi.org/10.1016/j.kscej.2024.100025

Roihan, A., Sunarya, P. A., & Rafika, A. S. (2020). Pemanfaatan Machine Learning dalam Berbagai Bidang: Review paper. *Jurnal Khatulistiwa Informatika*, 5(1), 490845. https://doi.org/10.31294/ijcit.v5i1.7951

Saidah, H., Budianto, M. B., & Hanifah, L. (2017). Analisa indeks dan sebaran kekeringan menggunakan metode Standardized Precipitation Index (SPI) dan Geographical Information System (GIS) untuk Pulau Lombok. *Jurnal Spektran*, 5(2), 173–179.

Silvianugroho, S., Prasetyo, S. Y. J., & Hartomo, K. D. (2019). Penentuan Wilayah Resiko Bencana Kekeringan di Jawa Tengah Menggunakan Machine Learning dan Indeks Vegetasi pada Citra Landsat 8 OLI. *Indonesian Journal of Computing and Modeling*, 2(2), 17–24. https://ejournal.uksw.edu/icm/article/view/2952

Supari, S., Tangang, F., Salimun, E., Aldrian, E., Sopaheluwakan, A., & Juneng, L. (2018). ENSO modulation of seasonal rainfall and extremes in Indonesia. *Climate Dynamics*, 51(7), 2559–2580. https://doi.org/10.1007/s00382-017-4028-8

Taufik, M., Torfs, P. J. J. F., Uijlenhoet, R., Jones, P. D., Murdiyarso, D., & Van Lanen, H. A. J. (2017). Amplification of wildfire area burnt by hydrological drought in the humid tropics. *Nature Climate Change*, 7(6), 428–431. https://doi.org/10.1038/nclimate3280

Widyastuti, R., Tambunan, M. P., Taqyuddin, T., & Tambunan, R. P. (2020). Pola Sebaran Kekeringan di Kecamatan Simpenan Menggunakan Metode SPI (Standardized Precipitation Index). *Jurnal Geosaintek*, 6(1), 19–24. https://journal.its.ac.id/index.php/geosaintek/article/view/7312

Yuningsih, Y., Febrianti. D., & Norman, Y. (2022). Analisis Kekeringan Standardized Precipitation Index (SPI) Akibat Pengaruh dari ENSO dan IOD di Wilayah Utara Banten. *Buletin Meteorologi, Klimatologi dan Geofisika*, 2(5), 39–49. https://www.balai2bmkg.id/index.php/buletin_mkg/article/view/42

© 2026 Dept. of Geophysics Hasanuddin University

ISSN: 2579-5821 (Print)
ISSN: 2579-5546 (Online)
URL address: http://journal.unhas.ac.id/index.php/geocelebes
DOI: 10.70561/geocelebes.v10i2.53104

Jurnal Geocelebes Vol. 10 No. 2, October 2026, 413 – 431

Intraseasonal Ocean Surface Variability Response to the Madden-Julian Oscillation: A Comparative Study of the Malacca Strait and the Indian Ocean

Nabila Afifah Azuga[1,2]*, Ahmad Dhuha Habibullah[3], Bintal Amin[1], Rianti Putri[1], Mubarak[1], Ilham Ilahi[1], Rifardi[1]

[1]Department of Marine Sciences, Faculty of Fisheries and Marine, University of Riau, Pekanbaru, 28293, Indonesia
[2]Center for Peatland and Disaster Studies (CPDS), University of Riau, Pekanbaru, 28293, Indonesia
[3]Independent Researcher, West Jakarta, 11610, Indonesia

*Corresponding author. Email: nabila.afifahazuga@lecturer.unri.ac.id

Manuscript received: 29 July 2026; Received in revised form: 4 October 2026; Accepted: 11 October 2026

Abstract

The Madden–Julian Oscillation (MJO) is the dominant mode of tropical intraseasonal variability, strongly modulating atmospheric convection and upper-ocean conditions across the Maritime Continent. However, its influence on narrow semi-enclosed straits relative to adjacent open-ocean regions remains insufficiently understood. This study investigated phase-dependent atmospheric and ocean-surface responses to active MJO events in the Malacca Strait (MS) and eastern Indian Ocean (IO) using daily ERA5 reanalysis and Copernicus Marine Service data for 2000-2025. Variables were interpolated onto a common 0.25° × 0.25° grid, converted to daily anomalies, and classified into eight MJO phases using the OLR-based MJO Index (OMI). Power spectral density and phase composite analyses were applied to outgoing longwave radiation (OLR), surface wind, precipitation, sea surface temperature (SST), sea surface salinity (SSS), and significant wave height (SWH). Both regions exhibited dominant OLR variability at 43-45 days, with stronger spectral power and more coherent convective signals found in the eastern IO. During phases 4-6, enhanced convection was associated with negative OLR anomalies, stronger westerly winds, and increased precipitation, whereas these responses were weaker within the MS. SST shifted from positive anomalies during phases 1-3 to negative anomalies during phases 5-7, while SSS freshening occurred earlier and more extensively in the eastern IO. SWH also increased more strongly in the eastern IO. These findings demonstrate that the semi-enclosed MS spatially modulates and attenuates MJO-related atmosphere-ocean responses, with implications for subseasonal marine monitoring and forecasting across the Maritime Continent.

Keywords: Intraseasonal variability; Maritime continent; Ocean surface anomalies; Outgoing longwave radiation; Phase composite analysis.

Citation: Azuga, N. A, Habibullah, A. D., Amin, B., Mubarak, M., Ilahi, I., & Rifardi, R. (2026). Intraseasonal Ocean Surface Variability Response to the Madden-Julian Oscillation: A Comparative Study of the Malacca Strait and the Indian Ocean. *Jurnal Geocelebes*, 10(2): 413–431, doi: 10.70561/geocelebes.v10i2.53104

Introduction

The Madden-Julian Oscillation (MJO) is known as the dominant mode of tropical intraseasonal variability, with convective activity that typically develops over the Indian Ocean (IO) and dissipates over the western Pacific with an average speed of ~5 m/s, characterized by eastward-propagating convective disturbances on a timescale of approximately 30-90 days (Barret et al., 2021; Worku et al., 2020; Lumbangaol & Yu, 2026; Marshall et al., 2015). Its propagation is divided into eight phases according to the geographical position of the main convective envelope (Kiladis et al., 2014; Da Silva & Matthews, 2021). As one of the primary drivers of tropical climate variability, the MJO modulates atmospheric circulation,

© 2026 Dept. of Geophysics Hasanuddin University

cloudiness, precipitation, and surface wind over the Indo-Pacific region (Xavier et al., 2014; Da Silva & Matthews, 2021). These atmospheric variations strongly influence ocean surface conditions through changes in turbulent heat fluxes, wind-induced mixing, freshwater input from precipitation, and wave generation (Karlowska et al., 2024; Baeda et al., 2019; DeMott et al., 2015). Consequently, variables such as outgoing longwave radiation (OLR), surface wind, precipitation, sea surface temperature (SST), sea surface salinity (SSS), and significant wave height (SWH) exhibit pronounced intraseasonal variability associated with MJO activity (Baeda et al., 2019; DeMott et al., 2015; Marshall et al., 2015; Hilmi et al., 2018; Ikuyajolu et al., 2024).

Previous studies have demonstrated that enhanced MJO convection is typically associated with negative OLR anomalies, intensified surface winds, increased precipitation, upper-ocean cooling, sea-surface freshening, and stronger wave activity. Conversely, suppressed convective phases are generally associated with positive OLR anomalies, weaker winds, reduced rainfall, and gradual recovery of upper-ocean thermal conditions (Lumbangaol & Yu, 2026; Savarin & Chen, 2022; Jiang et al., 2020). Numerous observational, reanalysis, and numerical modeling studies have investigated these responses in different tropical basins, including the IO, western Pacific, and the MC (DeMott et al., 2015; Du et al., 2025; Bi & Yuan, 2026). Nevertheless, most previous research has focused on individual atmospheric and oceanic variables, specific MJO events, or broad ocean basins rather than assessing the multiple atmosphere-ocean variables simultaneously over contrasting marine environments.

The MC consists of numerous islands, shallow marginal seas, narrow straits, and adjacent open oceans. The Malacca Strait (MS) is a shallow, semi-enclosed waterway with restricted fetch, strong tidal mixing, and substantial influence from the surrounding landmasses (Lee et al., 2019; Zhao et al., 2025), while the adjacent eastern IO is a broad open ocean directly exposed to large-scale atmospheric forcing (Azuga et al., 2020; Napitupulu et al., 2022; Thomas et al., 2024). Their contrasting bathymetry, coastline geometry, and water exchange may produce different magnitudes, spatial patterns, and timing of SST, SSS, and SWH responses (Renkl et al., 2024), yet direct quantitative comparisons of atmospheric forcing and ocean-surface responses across all eight MJO phases remain limited. These two regions were selected because their close geographic proximity but markedly different bathymetric and geographical settings provide a suitable natural comparison for assessing how the same large-scale MJO forcing is modified across semi-enclosed and open-ocean environments. Hence, it is still unclear to what extent the open ocean response observed in the eastern IO can be applied to the semi-enclosed MS, where shallow bathymetry, surrounding landmasses, restricted fetch, and water exchange with adjacent seas may modify MJO-related SST, SSS, and SWH responses.

To address this gap, six atmospheric and oceanic variables, namely OLR, surface wind, precipitation, SST, SSS, and SWH, were examined through phase-based composite analysis across MJO phases 1-8, using daily ERA5 reanalysis and Copernicus Marine Service salinity data for 2000-2025. ERA5 was selected for the atmospheric variables and SST because of its consistent long-term daily coverage and 0.25° × 0.25° spatial resolution, while Copernicus Marine was used for SSS because daily salinity data were available for the study period. To ensure consistency among the datasets, all variables were interpolated to a common 0.25° × 0.25° grid prior to analysis. By directly comparing a

© 2026 Dept. of Geophysics Hasanuddin University

semi-enclosed strait with an open ocean environment, this study aimed to determine how regional geographical and oceanographic conditions shape the magnitude, spatial pattern, and timing of MJO-related variability.

Materials and Methods

Study Area

The study area covered the Malacca Strait and the adjacent Indian Ocean off Sumatra, within approximately 95.5-104°E and 0-6°N (Figure 1). The open Indian Ocean (IO) domain was defined within this bounding box and, after ocean masking, covered approximately 127,533.26 km^2 and contained 147 OLR grid cells. The open IO domain is indicated by the green boundary, while the MS is indicated by the red boundary. The bathymetric gradient shows that most of the MS is very shallow, generally less than 100 m deep, whereas depth increases rapidly toward the western IO, exceeding 5,000 m in the deepest offshore area. The bathymetric contours illustrate the transition from the shallow waters around Sumatra and the offshore islands to the deep open ocean basin.

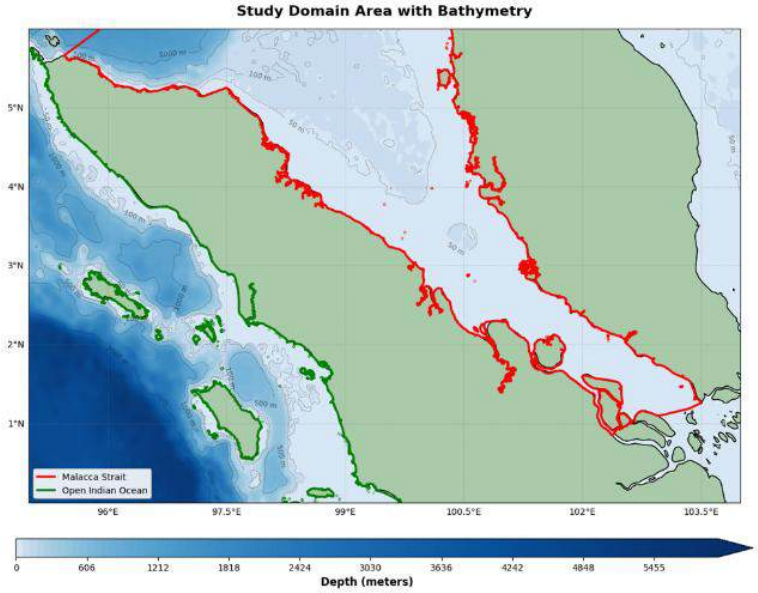


Figure 1. Map of study area and bathymetry of the Malacca Strait and the adjacent Indian Ocean, showing the regional masks used in the study.

Data Sources & Preprocessing

Daily atmospheric and ocean-surface data were collected for the period January 2000-December 2025. ERA5 reanalysis at a horizontal resolution of 0.25° × 0.25° was used to obtain top net thermal radiation (TNR), 10-m zonal and meridional wind components, total precipitation, and sea surface temperature (SST), whereas significant wave height (SWH) was available at a coarser resolution of 0.5° × 0.5° (Hersbach et al., 2020). To ensure spatial consistency among all variables, the SWH fields were interpolated onto the common 0.25° × 0.25° analysis grid using bilinear interpolation prior to subsequent analyses.

OLR was derived from the ERA5 top net thermal radiation field. Because ERA5 defines top net thermal radiation as positive downward, whereas OLR is conventionally expressed as upward longwave flux, the sign was reversed prior to analysis according to the standard ECMWF convention by (Hersbach et al., 2020) and written as follows:

$$OLR = -TNR \quad (1)$$

where TNR is the ERA5 top net thermal radiation W/m^2. This sign reversal converts

© 2026 Dept. of Geophysics Hasanuddin University

the ERA5 downward-positive convention into the standard meteorological convention for OLR, in which larger positive values represent greater outgoing longwave radiation emitted from the Earth-atmosphere system to space.

Daily sea surface salinity (SSS) was obtained from the Copernicus Marine Service and interpolated onto the common 0.25° × 0.25° analysis grid to match the ERA5 products. Daily principal components and amplitudes of the OLR-based Madden-Julian Oscillation Index (OMI) were used to identify active MJO conditions and classify each day into one of the eight MJO phases following Kiladis et al. (2014). All datasets were spatially subset to the MS and IO domains before further analysis.

The state of the MJO was classified using the OMI developed by Kiladis et al. (2014) and computed following the open-source implementation of Hoffmann et al. (2021). The OMI is derived from an empirical orthogonal function (EOF) analysis of 20-96-day bandpass-filtered OLR anomalies averaged over 20°S-20°N, producing two leading principal components (PC1 and PC2) that describe the amplitude and propagation of the MJO.

Following Wheeler & Hendon (2004) and Kiladis et al. (2014), the daily MJO amplitude (A) was calculated as:

$$A = \sqrt{PC1^2 + PC2^2} \quad (2)$$

where A represents the strength of the MJO signal.

The MJO phase was determined from the angular position of the two principal components in the PC1-PC2 phase space (Wheeler & Hendon, 2004),

$$\theta = \text{atan2}\,(PC1, PC2) \quad (3)$$

where θ is the phase angle measured counterclockwise from the positive PC1 axis.

The phase angle (θ) was subsequently divided into eight equal 45° sectors, corresponding to the eight canonical MJO phases defined by Wheeler & Hendon (2004) and Kiladis et al. (2014), using the floor discretization function (Hoffmann et al., 2021) and is written as follows:

$$\text{Phase} = \left\lfloor \frac{\theta + 180^\circ}{45^\circ} \right\rfloor + 1, \quad (1 \le \text{Phase} \le 8), \quad (4)$$

where the phase index is wrapped cyclically such that values exceeding Phase 8 return to Phase 1.

Following the standard practice, only days with OMI amplitude ≥ 1 were classified as active MJO events, whereas days with amplitude < 1 were excluded to avoid contamination from weak or poorly defined MJO conditions. Although the multivariate Real-time Multivariate MJO (RMM) index (Wheeler & Hendon, 2004) remains widely used, the OMI was selected because it is derived solely from OLR observations, making it more directly linked to the convective and radiative processes investigated in this study.

Power Spectral Density (PSD) Analysis

PSD analysis was performed to identify the dominant temporal variability of regional-mean OLR anomalies associated with the MJO. The PSD was estimated using Welch's method (Welch, 1967), as implemented in the *scipy.signal.welch* function of the SciPy scientific computing library (Virtanen et al., 2020). Welch's method with the window length of 1024 days; overlap percentage of 50%, and the window type Hann window may improve the statistical stability of spectral estimates by dividing the time series into overlapping segments, applying a window function to each segment, computing the modified periodogram of every segment, and averaging the resulting spectra to reduce the variance inherent in the classical periodogram. The resulting frequency spectrum was converted to oscillation periods. Spectral peaks within the 30-90-

© 2026 Dept. of Geophysics Hasanuddin University

day band were interpreted as characteristic signatures of the MJO variability.

Phase Composite and Regional Mean Analysis

Prior to the composite analysis, daily anomaly fields were computed to isolate the intraseasonal variability. The climatological reference period used for this formulation was 2000 to 2025. Daily climatologies were first established by calculating the long-term average for each specific day of the year across the entire 26-year period. Daily anomaly fields were then formulated by subtracting this day-of-year climatological mean from the raw daily observations. Once the anomalies were calculated, they were grouped according to the eight OMI phases to characterize the atmospheric and oceanic conditions associated with each active MJO phase. Composite maps were subsequently obtained by averaging all daily anomaly fields belonging to the same phase, following standard climate composite techniques (Wheeler & Hendon, 2004; Wilks, 2011).

$$\bar{X}'_p(i,j) = \frac{1}{N_p}\sum_{k=1}^{N_p} X'_k(i,j) \qquad (5)$$

where $\bar{X}'_p(i,j)$ is the composite anomaly for phase p, N_p is the number of active MJO days assigned to that phase, and $X'_k(i,j)$ is the anomaly field on the k-th day.

To quantify the temporal evolution within each study region, regional mean anomalies were calculated by averaging all grid cells within the MS and eastern IO domains (von Storch & Zwiers, 1999; Wilks, 2011),

$$\bar{X}'_R(t) = \frac{1}{N_R}\sum_{i=1}^{N_R} X'_i(t) \qquad (6)$$

where N_R is the number of grid cells within region R. The regional means were subsequently averaged by MJO phase to compare the magnitude and evolution of atmospheric and ocean-surface responses between the two domains.

Results and Discussion

Distribution of Active MJO Days

The analysis of the 2000–2025 period identifies a total of 5,513 active MJO days, revealing significant variations in occurrence among the eight phases. The highest concentration was found in phase 5, which accounted for 796 days (14.4% of the total), closely followed by phase 4 (787 days, 14.3%) and phase 8 (784 days, 14.2%). Conversely, the lowest count occurred in phase 6, representing just 552 days (10.0%), as depicted in Figure 2.

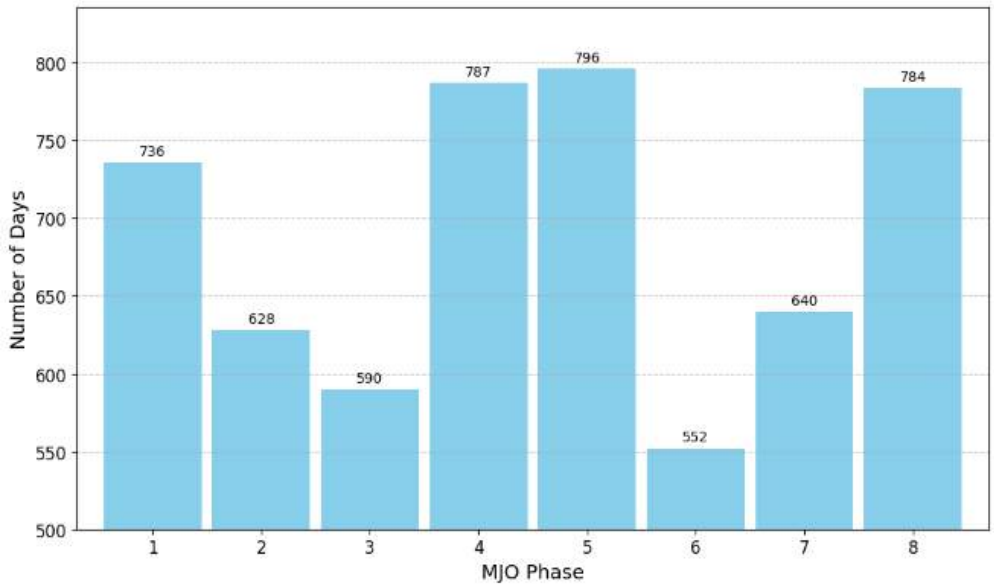


Figure 2. Number of Active MJO days in phases 1-8 during 2000-2025.

© 2026 Dept. of Geophysics Hasanuddin University

This phase-to-phase variation in active-day counts highlights differences in the occurrence and persistence of active MJO conditions. However, we acknowledge that the number of active days alone cannot directly represent propagation speed, as these totals are influenced by a combination of multiple factors, including event duration, overall event frequency, and amplitude persistence. MJO propagation is heavily dependent on coupled large-scale circulation and moist convective processes (Adames et al., 2017). Therefore, while the relatively high number of active days observed in phases 4–5 aligns with the longer residence times over the Maritime Continent reported by Yadav & Straus (2017), who found that events can stall or propagate slowly in this region, this metric alone only suggests, rather than directly proves, variations in propagation speed across our study period.

Intraseasonal Outgoing Longwave Radiation (OLR) Variability

PSD analysis shows clear intraseasonal variability in the regional-mean OLR anomaly for both the MS and the adjacent IO, with both regions peaks at approximately 43-45 days (Figure 3). The IO reached a maximum spectral power at about 39-43 days (PSD ≈ 39), while the MS peaked over a broader 26-44-day band with lower power (PSD ≈ 25). This difference indicates that the regional convective signal was stronger and more coherent over the open IO, although the weaker spectral power in the MS does not imply an absence of MJO-related variability; the intraseasonal signal remains detectable but is less pronounced in the regional OLR variance.

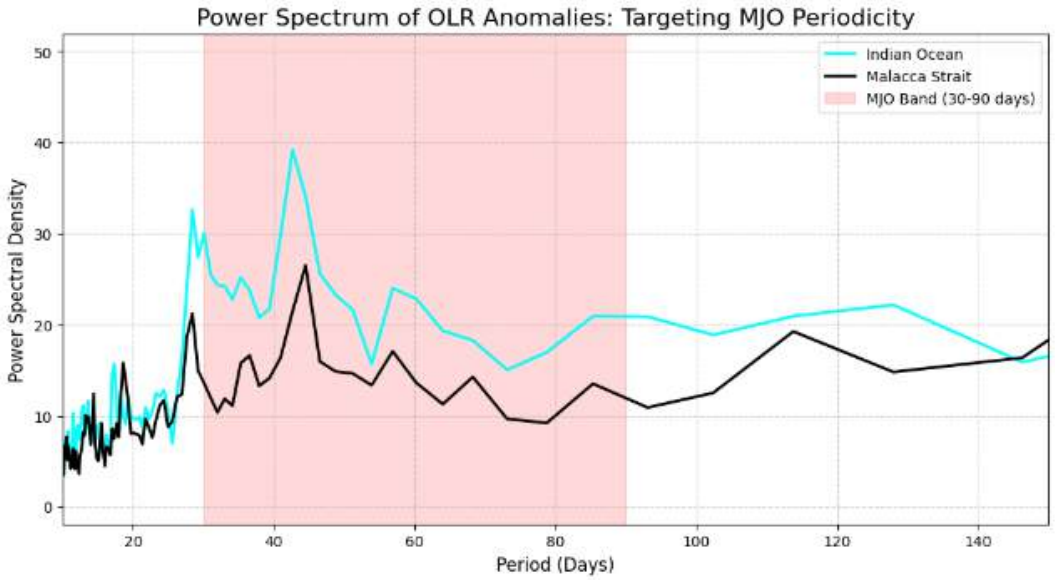


Figure 3. PSD plot of regional-mean OLR anomalies over the Malacca Strait (black) and the Indian Ocean (cyan) during 2000-2025. The shaded area represents the 30-90-day MJO intraseasonal period.

The dominant 43-45 days period found in this study was consistent with the established temporal characteristics of the MJO, found by Lin (2022), which showed that tropical wavenumber-frequency spectra commonly exhibited enhanced MJO power within the 30-60-day range, particularly in large-scale OLR and zonal-wind variability. Similarly, research by Neena et al. (2022) analyzed the OLR and atmospheric circulation data spanning from 1979-2019 and revealed that the wavenumber-frequency analysis identified MJO-related convective variability within the 30-90 day period. The spatial distribution of MJO-filtered OLR variance showed pronounced activity over the IO and several other tropical ocean basins. Among the three regional domains examined, the IO exhibited the largest

© 2026 Dept. of Geophysics Hasanuddin University

standard deviation of the regional MJO index, indicating stronger MJO-related convective variability than in the selected Pacific and Atlantic domains. In addition, the comparatively strong MJO-related OLR variability over the Indian Ocean is consistent with the large amplitude of MJO-filtered OLR anomalies and the strong tropospheric convection-circulation coupling reported for this region. Previous studies also show that MJO evolution involves interactions among column moisture, large-scale circulation, cloud processes, and surface turbulent fluxes, although no single process can be identified as the sole cause of the larger spectral power observed in the present study (Kim et al., 2018; Jiang et al., 2020; Neena et al., 2022).

OLR and Surface-Wind Response during MJO Active Phase in Malacca Strait and Indian Ocean

OLR represents the thermal infrared energy emitted by the Earth-atmosphere system to space. Because deep convective clouds have cold, high tops that emit less longwave radiation, negative OLR anomalies are a standard proxy for enhanced deep convection, while positive anomalies indicate suppressed convection. Phase composites of OLR can consequently describe the location, strength, and temporal evolution of MJO-related convection (Barrett et al., 2021; Zheng et al., 2024; Veerbhan & Kumar, 2025).

OLR and surface-wind composites (Figure 4) show a transition from suppressed convection during phases 1-3 to enhanced convection during phases 4-6. The IO generally exhibits stronger OLR anomalies than the MS, with the strongest negative anomalies occurring during the enhanced-convection phases. In phase 6, both regions show strong negative anomalies, reaching approximately -13.88 W/m^2. The convective signal weakens during phase 7 and reverses to positive anomalies in phase 8, while the surface-wind circulation changes markedly between phases 1-3 and 4-6.

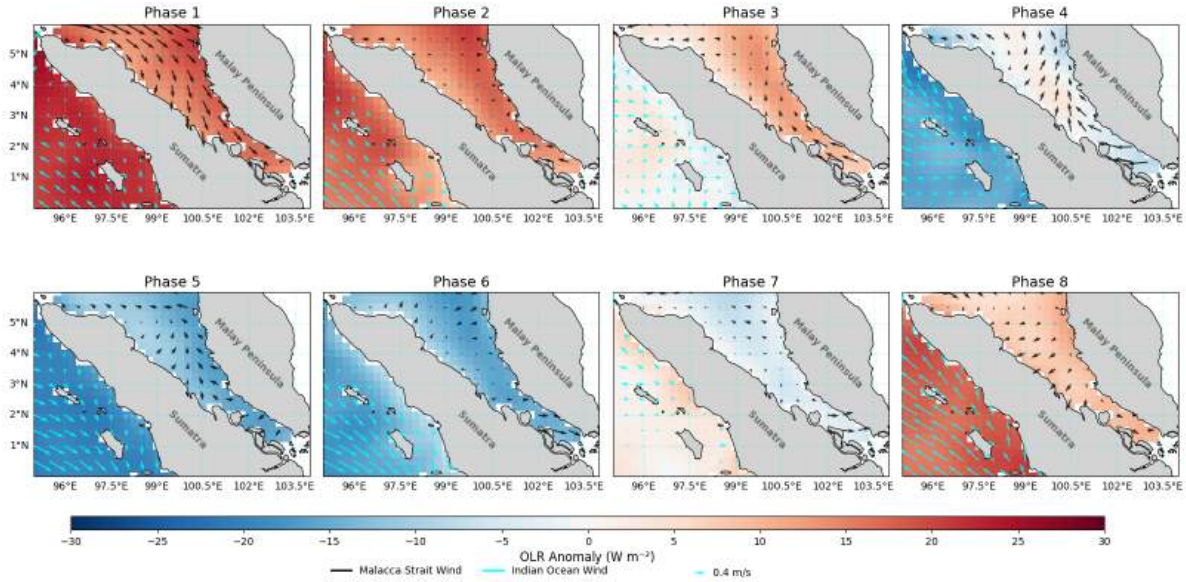


Figure 4. Spatial composites of OLR and 10-m surface-wind anomalies. Black vectors represent the Malacca Strait and cyan vectors represent the Indian Ocean during active MJO phases 1-8 for 2000-2025.

The shifting from positive OLR anomalies in phases 1–3 to negative anomalies in phases 4–6 (as depicted in Figure 5) represents the eastward development of the MJO convective system from the eastern Indian Ocean toward the western MC. The earlier decrease in OLR over the IO during phase 3, followed by stronger negative anomalies during phases 4-5, suggested that enhanced convection initially intensified

© 2026 Dept. of Geophysics Hasanuddin University

over the open ocean before extending toward the Malacca Strait. Kang et al. (2022) reported a similar phase evolution over the southern MC, where low-level zonal wind convergence strengthened during phase 4, while upward motion and precipitation peaked in phase 5. Westerly lower-tropospheric wind anomalies also accompanied the phase 5 precipitation increase. Therefore, the strongest negative OLR anomaly observed during phase 5 is consistent with the established sequence from low-level convergence to intensified deep convection.

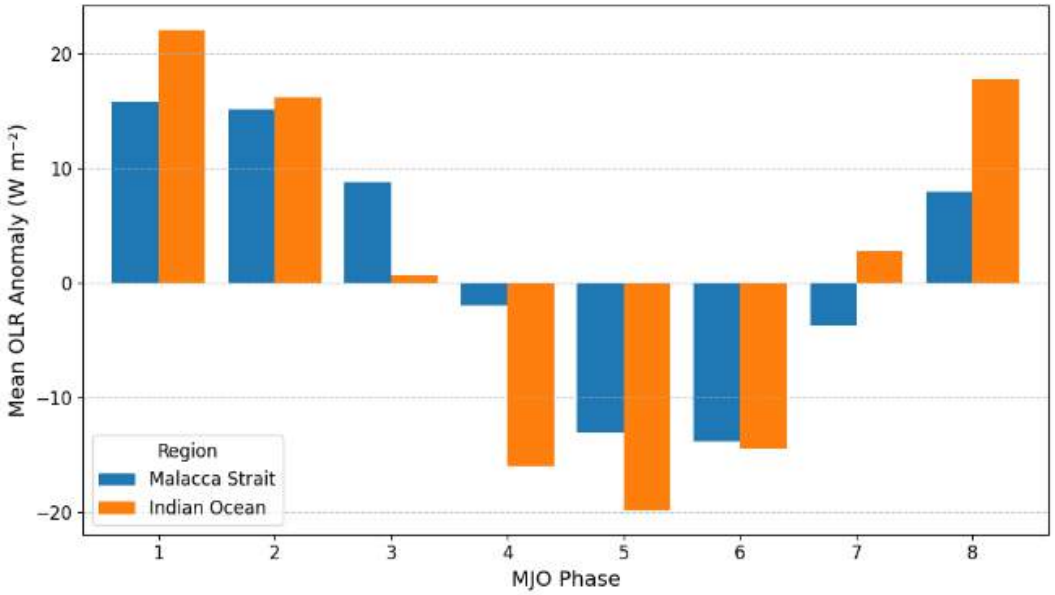


Figure 5. Regional-mean OLR anomaly during MJO phases 1-8. Bars represent the spatially averaged OLR anomalies for each regional domain. Positive values indicate suppressed convection, whereas negative values indicate enhanced convection.

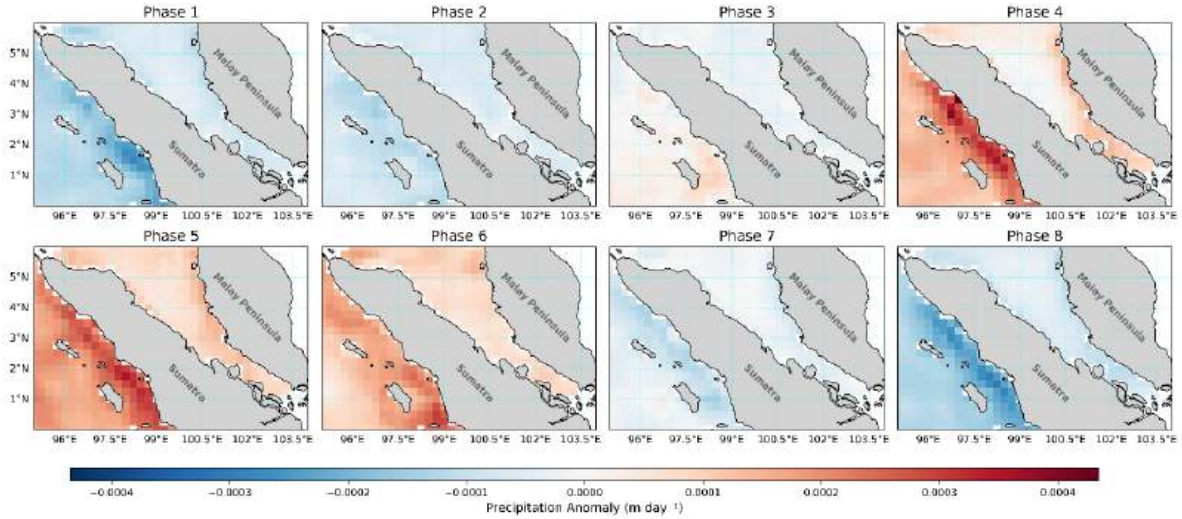


Figure 6. Spatial composite precipitation anomalies during MJO phases 1-8 over the Malacca Strait and the adjacent Indian Ocean during active MJO phases 1-8 for 2000-2025.

The larger negative OLR anomalies over the IO during phases 4-5 are consistent with enhanced MJO convection over the eastern IO and western MC. Karlowska et al. (2024) and Barrett et al. (2021) similarly reported enhanced convection and stronger negative OLR anomalies over the eastern IO during active MJO phases, before the MJO propagated into the MC. However, these studies did not specifically examine the MS or quantify the difference in OLR response between the open ocean and the strait. The present results further show that the OLR response in the MS was weaker

© 2026 Dept. of Geophysics Hasanuddin University

and more spatially heterogeneous than in the IO. During phases 4 and 5, the spatial standard deviation of OLR anomalies was 3.76 and 2.41 W/m^2 in the MS, compared with 1.66 and 1.06 W/m^2 in the IO, respectively. The larger spatial variability in the MS indicates a less uniform convective response, which may contribute to the weaker regional-mean anomaly through spatial cancellation. This contrast suggests that the MJO-related OLR response observed over the open IO may not be directly representative of the response within the semi-enclosed MS.

Response of Precipitation during MJO Active Phase in Malacca Strait and Indian Ocean

The spatial composites in Figure 6 showed a clear phase-dependent evolution of precipitation anomalies over the IO and MS. Negative anomalies dominated phases 1-2, followed by increasing rainfall during phases 4-6, with the strongest and most extensive positive anomalies over the eastern IO and western waters of Sumatra. A two-tailed Student's t-test confirms that these positive precipitation anomalies across phases 4-6 are highly statistically significant ($p < 0.001$) for both regional domains. It indicates a robust MJO-driven convective signal. Precipitation decreased again during phases 7–8. Compared with the IO, the MS generally showed weaker and less spatially continuous anomalies.

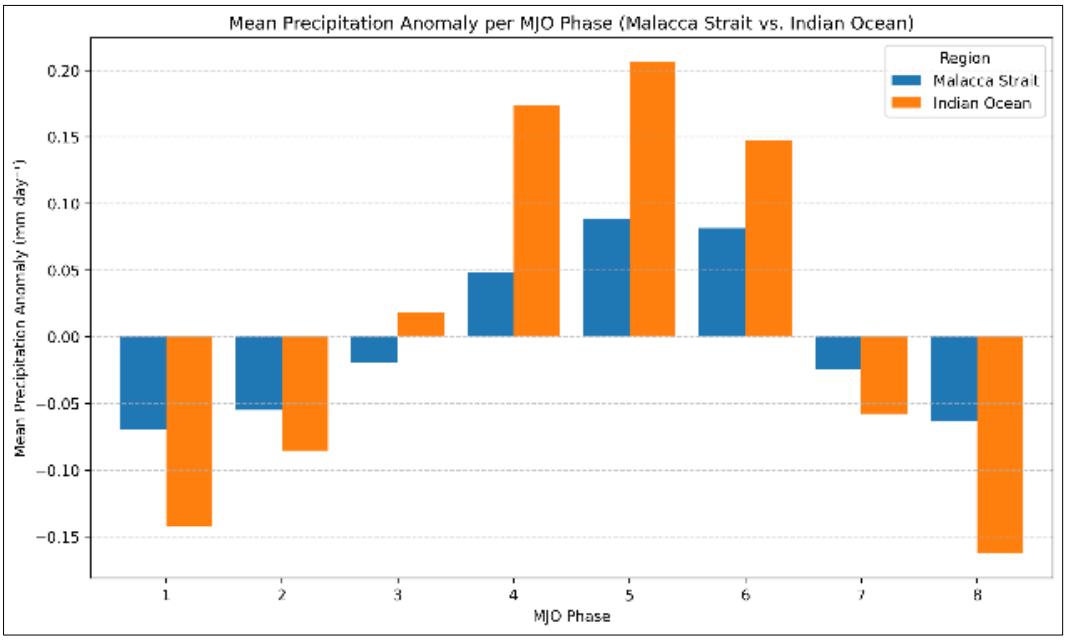


Figure 7. Regional-mean precipitation anomaly during MJO phases 1-8. Bars represent the spatially averaged precipitation anomalies for each regional domain.

Figure 7 confirmed a similar sequence of patterns in both regions, although the IO consistently showed larger amplitudes than the MS. The IO experienced a pronounced rainfall peak in phase 5, more than twice as large as that in the MS. Conversely, dry anomalies during phase 8 were also substantially stronger over the open ocean. The divergence in phase 3, where the IO showed a weak positive anomaly while the MS remained slightly negative, marked the earliest onset of the wet phase over the open water.

The positive precipitation anomalies during phases 4–6 are in line with the enhanced oceanic rainfall reported over the western MC during active MJO conditions. Kim et al. (2022) found that oceanic precipitation increased during phases 4–5, with the largest ocean-to-land precipitation ratio occurring in phase 5. In contrast, precipitation weakened during phases 1–2 and 7–8, when the active MJO convection

© 2026 Dept. of Geophysics Hasanuddin University

was located outside the study region. The corresponding negative OLR anomalies during phases 4–6 provide additional evidence of greater high-cloud cover and deep convective activity during the wetter phases, whereas positive OLR anomalies coincided with reduced precipitation during the suppressed phases.

The larger precipitation anomalies over the IO were consistent with the stronger moisture sensitivity of oceanic rainfall reported by Chen et al. (2021). In phase 5, the IO anomaly was more than twice that over the MS, although both regions followed a similar phase evolution. The weaker MS response may reflect the influence of nearby landmasses, coastal circulation, and the diurnal cycle, which were not separated in previous analyses of phases 4-5 over the western MC (Kim et al., 2022). Therefore, precipitation responses observed over the open IO may not directly represent rainfall variability within the MS during active MJO phases.

Response of Sea Surface Temperature (SST) during MJO Active Phase in Malacca Strait and Indian Ocean

SST is a critical indicator of air-sea interaction during MJO episodes because differences in cloud cover, surface winds, and air-sea heat fluxes can modify the upper-ocean heat balance (Karlowska et al., 2024). Spatial composites (Figure 8) showed positive SST anomalies through phases 1–4, which reach their largest extent over the IO in phases 2–3 before weakening by phase 4, especially in the MS. Negative anomalies then emerged across both regions in phases 5–7, with the most extensive cooling observed over the IO in phase 6, followed by a peak cooling response over the MS in phase 7. This indicates a one-phase lag in the peak SST cooling response of the MS relative to the IO. The cooling anomalies gradually weakened during phases 7–8.

Positive SST anomalies during phases 1–3 indicate warming before the development of strong convection, consistent with reduced cloud cover and weaker winds reported during the early MJO phases (Cui et al., 2024). SST remained slightly positive in phase 4 despite the onset of negative OLR and increased precipitation, suggesting a lagged ocean response to atmospheric forcing. SST subsequently became negative during phases 5–7, consistent with MJO-related cooling associated with reduced solar heating, evaporation, and mixing (Chandra et al., 2024). The evolution of negative SST anomalies reveals a distinct temporal lag between the two regional domains. Maximum cooling in the Malacca Strait peaked during phase 7, occurring one full phase later than the phase 6 peak observed over the open Indian Ocean. This delayed thermal response within the strait suggests that the local upper-ocean heat balance is not driven solely by instantaneous atmospheric forcing, but is instead modulated by complex regional oceanographic dynamics. Given the shallow bathymetry of the Malacca Strait, the water column is continuously subjected to intense tidal mixing. This strong vertical mixing can redistribute heat throughout the water column. Horizontal advection driven by coastal currents may continuously transport varying water masses from the adjacent Andaman and South China Seas. While a complete oceanic heat budget analysis would be necessary to quantify these individual driving factors, the combination of restricted coastal geometry, strong tidal mixing, and horizontal advection provides a highly plausible physical framework for the lagged SST response observed within the strait (Chen et al., 2014; Kurniawan et al., 2021).

© 2026 Dept. of Geophysics Hasanuddin University

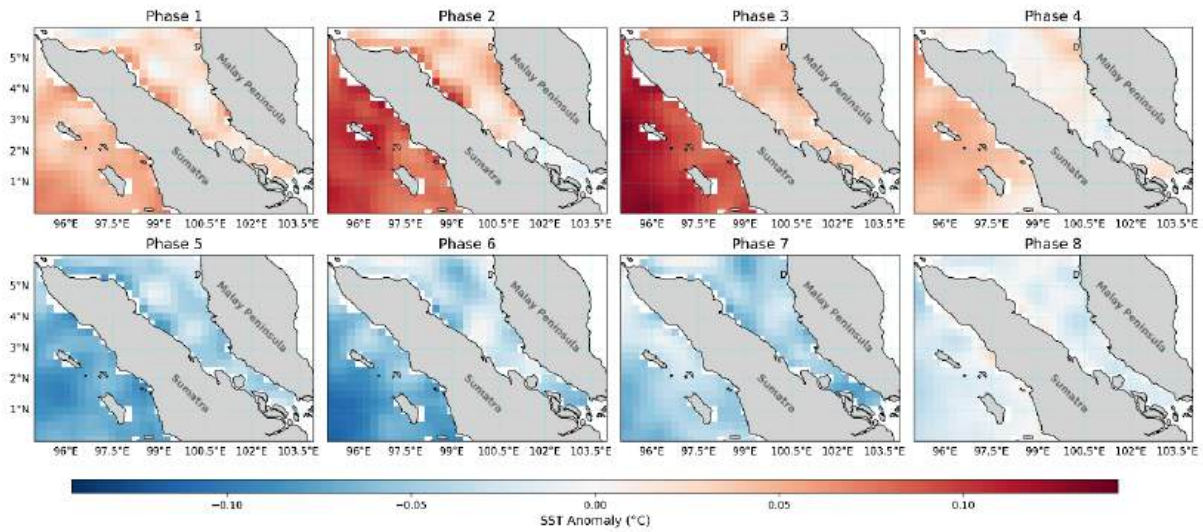


Figure 8. Spatial composites of sea surface temperature anomalies over the Malacca Strait and adjacent Indian Ocean during active MJO phases 1-8 for 2000-2025.

The regional means of SST, as depicted in Figure 9, confirmed that there is a shift from warming to cooling across MJO phases. The SST response exhibited a coherent warm-to-cool cycle across the MJO. Maximum warming was observed in phase 3 for both regions, but the amplitude over the IO was nearly three times that in the MS. The cooling phase extended from phases 5 to 7, with the strongest negative anomaly over the IO occurring in phase 6. The MS cooling was consistently weaker and peaked later in phase 7, reflecting the combined effects of reduced wind fetch and shallower mixed-layer dynamics that dampened the thermal response. Overall, both regions displayed a similar warm-to-cool sequence, but the IO generally exhibited larger SST anomaly amplitudes.

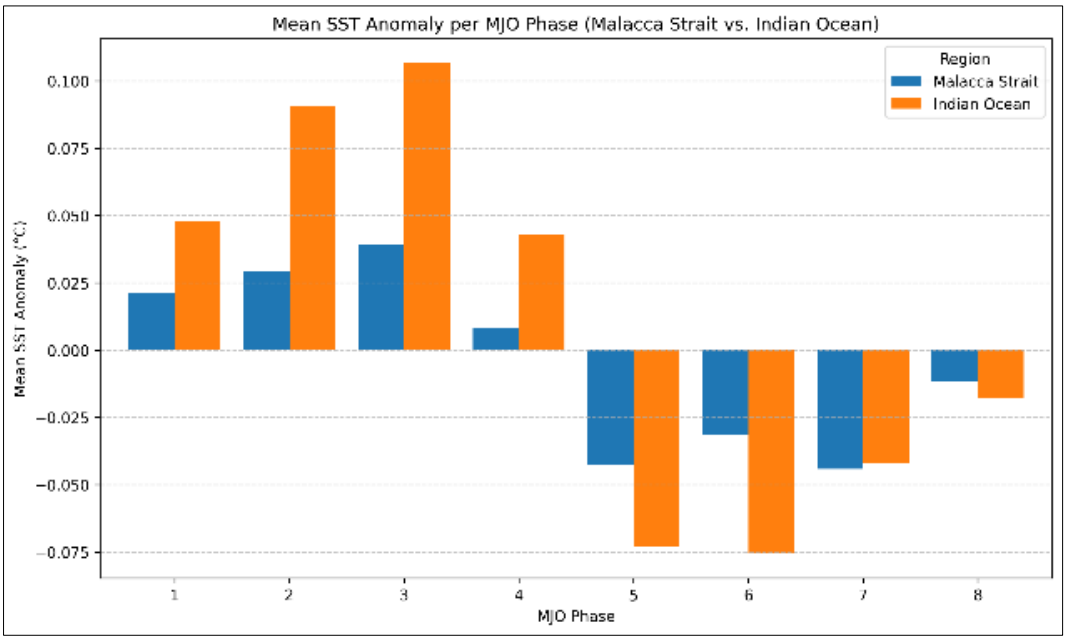


Figure 9. Regional-mean SST anomaly during MJO phases 1-8. Bars represent the spatially averaged SST anomalies for each regional domain.

© 2026 Dept. of Geophysics Hasanuddin University

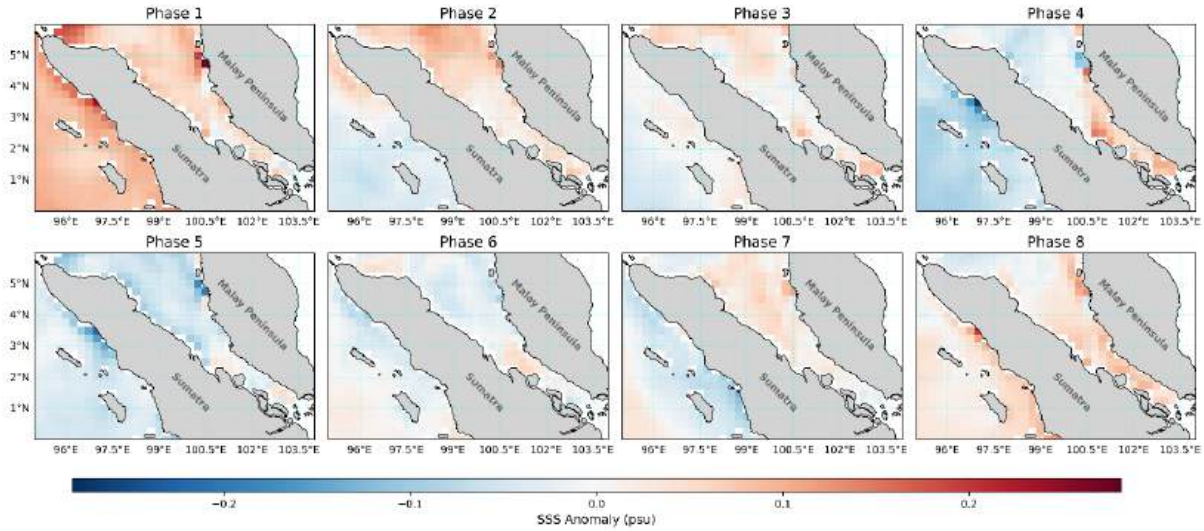


Figure 10. Spatial composites of sea surface salinity anomalies over the Malacca Strait and adjacent Indian Ocean during active MJO phases 1-8 for 2000-2025.

The narrow, shallow bathymetry of the strait likely strengthens tidal and wind-driven circulation, promoting upwelling and horizontal advection that dampen the surface thermal signal (Mandal et al., 2021), while net surface heat flux dominates the large-scale mixed-layer response and ocean advection becomes more important at smaller scales (Karlowska et al., 2024). The shallow water column in the strait also allows wind mixing to penetrate the full depth and distribute the heat over a smaller volume, further reducing the surface response compared with the deeper, more sensitive mixed layer of the open IO.

Sea Surface Salinity Response during MJO Active Phase in Malacca Strait and Indian Ocean

SSS reflects the surface freshwater balance, where positive anomalies indicate saltier conditions and negative anomalies indicate freshening (Yu, 2023). Spatial composites (Figure 10) showed positive anomalies in both regions during phase 1. During phases 2 and 3, the MS stayed mostly positive while the IO shifted slightly negative, and the most extensive IO freshening developed in phase 4, when the MS instead showed adjacent positive and negative anomalies on its eastern and western sides. The low regional mean in phase 4 resulted from spatial heterogeneity (spatial standard deviation of 0.050 psu in the MS versus 0.026 psu in the IO), where these adjacent positive and negative anomalies largely canceled each other out. Negative anomalies were stronger across the MS in phase 5 as IO freshening weakened. Both regions show weak negative means in phase 6 (about -0.012 psu in the MS and -0.007 psu in the IO), and a clear contrast appeared in phase 7, with positive MS anomalies against continued IO freshening, before positive anomalies prevailed in both regions by phase 8.

Additionally, the regional mean of SSS over the IO shifted from a positive anomaly in phase 1 to negative anomalies during phases 2–7, with the strongest freshening occurred in phase 4 (Figure 11). The MS showed a less regular pattern, as positive anomalies weakened during phases 1–3, approached zero in phase 4, and became weakly negative during phases 5–6. The near-zero mean in phase 4 resulted from adjacent positive and negative anomalies that largely canceled each other in the regional average, as shown in Figure 10.

© 2026 Dept. of Geophysics Hasanuddin University

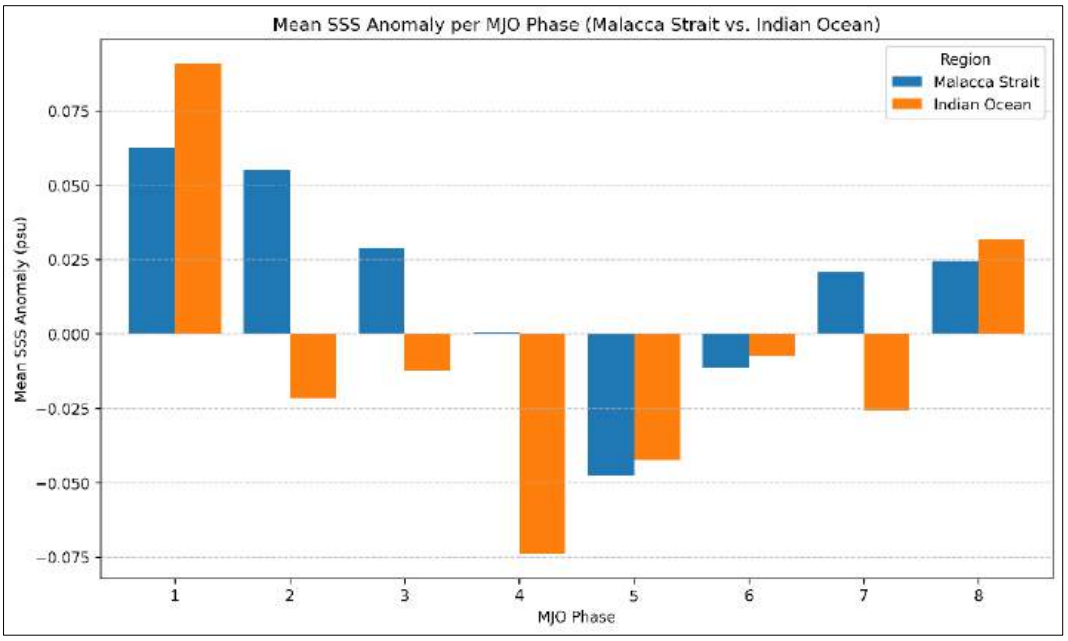


Figure 11. Regional-mean SSS anomaly during MJO phases 1-8. Bars represent the spatially averaged SSS anomalies for each regional domain.

These patterns generally followed variations in freshwater input and upper-ocean redistribution during the MJO cycle, where reduced precipitation in phases 1-2 limited surface freshening, while increased rainfall during the transition toward active convection deposited fresher, less dense water at the surface. Near-surface rain layers that developed during this transition and were later eroded by stronger wind mixing (Shackelford et al., 2024) are consistent with the IO freshening peak seen here in phase 4. The weaker and delayed MS freshening signal, however, indicates that SSS is not solely controlled by precipitation. Horizontal advection and turbulent mixing jointly shape salinity variability in the equatorial IO (Chi et al., 2021), while MS salinity has separately been linked to water transport and inflow salinity (Zhao et al., 2025). The present comparison suggests that precipitation dominates the IO signal, whereas tidal mixing and exchange with adjacent water masses play a larger role in the MS.

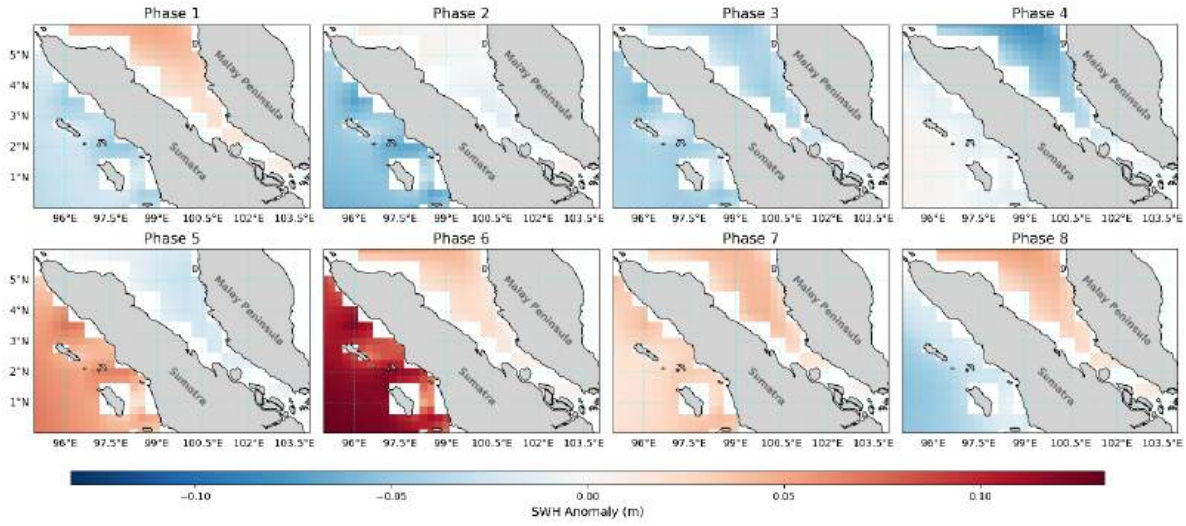


Figure 12. Spatial composites of significant wave height anomalies over the Malacca Strait and adjacent Indian Ocean during active MJO phases 1-8 for 2000-2025.

© 2026 Dept. of Geophysics Hasanuddin University

Significant Wave Height Response during MJO Active Phase in Malacca Strait vs Indian Ocean

The spatial composites in Figure 12 showed contrasting phase-dependent SWH responses over the IO and MS. During phase 1, positive anomalies occurred over much of the MS, whereas negative anomalies dominated the IO. Negative anomalies became more widespread during phases 2–4, with the strongest reduction over the IO during phases 2–3 and over the MS during phase 4. The pattern changed during phase 5, when positive anomalies developed over the IO, while the MS remained weakly negative. Positive anomalies then expanded across both regions during phases 6–7, with the largest and most extensive increase over the IO in phase 6. A regional contrast returned in phase 8, when positive anomalies persisted over the MS, but negative anomalies reappeared over the IO.

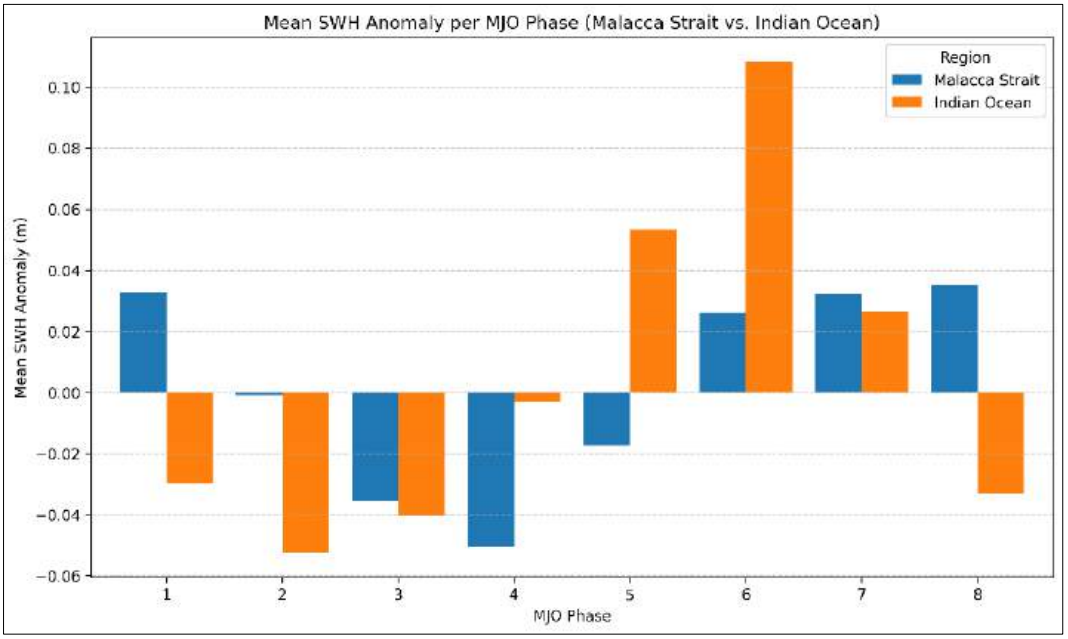


Figure 13. Regional-mean SWH anomaly during MJO phases 1-8. Bars represent the spatially averaged SWH anomalies for each regional domain.

The phase-dependent SWH response was closely associated with surface-wind forcing during the MJO cycle. The stronger IO response in phases 5–6 coincided with stronger wind anomalies in the preceding phases, which peaked in phases 4–5, representing a lag of approximately one phase or 5–7 days. Thus, the phase 6 SWH peak was likely related to accumulated wind forcing rather than an instantaneous response. Previous work has also reported MJO-related wave responses in the Riau Archipelago (Napitupulu et al., 2022). In contrast, the MS showed a weaker and less phase-coherent response, which may be partly related to its constrained wave environment and the effects of fetch, bathymetry, and topographic sheltering (Xu et al., 2026). However, these factors were not directly evaluated in the present study.

The regional means in Figure 13 show that the SWH response differed between the IO and MS. A stronger positive response was observed in the IO, with a peak in phase 6, whereas a weaker and more variable response was observed in the MS, with positive anomalies present during phases 6-8. The stronger response in the IO may be associated with contributions from locally generated waves and remote swell, whereas the weaker response in the MS may be partly related to its restricted fetch and surrounding landmasses, which limit wave development (Gao et al., 2023). The broader and delayed response in the MS

© 2026 Dept. of Geophysics Hasanuddin University

indicates that the SWH response to MJO-related wind forcing differed between the semi-enclosed strait and the open IO.

Spatial averaging over the small, heterogeneous MS domain contributes to its reduced amplitude, since adjacent anomalies partly cancel (Mandal et al., 2021), but physical mechanisms, including fetch limitation, shallow bathymetry, and tidal mixing, also genuinely dampen the MJO signal in the strait. Distinguishing these contributions would require higher-resolution data.

Conclusion

This study found clear differences in MJO-related variability between the Malacca Strait (MS) and the eastern Indian Ocean (IO). Both regions showed intraseasonal OLR variability within the MJO timescale, but the IO exhibited stronger spectral power and atmospheric responses, particularly during the enhanced convection phases. The ocean-surface responses also differed between the two regions, with SST changing from warming during phases 1–4 to cooling during phases 5–7, reaching maximum cooling in phase 6 in the IO and one phase later, in phase 7, in the MS. SSS freshening and SWH responses were also stronger and more consistent in the IO than in the MS. Overall, the results show that the magnitude, spatial pattern, and timing of MJO-related variability differ between the open IO and semi-enclosed MS, indicating that regional geographical and oceanographic conditions shape the ocean-surface response to the MJO.

Acknowledgements

This research was funded by DIPA Universitas Riau through the Riset Peningkatan Kapasitas Dosen Muda (RIPEKDOM) research scheme managed by the Institute for Research and Community Service Universitas Riau (LPPM UNRI), based on Contract No. 591/UN.19.5.1.3/AL.04.03/2026. The author would like to thank Universitas Riau and LPPM UNRI for the financial support and administrative facilities provided during this research.

Author Contribution

NAA contributed to conceptualization, methodology, formal analysis, investigation, visualization, project administration, writing the original draft, and reviewing and editing the manuscript. ADH contributed to conceptualization, data curation, software, formal analysis, visualization, and reviewing and editing the manuscript. BA contributed to supervision. RP contributed to validation. M contributed to supervision. II contributed to validation. R contributed to supervision and validation. All authors read and approved the final manuscript.

Conflict of Interest

The authors declare that there are no financial or personal relationships that could have influenced the research presented in this manuscript.

References

Adames, Á. F., Kim, D., Sobel, A. H., Del Genio, A., & Wu, J. (2017). Characterization of Moist Processes Associated with Changes in the Propagation of the MJO with Increasing CO_2. *Journal of Advances in Modeling Earth Systems*, 9(8), 2946–2967. https://doi.org/10.1002/2017MS001040

Azuga, N. A., Galib, M., & Elizal, E. (2020). Analyzing the Effect of Indian Ocean Dipole Phenomenon to the Anomalies Distribution of Sea Surface Temperature in West Sumatera. *Asian Journal of Aquatic Sciences*, 3(3), 260–270.

Baeda, A. Y., Pao'tonan, C., & Abdullah, D. (2019). The Correlation between Sea Surface Temperature and MJO

© 2026 Dept. of Geophysics Hasanuddin University

Incidence in Indonesian Waters. *IOP Conference Series: Earth and Environmental Science*, 235, 012020. https://doi.org/10.1088/1755-1315/235/1/012020

Barrett, B. S., Densmore, C. R., Ray, P., & Sanabia, E. R. (2021). Active and Weakening MJO Events in the Maritime Continent. *Climate Dynamics*, 57(1), 157–172. https://doi.org/10.1007/s00382-021-05699-8

Bi, Y., & Yuan, C. (2026). Changes in the Impact of MJO-Induced Oceanic Kelvin Waves on ENSO during 1981-2021. *Atmospheric and Oceanic Science Letters*, 100792. https://doi.org/10.1016/j.aosl.2026.100792

Chandra, A., Keenlyside, N., Svendsen, L., & Singh, A. (2024). Processes Driving Subseasonal Variations of Upper Ocean Heat Content in the Equatorial Indian Ocean. *Journal of Geophysical Research: Oceans*, 129(2), e2023JC020074. https://doi.org/10.1029/2023JC020074

Chen, H., Malanotte-Rizzoli, P., Koh, T. Y., & Song, G. (2014). The relative importance of the wind-driven and tidal circulations in Malacca Strait. *Continental Shelf Research*, 88, 92–102. https://doi.org/10.1016/j.csr.2014.07.012

Chen, S., Wong, N. Z., Ma, D., Chan, P. W., & Kuang, Z. (2021). Dependence of Precipitation on Precipitable Water Vapor over the Maritime Continent and Implications to the Madden-Julian Oscillation. *Geophysical Research Letters*, 48, e2021GL094648. https://doi.org/10.1029/2021GL094648

Chi, N.-H., Lien, R.-C., & D'Asaro, E. A. (2021). The Mixed Layer Salinity Budget in the Central Equatorial Indian Ocean. *Journal of Geophysical Research: Oceans*, 126(6), 1–18. https://doi.org/10.1029/2021JC017280

Cui, Z., Li, Y., Guo, Y., & Wang, F. (2024). Impacts of the Madden-Julian Oscillation on Marginal Sea Heatwaves of the Southeastern Tropical Indian Ocean. *Journal of Geophysical Research: Oceans*, 129(7), e2023JC020867. https://doi.org/10.1029/2023JC020867

Da Silva, N. A., & Matthews, A. J. (2021). Impact of the Madden-Julian Oscillation on Extreme Precipitation over the Western Maritime Continent and Southeast Asia. *Quarterly Journal of the Royal Meteorological Society*, 147(739), 3434–3453. https://doi.org/10.1002/qj.4136

DeMott, C. A., Klingaman, N. P., & Woolnough, S. J. (2015). Atmosphere-Ocean Coupled Processes in the Madden-Julian Oscillation. *Reviews of Geophysics*, 53(4), 1099–1154. https://doi.org/10.1002/2014RG000478

Du, D., Subramanian, A. C., Han, W., Lim, Y.-K, Hackert, E., & Molod, A. (2025). Assessing the Impact of Satellite Sea Surface Salinity Assimilation on Predicting the MJO Propagation across Maritime Continent in NASA GEOS-S2S-2 Model. *Journal of Climate*, 38(22), 6463–6473. https://doi.org/10.1175/JCLI-D-24-0579.1

Gao, Y., Schmitt, F. G., Hu, J., & Huang, Y. (2023). Probability-Based Wind-Wave Relation. *Frontiers in Marine Science*, 9, 1085340. https://doi.org/10.3389/fmars.2022.1085340

Hersbach, H., Bell, B., Berrisford, P., Hirahara, S., Horányi, A., Muñoz-Sabater, J., Nicolas, J., Peubay, C., Radu, R., Schepers, D., Simmons, A., Soci, C., Abdalla, S., Abellan, X., Balsamo, G., Bechtold, P., Biavati, G., Bidlot, J., Bonavita, M., De Chiara,

© 2026 Dept. of Geophysics Hasanuddin University

G., Dahlgren, P., Dee, D., Diamantakis, M., Dragani, R., Flemming, J., Rorbes, R., Fuentes, M., Geer, Al., Haimberger, L., Healy, S., Hogan, R. J., Hólm, E., Janisková, M., Keeley, S., Laloyaux, P., Lopez, P., Lupu, C., Radnoti, G., de Rosnay, P., Rozum, I., Vamborg, F., Villaume, S., & Thépaut, J. N. (2020). The ERA5 global reanalysis. *Quarterly journal of the royal meteorological society*, 146(730), 1999–2049. https://doi.org/10.1002/qj.3803

Hilmi, I., Ningsih, N. S., Sofian, I., Hanifah, F., & Rizal, A. M. (2018). The study of MJO impact on wave height and wind speed in Indonesian Seas. *IOP Conference Series: Earth and Environmental Science*, 162, 012004.

Hoffmann, C. G., Kiladis, G. N., Gehne, M., & von Savigny, C. (2021). A Python Package to Calculate the OLR-Based Index of the Madden-Julian-Oscillation (OMI) in Climate Science and Weather Forecasting. *Journal of Open Research Software*, 9(1), 9. https://doi.org/10.5334/jors.331

Ikuyajolu, O. J., Van Roekel, L., Brus, S. R., Thomas, E. E., Deng, Y., & Benedict, J. J. (2024). Effects of Surface Turbulence Flux Parameterizations on the MJO: The Role of Ocean Surface Waves. *Journal of Climate*, 37(10), 3011–3036. https://doi.org/10.1175/JCLI-D-23-0490.1

Jiang, X., Adames, Á. F., Kim, D., Maloney, E. D., Lin, H., Kim, H., Zhang, C., DeMott, C. A., & Klingaman, N. P. (2020). Fifty Years of Research on the Madden-Julian Oscillation: Recent Progress, Challenges, and Perspectives. *Journal of Geophysical Research: Atmospheres*, 125(17), e2019JD030911. https://doi.org/10.1029/2019JD030911

Kang, D., Kim, D., Rushley, S., & Maloney, E. (2022). Seasonal Locking of the MJO's Southward Detour of the Maritime Continent: The Role of the Australian Monsoon. *Journal of Climate*, 35(24), 8153–8168. https://doi.org/10.1175/JCLI-D-22-0234.1

Karlowska, E., Matthews, A. J., Webber, B. G. M., Graham, T., & Xavier, P. (2024). The Relative Importance of Ocean Advection and Surface Heat Fluxes during the Madden-Julian Oscillation in a Coupled Ocean-Atmosphere Model. *Journal of Geophysical Research: Oceans*, 129(11), e2024JC021515. https://doi.org/10.1029/2024JC021515

Kiladis, G. N., Dias, J., Straub, K. H., Wheeler, M. C., Tulich, S. N., Kikuchi, K., Weickmann, K. M., & Ventrice, M. J. (2014). A Comparison of OLR and Circulation-Based Indices for Tracking the MJO. *Monthly Weather Review*, 142(5), 1697–1715. https://doi.org/10.1175/MWR-D-13-00301.1

Kim, D., Kang, D., Ahn, M.-S., DeMott, C., Hsu, C.-W., Yoo, C., Leung, L. R., Hagos, S., & Rasch, P. J. (2022). The Madden-Julian Oscillation in the Energy Exascale Earth System Model Version 1. *Journal of Advances in Modeling Earth Systems*, 14(2), e2021MS002842. https://doi.org/10.1029/2021MS002842

Kim, J.-E., Zhang, C., Kiladis, G. N., & Bechtold, P. (2018). Heating and Moistening of the MJO during DYNAMO in ECMWF Reforecasts. *Journal of the Atmospheric Sciences*, 75(5), 1429–1452. https://doi.org/10.1175/JAS-D-17-0170.1

Kurniawan, A., Tay, S. H. X., & Ooi, S. K. (2021). Numerical investigation of tide and sea level anomalies propagation in Malacca Strait. TAO: *Terrestrial, Atmospheric and Oceanic*

© 2026 Dept. of Geophysics Hasanuddin University

Sciences, 32(4), 571–582. https://doi.org/10.3319/TAO.2021.10.12.01

Lee, T., Fournier, S., Gordon, A. L., & Sprintall, J. (2019). Maritime Continent Water Cycle Regulates Low-Latitude Chokepoint of Global Ocean Circulation. *Nature Communications*, 10, 2103. https://doi.org/10.1038/s41467-019-10109-z

Lin, H. (2022). The Madden-Julian Oscillation. *Atmosphere-Ocean*, 60(3-4), 338–359. https://doi.org/10.1080/07055900.2022.2072267

Lumbangaol, A., & Yu, J.-Y. (2026). Energetic Controls of MJO-Modulated Extreme Precipitation over the Maritime Continent: A Composite Analysis. *Climate Dynamics*, 64(4), 1–15. https://doi.org/10.1007/s00382-026-08157-5

Mandal, S., Behera, N., Gangopadhyay, A., Susanto, R. D., & Pandey, P. C. (2021). Evidence of a Chlorophyll "Tongue" in the Malacca Strait from Satellite Observations. *Journal of Marine Systems*, 223, 103610. https://doi.org/10.1016/j.jmarsys.2021.103610

Marshall, A. G., Hendon, H. H., Durrant, T. H., & Hemer, M. A. (2015). Madden Julian Oscillation Impacts on Global Ocean Surface Waves. *Ocean Modelling*, 96, 136–147. https://doi.org/10.1016/j.ocemod.2015.06.002

Napitupulu, G., Tarya, A., Pratama, I. G. M. Y., & Winardhie, I. S. (2022). Variability Analysis of Significant Wave Heights and Wind Waves in Riau Archipelago Sea Part ALKI 1. *Jurnal Pesisir dan Laut Tropis*, 10(3), 241–255.

Neena, J. M., Suhas, E., & Jiang, X. (2022). Modulation of the Convectively Coupled Kelvin Waves by the MJO over Different Domains. *Journal of Climate*, 35(21), 7025–7039. https://doi.org/10.1175/JCLI-D-21-0641.1

Renkl, C., Oliver, E. C. J., & Thompson, K. R. (2024). Downscaling the Ocean Response to the Madden-Julian Oscillation in the Northwest Atlantic and Adjacent Shelf Seas. *Climate Dynamics*, 62(7), 6719–6744. https://doi.org/10.1007/s00382-024-07233-y

Savarin, A., & Chen, S. S. (2022). Pathways to Better Prediction of the MJO: 2. Impacts of Atmosphere-Ocean Coupling on the Upper Ocean and MJO Propagation. *Journal of Advances in Modeling Earth Systems*, 14(6), e2021MS002929. https://doi.org/10.1029/2021MS002929

Shackelford, K., DeMott, C. A., van Leeuwen, P. J., Mazloff, M. R., & Sun, R. (2024). A Cold Lid on a Warm Ocean: Indian Ocean Surface Rain Layers and Their Feedbacks to the Atmosphere. *Journal of Geophysical Research: Atmospheres*, 129, e2023JD039272. https://doi.org/10.1029/2023JD039272

Thomas, E. A., Bond, T., Kolbusz, J. L., Niyazi, Y., Swanborn, D. J. B., & Jamieson, A. J. (2024). Deep-Sea Ecosystems of the Indian Ocean >1000 m. *Science of the Total Environment*, 957, 176794. https://doi.org/10.1016/j.scitotenv.2024.176794

Veerbhan, K., & Kumar, D. (2025). Understanding Heat Retention and Release through Outgoing Longwave Radiation Dynamics in the Upper Gangetic Alluvial Plain. *World Journal of Advanced Research and Reviews*, 27(1), 1660–1672. https://doi.org/10.30574/wjarr.2025.27.1.2691

Virtanen, P., Gommers, R., Oliphant, T. E., Haberland, M., Reddy, T., Cournapeau, D., Burovski, E., Peterson, P., Weckesser, W., Bright,

© 2026 Dept. of Geophysics Hasanuddin University

J., van der Walt, S. J., Brett, M., Wilson, J., Millman, K. J., Mayorov, N., Nelson, A. R. J., Jones, E., Kern, R., Larson, E., Carey, C. J., Polat, I., Feng, Y., Moore, E. W., VanderPlas, J., & SciPy 1.0 Contributors. (2020). SciPy 1.0: Fundamental Algorithms for Scientific Computing in Python. *Nature Methods,* 17(3), 261–272. https://doi.org/10.1038/s41592-019-0686-2

von Storch, H., & Zwiers, F. W. (1999). *Statistical Analysis in Climate Research*. Cambridge: Cambridge University Press.

Welch, P. D. (1967). The Use of Fast Fourier Transform for the Estimation of Power Spectra: A Method Based on Time Averaging over Short, Modified Periodograms. *IEEE Transactions on Audio and Electroacoustics,* 15(2), 70-73. https://doi.org/10.1109/TAU.1967.1161901

Wheeler, M. C., & Hendon, H. H. (2004). An All-Season Real-Time Multivariate MJO Index: Development of an Index for Monitoring and Prediction. *Monthly Weather Review*, 132(8), 1917–1932. https://doi.org/10.1175/1520-0493(2004)132%3C1917:AARMMI%3E2.0.CO;2

Wilks, D. S. (2011). *Statistical Methods in the Atmospheric Sciences* (3rd ed.). Academic Press. https://doi.org/10.1016/b978-0-12-385022-5.00001-4

Worku, L. Y., Mekonnen, A., & Schreck, C. J. (2020). The Impact of MJO, Kelvin, and Equatorial Rossby Waves on the Diurnal Cycle over the Maritime Continent. *Atmosphere*, 11(7), 711. https://doi.org/10.3390/atmos11070711.

Xavier, P., Rahmat, R., Cheong, W. K., & Wallace, E. (2014). Influence of Madden-Julian Oscillation on Southeast Asia Rainfall Extremes: Observations and Predictability. *Geophysical Research Letters*, 41(12), 4406–4412. https://doi.org/10.1002/2014GL060241

Xu, X., Sasmal, K., & Tkalich, P. (2026). High-Resolution Wave Climate Analysis in Complex Tropical Straits Using Triple-Nested Unstructured WW3 Modeling. *Applied Ocean Research*, 168, 104978. https://doi.org/10.1016/j.apor.2026.104978

Yadav, P., & Straus, D. M. (2017). Circulation Response to Fast and Slow MJO Episodes. *Monthly Weather Review*, 145(5), 1577–1596. https://doi.org/10.1175/MWR-D-16-0352.1

Yu, L. (2023). Connecting Subtropical Salinity Maxima to Tropical Salinity Minima: Synchronization Between Ocean Dynamics and the Water Cycle. *Progress in Oceanography*, 219, 103172. https://doi.org/10.1016/j.pocean.2023.103172

Zhao, Z., Sprintall, J., & Du, Y. (2025). The Interbasin Modulation from Indo-Pacific Climate Modes on the Salinity Transport through the Malacca Strait. *Geoscience Letters*, 12(1), 46. https://doi.org/10.1186/s40562-025-00415-4

Zheng, M., Wu, T., Xin, X., Liu, X., Lu, Y., Jie, W., Xie, C., & Zhou, Y. (2024). Simulation of MJO with Improved Deep Convection Scheme in Different Resolutions of BCC-CSM2 Models. *Climate Dynamics*, 62, 2161–2185. https://doi.org/10.1007/s00382-023-07015-y

© 2026 Dept. of Geophysics Hasanuddin University

ISSN: 2579-5821 (Print)
ISSN: 2579-5546 (Online)
URL address: http://journal.unhas.ac.id/index.php/geocelebes
DOI: 10.70561/geocelebes.v10i2.52858

Jurnal Geocelebes Vol. 10 No. 2, October 2026, 432 – 442

Comparison of Window Scan and Digital Outcrop Model Approaches for Fracture Characterisation Along the Lampung–Panjang Fault Zone

Rezki Naufan Hendrawan, David Kurniawan, Muhammad Eval Juni Wijaya, Luhut Pardamean Siringoringo

Geology Department, Institut Teknologi Sumatera, South Lampung 35365, Indonesia.

*Corresponding author. Email: rezki.hendrawan@gl.itera.ac.id

Manuscript received: 18 June 2026; Received in revised form: 15 October 2026; Accepted: 26 October 2026

Abstract

Fracture characterisation is an important component of structural geological studies because fracture orientation and distribution provide insights into tectonic deformation and rock mass behaviour. However, conventional field-based fracture measurements are often constrained by limited outcrop accessibility and observation coverage. This study evaluated the applicability of Digital Outcrop Models generated from unmanned aerial vehicle photogrammetry for fracture characterisation within crystalline rocks along the Lampung–Panjang Fault zone, southern Sumatra, Indonesia. Fracture data were collected from four outcrops using both the window scan method and digital measurements derived from georeferenced three-dimensional outcrop models. The aerial imagery was processed to generate orthomosaics and digital outcrop models, from which fracture traces were identified and analyzed. A total of 124 fractures were measured using the window scan method, whereas 319 fractures were extracted from the digital outcrop models. Results showed that both approaches consistently identified dominant northwest–southeast and northeast–southwest fracture orientations across the study area. Although differences were observed in dip distributions and contour dispersion, the digital outcrop models preserved the principal fracture patterns recognized in the field while providing a larger dataset and broader spatial coverage. These findings demonstrated that digital outcrop models can reliably represent fracture geometries and serve as an effective alternative to conventional measurements, particularly in inaccessible outcrops. The study highlights the potential of drone-based photogrammetry to improve the efficiency and completeness of structural geological mapping and fracture characterisation.

Keywords: Fracture characterisation; Digital outcrop model; Photogrammetry; Structural geology

Citation: Hendrawan, R. N., Kurniawan, D., Wijaya, M. E. J. & Siringoringo, L. P. (2026). Comparison of Window Scan and Digital Outcrop Model Approaches for Fracture Characterisation Along the Lampung–Panjang Fault Zone. *Jurnal Geocelebes*, 10(2): 432–442, doi: 10.70561/geocelebes.v10i2.52858

Introduction

The Lampung–Panjang Fault is one of the strike-slip faults in Lampung Province, cutting across various lithologies distributed from South Lampung Regency through Bandar Lampung City to Metro City (Mangga et al., 2010). The fault exhibits a northwest–southeast (NW–SE) trend and is characterized by left-lateral displacement (Rasimeng et al., 2024; Sarkowi et al., 2025; Sulandari et al., 2023). Fault activity generated some kind of morphology for example elongate hills, valleys, wavy flat, and mountains. This fault also developed fractures with high intensity especially on brittle rocks in the surrounding area of Fault. These fractures provide valuable records of tectonic processes and play an important role in structural geological investigations.

Fracture distributions are widely developed within crystalline rocks, including both igneous and metamorphic lithologies, along the Lampung-Panjang Fault zone (Haerudin et al., 2026). Traditionally, geologists have employed scanline and

© 2026 Dept. of Geophysics Hasanuddin University

window scan methods to assess fracture intensity, density, and spatial distribution in the field (Bistacchi et al., 2020; Koesmawardani et al., 2021; Watkins et al., 2015). However, the complex topography and variable outcrop accessibility associated with fault-related landscapes often limit the effectiveness of conventional measurements. Consequently, alternative approaches are required to obtain more comprehensive fracture datasets. One promising method is the use of Digital Outcrop Models (DOMs) or Digital Surface Models (DSMs) generated from unmanned aerial vehicle (UAV)-based photogrammetry, which enable detailed fracture mapping and analysis from high-resolution three-dimensional outcrop representations (Osterman, 2017; Panara et al., 2023; Rossi et al., 2017).

While previous digital discontinuity assessments in Indonesia (Koesmawardani et al., 2020) validated DOM applications against scanline/window measurements in granitic rocks at Muaro Silokek—reporting directional variances within ±8°—their evaluation focused primarily on homogenous basement exposures. The applicability and statistical consistency of DOM workflows across heterogeneous crystalline and metamorphic lithologies (e.g., Way Galih Schist) subjected to active strike-slip deformation along the Lampung–Panjang Fault Zone remain systematically unquantified. This study addresses this gap by implementing a nested multi-scale comparative framework (1 × 1 m field plots, co-located 3 × 3 m DOM windows, and full-outcrop DOMs) combined with 3D spherical statistics.

Photogrammetry is a method of acquiring information about physical objects by recording, measuring, and interpreting patterns from aerial photographs captured using drones (Bemis et al., 2014; Liu et al., 2022). The resulting aerial imagery is then processed to generate a DOM, which provides a detailed three-dimensional representation of the outcrop (Liang et al., 2022). Numerous studies have demonstrated the capability of DSMs/DOMs to collect fracture-related data, including the automatic identification and extraction of fracture networks (Martinelli et al., 2020; Menegoni et al., 2023). DOM method should be applied at the study site to generate a three-dimensional outcrop model, which can subsequently be analyzed using specialized software for structural interpretation and fracture characterisation (Assali et al., 2014; Fardana et al., 2024; Panara et al., 2023; 2024; Triantafyllou et al., 2019).

Materials and Methods

The study area is part of the Way Galih Schist (Pzgs), which consists of greenschist-facies amphibole schist and orthogneissic dioritic amphibolite (Mangga et al., 2010). These rocks are distributed along a northwest–southeast trend that parallels both the Great Sumatran Fault system and the Lampung–Panjang Fault (Figure 1). This geological setting provides an excellent opportunity to investigate fracture characteristics associated with long-term tectonic processes.

DOM are digital representations of surface geometry derived from a collection of three-dimensional coordinate points, providing a detailed depiction of the shape and topography of a surface or rock outcrop (Caravaca et al., 2020; Nesbit et al., 2018). When accurately georeferenced in terms of location, orientation, and scale, DOMs enable the efficient extraction of lithological and structural data, particularly for the characterization of discontinuities such as faults, fractures, joints, and bedding planes (Triantafyllou et al., 2019). The increasing use of unmanned aerial vehicles (UAVs) in geological mapping has facilitated the generation of high-resolution DOMs, allowing researchers to identify and analyze structural features with greater precision (Burnham et al., 2022).

© 2026 Dept. of Geophysics Hasanuddin University

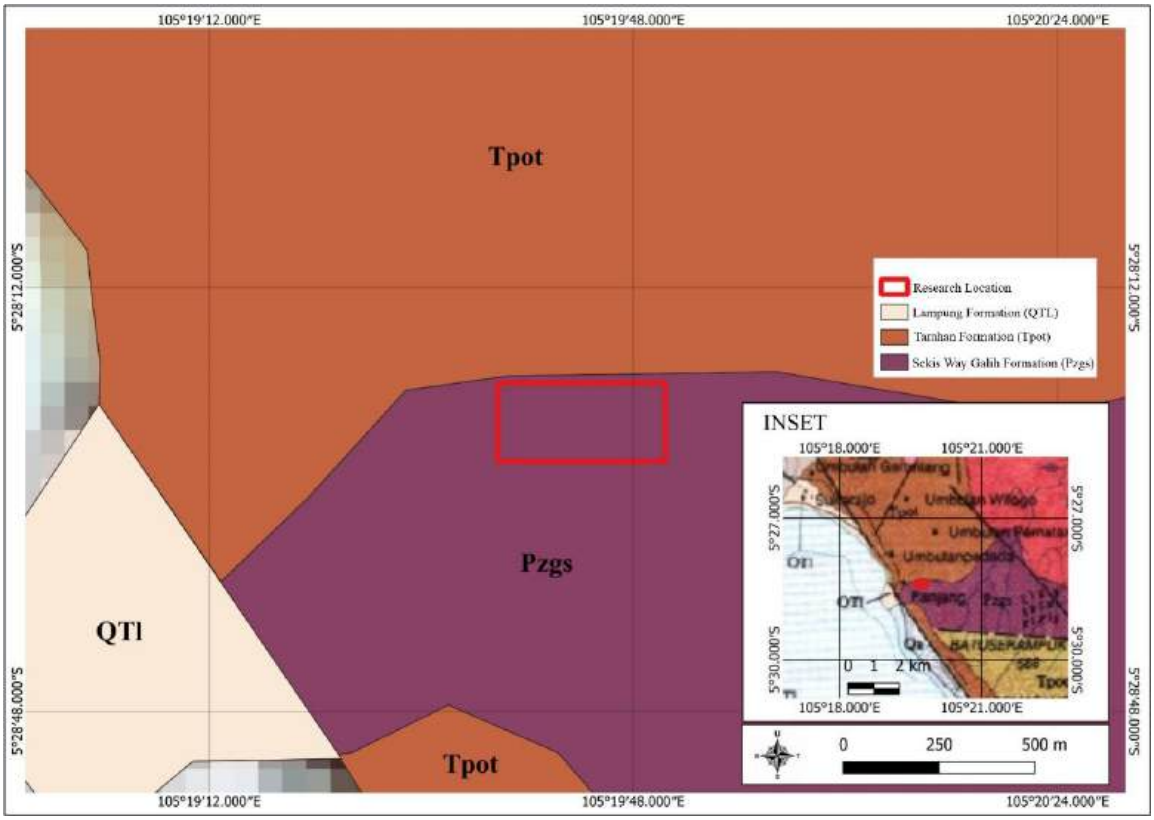


Figure 1. Section of geological map of Tanjungkarang (Mangga et al., 2010).

Previous studies have demonstrated the effectiveness of drone-based photogrammetry for automated fracture extraction and the mapping of various discontinuity surfaces within rock outcrops (Zeng et al., 2025). Compared to conventional field surveys, DOMs offer significant advantages by enabling measurements of orientation, thickness, and geometric relationships of structural features that may be inaccessible, poorly exposed, or too large to assess directly in the field (Menegoni et al., 2023). Fractures can be detected and mapped by interpreting linear features preserved within the digital models, providing a comprehensive framework for structural geological analysis (Perozzo et al., 2025).

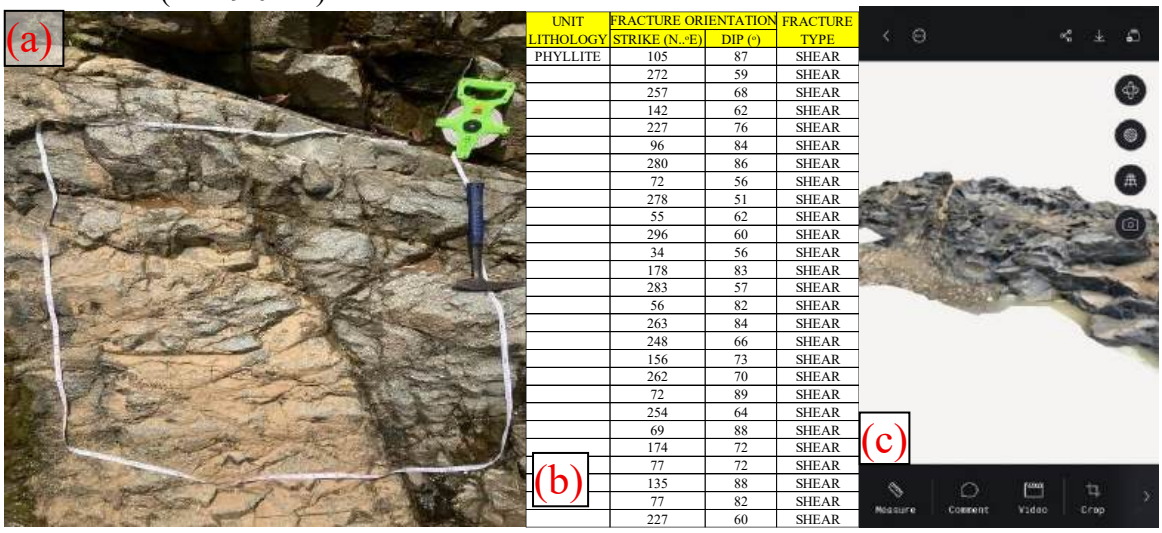
The study commenced with the acquisition of fracture data through a combination of field measurements and aerial photogrammetric surveys. Field-based fracture measurements were conducted using the window scan method within a 1 m × 1 m sampling area (Figure 2a and Figure 2b), with observation sites selected based on the abundance and intensity of fractures exposed on the outcrops (Farny, 2017; Koesmawardani et al., 2021; Watkins et al., 2015). Fracture mapping was performed concurrently with lithological observations to provide a geological context for the structural data. To support digital outcrop reconstruction, aerial imagery was collected using a DJI Mini 3 unmanned aerial vehicle, while an iPhone 15 Pro equipped with LiDAR technology was utilized to complement the data acquisition and improve three-dimensional surface characterisation.

Aerial imagery captured by a DJI Mini 3 drone was processed in Agisoft Metashape to generate georeferenced orthomosaics and 3D textured meshes, complemented by LiDAR close-range scans acquired via an iPhone 15 Pro Polycam (Figure 2c). Internal spatial scale accuracy was calibrated using physical scale bars (1.0 m × 1.0 m window frames) placed on the outcrop faces, yielding a mean relative distance residual of ≤1.8 cm (1.5% scale error). Fracture orientation extraction in

© 2026 Dept. of Geophysics Hasanuddin University

CloudCompare was performed using planar surface fitting with the Compass plugin, maintaining an angular orientation uncertainty within ±2.5°.

To overcome area-dependent dataset discrepancies between manual field scans and digital models, fracture intensity was normalized using the two-dimensional areal lineation density parameter (P21, expressed in m/m^2; (Sanderson & Nixon, 2018)). For the field dataset, total cumulative fracture trace length (L) within each 1.0 m × 1.0 m sampling frame (A = 1.0 m^2) was digitized from high-resolution field orthophotos calibrated against physical tape measurements. For the digital outcrop models, co-located 3.0 m × 3.0 m square sub-windows (A = 9.0 m^2) centered on the field scanplots were extracted. All visible discontinuity traces within the sub-windows were manually mapped on the georeferenced 3D meshes in CloudCompare to calculate total cumulative trace length. Fracture density P21 was then computed as the ratio of total trace length to observation area (P21 = L / A) (Andrews et al., 2019). Furthermore, spherical mean poles, Fisher concentration parameters (κ), and 3D angular misfits (γ) were calculated from lower-hemisphere normal vectors. Non-parametric two-sample Kolmogorov–Smirnov (K-S) tests were executed on circular-transformed axial strike angles (% 180) and dip angles to evaluate statistical equivalence across methods.



UNIT LITHOLOGY	FRACTURE ORIENTATION STRIKE (N..°E)	DIP (°)	FRACTURE TYPE
PHYLLITE	105	87	SHEAR
	272	59	SHEAR
	257	68	SHEAR
	142	62	SHEAR
	227	76	SHEAR
	96	84	SHEAR
	280	86	SHEAR
	72	56	SHEAR
	278	51	SHEAR
	55	62	SHEAR
	296	60	SHEAR
	34	56	SHEAR
	178	83	SHEAR
	283	57	SHEAR
	56	82	SHEAR
	263	84	SHEAR
	248	66	SHEAR
	156	73	SHEAR
	262	70	SHEAR
	72	89	SHEAR
	254	64	SHEAR
	69	88	SHEAR
	174	72	SHEAR
	77	72	SHEAR
	135	88	SHEAR
	77	82	SHEAR
	227	60	SHEAR

Figure 2. (a) Example of window scan method on outcrop; (b) fractures data list; (c) 3D model from Polycam.

Results

The study area is composed of crystalline rock units, including schist, phyllite, and andesite, exposed at four observation sites (Figure 3). Lithological characterization was carried out using two representative rock samples collected from outcrops DK1.1 and DK1.3. Petrographic analysis was conducted to determine the mineralogical composition, texture, and microstructural characteristics of the rocks, complementing field-based lithological observations. The combined field and microscopic analyses identified the DK1.1 outcrop as andesite, whereas the remaining representative sample was classified as phyllite. These lithologies constitute the principal fractured rock units investigated in this study.

Fracture data were collected from four observation sites, where the dominant fracture type identified was shear fractures. A total of 124 fracture measurements were obtained using the window scan method. Stereonet contour analysis reveals that each observation site exhibits contour concentrations in different quadrants, indicating local variations in fracture orientation (Figure 4). However, when viewed collectively, the fracture population

© 2026 Dept. of Geophysics Hasanuddin University

displays a predominant northwest–southeast trend. These results are subsequently compared with fracture orientation measurements derived from the DOM.

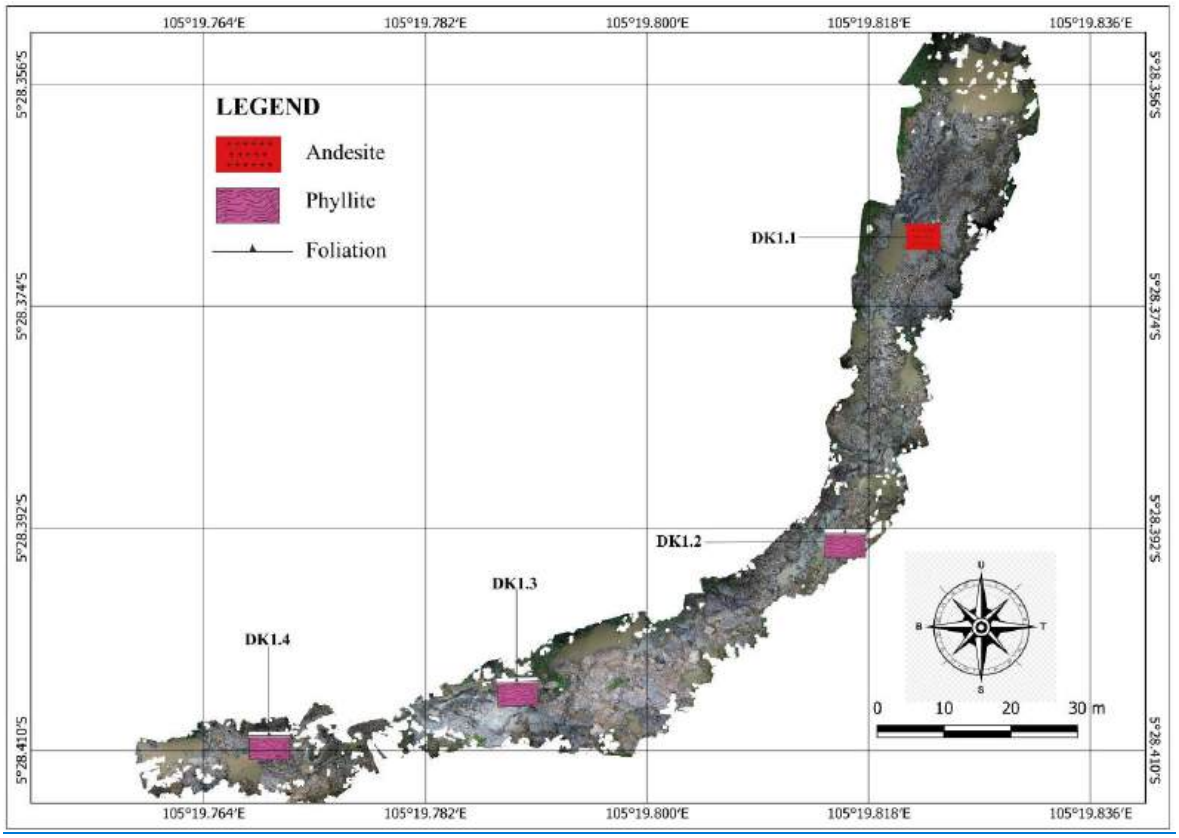


Figure 3. Lithology map in study area.

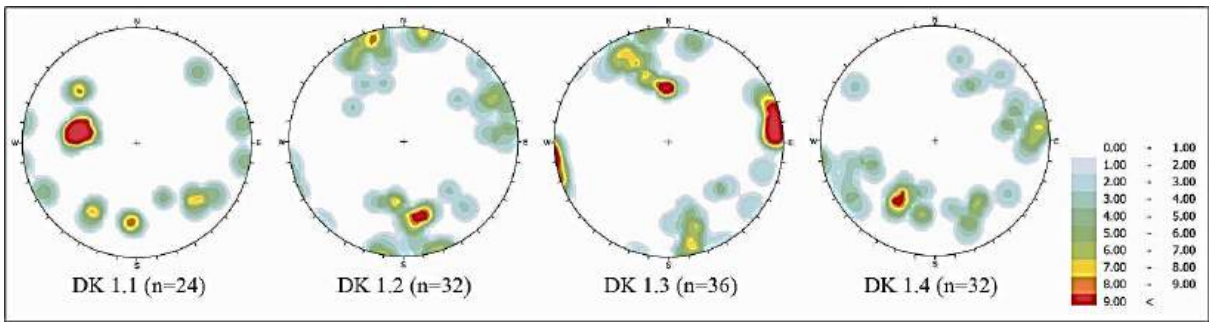


Figure 4. Fracture contours collected by window scan method at each site.

Digital outcrop modelling was conducted at all four observation sites (Figures 5). Fracture picking was performed after the outcrops had been reconstructed into georeferenced three-dimensional models. Fracture analysis on the DOMs covered the entire accessible outcrop surface, allowing a more comprehensive assessment than conventional field measurements. A total of 319 fractures were identified and mapped across the four sites. The orientation data from each site were subsequently presented using rose diagrams and analyzed through stereonet contour plots (Figure 6) to characterize the dominant fracture patterns and their spatial distribution.

Across the four observation sites (DK1.1 to DK1.4) on Table 1, field window scans yielded normalized fracture density (P21) ranging from 10.00 m/m^2 (DK1.1) to 12.77 m/m^2 (DK1.3). Co-located 3 × 3 m DOM sub-windows yielded lower absolute P21 values, ranging from 3.73 m/m^2 (DK1.4) to 5.08 m/m^2 (DK1.3), establishing a systematic field-to-DOM offset ratio

© 2026 Dept. of Geophysics Hasanuddin University

between 2.11 and 2.86. Despite this offset, relative spatial variability was perfectly preserved, with site DK1.3 exhibiting the highest P21 intensity in both field (12.77 m/m^2) and DOM (5.08 m/m^2) datasets. Based on Table 2, 3D angular misfits between 3x3 m DOM and full-outcrop DOMs remained exceptionally low (γ = 9.2° to 17.4°). Two-sample K-S tests for strike distributions revealed no statistically significant differences between field scans and local DOM windows at DK1.1 (D = 0.239, p = 0.514) and DK1.3 (D = 0.361, p = 0.080). Conversely, dip distributions exhibited statistically significant variance ($p < 0.001$) across all sites, with DOM measurements yielding systematically lower dip angles (mean dip 8.3°–29.4°) than field compass readings (mean dip 30.5°–54.1°).

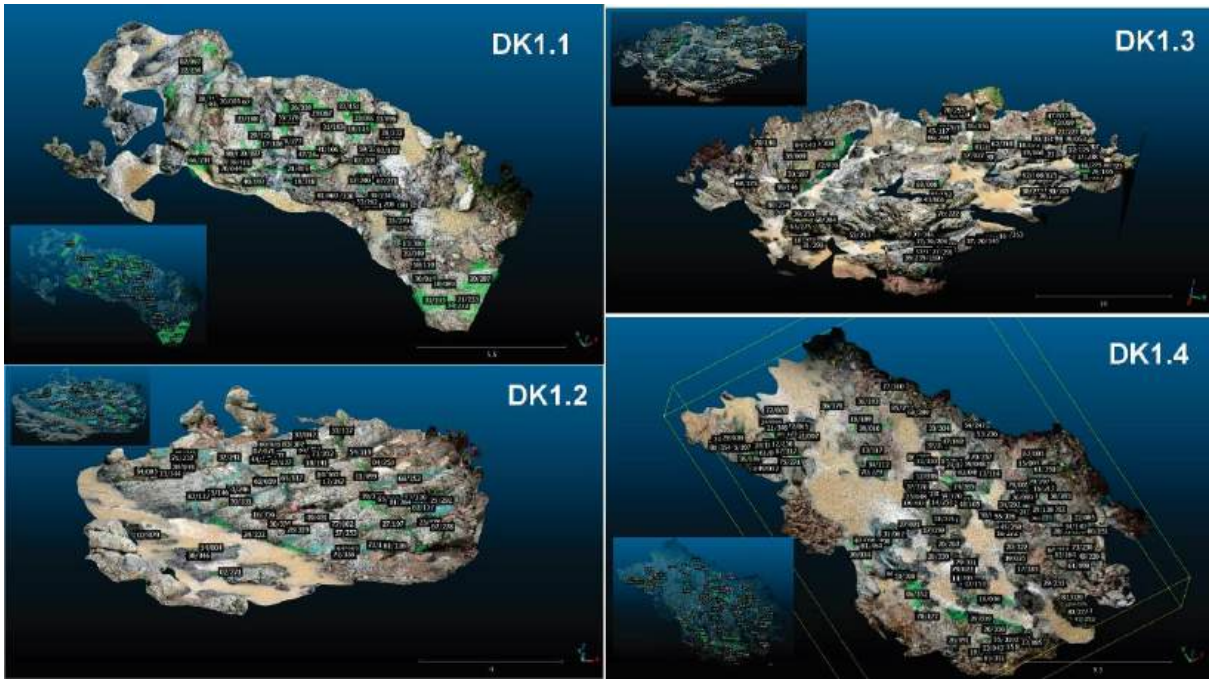


Figure 5 Digital Outcrop Model with Fracture Analysis at each site (inset: fracture distribution).

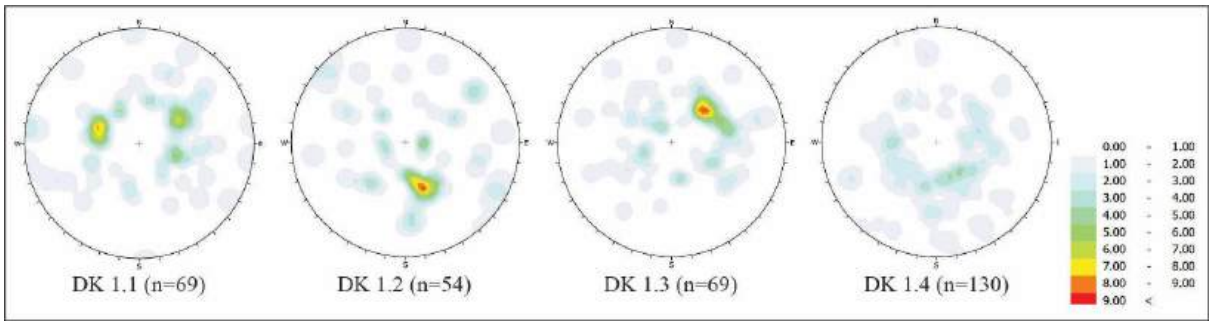


Figure 6. Fracture contours collected by picking from the DOM at each site.

Table 1. Fracture Density (P21).

Station	Scale	Area (A, m^2)	Length (L, m)	Density P21 (m/m^2)	Offset Ratio (P21 Field/ P21 DOM)
DK1.1	Field 1 × 1 m	1.0	10.00	10.00	2.11
	DOM 3 × 3 m	9.0	42.75	4.75	
DK1.2	Field 1 × 1 m	1.0	10.85	10.85	2.28
	DOM 3 × 3 m	9.0	42.84	4.76	
DK1.3	Field 1 × 1 m	1.0	12.77	12.77	2.51
	DOM 3 × 3 m	9.0	45.72	5.08	
DK1.4	Field 1×1 m	1.0	10.66	10.66	2.86
	DOM 3 × 3 m	9.0	33.57	3.73	

© 2026 Dept. of Geophysics Hasanuddin University

Table 2. Spatial orientation statistic result.

Sites	Scale	N	Strike Dip (RHR)	Fisher (κ)	Angular Misfit vs Field 1x1 (γ)	Angular Misfit (3x3 vs Full)	K-S Test Strike (D, p-value)	K-S Test Strike (D, p-value)
DK1.1	Field 1 × 1 m	23	N 328.3°E / 33.7°	1.86	–	–	–	–
	DOM 3 × 3 m	18	N 071.1°E / 10.8°	3.79	37.5°	9.2°	D=0.239, p=0.514	D=0.778, p<0.001
	DOM Full	69	N 125.9°E / 9.0°	3.15	42.2°	–	D=0.188, p=0.546	D=0.580, p<0.001
DK1.2	Field 1 × 1 m	32	N 166.8°E / 30.5°	1.44	–	–	–	–
	DOM 3 × 3 m	26	N 300.5°E / 11.2°	2.98	39.0°	11.5°	D=0.368, p=0.029	D=0.623, p<0.001
	DOM Full	54	N 229.5°E / 8.3°	2.81	27.6°	–	D=0.240, p=0.165	D=0.617, p<0.001
DK1.3	Field 1 × 1 m	36	N 138.2°E / 54.1°	1.76	–	–	–	–
	DOM 3 × 3 m	18	N 144.5°E / 29.4°	7.03	25.1°	17.4°	D=0.361, p=0.080	D=0.778, p<0.001
	DOM Full	69	N 130.6°E / 12.6°	3.66	41.7°	–	D=0.286, p=0.032	D=0.667, p<0.001
DK1.4	Field 1 × 1 m	32	N 250.4°E / 39.8°	1.79	-	–	–	–
	DOM 3 × 3 m	33	N 211.0°E / 16.4°	2.66	28.7°	10.6°	D=0.356, p=0.022	D=0.513, p<0.001
	DOM Full	130	N 251.7°E / 12.4°	3.06	27.4°	–	D=0.319, p=0.008	D=0.599, p<0.001

Discussion

The comparison of stereonet contour plots reveals that the primary difference between the two methods lies in the dip distribution and the degree of data dispersion. The DOM results generally exhibit a broader contour distribution than the window scan method. This difference is related to the wider observation coverage provided by DOM, which encompasses nearly the entire outcrop surface. As a result, in addition to recording shear fractures, the method may also capture other discontinuity surfaces, such as tension joints, foliation planes, and exposed bedding planes.

In contrast, field measurements using the window scan method were conducted within relatively small observation areas (1 × 1 m), resulting in datasets that are more focused on specific fracture populations. Furthermore, the use of a geological compass in the field may introduce measurement uncertainties due to limited access to fracture surfaces, irregular outcrop geometries, and potential errors in orientation readings. These factors may explain why the dip values obtained from the two methods are not always identical, despite displaying similar orientation trends.

The results indicate that the window scan and DOM methods produce generally consistent fracture orientation patterns across the four investigated outcrops. This consistency suggests that the DOM approach is capable of representing fracture geometries with a level of reliability comparable to conventional field measurements. Therefore, DOM can serve as an effective alternative for acquiring fracture orientation data, particularly in areas that are difficult to access or have limited outcrop exposure.

At outcrops DK1.1, DK1.2, and DK1.3, both methods yield relatively similar dominant orientations, demonstrating a high degree of agreement. A notable difference is observed at DK1.4, where the

© 2026 Dept. of Geophysics Hasanuddin University

window scan method shows a contour pole concentration within the third quadrant, corresponding to a northwest–southeast orientation, whereas the DOM results display a more dispersed trend distributed across two different quadrants. This discrepancy is likely attributable to the larger dataset obtained through DOM, which provides a more representative characterisation of the overall fracture population within the outcrop. In contrast, the window scan method captures fractures only within a limited observation area and is therefore more susceptible to local-scale bias. This pattern suggests that DOM is capable of recording a broader range of fracture orientations than conventional field measurements.

Although differences in contour concentration positions are observed in several outcrops, both methods consistently indicate similar principal orientation trends. This demonstrates that DOM preserves the dominant fracture orientation characteristics identified through field measurements while simultaneously increasing the quantity of data and the spatial extent of observations. Consequently, the application of DOM can be considered an effective approach for fracture characterisation in crystalline rocks, particularly in studies requiring extensive spatial coverage and high-density structural datasets.

The systematic offset in normalized fracture illustrates the resolution censoring effect (truncation limit) inherent to photogrammetric 3D models. Field observations within 1 × 1 m plots allow human geologists to detect fine-scale micro-fractures (<5 cm length), whereas DOM trace mapping is constrained by mesh density and image pixel resolution, filtering out sub-centimetric discontinuities. Nevertheless, the preservation of relative density trends, where DK1.3 consistently exhibits peak P21 values across both methods confirms that DOM workflows effectively capture spatial strain gradient variations along the fault zone.

The systematic divergence in dip angle distributions ($p < 0.001$) highlights fundamental sampling biases inherent to each observation technique. Aerial UAV photogrammetry operating from a top-down perspective preferentially exposes sub-horizontal to gently dipping fracture traces exposed on outcrop floors and bench surfaces. In contrast, manual field compass readings are constrained by physical reach, biasing field geologists toward steeply dipping to vertical fracture planes exposed on cliff faces. Consequently, DOM workflows should not be viewed as a standalone replacement for field measurements, but rather as a complementary system requiring targeted field compass calibration for dip orientation.

Conclusion

This study demonstrates that UAV-based Digital Outcrop Models provide a statistically reliable and highly efficient complementary framework for fracture orientation and intensity mapping in crystalline rocks along the Lampung–Panjang Fault Zone. While DOM workflows accurately reproduce field strike distributions ($p > 0.05$) and preserve relative P21 density variations across sites, photogrammetric resolution cut-offs reduce absolute P21 values by a factor of ~2.1 to 2.8 relative to field plots. Systematic dip variations ($p < 0.001$) further underscore the need for targeted field compass calibration. Co-located 3x3 m DOM sub-windows effectively bridge the scale gap between localized field plots and macro-scale outcrop trends, confirming DOM photogrammetry as an essential upscaling tool for structural geology.

Acknowledgements

This manuscript is an output of the research grant from Institut Teknologi Sumatera

© 2026 Dept. of Geophysics Hasanuddin University

(grant number: 1998w/IT9.2.1/PT.01.03/2025).

Author Contribution

RNH: Conceptualization, visualization, writing; DK: data curation, investigation, software; MEJ: project administration, visualization; LPS: validation.

Conflict of Interest

The authors declare no conflict of interest.

References

Andrews, B. J., Roberts, J. J., Shipton, Z. K., Bigi, S., Tartarello, M. C., & Johnson, G. (2019). How do we see fractures? Quantifying subjective bias in fracture data collection. *Solid Earth*, 10, 487–516. https://doi.org/10.5194/se-10-487-2019

Assali, P., Grussenmeyer, P., Villemin, T., Pollet, N., & Viguier, F. (2014). Surveying and modeling of rock discontinuities by terrestrial laser scanning and photogrammetry: Semi-automatic approaches for linear outcrop inspection. *Journal of Structural Geology*, 66, 102–114. https://doi.org/10.1016/j.jsg.2014.05.014

Bemis, S. P., Micklethwaite, S., Turner, D., James, M. R., Akciz, S., Thiele, S. T., & Bangash, H. A. (2014). Ground-based and UAV-Based photogrammetry: A multi-scale, high-resolution mapping tool for structural geology and paleoseismology. *Journal of Structural Geology*, 69, 163–178. https://doi.org/10.1016/j.jsg.2014.10.007

Bistacchi, A., Mittempergher, S., Martinelli, M., & Storti, F. (2020). On a new robust workflow for the statistical and spatial analysis of fracture data collected with scanlines (or the importance of stationarity). *Solid Earth*, 11, 2535–2547. https://doi.org/10.5194/se-11-2535-2020

Burnham, B. S., Bond, C. E., Flaig, P. P., van der Kolk, D. A., & Hodgetts, D. (2022). Outcrop conservation: Promoting accessibility, inclusivity, and reproducibility through digital preservation. *The Sedimentary Record*, 20(1), 5–14. https://doi.org/10.2110/sedred.2022.1.2

Caravaca, G., Le Mouélic, S., Mangold, N., L'Haridon, J., Le Deit, L., & Massé, M. (2020). 3D digital outcrop model reconstruction of the Kimberley outcrop (Gale crater, Mars) and its integration into Virtual Reality for simulated geological analysis. *Planetary and Space Science*, 182, 104808. https://doi.org/10.1016/j.pss.2019.104808

Fardana, Y. C., Setianto, A., & Husein, S. (2024). Digital Fracture Porosity Measurement using Digital Outcrop Modelling (DOM). *IOP Conference Series: Earth and Environmental Science*, 1373, 012055. https://doi.org/10.1088/1755-1315/1373/1/012055

Farny, N. J. (2017). Comparing Rock Discontinuity Measurements Using Geological Compass, Smartphone Application, and Laser Scanning Methods. *Environmental & Engineering GeoScience*, 23(2), 97–112. https://doi.org/10.2113/gseegeosci.23.2.97

Haerudin, N., Darmawan, I. G. B., Mulyasari, R., Karyanto, K., & Persada, C. (2026). Identifying The Seismic Risk Zoning Along The Lampung-Panjang Fault and Surroundings based on A Comprehensive Gravity and Microtremor Analysis. *Earth and Planetary Science*, 3, 3–14. https://doi.org/10.21303/2461-

© 2026 Dept. of Geophysics Hasanuddin University

4262.2026.003948

Koesmawardani, W. T., Burhannudinnur, M., & Maulana, G. F. (2020). Identification of Natural Fractures Using Digital Outcrop Model (DOM) and Filedwork Data at Granitic Basement Rocks Muaro Silokek, West Sumatra. *Technology Reports of Kansai University*, 62(03), 645–654. https://www.researchgate.net/publication/344460189_Identification_of_Natural_Fractures_Using_Digital_Outcrop_Model_DOM_and_Filedwork_Data_at_Granitic_Basement_Rocks_Muaro_Silokek_West_Sumatra

Koesmawardani, W. T., Sapiie, B., & Rudyawan, A. (2021). Fracture characterization with fieldwork data and its implication for basement fracture reservoir at Muaro Silokek Granitic Outcrops. *IOP Conference Series: Materials Science and Engineering*, 1098(6), 062019. https://doi.org/10.1088/1757-899x/1098/6/062019

Liang, B., Liu, Y., Shao, Y., Wang, Q., Zhang, N., & Li, S. (2022). 3D quantitative characterization of fractures and cavities in Digital Outcrop texture model based on Lidar. *Energies*, 15(5), 1627. https://doi.org/10.3390/en15051627

Liu, Y., Chen, J., Tan, C., Zhan, J., Song, S., Xu, W., Yan, J., Zhang, Y., Zhao, M., & Wang, Q. (2022). Intelligent scanning for optimal rock discontinuity sets considering multiple parameters based on manifold learning combined with UAV photogrammetry. *Engineering Geology*, 309, 106851. https://doi.org/10.1016/j.enggeo.2022.106851

Mangga, S. A., Amirudin, A., Suwarti, T., Gafoer, S., & Sidarto, S. (2010). *Peta Geologi Lembar Tanjungkarang, Sumatera*. Pusat Survei Geologi. https://geologi.esdm.go.id/geomap/pages/preview/peta-geologi-lembar-tanjungkarang-sumatera

Martinelli, M., Bistacchi, A., Mittempergher, S., Bonneau, F., Balsamo, F., Caumon, G., & Meda, M. (2020). Damage Zone Characterization combining scan-line and scan-area analysis on a km-scale Digital Outcrop Model: The Qala Fault (Gozo). *Journal of Structural Geology*, 140, 104144. https://doi.org/10.1016/j.jsg.2020.104144

Menegoni, N., Giordan, D., Inama, R., & Perotti, C. (2023). DICE : An open-source MATLAB application for quanti fi cation and parametrization of digital outcrop model-based fracture datasets. *Journal of Rock Mechanics and Geotechnical Engineering*, 15(5), 1090–1110. https://doi.org/10.1016/j.jrmge.2022.09.011

Nesbit, P. R., Durkin, P. R., Hugenholtz, C. H., Hubbard, S. M., & Kucharczyk, M. (2018). 3-D stratigraphic mapping using a digital outcrop model derived from UAV images and structure-from-motion photogrammetry. *Geosphere*, 14(6), 2469–2486. https://doi.org/10.1130/GES01688.1

Osterman, F. (2017). *Comparison of Photogrammetry Interpretation with Physical Structural Field Measurements*. Uppsala University. https://uu.diva-portal.org/smash/record.jsf?pid=diva2:1111024

Panara, Y., Chandra, V., Finkbeiner, T., Petrovic, A., Zühlke, R., Khanna, P., & Vahrenkamp, V. (2023). Fracture intensity and associated variability: A new methodology for 3D digital outcrop model analysis of carbonate reservoirs. *Marine and Petroleum Geology*, 158, 106532. https://doi.org/10.1016/j.marpetgeo.2023.106532

Panara, Y., Menegoni, N., Finkbeiner, T., Zühlke, R., & Vahrenkamp, V. (2024). High-resolution analysis of 3D fracture networks from Digital

© 2026 Dept. of Geophysics Hasanuddin University

Outcrop Models, correlation to plate-tectonic events and calibration of subsurface models (Jurassic, Arabian Plate). *Marine and Petroleum Geology*, 167, 106998. https://doi.org/10.1016/j.marpetgeo.2024.106998

Perozzo, M., Menegoni, N., Crispini, L., Federico, L., Seno, S., & Maino, M. (2025). Quantitative characterization of fracture network in large sheath-fold: field and UAV-based digital outcrop model analysis (Ligurian Alps, Italy). *Journal of Structural Geology*, 201, 105551. https://doi.org/10.1016/j.jsg.2025.105551

Rasimeng, S., Fahruddin, F., Valentin, F., Aurora, T. G., & Nurlaili, J. (2024). Subsurface Interpretation of the Panjang Fault Area, Lampung, Based on Geomagnetic Method. *Jurnal Geocelebes*, 8(1), 37–50. https://doi.org/10.20956/geocelebes.v8i1.28303

Rossi, M., Olsson, P.-I., Johanson, S., Fiandaca, G., Bergdahl, D. P., & Dahlin, T. (2017). Mapping geological structures in bedrock via large-scale direct current resistivity and time-domain induced polarization tomography. *Near Surface Geophysics*, 15(6), 657–667. https://doi.org/10.3997/1873-0604.2017058

Sanderson, D. J., & Nixon, C. W. (2018). Topology, connectivity and percolation in fracture networks. *Journal of Structural Geology*, 115, 167–177. https://doi.org/10.1016/j.jsg.2018.07.011

Sarkowi, M., Damayanti, L., Rosadi, V. A., Pinandita, A. H., Fajriyanto, F., Hendrawan, R. N., Wibowo, A., & Wibowo, R. C. (2025). Fault Identification Using Inversion Modeling and Gradient Method of Gravity Data in Bandar Lampung City. *IOP Conference Series: Earth and Environmental Science*, 1517, 012016. https://doi.org/10.1088/1755-1315/1517/1/012016

Sulandari, B., Suteja, A., Hadibroto, H., Nurmaliah, N., Setyanta, B., & Garniwa, A. (2023). Deliniasi Struktur Sesar Lampung-Panjang dan Identifikasi Potensi Sumberdaya Alam Berdasarkan Anomali Magnet Daerah Bandar Lampung. *Jurnal Geologi Dan Sumberdaya Mineral*, 24(4), 195–203. https://doi.org/10.33332/jgsm.geologi.v24i4.721

Triantafyllou, A., Watlet, A., Le Mouélic, S., Camelbeeck, T., Civet, F., Kaufmann, O., Quinif, Y., & Vandycke, S. (2019). 3-D digital outcrop model for analysis of brittle deformation and lithological mapping (Lorette cave, Belgium). *Journal of Structural Geology*, 120, 55–66. https://doi.org/10.1016/j.jsg.2019.01.001

Watkins, H., Bond, C. E., Healy, D., & Butler, R. W. H. (2015). Appraisal of fracture sampling methods and a new workflow to characterise heterogeneous fracture networks at outcrop. *Journal of Structural Geology*, 72, 67–82. https://doi.org/10.1016/j.jsg.2015.02.001

Zeng, Q.-H., Wang, W.-Z., Ma, Z.-G., Shen, J., Shao, Y., Deng, F., & Wang, Q. (2025). Cavity and Fracture Extraction of CarbonateRocks Digital Outcrop Model. *Proceedings of the International Field Exploration and Development Conference 2024*, 209–219. https://doi.org/10.1007/978-981-96-2706-6_16

© 2026 Dept. of Geophysics Hasanuddin University

ISSN: 2579-5821 (Print)
ISSN: 2579-5546 (Online)
URL address: http://journal.unhas.ac.id/index.php/geocelebes
DOI: 10.70561/geocelebes.v10i2.53132

Jurnal Geocelebes Vol. 10 No. 2, October 2026, 443 – 470

Projected Changes in Rainy Season Onset, Retreat, and Duration over the Brantas Watershed Using Downscaled CMIP6 Climate Models

Gilang Aulia Herlambang, Lalu Muhamad Jaelani

Geomatics Engineering, Institut Teknologi Sepuluh Nopember, Surabaya 60111, Indonesia.

Corresponding author. Email: gilangauliaherlambang@gmail.com

Manuscript received: 31 July 2026; Received in revised form: 26 October 2026; Accepted: 31 October 2026

Abstract

This study evaluates projected changes in rainy-season onset, retreat, duration, and peak timing across the Brantas Watershed, Indonesia, using five downscaled CMIP6 climate models under SSP2-4.5 and SSP5-8.5 scenarios. Daily precipitation was downscaled to approximately 0.05° resolution using the BCCAQ method. Rainy-season characteristics were determined using the Indonesian Agency for Meteorology, Climatology, and Geophysics (BMKG) 10-daily criteria and compared with the accumulated rainfall anomaly method. Historical validation against rain-gauge observations (2000–2014) showed generally better performance for the BMKG method, with onset and retreat RMSE values of approximately 12–22 days. Projections indicated an advance in rainy-season onset of approximately 43–53 days and an increase in duration of 41–58 days relative to the 1981–2014 baseline. Retreat timing remained relatively stable under the BMKG method. However, a statistically significant increasing trend in duration was identified only under SSP5-8.5. The anomaly method showed smaller and less consistent duration changes, ranging from −7.9 to +8.5 days. Peak rainfall timing tended to occur earlier, particularly under SSP5-8.5, although substantial interannual variability persisted. These findings highlight the influence of seasonal determination methods on projected rainfall characteristics and provide relevant information for agricultural planning and water-resource management.

Keywords: BCCAQ downscaling; Brantas Watershed; CMIP6; SSP scenarios; Rainy season.

Citation: Herlambang, G. A., & Jaelani, L. M. (20xx). Projected Changes in Rainy Season Onset, Retreat, and Duration over the Brantas Watershed Using Downscaled CMIP6 Climate Models. *Jurnal Geocelebes*, 10(2): 443–470, doi: 10.70561/geocelebes.v10i2.53132

Introduction

Climate change is widely acknowledged as a paramount environmental crisis of the twenty-first century, with documented and anticipated consequences for ecosystem stability, food security, water resources, and global economic resilience (IPCC, 2023). The Intergovernmental Panel on Climate Change (IPCC) assessed global mean surface temperature in 2011–2020 as approximately 1.1°C above the 1850–1900 average; the 1.5°C warming level is projected to be reached in the near term under many assessed scenarios (IPCC, 2021; IPCC, 2023). Continued warming is expected to influence atmospheric circulation, precipitation variability, and hydroclimatic extremes, although the magnitude and direction of local precipitation changes differ among regions and models.

The effects of climate change are expected to be particularly noticeable in tropical regions, where climate systems are often more sensitive to external forcing. Indonesia, located within the Asian–Australian monsoon domain (Mulsandi et al., 2024), experiences precipitation variability that is strongly influenced by the interaction between monsoonal circulation, El Niño–Southern Oscillation (ENSO), and the Indian Ocean Dipole (IOD) (Supari et al., 2018, 2020; Kurniadi et al., 2023). These factors contribute to

© 2026 Dept. of Geophysics Hasanuddin University

considerable spatial and temporal heterogeneity in rainfall distribution across the archipelago (Kurniadi et al., 2023; Sudarman et al., 2024; Yulizar & Asdak, 2025). In addition to affecting total annual precipitation, climate change may also alter the seasonal characteristics of rainfall, including the timing of rainy season onset, cessation, and overall duration. Such changes are potentially important for agricultural planning, irrigation management, and adaptation strategies, as many agricultural systems remain highly dependent on seasonal rainfall patterns (Adriat et al., 2025; Shrestha et al., 2025). This highlights the need for localized climate assessments that can provide more detailed information for regions with high dependence on water resources.

The Brantas Watershed in East Java, Indonesia, is an important river basin that supports agricultural production, water supply, flood management, and hydropower generation (BBWS Brantas, 2011; Wiwoho et al., 2023). Seasonal rainfall is closely linked to water availability and agricultural activities, making changes in rainy-season timing and duration important considerations for watershed management (Kwawuvi et al., 2022; Long et al., 2023). Studies in the Oti River Basin in West Africa and the Xiang River Basin in China have demonstrated that rainy-season onset, cessation, and duration can vary over time, with potential implications for agricultural planning and water management (Kwawuvi et al., 2022; Long et al., 2023).

Furthermore, CMIP6-based projections indicate that future changes in rainy-season onset, retreat, and duration may differ across monsoon regions and emission scenarios (Moon & Ha, 2020; Taguela et al., 2026). These findings highlight the importance of assessing seasonal rainfall timing alongside changes in precipitation amounts when investigating future climate impacts on water resources and agricultural systems (Kwawuvi et al., 2022; Moon & Ha, 2020). In the Brantas Watershed, previous research has examined rainfall variability, agricultural productivity, and future precipitation projections (Wiwoho et al., 2023, 2025; Herlambang & Jaelani, 2026). Further investigation of projected changes in rainy-season onset, retreat, duration, and peak timing can complement these studies by providing additional information on the seasonal distribution of rainfall relevant to water resource management and climate adaptation.

For future climate projections, the Coupled Model Intercomparison Project Phase 6 (CMIP6) provides a widely used set of global climate model (GCM) simulations under various Shared Socioeconomic Pathways (SSPs) (Eyring et al., 2016; O'Neill et al., 2016; Tebaldi et al., 2021). However, GCM outputs are generally produced at coarse spatial resolutions and may contain systematic biases that limit their direct application for local-scale studies, especially in tropical areas where precipitation processes are complex and highly variable (Chen et al., 2021; IPCC, 2021). To address this limitation, downscaling and bias correction techniques are often applied to improve the representativeness of GCM data at regional and local levels (Gebrechorkos et al., 2023; Raghavan et al., 2018). One such method is the Bias Correction Constructed Analogues with Quantile Mapping Reordering (BCCAQ), which combines the spatial pattern preservation capability of Constructed Analogues with the statistical distribution correction of Quantile Mapping (Cannon et al., 2015; Werner & Cannon, 2016). Studies have shown that BCCAQ effectively reduces systematic biases and enhances the representation of precipitation variability and extreme events in downscaled climate projections (Werner & Cannon, 2016; Gebrechorkos et al., 2023). The application of bias correction and

© 2026 Dept. of Geophysics Hasanuddin University

downscaling is now considered a necessary step for generating climate information suitable for local impact assessments (Lafferty & Sriver, 2023).

In recent years, BCCAQ-downscaled CMIP6 data have been increasingly employed in climate-related studies in Indonesia, including analyses of temperature changes, rainfall characteristics, extreme climate indices, and hydrological responses (Kurniadi et al., 2023, 2024; Yulizar & Asdak, 2025; Herlambang & Jaelani, 2026). However, most of these studies have concentrated on changes in the magnitude of climate variables, while less attention has been given to the seasonal timing of rainfall (onset, retreat, and duration) at watershed scales. For instance, while Hariadi et al. (2022) evaluated the onset and cessation of the rainy season across Southeast Asia, their analysis was conducted at a broad regional scale rather than at a specific watershed scale.

The novelty of this study lies in its comprehensive watershed-scale assessment of rainy season timing in the Brantas Watershed. Unlike previous regional studies that focused primarily on precipitation magnitudes, this study specifically quantifies the projected shifts in onset, retreat, duration, and peak timing at a high spatial resolution (~5.5 km) using newly BCCAQ CMIP6 data. Furthermore, this study provides a critical methodological comparison between the operational BMKG threshold method and the international cumulative anomaly method, offering a robust framework for assessing seasonal rainfall shifts in complex tropical terrains.

This study investigates projected changes in rainy-season characteristics across the Brantas Watershed using BCCAQ-downscaled CMIP6 precipitation data. The specific objectives are to: (1) evaluate the performance of five CMIP6 climate models against observational precipitation data using statistical metrics; (2) quantify projected changes in rainy-season onset, retreat, duration, and peak timing under the SSP2-4.5 and SSP5-8.5 scenarios across the near-term (2015–2040), mid-term (2041–2070), and long-term (2071–2099) periods relative to the 1981–2014 baseline; and (3) compare the projected changes in rainy-season onset, retreat, and duration derived using the BMKG and rainfall-anomaly methods, considering their temporal trends and spatial variability. The findings are expected to support climate adaptation planning, water resource management, and agricultural scheduling in the Brantas Watershed. It should be noted that the scope of this study is limited to the evaluated GCMs, the two selected seasonal determination methods, and the specific projection periods, which may not fully capture all possible future climate trajectories.

Materials and Methods

Study Area

The Brantas Watershed (DAS Brantas) is located in East Java Province, Indonesia, between approximately 111°30′–112°55′ East Longitude and 7°01′–8°15′ South Latitude, with a catchment area of about 11,800 km² and a main river length of approximately 320 km (BBWS Brantas, 2011; Wiwoho et al., 2023). The geographical location and spatial extent of the study area are presented in Figure 1. The upstream portion of the watershed is situated in the mountainous region of Batu City and Malang Regency, while the river flows through the central area, which is predominantly characterized by agricultural land and settlements, before discharging into the Madura Strait. The watershed is supported by several multipurpose reservoirs, including Sutami (Karangkates), Lahor, Selorejo, Wlingi, and Lodoyo, which serve functions such as flood control, raw water supply, irrigation, and hydropower generation (BBWS

© 2026 Dept. of Geophysics Hasanuddin University

Brantas, 2011). The topographic conditions of the Brantas Watershed vary considerably, ranging from volcanic mountainous areas in the upstream section to lowland coastal plains in the downstream section. These variations contribute to spatial differences in rainfall distribution across the watershed, suggesting that an assessment of changes in rainy season characteristics should consider spatial approaches to better represent the heterogeneity of precipitation patterns within the watershed.

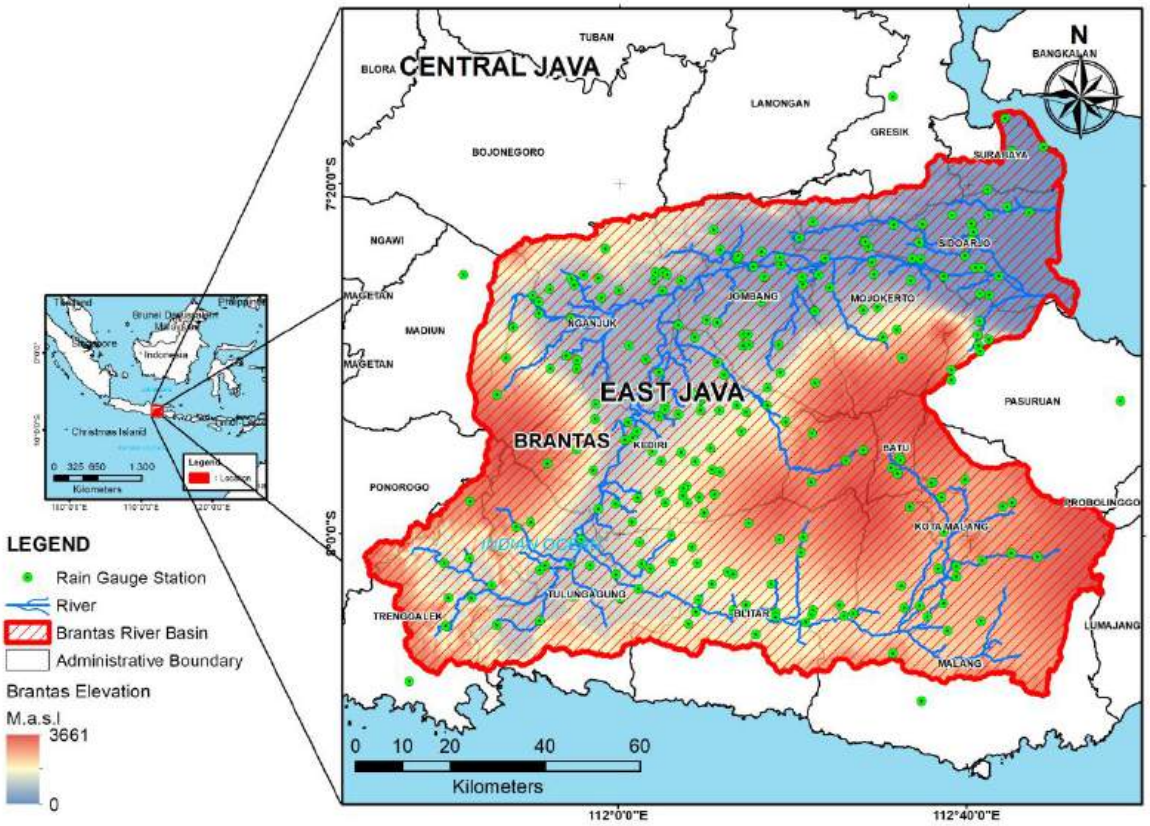


Figure 1. Geographic location and spatial characteristics of the Brantas Watershed, East Java, Indonesia, showing the watershed boundary, digital elevation model (DEM), and spatial distribution of 216 rain gauges within the watershed, selected from 221 available stations.

Data

Observational Precipitation Data

Two precipitation datasets were utilized in this study. The first was the Climate Hazards Group InfraRed Precipitation with Station data version 2.0 (CHIRPS v2.0) (Funk et al., 2015), available at a spatial resolution of 0.05o (approx. 5.5 km) and a daily temporal resolution. CHIRPS v2.0 was employed as the observational reference (training target) for calibrating and downscaling the CMIP6 climate models using the BCCAQ method over the baseline period of 1981–2014. Although CHIRPS exhibits known limitations in capturing exact daily rainfall timing and fine-scale orographic precipitation (Rahmawati & Lubczynski, 2018; Wiwoho et al., 2021), aggregating daily estimates into dasarian (10-day) totals substantially mitigates daily temporal noise and uncertainties (Dinku et al., 2018; Wiwoho et al., 2021), rendering it suitable for robust rainy-season onset and retreat detection across regional domains. CHIRPS has also been evaluated against rain-gauge observations in Indonesia, including the Brantas Watershed (Ferijal et al., 2025; Wiwoho et al., 2021), and in other regions (Bai et al., 2018; Dinku et al., 2018; Paredes-Trejo et al., 2017).

© 2026 Dept. of Geophysics Hasanuddin University

The second dataset comprised daily rain-gauge observations provided by the Indonesian Agency for Meteorology, Climatology, and Geophysics (BMKG) and the Department of Public Works and Water Resources (PU SDA) of East Java Province for the validation sub-period of 2000–2014. A total of 221 rain-gauge stations were available, of which 216 were located within the Brantas Watershed and met the quality-control criteria. The remaining five stations were located outside the watershed boundary and were excluded from the watershed-scale validation. Quality-control procedures included screening for non-physical values, identifying prolonged frozen values, and enforcing a minimum data-completeness threshold of 85% across the 2000–2014 period.

While CHIRPS drove the BCCAQ calibration process, the independent rain-gauge observations (restricted to 2000–2014) served strictly as an external validation dataset to evaluate the performance of the downscaled precipitation estimates. Although complete independence between gridded products and station data can be challenging due to station incorporation in CHIRPS generation, this gauge-based evaluation provides a rigorous assessment of how closely the BCCAQ-adjusted outputs reproduce observed station-scale variability across the watershed.

CMIP6 Climate Model Data and SSP Scenarios

Projected precipitation data were obtained from the Coupled Model Intercomparison Project Phase 6 (CMIP6) via the Earth System Grid Federation (ESGF) portal. Five GCMs MIROC-ES2L, EC-Earth3-Veg-LR, IPSL-CM6A-LR, NorESM2-MM, and GFDL-ESM4 were selected based on previous regional precipitation evaluations across Southeast Asia and Indonesia. Specifically, MIROC-ES2L demonstrated strong performance over the Brantas River Basin (Herlambang & Jaelani, 2026), EC-Earth3-Veg-LR, IPSL-CM6A-LR, and GFDL-ESM4 were identified among the top-performing models for reproducing precipitation dynamics and seasonal cycles across Southeast Asia (Iqbal et al., 2021; Liu et al., 2023; Pimonsree et al., 2023), and NorESM2-MM showed robust skill across regional evaluations (Kurniadi et al., 2023; Liu et al., 2022). Retaining these five structurally independent models provides a manageable multi-model ensemble to account for structural uncertainty and capture differences in projected climate responses (Tebaldi et al., 2021). The detailed specifications of the five selected CMIP6 models, including their development institutions and native spatial resolutions, are summarized in Table 1.

Table 1. Specifications of the five CMIP6 Global Climate Models (GCMs) used in this study.

Model	Institution (Country)	Native Resolution (Lat × Lon)	Reference
EC-Earth3-Veg-LR	EC-Earth Consortium (Europe)	~1.0° × 1.0°	Döscher et al. (2022)
GFDL-ESM4	NOAA-GFDL (USA)	~1.0° × 1.25°	Dunne et al. (2020)
IPSL-CM6A-LR	IPSL (France)	~1.26° × 2.5°	Boucher et al. (2020)
MIROC-ES2L	MIROC (Japan)	~2.8° × 2.8°	Hajima et al. (2020)
NorESM2-MM	NCC (Norway)	~1.0° × 1.0°	Seland et al. (2020)

Rather than re-using existing downscaled outputs, raw daily GCM series were newly downscaled in this study to a 0.05° spatial resolution over the Brantas Watershed via the BCCAQ method. To prevent circular reasoning, the initial model selection based on macro-climatological skill is strictly separated from the validation in Section 2.4, which independently evaluates these newly downscaled products against daily rain-gauge observations across higher-order daily variability, extreme

© 2026 Dept. of Geophysics Hasanuddin University

precipitation indices, and rainy-season onset/ retreat dynamics.

The historical baseline covers 1981–2014, corresponding to the period used to calibrate the BCCAQ method against CHIRPS v2.0 precipitation data. In contrast, validation against ground-based daily rainfall observations is restricted to the 2000–2014 sub-period, aligning with station data availability and quality control criteria.

Future projections were extracted under two Shared Socioeconomic Pathways: SSP2-4.5, describing a "middle-of-the-road" pathway, and SSP5-8.5, representing a fossil-fuel-intensive, high-emissions pathway (Riahi et al., 2017). Together, they provide a robust foundation for assessing precipitation changes across a moderate-to-high range of future forcing scenarios (IPCC, 2021). Future changes are evaluated over three distinct 30-year time horizons: 2015–2040 (near-term), 2041–2070 (mid-century), and 2071–2099 (end-century). These time horizons enable a comprehensive evaluation of progressive climate shifts throughout the twenty-first century, while internal climate variability is acknowledged as a potential source of uncertainty in near-term projections.

BCCAQ Statistical Downscaling

The native spatial resolution of CMIP6 GCM outputs (100–250 km) is too coarse to capture fine-scale precipitation variability across the topographically complex Brantas Watershed. To bridge this spatial scale gap, raw daily precipitation series from the five selected CMIP6 models were downscaled using the Bias Correction/ Constructed Analogues with Quantile Mapping Reordering (BCCAQ) method (Werner & Cannon, 2016). BCCAQ is a hybrid statistical downscaling technique that integrates Constructed Analogues (CA) spatial downscaling with Quantile Delta Mapping (QDM) bias correction (Cannon et al., 2015).

Rather than performing daily-scale bias correction, the BCCAQ algorithm executes a multi-step integration process:

1. Bias Correction: Raw daily GCM outputs at their native resolutions are first bias-corrected against a coarse-aggregated observational reference using QDM (Cannon et al., 2015). QDM adjusts historical and future GCM quantiles while explicitly preserving the model's projected relative change signals across all quantiles, ensuring that climate change signals in extreme values are retained.
2. Constructed Analogues (CA) Spatial Downscaling: Daily large-scale atmospheric patterns from the GCM are constructed as optimal linear combinations of N analog days selected from the historical observational record, downscaling the spatial pattern to the fine observational grid (Werner & Cannon, 2016).
3. Quantile Mapping Reordering: To preserve spatial co-variability and prevent artificial variance reduction in extreme events, high-resolution QDM outputs at each target grid cell are reordered based on the rank structure derived from the CA spatial patterns (Werner & Cannon, 2016).

Downscaling was executed using CHIRPS v2.0 daily precipitation data at its native spatial resolution of ~0.05° (5x5 km) as the observational target dataset over the 34-year calibration period (1981–2014). Key algorithmic parameters were configured as follows (Cannon et al., 2015; Werner & Cannon, 2016):

- Wet-day threshold: Set to 0.1 mm/day to differentiate wet and dry states and avoid trace-precipitation bias during quantile mapping.
- Number of analogues (N): Configured to N = 30 historical analog days to construct spatial patterns while

© 2026 Dept. of Geophysics Hasanuddin University

preventing over-smoothing of local orographic extremes.
- QDM distribution: Empirical cumulative distribution functions (eCDFs) were constructed non-parametrically using 100 quantiles evaluated across a rolling 31-day centered window to account for seasonal non-stationarity without parametric distribution assumptions.

The resulting dataset provides continuous, high-resolution (~0.05º, 5.5 km) daily precipitation projections across the Brantas Watershed for both the historical baseline (1981–2014) and future projection horizons (2015–2100) under SSP2-4.5 and SSP5-8.5.

GCM Performance Evaluation and Model Selection

To assess the fidelity of the downscaled climate simulations over the Brantas Watershed, outputs from all five downscaled CMIP6 models (MIROC-ES2L, EC-Earth3-Veg-LR, IPSL-CM6A-LR, NorESM2-MM, and GFDL-ESM4) were evaluated against observed ground-based daily precipitation during the independent historical sub-period (2000–2014). Observational data were obtained from 216 rain-gauge stations located within the Brantas Watershed that met the quality-control criteria. Although 221 stations were initially available, five stations located outside the watershed boundary were excluded from the validation. The selected station records were spatially interpolated using Ordinary Kriging to produce reference precipitation fields at a 0.05° grid resolution for comparison with the downscaled CMIP6 outputs. Because the BCCAQ downscaling procedure was calibrated exclusively against CHIRPS v2.0 over 1981–2014, evaluating the downscaled outputs against station-interpolated surfaces over 2000–2014 serves as an independent split-sample validation.

Model performance was evaluated across both daily rainy-season characteristics. First, general model performance was quantified using four statistical metrics: Correlation Coefficient (CC) for temporal coherence, Root Mean Square Error (RMSE) and Percent Bias (PBias) for magnitude deviations, and Standard Deviation Ratio (StdRatio) for spatial variability (Prasetya et al., 2026). These metrics were integrated using Taylor diagrams and heatmaps to visually compare spatial and temporal performance across models. Second, to rigorously test the daily-scale performance of the BCCAQ outputs, historical simulations were explicitly evaluated against observations for rainy-season dynamics, including onset date, retreat date, duration, and peak rainfall intensity, following previous evaluations of simulated rainy-season onset and cessation (Dunning et al., 2017; Hariadi et al., 2022).

Rather than using model rankings to assign differential weights or eliminate lower-ranked models, all five GCMs were retained to construct an unweighted multi-model ensemble based on the simple arithmetic mean. This approach preserves the representation of structural uncertainty and inter-model spread across future climate projections, aligning with multi-metric evaluation benchmarking frameworks for regional climate change studies in Southeast Asia (Gupta et al., 2025; Iqbal et al., 2021; Pimonsree et al., 2023; Prasetya et al., 2026; Shakeel et al., 2025; Zabihi & Ahmadi, 2024).

Determination of Rainy Season Onset, Retreat, and Duration

The rainy season characteristics in this study were defined using three main parameters: onset, retreat (or cessation), and rainy season duration, which collectively describe the timing, length, and variability of the rainy season in a given region (Bombardi et al., 2020). Various methods have been developed in

© 2026 Dept. of Geophysics Hasanuddin University

the international literature to determine these parameters, ranging from cumulative rainfall threshold approaches, two-phase regression analysis on cumulative rainfall data, to wavelet transform-based methods, each with different characteristics and levels of sensitivity to noise in precipitation data (Bombardi et al., 2020). This study combined two complementary approaches: the operational 10-daily (dasarian) criteria established by the Indonesian Agency for Meteorology, Climatology, and Geophysics (BMKG) as the primary method, which is operationally relevant in Indonesia, and the accumulated rainfall anomaly approach, which is commonly used in international CMIP6 scientific literature, as a comparative method to strengthen the scientific validity of the results.

BMKG 10-Daily (Dasarian) Criteria

The primary method used in this study follows the operational criteria established by the Agency for Meteorology, Climatology, and Geophysics of Indonesia (BMKG, 2022), which divide each month into three 10-day periods (dasarian): Dasarian I (days 1–10), Dasarian II (days 11–20), and Dasarian III (days 21 to the end of the month).

To avoid truncating the natural wet season of Indonesia which is dominated by the Asian winter monsoon and typically spans from late November through April across the calendar year boundary (BMKG, 2022) the search window for determining seasonal characteristics was set according to the hydrological year spanning from 1 August to 31 July of the following year. Within this defined annual search window, the rainy season parameters were calculated as follows:

a. Rainy season onset is defined as the first dasarian in which the 10-day rainfall total reaches or exceeds 50 mm, followed by two subsequent dasarians that also meet this criterion, thus constituting three consecutive dasarians with rainfall 50 mm (BMKG, 2022).
b. Rainy season retreat (marking the onset of the dry season) is defined as the first dasarian in which the 10-day rainfall total falls below 50 mm, followed by two subsequent dasarians that also remain below this threshold.
c. Rainy season duration is calculated as the total number of dasarians between onset and retreat.
d. Rainy season peak is determined as the period of three consecutive dasarians with the highest accumulated rainfall within a single seasonal year.

The 10-daily (dasarian) criteria were selected because they represent the official operational standard used by BMKG for seasonal forecasting and planting calendar determination in Indonesia (BMKG, 2022). Consequently, the results are directly relevant to agricultural and water resource management frameworks in the Brantas Watershed.

Accumulated Rainfall Anomaly Method (Complementary Approach)

As a comparative method, this study also applied the accumulated rainfall anomaly approach developed by Liebmann et al. (2007), which has been widely adopted in regional climate studies and precipitation evaluations across Indonesia and Southeast Asia (Hariadi et al., 2022; Dunning et al., 2018). This method calculates the accumulation of daily rainfall anomalies relative to the mean annual daily rainfall, with the general formulation given in Equation (1) (Liebmann et al., 2007; Dunning et al., 2018):

$$A(t) = \sum_{n=1}^{t} (R_n - \bar{R}) \qquad (1)$$

where $A(t)$ is the accumulated anomaly value on day t, $R(n)$ is the daily rainfall on day n, and $\bar{R}$ is the mean rainfall across the hydrological year (Liebmann et al., 2007; Dunning et al., 2018; Hariadi et al., 2022).

© 2026 Dept. of Geophysics Hasanuddin University

To avoid splitting the continuous wet season over the Brantas Watershed across calendar year boundaries, the accumulation calculation was executed on a hydrological year basis starting on 1 August corresponding to the climatologically driest period of the year and extending through 31 July of the following year.

Within this seasonal-year frame, rainy season onset is defined as the day when $A(t)$ reaches its absolute minimum value, marking the transition from dry-season conditions to daily rainfall consistently exceeding the annual mean. Conversely, rainy season retreat is defined as the day when $A(t)$ reaches its absolute maximum value, representing the transition back to conditions below the annual mean (Liebmann et al., 2007; Dunning et al., 2018). Rainy season duration is subsequently determined as the total number of days elapsed between the identified onset and retreat dates.

Trend and Statistical Significance Analysis

Temporal trends in rainy-season characteristics were assessed using the modified Mann–Kendall (MMK) test, which accounts for serial autocorrelation in climate time series (Hamed & Rao, 1998). Trend magnitudes were estimated using Sen's slope estimator and expressed in days per decade. Statistical significance was initially evaluated at $p < 0.05$. For spatial analyses involving multiple grid cells, the false discovery rate (FDR) procedure of Benjamini & Hochberg (1995) was applied at a significance level of $\alpha = 0.10$ to account for multiple testing.

The inter-model signal-to-noise ratio (SNR) was calculated as the absolute ensemble-mean change divided by the standard deviation of changes across the five climate models. An SNR greater than 1 indicates that the magnitude of the ensemble-mean signal exceeds the inter-model standard deviation, whereas a lower value indicates greater relative inter-model uncertainty. SNR was interpreted as a measure of signal strength rather than as a statistical significance test.

Differences between future projection periods and the historical baseline were also assessed using Welch's t-test on the ensemble-mean annual time series for each grid cell. This test accommodates unequal variances between the two periods. Grid cells with fewer than five valid annual values in either comparison period were excluded. FDR-adjusted significance results were reported separately from temporal trend significance. Where insufficient valid baseline observations prevented a reliable comparison, the corresponding significance result was reported as not applicable (N/A).

Spatial Change Analysis

Changes in rainy season characteristics were analyzed by calculating the differences (anomalies) between onset, retreat, and rainy season duration values for each projection period (SSP2-4.5 and SSP5-8.5; near-term 2015–2040, mid-term 2041–2070, and long-term 2071–2099) relative to the climatological values of the historical period, for each grid cell across the entire Brantas Watershed. Changes in onset and retreat are expressed in days, with positive values indicating a delay (later occurrence) and negative values indicating an advance (earlier occurrence), while changes in duration are also expressed in days, with positive values indicating a lengthening and negative values indicating a shortening of the rainy season. The calculated results were then mapped spatially using Geographic Information System (GIS) software to identify patterns and areas with notable changes within the Brantas Watershed, thereby providing a comprehensive picture of the spatial variation in climate change impacts on rainy season characteristics across the study area.

© 2026 Dept. of Geophysics Hasanuddin University

Both approaches were applied consistently to the BCCAQ-downscaled precipitation data, for both the historical baseline period (1981–2014) and the projection periods under the SSP2-4.5 and SSP5-8.5 scenarios. Onset, retreat, and rainy season duration values were calculated for each grid pixel at the downscaled resolution across the entire Brantas Watershed and for each year within the simulation period. These values were then averaged across each time horizon (historical, near-term, mid-term, and long-term) to produce representative climatological values, ensemble means, and anomaly fields for each period.

Results and Discussion

Model Performance Evaluation of CMIP6 against Observational Data

Model validation was conducted by comparing the outputs of five CMIP6 global climate models namely MIROC-ES2L, EC-Earth3-Veg-LR, IPSL-CM6A-LR, NorESM2-MM, and GFDL-ESM4 against observational reference data. Model performance was evaluated using several statistical indicators, including Correlation Coefficient (CC, [-]), Root Mean Square Error (RMSE, mm/day), Percent Bias (PBias, %), Standard Deviation (Std Dev, mm/day), and Standard Deviation Ratio (StdRatio, [-]). In addition to numerical metric-based evaluation, the analysis was reinforced through visualization using heatmaps and Taylor diagrams to assess pattern agreement, variability, and the degree of deviation of each model relative to observations. The validation results are presented in Figures 2 and 3, with detailed numerical values provided in Table 2.



Figure 2. Comparison of the performance of five CMIP6 models based on statistical indicators evaluated against observational data.

Based on Figure 2, illustrates variations in model performance across the evaluated statistical indicators. Overall, each model exhibited distinct capabilities in representing historical precipitation characteristics over the Brantas Watershed. Among the five models, MIROC-ES2L showed relatively highest overall performance, as indicated by the lowest RMSE (3.17 mm/day) and the highest correlation coefficient (CC = 0.79). The lower error metric indicates closer agreement between model simulations and observations, while the higher correlation demonstrates a strong ability to capture observed precipitation variability patterns. Furthermore, a PBias value of -0.94% indicates minimal systematic bias, while a

© 2026 Dept. of Geophysics Hasanuddin University

StdRatio of 1.10 effectively reproduces the amplitude of observed variability.

The remaining four models also demonstrated competitive performance and complementary strengths in representing regional climate features. GFDL-ESM4 exhibited strong fidelity with a low error metric (RMSE = 3.28 mm/day), a high correlation coefficient (CC = 0.75), a near-unity standard deviation ratio (StdRatio = 1.03), and a slight positive bias (PBias = 0.86%). NorESM2-MM and EC-Earth3-Veg-LR produced comparable error ranges (RMSE of 3.36 mm/day and 3.49 mm/day; CC of 0.76 and 0.74, respectively), with EC-Earth3-Veg-LR displaying a slight dry bias (PBias = -4.34%) and NorESM2-MM showing a moderate wet bias (PBias = 9.01%). IPSL-CM6A-LR presented a higher amplitude of simulated variability (StdRatio = 1.28) and a wet bias (PBias = 9.60%), yet retained a strong pattern correlation (CC = 0.76).

Overall, while the downscaled models demonstrated reasonable capability in capturing the mean state and seasonal variability under the BMKG threshold method, the evaluation results based on the heatmap were further reinforced by the Taylor diagram in Figure 3, which integrates information on correlation, standard deviation, and RMSE within a single spatial representation. Model positions closer to the observational reference point indicate higher levels of agreement, as they reflect a combination of good correlation, standard deviation close to that of observations, and smaller errors.

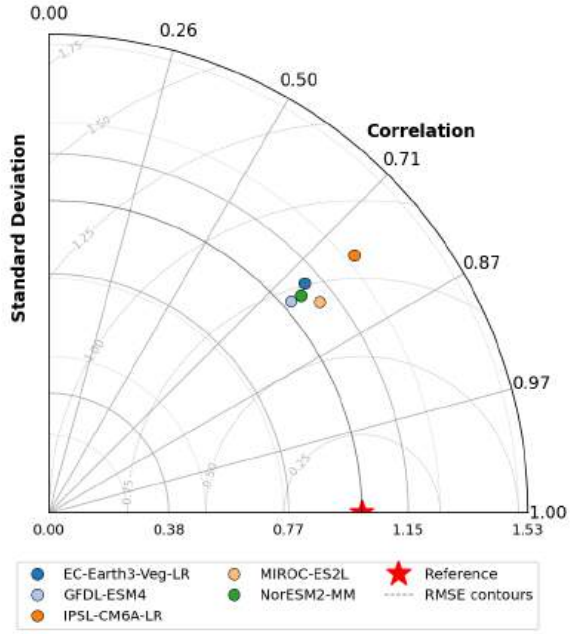


Figure 3. Taylor diagram evaluating the performance of five CMIP6 models against observational data.

In Figure 3, MIROC-ES2L is positioned relatively closest to the observational reference point, exhibiting the lowest RMSE (3.17 mm/day) and highest correlation coefficient (0.79) among the evaluated models. GFDL-ESM4 and NorESM2-MM occupied closely adjacent intermediate positions, reflecting strong correlation values and standard deviation ratios close to unity. Conversely, EC-Earth3-Veg-LR and IPSL-CM6A-LR exhibited slightly greater distances from the reference point, primarily driven by moderate dry/wet biases and higher standard deviation differences, while still maintaining high pattern correlation (CC = 0.74).

Overall, the results from the statistical metrics, heatmap, and Taylor diagram

© 2026 Dept. of Geophysics Hasanuddin University

consistently identified differences in capability among the CMIP6 models. MIROC-ES2L showed relatively exhibited the highest overall performance based on the combined evaluation of RMSE, CC, PBIAS, StdDev and StdRatio values, suggesting that this model achieved the highest level of agreement in representing historical precipitation characteristics over the Brantas Watershed. GFDL-ESM4 and NorESM2-MM also demonstrated robust performance, particularly in capturing variability amplitude with standard deviation ratios near unity (StdRatio = 1.03 and 1.06, respectively). The remaining models (EC-Earth3-Veg-LR and IPSL-CM6A-LR) provided complementary value by spanning the range of inter-model uncertainty, which is a key requirement of the multi-model ensemble framework.

Expanding this evaluation to seasonal transition dynamics, Table 2 provides a quantitative breakdown of historical onset, retreat, and duration evaluated against station observations for both the operational BMKG method and the ANOMALY method.

Table 2. Historical validation metrics of CMIP6 models against station observations (2000–2014) for BMKG and Anomaly methods.

Model	Method	Param	Obs Mean Days	Model Mean Days	Bias Days	Rmse Days	Spatial Corr
EC-Earth3-Veg-LR	BMKG	onset	126.2	132.4	6.2	13.8	0.74
		retreat	266.9	276.2	9.3	18	0.39
		duration	140.9	141.4	0.5	19.2	0.75
	ANOMALY	onset	109.1	203.2	94	94.4	0.5
		retreat	263	288.9	25.9	27.2	0.09
		duration	153.8	85.7	-68.1	68.9	0.52
GFDL-ESM4	BMKG	onset	125.8	144.3	18.5	21.5	0.76
		retreat	267	253.2	-13.8	20.4	0.46
		duration	141.4	107.6	-33.8	39	0.74
	ANOMALY	onset	107.7	120.1	12.4	14.1	0.68
		retreat	263.1	249.4	-13.7	15.4	0.17
		duration	155.4	129.2	-26.1	27.6	0.55
IPSL-CM6A-LR	BMKG	onset	126.2	124.4	-1.8	12	0.79
		retreat	266.9	255.8	-11.1	17.4	0.56
		duration	140.9	133.9	-6.9	17.1	0.85
	ANOMALY	onset	109.1	196.8	87.6	88	0.56
		retreat	263	289.1	26.2	27.6	0.12
		duration	153.8	92.3	-61.5	62.7	0.54
MIROC-ES2L	BMKG	onset	126.2	115.9	-10.4	14.8	0.78
		retreat	266.9	269	2.1	13.2	0.73
		duration	140.9	153	12.2	19.1	0.87
	ANOMALY	onset	109.1	200.4	91.3	91.6	0.53
		retreat	263	281.7	18.7	20.7	0.16
		duration	153.8	81.3	-72.5	73.3	0.52
NorESM2-MM	BMKG	onset	125.8	140.3	14.6	21.1	0.77
		retreat	267	255.7	-11.3	20.6	0.37
		duration	141.4	115	-26.4	31.4	0.82
	ANOMALY	onset	107.7	117.3	9.6	12.5	0.7
		retreat	263.1	251.1	-12	13.5	0.27
		duration	155.4	133.8	-21.6	23.6	0.61

Table 2 shows that model performance depended on both the seasonal parameter and the method used to identify it. The BMKG method generally produced stronger spatial correlations and lower errors for duration, whereas the Anomaly method performed comparatively well for onset and retreat in selected models. These results indicate that neither method consistently outperformed the other for

© 2026 Dept. of Geophysics Hasanuddin University

every model and parameter. RMSE values ranged from 12.0 to 21.5 days for onset, 13.2 to 20.6 days for retreat, and 17.1 to 39.0 days for duration. Spatial correlation coefficients reached 0.79 for onset, 0.73 for retreat, and 0.87 for duration. MIROC-ES2L and IPSL-CM6A-LR showed particularly strong spatial agreement for duration, with correlation coefficients of 0.87 and 0.85, respectively.

In contrast, the Anomaly method exhibited substantial errors for onset and duration in several models. Onset RMSE ranged from 12.5 to 94.4 days, while duration RMSE ranged from 23.6 to 73.3 days. Retreat RMSE was comparatively lower, ranging from 13.5 to 27.6 days. Spatial correlations for retreat were also generally weak, ranging from 0.09 to 0.27. These results indicate that the Anomaly method did not perform consistently across models and rainy-season parameters, particularly for onset and duration.

Given the different strengths and limitations of individual models, the five-model ensemble provides a basis for examining inter-model variability and structural uncertainty in future projections. However, the reliability of the resulting projections remains dependent on model performance, the seasonal-index method, and the consistency of the projected responses across models.

Temporal and Spatial Analysis of Changes in Rainy Season Characteristics under SSP2-4.5 and SSP5-8.5 Scenarios

To evaluate the response of rainy season characteristics to climate change, the analysis was conducted using both the BMKG method and the anomaly method, considering three main parameters: onset, retreat, and duration. The evaluation was carried out across three projection periods: near-term (2015–2040), mid-term (2041–2070), and far-term (2071–2099). The temporal statistical results were then combined with spatial distributions to identify patterns of change in rainy season characteristics under the SSP2-4.5 and SSP5-8.5 scenarios, as presented in Figure 4 and 5.

Based on the BMKG method mapping results (Figure 4), the changes in rainy season characteristics showed different responses between the SSP2-4.5 and SSP5-8.5 scenarios. Overall, the onset parameter exhibited a consistent advance under both scenarios, while the retreat parameter remained relatively stable. Consequently, the duration parameter showed a tendency to lengthen, primarily driven by the earlier onset rather than by changes in retreat timing.

For the onset parameter, ensemble median derived using the BMKG method indicated an earlier rainy-season onset in all three projection periods relative to the 1981–2014 baseline. Under SSP2-4.5, the median changes were −45.1 days in the near term, −50.3 days in the mid term, and −53.2 days in the long term. Under SSP5-8.5, the corresponding changes were −42.8, −45.1, and −45.3 days. These values describe the median projected changes and should not be interpreted as evidence of uniform changes across all grid cells or models.

The retreat parameter, in contrast, showed only small changes. Under SSP2-4.5, the median change ranged from +1.4 days (near-term) to −0.4 days (long-term), while under SSP5-8.5 it ranged from −8.9 days (near-term) to −5.6 days (long-term). These results suggest that the retreat timing of the rainy season is relatively insensitive to the emission scenario, at least as detected by the BMKG threshold criterion.

© 2026 Dept. of Geophysics Hasanuddin University

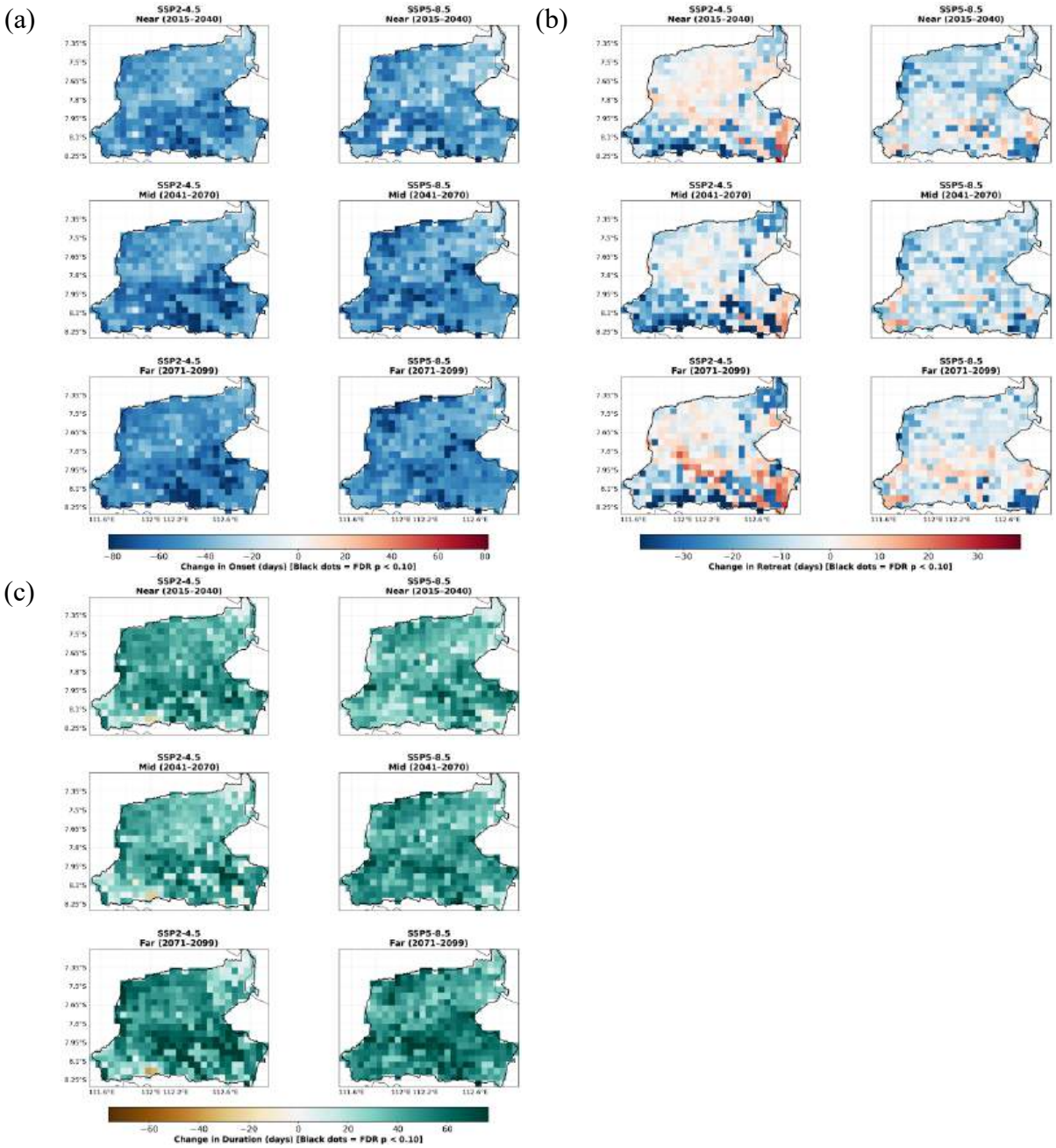


Figure 4. Spatial distribution of changes in (a) rainy season onset, (b) rainy season retreat, and (c) rainy season duration based on the BMKG method under SSP2-4.5 and SSP5-8.5 scenarios for the near-term (2015–2040), mid-term (2041–2070), and long-term (2071–2099) periods.

Changes in duration followed the pattern of onset and retreat. Under both scenarios, the rainy season duration lengthened substantially: +46.5 days (near-term), +41.0 days (mid-term), and +58.0 days (long-term) under SSP2-4.5; and +43.9, +44.7, and +51.1 days under SSP5-8.5. The spatial distribution (Figure 4c) showed widespread lengthening across the basin, consistent with the earlier onset identified in Figure 4a. Notably, the magnitude of duration lengthening was comparable between scenarios in the near-term and mid-term, but larger under SSP5-8.5 in the long-term period, suggesting an increasing response with higher emission forcing.

These values represent median changes relative to the 1981–2014 baseline for each projection period, rather than the temporal trend throughout 2015–2099. The period-specific median changes should be distinguished from the temporal trend estimates in Table 3. For the BMKG

© 2026 Dept. of Geophysics Hasanuddin University

method, duration showed a statistically significant increasing trend under SSP5-8.5 (Sen's slope = +2.573 days/decade, p = 0.0001), whereas the trend under SSP2-4.5 was not statistically significant (p = 0.0651). The Anomaly method yielded a contrasting significant decreasing trend under SSP5-8.5, highlighting the sensitivity of the projected duration response to the method used to define the rainy season

The anomaly method (Figure 5) quantified the magnitude of temporal deviation from the 1981–2014 climatology in days. In contrast to the BMKG method, which measures the absolute position of the rainy season, the anomaly method measures the relative shift of the seasonal cycle. The comparison between the two methods therefore provides complementary insight into the physical response of the rainy season to climate change.

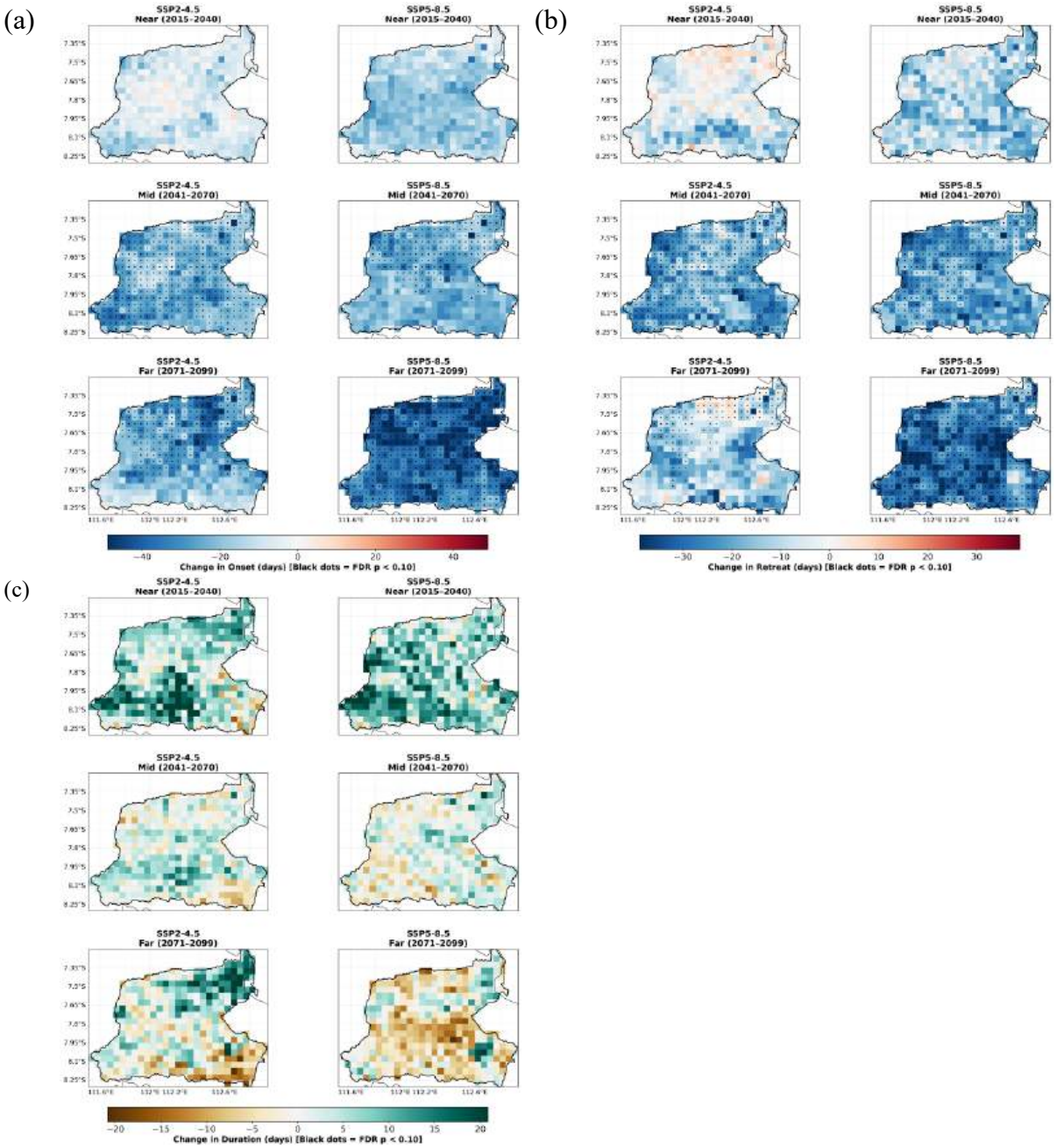


Figure 5. Spatial distribution of changes in (a) rainy season onset, (b) rainy season retreat, and (c) rainy season duration based on the anomaly method under SSP2-4.5 and SSP5-8.5 scenarios for the near-term (2015–2040), mid-term (2041–2070), and long-term (2071–2099) periods.

© 2026 Dept. of Geophysics Hasanuddin University

For onset, the Anomaly method indicated an earlier rainy-season onset under both scenarios, although the magnitude varied across projection periods. Under SSP2-4.5, the median onset changes were −6.1 days in the near-term period, −21.0 days in the mid-term period, and −23.9 days in the long-term period. Under SSP5-8.5, the corresponding changes were −20.2, −21.9, and −40.0 days. The inter-model signal-to-noise ratios ranged from 0.73 to 1.61 under SSP2-4.5 and from 1.95 to 4.06 under SSP5-8.5. These results indicate that the projected advance varied in magnitude and robustness across scenarios and periods

For retreat, the Anomaly method indicated an earlier retreat in all projection periods, in contrast to the relatively stable retreat timing derived using the BMKG method. Under SSP2-4.5, the median retreat changes were −5.4, −16.6, and −11.0 days in the near-term, mid-term, and long-term periods, respectively. Under SSP5-8.5, the corresponding changes were −11.6, −19.5, and −28.3 days. However, the signal-to-noise ratios varied considerably, ranging from 0.65 to 1.34 under SSP2-4.5 and from 0.74 to 2.77 under SSP5-8.5. Therefore, the direction of the median changes should be distinguished from the robustness of the projected response across models and grid cells.

For duration, the ANOMALY method produced small and inconsistent changes compared with the BMKG method. Under SSP2-4.5, the median duration changes were +2.2 days in the near-term period, +1.9 days in the mid-term period, and −3.6 days in the long-term period. Under SSP5-8.5, the corresponding changes were +8.5, −1.3, and −7.9 days. The signal-to-noise ratios ranged from 0.35 to 0.70 under SSP2-4.5 and from 0.07 to 0.14 under SSP5-8.5, indicating that the ensemble signal was generally weak relative to inter-model variability. The FDR-significant area was also negligible in most periods. Consequently, the Anomaly results do not support a robust conclusion regarding the direction or magnitude of future duration changes.

Table 3 summarizes the temporal trend estimates for rainy-season onset, retreat, and duration under SSP2-4.5 and SSP5-8.5 for both the BMKG and Anomaly methods. The table reports Sen's slope, the corresponding p-value, ensemble significance, and the dominant direction of change across models. In the BMKG method, onset and retreat are represented by their timing within the defined seasonal calendar, whereas duration represents the interval between these two transitions. In the Anomaly method, changes in timing and duration are expressed as differences from the 1981–2014 baseline. These quantities are interpreted separately because seasonal timing indices and duration have different meanings and should not be compared as equivalent measures.

Table 3. Summary of statistics and trend analysis for rainy season onset, retreat, & duration derived from the BMKG & anomaly methods under the SSP2-4.5 & SSP5-8.5 scenarios during the 2015–2099 projection period.

Method	Parameter	Scenario	Slope (days/decade)	Sig P	Ensemble Sig	Agreement
Anomaly	duration	SSP2-4.5	-0.3793	0.8954	No	Mostly decline
	onset	SSP2-4.5	-0.1196	0.0852	No	Mostly decline
	retreat	SSP2-4.5	-1.4943	0.0145	Yes	Mostly decline
BMKG	duration	SSP2-4.5	0.7228	0.0651	No	Mostly increase
	onset	SSP2-4.5	-0.6793	0.1771	No	Mostly decline
	retreat	SSP2-4.5	-0.8495	0.2121	No	Mostly decline
Anomaly	duration	SSP5-8.5	-3.3405	0.0142	Yes	Mostly decline
	onset	SSP5-8.5	-3.329	0.0279	Yes	Mostly decline
	retreat	SSP5-8.5	-0.9367	0.2449	No	Mostly decline
BMKG	duration	SSP5-8.5	2.573	0.0001	Yes	Consistent increase
	onset	SSP5-8.5	-0.2523	0.6636	No	Consistent decline
	retreat	SSP5-8.5	0.395	0.3763	No	Consistent increase

© 2026 Dept. of Geophysics Hasanuddin University

The modified Mann–Kendall trend analysis (Table 3) identified different temporal trends between the BMKG and Anomaly methods. Under the BMKG method, rainy-season duration under SSP5-8.5 showed a statistically significant increasing trend (Sen's slope = +2.57 days/decade, p = 0.0001), whereas onset and retreat showed no statistically significant trends at the 0.05 level. Under the Anomaly method, statistically significant trends were detected for onset under SSP5-8.5 (−3.329 days/decade, p = 0.0279), retreat under SSP2-4.5 (−1.4943 days/decade, p = 0.0145), and duration under SSP5-8.5 (−3.3405 days/decade, p = 0.0142). For anomaly-based duration under SSP5-8.5, the negative temporal trend indicates an overall tendency toward shorter rainy seasons during 2015–2099. However, the period-specific median changes relative to the 1981–2014 baseline were +8.5 days in the near term, −1.3 days in the mid term, and −7.9 days in the long term (Table 4). These values describe changes in separate projection periods, whereas the trend estimate represents the temporal tendency across the full projection period; therefore, the two results are not necessarily contradictory. Nevertheless, the low SNR values (0.07–0.14) and negligible FDR-significant area (0–0.3%) indicate that the anomaly-based duration signal is weak relative to inter-model variability and lacks substantial spatial significance. Consequently, the statistically significant temporal trend should not be interpreted as evidence of a robust, spatially consistent response across the watershed.

Tabel 4. Cross-method comparison of projected changes in rainy season onset, retreat, and duration (days) under SSP2-4.5 and SSP5-8.5.

Para-meter	Scenario	Period	BMKG Median	Anomaly Median	Diffe-rence	BMKG SNR	Anomaly SNR	BMKG FDR	Anomaly FDR
Onset	SSP2-4.5	2015-2040	-45.1	-6.1	-39	19.55	0.73	N/A	0
		2041-2070	-50.3	-21	-29.3	8.02	1.61	N/A	91
		2071-2099	-53.2	-23.9	-29.4	11.76	1.46	N/A	54.5
	SSP5-8.5	2015-2040	-42.8	-20.2	-22.7	1.45	1.95	N/A	0
		2041-2070	-45.1	-21.9	-23.3	2.4	4.06	N/A	46.5
		2071-2099	-45.3	-40	-5.3	2.54	2.32	N/A	97.7
Retreat	SSP2-4.5	2015-2040	1.4	-5.4	6.8	0.25	0.65	N/A	0
		2041-2070	-1.4	-16.6	15.2	0.64	1.34	N/A	85.1
		2071-2099	-0.4	-11	10.6	0.43	0.71	N/A	29.1
	SSP5-8.5	2015-2040	-8.9	-11.6	2.8	0.61	0.74	N/A	1
		2041-2070	-8.7	-19.5	10.8	0.91	2.77	N/A	65.8
		2071-2099	-5.6	-28.3	22.8	0.48	1.56	N/A	96.7
Duration	SSP2-4.5	2015-2040	46.5	2.2	44.3	2.49	0.53	N/A	0
		2041-2070	41	1.9	39.1	1.96	0.7	N/A	0.3
		2071-2099	58	-3.6	61.6	1.6	0.35	N/A	0
	SSP5-8.5	2015-2040	43.9	8.5	35.3	1.45	0.07	N/A	0.3
		2041-2070	44.7	-1.3	46	3.32	0.14	N/A	0
		2071-2099	51.1	-7.9	59	4.24	0.13	N/A	0

To compare the two methods, Table 4 presents the ensemble-median changes in onset, retreat, and duration for each scenario and projection period, together with the difference between methods, SNR values, and the percentage of grid cells showing FDR-significant changes where available. First, the advance of onset was consistently larger under the BMKG method (median −45 to −53 days) than under the anomaly method (median −6 to −40 days) for both scenarios and all periods. The difference may reflect the distinct ways in which the two methods identify seasonal transitions. The BMKG method is based on a predefined rainfall threshold, whereas the Anomaly method relies on deviations in

© 2026 Dept. of Geophysics Hasanuddin University

the accumulated rainfall cycle relative to the historical reference. Consequently, the methods may respond differently to changes in rainfall amount, timing, and within-season distribution. The present analysis does not independently establish which of these factors explains the observed differences.

Second, retreat showed opposite responses between the two methods. Under BMKG, retreat remained approximately stable (median change between −8.9 and +1.4 days) with low inter-model agreement (SNR = 0.25–0.91). Under the Anomaly method, the ensemble-median retreat change was negative in all projection periods, ranging from −5.4 to −28.3 days. For the long-term SSP5-8.5 period, 96.7% of grid cells were reported as FDR-significant. This spatial significance result should be interpreted separately from inter-model agreement and SNR, which describe different aspects of projection robustness.

Third, duration showed a substantial lengthening under the BMKG method (median +41 to +58 days) with moderate to high SNR (1.5–4.2). In contrast, the anomaly method showed only weak and inconsistent duration changes (median between −7.9 and +8.5 days) with very low SNR (0.07–0.70) and negligible FDR significance (< 1% in most periods). The larger signal under BMKG is consistent with the advance of onset being only partially offset by changes in retreat timing, whereas under the anomaly method, onset and retreat advance together, leaving duration approximately unchanged.

The projected changes varied spatially across the Brantas Watershed. At the ensemble-median level, both methods indicated an earlier onset, whereas retreat responses differed between methods and duration lengthening was evident primarily in the BMKG results. These basin-wide summaries do not imply uniform responses across all grid cells or models. The spatial patterns should therefore be interpreted together with the reported SNR and FDR results. However, attributing these variations to specific local drivers requires further analysis beyond the scope of this study.

Dynamics of Rainy Season Peak under Climate Change Scenarios

In addition to changes in rainy season onset and retreat, the timing of the rainy season peak represents an important indicator for understanding changes in the temporal distribution of rainfall within future climate systems. Shifts in the timing of peak rainfall may affect periods of maximum water availability, cropping patterns, and the risk of hydrometeorological events associated with seasonal rainfall intensity. Therefore, an analysis of the rainy season peak was conducted to evaluate changes in its spatial distribution and temporal variation under the SSP2-4.5 and SSP5-8.5 scenarios during the 2015–2099 projection period. The spatial distribution of rainy season peak timing is presented in Figure 6, while the temporal variation is shown in Figure 7.

Based on Figure 6, the spatial distribution of rainy season peak timing showed considerable regional variation under both scenarios. Overall, the northern part of the study area was predominantly characterized by earlier peak rainfall occurrence (approximately 100–140 days since 1 August, corresponding to mid-November to late December), while the southern region showed relatively later peak timing (approximately 160–200 days, corresponding to early January to mid-February). This north-to-south spatial gradient suggests that the distribution of maximum rainfall does not occur uniformly but rather follows the regional characteristics of the study area.

© 2026 Dept. of Geophysics Hasanuddin University

The differences in peak timing between regions indicate a clear spatial gradient. Areas located closer to the pathway of moist air mass inflow or those with more rapid atmospheric responses to seasonal transitions tended to experience earlier rainfall peaks, while other areas experienced delays due to differences in geographical conditions. However, identifying the specific atmospheric or topographic drivers behind this gradient requires further dedicated analysis.

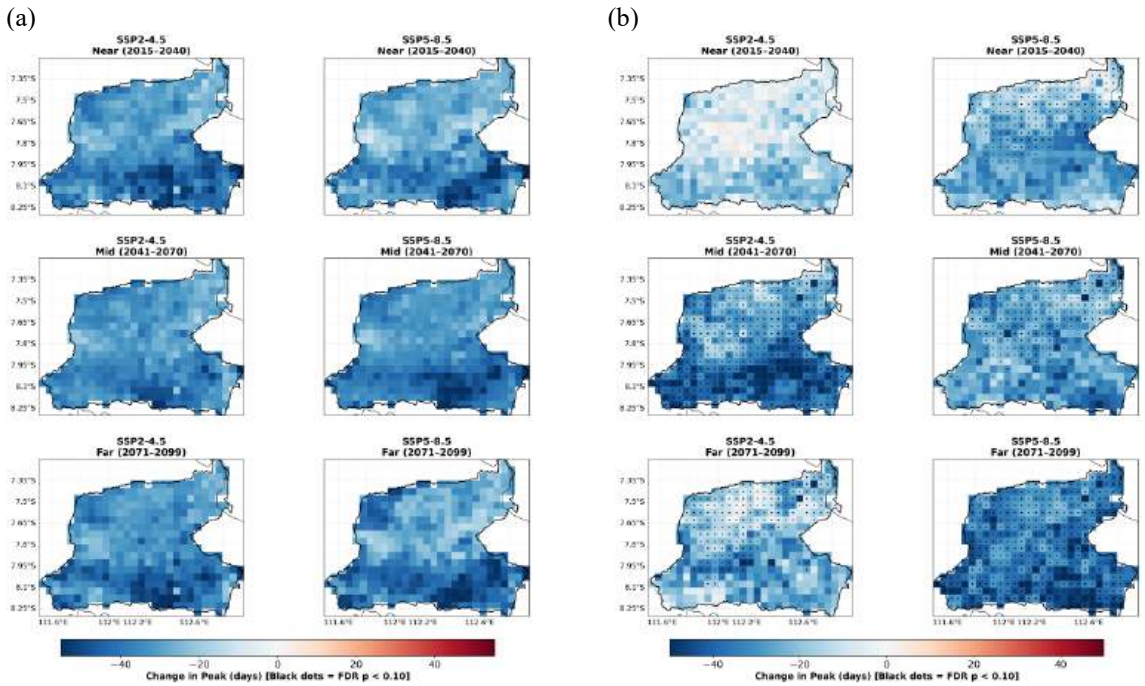


Figure 6. Spatial distribution of rainy season peak timing under SSP2-4.5 and SSP5-8.5 during 2015–2099 based on (a) BMKG and (b) anomaly methods.

Under the SSP2-4.5 scenario, most areas showed rainy season peak timing in the range of 100 to 150 days (mid-November to late December), with some southern areas reaching up to 200 days (mid-February). This distribution suggests that the spatial pattern of peak rainfall still generally maintained its overall characteristics, although local variations between areas were evident. This condition indicates that under the moderate emission scenario, changes in rainy season peak timing were more a matter of regional variation rather than widespread shifts in pattern.

Under SSP5-8.5, the mapped peak-timing index retained a broadly similar spatial pattern to that under SSP2-4.5, with values reaching approximately 210 days in parts of the southern and southeastern watershed. Because these maps show absolute timing rather than changes relative to the historical baseline, they do not establish whether peak rainfall becomes systematically later under the higher-emission scenario. These changes suggest differences in regional response to increased climate forcing. However, since the northern areas still maintained relatively earlier peak rainfall characteristics, the observed changes did not indicate a uniform shift across the entire region.

Spatially, these results suggest that higher emission scenarios do not directly lead to uniform changes in rainy season peak timing across all areas. Rather, the response of peak rainfall appears to remain controlled by a combination of large-scale climate changes and local factors that influence rainfall distribution. This differs from some other rainy season parameters, such as retreat and duration, which in

© 2026 Dept. of Geophysics Hasanuddin University

previous analyses showed more consistent changes across periods.

In addition to spatial distribution analysis, the temporal variation in rainy season peak timing during the 2015–2099 period is shown in Figure 7. The thin lines represent the annual values for each scenario, the thick lines represent the 5-year moving average to illustrate medium-term variations, and the dashed lines indicate the Sen's slope trend during the projection period. The y-axis represents the peak timing expressed in days since 1 August of the hydrological year (Day 0 = 1 August; for reference, Day 100 ≈ 9 November, Day 150 ≈ 29 December, and Day 200 ≈ 17 February).

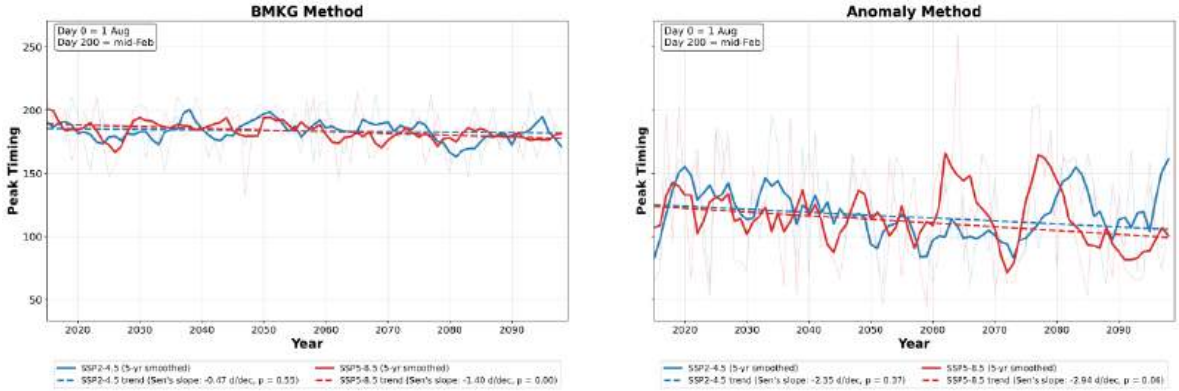


Figure 7. Temporal variation of rainy season peak timing under SSP2-4.5 and SSP5-8.5 scenarios during the 2015–2099 period.

Based on Figure 7, under the BMKG method (left panel), the timing of the rainy season peak fluctuated between approximately 160 and 200 days (early January to mid-February), indicating considerable inter-annual variability. Despite this variability, the Sen's slope analysis showed a decreasing trend of −0.61 days/decade ($p = 0.07$) under SSP2-4.5 and −1.24 days/decade ($p < 0.01$) under SSP5-8.5. The reported negative Sen's slope under SSP5-8.5 (−1.24 days/decade, $p < 0.01$) suggests an apparent shift toward earlier peak timing. However, this interpretation remains provisional because peak timing is a seasonal index that may wrap around the seasonal-cycle boundary. The direction and significance of the trend should be confirmed using an appropriate treatment of the seasonal index and its uncertainty.

Conversely, under the Anomaly method (right panel), the peak timing showed a much larger amplitude of inter-annual variability, fluctuating between approximately 50 and 160 days (late September to early January). The trend analysis revealed a decreasing trend of −1.27 days/decade ($p = 0.14$) under SSP2-4.5 and −2.28 days/decade ($p = 0.02$) under SSP5-8.5. The large interannual variability and SNR values below 1.5 indicate that the projected peak-timing signal under the Anomaly method is relatively weak compared with its variability. This suggests limited robustness of the projected response, although a direct comparison of robustness between methods requires consistent SNR definitions and uncertainty estimates.

When compared to changes in onset and retreat, the peak rainfall parameter showed a more moderate shift. Changes in onset and retreat can affect the length of the rainy season, while peak timing describes the distribution of maximum rainfall within that period. Therefore, even though the rainy season may undergo changes in duration under some scenarios, the period of maximum rainfall occurrence exhibited a slight, statistically significant advance (particularly under SSP5-8.5), although it was largely masked by high inter-annual variability.

© 2026 Dept. of Geophysics Hasanuddin University

Overall, the results suggest that changes in the rainy season peak were characterized by high spatial and inter-annual variation, rather than a uniform systematic shift across the entire basin. The SSP5-8.5 scenario showed greater temporal variability compared to SSP2-4.5, but both scenarios still maintained relatively similar ranges of peak rainfall timing throughout the twenty-first century. These findings suggest that within the study area, climate change may potentially affect the stability of peak rainfall timing, while regional factors and natural atmospheric variability continue to play important roles in determining the temporal dynamics of maximum rainfall.

These findings provide critical insights into the future dynamics of the rainy season over the Brantas Watershed. The projected earlier onset under both scenarios is broadly consistent with previous studies reporting changes in rainy-season timing over parts of the Maritime Continent (Adriat et al., 2025; Hariadi et al., 2022). However, differences in study area, observational references, and seasonal-index definitions should be considered when comparing the magnitude and proposed mechanisms of these changes. However, our findings diverge regarding the rainy season duration. While this study projects a substantial lengthening of duration (+41 to +58 days) based on the BMKG method, previous studies (Wiwoho et al., 2023) reported a relatively stable duration. This discrepancy likely arises from methodological differences. The BMKG threshold method is highly sensitive to the intensification of extreme rainfall, whereas the cumulative Anomaly method captures the relative shift of the seasonal cycle (Dunning et al., 2018).

The stark contrast between these two approaches highlights an important methodological insight: for tropical watersheds characterized by high daily rainfall variability, cumulative Anomaly indices are highly sensitive to daily-scale noise. These findings suggest that the BMKG threshold method may be more suitable for operational applications involving rainy-season duration in the Brantas Watershed, given its stronger historical validation for this parameter. However, method performance varied across parameters and models, so the suitability of either method should be assessed against the specific application and validation metric

Despite these valuable insights, this study has several limitations that should be acknowledged. First, the historical validation was restricted to CMIP6 models and relied on an observational period (2000–2014) that, while independent of the BCCAQ calibration against CHIRPS, still contains inherent uncertainties. Future studies should incorporate pre-2000 observational data to enable a strictly independent validation. Second, the anomaly method exhibited substantial deviations during historical validation, which limits its utility for future projections in this region. Third, the attribution of spatial variations in peak timing to specific local drivers was beyond the scope of this study and requires further dedicated analysis using high-resolution topographic data and large-scale climate indices.

Based on these findings, several recommendations can be made. For water resource managers and agricultural planners in the Brantas Watershed, the projected earlier onset and longer rainy season imply that cropping calendars and reservoir operation strategies may need to be adjusted to accommodate the shifting hydrological cycle. Furthermore, future research should expand the multi-model ensemble by including a wider range of CMIP6 models and integrating large-scale atmospheric dynamics with local geographical factors to fully understand

© 2026 Dept. of Geophysics Hasanuddin University

the spatial heterogeneity of rainy season changes.

Conclusion

This study evaluated projected changes in rainy-season onset, retreat, and duration across the Brantas River Basin under the SSP2-4.5 and SSP5-8.5 scenarios using the BMKG and Anomaly methods. The results revealed differences between the two methods in both the magnitude and direction of projected changes. The BMKG method generally indicated larger changes in seasonal timing and duration, whereas the Anomaly method produced smaller and more variable changes. Trend analysis also identified significant changes in selected parameters, including decreasing anomaly-based onset and duration under SSP5-8.5, as well as increasing BMKG-based duration under the same scenario. These findings highlight the importance of considering methodological differences when interpreting future rainy-season characteristics.

Despite these trends, the strength and spatial consistency of projected changes varied across scenarios and periods. In particular, low signal-to-noise ratios and limited FDR-significant areas for anomaly-based duration indicate substantial uncertainty relative to inter-model variability. Therefore, statistically significant temporal trends should not automatically be interpreted as robust spatial responses across the basin. The findings demonstrate that combining temporal trend analysis with ensemble agreement, signal-to-noise ratios, and spatial significance assessments provides a more comprehensive basis for evaluating future rainy-season changes. This approach can support climate adaptation and water-resource planning in the Brantas River Basin while accounting for uncertainty in future rainfall-season dynamics.

Acknowledgements

The authors gratefully acknowledge the Indonesia Agency for Meteorology, Climatology, and Geophysics (BMKG) for providing operational climate data and for the establishment of the dasarian-based rainy season criteria used in this study. We also thank the Earth System Grid Federation (ESGF) for providing access to CMIP6 model outputs, and the Climate Hazards Group for making the CHIRPS precipitation dataset publicly available.

Author Contribution

Gilang Aulia Herlambang: Conceptualization, data curation, formal analysis, investigation, methodology, validation, visualization, and writing – original draft.
Lalu Muhamad Jaelani: Conceptualization, methodology, project administration, supervision, and writing – review and editing.

Conflict of Interest

The authors declare no conflicts of interest. No financial or personal relationships with other people or organizations have inappropriately influenced or biased the work presented in this study. The funders had no role in the design of the study; in the collection, analyses, or interpretation of data; in the writing of the manuscript; or in the decision to publish the results.

References

Adriat, R., Aprilina, A., Satyawardhana, H., Ihwan, A., & Sutanto, Y. (2025). Identification of variations in the onset of the rainy and dry seasons in Indonesia. *Journal of Bioresources and Environmental Sciences,* 4(2), 102–111. https://doi.org/10.61435/jbes.2025.19960

Bai, L., Shi, C., Li, L., Yang, Y., & Wu, J. (2018). Accuracy of CHIRPS

© 2026 Dept. of Geophysics Hasanuddin University

satellite-rainfall products over mainland China. *Remote Sensing*, 10(3), 362. https://doi.org/10.3390/rs10030362

BBWS Brantas. (2011). *Profil Wilayah Sungai Brantas*. Balai Besar Wilayah Sungai, Direktorat Jenderal Sumber Daya Air, Kementerian Pekerjaan Umum. https://sda.pu.go.id/balai/bbwsbrantas/

Benjamini, Y., & Hochberg, Y. (1995). Controlling the false discovery rate: A practical and powerful approach to multiple testing. *Journal of the Royal Statistical Society: Series B (Methodological), 57*(1), 289–300. https://doi.org/10.1111/j.2517-6161.1995.tb02031.x

BMKG. (2022). *Normal standar iklim 1991–2020 (Buku ZOM 9120)*. Badan Meteorologi, Klimatologi, dan Geofisika. https://iklim.bmkg.go.id/bmkgadmin/storage/buletin/Buku_ZOM9120_versi_cetak.pdf

Bombardi, R. J., Moron, V., & Goodnight, J. S. (2020). Detection, variability, and predictability of monsoon onset and withdrawal dates: A review. *International Journal of Climatology,* 40(2), 641–667. https://doi.org/10.1002/joc.6264

Boucher, O., Servonnat, J., Albright, A. L., Aumont, O., Balkanski, Y., Bastrikov, V., Bekki, S., Bonnet, R., Bony, S., Bopp, L., Braconnot, P., Brockmann, P., Cadule, P., Caubel, A., Cheruy, F., Codron, F., Cozic, A., Cugnet, D., D'Andrea, F., Davini, P., de Lavergne, C., Denvil, S., Deshayes, J., Devilliers, M., Ducharne, A., Dufresne, J.-L., Dupont, E., Éthé, C., Fairhead, L., Falletti, L., Flavoni, S., Foujols, M.-A., Gardoll, S., Gastineau, G., Ghattas, J., Grandpeix, J.-Y., Guenet, B., Guez, L. E., Guilyardi, E., Guimberteau, M., Hauglustaine, D., Hourdin, F., Idelkadi, A., Joussaume, S., Kageyama, M., Khodri, M., Krinner, G., Lebas, N., Levavasseur, G., Lévy, C., Li, L., Lott, F., Lurton, T., Luyssaert, S., Madec, G., Madeleine, J.-B., Maignan, F., Marchand, M., Marti, O., Mellul, L., Meurdesoif, Y., Mignot, J., Musat, I., Ottlé, C., Peylin, P., Planton, Y., Polcher, J., Rio, C., Rochetin, N., Rousset, C., Sepulchre, P., Sima, A., Swingedouw, D., Thiéblemont, R., Traore, A. K., Vancoppenolle, M., Vial, J., Vialard, J., Viovy, N., & Vuichard, N. (2020). Presentation and evaluation of the IPSL-CM6A-LR Climate Model. *Journal of Advances in Modeling Earth Systems*, 12(7), e2019MS002010. https://doi.org/10.1029/2019MS002010

Cannon, A. J., Sobie, S. R., & Murdock, T. Q. (2015). Bias correction of GCM precipitation by quantile mapping: How well do methods preserve changes in quantiles and extremes? *Journal of Climate,* 28(17), 6938–6959. https://doi.org/10.1175/JCLI-D-14-00754.1

Chen, C.-A., Hsu, H- H., & Liang, H.-C. (2021). Evaluation and comparison of CMIP6 and CMIP5 model performance in simulating the seasonal extreme precipitation in the Western North Pacific and East Asia. *Weather and Climate Extremes*, 31, 100303. https://doi.org/10.1016/j.wace.2021.100303

Dinku, T., Funk, C., Peterson, P., Maidment, R., Tadesse, T., Gadain, H., & Ceccato, P. (2018). Validation of the CHIRPS satellite rainfall estimates over eastern Africa. *Quarterly Journal of the Royal Meteorological Society*, 144, 292–312. https://doi.org/10.1002/qj.3244

Dunne, J. P., Horowitz, L. W., Adcroft, A. J., Ginoux, P., Held, I. M., John, J. G., Krasting, J. P., Malyshev, S., Naik, V., Paulot, F., Shevliakova, E., Stock,

© 2026 Dept. of Geophysics Hasanuddin University

C. A., Winton, M., Zadeh, N., Balaji, V., Blanton, C., Dunne, K. A., Dupuis, C., Durachta, J., Dupuis, R., Gauthier, P. P. G., Griffies, S. M., Guo, H., Hallberg, R. W., Harrison, M., He, J., Hurlin, W., McHugh, C., Menzel, R., Milly, P. C. D., Nikonov, S., Paynter, D. J., Ploshay, J., Radhakrishnan, A., Rand, K., Reichl, B. G., Robinson, T., Schwarzkopf, D. M., Sentman, L. T., Underwood, S., Vahlenkamp, H., Winton, M., Wittenberg, A. T., Wyman, B., Zeng, Y., & Zhao, M. (2020). The GFDL Earth System Model Version 4.1 (GFDL-ESM4.1): Overall coupled model description and simulation characteristics. *Journal of Advances in Modeling Earth Systems*, 12(11), e2019MS002015. https://doi.org/10.1029/2019MS002015

Döscher, R., Acosta, M., Alessandri, A., Anthoni, P., Arsouze, T., Bergman, T., Bernardello, R., Boussetta, S., Caron, L.-P., Carver, G., Castrillo, M., Catalano, F., Cvijanovic, I., Davini, P., Dekker, E., Doblas-Reyes, F. J., Docquier, D., Echevarria, P., Fladrich, U., Fuentes-Franco, R., Gröger, M., von Hardenberg, J., Hieronymus, J., Karami, M. P., Keskinen, J.-P., Koenigk, T., Makkonen, R., Massonnet, F., Ménégoz, M., Miller, P. A., Moreno-Chamarro, E., Nieradzik, L., van Noije, T., Nolan, P., O'Donnell, D., Ollinaho, P., van den Oord, G., Ortega, P., Tintó Prims, O., Ramos, A., Reerink, T., Rousset, C., Ruprich-Robert, Y., Le Sager, P., Schmith, T., Schrödner, R., Serva, F., Sicardi, V., Sloth Madsen, M., Smith, B., Tian, T., Tourigny, É., Uotila, P., Vancoppenolle, M., Wang, S., Wårlind, D., Willén, U., Wyser, K., Yang, S., Yepes-Arbós, X., & Zhang, Q. (2022). The EC-Earth3 Earth system model for the Coupled Model Inter-comparison Project 6. *Geoscientific Model Development*, 15(7), 2975–3020. https://doi.org/10.5194/gmd-15-2973-2022

Dunning, C. M., Allan, R. P., & Black, E. (2017). Identification of deficiencies in seasonal rainfall simulated by CMIP5 climate models. *Environmental Research Letters,* 12, 114001. https://doi.org/10.1088/1748-9326/aa869e

Dunning, C. M., Black, E., & Allan, R. P. (2018). Later wet seasons with more intense rainfall over Africa under future climate change. *Journal of Climate*, 31(23), 9719–9738. https://doi.org/10.1175/JCLI-D-18-0102.1

Eyring, V., Bony, S., Meehl, G. A., Senior, C. A., Stevens, B., Stouffer, R. J., & Taylor, K. E. (2016). Overview of the Coupled Model Intercomparison Project Phase 6 (CMIP6) experimental design and organization. *Geoscientific Model Development,* 9(5), 1937–1958. https://doi.org/10.5194/gmd-9-1937-2016

Ferijal, T., Mechram, S., Fauzi, A., & Ferdiansyah, T. (2025). Performance analysis of satellite-derived precipitation data in Aceh, Indonesia. *International Journal of Geoinformatics*, 21(7), 1–15. https://doi.org/10.52939/ijg.v21i7.4311

Funk, C., Peterson, P., Landsfeld, M., Pedreros, D., Verdin, J., Shukla, S., Husak, G., Rowland, J., Harrison, L., Hoell, A., & Michaelsen, J. (2015). The climate hazards infrared precipitation with stations—a new environmental record for monitoring extremes. *Scientific Data,* 2, 150066. https://doi.org/10.1038/sdata.2015.66

Gebrechorkos, S. H., Leyland, J., Slater, L., Wortmann, M., Ashworth, P. J., Bennett, G. L., Boothroyd, R., Cloke, H., Delorme, P., Griffith, H., Hardy,

© 2026 Dept. of Geophysics Hasanuddin University

R., Hawker, L., McLelland, S., Neal, J., Nicholas, A., Parsons, D. R., Tatem, A. J., Vahidi, E., & Darby, S. E. (2023). A high-resolution daily global dataset of statistically downscaled CMIP6 models for climate impact analyses. *Scientific Data,* 10, 611. https://doi.org/10.1038/s41597-023-02528-x

Gupta, R., Prakash, P., & Chembolu, V. (2025). Multi criteria evaluation of downscaled CMIP6 models in predicting precipitation extremes. *Atmospheric Research*, 315, 107921. https://doi.org/10.1016/j.atmosres.2025.107921

Hajima, T., Watanabe, M., Yamamoto, A., Tatebe, H., Noguchi, M. A., Abe, M., Ohgaito, R., Ito, A., Yamazaki, D., Okajima, H., Ito, A., Takata, K., Ogochi, K., Watanabe, S., & Kawamiya, M. (2020). Develop-ment of the MIROC ES2L Earth system model and the evaluation of biogeochemical processes and feedbacks. *Geoscientific Model Development*, 13(5), 2197–2244. https://doi.org/10.5194/gmd-13-2197-2020

Hamed, K. H., & Rao, A. R. (1998). A modified Mann-Kendall trend test for autocorrelated data. *Journal of Hydrology,* 204(1–4), 182–196. https://doi.org/10.1016/S0022-1694(97)00125-X

Hariadi, M. H., van der Schrier, G., Steeneveld, G.-J., Sopaheluwakan, A., Tank, A. K., Roberts, M. J., Moine, M.-P., Bellucci, A., Senan, R., Tourigny, E., & Putrasahan, D. (2022). Evaluation of onset, cessation and seasonal precipitation of the Southeast Asia rainy season in CMIP5 regional climate models and HighResMIP global climate models. *International Journal of Climatology,* 42(5), 3007–3024. https://doi.org/10.1002/joc.7404

Herlambang, G. A., & Jaelani, L. M. (2026). Assessing future precipitation patterns in the Brantas River Basin through downscaling of CMIP6 GCMs. *IOP Conference Series: Earth and Environmental Science,* 1607(1), 012036. https://doi.org/10.1088/1755-1315/1607/1/012036

IPCC. (2021). *Climate Change 2021: The Physical Science Basis. Contribution of Working Group I to the Sixth Assessment Report of the Intergovernmental Panel on Climate Change*. Intergovernmental Panel on Climate Change. Cambridge University Press. https://doi.org/10.1017/9781009157896

IPCC. (2023). *Climate Change 2023: Synthesis Report. Contribution of Working Groups I, II and III to the Sixth Assessment Report of the Intergovernmental Panel on Climate Change* (H. Lee & J. Romero, Eds.). Intergovernmental Panel on Climate Change. https://doi.org/10.59327/IPCC/AR6-9789291691647

Iqbal, Z., Shahid, S., Ahmed, K., Ismail, T., Ziarh, G. F., Chung, E.-S., & Wang, X. (2021). Evaluation of CMIP6 GCM rainfall in mainland Southeast Asia. *Atmospheric Research,* 254, 105525. https://doi.org/10.1016/j.atmosres.2021.105525

Kurniadi, A., Weller, E., Kim, Y.-H., & Min, S.-K. (2023). Evaluation of Coupled Model Intercomparison Project Phase 6 model-simulated extreme precipitation over Indonesia. *International Journal of Climatology,* 43(1), 174–196. https://doi.org/10.1002/joc.7744

Kurniadi, A., Weller, E., Salmond, J., & Aldrian, E. (2024). Future projections of extreme rainfall events in Indonesia. International *Journal of*

© 2026 Dept. of Geophysics Hasanuddin University

Climatology, 44(1), 160–182. https://doi.org/10.1002/joc.8321

Kwawuvi, D., Mama, D., Agodzo, S. K., Hartmann, A., Larbi, I., Bessah, E., Abraham, T., Dotse, S.-Q., & Limantol, A. M. (2022). An investigation into the future changes in rainfall onset, cessation and length of rainy season in the Oti River Basin, West Africa. *Modeling Earth Systems and Environment,* 8(4), 5077–5095. https://doi.org/10.1007/s40808-022-01410-w

Lafferty, D. C., & Sriver, R. L. (2023). Downscaling and bias-correction contribute considerable uncertainty to local climate projections in CMIP6. *npj Climate and Atmospheric Science,* 6, 158. https://doi.org/10.1038/s41612-023-00486-0

Liebmann, B., Camargo, S. J., Seth, A., Marengo, J. A., Carvalho, L. M. V., Allured, D., Fu, R., & Vera, C. S. (2007). Onset and end of the rainy season in South America in observations and the ECHAM 4.5 atmospheric general circulation model. *Journal of Climate,* 20(10), 2037–2050. https://doi.org/10.1175/JCLI4122.1

Liu, S., Raghavan, S. V., Nguyen, N. S., & Ona, B. J. (2022). Evaluations of the sixth phase of Coupled Model Intercomparison Project model performance on precipitation over Southeast Asia based on the moisture budget. *International Journal of Climatology*, 42(14), 7087–7102. https://doi.org/10.1002/joc.7631

Liu, S., Raghavan, S. V., Ona, B. J., & Nguyen, N. S. (2023). Bias evaluation in rainfall over Southeast Asia in CMIP6 models. *Journal of Hydrology*, 621, 129593. https://doi.org/10.1016/j.jhydrol.2023.129593

Long, Y., Zheng, M., He, H., & Yan, S. (2023). Interannual variabilities in the onset and demise of rainy season: Implications for water management. *Water Resources Management,* 37(12), 4933–4948. https://doi.org/10.1007/s11269-023-03589-8

Moon, S., & Ha, K.-J. (2020). Future changes in monsoon duration and precipitation using CMIP6. *npj Climate and Atmospheric Science,* 3, 45. https://doi.org/10.1038/s41612-020-00151-w

Mulsandi, A., Koesmaryono, Y., Hidayat, R., Faqih, A., & Sopaheluwakan, A. (2024). Detecting Indonesian monsoon signals and related features using space–time singular value decomposition (SVD). *Atmosphere*, 15(2), 187. https://doi.org/10.3390/atmos15020187

O'Neill, B. C., Tebaldi, C., van Vuuren, D. P., Eyring, V., Friedlingstein, P., Hurtt, G., Knutti, R., Kriegler, E., Lamarque, J.-F., Lowe, J., Meehl, G. A., Moss, R., Riahi, K., & Sanderson, B. M. (2016). The Scenario Model Intercomparison Project (ScenarioMIP) for CMIP6. *Geoscientific Model Development,* 9(9), 3461–3482. https://doi.org/10.5194/gmd-9-3461-2016

Paredes-Trejo, F. J., Barbosa, H. A., & Kumar, T. V. L. (2017). Validating CHIRPS-based satellite precipitation estimates in Northeast Brazil. *Journal of Arid Environments*, 139, 26–40. https://doi.org/10.1016/j.jaridenv.2016.12.009

Pimonsree, S., Kamworapan, S., Gheewala S. H., Thongbhakdi, A., & Prueksakorn, K. (2023). Evaluation of CMIP6 GCMs for simulating precipitation over Thailand and Indonesia. *Atmospheric Research, 282*, 106522. https://doi.org/10.1016/j.atmosres.2022.106522

Prasetya, R. P., Djuhana, D., Saputro, A. H. H., & Permana, D. S. (2026).

© 2026 Dept. of Geophysics Hasanuddin University

Evaluation and ranking of NEX-GDDP-CMIP6 models based on monthly precipitation climatology over Indonesia. *Frontiers in Climate,* 8, 1748663. https://doi.org/10.3389/fclim.2026.1748663

Raghavan, S. V., Hur, J., & Liong, S.-Y. (2018). Evaluations of NASA NEX-GDDP data over Southeast Asia: Present and future climates. *Climatic Change*, 148, 503–518. https://doi.org/10.1007/s10584-018-2213-3

Rahmawati, N., & Lubczynski, M. W. (2018). Validation of satellite daily rainfall estimates in complex terrain of Bali Island, Indonesia. *Theoretical and Applied Climatology*, 134, 513–532. https://doi.org/10.1007/s00704-017-2290-7

Riahi, K., van Vuuren, D. P., Kriegler, E., Edmonds, J., O'Neill, B. C., Fujimori, S., Bauer, N., Calvin, K., Dellink, R., Fricko, O., Lutz, W., Popp, A., Cuaresma, J. C., KC, S., Leimbach, M., Jiang, L., Kram, T., Rao, S., Emmerling, J., Ebi, K., & Tavoni, M. (2017). The Shared Socioeconomic Pathways and their energy, land use, and greenhouse gas emissions implications: An overview. *Global Environmental Change, 42*, 153–168. https://doi.org/10.1016/j.gloenvcha.2016.05.009

Seland, Ø., Bentsen, M., Olivié, D., Toniazzo, T., Gjermundsen, A., Graff, L. S., Debernard, J. B., Gupta, A. K., He, Y.-C., Kirkevåg, A., Schwinger, J., Tjiputra, J., Aas, K. S., Bethke, I., Fan, Y., Griesfeller, J., Grini, A., Guo, C., Ilicak, M., Karset, I. H. H., Landgren, O., Liakka, J., Moseid, K. O., Nummelin, A., Spensberger, C., Tang, H., Zhang, Z., Heinze, C., Iversen, T., & Schulz, M. (2020). Overview of the Norwayn Earth System Model (NorESM2) and key climate response of CMIP6 simulations. *Geoscientific Model Development*, 13(12), 6165–6200. https://doi.org/10.5194/gmd-13-6165-2020

Shakeel, M., Abbas, H., Ali, Z., Tariq, A., Almazroui, M., & Kader, S. (2025). A novel framework for future drought characterization under ranked-based subset selection and weighted aggregative multi-modal ensemble of global climate models. *Journal of Environmental Management*, 392, 126692. https://doi.org/10.1016/j.jenvman.2025.126692

Shrestha, B. B., Rasmy, M., Ushiyama, T., Acierto, R. A., Kawamoto, T., Fujikane, M., Shinya, T., & Kubota, K. (2025). Assessment of future risk of agricultural crop production under climate and social changes scenarios: A case of the Solo River basin in Indonesia. *Journal of Flood Risk Management,* 18(1), e13052. https://doi.org/10.1111/jfr3.13052

Sudarman, G. G., Hadi, T. W., Ningsih, N. S., Sopaheluwakan, A., Syahputra, M. R., & Marpaung, F. (2024). Nonstationary changes in annual rainfall over Indonesia's maritime continent. *Advances in Meteorology*, 2024, 9392844. https://doi.org/10.1155/2024/9392844

Supari, Tangang, F., Salimun, E., Aldrian, E., Sopaheluwakan, A., & Juneng, L. (2018). ENSO modulation of seasonal rainfall and extremes in Indonesia. *Climate Dynamics*, 51, 2559–2580. https://doi.org/10.1007/s00382-017-4028-8

Supari, S., Tangang, F., Juneng, L., Cruz, F., Chung, J. X., Ngai, S. T., Salimun, E., Mohd, M. S. F., Santisirisomboon, J., Singhruck, P., PhanVan, T., Ngo-Duc, T., Narisma, G., Aldrian, E., Gunawan, D., & Sopaheluwakan, A. (2020). Multi-model projections of precipitation extremes in Southeast Asia based on CORDEX-Southeast

© 2026 Dept. of Geophysics Hasanuddin University

Asia simulations. *Environmental Research,* 184, 109350. https://doi.org/10.1016/j.envres.2020.109350

Taguela, T. N., Raji, I., Akinsanola, A. A., Singhai, P., Adeyeri, O. E., Wainwright, C. M., & Barimalala, R. (2026). Impacts of 1.5°C and 2.0°C global warming on the onset, cessation, and length of the rainy season in global land monsoon regions. *Advances in Atmospheric Sciences,* 43, 87–102. https://doi.org/10.1007/s00376-025-4386-9

Tebaldi, C., Debeire, K., Eyring, V., Fischer, E., Fyfe, J., Friedlingstein, P., Knutti, R., Lowe, J., O'Neill, B., Sanderson, B., van Vuuren, D., Riahi, K., Meinshausen, M., Nicholls, Z., Tokarska, K. B., Hurtt, G., Kriegler, E., Lamarque, J.-F., Meehl, G., Moss, R., Bauer, S. E., Boucher, O., Brovkin, V., Byun, Y.-H., Dix, M., Gualdi, S., Guo, H., John, J. G., Kharin, S., Kim, Y.H., Koshiro, T., Ma, L., Olivié, D., Panickal, S., Qiao, F., Rong, X., Rosenbloom, N., Schupfner, M., Séférian, R., Sellar, A., Semmler, T., Shi, X., Song, Z., Steger, C., Stouffer, R., Swart, N., Tachiiri, K., Tang, Q., Tatebe, H., Voldoire, A., Volodin, E., Wyser, K., Xin, X., Yang, S., Yu, Y., & Ziehn, T. (2021). Climate model projections from the Scenario Model Intercomparison Project (ScenarioMIP) of CMIP6. *Earth System Dynamics*, 12(1), 253-293. https://doi.org/10.5194/esd-12-253-2021

Werner, A. T., & Cannon, A. J. (2016). Hydrologic extremes – an intercomparison of multiple gridded statistical downscaling methods. *Hydrology and Earth System Sciences,* 20(4), 1483–1508. https://doi.org/10.5194/hess-20-1483-2016

Wiwoho, B. S., Astuti, I. S., Alfarizi, I. A. G., & Sucahyo, H. R. (2021). Validation of three daily satellite rainfall products in a humid tropic watershed, Brantas, Indonesia: Implications to land characteristics and hydrological modelling. *Hydrology*, 8(4), 154. https://doi.org/10.3390/hydrology8040154

Wiwoho, B. S., Astuti, I. S., Purwanto, P., Deffinika, I., Alfarizi, I. A. G., Sucahyo, H. R., Gusti, R., Herwanto, M. T., & Herlambang, G. A. (2023). Assessing long-term rainfall trends and changes in a tropical watershed Brantas, Indonesia: An approach for quantifying the agreement among satellite-based rainfall data, ground rainfall data, and small-scale farmers questionnaires. *Natural Hazards,* 117, 2535–2562. https://doi.org/10.1007/s11069-023-05969-0

Wiwoho, B. S., Dargusch, P., & Astuti, I. S. (2025). An analysis of rainfall variability and its association with agricultural productivity in the Brantas River Basin, Indonesia: Insights from a 26-year analysis. *Ecohydrology & Hydrobiology,* 25(4), 100674. https://doi.org/10.1016/j.ecohyd.2025.100674

Yulizar, Y., & Asdak, C. (2025). The joint variation of temperature and precipitation across Indonesia: A seasonal and regional analysis. *Theoretical and Applied Climatology,* 156(11), Article 624. https://doi.org/10.1007/s00704-025-05872-7

Zabihi, O., & Ahmadi, A. (2024). Multi-criteria evaluation of CMIP6 precipitation and temperature simulations over Iran. Journal of Hydrology: Regional Studies, 52, 101707. https://doi.org/10.1016/j.ejrh.2024.101707

© 2026 Dept. of Geophysics Hasanuddin University



Indexing and Abstracting

The work is licensed under CC Attribution-NonCommercial-ShareAlike 4.0.



GEOFISIKA
UNIVERSITAS HASANUDDIN

ISSN 2579-5546



